11th Space Simulation Conference

*Proceedings of a symposium
held at Lyndon B. Johnson Space Center
Houston, Texas
September 23-25, 1980*

NASA

11th Space Simulation Conference

Proceedings of a symposium sponsored by
National Aeronautics and Space Administration,
Institute of Environmental Sciences,
The American Institute for Aeronautics and Astronautics, and
The American Society for Testing and Materials and held at
Lyndon B. Johnson Space Center, Houston, Texas
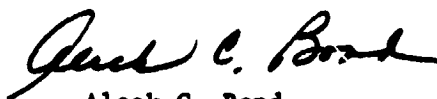September 23-25, 1980

PREFACE

The Eleventh Space Simulation Conference, held at the NASA Lyndon B. Johnson Space Center (JSC), September 23 to 25, 1980, was sponsored jointly by the Institute of Environmental Sciences (IES) and the Johnson Space Center and supported by the American Institute of Aeronautics and Astronautics and the American Society for Testing and Materials. This series of symposia has been especially useful and effective over the past two decades in bringing together national and international scientists and engineers for technical discussions and exchanges relating to findings and advances in space simulation and aerospace testing technology.

The Eleventh Space Simulation Conference program was favored with a wide spectrum of interesting and important subject areas ranging from specialized issues dealing with space and entry environments to the environmental testing of systems and complete spacecraft. The program included papers concerned with integrated testing of Space Shuttle systems and complete satellites, space contamination, thermal protection, sensor development, and other related subject areas of current interest to the scientific and technical communities. The subject area of test facilities is well represented with papers that describe several new and unique facilities developed to meet the demanding requirements for high fidelity simulation of test environments.

The Johnson Space Center was pleased to host this conference since it offered a continuing opportunity for maintaining direct rapport and interaction with the technical community in an area that is vitally important to our space flight programs. Additionally, with the approaching flight test phase of the Space Shuttle, it provided for the timely reporting on the test and development of a number of key systems of the Orbiter vehicle.

This document is a compilation of papers presented at the conference. It is a product that represents the efforts of many individuals. In this regard, I wish to thank the authors for the fine quality of the papers, the General Conference Committee including the Technical Program Committee for the review and selection of papers and for developing the overall program, as well as the numerous other individuals who provided active support in the various facets of the symposium preparations. I particularly wish to acknowledge and thank George F. Wright, Technical Program Chairman, Sandia Laboratories; James S. Moore, Operations Chairman, JSC; and Viljar Sova, JSC, for their dedicated and expert handling of their respective areas of responsibility and for their invaluable aid and assistance throughout the planning and conduct of this conference. Likewise, I wish to extend my thanks and gratitude to Betty L. Peterson, Executive Director, IES, and Janet A. Ehmann, Assistant to the Director, IES, for their fine handling of many of the administrative details of the conference, and to John D. Campbell, IES Meeting Manager, for advice and counsel on many conference matters.

Aleck C. Bond
General Chairman

PRECEDING PAGE BLANK NOT FILMED

COMMITTEES FOR

11TH SPACE SIMULATION CONFERENCE

MEETING MANAGEMENT COMMITTEE

General Chairman: Aleck C. Bond, NASA Lyndon B. Johnson
                              Space Center
Operations Chairman: James S. Moore, NASA Lyndon B. Johnson
                              Space Center
Technical Program Chairman: George F. Wright, Jr., Sandia Laboratories
IES Meeting Manager: John D. Campbell, Perkin-Elmer Corporation
IES Executive Director: Betty L. Peterson, Institute of Environmental
                              Sciences

TECHNICAL PROGRAM COMMITTEE

R. Kruger, NASA Goddard Space Flight Center
E. N. Borson, The Aerospace Corporation
A. R. Lunde, The Boeing Company
C. H. Duncan, NASA Goddard Space Flight Center
R. Murray, General Electric Company, Space Division
E. S. J. Wang, McDonnell Douglas Corporation
H. Lewis, ARO, Inc.
Dr. C. G. Miller, Jet Propulsion Laboratory
R. J. Piotrowski, NASA Lyndon B. Johnson Space Center

JOINT POLICY COMMITTEE

IES

John D. Campbell, Perkin-Elmer Corporation
George Frankel, Grumman Aerospace

ASTM

Eugene N. Borson, The Aerospace Corporation
Charles H. Duncan, NASA Goddard Space Flight Center

AIAA

Dr. Charles Miller, Jet Propulsion Laboratory
Dwight Reilly, NASA Lewis Research Center

CONTENTS

Section   Page

SESSION I: SPACECRAFT AND SYSTEMS 1

Chairman: T. Gindorf, Jet Propulsion Laboratory

Organizer: E. S. J. Wang, McDonnell Douglas Corporation

SESSION II: SPACECRAFT AND SYSTEMS 2

Chairman: T. Gindorf, Jet Propulsion Laboratory

Organizer: E. S. J. Wang, McDonnell Douglas Corporation

PRECEDING PAGE BLANK NOT FILMED

COMPREHENSIVE TESTING OF A DEFENSE SYSTEMS COMMUNICATIONS SATELLITE

Neil K. Shirk
Stafford J. Keer

ABSTRACT

This paper reviews the system level testing of the Defense Satellite
Communications System III program concentrating on the results of the systems
tests of the DSCS III Development Test Model (DTM). The DSCS III Development
Test Model consisted of engineering components interconnected in an open bench
layout. The DTM tests were performed to demonstrate satellite electrical per-
formance characteristics, and to uncover design deficiencies and interface
problems. The availability of the DTM test results prior to the fabrication
of the flight model hardware permitted the incorporation of necessary design
changes with a minimum impact on program costs and schedules.

DSCS III SATELLITE

Mission Description

The goal of the DSCS III program is to provide a network of four opera-
tional communication satellites and two on-orbit spares in synchronous orbit.
Each satellite is designed to have a life expectancy of ten years and the
capability of being launched from a Titan booster or the Space Shuttle.

The six channel communications payload has anti-jam capability and nu-
clear survivability provisions. The primary system utilizes SHF (X-Band)
frequencies to serve the Department of Defense World Wide Military Command
and Control Communications System (WWMCCS), the ground mobile forces, the
Defense Communications System (DSC), Navy Fleet Communications, the White
House Communications Agency, and Allied Communications Network such as NATO.
A secondary communications payload is an Air Force Satellite Communications
Single Channel Transponder which provides service to Air Force elements.
Figure 1 illustrates typical satellite system operation.

TYPICAL SYSTEM OPERATION

AN/WSC-2

AN/FSC-78(HT)

AN/ASC-24

AN/MSC-46

AN/TSC-54 SCF REMOTE DSCS
TRACKING STATION TERMINALS AN/TSC-86
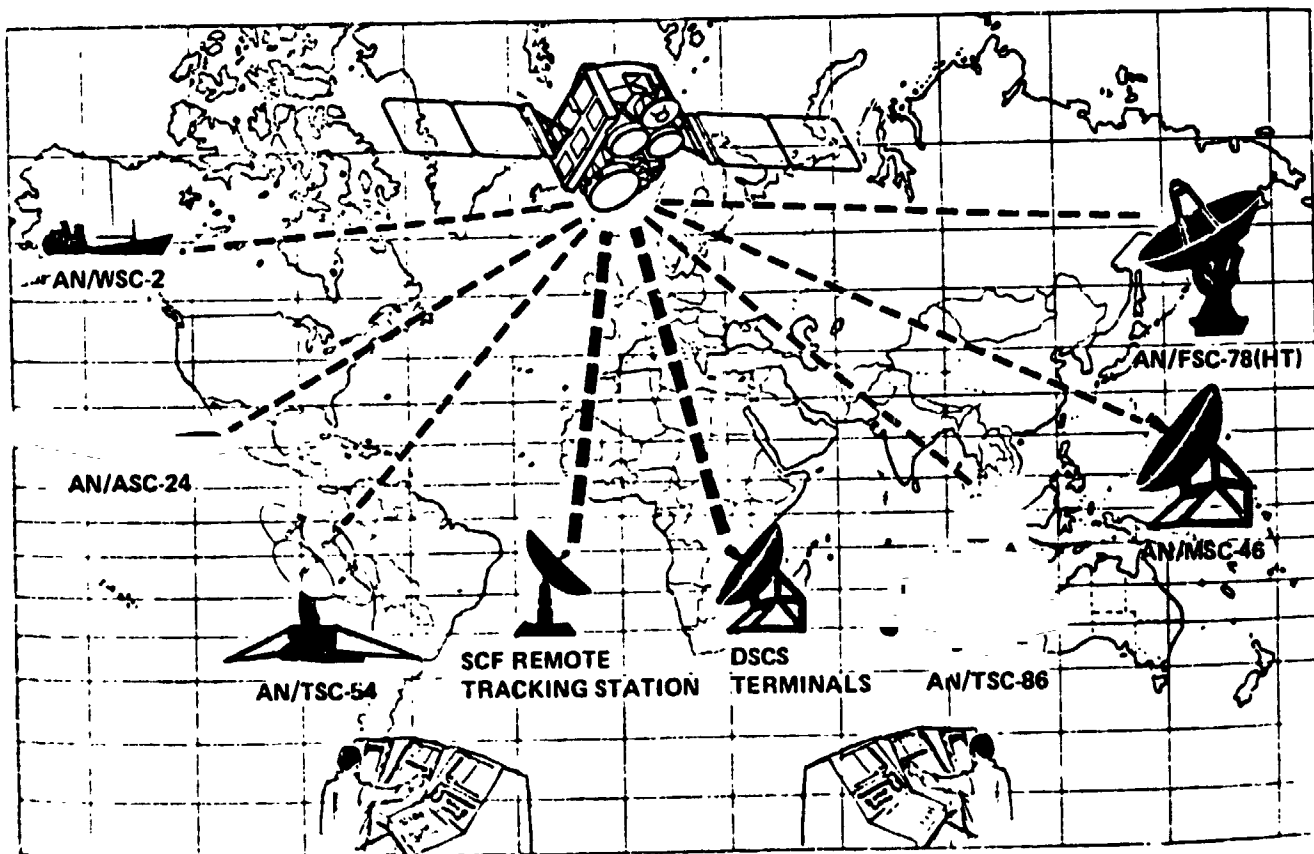
**SPACE AND MISSILE SYSTEMS ORGANIZATION
SATELLITE CONTROL FACILITY (SCF)**

Ground control complex at Sunnyvale, Cal. monitors and controls the housekeeping of the DSCS III spacecraft via its Remote Tracking Station Network. The SCF also provides backup Communication Configuration Control functions.

**DEFENSE COMMUNICATIONS AGENCY
SATELLITE CONFIGURATION CONTROL ELEMENT
(SCCE)**

SCCE's provide in-band command and control of the payload configurations to meet worldwide user requirements. They also display selected payload and telemetry data.

Figure 1

The satellite weighs approximately 1870 pounds, with additional pro-
pellant load up to 600 lbs. The attitude control subsystem provides three
axis stabilization and maintains pointing of the communications antennas to-
wards the earth. Power to operate the satellite is collected by two uni-
directional drive solar arrays. Command control and performance monitoring
are accomplished by either S-Band or X-Band Telemetry Tracking and Command
subsystems. Key satellite design and performance characteristics are listed
in Figure 2.

ITEM	KEY FEATURES	ITEM	KEY FEATURES
craft nary	• 3-Axis Stabilized • Single Axis Sun Oriented • Large North/South Viewing Panels for Passive Heat Rejection • 10-Year Design Life • North/South Stationkeeping • Reliability Exceeds .7 at 7 Years • Low Life-Cycle Cost	Electrical Power Subsystem (cont.)	• Fully Redundant • Rapid Response to Load Changes • Load Fault Isolation • Transient Protection
stem	• Command and Telemetry Interface with SCF, DCS Terminals, and Shuttle • Rapid MBA Reconfiguration • Incorporation of S Band and SHF COMSEC Equipment	Propulsion Subsystem	• Hydrazine Propulsion System with Redundant Thrusters and Tanks • 600 Lb. Capacity • FLTSATCOM Tanks • 1.0 Lb. Thrusters
nel ponder	• SHF and UHF Receive Frequency Capability • Compatible with initial AFSATCOM I System • High A/J performance with AFSATCOM II Modulation • Wide bandwidth, fast response synthesizer • Digital matched filter MFSK/FSK demodulator • Integral operational command via comm channel • High power UHF P.A. at 60% power efficiency	Thermal Subsystem	• Passive • North/South Radiator Panels using Optical Solar Reflectors • Imposes no Satellite Operational Restrictions • Survive Failure Modes Including Attitude Loss and Total Battery Failure
ude rol ystem	• Autonomous initial acquisition and operation • Time Shared Central Digital Processor for all Control Modes • Earth & Sun Sensors for Attitude Sensing • Four Skewed Reaction Wheels • .08°R, .08°P, 0.5°Y Control Accuracy	Structure Subsystem	• Accessibility/Modularity • Parallel Subsystem Assembly and Test • North/South Array Through Drive Shaft • Independent Propulsion Module • Vibration Damped Equipment Panels • Lightweight/Stiff/Dimensionally Stable • Growth and Option Flexibility
trical r ystem	• Regulated Bus — 28V ± 1% — 126 sq. ft. Solar Array — 1100 Watts Output (BOL) • 96 AHr NiCd Battery Capacity	Survivability	• Overall Hardening Approach is based Upon JCS Guidelines
		Launch Vehicle	• Titan IIIC • Shuttle • Titan 34D IUS

Figure 2

SUBSYSTEM DESCRIPTIONS

Electrical Power and Distribution

The Electrical Power and Distribution Subsystem (EPDS) provides for the conversion of solar energy to electric power, the regulation and distribution of power to the satellite subsystems (loads), and the storage of electrical energy in three nickel-cadmium batteries for use during eclipse periods.

The generation, regulation and storage of power is accomplished in the following components:

- Two Solar Arrays (2 solar panels per array)
- One Power Regulation Unit
- Two Shunt Dissipators
- Three Nickel Cadmium Batteries

Power distribution is accomplished by:

- South Power Controller
- North Power Controller
- Ordnance Controller
- Electrical Harness

3

Telemetry, Tracking and Command

The Telemetry, Tracking and Command Subsystem provides for the reception, decryption and decoding of commands; reception, filtering and transmission of the ranging signal; and formatting, encryption and transmission of satellite telemetry.

Attitude Control Subsystem

The Attitude Control Subsystem provides the function of attitude sensing, signal processing, drive signals for control actuation, control of Solar Array positioning, BFN reconfiguration and GDA positioning. The ACS also processes commands for mode switching and command data storage, and outputs telemetry to the CTU.

Communications Transponder Subsystem

The Communications Transponder Subsystem provides six SHF communications channels, each powered by its own TWT amplifier. Signals are received and transmitted through an interconnected set of antennas which includes:

- Two earth coverage receive horns
- Two earth coverage transmit horns
- One 61 beam receive antenna for selective coverage
- Two 19 beam transmit antennas for selective coverage
- One high-gain gimballed dish transmit antenna for adjustable coverage.

DSCS III TEST PROGRAM

Test Philosophy

The General Electric approach to the development of long life satellites is based on the concept that on-orbit failures which result in mission failure or degradation of performance can be eliminated from flight systems by three major techniques:

1. Failure prevention by thorough design
2. Failure removal by proper inspection and establishment of test screens
3. Failure protection by adequate redundancy and backup operational modes.

Strong emphasis is placed on comprehensive performance and environmental tests to provide effective screens to eliminate design deficiencies, inferior material and poor workmanship. These tests are progressive in nature, starting with the piece part level, followed by development tests of components, subsystems and development models, and continuing through the qualification and acceptance test at each level of assembly, and culminating with the final acceptance and certification of the flight satellite.

Maximum emphasis is placed on the comprehensive testing at the component and lower levels of assembly where defects are most easily detected and rework has a minimum impact on cost and schedule. Testing at the subsystem level of assembly is applied on certain subsystems which require unique performance characteristics to be verified that are impractical, or too costly, to verify at the satellite level of integration. Major emphasis is also applicable at the satellite level where the system is fully configured for flight verification of system compatibility and performance under environmental conditions representative of the mission.

DSCS III Test Program

1. Development Testing

Development tests were used to verify critical design areas prior to the design freeze and to prove the adequacy of the system design with respect to performance requirements. The development program included material and specimen evaluations, breadboard tests of circuits and subassemblies and integrated systems tests employing Structural, Thermal and Electrical Development Test Models.

2. Qualification Testing

Qualification testing provided verification of hardware design by subjecting parts, components, and critical subsystems to environmental levels and durations in excess of what they are expected to experience during flight. The assembled Qualification Satellite in turn undergoes a complete program of environmental tests.

3. Acceptance Testing

The components, subsystems and satellite which comprise the flight satellites follow the same test program as the qualification units, except that the environmental test stress levels are lower in magnitude and shorter in duration.

DEVELOPMENT TEST MODEL

The DSCS III Development Test (DTM) provided an electrical systems representation of the satellite by interconnecting engineering model components in an open bench layout. This configuration served as a systems level test screen for the early detection of system incompatibilities and design problems.

Test Objectives

The primary objectives of the DSCS III Development Test Model tests were:

5

- To validate electrical systems compatibility at the satellite systems level.
- To demonstrate ground software/satellite compatibility.

Some of the secondary objectives that were also accomplished during DTM testing are as follows:

- To develop electrical integration and performance procedures for the qualification and flight satellites.

- To demonstrate electrical auxiliary ground equipment/satellite compatibility.

- To train test personnel.

- To obtain engineering test data for preliminary design evaluation.

Test Configuration

The DTM system tests were performed in the open bench layout as depicted in Figure 3.
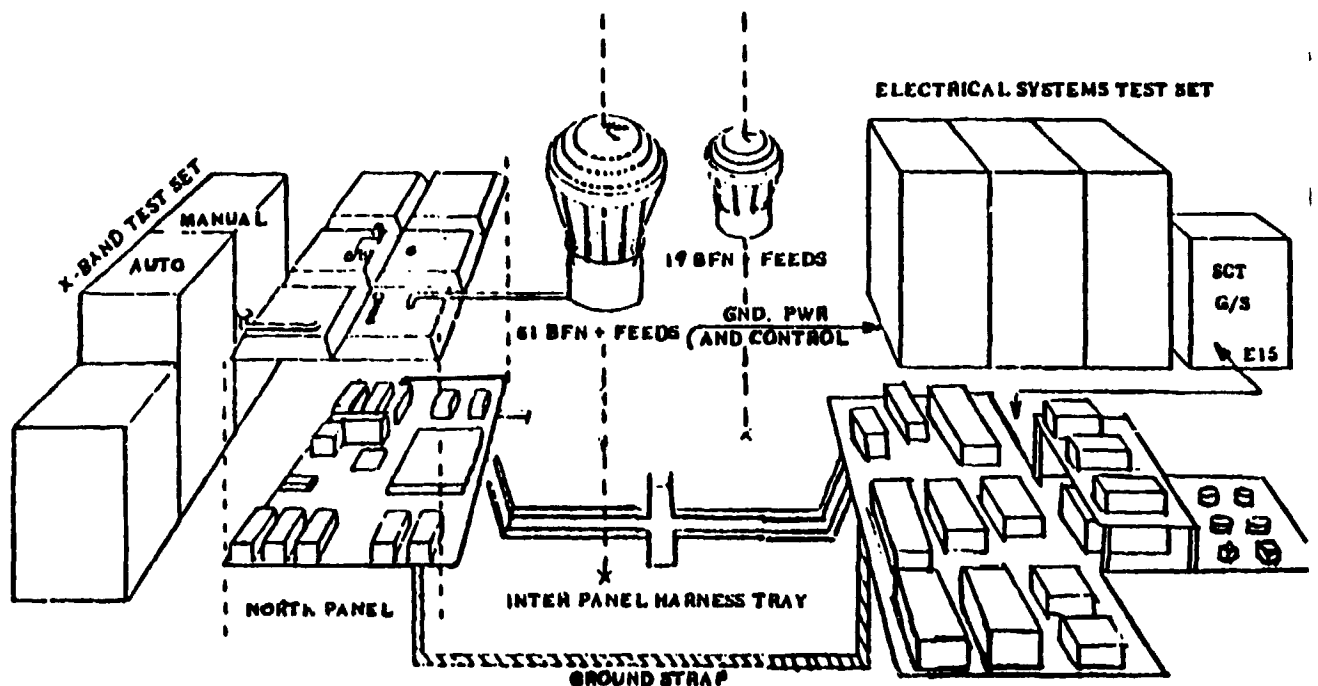
Figure 3. Development Test Model (DTM)

Test Sequence

The sequence of tests established for the DTM correspond to the integration and ambient functional tests that the qualification and flight satellites would undergo. The only additional environment to which the DTM was exposed was the EMC environment. Figure 4 illustrates the DTM test sequence and duration. During all powered testing the command and telemetry software were employed.

Test anomalies are documented by means of a problem report system. In this system all potential problems, or unexplained occurrences relating to test procedures, electrical AGE, software, hardware, drawings and test data are reported. The problem report is addressed to the responsible engineer, or analyst, to investigate. Once the cause of the problem is diagnosed, corrective action is defined. The problem report remains open until the corrective action is completed. Upon successful resolution of the problem, the Problem Report Review Board will concur in closing the problem report. For the DTM testing, the Problem Report Review Board consisted of representatives from Systems Test, Engineering and Product Assurance.

In the performance of the DSCS DTM tests, a total of 249 problem reports were written. The problem report breakdown per failure types, and subsystem occurrence are presented in Table I. Currently the Qualification satellite is in the integration phase of testing. To date, 249 problem reports have been written, and Table II presents the same breakdown for the Qualification satellite problem reports. It should be noted that the Qualification satellite includes more actual hardware than the DTM, as well as a complete set of operational software, much of which was not available for DTM.

Test Results

The DTM tests provided verification of 85% of the spacecraft system level electrical performance requirements as delineated in the prime item specification. These results were limited primarily by the test configuration and the available hardware.

Summary

The DTM test program served its purpose well, in that several hardware problems which required redesigns were uncovered. In addition, those portions of the Operations Software which were available at the time were exercised and necessary redesigns incorporated.

Hardware Redesigns

Hardware redesigns generated by the DTM test program are herein summarized by subsystem.

7

JAN	FEB					MAR				APR					MAY				JUN				JUL				AUG				SEP		
4	5	6	7	8	9	10	11	12	13	14	15	16	17	18	19	20	21	22	23	24	25	26	27	28	29	30	31	32	33	34	35	36	37	38

●ACE
●EARTH SENSOR
●RATE GYRO
●SUN SENSOR
●REACTION
    WHEELS

●RE-INTEG.
    EARTH SENSOR
    RATE GYRO

● CTU Noise Investigation
● SPC B Secondary Voltage
● X-Band Electric Field Test
● TDAL Gain Set & Ferrite
    Switching
● Reg Bus AC current noise
    measurements
● IFU B Timing Pulses
● Thruster Harness Check
● Comm CH. Phase Linearity
● X-Band U/L compatibility

●CTU
●K123
●K128

●NPC
●BEACONS
●S/F
●SHF/S

●CTU
    REINTEG.

●PRU (BB)

●PRU (EM)
●61 RFM

●ACE/BFN
    COMPAT.

●SPC ●RTU
        ●19BFN

●JLE
    INTEG.

| PWR
INTEG. | TT&C
INTEG. | ACS
INTEG. | S
BND
INTEG. | BCN
INTEG. | 19
BFN
INTEG. | PRU
(EM)
INTEG. | COMM
INTEG. | SCT
INTEG. | X-BAND
INTEG. | ACS
RE-INTEGRATION | EMC | PERF.
COMPT.
TEST. | T R A N S I E N T S | REWORK
VERIFI-
CATION
&
OPEN
ITEMS |

●S-BAND XPDR

Figure 4.- DTM test schedule.

8

TABLE I

DTM PROBLEM REPORTS

Category	Nature of Problem	Quantity	% of Total
Satellite Hardware			
	Design	27	
	Failure	14	
	Workmanship	17	
		58	23.3
Ground Station			
	Design	3	
	Failure	15	
	Workmanship	6	
		24	9.6
Software			
	Design	27	10.8
Documentation			
	SW Data Base	9	
	Procedures	11	
	Drawings & Specs	23	
	Duplication of Problem Report	32	
		75	30.1
Test Related			
	Test Errors	31	
	Test Configuration Limitation	14	
		45	18.1
Unresolved		20	8.1

TABLE II

QUAL PROBLEM REPORTS

Category	Nature of Problem	Quantity	% of Total
Satellite Hardware			
	Design	3	
	Failure	3	
	Workmanship	11	
		17	6.8
Ground Station			
	Design	4	
	Failure	25	
	Fabrication	7	
	Documentation	7	
		43	17.3
Software			
	Design	25	
	Documentation	2	
	Operation	2	
		29	11.6
Documentation			
	SW Data Base	40	
	Procedures	52	
	Drawings & Specs	23	
	Duplication of P.R.	13	
		128	51.4
Test Related			
	Test Errors	14	
	Test Config/Limitations	6	
	Test Equip. Failures	2	
		22	8.8
Unresolved		10	4.1

Electrical Power and Distribution Subsystem

● Oscillations on the regulated voltage bus traced to marginal capacitance value in the power regulator feedback loop.

Attitude Control Subsystem

● Incorrect phasing of the reaction wheel tachometer signals.
● Incorrect phasing of the gimballed dish antenna motor drives.
● Several logic and timing signal problems associated with the imbedded software in the attitude control electronics.

S-Band Telemetry, Tracking and Command

● Logic circuitry in command, telemetry unit disabled telemetry unit when both X-band decryptor units were powered off.

● Command counter bit stream presented to telemetry processor in reverse order.

● Several logic and timing signal problems in association with other hardware units.

X-Band Telemetry, Tracking and Command

● Phasing of clock timing signal inverted.

● Interface problem in ground encryption equipment.

● Faulty cross-strapping design with two groups of redundant equipment.

SHF Communications Transponder

● Improper loading of ferrite switches in command interface unit.

● Improper phasing of digital timing signals in command interface unit.

Software Redesigns

During the development testing of the hardware the majority of software modules were in the development phase themselves. Sufficient software was available to provide S-band and X-band command generation and telemetry processing of the normal housekeeping functions and to provide a limited capability for antenna reconfigurations. Since the software is primarily designed for an orbit operation, some design modifications were required to accommodate in-house testing. However, the command and telemetry software modules were tested and several design modifications defined.

11

CONCLUSIONS

Satellite hardware problems have been reduced - by a factor of three - between the DTM and the qualification satellite integration tests and satellite design problems have been reduced by a factor of nine.

Testing and troubleshooting at the DTM level was less expensive since the number of people in a DTM test crew was fewer than the number of people in a Qual or Flight test crew.

The rework of qualification hardware to incorporate design changes impacts program costs in two ways, viz.:

(1) Cost for requalification tests of hardware
(2) Cost for down time and schedule slip at systems test level.

The 27 design problems in DTM effected nine different components which would have required (if not detected in DTM) requalification of each of these components at the qualification satellite test level.

The cost of down time and schedule slips at the system test level which would impact the launch date, etc. is unmeasurable.

The substantial complexity of the DSCS III satellite necessitates the use of systems level development tests such as the DTM tests in order to accomplish verification of electrical systems compatibility and system design with minimum impact on program costs and schedules.

EFFECTIVENESS OF SPACECRAFT TESTING PROGRAMS

Dr. A. Krausz

ABSTRACT

This paper departs from the usual subject of the Space Simulation Conference and concerns itself with the need for testing under simulated mission operational conditions and reviews the results of such tests from the point of view of the user. It presents a brief overview of the usual test sequences for high reliability, long life spacecraft and will analyze the effectiveness of the testing program in terms of the defects which are discovered by such tests. The need for automation, innovative mechanical test procedures and design for testability will be discussed.

INTRODUCTION

As our spacecraft have become progressively more complex and their missions have become more sophisticated and of longer duration, it has become increasingly important to improve the methods for verifying design and workmanship prior to making the decision to launch. Such verification is based on an extensive testing program which duplicates operation over a range of worst case mission scenarios and simulates exposure to launch, boost and space flight environments.

Since a typical spacecraft may cost $40 million, contain 60,000 electronic piece parts and must last 7 to 10 years in orbit, it clearly is wise to learn as much as possible about how well it can be expected to perform in space. A comprehensive test program must progress in a logical manner from development testing, through qualification and acceptance testing to flight readiness checkout at the launch site. In addition, the test program must include development, qualification and acceptance tests at progressively higher levels of assembly starting with parts and continuing through unit level (i.e., component, black box or assembly) to subsystem, spacecraft and system level tests. The real challenge lies in choosing the most perceptive and cost effective test procedures and environmental exposures at each assembly level. These must be tailored to the specific spacecraft and mission at hand but can be summarized for purposes of this paper as described below.

PARTS TESTING

Current procedures for piece-part testing are based on a large body of engineering data and various analyses of the physics of failure for the different kinds of parts. Standardization of test procedures has been fostered by the government and the electronic parts industry. For example, MIL-STD-883 defines screening tests for micro-electronic devices and is intended to yield an in-equipment failure rate of less than .004% per thousand hours for high reliability (Class S) parts. Detailed screening, sampling and lot qualification tests are specified, including temperature cycling, burn-in, particle impact noise detection (PIND), radiographic

inspection and life tests, among others. Comparable specifications and procurement standards exist for other electronic parts and are reflected in the design manuals and procedures used by individual aerospace contractors. These procedures have resulted in a significant drop in part failures during subsequent unit level testing.

COMPONENT TESTS

Unit or component-level test procedures are designed to verify all functional performance requirements over a range of environmental exposures without disassembly or change in the configuration of the component as installed in the spacecraft. For electronic components this usually requires that test points be brought out to a special test connector; this makes it possible to inject test signals and observe the resulting response, waveforms, logic levels, etc. Computer controlled special test equipment is required for functional checkout of digital components and complicated electronic components which have several modes of operation and process a variety of signals. Mechanical and electromechanical components also require special purpose test equipment and test fixtures for functional checkout but generally do not require automated testing.

The environmental tests for component-level qualification and acceptance are specified in MIL-STD-1540A "Test Requirements for Space Vehicles". The newer spacecraft projects, especially those for important military missions, use the approach spelled out by this document. It involves functional testing before, during and after exposure to pyroshock, random vibration or acoustics, thermal cycling, vacuum and EMI. Depending on the nature of the component, thermal cycling is performed at ambient pressure or in a vacuum chamber. In either case at least eight temperature cycles should be applied to expose any workmanship or design defects before acceptance. Test levels and duration vary from unit to unit but should be selected to accelerate detection of inherent defects without inducing damage or degradation of good equipment.

SPACECRAFT TESTS

A simplified version of a typical spacecraft-level test flow is shown in Figure 1. There are three separate phases, namely an integration phase, an environmental qualification or acceptance phase and a prelaunch verification phase. During the integration phase the various components, subassemblies and harnesses which have undergone testing at the component and part level are installed on the spacecraft structure and interconnected to form subsystems and related equipment groups. Physical inspection and functional tests are performed under ambient conditions to verify interfaces and correctness of the assembly procedures. The environmental qualification or acceptance phase consists of functional performance tests under various environmental conditions to demonstrate that the full range of performance requirements is met. The usual approach is to conduct end-to-end tests which closely simulate the actual in-orbit mission. Large deployable appendages such as solar arrays and antennas are usually tested separately and may be removed during various electrical functional tests. The prelaunch verification tests are performed at the launch site and vary greatly from program to program. On some spacecraft a full functional test is performed

14

prior to installing the spacecraft on the booster. In other cases only on-stand interface and command compatibility tests are conducted in addition to ordnance circuit checkout and fueling operations.

PHASE I - INTEGRATION

```
INSTALL          PRESS. &
PROPULSION       LEAK TEST
UNITS

INSTALL          CONTINUITY      INSTALL       FUNCTIONAL      MATE         ALIGNMENT
CABLES &         TEST            ELEC.         TESTS           SUB          TEST
SENSORS                          UNITS                         SYST.

INSTALL          MECHAN.
APPENDAGES       FUNCT.
& MMAs           TESTS
```

PHASE II - ENVIRONMENTAL ACCEPTANCE

```
FULL      EMC     PYRO     ABBREV.    ACOUSTIC &    ABBREV.    T/V     FULL
FUNCT.    TEST    SHOCK    FUNCT.     VIBRATION     FUNCT.     TEST    FUNCT.
TEST                      TEST       TESTS          TEST               TEST
```

PHASE III - PRELAUNCH VERIFICATION

```
SHIP
TO
ELS

          FUNCT.     PROPELL.    INTERFACE       ON-STAND      LAUNCH
          TEST       LOADING     VERIFICATION    FUNCT.
                                                 TEST
```

Figure 1 - Spacecraft Test Flow

EVALUATION OF TEST RESULTS

The ultimate objective is to launch spacecraft which will operate flawlessly in orbit for their specified lifetime or longer. We therefore strive for failure-free acceptance testing under conditions which closely simulate orbital conditions. Discrepancies which are discovered during acceptance testing are corrected prior to launch. In Figures 2 and 3 we have attempted to correlate orbital performance to performance during acceptance testing prior to launch. The average number of on-orbit and acceptance test discrepancies for four different projects representing a total of 25 spacecraft was normalized with respect to spacecraft complexity as measured in terms of part count and the average number of defects per 1000 parts was plotted for each project. Note that lower defect rates during acceptance testing yield better on-orbit performance. This is

also borne out by Figure 3 which plots normalized on-orbit discrepancies against spacecraft level acceptance test discrepancies fo 12 individual spacecraft comprising three separate projects.

PROJECT A - 3 MILITARY COMSATS
PROJECT B - 3 SCIENTIFIC SPACECRAFT
PROJECT C - 7 CLASSIFIED SPACECRAFT
PROJECT D - 12 COMMERCIAL COMSATS

ON ORBIT DISCREPANCIES PER 1000 PARTS

TOTAL TEST DEFECTS PER 1000 PARTS
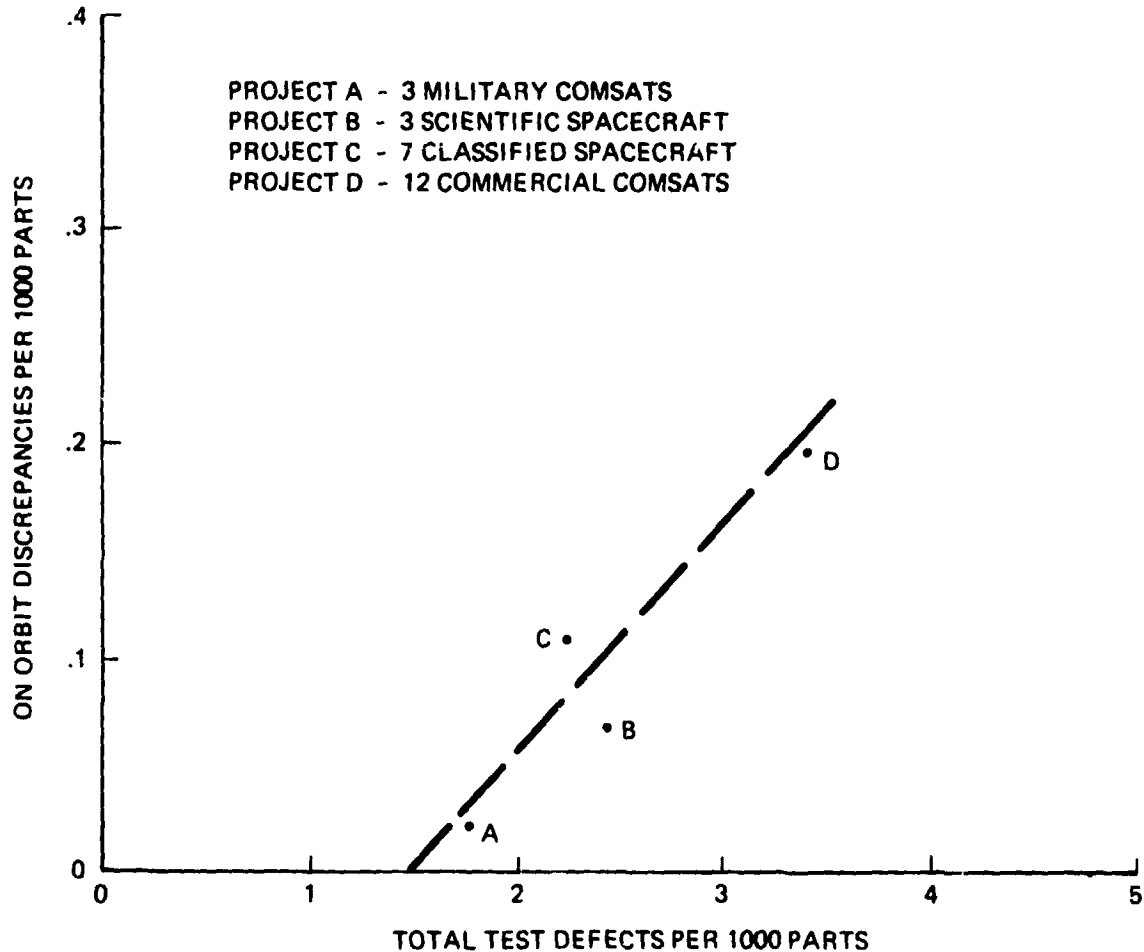
Figure 2 - Orbital Performance Correlation by Project

ANALYSIS OF TEST PROGRAM

In order to determine whether the current approach of duplicating antici-pated operating modes and simulating space environments during the qualifica-tion and acceptance test program is really effective in locating all potential defects, we reviewed the actual test history for two recent spacecraft projects in more detail. Tables 1 ar 2 give the number and type of discrepal.:ies which were found during successive phases of the testing program and during orbital operation. Project A consists of a qualification test spacecraft and three identical flight spacecraft all of which are currently operating in orbit. Each satellite contains approximately 58,000 electronic parts including about 5500 integrated circuits. Project B consists of three scientific satellites, all of which have been launched. The first of the

three spacecraft served as both a prototype and flight vehicle since there was no separate qual spacecraft. Not including the scientific payload, each satellite contains approximately 30,000 electronic parts. The data of Table 2 does not include discrepancies found in the scientific instruments payloads since these were GFE.
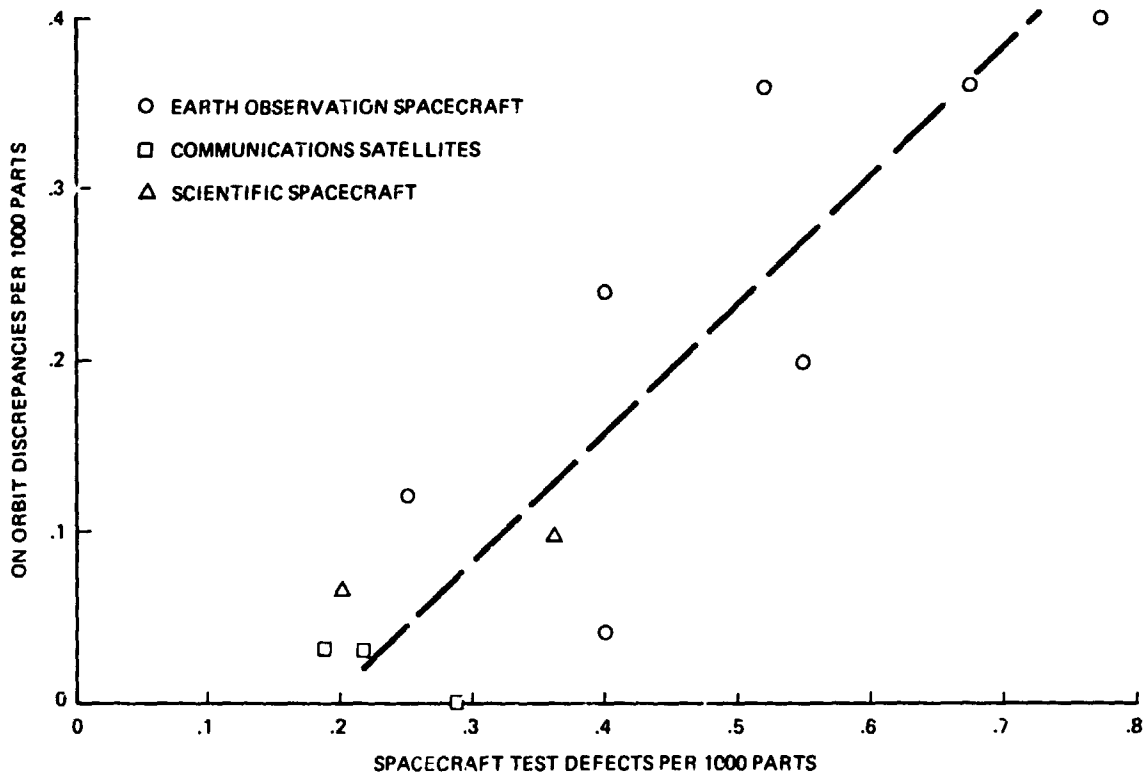
Figure 3 - Orbital Performance vs. System Test Results

Both Tables 1 and 2 provide the number of test discrepancies due to defects in the equipment under test, due to defects in test procedures and due to causes which are not related to any defect. Note that 367 and 174 product defects respectively were found during component level qualification and acceptance testing which were corrected prior to start of spacecraft level testing. Additional component defects were found during spacecraft level testing in the factory and at the launch site and during on-orbit operation. These additional discrepancies are called "escapes" because they escaped detection during component qual or acceptance testing. The escape ratio E_c is simply the ratio of component test escapes to total component defects. Similarly, the on-orbit discrepancies or performance anomalies are escapes from the ground test program if it is assumed that there are no spontaneous failures due to wearout or other causes during the mission life of the spacecraft. The escape ratio E_0 then is the ratio of on-orbit discrepancies to total discrepancies. The purpose of these ratios and the data of Tables 1 and 2 is to provide a broad overview of what results can be expected from typical testing programs.

17

Table 1.   PROJECT A - CAUSE OF TEST DISCREPANCIES

DEFECT/CAUSE OF DISCREPANCY	TEST LEVEL				ESCAPE RATIO	
	COMPONENT	SPACECRAFT	LAUNCH BASE	ON ORBIT	E_c	E_o
PRODUCT DEFECTS						
PART FAILURE	68	10	1		13.9	
COMPONENT MANUFACTURING	112	19		1	14.5	0.7
COMPONENT DESIGN	174	28			13.8	
SPACECRAFT ASSEMBLY		14				
SPACECRAFT DESIGN		16	1	3		15
TEST INDUCED	13	5				
UNDETERMINED		11				
TOTAL	367	103	2	4	14.3%	0.04%
PROCEDURE DEFECTS						
DOCUMENTATION	110	34				
TEST EQUIPMENT	41	23	1			
OPERATOR ERROR	35	16	1			
TEST SETUP	18	3	1			
TOTAL	204	76	3			
NON-DEFECTS						
WITHIN TOLERANCE/WAIVER	78	21	2	4		
UNABLE TO REPEAT PROBLEM	29	13		1		
TOTAL	107	34	2	6		

NOTES: 4 spacecraft, 3 in orbit, 3 years of orbital performance

To gain further insight into the effectiveness of environmental simulation for spacecraft level testing we have broken down the product defect discrepancies as shown in Tables 3 and 4 for Projects A and B respectively. Note that in both projects about 40% of the spacecraft acceptance test defects were found during the integration phase (Figure 1). Project A spacecraft received a temperature cycling test in a thermal chamber at ambient pressure during which 15 discrepancies were observed. During the subsequent T/V test four component failures occurred, all on the qualification spacecraft. These failures most likely were not induced by the vacuum environment since each of the failed components had previously passed a T/V test as part of the component acceptance sequence. Also note that on Project B only one component discrepancy was found during spacecraft T/V whose discovery cannot be credited to vacuum exposure. It appears therefore that exposure to vacuum as part of spacecraft level acceptance testing is not as profitable as testing over the widest possible temperature range in a thermal chamber. The merit of temperature cycling at the spacecraft level has also been demonstrated on a classified project as described in Reference 1.

Careful analysis of the discrepancy data for Projects A and B and several other projects leads to the following additional conclusions:

a) A majority of on-orbit discrepancies are due to subtle design defects which were not or could not be discovered during the qualification and acceptance test program.

b) Repetitive room ambient testing over a variety of mission scenarios and using different test methods will disclose more defects than simple environmental exposure without electrical stress.

Although it is impossible to achieve reliable operation in orbit by testing alone, it seems axiomatic that the more testing and the more variation in testing which is conducted, the better the orbital performance. This justifies the use of automated test equipment and requires design of spacecraft for testability as described below.

Table 2.   PROJECT B - CAUSE OF TEST DISCREPANCIES

DEFECT/CAUSE OF DISCREPANCY	TEST LEVEL				ESCAPE RATIO	
	COMPONENT	SPACECRAFT	LAUNCH BASE	ON ORBIT	E_c	E_o
PRODUCT DEFECTS						
PART FAILURE	38	4		1	13.6	2.3
COMPONENT MANUFACTURING	79	5	1	-	17.0	-
COMPONENT DESIGN	45	19	4	5	38.3	6.8
SPACECRAFT ASSEMBLY	-	18	-	-		
SPACECRAFT DESIGN		11	2	1		
TEST INDUCED	6	-	2			
UNDETERMINED	6	4	1			
TOTAL	174	61	11	7	19.8	2.9%
PROCEDURE DEFECTS						
DOCUMENTATION	55	23	1			
TEST EQUIPMENT	62	4	1			
OPERATOR ERROR	50	13				
TEST SETUP	35	7	3			
TOTAL	202	47	5			
NON-DEFECTS						
WITHIN TOLERANCE/WAIVER	21	21	2			
UNABLE TO REPEAT PROBLEM	35	7	1	1		
TOTAL	56	28	3	1		

NOTES: 2 spacecraft, 3 on orbit, 4 years of orbital performance
Experiment TDRs not included

AUTOMATED TESTING

An objective of the spacecraft acceptance test sequence is to exercise all equipment and verify all the operating modes which the spacecraft will encounter during its space mission. To get an idea of the complexity of such a comprehensive spacecraft test (CST) consider the Tracking and Data Relay Satellite (TDRS) shown in Figure 4, which is currently under development at TRW. The TDRS system provides two-way communications with a large ground station for up to 20 spacecraft users in low earth orbits including the shuttle orbiter. In addition, it provides twelve 18 MHz repeater channels at C band for commercial communication satellite service. Altogether, there are more than 60 switchable RF communications links. Each TDRS contains 172 active electronic units which contain approximately 55,000 parts of which 4500 are integrated circuits. One thousand seventy-six discrete and 58 serial ground commands are available for configuration control, redundancy switching and power management during on-orbit operation. One thousand two hundred eighty-eight performance and status parameters are telemetered to the ground.

19

Table 3. PROJECT A - LOCATION OF TEST DISCREPANCIES

TEST/DEFECT	ELECTRONIC COMPONENTS			PROPULSION/STRUCTURE			HARNESS		TOTAL DEFECTS
	Part	Workman-ship	Design	Part	Workman-ship	Design	Workman-ship	Design	
UNIT ACCEPTANCE	68	100	167		12	7			354
SPACECRAFT ACCEPTANCE	·11	15	25	2	23	2	7	2	87
Integration	(3)	(6)	(12)	(1)	(11)	(1)	(3)	(1)	(38)
First Functional	(3)	(2)	(5)						(10)
Temperature	(2)	(2)	(7)		(1)		(2)	(1)	(15)
EMC/IM	(1)	(1)	(1)		(4)		(1)		(8)
Dynamics									
Post Dynamics					(4)		(1)		(5)
T/V Test	(2)	(2)							(4)
Preship Functional		(2)			(3)	(1)			(6)
Launch Base				(1)					(1)
ON ORBIT			1		1	2			4

Table 4. PROJECT B - LOCATION OF TEST DISCREPANCIES

| TEST/DEFECT	ELECTRONIC COMPONENTS			PROPULSION/STRUCTURE			HARNESS		TOTAL DEFECTS
	Part	Workman-ship	Design	Part	Workman-ship	Design	Workman-ship	Design	
UNIT ACCEPTANCE	35	79	43	3		2			162
SPACECRAFT ACCEPTANCE	5	6	23		7	1	11	12	65
Integration			(9)		(5)	(1)	(2)	(9)	(26)
EMC		(2)	(1)				(1)	(1)	(5)
First Functional	(1)	(2)	(4)		(1)		(3)		(11)
Dynamic Environment	(1)	(1)	(1)				(1)		(4)
Post Dynamic Functional	(1)		(2)				(2)		(5)
T/V Environment			(1)						(1)
Preship Functional	(1)		(1)		(1)		(2)		(5)
ETR	(1)	(1)	(4)					(2)	(8)
ON ORBIT	1		5			1			7
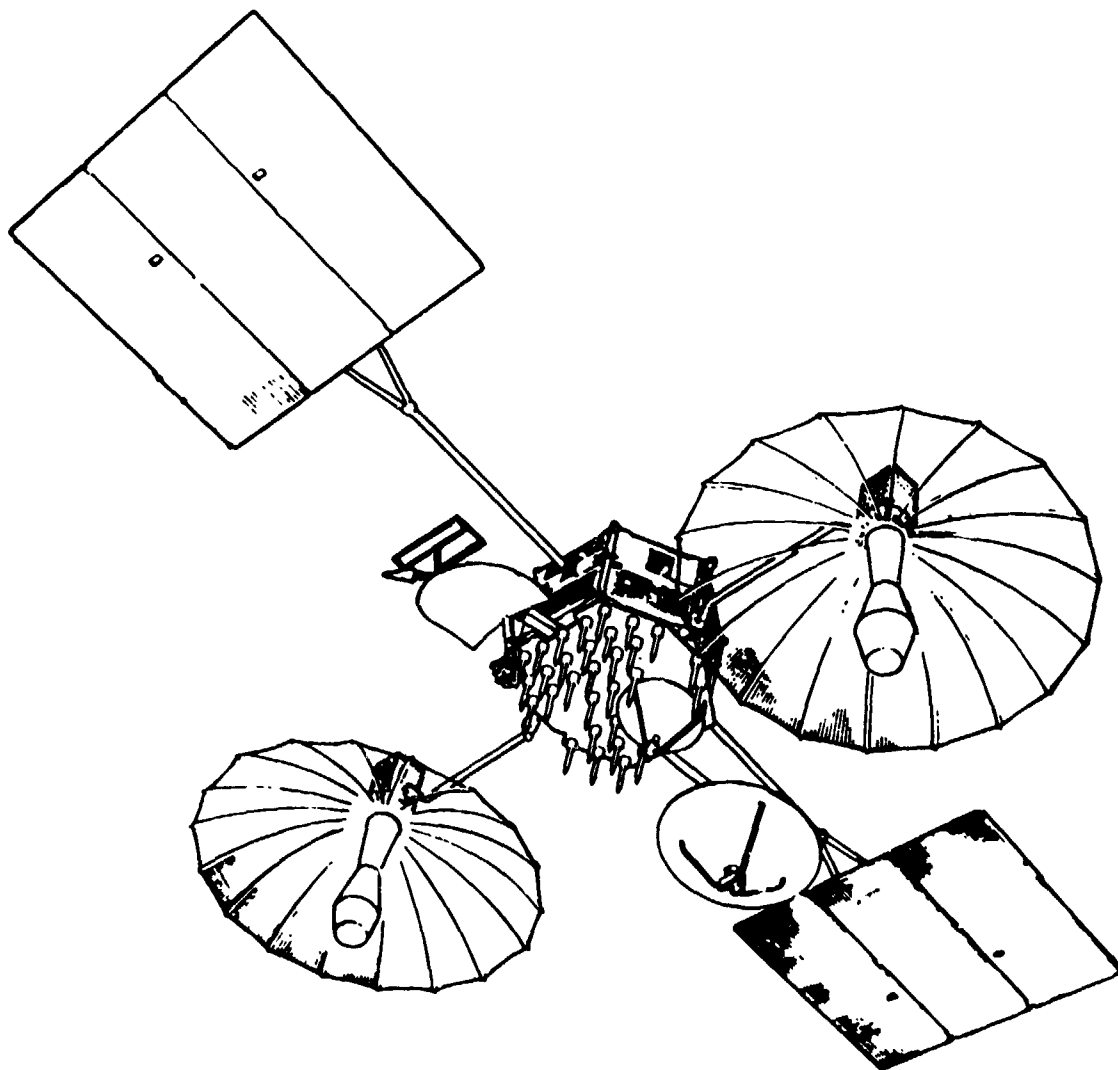
Figure 4. TDRS Spacecraft Configuration

Because of this complexity, a computer is required for generating command sequences, processing of telemetry data, conversion of RF measurements to performance parameters appearing in requirements specifications and for recording test results. In addition, a computer is needed to control the test equipment which supplies the RF signals, sensor stimuli and electrical power which are required for operation of the spacecraft.

The significance of computer based automated testing must be recognized by program managers and test facility managers. Although computers with sufficient speed and memory capacity to handle almost any spacecraft system test requirement are readily available, the software needed for conducting the test and processing the data must be designed for the specific spacecraft and costs significantly more than the computer hardware. Standardized software

and distributed processors are being used wherever possible to reduce this high cost, but a lot more effort and innovation is required to arrive at optimized automated test systems.

TESTABILITY

Another issue which is of major concern to system test organizations is the basic testability of complex spacecraft. Over the last 10 to 15 years we have seen a change in the characteristics of spacecraft so that today we have more and more digital equipment using LSI and on-board processing and much larger and more complicated mechanical structures. In addition, the cross-strapping and reconfiguration capability of the electronic equipment is so great that it is very difficult to validate all anticipated operating modes prior to flight. It is, therefore, very important for test people to partici-pate in the design of a spacecraft from the start in order to influence the following design features:

- selection of test points and location of test connectors

- equipment layout and clearances to enable replacement of faulty units

- provision of accelerated command capability for automated testing

- selection of telemetry measurements

- design of on-board computers for reprogrammability and interfacing with ground test equipment

- accessability for x-ray and visual inspection of critical connectors

- mechanical design which enables functional testing of mechanisms

- location of hard points to allow safe support during testing and transportation

- use of test-only sensors vs. flight telemetry

Several of these points may appear trivial or obvious, but experience has shown that their importance must not be underestimated. Another observation which should influence future activities is the fact that through automation and improved test equipment we have kept pace with the increasing complexity of electronic and electrical equipment aboard a spacecraft. On the other hand, our mechanical and structural test procedures have not changed signifi-cantly during the last 10 years. Acoustic and vibration test facilities are available but methods for conducting deployment tests under simulated zero gravity conditions are still relatively crude. On-orbit testing using the shuttle as a base may prove to be a viable option in the future and deserves further study.

CONCLUSIONS AND RECOMMENDATIONS

Performance during acceptance testing affects performance in orbit. Comprehensive testing over a wide range of usage and environmental conditions has been a major contributor to the excellent success record of spacecraft which have been launched.

Severe thermal thermal cycling over the maximum allowable temperature range rather than extended thermal vacuum exposure should be used to detect workmanship and design defects at the spacecraft level.

Test engineers and project managers must be aware of the large cost and schedule requirements for generating the software which controls the automated test procedures.

Methods for testing the deployment of appendages and/or verifying mechanical characteristics of large structures will have to be improved as structures become larger and more flexible and dynamic interactions which influence alignment and pointing accuracies become more critical.

Test engineers must participate in early spacecraft design decisions and exert greater influence to insure that testability is achieved.

REFERENCES

1. C. E. Nelson, "System Level Reliability Thermal Cycling", Proceedings of the 5th Aerospace Testing Seminar, Institute of Environmental Sciences, 19-21 September 1979, p. 69.

R. F. TESTING OF THE THIRD GENERATION DEFENSE COMMUNICATION SATELLITE

John Sargent *
Dr. Michael Massaro **

Abstract

This paper will describe the approach taken to test, on a system level, a completed DSCS Communications Satellite. Areas to be described are measuring RF isolation of separate communications subsystems and a test method which insures that one RF subsystem does not interfere with another. In addition, the method of complying with MIL-STD-1541 in the area of demonstrating safety of electroexplosive devices in an RF field will be discussed.

INTRODUCTION

In January of 1977 a contract for the third generation Defense Satellite Communication System was awarded to the General Electric Space Division. This newer generation satellite is unique compared to earlier generations in that it has a six channel transponder designed for both frequency and time domain access operation and real-time commandable uplink and downlink multibeam antennas. On the satellite the six SHF channels can be received via one of two earth coverage horns, or a 61 element, switchable multibeam antenna (MBA) and transmitted via one of two earth coverage horns, a gimballed high-gain reflector antenna (GDA), or one of two 19 element switchable multibeam antennas. In addition, there are two omnidirectional S-Band antennas for TT&C operation, and a Single Channel Transponder operating at UHF and SHF. Thus, there are a total of twelve antennas, two SHF earth coverage Transmit horns, two earth coverage Receive horns, one 61 MBA Receive antenna, a GDA Transmit antenna, a UHF Transmit and Receive Antenna, and finally, two S-Band omni antennas.

The RF testing of the DSCS III satellite represents a unique challenge from a technical standpoint, as well as from an implementation standpoint regarding needed facilities and test equipment.

This paper presents the test philosophy, test approach and test acceptance criteria and expected test results of the DSCS III satellite RF tests. In particular, the following tests will be discussed:

- Antenna Isolation
- RF Self Compatibility Performance
- Radiated Electro Magnetic Susceptibility
- Intermodulation Product Generation

All of the above satellite tests will be performed in a large anechoic room which was designed to absorb most of the RF energy radiated from the spacecraft in order to closely duplicate free space. The above tests are being conducted to verify basic program design performance parameters or to determine compliance

* System Test Engineer   ** EMC Engineer
  General Electric Space Division
  Valley Forge, Pa.

with the design and test requirements of MIL-STD-1541, which has been applied
to the program. The antenna isolation test and the RF self compatibility
performance test are performed to satisfy both requirements; whereas, the
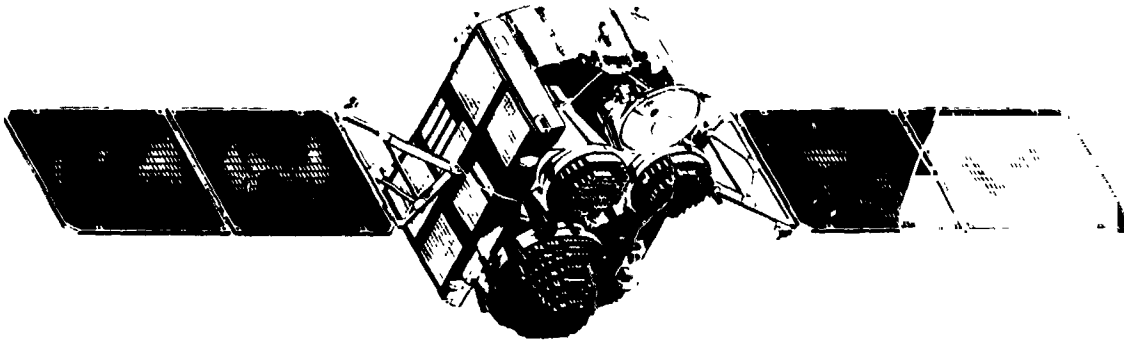Radiated EMISM test satisfies only the latter, and the IMP test the former.

Figure 1 - DSCS Satellite

DSCS III Satellite Description

The Defense Communications Satellite, due for launch early in 1981, is
a third generation communication satellite which, during its 10 year design
life, will act as a repeater in space for our defense forces. The satellite,
which is presented in Figure 1, is a three-axis stabilized synchronous orbit
satellite whose body size measures 6 1/2 feet wide (38 feet including solar
array), 6.75 feet long and 6.5 feet high, weighing 2200 pounds. Ten communi-
cation antennas are mounted on its earth viewing face. Antennas operating at
X-band consist of two receive earth coverage horns, two transmit earth cov-
erage horns, two 19 beam transmitter antennas, one 61 beam receive antenna and
one gimball dish. At UHF there are separate receive and transmit antennas.
At S-band there are two antennas, one on earth viewing and one on space facing
side used for telemetry and command functions. The north face of the satel-
lite contains the communications and the south panel, which contains the power
controller and regulation unit, attitude control, command decoder, telemetry
unit, data encrypters, decrypters and batteries. All subsystems are fully re-
dundant and may be cross strapped. Frequency spectrum covered by the communi-
cations payload is 7900 to 8400 MHz for X-band receive, 7250 to 7750 MHz for
X-band transmit. This transmit band is divided into 6 bands or channels whose
downlink transmit power is provided by two 40 watt and four 10 watt TWT's.
There are two standard SGLS channels number 12 and 16 for S-band TT&C control.

25

In addition, there is a single channel transponder whose UHF downlink communicates to all AFSATCOM equipped force elements. Access to AFSATCOM transponder is via UHF; X-band direct, X or S-band TT&C. DSCS III has two beacons operating with identical simultaneous modulation. Telemetry is impressed on the beacon modulation using an interplex modulation of two telemetry streams modulated on two subcarriers. One telemetry stream is time shared between a PN code and SCT telemetry data. Main telemetry is 61 K bits in length with a 1 K BPS rate. The Transmit and Receive frequencies are indicated in Figure 2.

Designation of Tests

Early in the program ground rules were agreed to which determine which tests were to be automated and which were to be manual. These ground rules were:

a) Are the measurements of a repetitive nature, such as transponder power output across the band?

b) Will the automation reduce overall test time?

c) Will the test be used repetitively on each satellite, or is it just for qualification of one satellite?

d) Will the additional complexity of the test which includes computer operators and software programmers be recoverable in shortened test time? Thus, a five-hour manual test shortened to one hour through automation may not be cost effective if it takes 4 times the number of people to run the test.

SATELLITE SYSTEM RF TESTS

Antenna Isolation

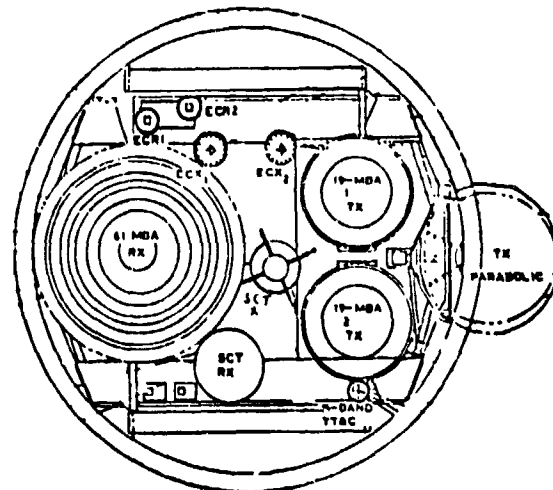| Ant	Ch	MHz	BW	Ant	Ch	MHz	BW
HBA1	1	7200	60	ECR1	3	8172	75
	3	7467	75		4	8285	60
HBA2	2	7365	60		5	8370	60
	4	7560	60	ECR2	1	8005	60
ECX2	4	7560	60		2	8010	30
	6	7725	50		6	7925	50
BEACON		7605		HBR	1	8005	60
ECX1	3	7457	75		2	8090	60
	5	7645	60		3	8172	75
BEACON		7600			4	8285	60
DISH	1	7580	60	UHF	R	360	90
	2	7365	60		T	247	20
	4	7560	60	S	R	1807	1823
					T	2257	2277

Figure 2

Since the spectrum of frequencies of the satellite is so broad band, there exist many possibilities for one subsystem to interfere with another by means of spurious responses, intermodulation products, or adjacent channel noise. To prevent this from happening, the harmonic content of each transmitter is minimized by careful design. By measuring the satellite's receiver thresholds - that is - the minimum signal necessary to operate the system and a transmitter's fundamental and harmonic output at a specific frequency, the magnitude of isolation which must exist between the two on-board RF subsystems to prevent intrasystem interference can be determined.

On the DSCS satellite there exist high field strengths from all transmit antennas, and therefore large isolation values were required of the antenna systems. It was decided to measure isolation across the antenna's entire operating band to insure that any peaks in the antenna's coupling from one antenna to another would not be overlooked.

There are many ways to make isolation measurements - phase lock receivers, network analyzers, and tracking generators. Each system was evaluated for ease of use and minimization of set up time. It was decided that because of the wide band of frequencies to be covered, the sweep generator and spectrum analyzer approach would be employed. There are over 50 combinations of pairs of antenna measurements to be made. Since the sweep generator power source had to be coupled to many antenna ports, and since there would be frequent connection changes, the use of waveguide as the test signal path was impractical. Therefore, all antenna ports using waveguide are transitioned to coax for connection to the test equipment. To prevent the sensitive spectrum analyzer from measuring the leakage from coax used for the tests and mistaking it for antenna leakage, solid shield short length heliax cable will be used for interconnection. Reflected energy from the walls of the facility are expected to be low and in the order of -70 dBc, as shown in Table I. Being so low in amplitude, they will not interfere with the isolation measurement.

BAND	PATH	ANT. SIDE LOBE	ABSORBER	TOTAL ATT.
UHF	30	32	10	70
S	42	6	25	73
X	45	50	30	125

TABLE I - RF ISOLATION FROM FACILITY

Although the test is repetitive in nature and thereby qualifies for automation, it will be performed manually because the test will only be done on the Qual vehicle. Antenna isolation is affected by antenna position, type of antenna geometric layout, operating frequencies and load matching networks.

These relationships should not change from satellite to satellite. Preliminary design data indicates that isolation is 10 dB better than acceptance levels, and therefore there is little chance of risk in performing this test on only one satellite.

RF SELF COMPATIBILITY PERFORMANCE

Up to the point in time where this test is performed, the satellite has been tested in a hard wire configuration where antennas were not connected to operating subsystems. During this test the satellite will radiate through its antennas and system performance tests via air link for the first time. The purpose of the test is a) to insure there is no mutual RF interference between two subsystems - that is - satellite receivers listening to their own on-board transmitters, and b) the RF field around the satellite does not leak into a performing subsystem and effect its operation. The first is detected by spectrum analysis of the transmitted signal. The second is measured by offsets in telemetry from those values recorded in a baseline measurement.

An optimistic test plan would exercise the spacecraft in every possible configuration in all modes and insure proper operation, but considering the fact that the 6-channel comm transponder alone has 155,000 possible operating modes, this is impractical. Therefore, we must scope our tests to only those configurations which can realistically be affected. A study was performed and ground rules made to simplify the tasks necessary for an uncompromising compatibility test. A summary of this study was as follows:

a) Attitude control system is affected by RF because the sensitive sun and earth sensors measuring satellite attitude are within the radiation field of the antennas.

b) The Single Channel Transponder's receiver may incorrectly AGC due to RF leakage entering the X or UHF receivers.

c) The X-band communications channels may be affected by RF leakage into their mixer stages and cause spurious outputs within their channels.

d) Power subsystem may incorrectly regulate due to RF leakage onto power controller sense lines.

To test for these effects and others, the satellite is configured by air link to a minimum power configuration and each subsystem is powered up by itself, and baseline measurements recorded. As an example, the attitude control system is initialized to a stable null condition and all sensor outputs recorded. The single channel transponder is configured by UHF and is placed in a bypass mode where it operates as a true transponder. In this configuration the uplink power is varied and a bit error rate curve is generated. Comm transponder outputs in each channel are monitored by spectrum analyzer under no uplink and noise power measurements made. Command threshold measurements are made on the command system and minimum uplink power points are established for S-band and X-band commanding. Beacon modulation

spectrum measurements are made and center frequency is accurately established.

These tests are ther. repeated on each subsystem while all other systems are fully on. If there is any interference, it will show up on that subsystem by a delta in performance as measured either directly on a spectrum analyzer or on telemetry by changes from baseline values previously recorded.

Radiated EMISM Spray Test - Figure 3

The RF Radiated Spray Test must demonstrate that the various subsystems of the vehicle could operate within their specified performance limits if the environmental field-strengths were increased 6 dB above their nominal levels. That is, electromagnetic radiated interference safety margins, (EMISM) must be established for the various subsystems of the spacecraft. An EMISM must be demonstrated for the following coupling modes:

(1) Transmit antenna-to-component case radiated field coupling.

(2) Transmit antenna-to-wire bundle and cable radiated field coupling.

(3) Transmit antenna-to-electroexplosive device case and wire harness radiated field coupling.
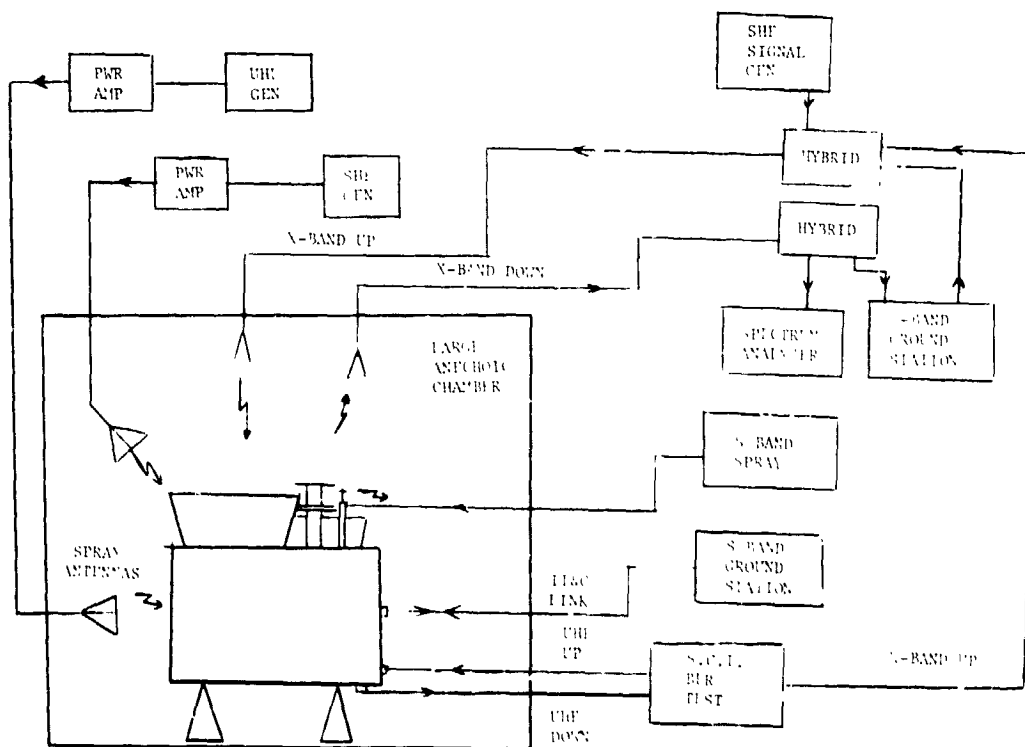

Figure 3

This test is accomplished by first measuring the ambient fields around the vehicle at the transmitter fundamental frequencies and large harmonics. It was decided to use a Radiation Hazard probe (RADHAZ) type instrument to measure the ambient fields. RADHAZ probes are typically broadband, omnidirectional and polarization independent, and are thus ideal for probing unknown field distributions. However, RADHAZ probes have low sensitivity with minimum discernible fields on the order of about 2.0 V/m. Consequently, this limit was used to establish the lower limit of the intensity of the spray field at a level of 5 V/m.

After establishing the ambient field levels, the S/C is then sprayed a level that is 6 dB greater in intensity at each of the measured frequencies. During the spray test at each frequency, selected critical performance parameters are monitored to determine if acceptance limits have been exceeded. For example, for the SHF transponders, spurious sideband levels are measured. For the TT&C system X-Band and S-Band downlink telemetry is monitored for upsets and changes. For the Single Channel Transponder system, a Bit error rate test is performed.

The test is performed for the Electro-explosive device system (EED) by first determining the largest environmental field strength that the EED system, EED device, case and control cable will experience. The environment in this case refers to the fields that exist at the launch pad, the fields produced by pre-launch tests, or the fields produced by the launch vehicle. The test is performed to ensure that the RF environment does not cause a false firing of the EED. A 20 dB safety margin must be established, i.e., the EED must be sprayed with an effective field that is a numerical factor of 10 higher than the maximum ambient environmental field. For DSCS III the maximum overage environmental field strength was a level of 60 V/m produced by the launch vehicle. Since the test field strength for this case (600 V/m) was enormous, an effective field strength of 600 V/m can be produced by removing the shield from the EED harnesses and spraying at a field strength of 6 V/m. This reduction in the spray intensity is based on the fact that the shields can produce 40 dB of attenuation to external fields. The harness is sprayed at this level for 2 months and a non firing of the EED is the pass criteria.

Internal Product (IMP Testing)

When a non linear electrical device on the satellite is simultaneously sprayed with RF at two different frequencies, doubling and mixing actions take place which can produce and self generate a third frequency. If this self generated signal lies within a satellite's receive pass band, and is strong enough to be "seen" by the satellite's receive antenna, the satellite will amplify this signal and rebroadcast it on the downlink. This extra signal is capable of saturating the transponder's power and rendering - in extreme cases - the channel useless. Examples of elements which cause IMP generation are loose waveguide points, dissimilar metals in waveguide switches, and antenna elements poorly joined. They are usually parts which are exposed to high power.

Recognizing the importance of this test, it is planned to be performed three times in the satellite test cycle. First, after initial satellite assembly in order to prove workmanship quality. Second, after acoustic noise exposure to prove structural integrity, and a third time after pyro shock exposure. Since this test is so discretely repetitive and must be performed on every satellite, it is a prime candidate for automation.

To perform this test a "full up" satellite is required. The test must be air linked in order to allow the IMP to ring around into a receive antenna port.

The test philosophy is as follows. An intermod measurement pair is selected, such as those shown in Figure 4.

Xmit Ant.	Xmit Freq.	Rec Ant.	Rec. Freq.
Dish	7335	Earth Horn	8060
Earth Horn	7750	Earth Horn	7950

IMP Rec. Ant.	IMP/R Freq.	IMP/Xmit Freq.	Imp Ant
M Beam	8165	7440	Earth Horn 1

Figure 4

Two uplink signal generators are programmed to 8060 and 7950 GHz and the signals sent to the satellite are received on earth horn #1. The signals are translated 750 MHz down in frequency, amplified and transmitted from the satellite dish and earth horn #1 antennas. If there is a non linear IMP generator, it will mix the two transmit frequencies and the resultant third order internal product will fall at 8165 MHz. This is a receive frequency IMP which will be translated down 750 MHz, amplified and rebroadcast on 7440 GHz. It is to this frequency the spectrum analyzer is tuned. Baseline noise power measurements out of the satellite are made at this frequency at a bandwidth of 10 KHz to determine amplitude of pure noise with no uplink established. Once this noise power is quantized, the two uplink signals are sent and power again measured at the IMP frequency. If power increases 8 dB with uplink signals present, there is an indication of an intermod product signal.

Considerable care in the selection of test equipment has been exercised to insure that the uplink signal path does not in itself generate IMP products. Two separate uplink antennas will be used to keep the two uplink test signals separate until they ultimately mix within the satellite. Low power from the uplink signal generators - in the order of -30 dBM - will be used for the test signals to prevent IM products from being generated on the uplink and

close coupling to the receive antennas will achieve immunity to generating IM products on the uplink.

By testing all possible pairs of transmit and receive ports across all possible IMP frequencies, we will eliminate any "surprise" signals from being self generated by the satellite after launch.

CONCLUSIONS

As in every satellite test program there exists a myriad of component and subsystem tests which prove proper subsystem design. However, it is only at the system level test where proper satellite operation is proven. This is accomplished by verifying test parameters under true orbit simulation.

In this DSCS program, with regard to RF system test parameters, we have attempted to assume nothing. We have replaced "test by analysis" with analysis then test. By completely testing a satellite in a mode which duplicates its operation in orbit, then linking this with testing for a proper margin of proper system operation, a high level of confidence for correct system operation is achieved.

PYROTECHNIC SHOCK AT THE ORBITER/EXTERNAL TANK FORWARD ATTACHMENT

William F. Rogers, David S. Grissom, and Larry R. Rhodes*

ABSTRACT

During the initial certification test of the forward structural attachment of the Space Shuttle Orbiter to the External Tank, pyrotechnic shock from actuation of the separation device resulted in structural failure of the thermal protection tiles surrounding the attachment. Because of the high shock associated with the separation bolt, the development of alternative low-shock separation designs was initiated. Two concepts that incorporate a 5.08-centimeter (2-inch) frangible nut as the release device have been developed and tested at the NASA Lyndon B. Johnson Space Center.

INTRODUCTION

Pyrotechnic-actuated devices are used to release the External Tank (ET) (fig. 1) during separation of the Space Shuttle Orbiter from the ET. These devices must meet the system design requirements to sustain the flight loads and to separate cleanly at the moment of release. At the forward structural attachment, the device must also meet close-tolerance aerothermodynamic smoothness requirements for the Orbiter outer mold line following separation.

During the initial certification test of the forward attachment, pyrotechnic shock from actuation of the separation device resulted in structural failure of the thermal protection tiles surrounding the attachment. The test data also indicated that shock levels transmitted to the forward avionics bay of the Orbiter would exceed the qualification levels of some of the equipment.

To meet these diverse design requirements and to quickly obtain test data on alternative low-shock separation designs at the NASA Lyndon B. Johnson Space Center (JSC) and at the prime contractor facility, two designs incorporating a 5.08-centimeter (2-inch) frangible nut were investigated. The 5.08-centimeter (2-inch) frangible nut was chosen for this application because (1) it could withstand the structural flight loads at the Orbiter forward attachment, (2) the pyrotechnic shock from this device would be low compared to that of the baseline separation bolt design, and (3) hardware to perform development tests was readily available. These designs were investigated as possible substitutes for the baseline separation bolt in the event that baseline modifications were not satisfactory.

---
*NASA Lyndon B. Johnson Space Center, Houston, Texas.

DESIGN REQUIREMENTS

The separation system design requirements can be divided into two general categories: structural and mechanical. The separation hardware is the primary structural load path between the Orbiter and the ET; hence, the hardware must satisfy the overall structural design requirements of the spacecraft for the prelaunch, launch, and boost environments. For separation, the system acts as a mechanical device and must satisfy the design requirements to ensure a safe separation.

The mechanical design requirements for the Orbiter/ET separation are

1. To provide release of the Orbiter from the ET for normal and abort separation

2. To preclude degradation of Orbiter functional systems after separation

3. To satisfy aerothermal smoothness criteria after separation

4. To separate without releasing debris

5. To incorporate acceptable assembly and mating procedures

To satisfy these design requirements and to develop a separation system with low-shock characteristics, the 5.08-centimeter (2-inch) frangible nut was chosen. This nut was selected because it has the strength to withstand the structural flight loads at the forward attachment, data indicate that pyrotechnic shock would be low compared to that of the baseline design, and the hardware is readily available to perform development tests.

Selection of a design to meet specific requirements generally involves some compromises. For example, the baseline shear-bolt design meets the requirements for a clean separation and a smooth outer mold line exceedingly well with a relatively simple device. The piston ejects the severed stud with a high force so that the potential for hangup is virtually nonexistent. The stud has to move only about 2.54 centimeters (1 inch) to clear the Orbiter outer mold line and, even under side-load conditions for a separation during an abort, separation is positive. Unfortunately, the pyrotechnic shock associated with this device damages tiles adjacent to the attach point and may adversely affect the operation of avionics equipment located nearby.

The low-shock devices that have been investigated by JSC and the prime contractor have a potential to hang up under the side-load conditions associated with an abort separation. This problem has become a significant challenge in developing a low-shock system and is receiving emphasis in an ongoing design and test effort.

BASELINE SEPARATION SYSTEM

The major components for separation of the Orbiter from the ET are shown in figure 1. At the forward attachment, release is accomplished by the shear-type separation bolt (fig. 2). After the piston shears the bolt shank, it pushes the lower section of the shank free of the spherical bearing and the bottom of the piston stops flush with the outer surface of the bearing. This design results in a dual-shock effect. As the pyrotechnic cartridge pressurizes the volume above the piston, there is a recoil effect. The primary shock, however, is caused by the piston shearing the bolt shank and then stopping as it impacts the shoulder of the shank. At the two aft attachments, a 6.35-centimeter (2.5-inch) frangible nut is used as the release device. After the Orbiter is separated from the ET, doors close to cover the cavities that remain after structural release.

FRANGIBLE NUT - ORBITER SIDE

A primary objective in quickly developing an alt.rnate separation concept was to minimize the impact to the system in terms of design changes to the Orbiter and the ET. To develop, prove, and implement a new separation system, there would have to be virtually no structural changes or significant redesign to either vehicle. By locating the frangible nut on the Orbiter side and providing blast-containment and bolt-reaction capabilities within the existing volume, no changes would be required on the ET side of the separation plane.

The initial focus of attention was to develop a means of blast containment. With increased Orbiter weight being highly undesirable and with a restricted volume to work in, the goal was to develop a relatively lightweight cloth bag container fabricated from Kevlar, a registered DuPont trademark for a family of aromatic polyamide fibers characterized by high tensile strength. The bag was cylindrically constructed with one end closed and the other end secured to a mounting structure by a compressive V-clamp. Figure 3 shows the test configuration and indicates how the bag completely contains the frangible nut and any debris resulting from an explosion.

Initial test objectives were to determine the capability of the fabricated Kevlar material to withstand the explosive elements and to verify the bag retention design. As these tests were being planned and cond cted, a design effort to provide a bolt retraction mechanism compatible wit the Kevlar blast container was initiated. A series of tests (discussed in the section on test results) was conducted and proved the lightweight Kevlar bag to be very successful; however, the concept was abandoned in favor of a design using the explosive elements on the ET side and the design of the bolt retraction mechanism was stopped.

35

FRANGIBLE NUT - ET SIDE

A design that relocated the pyrotechnics to the ET side of the separation plane (fig. 4) was chosen as the preferred approach. The primary reasons for this change were to completely remove the explosive shock condition from the Orbiter structure and to provide the allocated Orbiter separation volume for a bolt retraction mechanism. It had become evident in earlier efforts that an acceptable bolt retraction mechanism would require considerable volume and that this would probably be the main design driver. By relocating the frangible nut to the ET side, the bolt could be shortened to a length compatible with retraction into the existing Orbiter volume.

The basic design approach was to machine a slot in the ET yoke fitting for locating the frangible nut. Pyrotechnic ignition wires are routed through a hole in the main attachment bolt from the Orbiter to the frangible nut. An appropriate potting compound is used to secure the wires and to fill the void remaining at the bottom surface. The bottom of the retracted bolt acts as a closeout at the separation plane. A wire-cutting feature was added to the system; this device, upon actuation of the nut pyrotechnics, severs the wires at the bottom of the bolt and results in a smooth closeout surface. A rugged, all-metal blast container lined with an energy-absorbing material to dampen the explosive effects is attached to the yoke fitting and encloses the frangible nut. The bolt is spring-loaded on the underside of the head to provide retract energy.

The initial objectives were to determine the modifications required to the ET yoke fitting and to develop means for blast containment. The test objectives for the first phase were to evaluate the blast container integrity and to obtain engineering data on bolt energy due to release of the 445-kilonewton (100 000-pound) preload. In the second phase of development, a wire-cutting mechanism and a bolt-retract system were added. Both phases of testing were developmental and did not include side loads or other specific conditions existing during flight separation.

TEST FACILITY DESCRIPTION

Testing was conducted in the Pyrotechnics Test Facility of the Thermochemical Test Area at JSC. The primary purpose of the Thermochemical Test Area is to support the development, evaluation, and qualification of spacecraft electrical power, hydraulic, propulsion, and pyrotechnic subsystems.

The Protechnics Test Facility includes the electronics and mechanical shops, an explosives handling and loading room, and four test cells that are used for testing pyrotechnics ranging from a few milligrams of explosive charge to small rocket motors. Ready storage for pyrotechnic igniters and charges is provided by two magazettes. One of the test cells is shown in figure 5.

TEST RESULTS

Frangible Nut - Orbiter Side

The first test of the Kevlar blast container used a 1.91-centimeter (0.75-inch) nut with two NASA standard detonators (NSD's). The bag was secured to the test fixture with two hose clamps. In this test, the bag failed where the top was sewn to the cylindrical sleeve. The next bag was reinforced with straps that cross over the top of the bag. A second test used the two NSD's with boosters but without a nut. This bag was secured to the test fixture with a 1.27-centimeter (0.5-inch) stainless steel band using a banding tool. Small penetrations were found in the bag but were not considered an issue because a nut would have absorbed much of the energy of the pyrotechnic fragments.

For the next test, a 5.08-centimeter (2-inch) pyrotechnic-actuated frangible nut was used to test a third bag. This bag was secured to the test fixture with a 1.91-centimeter (0.75-inch) stainless steel band. The bag successfully contained all particles and, at this point, confidence in the bag was high. However, it was determined that the banding tool could not be used for the Shuttle because of access constraints.

A series of four tests using 5.08-centimeter (2-inch) nuts was conducted to develop a three-piece clamp for holding the bag. In the first test, the 0.79-centimeter (0.31-inch) bolts holding the clamp segments failed. High-speed motion pictures indicated two primary dynamics: the pressure wave from the blast loads the entire bag, and the nut halves are propelled radially and strike the clamp. One-centimeter (0.38-inch) bolts were used for the next test. The bag and clamp assembly blew off the fixture because the clamp did not have enough interference with the fixture. A tighter clamp was made and two demonstration tests confirmed the design adequacy. This final configuration is shown in figure 6.

Frangible Nut - ET Side

Two tests of the frangible-nut ET-side configuration have been conducted. The primary objective of the first test was to demonstrate the effectiveness of the steel blast-containment device. A secondary objective was to measure the velocity of the bolt resulting from the release of strain energy. Two carbon rods were placed in the path of the bolt and spaced at a prescribed distance. Electrical current passing through the rods was recorded on high-speed analog tape. Interruption of the signal would signify rod breakage due to bolt travel and provide displacement and time information for calculating velocity. High-speed motion pictures also recorded the motion of the bolt. The test setup is shown in figure 5.

After the nut was separated, the bolt began to spring upward. The first carbon rod was broken; however, the bolt only traveled approximately 3.81 centimeters (1.5 inches). From the motion pictures, it could be seen that the yoke fitting was falling and rotating, possibly binding the bolt.

Inspection of the bolt threads indicated that the nut fragments may have interfered with bolt movement. The blast-containment device was completely effective.

The primary objective of the second test was to determine the performance of the guillotine used to cut the pyrotechnic lead wires. The secondary objective was to determine the effectiveness of the bolt-retracting spring and the bolt catcher. The lead wires were cleanly severed by the guillotine, and the bolt retracted and locked as designed.

SHOCK DATA COMPARISON

Shock-response spectra for the baseline shear bolt and for the frangible-nut ET-side configuration are shown in figure 7. These data were obtained from tests conducted at the prime contractor facility. The test article included a complete forward structural attachment and a representative portion of the Orbiter forward fuselage structure. Also shown in figure 7 is an apparent structural limit for the thermal protection system (TPS) obtained from component tests of TPS tiles. It is evident that the frangible-nut ET-side configuration produces shock levels that are well within the TPS capability boundary. A test of the frangible-nut Orbiter-side configuration had also been planned using this structural representative test article. This test was canceled when the decision was made to minimize the number of mechanical concepts under consideration to reduce shock levels. Modifications to the baseline shear bolt were also tested, and the results are summarized in figure 7.

CONCLUDING REMARKS

Because of pyrotechnic shock generated at the Orbiter forward structural attachment by the baseline pyrotechnic separation bolt, the development of alternative low-shock separation designs was initiated. Two designs, which used a 5.08-centimeter (2-inch) frangible nut as the release device, were tested at JSC. The results of these tests have demonstrated the feasibility of these designs for application to the Orbiter forward attachment. Data from a test of one of the designs at the prime contractor facility have shown that shock levels are substantially reduced and well within the capability of the TPS tiles and the Orbiter avionics equipment located nearby. Additional testing of the frangible-nut ET-side configuration is planned at JSC. This series of tests will include the effects of externally applied loads at separation and will provide additional confidence in this system as a potential substitute for the baseline separation system.
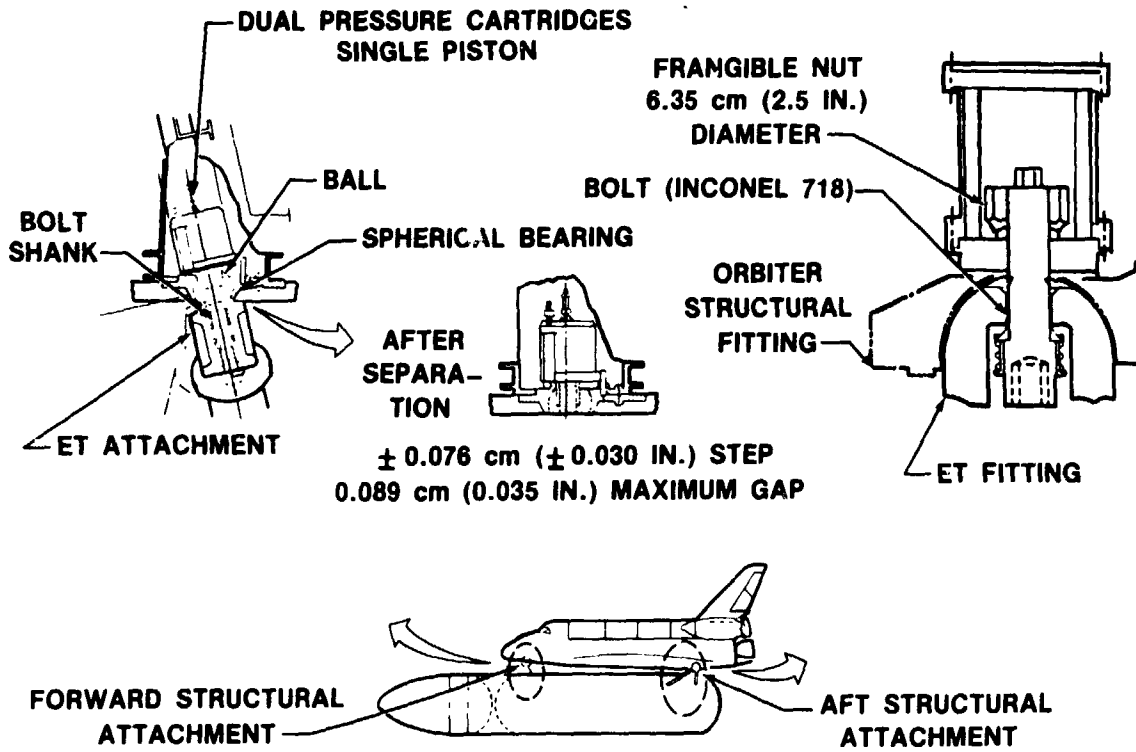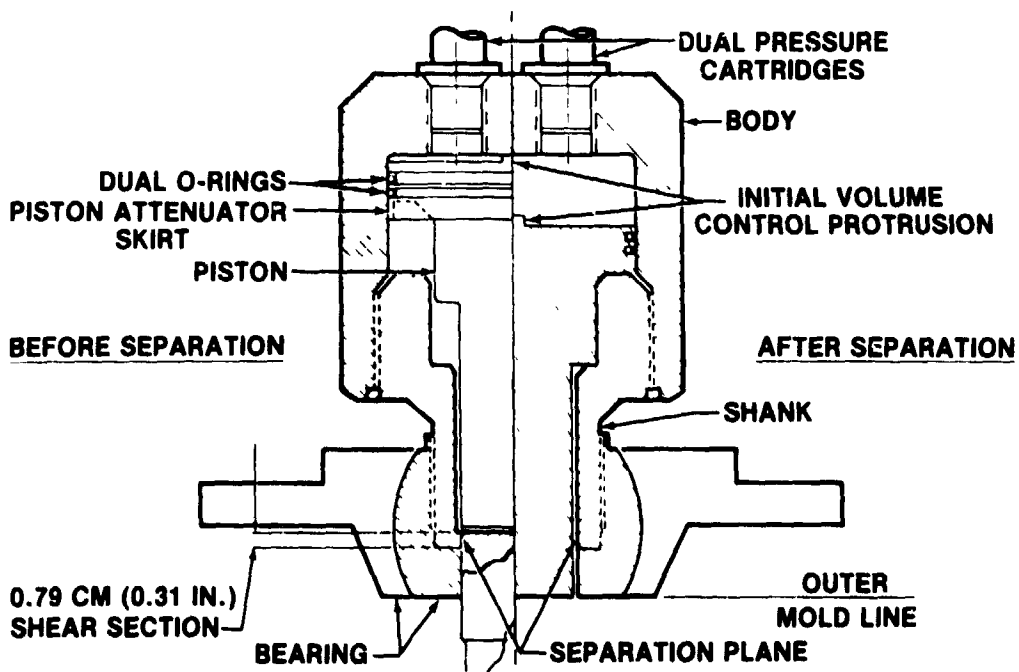
Figure 1.- Orbiter/ET separation system.
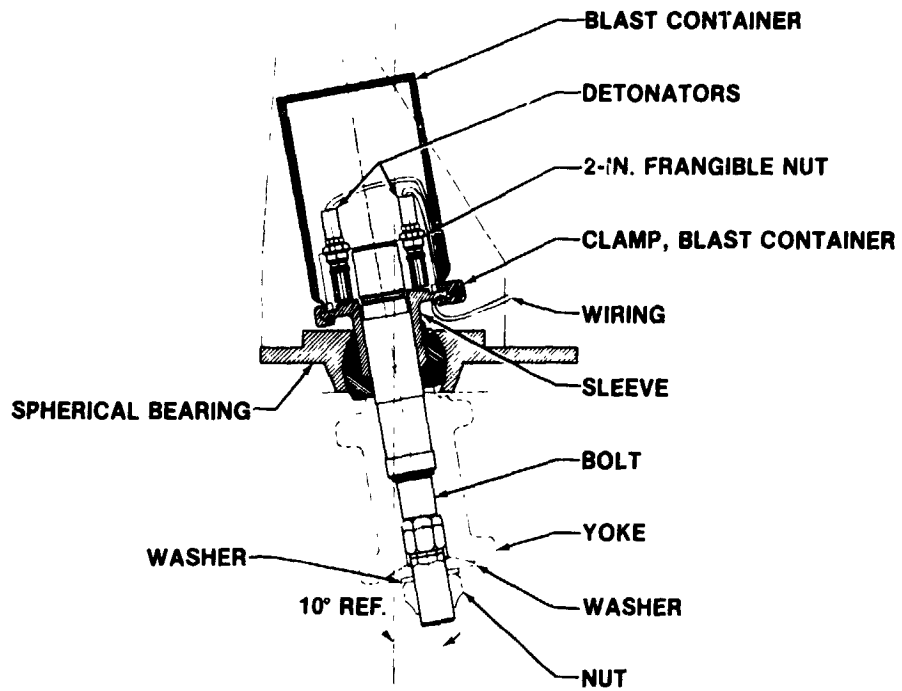

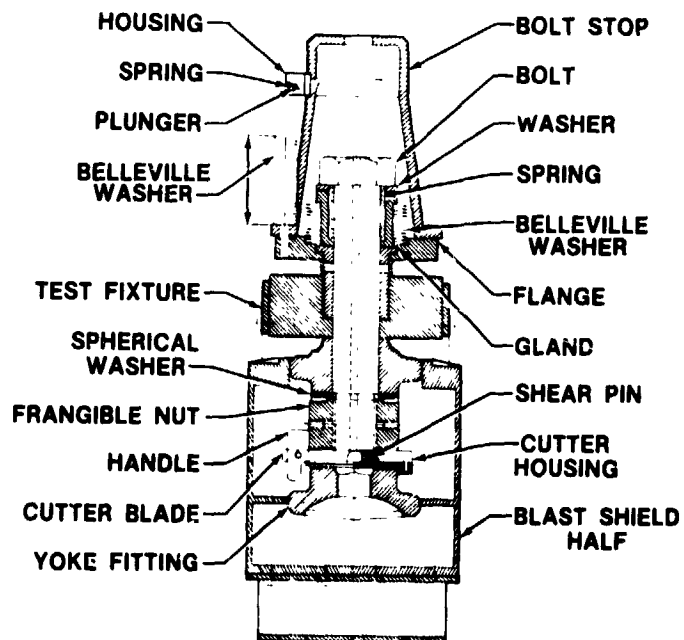Figure 2.- Shear flange separation bolt.

39

Figure 3.- Frangible-nut Orbiter-side configuration.

SECTION LOOKING OUTBOARD THROUGH
CENTER OF TEST FIXTURE

Figure 4.- Frangible-nut ET-side configuration.

40

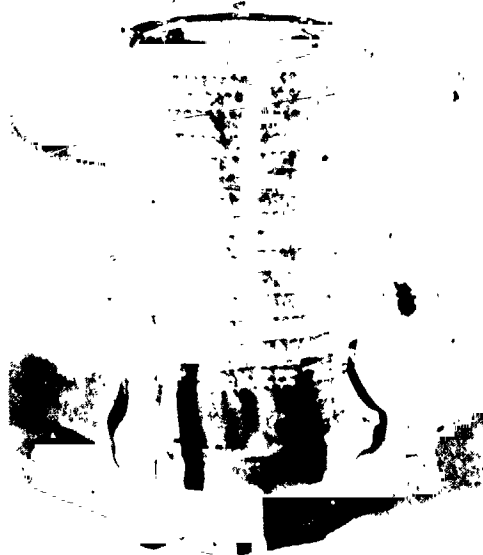Figure 5.- Frangible-nut ET-side test configuration.

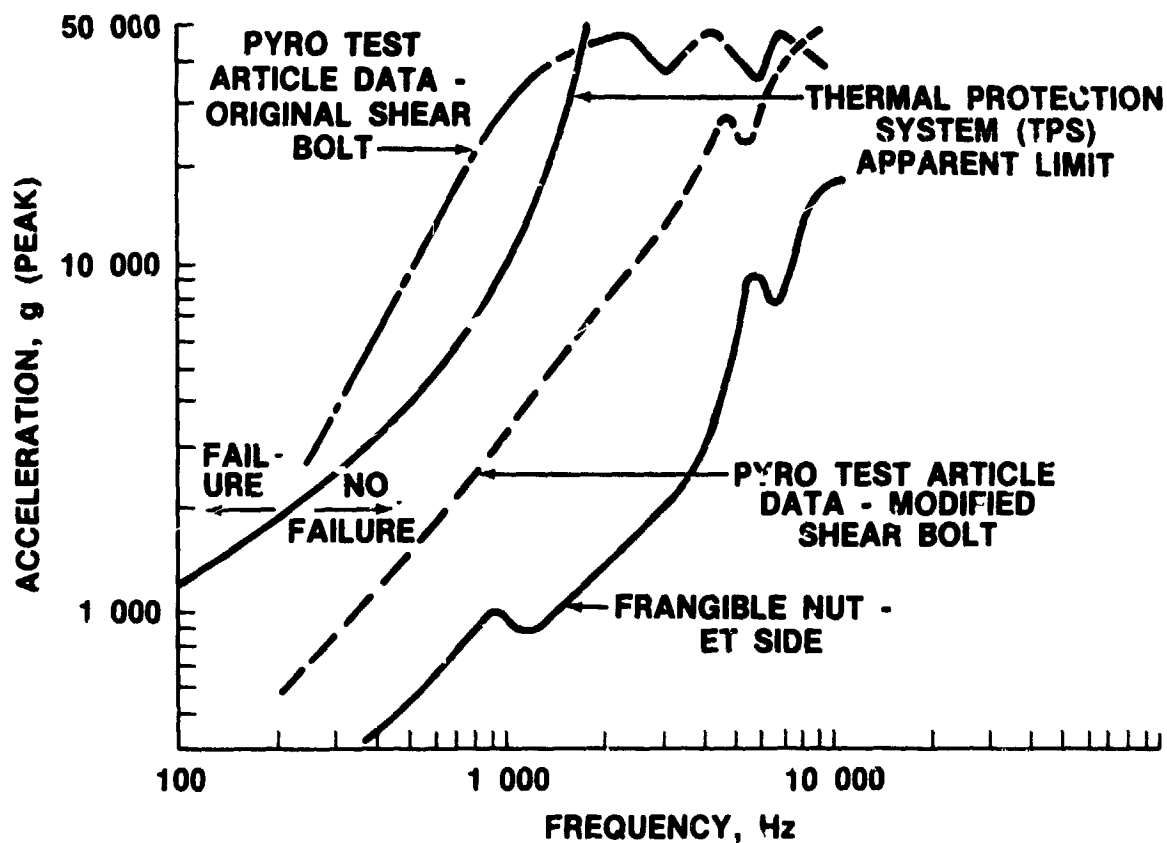Figure 6.- Frangible-nut Orbiter-side test configuration.

41

Figure 7.- Pyrotechnic shock-response spectra of the forward separation
system.

THERMODYNAMIC PERFORMANCE TESTING OF THE ORBITER FLASH EVAPORATOR SYSTEM

James R. Jaax*

Michael A. Melgares**

James R. Frehm+

ABSTRACT

System level testing of the Space Shuttle Orbiter's Development Flash Evaporator System (FES) was conducted at the Johnson Space Center during May/June 1978, and January/February 1979. Testing was performed in a thermal vacuum chamber capable of simulating ambient ascent, orbital, and entry temperature and pressure profiles. The test article included the evaporator assembly, high load and topping exhaust duct and nozzle assemblies, and feedwater supply assembly. Steady state and transient heat load, water pressure/ temperature and ambient pressure/temperature profiles were imposed by specially designed supporting test hardware. Testing in 1978 verified evaporator and duct heater thermal design, determined FES performance boundaries and assessed topping evaporator plume characteristics. Testing in 1979 combined the FES with the other systems in the Orbiter active thermal control subsystem (ATCS). The FES met or exceeded all nominal and contingency performance requirements during operation with the integrated ATCS. During both tests stability problems were encountered during steady state operations which resulted in subsequent design changes to the water spray nozzle and valve plate assemblies.

INTRODUCTION

Successful performance by the FES is dependent upon the combined operation of its 4 major assemblies: evaporator core, feedwater nozzles and controllers assembly; feedwater lines, accumulators and heaters assembly; exhaust ducts and heaters assembly, and exhaust duct nozzles assembly. Extensive component level testing of the evaporator assembly had been completed but with simulators for the other assemblies due to the large chamber volume required. Chamber A of the Space Environment Simulation Laboratory at the Johnson Space Center offered the space environment simulation and physical volume necessary for layout of the duct, nozzle and feedwater assemblies of the FES. Special support equipment capable of simulating transient heat load and feedwater pressure and temperature profiles were needed. Hardware to fully assemble and test the FES was obtained. Special structures were provided for assessing orientation and vehicle surface effects. Instrumentation, displays and controls for engineering data and flight performance evaluation were significant drivers on the development of the test facility's data management system. Test conduct followed the test plans allowing deviations to work around hardware and support equipment malfunctions.

*NASA, Johnson Space Center, Houston, Texas 77058
**Hamilton Standard, Division of United Technologies Corporation, Houston, Texas
+Rockwell International, Houston, Texas 77058

FLIGHT SYSTEM DESCRIPTION

The FES is the Orbiter's sole heat sink during ascent and down to 30,480m (100,000 feet) altitude during entry on a nominal mission. During orbital operations the FES supplements the radiator system to provide a constant coolant temperature to the Orbiter. The FES removes heat from the Orbiter coolant loops by evaporating in a heat exchanger at low ambient pressure expendable water generated as a byproduct of the fuel cells in the Orbiter electrical power system. The FES is designed to be automatically activated and deactivated as a function of altitude and radiator system performance. Manual control override capability is provided. Water vapor produced during FES operation is discharged overboard through 3 sonic nozzles. Two nozzles are located at positions on the aft fuselage which minimize both the propulsive effects and the particle and gas contamination of the space environment viewed by the payload bay. The FES components are located in the midbody and aft sections of the Orbiter as shown in Figure 1.

The high load and topping evaporators are identical in design. The evaporator, shown schematically in Figure 2, consists of three basic parts; the evaporator core, the water valve/nozzle mounting plate, and the anti-carryover device. The core is a cylindrical dual passage heat exchanger consisting of three concentric cylinders separated by two ruffled finned passages. Evaporant water is sprayed on the inner surface of the core to cool the dual freon loops flowing in the separated finned passages. The water valve/nozzle mounting plate is a pin fin heat exchanger for passing hot freon through to keep the water spray nozzles warm and thereby prevent ice buildup. The anti-carryover plate is a pin fin heat exchanger for passing hot freon through to allow the evaporation of water particles that did not impinge on, or rebound from, the cylindrical wall. The surfaces of the core and anti-carryover device exposed to the water spray are grooved to increase the surface area available for water evaporation. Freon flow through the core is longitudinal from the steam outlet end to the water spray nozzle end of the evaporator. The freon loop having the inside passage (next to the inner cylinder) in one evaporator core has the outside passage in the other evaporator core. On the water valve/nozzle mounting plate are two identical water valve/nozzle assemblies. One assembly consisting of the pulser valves and spray nozzles is dedicated to the primary feedwater supply, and the other is dedicated to the secondary feedwater supply. The feedwater valves are pulsed open at a variable frequency, dependent upon heat load, to meter feedwater to the spray nozzle. The spray nozzles have swirl slots and a swirl chamber to distribute feedwater over the interior surfaces of the evaporators. There are two nozzle sizes: 23 kb/hr (50 lb/hr) installed in the topping evaporator and 61 kg/hr (135 lb/hr) installed in the high load evaporator. Three electronic controllers are used to perform the temperature control function for both the high load and topping evaporators.

The overboard venting of the steam generated by the FES is accomplished by two insulated and electrically heated ducts as shown schematically in Figure 3. The high load evaporator has a nominal 0.15m (6 in) diameter, 2.29m (90 in) long duct with two 90-degree bends. The topping evaporator has a non-propulsive exhaust duct system composed of a 0.15m (6 in) diameter, 2.08m (82 in) long section with one 90-degree bend and two 0.1m (4 in)

diameter, 4.32 m (170 in) long sections with three 90-degree bends; both of which terminate with sonic nozzles. Water that is not evaporated in the evaporator is called carryover. It results from the spray nozzle dribble volume, steam drag effects on the main water spray, deflection of water particles, and inefficiency of the evaporator process. The exhaust duct heaters are sized to handle up to 3 percent water carryover. The exhaust duct heaters are divided into zones with individual zone configurations and power requirements. The ducts are insulated to minimize environmental heat losses.

The FES feedwater supply system contains the primary and secondary feedwater lines and accumulators. A detailed description of the FES is provided in Reference 1.

TEST FACILITY

Both tests were conducted in Chamber A of the Space Environment Simulation Laboratory. A schematic representation of the test article layout for the 1978 test is shown in Figure 4. A similar layout, without the equipment for plume distribution assessment, was used in the 1979 test. Test article elements were mounted at floor level elevation inside the chamber as shown in Figure 5. Special test support elements supporting the test article were located on the first and third levels around the chamber. Roughing, cryogenic and diffusion pumping was used to obtain 1.3×10^{-4} N/M^2 (10^{-5} torr) chamber pressure. Up to 11 diffusion pumps were activated to handle the water vapor load during FES operation. The chamber's entire liquid nitrogen shroud was cooled to liquid nitrogen temperature to obtain the required environment for FES plume measurements, duct heater assessment and FES water vapor collection. One zone of helium was used to maintain chamber pressure. Ten controlled partial chamber repressurizations down to 200 N/M^2 (15 torr) were conducted simulating the ambient pressure environment during a typical Orbiter entry profile. A slower (12 hour) method, sublimation repressurization, using dry nitrogen and heaters to minimize water condensation in the thermal blankets of the test article, was used to bring the chamber to sea level conditions. During repressurization television operation was prohibited to prevent corona effected damage. Facility chilled water, hot water, cooling water and compressed air were supplied to elements of the test support equipment. Special user AC and DC power requirements were supplied by a 400 Hertz motor-generator set and regulated power supplies.

TEST ARTICLE

For both tests development, and inhouse FES hardware were assembled in a test configuration which represented the total flight system.

The development evaporator assembly contained flight-type high-load and topping cores, feedwater valves and nozzles and electronic controllers. Between tests a modified design of the topping feedwater nozzles was installed

to obtain a better water spray distribution for improving low control temperature performance. During the 1979 test the topping feedwater nozzles were coated with thermal grease and an insert (shim) which recessed the water nozzles to be flush with the valve plate was installed to obtain better thermal conductivity and minimize possible icing nucleation sites within the core. A thermal blanket of multilayer insulation protected the assembly from the chamber environment.

A feedwater supply assembly duplicating the dual 30.48m (100 feet) stainless steel lines of the flight configuration was provided. Accumulators simulating the function of the flight accumulators were included in both tests. Thermal conditioning of the water in the feedwater lines, simulating orbital conditions, was provided by multilayer insulation, electric heaters and a counterflow concentric tube heat exchanger. A combination of computer and set point controlled heater circuits protected the feedwater system during nonflowing periods.

The exhaust duct heater assembly was installed such that steam flow would never be opposed to gravity (vertical upward), only horizontal and vertical down. Both the high load and topping ducts were equipped with heaters subdivided into discrete zones. Each heater circuit was individually powered by a computer controlled power supply. During the 1979 test heater density and temperature control bands were preset at the levels planned for the early Shuttle flights. A special 20 watt heater blanket was wrapped   . around the high load duct system to replace the function of heaters failed during the 1978 test.

During the 1978 test one topping nozzle was oriented to exhaust into the main chamber volume for plume measurements. The other nozzles in the 1978 tests and all nozzles in the 1979 test were oriented to exhaust behind the chamber cold walls. In addition, in the 1979 test four liquid nitrogen panels were installed between the FES ducts and the center of the chamber to ensure that the water vapor plumes impinged directly upon the cold walls.

TEST SUPPORT HARDWARE

Several independently controlled support systems were provided to simulate the various Orbiter fluid, thermal, electrical and structural interfaces with the FES.

The Orbiter Coolant Thermal Simulator delivered Freon-21 at rates up to 1361 kg/hr (3000 lb/hr) per loop at temperature ranges of -1 to 66°C (30 to 150°F) to simulate the full spectrum of Orbiter ATCS operating conditions and heat loads. Manual and automatic (drum recorder) temperature control capable of introducing FES inlet temperature ramps of 1.7°C (3°F) per second was provided. Two coolant loops were provided, with provision to stop flow in either loop.

The Flash Evaporator Feedwater Supply simulator delivered deionized water from two 0.04m^3 (10 gallon) tanks at pressures up to 10.4 x 10^5 N/M^2 gage (150 psig) and rates up to 91 kg/hr (200 lb/hr) to the FES. Manual

46

controls capable of simulating the ascent and entry pressure transients and electronic weight scales for measuring water consumption rates were provided. Both primary and secondary water systems were provided.

A Feedwater Thermal Conditioning System conditioned the feedwater to provide 7.2°C (45°F) to 66°C (150°F) delivered water to the FES at demand rates up to 91 kg/hr (200 lb/hr). Computer and set point controllers were used to introduce ramps up to 5.6°C (10°F) per minute, multilayer insulation blankets and 21 electrical heaters provided freeze protection for the feedwater lines during no-flow test periods. A 9 kW heater and a liquid nitrogen heat exchanger were available to trim the water temperature.

A FES power and control console provided electrical and control interfaces to the FES. This console provided the normal Orbiter control functions, special test control functions, specific failure mode operations and special monitoring equipment for FES operation and evaluation.

The FES was mounted on a multi-orientation support stand. The aluminum structure permitted configuration of the FES evaporators in three different orientations: vertical up, vertical down, and horizontal. This permitted the study of gravity effects on evaporator performance. The stand was thermally isolated from the evaporator, exhaust ducts, and chamber floor by teflon pads.

Two adjustable Orbiter fuselage surface simulators were provided in the chamber adjacent to one of the topping evaporator exhaust duct nozzles to study the effect of plume characteristics on Orbiter structure and payloads.

During buildup, servicing, and operation of the FES test, additional test support equipment was provided.
    a. In chamber closed circuit television coverage by 6 cameras of the 3 FES exhaust nozzles and Orbiter surface simulators.
    b. Vacuum pump with cryo trap and micro gage for servicing the freon and water loops.
    c. Helium leak check test equipment.
    d. Gas analyzer, first aid, and protective equipment for handling leaks or spills of Freon-21.
    e. Heaters and temperature controllers to maintain FES exhaust duct pressure instrumentation lines above 50°F.
    f. Wang 2200 Mini-Computer system for off-line processing of test data for anomoly investigations and FES water carryover determination.

DATA MANAGEMENT

The test facility's Flexible Data System (FLEX) Hewlett Packard 2117 computer provided the real time control and data acquisition/process/display services for both tests. Raw data from temperature, pressure, flow ate, frequency, current and voltage instrumentation was simulataneously displayed, used in calculations and stored.

47

Instrumentation

Extensive engineering test instrumentation was installed for the 1978 tests to obtain performance data on the evaporator core, duct heater system and water vapor plume. Much of this instrumentation was removed for the 1979 test as the test program matured from detailed component performance assessment to system interaction with other ATCS systems assessment. The 1979 test instrumentation was used to obtain detailed system performance data and evaluate the timeliness and meaningfulness of flight data. The following is a summary of the thermal performance instrumentation required for the test article and support equipment for both tests.

	1978 Test	1979
Surface Thermocouples	200	48
Immersion Platinum Probe	6	24
Current transducers	71	25
Voltage transducers	21	17
Turbine flowmeters	5	2
Baratron pressure sensors	6	6
Pressure transducers	25	6
Frequency	1	1

Thermal performance test instrumentation was sampled at 2, 3, 5, 10, 15, or 30 seconds intervals depending on the dynamic response required from the measurements. Special high response pressure transducers monitored by high speed stripchart recorders were included to detect feedwater and steam pressure transients in both tests.

Plume performance instrumentation included 2 particle spectrometers to detect ice particle formation in the chamber, 9 quality crystal oscillators to measure surface contamination, 4 ionization gages to determine plume flow field characteristics and 3 baratron pressure transudcers to measure low pressures in the $1.3 \times 10^{-2} N/M^2$ (1×10^{-4} torr) range.

Real Time Processing

FLEX software for the 1978 test was configured to acquire and process 896 real measurements, calculate 156 pseudo measurements and compute stimuli for 100 control channels for the test article, support equipment and facility systems. Formats for 37 pages were defined and available for display at 12 interactive terminals with CRT's. Data displays could be made into hard copy through "instantaneous" system SCOOPS (upon keyboard command). A similar software capability was provided for the 1979 test.

During both tests team members maintained data logs, recording real time observations and impressions of test article performance. FLEX made a permanent record of real and pseudo measurements on test history magnetic tapes for post-test point data evaluation. During the test, 24-hour processing of selected portions of the test history tapes was provided by the IDSD (Institutional Data Systems Division) on the UNIVAC 1110 and 1108 EXEC 8 computer systems. Post-test time history plots of key parameters for assessing selected component performance were prepared by IDSD from the FLEX test history tape for selected test points. Microfilm and hard copy were provided of each plot.

TEST CONDUCT

Chamber occupancy for the 1978 test began in August 1977, and ended in June 1978 after 4 weeks of testing. Test article fluid charging began in March 1978 followed by 1 week of ambient checkout and 4 weeks of vacuum checkout testing. The test article and stand was removed in June then re-installed in August in Chamber A for the 1979 test buildup. Test article fluid charging for the 1979 test began in late December 1978 followed by 2 weeks of ambient checkout testing and 2 days of vacuum checkout testing. FES performance testing was completed during the 3 week "open loop" test period. The test article was reconfigured for "closed loop" testing. A 3 day vacuum checkout test preceded the 4 days of "closed loop" testing where FES performance as part of the integrated ATCS was assessed.

The 60 members of the 1978 test team manned 15 stations, providing 24 hour coverage with three 8 hour shifts. The control room had 6 stations including the test director responsible for the conduct of the test, technical supervision and control of the systems within the test article, operation of the test support and facility systems and real time assessment of the test article's performance. A similar layout of stations and responsibilities for FES operations was maintained for the 1979 test. During both tests standard hardline communication network protocol was observed by all test team members and a voice record tape of all communication channels was obtained.

During the 1978 test one control room CRT station displayed FES "flight" data in addition to engineering test information. This concept was expanded for the 1979 test, whereby at one CRT station, flight measurements identical to the flight data format were used by a "flight controller" test team member to monitor ATCS performance, including the FES, during mission simulations.

Steady state and transient heat load profiles based on pretest analytical predictions were used to assess FES capacity, water carryover, controller response, heater design, flight instrumentation adequacy, and plume charac-teristics (1978 test only). Timelining of the 224 steady state and 42 transient test points in the 1978 test followed the guidelines that test points requiring similar conditions shall be grouped in priority order and that proceeding from one group to another shall take the path of minimum change in existing conditions. All vertical FES assembly orientation testing was grouped into the first test week. Weekend reconfiguration allowed horizontal orientation to start the following week. Chamber pressure, chamber temperature, feedwater temperature and "ice free" duct pressure were the most time consuming parameters to establish. Using "drum plotters" to input transient heat load profiles for the FES provided uniform repeatable stimuli for the transient test points. High risk test points which "stressed" the test article or were predicted to result in ice buildup were conducted at the end of each test week. During each test point selected parameters were monitored continuously to minimize ice buildup in the test article. Test article hardware performance problems required almost daily assessment of the test timeline as diagnostic and problem solving test conditions were integrated into the test conduct.

The 1979 test included 21 open loop test points for performance mapping and constraint definition and 30 closed loop test points for assessment of FES operation with the integrated ATCS. Timelining guidelines were similar to those used in the previous test. All tests were conducted with the FES in the horizontal position.

TEST RESULTS

The system level tests of the FES achieved all planned test objectives, demonstrated that the FES meets or exceeds most performance requirements, and demonstrated the full compatibility of the FES hardware and controls within the Orbiter ATCS. During the conduct of both tests, hardware and procedure deficiencies were identified which have resulted in design and operation changes that improve FES performance and recommendations for reducing FES weight, power and volume requirements and are described in Reference 2.

Testing in 1978 concentrated on verifying the system design and determining the FES operating boundaries. Steam backpressure (boiler pressure) is a critical parameter in the operation of the FES. Initial testing provided the data for determining and verifying the topping exhaust nozzles throat diameter for obtaining the design on-orbit backpressure in the evaporator core. The remainder of the testing was dedicated to determining the thermodynamic performance of the FES during all planned and contingency FES operating modes, verifying topping evaporator plume characteristics. The topping evaporator performed successfully in both vertical and horizontal orientations. Instabilities in feedwater pressure (water hammer) during FES operation were confirmed and the effectiveness of an accumulator in reducing this effect verified. Maximum performance capability for all operating modes exceeded design requirements. However, significant problems were encountered during orbital simulations at moderate heat loads which subsequently resulted in a design change to the topping evaporator water spray nozzles. Unstable FES performance was observed during extended operation with feedwater temperatures above $38^{\circ}C$ ($100^{\circ}F$). Although many FES shutdowns occurred and ice verified to be in the core and ducts, each FES restart was successful when feedwater was below $38^{\circ}C$ ($100^{\circ}F$). Flight instrumentation was found adequate for monitoring FES status but inadequate for early detection (before FES shutdown) of an icing condition in the cores and ducts. Exhaust ducts and nozzle heaters thermal design was determined to be conservative and power density redistribution, fewer heaters and lower control temperatures were recommended. Topping evaporator plume characteristics were compatible with Orbiter design requirements. Periodic solar orientation of the Orbiter should prevent buildup of frost (particles less than 1 micron) observed on the fuselage simulator. Minimal thrust imbalance from the ducts was noted during topping evaporator operation.

For the 1979 test the FES was included with flight-type and functionally simulated portions of all systems within the Orbiter ATCS. Maximum thermodynamic performance test points verified that FES performance with the new topping evaporator water spray nozzles still exceeded design requirements. The FES met or exceeded all performance requirements during operation with the integrated ATCS. Testing verified with few identified shortcomings the

50

adequacy of proposed flight procedures, instrumentation, displays and controls for nominal and contingency operations. Coolant temperature instabilities encountered during high load evaporator operation at low heat loads resulted in a design change to the water spray nozzle and valve plate. Procedures were successfully developed and demonstrated for clearing ice out of the topping evaporator core and startup of the topping evaporator after inhibiting on orbit. Exhaust ducts and nozzle heater performance using the OV102 Orbiter power density was adequate but inefficient. A redistribution of the topping evaporator heaters would prevent non-iced heater zones from exceeding 177°C (350°F) after FES shutdown should ice collect at a thermostat location.

CONCLUSIONS

The FES development test program provided the data necessary for design verification and operational certification of the Orbiter FES. The successes, limitations, and shortcomings identified during the tests have resulted in a safer design with much greater understanding and confidence in the FES during normal and contingency operations. Through the daily coordination and cooperation by user and test facility personnel both tests were successfully planned and conducted with minimal impact on technical obejctives and within financial constraints.

REFERENCES

1. Jaax, J. R., "Orbiter Active Thermal Control Subsystem Description and Test History," Crew Systems Division CSD-SH-126, Johnson Space Center JSC 11295, July 20, 1978.
2. Jaax, J. R., "Integrated Active Thermal Control Subsystem Test Final Report," Crew Systems Division CSD-SH-143, Johnson Space Center JSC 14182, August 24, 1979.
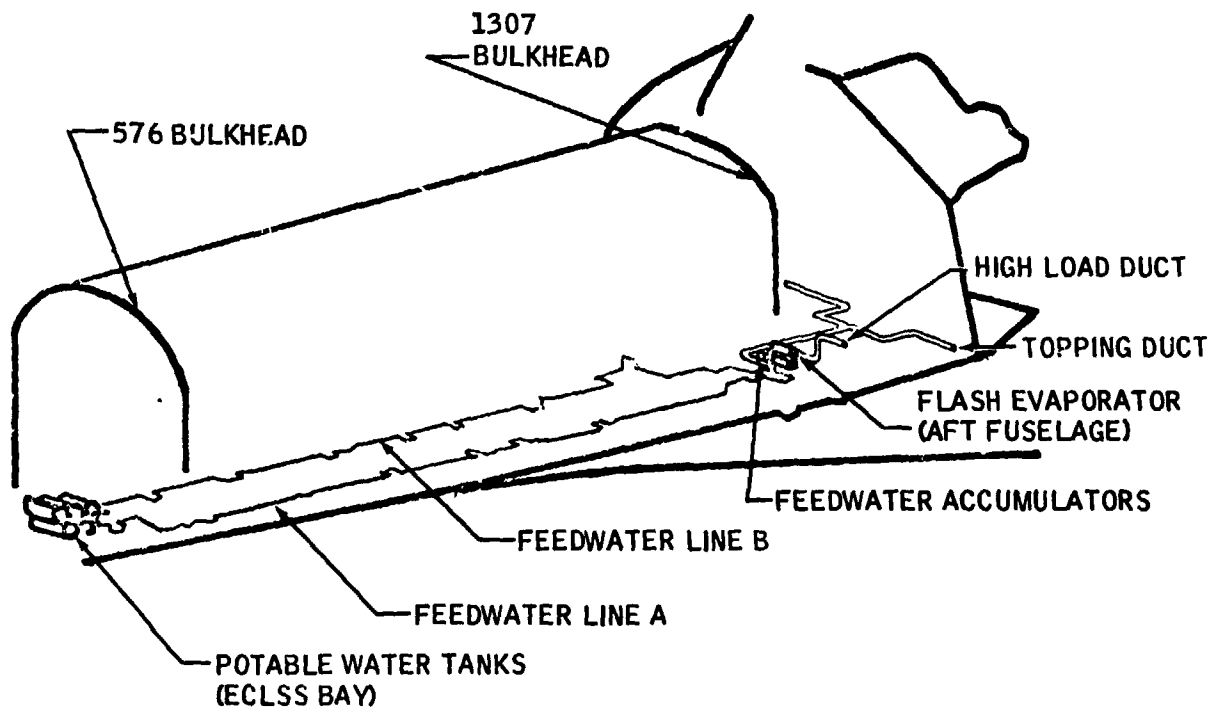
Figure 1   Flash Evaporator System Location in Space Shuttle
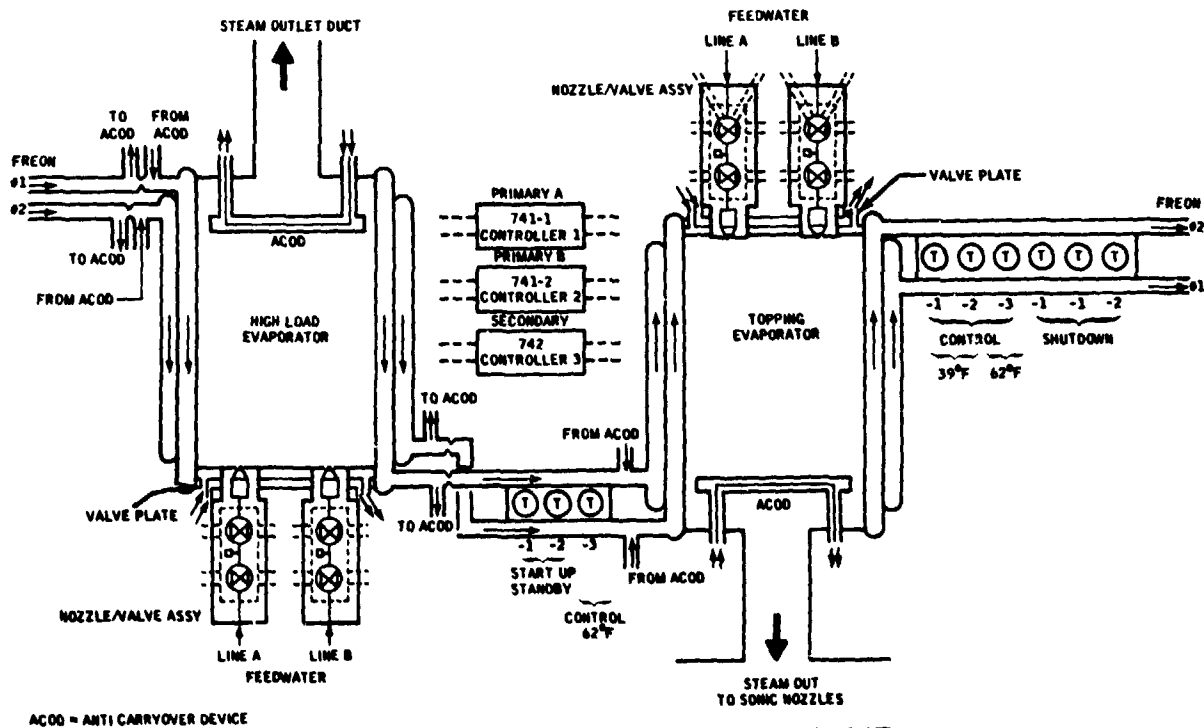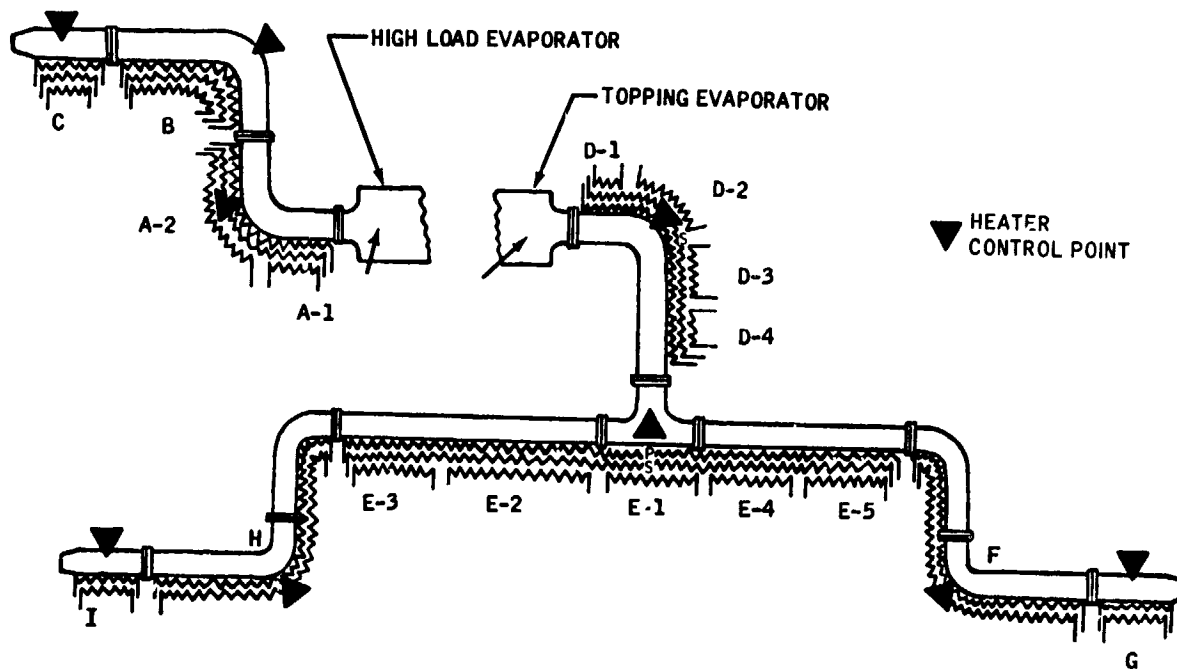

Figure 2   FES Evaporator Assembly Schematic
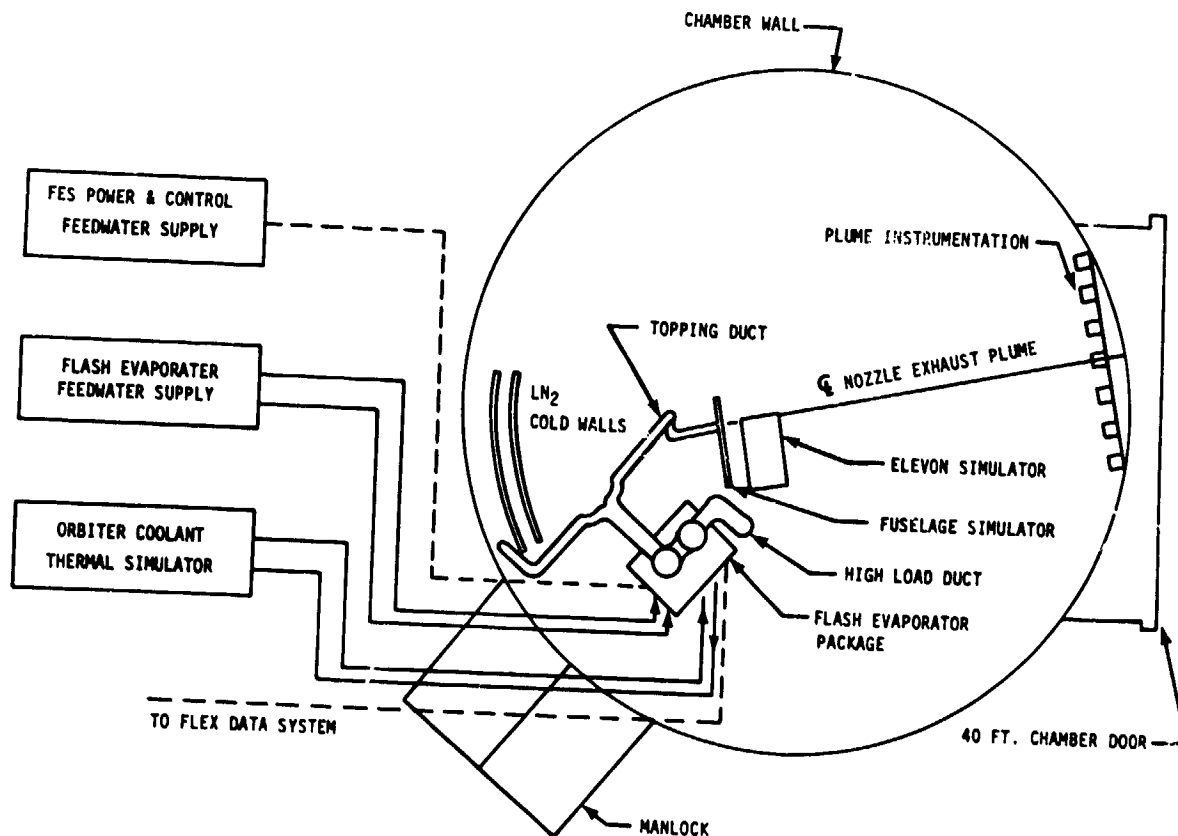
Figure 3   FES Duct and Nozzle Heater Schematic

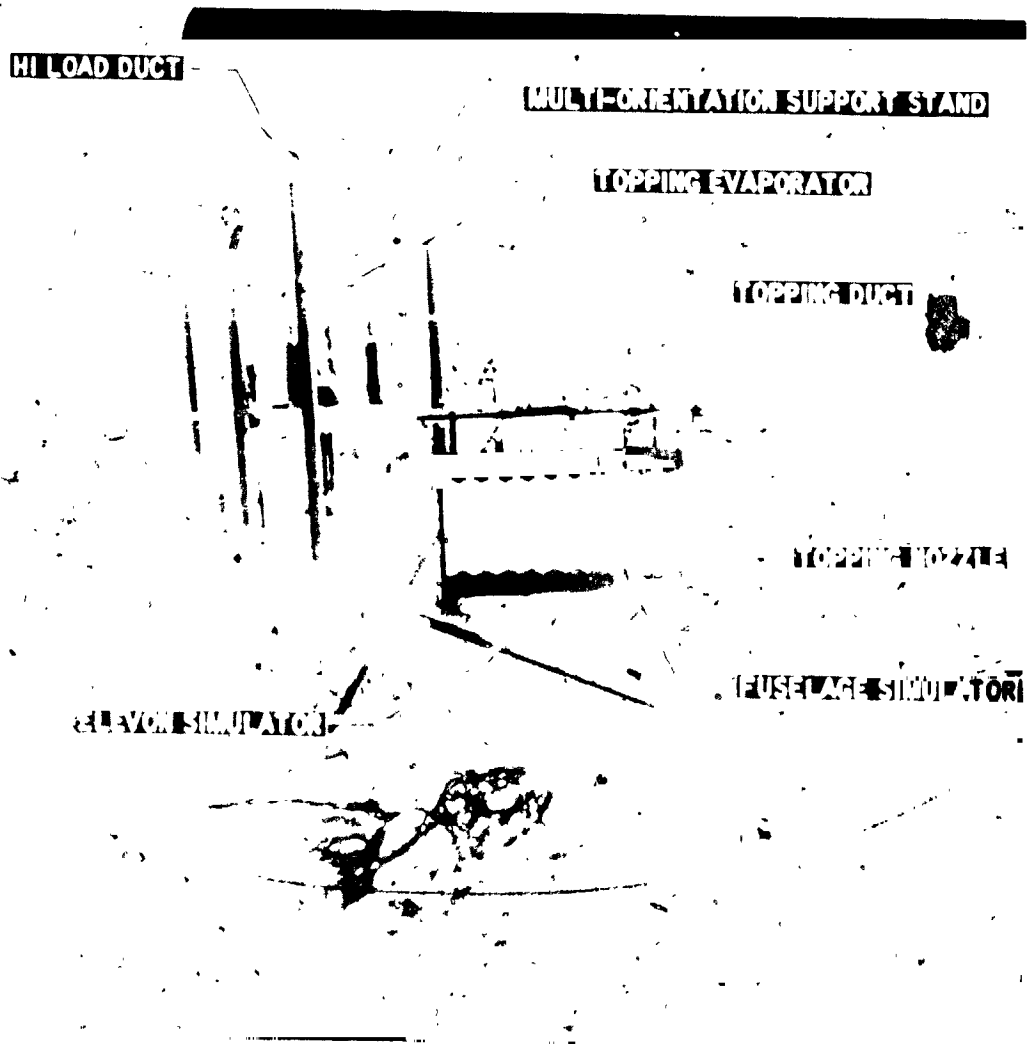Figure 4   Layout of Flash Evaporator System in Test Chamber A

53

Figure 5   FES Test Setup in Chamber A

ORBITER INTEGRATED ACTIVE THERMAL CONTROL SUBSYSTEM TEST

James R. Jaax*

ABSTRACT

Integrated subsystem level testing of the systems within the Orbiter
Active Thermal Control Subsystem (ATCS) was conducted at the Johnson Space
Center during January-February 1979. Testing was performed in a thermal
vacuum chamber capable of simulating ground, orbital, and entry temperature
and pressure profiles. The test article was in a closed loop configuration
that included flight-type and functionally simulated portions of all ATCS
components for collecting, transporting and rejecting orbiter waste heat.
Specially designed independently operating equipment simulated the transient
thermal input from the cabin, payload, fuel cells, freon cold plates, hydraulic
system and space environment. Test team members using data, controls and
procedures available to a flight crew controlled the operation of the ATCS.
ATCS performance met or exceeded all thermal and operational requirements
for planned and contingency mission support.

INTRODUCTION

Most components within the ATCS had successfully completed development
testing. However, because of the complex heat load sharing, manual and
automatic control and sequencing of ATCS heat sinks, multiple transient
heat loads imposed by the heat sources, and high degree of crew involvement
in ATCS operations, an integrated test for design verification data was
required to complete operational certification of the ATCS. Chamber A of
the Space Environment Simulation Laboratory at the Johnson Space Center
offered the space environment simulation and physical volume necessary for
layout and thermal isolation of the systems in the ATCS. Special support
equipment capable of simulating the thermal response of four major Orbiter
subsystems and the transient orbital environments were needed. Within the
ATCS, hardware to fully assemble and test one of the two coolant loops was
obtained; however, for closure of both coolant loops simulators for Orbiter
coldplate and radiator functions were needed. Instrumentation, displays
and controls duplicating flight configuration and data processing in addition
to engineering evaluation data were drivers on the development of the test
data management system. Test conduct followed established scenarios for
nominal and contingency activities allowing for real time development of
flight procedures and control functions.

FLIGHT SYSTEM DESCRIPTION

The ATCS collects, transports and rejects waste heat from Orbiter sub-
systems, equipment, and payloads from prelaunch through post-landing for

*NASA, Johnson Space Center, Houston, Texas 77058

each mission. Heat transport fluid (Freon-21) is pumped through twenty-seven centralized heat collection devices (liquid to liquid heat exchangers and pin-fin coldplates) and twelve expendable and radiative heat sinks. Two separate but parallel routed coolant loops are required to perform the ATCS thermal management function. The ATCS components are located in the midbody and aft sections of the Orbiter as shown in Figure 1. A simplified fluid schematic containing external views of the major ATCS components is shown in Figure 2. Displays on Cathode Ray Tubes (CRT), meters and controls for the ATCS are located on the Orbiter flight deck.

Systems within the ATCS providing heat rejection include the Ground Support Equipment (GSE) heat exchanger, flash evaporator system, radiator system and ammonia boiler system. During ground operations (prelaunch and within 15 minutes after landing) the Orbiter heat load is rejected through the GSE heat exchanger to a ground coolant unit. The Flash Evaporator System (FES) is the Orbiter's sole heat sink during ascent until the payload bay doors are opened and during entry down to 30,480m (100,000 feet) altitude. During orbital operations the FES supplements the radiator system to provide a constant coolant temperature to the Orbiter. The FES removes heat by evaporating in a heat exchanger at low ambient pressure water generated as a byproduct by the fuel cells in the Orbiter's electrical power system. The radiator system includes 8 radiator panels attached to the inside of the payload bay doors. Four of the panels can be deployed away from the doors to allow radiation from both sides of a panel. The ammonia boiler system (ABS) is the Orbiter's heat sink during entry, below 36,576m (120,000 feet), and post-landing until ground cooling is provided through the GSE heat exchanger. The ABS removes heat by boiling liquid anhydrous ammonia and venting the vapor overboard. A detailed description of the ATCS is provided in reference 1.

TEST FACILITY

The test was conducted in Chamber A of the Space Environment Simulation Laboratory. The working volume of the Chamber is 16.8m (55 feet) in diameter and 27.4m (90 feet) in height. A schematic representation of the test article layout is shown in Figure 3. Test article elements were mounted at floor level elevation inside the chamber as shown in Figure 4. Special test support elements supporting the test article were located on the first level around the chamber. Roughing cryogenic and diffusion pumping was used to obtain 1.3×10^{-4} N/M^2 (10^{-5} torr) chamber pressure. One zone of helium with occasional use of an additional zone when test article fluid leaks were encountered was able to maintain chamber pressure. The chamber's entire liquid nitrogen shroud was cooled to liquid nitrogen temperatures to obtain the required environment for radiator performance evaluation and handle the water vapor load during FES operation. Six controlled partial chamber repressurizations down to 266.6 N/M^2 (20 torr) using dry nitrogen were conducted which simulated the ambient pressure environment during Orbiter entry. A slower (12 hour) method, sublimation repressurization, using dry nitrogen and heaters to minimize water condensation on the radiator panels and insulated surfaces, was used to bring the chamber to sea level conditions. During repressurization television and high voltage

equipment (infrared simulators) operation was prohibited to prevent corona effected damage. Facility chilled water, hot water, steam, gaseous nitrogen, liquid nitrogen and compressed air were supplied to elements of the test support equipment. Special user AC and DC power requirements were supplied by a 400-Hertz motor-generator set, regulated power supplies and special support hardware.

TEST ARTICLE

Development, qualification, flight and inhouse ATCS hardware were assembled in a test configuration which represented one (loop 2) of the Orbiter's two coolant loops. The other loop was simulated to provide proper conditions at the points in the ATCS where the two loops have common thermal interfaces. A summary list of the test article components and their source is shown in Table 1.

Radiator System

Four radiator panels were installed in the configuration shown in figures 3 and 4. To minimize gravity effects the aft panels were aligned with the plane formed by the panel edges tilted at an angle of 0.15 radians (8.75 degrees) with respect to the horizontal with the outboard edge above the inboard edge. The forward panels were placed behind the aft panels with the plane formed by the panel edges in a horizontal position. A liquid nitrogen shroud was installed between the forward and aft panels to prevent radiant interchange between the upward tilted aft panels and the forward panels. The radiator panels were suspended by cables attached to the environment simulator structure. Payload bay door simulators were installed below the two forward panels forming an angle of 0.62 radians (35.5 degrees) between the planes of the upper surfaces of the panels and doors representing the deployed position of the panels during on-orbit operations. Heaters on the door simulators, simulating the infrared flux originating from the doors, were controlled from a power console located outside the test chamber. The back side of the aft panels and the door simulators were insulated with multilayer insulation to minimize heat leak from these surfaces. Guard heaters were installed beneath the back side insulation of the aft radiator (panel 4) to prevent freezing during test points that required isolation of panel 4 from the coolant loop.

Earth and solar environment simulation was provided by infrared lamps capable of simulating both skewed and orbital cycle flux environments. Flux from the lamps was input through the upper surface of the radiators by an array of nine rows of lamps each under separate computer control. Radiometers to measure heat flux were mounted flush with the upper surface of the radiators in the plane of the radiator. Two radiometers were placed in the opening of the cavity, formed by the forward radiators and the door simulators, directed into the chamber to determine chamber background flux. Structure holding the environment simulator was designed to minimize blockage thereby maximizing radiator panels view to chamber. Shutoff valves and a

57

modified flight type adapter tube to bypass the aft radiator panel were installed to allow 3-panel radiator system testing. Selection of either the 3- or 4-panel configuration was made from a control panel in the facility control room.

The radiator panels were plumbed into coolant loop 2. An Orbiter design interchanger heat exchanger was plumbed into loop 1 to simulate its radiator heat rejection capacity by either providing a constant "set point" outlet temperature of $3.3^{\circ}C$ ($38^{\circ}F$) or tracking the loop 2 radiator outlet temperature. Special valving allowed simulation of the 3 and 4 radiator flow characteristics.

Two radiator flow control assemblies (FCA) were installed to control flow to the radiator panels and simulator. Remote controlled motors allowed selection of 3 or 4 panel configuration for the two FCA mode control valves while at vacuum conditions. Activation and mode selection for FCA operation during testing was provided by a control panel located in the facility control room. A detailed description of the configuration and performance of the radiator system during this test is provided in references 2 and 3.

Flash Evaporator System

A special support stand as shown in Figure 4 housed the FES test article. The evaporator assembly was mounted in the horizontal position to minimize gravity effects on both evaporators. A thermal blanket of multilayer insulation protected the assembly from the chamber environment. A feedwater supply system duplicating the dual 30.48m (100 feet) lines of the flight configuration was provided. Thermal conditioning of the water in the feedwater supply lines, simulating orbital conditions, was provided by a counterflow concentric tube heat exchanger. A combination of computer and set point controlled heater circuits protected the feedwater system during nonflowing periods. The three exhaust duct nozzles were oriented to direct water vapor at the chamber cold walls. Four 1.8m by 3.7m (6 feet by 12 feet) liquid nitrogen panels were installed between the duct nozzles d the radiator panels to ensure that the water vapor plumes impinged d tly upon the cold walls. Both the high load and topping evaporator ducts a.. nozzles were equipped with heaters subdivided into discrete zones. Each heater circuit was independently powered by a computer controlled power supply having the preset heat density and temperature control bands specified for the early Shuttle flights. Activation and controls for FES operation during testing was provided by an evaporator power and control console located in the facility control room. A detailed description of the configuration and performance of the FES during this test is provided in references 3 and 4.

Ammonia Boiler System

The impact of the extensive facility modifications identified for handling ammonia vapor prior to release into the local atmosphere exceeded the benefits foreseen by including a functional ammonia boiler system in the test. Thus, only the boiler heat exchanger was included in the test planning. During installation activities this passive device was found to have

58

unrepairable internal leaks and was deleted from the test configuration.
The heat removal function of the ammonia boiler was simulated by the GSE
heat exchanger based on analytical correlation with prior test experience.

Freon Coolant Loop

The five ATCS heat exchangers (interchanger, payload, fuel cell, hydrau-
lics and GSE) were mounted on special support stands of aluminum unistrut
and teflon blocks to provide accessibility, common elevation (reduce gravity
effects) and thermal isolation from the structure of the test chamber.
Special actuation motors and television cameras were installed to allow remote
changing of the two flow proportioning module configuration during testing.
Individual controls for both flow proportioning modules were provided on a
control panel located in the facility control room.

Orbiter coldplates were unavailable, thus four simulators representing
the cumulative coldplate fluid volume and thermal input for each coolant
loop in the aft and midbody sections of the Orbiter was provided. Each
simulator contained a low wattage heater element submerged in a cylinder
with baffles to obtain turbulent fluid flow. The simulators used high
voltage (220 volt) power, thus were located outside the test chamber, satis-
fying safety concerns about possible corona discharge from high voltage
components in a vacuum. The simulators were located as a lumped mass at the
position of the last coldplate in the flight configuration of each coolant
loop. A thermal cutout attached to each heater element monitored fluid/
element temperature to prevent flashing and fluid decomposition. Variable
power setting controls were provided on a control panel located outside the
test chamber.

Both freon pump packages were mounted on special support, thermal isola-
tion stands. A control panel was provided in the facility control room for
activating and deactivating the pump packages.

All plumbing between ATCS components used flight design stainless steel
(CRES 21-6-9) thin wall tubing, 0.0004m (0.016 inch) thickness, covered with
a minimum of seven layers of multilayer insulation. Line lengths between
components were identical to the Orbiter except for the radiator simulator
portion of loop 1. Approximately 290m (950 feet) of 0.019m (0.75 inch)
diameter and 130m (425 feet) of 0.0095m (0.375 inch) diameter tubing was
installed. Special structural supports were used for routing line lengths
longer than the available distance between components. Flared 0.65 radian
(37.5 degree) "AN" fittings specially modified (bored to tubing internal
diameter) to reduce pressure drop were used to connect the tubing. All
system components were cleaned or verified to level 300. All lines were
leak tested at 1.38×10^6 n/m^2 gage pressure (200 psig) with helium gas and
proof pressure tested at 1.72×10^6 n/m^2 gage pressure (250 psig).

The number and types of line bends did not duplicate the Orbiter configu-
ration. Therefore, remote controlled air actuated metering valves were
installed near each pump inlet for adjusting total system flow. Manual
metering valves were located in both loops upstream of the interchanger,

59

payload heat exchanger, aft coldplate simulator and midbody coldplate simulator for pretest adjustment of flow distribution to obtain flight flowrates for the baseline flow configuration. Ball type shutoff valves (selected for low flow resistance when fully opened) were installed to permit open loop testing of the portion of the ATCS loops containing the heat rejection devices. A "jumper" line connected the remaining components permitting closed loop circulation by the pump packages for preventing coolant freezing during open loop testing. An additional shutoff valve was installed in loop 1 to isolate the coolant accumulators in the two loops from the small intercoolant loop leakage occurring in the FES during single coolant loop testing. During thermal vacuum testing several Jamesbury ball type shutoff valves developed internal leaks. Inspection of the valves following the test revealed the leaks were at the teflon seals which were deformed when coolant trapped in the valve body froze. To prevent this from reoccurring in future tests a hole will be drilled in the valve ball that allows the trapped fluid to "see" the upstream fluid.

Fully charged the test article contained approximately 272kg (600 pounds) of coolant (Freon-21). Special dryer filters were used to reduce the moisture level in the coolant to less than 10 parts per million prior to servicing. Coolant loop service ports were located outside the test chamber near the coldplate simulators. This easy accessibility allowed real time "topping off" of the coolant loops between test points for leakage makeup.

Duplication of flight thermal environment at each component location in the Orbiter was not required. Therefore, all nonradiator test article components were wrapped in multilayer insulation blankets to minimize heat leaks.

Prior to entering the test chamber after each chamber repressurization air samples were taken to measure Freon-21 concentration. The chamber was vented with ambient air until an acceptable concentration level (less than 10 parts per million) was obtained. Daily air samples were also taken outside the chamber at the test support equipment operators' stations.

TEST SUPPORT HARDWARE

Eight independently controlled support systems located outside the test chamber provided the thermal, pressure and consummable profiles required to simulate the operation of the Orbiter interfaces with the ATCS. Copper and stainless steel tubing insulated with 6 wraps of mylar inside the chamber and 0.013m (0.5 inch) thick armaflex outside the chamber provided the supply and return lines to the test article components. Pressure relief valves were provided in each line.

The Cabin Thermal Simulator delivered deionized water at 431 kg/hr (950 lb/hr) to the interchanger conditioned from 7.2°C (45°F) to simulate cabin heat loads up to 14,078 joule/sec (48,000 Btu/hr). Manual and automatic (drum recorder) temperature control capable of introducing ramps up

60

to 5.6°C (10°F) per minute was provided. Manual valves outside the chamber permitted selection of either or both of the supply lines to the interchanger.

The Payload Thermal Simulator delivered Freon-21 at rates up to 907 kg/hr (2000 lb/hr) to the payload heat exchanger conditioned from 7.2°C (45°F) to simulate payload heat loads up to 8,505 joule/sec (29,000 Btu/hr). Manual and automatic (drum recorder) temperature control capable of introducing ramps up to 5.6°C (10°F) per minute was provided. Manual valves outside the chamber permitted selection of either or both supply lines to the payload heat exchanger. Facility support requirements included water at 0.15 m³/minute (40 gal/minute) and 29°C (85°F), liquid nitrogen and gaseous nitrogen.

Hamilton Standard, the fuel cell heat exchanger vendor, provided, on loan, the test rig used to simulate the fuel cell subsystem thermal interface. The test rig was capable of delivering fuel cell fluid (fluorinent FC40) at flow rates of 181 to 1089 kg/hr (400 to 2411 lbs/hr) in each of 3 loops to the fuel cell heat exchanger at temperatures up to 121°C (250°F) to simulate fuel cell heat loads up to 14,078 joule/sec (48,000 Btu/hr). Manual valves outside the chamber controlling flowrate were capable of introducing ramps equivalent to a 11,732 joule/sec (40,000 Btu/hr) change within 1 minute. Facility support requirements included steam at 23 kg/hr (50 lbs/hr) and 1.2×10^{-6} n/m² gage pressure (175 psig) and gaseous nitrogen.

Hamilton Standard, the hydraulics heat exchanger vendor, provided, on loan, the test rig used to simulate the hydraulic subsystem thermal interface. The test rig was capable of delivering Orbiter hydraulic fluid flowrates from 0 to 907 kg/hr (0 to 2000 lb/hr) in each of 3 loops to the hydraulics heat exchanger over a temperature range of -18 to 21°C (0 to 70°F) to simulate heat removal by the hydraulic loops of up to 5866 joule/sec (20,000 Btu/hr). Manual valves outside the chamber controlled flowrate. Remote controlled bypass valves next to the test article allowed the hydraulic fluid to be conditioned prior to "shocking" the heat exchanger with an "instantaneous" heat load. Facility support requirements included ethylene glycol at 0.03 m³/minute (8 gallon/minute) and -26°C (-15°F), Freon-11 2.268 kg/hr (5000 lb/hr) at -1 to 85°C (30 to 185°F) and gaseous nitrogen.

The Radiator Thermal Simulator delivered Freon-21 at rates up to 1361 kg/hr (3000 lb/hr) to the loop 1 radiator system simulator conditioned from -1°C (30°F) to 21°C (70°F) for simulating radiator heat removal rates up to 16,131 joule/sec (55,000 Btu/hr). Manual and automatic (tracking) temperature control capable of introducing ramps up to 3°C (5°F) per minute was provided. A thermal cutout attached to each heater element monitored fluid/element temperature. Manual valves outside the chamber permitted selection of either or both supply lines to the radiator simulator heat exchanger. Facility support requirements were the same as required for the Payload Thermal Simulator.

The Ground Cooling Simulator delivered Freon-21 at 4,535 kg/hr (10,000 lb/hr) to the GSE heat exchanger conditioned from -12°C (10°F) to -1°C (30°F) for simulating ground cooling rates up to 43,995 joule/sec (150,000 Btu/hr). The flight method of manual temperature control by tracking test article response was used. Manual valves outside the chamber permitted selection of

either or both supply lines to the GSE heat exchanger. Remote controlled
bypass valves next to the test article allowed the ground coolant to be
conditioned prior to "shocking" the heat exchanger with an instantaneous
heatsink. Facility support requirements included water at 0.19 m^3/minute
(50 gallon/minute) and 30°C (86°F) and gaseous nitrogen.

The Flash Evaporator Feedwater Supply Cart delivered deionized water
from two 0.04 m^3 (10 gallon) tanks at pressures up to 10.4 x 10^5 n/m^2 gage
(150 psig) and rates up to 91 kg/hr (200 lb/hr) to the flash evaporator.
Manual controls capable of simulating the ascent pressure transients and
electronic weight scales for measuring water consumption rate were provided.
Facility support requirements included gaseous nitrogen and deionized water.

The feedwater thermal conditioning system conditioned the feedwater to
obtain 7.2°C (45°F) to 66°C (150°F) delivered water to the FES at demand
rates up to 91 kg/hr (200 lb/hr). Computer and set point controllers were
used to introduce ramps up to 5.6°C (10°F) per minute. Multilayer insula-
tion blankets and heaters provided freeze protection for the feedwater lines
during no-flow test periods.

During buildup, servicing and operation of the ATCS test additional
test support equipment was provided.

    a. In-chamber closed circuit television coverage by 8 cameras of the
3 FES exhaust nozzles, 2 flow proportioning valves position indicators,
2 FCA mode control valve position indicators, forward and aft radiator panels
coatings, environment simulator configuration and overall test configuration.
    b. Vacuum pump with cryo trap and micro gage for servicing the freon,
water, FC-40 and hydraulics loops.
    c. Helium leak check test equipment.
    d. Pneumatic pressure control system for automatic valve positioning
    e. Gas analyzer, first aid and protective equipment for handling leaks
or spills of Freon-21 or FC-40.
    f. Heaters and temperature controllers to maintain FES exhaust duct
pressure instrumentation lines above 10°C (50°F)
    g. Digital meters for the critical parameters that monitor health of
test article and support equipment during test facility power or data system
outages.
    h. Wang 2200 and Hewlett-Packard 9830 mini-computer systems for off-
line processing of test data for anomaly investigations and FES water carry-
over determination.

                          DATA MANAGEMENT

    Space Environment Test Division's Flexible Data System (FLEX) using
Hewlett-Packard 2112 and 2117 computers was the primary real time processor
of ATCS test data. Raw data from temperature, pressure, flow rate, frequency,
current and voltage instrumentation was simultaneously displayed, used in
calculations and stored.

Instrumentation

Within the test article flight and engineering test instrumentation were co-located for evaluation of response, recovery, and amplitude of changed change during transient operations. Additional engineering test instrumentation were selected and installed to obtain detailed system performance data and evaluate the timelines and meaningfulness of flight data. The following is a summary of the instrumentation required for the test article and support equipment:

440 Surface Thermocouples	7	Pressure transducers
114 Immersion Platinum Probes	6	Baratron Pressure Sensors
73 Current transducers	2	Wattmeters
61 Voltage transducers	2	Quantity sensors
30 Radiometers	2	Thermisters
21 Turbine flowmeters	1	Frequency meter

Data system sample rate of the 26 flight measurements was set at the flight level of 2 seconds. The remaining test instrumentation was sampled at 2, 3, 5, 10, 15 or 30 second intervals depending on the dynamic response required from that measurement.

Real Time Processing

FLEX software was configured to acquire and process 1068 real measurements, calculate 424 pseudo measurements and compute stimuli for 116 control channels for the test article, support equipment and facility systems. Formats for 162 pages were defined and available for display on 12 CRT's in the control rooms. Additional pages could be constructed real time. Data displays could be made into hard copy through "instantaneous" system or single page SCOOPS (upon keyboard command). Two TV cameras monitored a FLEX terminal display for retransmission of 2 FLEX data displays to several TV monitors installed at operator stations near the test support hardware.

Data logs, maintained by test team members, were used to record real time observations and impressions of test article performance. FLEX made a permanent record of the processed measurements on test history magnetic tapes for post-test point data evaluation. During the test, 24-hour processing of selected portions of the test history tapes was provided by the IDSD (Institutional Data Systems Division) on the UNIVAC 1110 and 1108 EXEC 8 computer systems. Post-test time history plots of key parameters for assessing selected component and subsystem performance were prepared by IDSD from the FLEX test history tape for each test point. Up to 6 measurements were put on a plot, 217 plots were formatted and combined into 25 performance evaluation groups. Microfilm and hard copy were provided of each plot.

63

TEST CONDUCT

Test chamber occupancy began in June 1978, and ended in March 1979 after 4 weeks of testing which included four 24-hour days of integrated closed loop testing. Test article fluid charging began in late December 1978 followed by 2 weeks of ambient checkout testing and 2 days of vacuum checkout testing. A 3 week "open loop" test of portions of the ATCS was completed prior to configuring the test article for "closed loop" testing. A 3 day vacuum checkout test preceded the "closed loop" test.

The 130 members of the test team manned 40 stations, providing 24-hour coverage with three 8-hour shifts. The test team included two control groups located in separate control rooms. The 15 stations of the test control group included the test director and were responsible for the conduct of the test, technical supervision and control of the systems within the test article and the operation of the test support and facility systems. The 5 stations of the data analysis control group were responsible for the test procedures, test sequencing, data collection and evaluation and success/failure assessment for each test point. Standard hardline communication network protocol was observed by all test team members. A voice record tape of all communication channels was obtained.

One CRT display in the test control room was dedicated for a "flight/test control" test team member to monitor ATCS performance. Flight measurements on a page identical to flight data format and ATCS controls similar to onboard controls were used by the "flight controller" to configure and control the ATCS. Pretest analytical predicitions of the transient heat loads seen at the ATCS interfaces with other Orbiter systems were used to simulate the ascent, on-orbit and entry portions of a typical mission. Credible failures cf selected components within the ATCS and of subsystems that interface ith the ATCS that may occur during ascent, on-orbit and entry mission phases were simulated. During each situation the "flight controller" used current flight procedures, instrumentation and displays to assess the situation, reconfigure and stablize the ATCS. When necessary during the conduct of the test special procedures were developed to assist in diagnostic activity, problem resolution and timeline constraints.

Timelining of the 30 closed loop test points followed the guidelines that test points requiring similar conditions shall be grouped in priority order and that proceeding from one group to another shall take the path of minimum change in existing conditions. Radiator environment and chamber pressure were the most time consuming parameters to establish. Using "drum plotters" to input transient heat load profiles at the various Orbiter interfaces to ATCS provided uniformity, repeatability and "first time" success for the majority of the test points. The successfulness of the simultaneous independent operation of the 8 heat sources was due largely to the time caken by the test team to understand the interrelationship (e.g., line lag, heat loss, etc.) of each supporting system with the test article during the checkout periods.

TEST RESULTS

The integrated ATCS achieved all planned test objectives, demonstrated the full compatibility of the integrated ATCS hardware and controls and demonstrated that the ATCS can meet or exceed all performance requirements. During the conduct of the test hardware, instrumentation and procedure changes which would improve subsystem performance, reduce crew involvement, stream-line subsystem operation and reduce weight, power and volume requirements were noted and are described in reference 3.

The ATCS successfully supported the prelaunch, ascent, on-orbit, entry and post-landing portions of a typical Shuttle mission. All ATCS fluid systems and mechanical hardware were functional throughout the test. No evidence of subsystem or component performance degradation with 6 cycles between sea level conditions and thermal vacuum exposure was found. The scheme for heat load sharing and manual/automatic control and sequencing of ATCS heat sinks met all requirements. ATCS thermal capacity and response during all mission phases met or exceeded require ents. All normal and failure related transients caused by interfacing Orbiter and payload sub-systems were accommodated without requiring configuration changes or special procedures. The test demonstrated that the current flight controls and procedures are satisfactory (with minor changes) for properly sequencing, monitoring and controlling the ATCS during normal mission and si lated failure operations. However, several "system transients" found to occur during normal ATCS operation will require both procedural and crew warning limit value changes. Several special procedures developed during the test to assist diagnostic activity, problem resolution and timeline constraints are recommended for inflight use. The test demonstrated that the current ATCS flight instrumentation, displays and warning limits are adequate for flight crew and real time ground controller monitoring of subsystem status. Routine and contingency activities were found in which crew time would be significantly reduced by making minor changes to existing instrumentation. The flight instrumentation was also verified to be adequate for satisfying flight test objectives and post-flight data evaluation. ATCS thermal charac-teristics during transient operation and flight test configurations were obtained for flight verification and math model correlation.

CONCLUSIONS

The integrated ATCS test program reaffirmed the value of system level testing under thermal vacuum conditions. The tangible benefits are the improvements to the hardware and procedures cited in the test report. Equally important are the intangible benefits derived from the confident and experience gained in the understanding of the signature of the ATCS by the personnel who will train the flight crews and monitor ATCS performance during the Shuttle missions. Daily coordination and cooperation y member of the user and service organizations made possible the successful planning, buildup, integration, checkout, operation and timely completion of the ATCS test without compromising either the technical objectives or financial constraints of the test.

REFERENCES

1. Jaax, J. R., "Orbiter Active Thermal Control Subsystem Description and Test History," Crew Systems Division CSD-SH-126, Johnson Space Center JSC 11295, July 20, 1978.
2. Behrend, A. F., G. D. Chandler, and H. R. Howell, "Thermal Vacuum Performance Testing fo the Space Shuttle Orbiter Radiator System," AIAA paper, September 1980.
3. Jaax, J. R., "Integrated Active Thermal Control Subsystem Test Final Report," Crew Systems Division CSD-SH-143, Johnson Space Center JSC 14182, August 24, 1979.
4. Jaax, J. R., M. A. Melgares, and J. R. Frahm, "Thermodynamic Performance Testing of the Orbiter Development Flash Evaporator System," AIAA paper, September 1980.
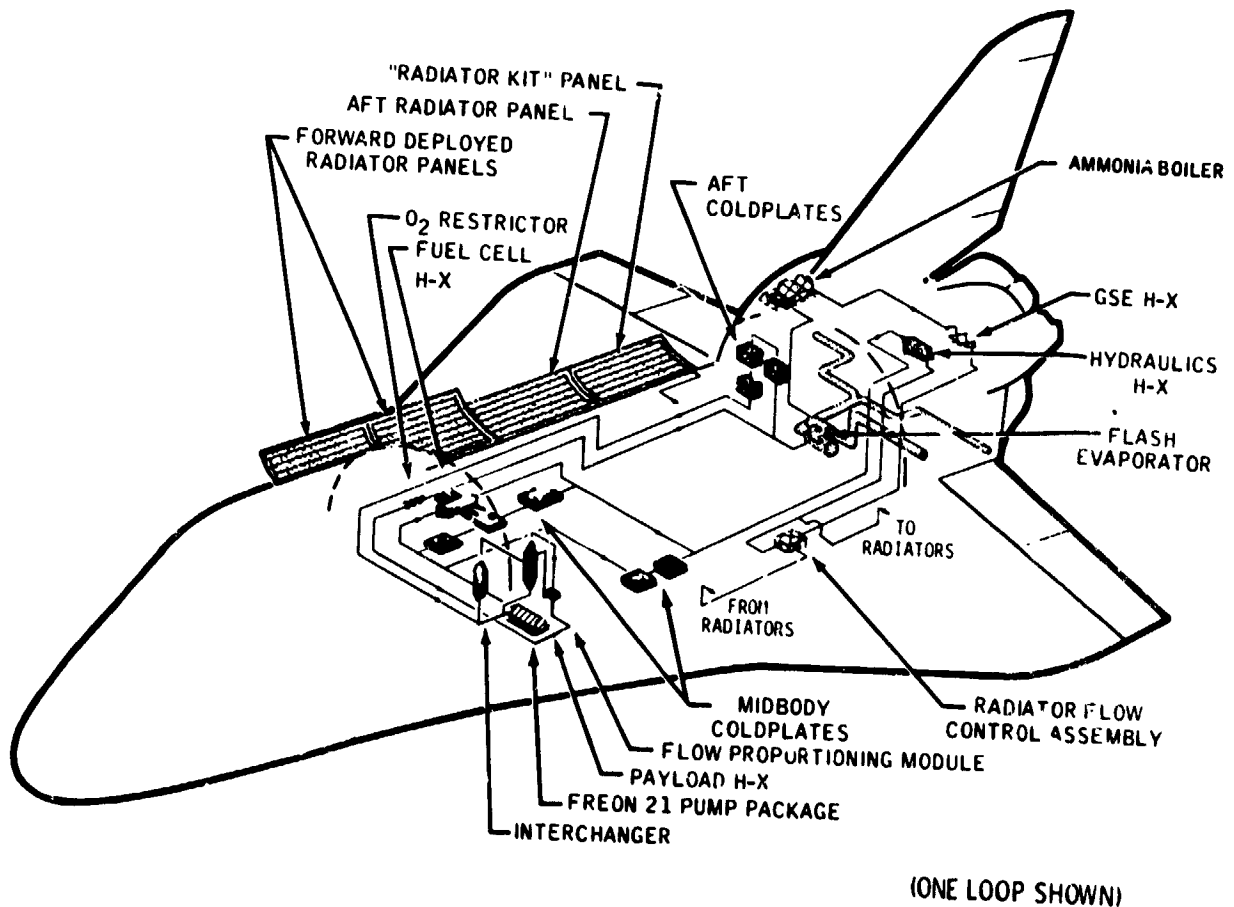
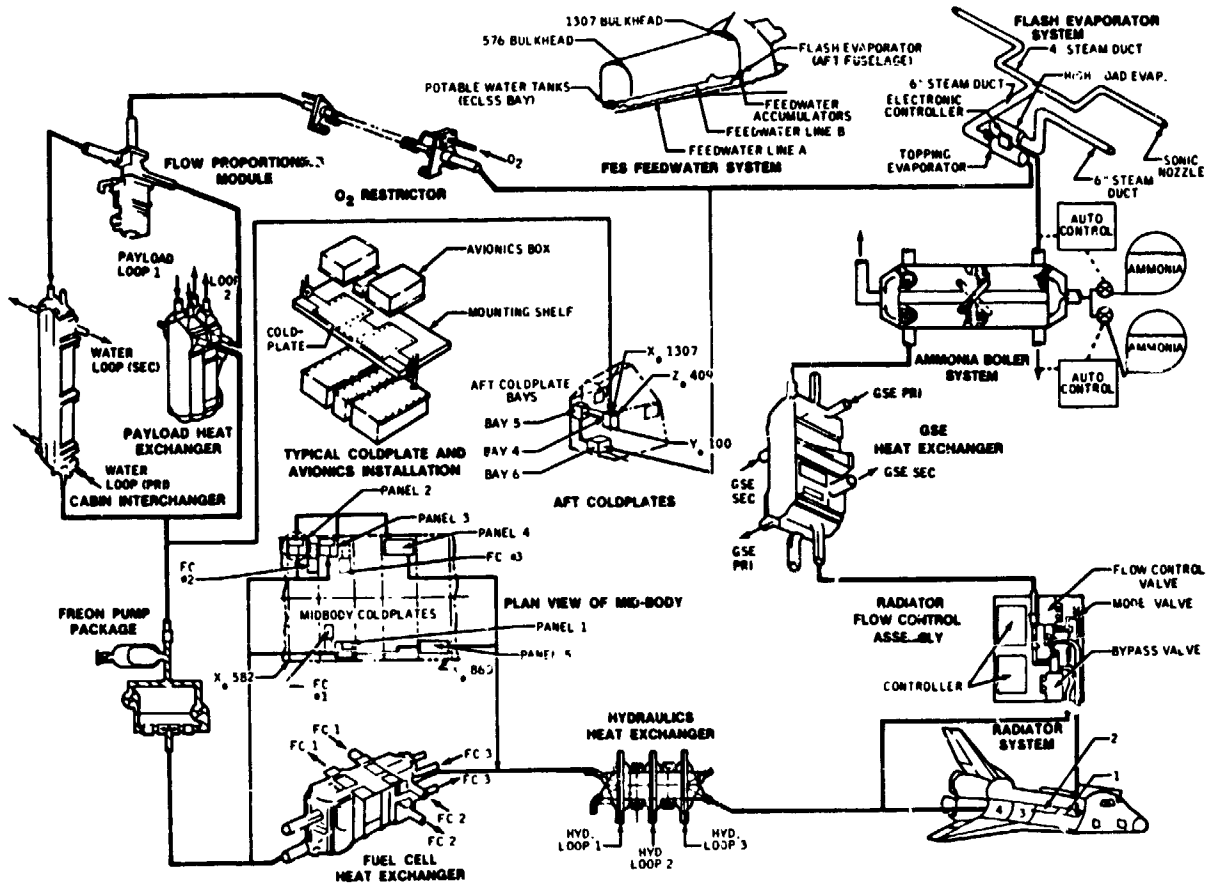Figure 1 Active Thermal Control Subsystem Location in Space Shuttle

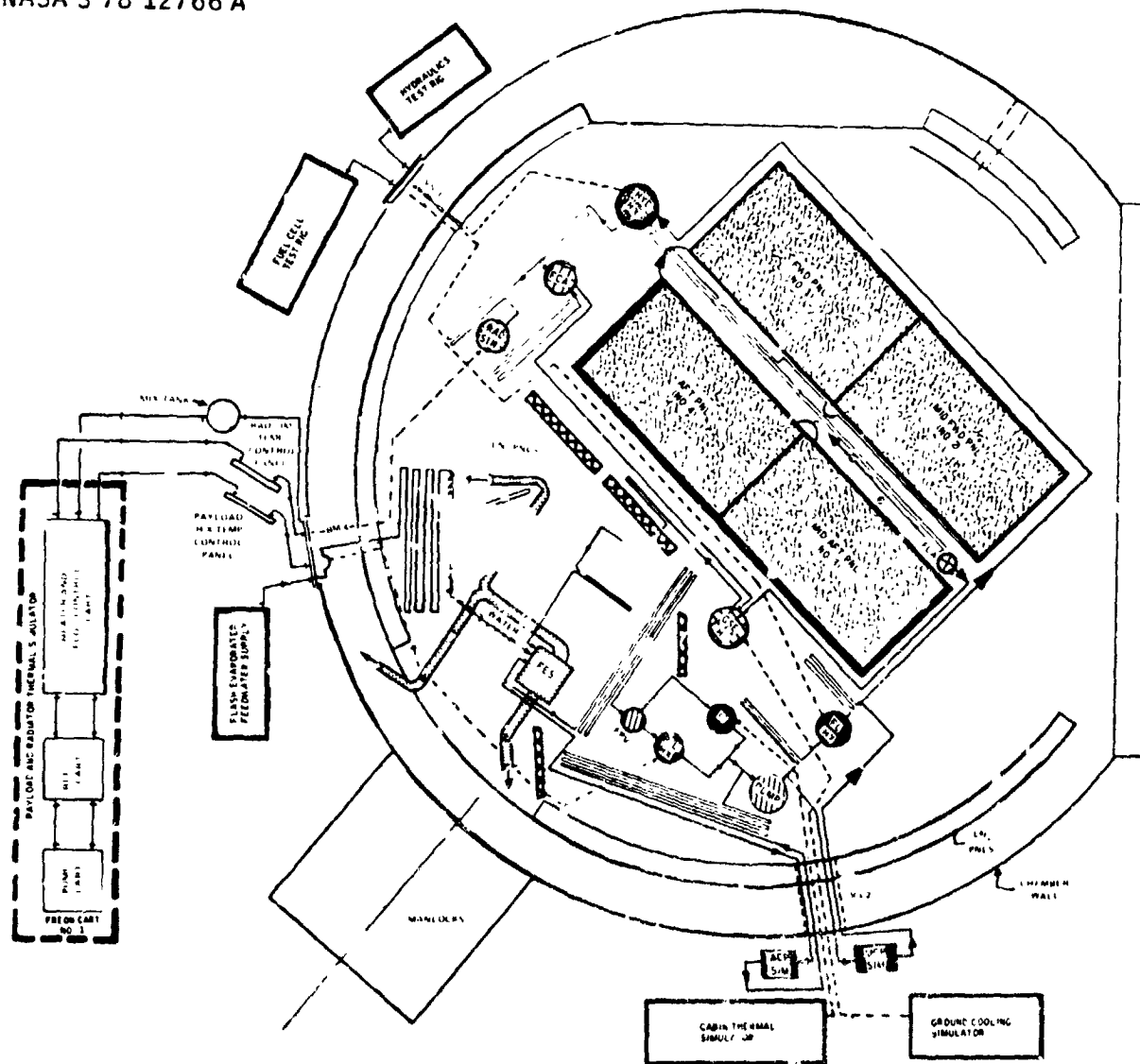Figure 2   Orbiter Active Thermal Control Subsystem Schematic

NASA S 78 12766 A

Figure 3   Layout of integrated ATCS in Test Chamber A

NASA National Aeronautics and
Space Administration

LN2 SHIELDS

R CAGE ASSEMBLY

FORWARD RADIATOR
PANEL (NO. 1)

PAYLOAD BAY DOOR
SIMULATORS

MID FORWARD RADIATOR
PANEL (NO. 2)
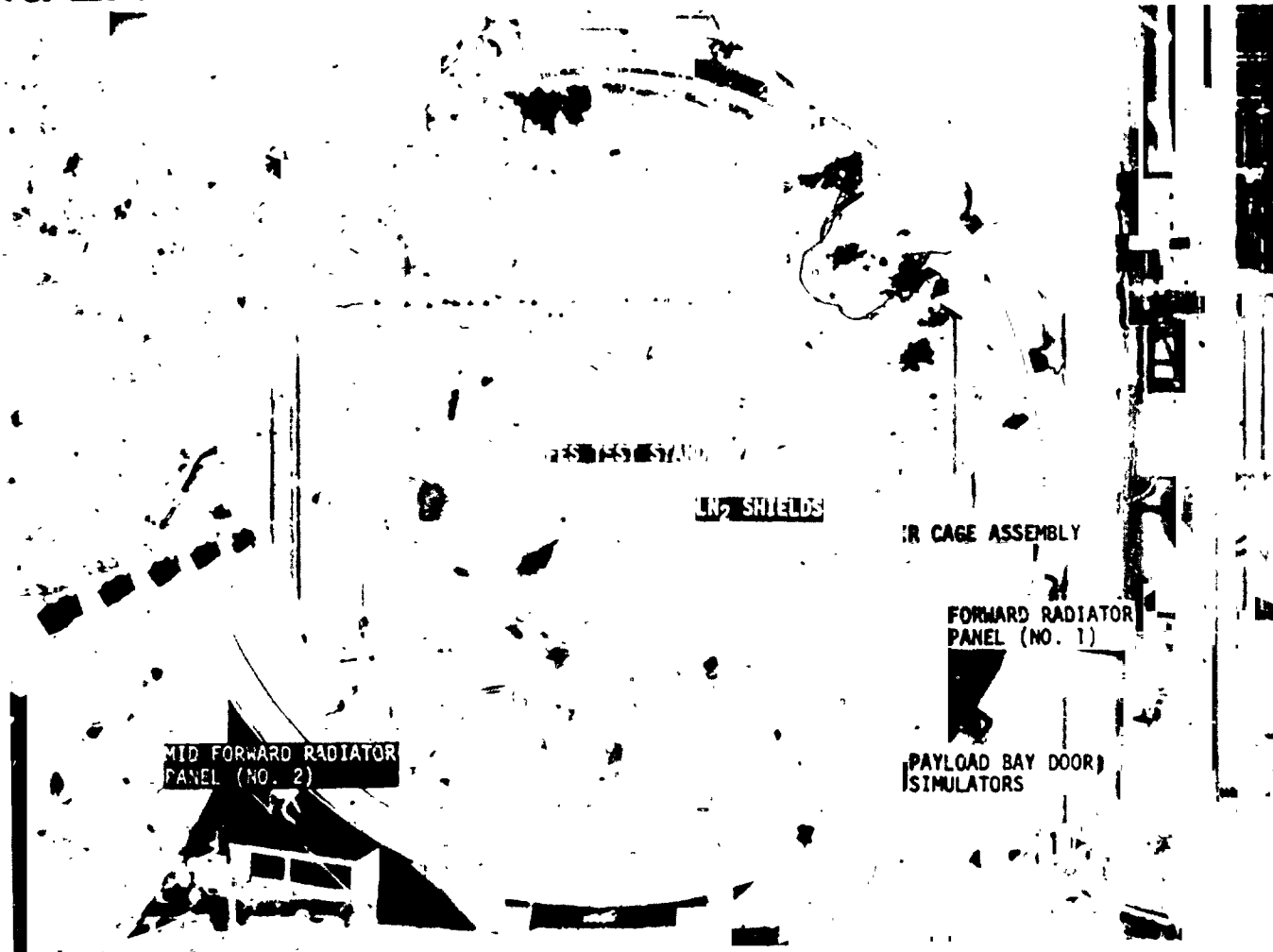
Figure 4   View of ATCS Test Configuration

Table I   Integrated ATCS Test Hardware

- **RADIATOR SYSTEM**
  - FLIGHT TYPE FLOW CONTROL ASSEMBLIES (DEVELOPMENT AND QUALIFICATION)
  - FLIGHT TYPE RADIATOR PANELS (RIGHT SIDE-LOOP 2)
    - TWO "FLIGHT/TEST" PANELS (FORWARD AND AFT)
    - TWO DEVELOPMENT PANELS (MIDFORWARD AND MIDAFT)
  - FLIGHT TYPE INTERPANEL PLUMBING
  - SIMULATED LEFTSIDE LOOP 1 RADIATOR SYSTEM *(RSECS INTERCHANGER)
- **FLASH EVAPORATOR SYSTEM**
  - FES PACKAGE (DEVELOPMENT UNIT)
    - FLIGHT TYPE HIGH LOAD AND TOPPING CORES
    - FLIGHT TYPE VALVE/NOZZLE ASSEMBLIES
    - FLIGHT TYPE CONTROLLERS
  - EXHAUST DUCT/NOZZLE SYSTEM
    - FLIGHT TYPE STRUCTURE/BELLOWS
    - FLIGHT TYPE EXHAUST NOZZLES
    - FLIGHT TYPE HEATERS (REDUCED REDUNDANCY)
    - FUNCTIONALLY SIMULATED HEATER CONTROL
  - FEEDWATER SYSTEM
    - FLIGHT TYPE PLUMBING LINE (SIZE AND LENGTH)
    - FUNCTIONALLY SIMULATED THERMAL CONTROL
    - FUNCTIONALLY SIMULATED ACCUMULATORS
- **AMMONIA BOILER SYSTEM**
  - NOT INCLUDED

- **FREON COOLANT LOOP**
  - FLIGHT TYPE FLOW PROPORTIONING MODULES (QUAL AND TEST UNITS)
  - FLIGHT TYPE INTERCHANGER (RSECS UNIT) - REDUCED PERFORMANCE CAPABILITY
  - FLIGHT TYPE PAYLOAD H-X (RSECS UNIT)
  - FLIGHT TYPE FREON PUMP PACKAGES - ONE PUMP PER PACKAGE (RSECS PUMPS, OV101 ACCUMULATORS)
  - FLIGHT TYPE FUEL CELL H-X (OV101 UNIT)
  - FLIGHT TYPE HYDRAULICS H-X (RSECS UNIT)
  - FUNCTIONALLY SIMULATED AFT COLDPLATES (HEAT, FLUID VOLUME AND ΔP)
  - FUNCTIONALLY SIMULATED MIDBODY COLDPLATES (HEAT, FLUID VOLUME AND ΔP)
  - FLIGHT TYPE GSE H-X (RSECS UNIT)
  - FLIGHT TYPE PLUMBING (LINE SIZE AND LENGTH)
  - FLIGHT TYPE INSTRUMENTATION EXCEPT FLOWRATE
- **INTERFACING ORBITER SYSTEMS**
  - FUNCTIONALLY SIMULATED CABIN WATER LOOP (HEAT, FLUID VOLUME, FLOW, FLUID)
  - FUNCTIONALLY SIMULATED PAYLOAD COOLANT LOOP (HEAT, FLOW, FLUID)
  - FUNCTIONALLY SIMULATED FUEL CELL COOLANT LOOPS (HEAT, FLOW FLUID)
  - FUNCTIONALLY SIMULATED HYDRAULICS COOLANT LOOPS (HEAT, FLOW, FLUID)
  - FUNCTIONALLY SIMULATED GSE COOLANT LOOP (HEAT, FLOW, FLUID)

*RSECS - REPRESENTATIVE SHUTTLE ENVIRONMENTAL CONTROL SYSTEM (CREW SYSTEMS DIVISION HARDWARE DEVELOPMENT, TEST AND EVALUATION PROGRAM)

USE OF CRYOPUMPS ON LARGE
SPACE SIMULATION SYSTEMS

L.E. McCrary[*]

ABSTRACT

The need for clean, oil-free space simulation systems has demanded the development of large, clean pumping systems. The assurance of optically dense liquid nitrogen baffles over diffusion pumps prevents backstreaming to a large extent, but does not preclude contamination from accidents or a control failure. Turbomolecular pumps or ion pumps achieve oil-free systems but are only practical for relatively small chambers. Large cryopumps have been developed and checked out which do achieve clean pumping of very large chambers. These pumps can be used as the original pumping system or can be retrofitted as a replacement for existing diffusion pumps.

INTRODUCTION

As spacecraft become more complicated, the need for simulation systems which more closely duplicate the space environment and prevent contamination to the spacecraft are needed. Cryogenically refrigerated surfaces have been used extensively for thermal sinks and for the creation of the vacuum environment. Hardgrove [1] discussed several existing vacuum chambers in 1972 and Wang, Collins, and Haygood [2] discussed general cryopumping in a paper in 1961. More recently, Wilson and Watts [3] evaluated the design and operational characteristics of a cryopumping system for a 2500 liter chamber.

Several other chambers at various facilities extensively use cryopumping to achieve an oil-free vacuum. However, extensive work is still being done in space simulation chambers evacuated by oil diffusion pumps which are well-trapped.

This paper discusses the development of a large 1.2 meter (48") diameter cryopump which has been developed to evacuate large space chambers. These pumps were designed to have high pumping speeds for all gases, including hydrogen and helium. They provide a vacuum environment which is oil-free and not subject to contamination from the pumping system.

The refrigeration system in the pump is supplemented by a liquid nitrogen (LN_2)-cooled shroud to prevent thermal radiation to the $15^\circ K$ surface.

TYPES OF CRYOPUMPS

The common LN_2-cooled or refrigerated baffle above diffusion pumps is used to pump water and to prevent backstreaming of the oil. This is, in effect, a cryopump for water vapor.

Liquid nitrogen-cooled shrouds used in chambers for cold walls are useful for pumping water and condensibles such as solvents and plasticizers, and to provide a thermal simulation of the space environment.

[*]High Vacuum Equipment Corp., Hingham, Massachusetts

The third type of cryopump is the $20^{\circ}K$ helium shrouds which are sometimes used in conjunction with the LN_2 shroud. These temperatures are obtained with a helium refrigerator and can be used with or without charcoal to supplement the pumping of H_2 and He. These cold panel pumps require large He refrigerators and are expensive to operate.

Another type of cryopump is one using liquid helium (LHe) as a refrigerant and is used most commonly in a research-size chamber.

The fifth kind of cryopump is the commercially available pump which bolts onto a flange and is used to replace or supplement other types of pumping such as diffusion pumps or turbomolecular pumps. These cryopumps have been available in sizes to 250mm (10") diameter and are now commercially available up to 500mm (20") diameter.

There is, however, a requirement for cryopumps larger than 500mm (20"). In the process of specifying and fabricating large space simulation chambers, High Vacuum Equipment Corp. has found it impractical to use many smaller cryopumps and has designed a 1.2m (48") diameter pump.

Since cryopumps normally are valved off from the system, and a multiplicity of valves and pumps add significant cost to the pumping system, it is highly desirable to use large cryopumps. If the pumps are separated from the chamber by a valve, they can be regenerated individually during long tests and can be placed back on-stream a a fresh pump.

Gate valves which seal in both directions (will hold vacuum with atmospheric pressure on either side) are preferable to poppet valves which will seal in only one direction. Poppet valves will not allow regeneration during te.., but will allow evacuation and preconditioning of the pumps before the chamber is evacuated for testing.

Neither gate valves nor poppet valves are required if the cryopumps do not require regeneration during testing. However, if the pumps should malfunction and warm up during the test, the gas which has cryocondensed onto the cold surface will be released from the pump and will return to the space chamber and possibly contaminate the test article. Therefore, valves are recommended which are automatically interlocked to close when the cryopump warms up above $25^{\circ}K$ or if the pressure in the chamber should rise to above a few microns.

4. DESIGN OF 1.2m CRYOPUMP

Smaller cryopumps which are commercially available use the first stage refrigerator to cool the radiation shield to $70-125^{\circ}K$ to diminish the heat load on the $15^{\circ}K$ pumping surface. For larger pumps, this becomes impractical without the use of multiple refrigerators and compressors. High Vacuum Equipment opted to cool the radiation shield (shroud) with LN_2 since LN_2 is readily available at larger space chambers to cool the shrouds, and the additional use of a few liters per day is not detrimental. For smaller cryopumps, the use of a refrigerated radiation shield is cost effective. The elimination of LN_2 is a big selling factor for cryopumps, but elimination of LN_2 at space chambers is not possible, so therefore it is cost-effective for very large cryopumps to

use LN_2.

High Vacuum Equipment developed a cryopump 1.2m (48") diameter, shown in Figure 1 This size was selected to optimize size, pumping speed, and standardization. The pump uses a LN_2-cooled entrance chevron radiation baffle, LN_2-cooled cylindrical walls, and an LN_2-cooled rear head shroud, which mates with the shield on the back head cooled by the first stage of the refrigerator. These cold surfaces completely surround the $15^\circ K$ surfaces. The LN_2 surfaces pump the water in the chamber and all readily-condensible gases. The $15^\circ K$ surfaces are used to pump the atmospheric gases, such as N_2, O_2, and Argon. The only gases not pumped by either the $77^\circ K$ or the $15^\circ K$ surfaces are the "noncondensible gases", Neon, H_2, and He. These gases are pumped by the $15^\circ K$ charcoal surface which is thermally isolated behind a $15^\circ K$ chevron. The charcoal covers a 250 x 650mm (10 x 25 inch) surface.

A silicon diode temperature sensor is used to monitor the temperature of the second stage sail and charcoal "box". The temperature sensor is normally attached to the sail to ensure that the thermal joint is sound between the second stage flange and the copper cold surfaces.

Eight of these pumps have been fabricated to date. One has been installed on a stainless steel, internally polished 2.1m (8' x 12') diameter x 3.7m long chamber at Rockwell International's Seal Beach facility. This chamber is the subject of another paper at this conference. One pump with a speed of approximately 38,000 1/sec has achieved an ultimate pressure in the unbaked stainless steel chamber in the mid 10^{-9} torr range with a room-temperature aluminum shroud. With a baked chamber and a $77^\circ K$ shroud, it may be possible to evacuate the chamber to the 10^{-10} torr range. The shroud is a standard tube-on-sheet shroud with a chevron baffle pumping port in the vicinity of the 1.3m (52") diameter horizontal poppet valve.

Three of these cryopumps are installed on the Canadian Communications Research Centre space simulation chamber at Shirley Bay, Ottawa, Ontario, scheduled for completion in December 1980. This system is schematically shown in Figure 2. Each cryopump is isolated from the chamber with a 1.2m (48") gate valve capable of sealing with atmospheric pressure in either direction. The CRC chamber is a vertical top-loading 7.3m (24') diameter, 10.7m (35') high stainless steel chamber which is internally polished. A LN_2 shroud encloses a working space of 6.7m (22') diameter by 10.7m (35') high. Ultimate pressures and pumpdown curves are not available at this time, but an ultimate of 5 x 10^{-9} torr with a cold shroud is anticipated.

In both of the above applications, the requirement for an oil-free chamber with no possibility of contamination was the driving factor for the specification of cryopumps instead of diffusion pumps. Likewise, in existing large chambers, the decision is either being made or considered, to replace the diffusion pumps with cryopumps. This retrofit is being done for the 8.8m (29') diameter x 19.8m (65') Martin-Marietta, Denver chamber. Four 1.2m (48") oil diffusion pumps are being replaced with an improved version of the pump discussed above. The four cryopumps for Martin are larger in diameter-1.3m (52"), but will still mate with the 1.2m (48") diameter standard flange. The increased diameter and increased spacing on the entrance chevron has increased the pumping speed to approximately 48,000 1/sec. This pumping speed has not

yet been measured, but conductance calculations indicate this substantial increase in pumping speed.

5. PUMPING SPEED MEASUREMENTS

The pumping speed of the pumps was measured using the AVS Standard Method 4.8, "Procedure for Measuring Speed of Pumps Without Working Fluid." An inclined manometer with silicone oil for the displacement fluid was used. Corrections were applied as defined by Stevenson (4) for the inclined manometer tube. Ion gauge corrections were made for the various gases. The pumping speed measurements are shown in Table I.

More extensive pumping speed tests are in process using the constant pressure gas flow measurement method used here and the partial pressure decay with time using a Residual Gas Analyzer (RGA). The pumping speed measurements illustrate the high pumping speeds achievable with cryopumps.

CONCLUSIONS

The use of large commercially available cryopumps is the most reliable means of achieving a vacuum environment which is assured of being free of contamination from the pumping system. To paraphrase Yarwood (5) the pump of the future is the cryopump. Cryopumps will be used instead of diffusion pumps in future systems and diffusion pumps will be replaced by cryopumps on existing systems to ensure the elimination of oil contamination.

REFERENCES

1. W.F. Hardgrove, "Cryogenic Applications for Environment Simulation", AIChE Symposium Series No. 125, <u>Vacuum Technology at Low Temperatures</u>, S.Alexander, editor, 1972, pp.31-39.

2. E.S.J. Wang, J.A. Collins, J.D. Haygood, "General Cryopumping Study," <u>Advances in Cryogenic Engineering</u>, Vol. 7, Plenum Press, N.Y., 1961.

3. N.G. Wilson, K.N. Watts, "Design and Operational Characteristics of the Cryopump High Vacuum System for the 2500-1 Target Chamber of the Helios Test Facility," J. Vac. Sci. Tech., Vol. 17, No.1, Jan/Feb. 1980, pp. 270-273.

4. D.L. Stevenson, "Improving the Accuracy of Metering Gas Flow and Computing Throughput," <u>Vacuum Symposium Transactions</u>, 1961, pp. 555-559.

4. J. Yarwood, "The Production of Vacuum: Past, Present, and Future," Vacuum, Vol. 29, No.8/9, Aug/Sept. 1979, pp. 313-317.

TABLE I

Gas	Pumping Speed l/sec.
Nitrogen	39,278 (Avg. of ˄ meas.)
Argon	30,575 (Avg. of 3 meas.)
Helium	5,729 (Avg. of 2 meas.)

15°K SAIL.

ACTIVATED CHARCOAL.

DIODE TEMP SENSOR.

77°K BAFFLE & SHROUD.

CTI MODEL 1020 REFRIGERATOR

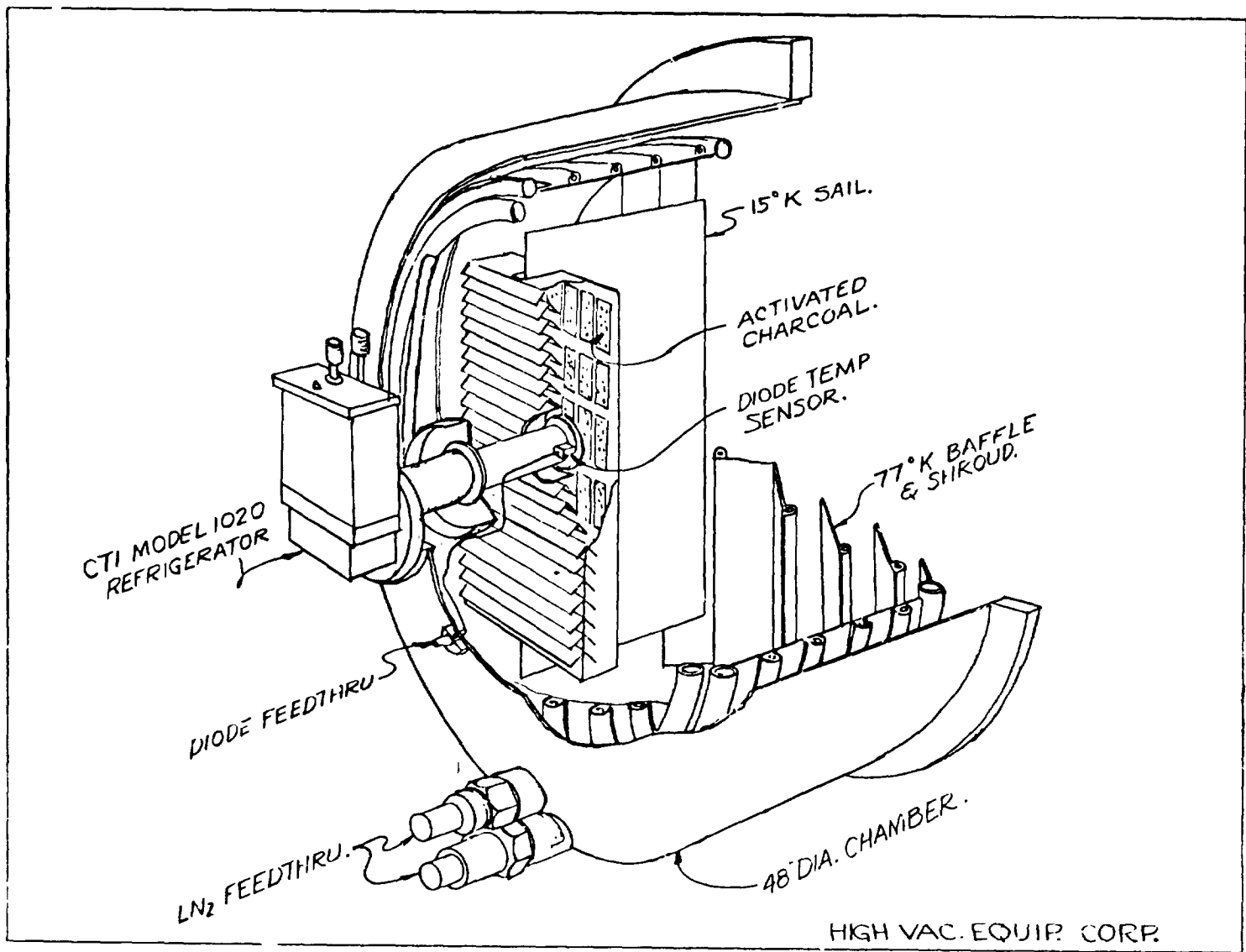DIODE FEEDTHRU

LN₂ FEEDTHRU.

48˝ DIA. CHAMBER.

HIGH VAC. EQUIP. CORP.
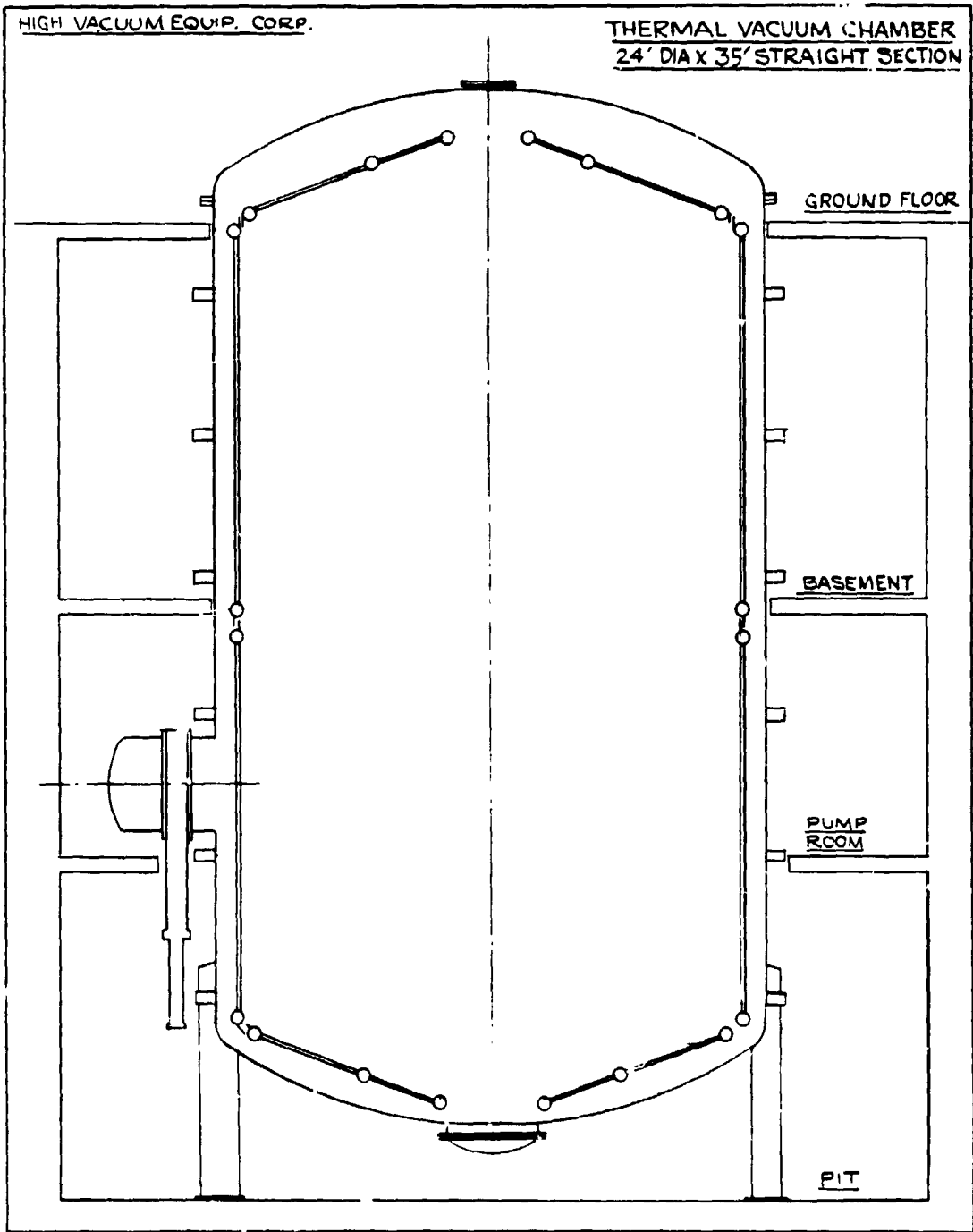
Figure 1   Schematic of 1.2 Meter Diameter Cryopump

Figure 2 CRC Thermal Vacuum Chamber

SHUTTLE REMOTE MANIPULATOR

SYSTEM HARDWARE TEST FACILITY

C.G. Wagner-Bartak*
J.A. Middleton*
J.A. Hunter**

ABSTRACT

The Shuttle Remote Manipulator (RMS) is designed and built for operations in a zero gravity environment. As such, the ground test facility for the integrated RMS must simulate conditions which will support verification of the overall system performance.

In order to allow ground test operations, a test facility was constructed with an area of 60 ft. x 120 ft. and extremely tight tolerances on floor flatness and slope. An air bearing support structure (Systems Test Rig - STR) was designed for the RMS to operate with 4 degrees of freedom.

This paper describes the RMS system test facility and systems tests conducted to date.

INTRODUCTION

The Space Shuttle Remote Manipulator (RMS) is an anthropomorphic, man-machine system primarily used for deploying and retrieving of payloads (satellites) in orbit. The National Research Council of Canada (NRCC) is funding the design, development, testing and evaluation of the first flight system. Detailed system requirements jointly formulated by NASA, NRCC and Spar Aerospace Limited, the prime contractor, define that the RMS shall be capable of deploying a 65,000 lb. payload and retrieving a 32,000 lbs. payload. The Manipulator Arm (MA) is 601 in. long and consists of a Shoulder (2 DOF), Elbow (1 DOF) and a Wrist (3 DOF) connected by upper and lower arm booms and a payload grappling device called the End Effector.(1)(2) The RMS system is illustrated in Figure 1.

Since the RMS is designed to operate in space environment, test and verification of expected performance require special facilities. In addition to ground tests, two simulation models are used to provide in depth analysis of performance under varying conditions.

*   Spar Aerospace Limited, RMS Division, Toronto, Canada
** National Research Council, Ottawa, Canada

SYSTEM DESIGN DESCRIPTION

The RMS is comprised of four major subsystems:

(a) Mechanical Arm Subsystem
(b) Display and Control (D&C) Subsystem
(c) Electrical Subsystem
(d) Software Subsys ...

Canada is responsible for the production of tne first three subsystems and the requirements definition of the fourth. The software subsystem is implemented within the Orbiter General Purpose Computer (GPC) which provides automated and semi-automated control of the RMS.

Control of the RMS is provided by the D&C Subsystem. This subsystem contains a Display and Control Panel, Translational Hand Controller (THC) and Rotational Hand Controller (RHC). These provide the Orbiter crew with control of the Mechanical Arm.

The D&C Subsystem interfaces with the Manipulator Controller Interface Unit (MCIU) which in turn provides the interface to both the GPC and the Electrical Subsystem within the Manipulator Arm. Both the D&C Subsystem and the MCIU form part of the Orbiter cabin equipment. The Mechanical Arm contains the balance of the electrical subsystem which provides control of each of the degrees of freedom as well as the Eno Effector.

RMS PERFORMANCE EVALUATION PROCESS

The verification process of the RMS is undertaken through non-real-time and real-time simulation analysis component tests system tests and orbital flight tests. Primary means of verification of overall performance prior to flight is through simulation and systems test. The benchmark simulation model of the RMS is the ron-real-time model "ASAD". ASAD incorporates up to thirty selectable flexible modes and is used to provide complete confirmation regarding the dynamics of operation such as deployment and retrieval of payload singularity management, automatic trajectories and arm positioning capability.

In order to evaluate operator interaction with the RMS a real-time simulation facility "SIMFAC" is used. The SIMFAC model is based on ASAD but is restructured to permit real-time processing.(3)

The requirements for the RMS Systems Test Rig (STR) were established as part of the verification process of simulation, analysis and test. It was recognized that an attempt to perform a completely representative test on the RMS would be extremely complex and expensive. A trade-off study addressed the following global requirements:

(a) The exercise of a fully assembled RMS in a 1-g laboratory environment.

(b) Test two models; an Engineering Model (EM), and a Flight Model (FM).

(c) The verification RMS performance.

(d) Provide hardware performance data in support of the computer simulation programs.

The most complicated STR appeared to be a true three-dimensional rig and the simplest was a two dimensional horizontal plane rig. Construction of the system integration and test floor area was based on the probability that a single plane system would be required. A 60' x 120' area was provided. As a result of the initial studies conducted, it was determined that a system based on planar motions would provide the best overall compromise between cost, schedule and performance.

The following requirements were an outgrowth of the study and provided the design drivers for the STR:

(a) Provide a qualitative assessment of system operation.

(b) Verify or substantiate those elements of the Contract End Item Specification which could only be done by an integrated system test.

(c) Support development testing; Primary Design Drivers were:

   i) Design to accommodate pitch and yaw coupled motions (serially).

   ii) Accommodate arms with varying weights from 600 lbs. to 1,000 lbs.

   iii) Friction .003.

   iv) Failsafe such that any failure within the support system would not damage the RMS.

   v) Accommodate the floor fluctuations up to .25 inches over 3 feet.

   vi) Minimum interaction with mechanical arm dynamics.

   vii) Permit joint to travel over the full operational range.

   viii) Permit the arm to float on the STR such that dynamic or parasitic coupling from the STR would be minimized.

The requirements for payload operations in the integration area with the RMS were based on limitations that could be expected with a coefficient of friction of approximately .0025. The minimum force capability requirement from a straight arm is approximately 12 lbs. The maximum payload size that can be driven on air bearings would be in the order of 4,000 lbs.,

C-2

81

assuming 20% loss in torque capability of the arm due to STR friction. On the basis of information which would be gained from loaded arm tests, it was decided not to use a large mass payload for the Engineering Model arm tests and restrict operations to the unloaded arm with a low mass payload (50 lbs). This would permit evaluation of system stability during track and capture of a payload.

THE SYSTEMS TEST RIG

The STR is shown in Figure 2. The Shoulder joint is anchored on a fixed base (plinth). The shoulder can be attached to the plinth in either the pitch coupled or yaw coupled mode. The upper arm boom is supported at the shoulder and elbow interface flanges by the upper arm STR. This section provides a single 8" air bearing pad at the Shoulder interface and two 8" pads at the Elbow. Spacing between the Elbow pads is designed to counteract any pad flutter instability and any tendency to tip during arm acceleration or braking.

The lower arm is supported in the same manner at the upper arm Elbow flange and Wrist electronics compartment interface flange. One air pad is provided at the Elbow and two at the Wrist interface (Figure 3).

The Wrist and End Effector are supported on three air pads as shown in Figure 2 such that loading is balanced between the pads.

CRITICAL DESIGN AREAS OF THE STR

Since the STR is used to assess performance of flight hardware, undue loading of the system must be avoided. In order to meet this requirement, operational loads greater than 50% of the endurance limit must be avoided. Drivers to the design of the STR become:

(a) Joint Accelerations.
(b) Static and Dynamic Stability of the STR.
(c) Braking of the MA under normal and joint seizure conditions.
(d) Failure of the air supply or air bearing pads.
(e) Variations in floor slope and lift off of the air bearings.

In order to meet the static loads requirements with an arm stiffness of 10 lbs. per inch deflection of the End Effector, the allowable variation in support height at the Elbow and Wrist is ±0.10 inches. Since the total height variation could be as high as 0.5 inches due to air bearing lift off and floor variations, a support mechanism that accommodates these changes becomes essential. In order to meet these requirements a constant force device was chosen to interface between MA support flanges and the air bearing system.

THE PLINTH (Figure 2)

The plinth is a rigid support to which the Shoulder is attached. The mounting arrangement provide for the MA Shoulder vertical center line to be held either parallel or perpendicular to the floor (depending on whether the arm is in pitch coupled or yaw coupled mode.

In order to cater for the worst case failure of a Shoulder seizure at maximum arm rate, a torque limiting breakout clutch is incorporated between the plinth and the Shoulder interface. The clutch is designed to slip between 1,000 and 1,500 foot-pounds and is adjustable.

UPPER AND LOWER ARM SUPPORT MODULES

The configuration of the support modules is shown in Figure 3. Five point support is provided to the MA in order to meet arm stress load requirements. The three air bearing pads are provided on each module for static and dynamic stability.

The main structural member is a 6 inch diameter thin wall aluminum tube which also acts as a plenum for the air supply system. The plenum is used as an additional supply of air in the event of failure of the air supply system. Castors are also provided as a backup support system in the event of failure of the primary air bearing system.

WRIST AND END EFFECTOR SUPPORT MODULE

The Wrist and End Effector module duplicates the support mechanisms of the upper and lower arm sections. The air pads are displaced about the center of gravity of the support weight. The support flange location is chosen to minimize the static moments on all three of the wrist joints.

FLEXIBLE SUPPORT MECHANISM

The flexible support mechanism arrangement as shown in Figure 4 minimizes moment and torsion transfer to the MA support flange while maintaining the support force constant. Vertical motion of ±2 inches is provided. This motion is balanced by a beam linkage which acts against the constant force device.

The constant force device is a double spring system which provides for a "constant" reaction load over a prescribed linear movement by equating load moments with spring moments through a linkage system. A low spring rate is attained (1 pound/inch) at a nominal 150 pounds-feet. By providing

adjustment of the lever ratio, a linear relationship is attained over ±10% variation of nominal load setting. Total load variation is less than ±2% over the full range of travel and ±1% over a ±2 inch travel.

Dynamic characteristics were measured for the linkage/constant force device over the velocity range of zero to 0.65 feet/second with a range of movement equivalent to 5 inches at the STR support paint. Test results indicated that, dynamically, the device operates within the ±2% load variation and showed no resonance conditions within the system bandwidth.

AIR BEARING SYSTEM

The air bearing system is based on an air pad of 8" diameter.

This pad was chosen on the basis of static and dynamic stability over the load range of 130 to 500 lbs. with a friction coefficient between 0.001 and 0.003.

Development testing indicated that the operating band of the air bearing system had a fairly narrow stability range as shown in Figure 5 and is sensitive to low load. In order to avoid this condition, each air pad incorporates its own separate plenum with the air supply entering through a choked nozzle. Because the main air supply is carried at a higher pressure than that of the pad operating pressure, failure of the air supply will cause gradual failure of each pad. Adequate time is therefore available to allow the control and safety system to sense a change in vertical displacement and initiate an orderly shutdown of the MA.

In order to evaluate the characteristics of the air bearing system a development setup was constructed consisting of three air pads, a static and dynamic load and safety castors. Tests were conducted on the task area floor which is made up of linoleum strips approximately three feet wide by 60 feet long.

Results of the friction tests verified the linoleum's friction coefficient of between .001 and .003. Static and dynamic friction are approximately identical since the internal fluid velocity is high compared with the imposed relative velocity between the bearing pad and the floor surface.

The relationship between drag force and support load was found to be essentially constant within the limits of intended load variation.

Tests were also conducted with a support load offset to simulate the effects of inertia forces causing an overturning moment about the air pads. To simulate the effect of floor slope, tests were carried out with pad slopes between 1 degree and 4 degrees relative to the floor. Results of these tests indicate that overturning moments and floor slopes which would be encountered would have negligible effect on the friction drag.

84

Measurement of pad liftoff was taken during the friction test. Liftoff was found to be 0.375 inches. Tests with the castors in place indicated that the pad would reinflate with 1/16" of clearance.

With a support weight load of 280 lbs. applied to the air pad the pressure and flow were set at 5.5 psig and 8.8 SCFM respectively. Tests over the entire floor surface produced a nominal friction of between 0.0015 and 0.002.

The total requirement based on stability requirements established the air supply requirement as 60 SCFM at 40 psig.

Tests indicated the natural frequency of the air pad system under unstable operation as 11.5 Hz @ 280 lbs. and 9.0 Hz @ 380 lbs. The system also indicated heavy damping with a peak amplitude of 0.05 inches.

MA/STR DYNAMICS ANALYSIS

The unloaded arm has a natural frequency of 0.5 Hz. Analysis using computer model and a total STR weight of 890 lbs. showed the first two natural frequencies to be 0.5 and 3.5 Hz. Laboratory tests indicated a natural frequency for an unloaded STR to be about 11 Hz. It is concluded that the two systems do not couple through the action of the small friction force passed through the constant force device.

CONTROL AND SAFETY SYSTEM

The control and safety console provides monitoring of the following,

(a)   Supply air pressure.

(b)   Floor clearance of each of the inflated air pads.

(c)   Support loads at each of the five interface stations.

(d)   Vertical support positions of the five interface stations.

(e)   Plinth slip clutch.

Should any of the monitored status indicators fall outside prescribed limits, an alarm is sounded and the failure location is annunciated. A signal is also fed to the RMS control computer which brings the arm to rest. The signals also provide an interlock to ensure the MA cannot be functioned until the STR is in full operational status.

SETUP OF THE STR

Based on development test results for the air pads and constant forces devices the STR was set up prior to delivery. When tested on the flat floor, the only adjustments required were the height and level of the five arm interfaces. Dynamic tests with simulated loads applied to the five interfaces indicated no tendency towards instability as well and the load variation well within the ±2% limits.

ENGINEERING MODEL RMS SYSTEMS TESTS

Systems tests of the Engineering Model (EM) RMS occurred in late 1978 and during 1979. The setup is shown in Figure 6. A Hewlitt Packard HP21MX was used as the system computer with software which represented the orbiter RMS software. The EM MA differs from the flight model in that aluminum arm booms are used instead of the light weight graphite epoxy booms. Although the EM boom stiffness is representative of flight, there is an additional weight of approximately 300 pounds. The purpose of the EM systems test was to provide data in the following areas:

(a) System stability and controllability.

(b) Software/hardware compatibility.

(c) System stiffness.

(d) Operation in the different control modes.

(e) Payload operations limited to the use of a small dolly.

(f) Stopping distance from maximum rate.

(g) Maximum tip force.

Initial tests conducted driving the Shoulder showed the STR friction to be about 122 foot-pounds; well within design predictions. Examination of joint motor current traces were used for evaluation of floor slope and fluctuation. Again, the floor showed minimal effects on overall system performance. Track and capture tasks were performed using a commercial television system with the small payload drawn along the floor at typical payload rates. Operators familiar with SIMFAC simulations were used for the above tasks. Generally, the operators felt that the EM system tended to show more damping and less amplitude excursions during step inputs. Part of this is believed to be caused by the loss of the cross axis degrees of freedom and flexibility but generally the system performed well within the anticipated performance domain.

Another test conducted was to command the arm at very low rates in a straight trajectory. Results indicated that an End Effector rate of

approximately 0.035 feet/second could be attained. This is very close to the lower limit of the design capability and indicates excellent characteristics of floor slope and waviness as well as action of the air bearings and constant force devices. Deviations from the straight line trajectory were approximately 4 inches in 20 feet. Based on a specified joint rate accuracy of ±0.7 radians/second at the motor and taking into effect the expected floor friction, the results were well within specification.

A comparison run was made between the simulation program ASAD and the RMS. The typical plot of results for the shoulder and elbow pitch joints is shown in Figure 7. As a general observation the EM arm appears to follow the input commands more closely than the ASAD program in spite of the higher EM arm inertia (factor-of two higher).

CONCLUSION

Results of Engineering Model system tests of the RMS have indicated that the system test facility has exceeded expectations in the use for evaluating performance of the RMS in a zero -g environment. As a result, more rigorous testing will be performed on the flight model than had been originally planned. Also, tests using a payload for evaluation of partially and fully constrained motions will be performed. This gives confidence in the RMS abilities to deploy and stow payloads in the orbiter retention system prior to the use of the Payload Deployment and Retrieval System in flight.

ACKNOWLEDGEMENTS

REFERENCES

1. Doetsch, K., "The Remote Manipulator System for the SPACE Shuttle Orbiter", Jahrestagung 1977 of the Deutsche Gesellschaft fur Luft-und Raumfahrt eV, Berlin, West Germany, September, 1977

2. Kumar, P., Truss, P., Wagner-Bartak, C.G., "System Design Features of the Space Shuttle Remote Manipulator", Proceedings of the Fifth World Congress on Theory of Machines and Mechanisms - 1979. Published by the American Society of Mechanical Engineers

3.   Stovman, J.A., Wagner-Bartak, C.G., Doetsch, K.H., "A Real Time
     Simulation Facility for the Development of Manipulator Systems with
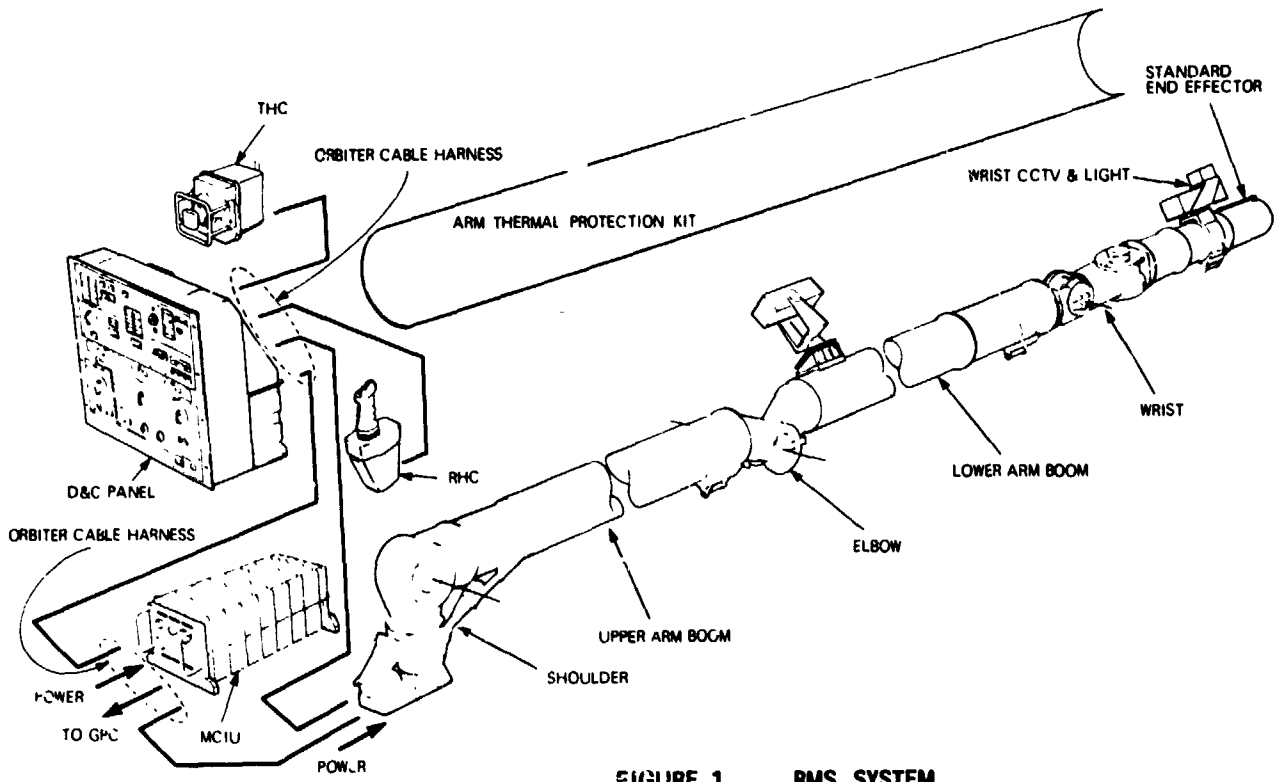   Man-in-the-Loop"
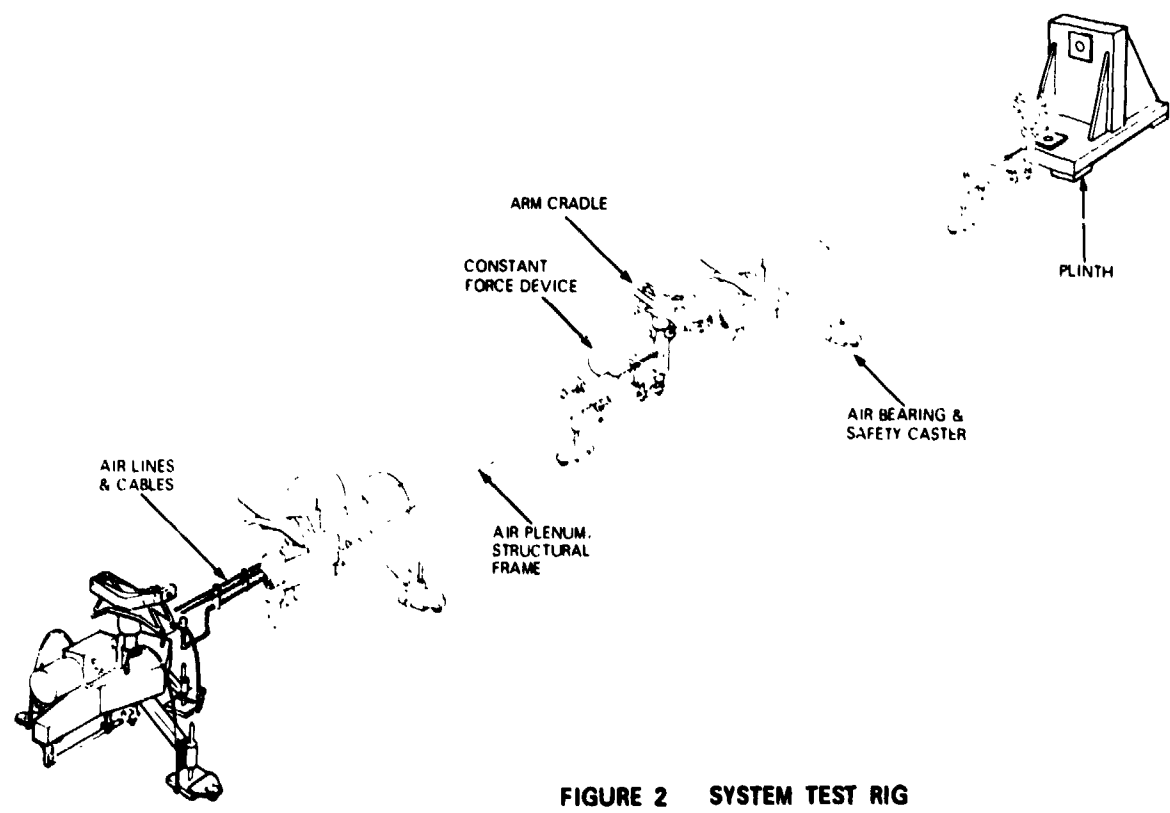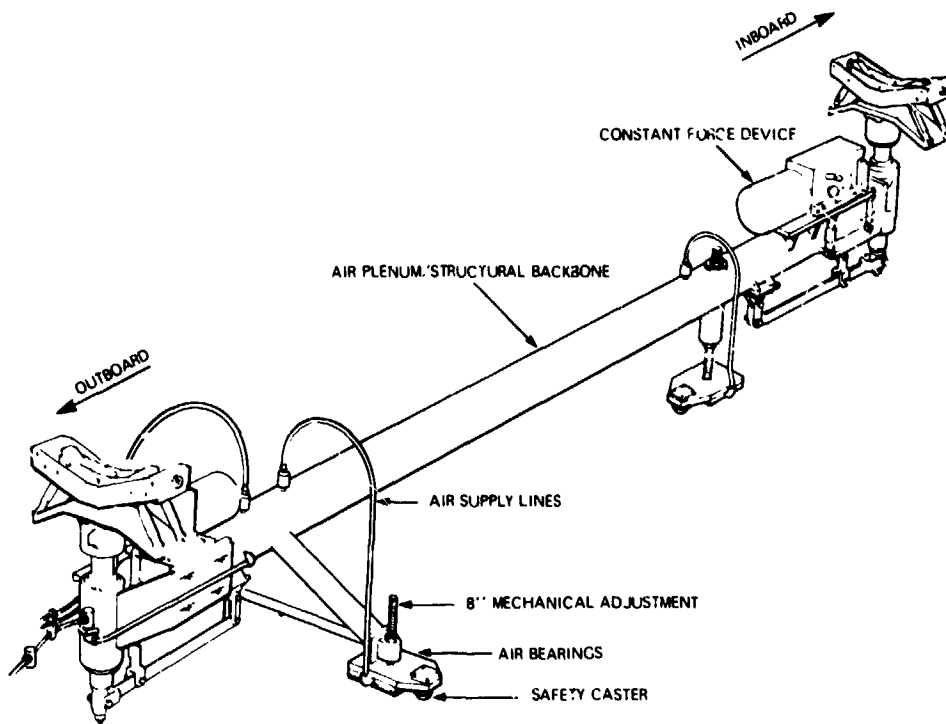
FIGURE 1   RMS SYSTEM

Labels in figure:
- THC
- ORBITER CABLE HARNESS
- STANDARD END EFFECTOR
- WRIST CCTV & LIGHT
- ARM THERMAL PROTECTION KIT
- WRIST
- LOWER ARM BOOM
- ELBOW
- RHC
- D&C PANEL
- ORBITER CABLE HARNESS
- UPPER ARM BOOM
- SHOULDER
- POWER
- TO GPC
- MCIU
- POWER

FIGURE 2   SYSTEM TEST RIG

Labels in figure:
- ARM CRADLE
- CONSTANT FORCE DEVICE
- PLINTH
- AIR BEARING & SAFETY CASTER
- AIR LINES & CABLES
- AIR PLENUM. STRUCTURAL FRAME

89

FIGURE 3   SYSTEM TEST RIG LOWER RMS ARM SUPPORT

INBOARD

CONSTANT FORCE DEVICE

AIR PLENUM/STRUCTURAL BACKBONE

OUTBOARD

AIR SUPPLY LINES

8'' MECHANICAL ADJUSTMENT

AIR BEARINGS

SAFETY CASTER

ARM CLAMP
CRADLE

CONSTANT FORCE
DEVICE

FLEXURE POSTS FOR
ROTARY MOTION

LOAD CELL
OUTLET

LOAD CELL
HOUSING

GROSS LONGITUDINAL
ADJUSTMENT

VERTICAL MOTION
HOUSING & BUSHINGS

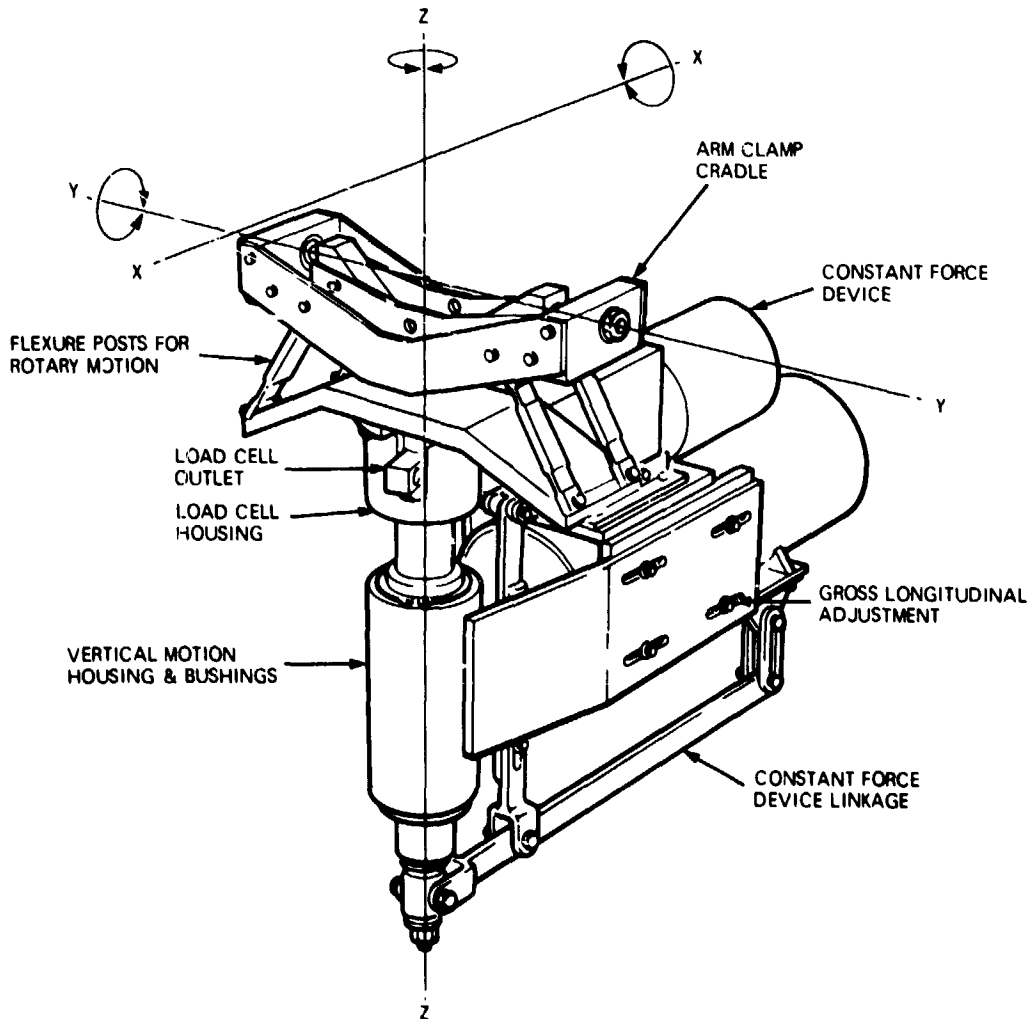CONSTANT FORCE
DEVICE LINKAGE

FIGURE 4   FLEXIBLE SUPPORT MECHANISM

90
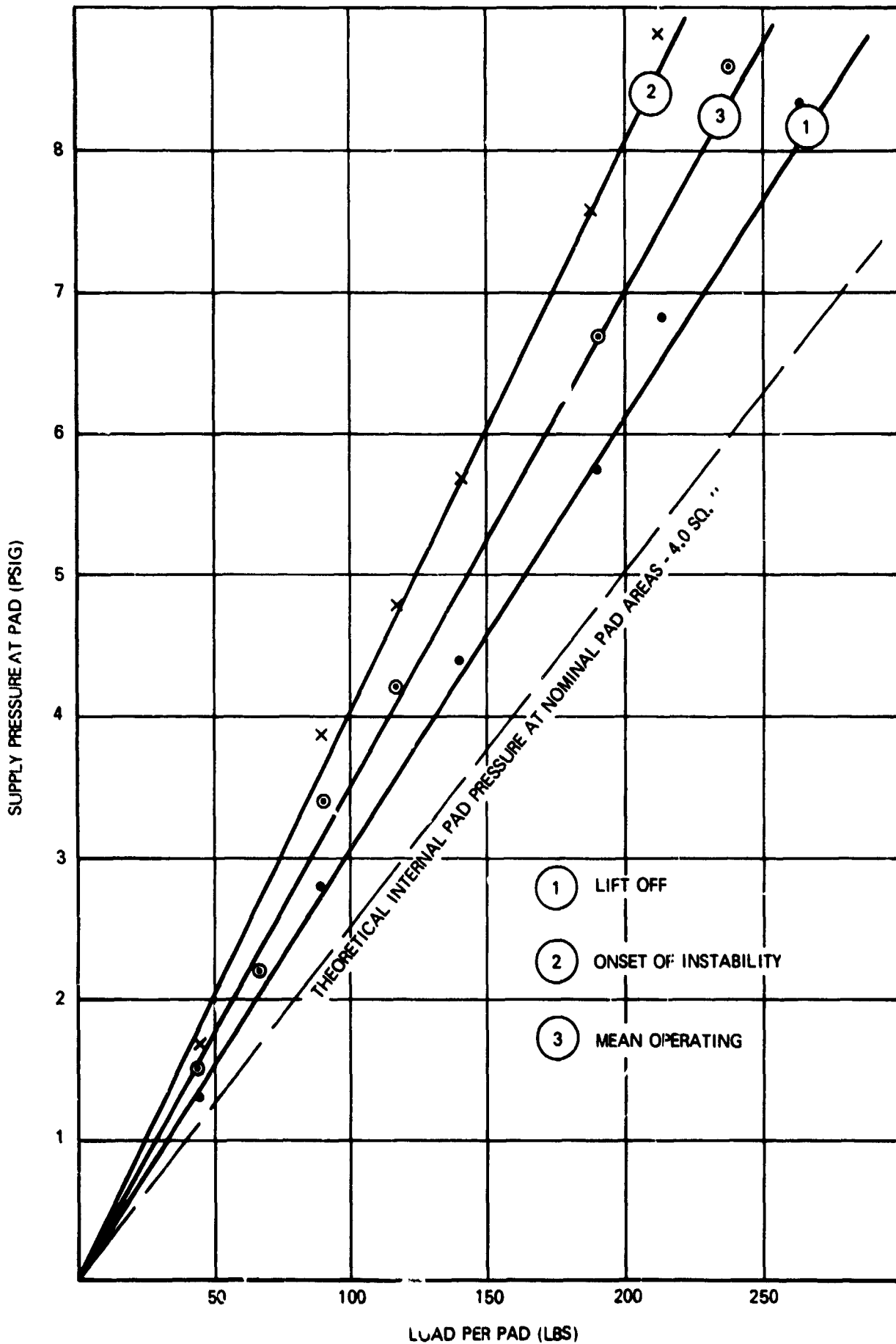
FIGURE 5   8'' NOMINAL DIAMETER PAD

91

FIGURE 6   MOUNTED SYSTEM TEST RIG DURING SIMULATED PAYLOAD TRACK & CAPTURE
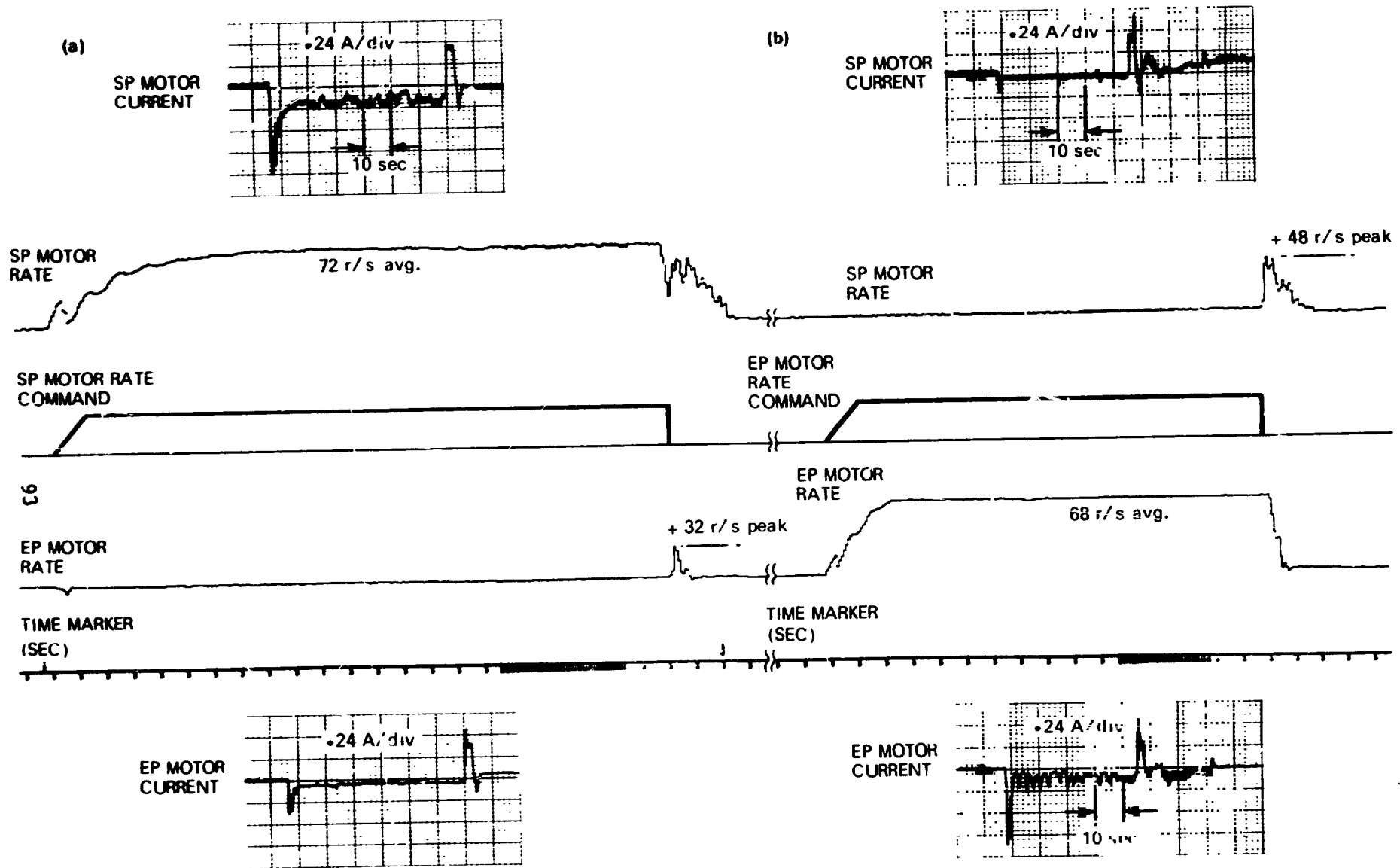
92

(a) SP MOTOR CURRENT · .24 A/div · 10 sec

(b) SP MOTOR CURRENT · .24 A/div · 10 sec

SP MOTOR RATE — 72 r/s avg.

SP MOTOR RATE — + 48 r/s peak

SP MOTOR RATE COMMAND

EP MOTOR RATE COMMAND

EP MOTOR RATE — 68 r/s avg.

EP MOTOR RATE — + 32 r/s peak

TIME MARKER (SEC)

TIME MARKER (SEC)

EP MOTOR CURRENT · .24 A/div

EP MOTOR CURRENT · .24 A/div · 10 sec

93

FIGURE 7   SINGLE JOINT MODE: (a) SHOULDER PITCH COMMAND (b) ELBOW PITCH COMMAND (EXTENDED ARM)

THE ROLE OF THE REAL-TIME SIMULATION FACILITY, SIMFAC, IN THE DESIGN, DEVELOPMENT AND PERFORMANCE VERIFICATION OF THE SHUTTLE REMOTE MANIPULATOR SYSTEM (SRMS) WITH MAN-IN-THE-LOOP

J.R. McCullough and A. Sharpe
Spar Aerospace Limited
Toronto, Ontario

K.H. Doetsch
National Research Council of Canada
Ottawa, Ontario

ABSTRACT

The Real-Time Simulation Facility, SIMFAC, is a powerful and adaptable engineering tool for the conduct of studies relating to man-in-the-loop manipulator systems. SIMFAC has played a vital role in the design, development and performance verification of the Shuttle Remote Manipulator System (SRMS) to be installed in the NASA Space Shuttle Orbiter. The facility provides for realistic man-in-the-loop operation of the SRMS by an operator in the Operator Complex, a flight-like crew station patterned after the Orbiter aft flight deck with all necessary man-machine interface elements, including SRMS displays and controls and simulated out-of-the-window and CCTV scenes. The characteristics of the manipulator system, including arm and joint servo dynamics and control algorithms, are simulated by a comprehensive mathematical model within the Simulation Subsystem of the facility.

Major studies carried out using SIMFAC include SRMS parameter sensitivity evaluations; the development, evaluation, and verification of operating procedures; and malfunction simulation and analysis of malfunction performance.

Amongst the most important and comprehensive man-in-the-loop simulations carried out to date on SIMFAC are those which support SRMS performance verification and certification when the SRMS is part of the integrated Orbiter-Manipulator System.

1   INTRODUCTION

The development of a general purpose, real-time Remote Manipulator Simulation Facility, SIMFAC, was initiated in 1974. The first application for this facility was created as a consequence of an agreement, reached between the Government of Canada and the U.S.A., that the Remote Manipulator System (RMS) for the National Aeronautic and Space Administration (NASA) Space Transportation System (STS) would be developed by a Canadian industrial team under contract to the National Research Council of Canada (NRCC), with Spar Aerospace Limited as the prime contractor.

The Shuttle Remote Manipulator System (SRMS) is intended for operation in space in a zero gravity (0-g) environment and as such, cannot be operated or fully tested in a 1-g, on-earth environment. SIMFAC provides evaluations of - and operator familiarization with - the SRMS performance characteristics that would be exhibited in the on-orbit environment and inputs to the design and development of the SRMS itself.

SIMFAC came into service in support of the SRMS Program early in 1977 and has since then been playing a most important role in the design development and performance verification of the SRMS. In addition, it has provided valuable data in support of the development of SRMS operating proceaures prior to actual orbital operations.

II THE SHUTTLE REMOTE MANIPULATOR SYSTEM (SRMS)

The SRMS is an anthropomorphic man/machine system with six control degrees-of-freedom for use on the Shuttle Orbiter in deploying, manipulating and retrieving a wide range of payloads (small to volumnous and massive) in space (Figure II-1).

The SRMS is operated in both automatic and manual modes from the aft port window location of the Orbiter crew compartment by an SRMS specialist using dedicated SRMS controls and with the aid of direct viewing and closed circuit television.

It is required that the manipulator be capable of safely deploying and retrieivng a 32,000 lb. cylindrical payload of diameter 15 feet and length 60 feet and, further, of deploying a 65,000 lb. payload of the same size.

Failsafe operation is a basic requirement of the SRMS design and a 10 year, 100 mission life is specified for the system.

The manipulator arm mechanical assembly comprises a series of six active joints and seven structural links, as shown in Figure II-2. These provide a gimbal order of shoulder yaw, shoulder pitch, elbow pitch, wrist pitch, wrist yaw and wrist roll. Each active joint of the manipulator arm is driven by a servo whose output, provided by a brushless DC motor, is transmitted to the arm via a high reduction gearbox.

A standard end effector is attached to the wrist for grappling and applying loads or motions to the payload or for releasing payloads into orbit. Mounted at the wrist roll joint is a wrist CCTV camera and viewing light assembly and near the elbow pitch joint there is provision for an elbow CCTV camera and pan and tilt unit assembly. These cameras, together with cameras in the Shuttle Orbiter cargo bay, provide specific and selectable views for the operator via the television monitors mounted in the RMS operating station in the crew compartment.

The arm, when fully extended, has a reach of approximately 50 feet and the arm booms are approximately 13 inches in diameter.

SRMS CONTROL

The manipulator arm is controlled from a Display and Controls (D&C) system using SRMS software resident in the Orbiter General Purpose Computer (GPC) through a Manipulator Controller Interface Unit (MCIU), all mounted within the Orbiter cabin. The MCIU supplies the data interface between the D&C system, SRMS software in the GPC and the manipulator arm.

The SRMS is a man-in-the-loop system, the operator forming an integral part of the control and monitoring system. Operator interaction and control, are effected by means of the following:

- Rotational and Translational Hand Controllers (RHC, THC) for Manual Augmented Mode Operation, which provide end effector translational and rotational velocity commands to the control algorithms within the SRMS software resident in the Orbiter GPC.

- The Display and Controls (D&C) panel (and electronics), which provides arm status data to the operator and performs secondary control functions.

- The mission keyboard, which provides operator access to the orbiter GFC.

- A GPC CRT which presents detailed SRMS status and health data to the operator.

The primary source of composite arm position and attitude data is the operator's own direct vision through the crew compartment aft bulkhead and overhead windows, augmented by CCTV views from the arm and payload bay-mounted camera. Figure II-3 shows the locations of the SRMS controls in the orbiter crew compartment.

CONTROL ALGORITHMS

The primary function of the SRMS control algorithms is to convert the various input drive commands into a resolved output rate demand for each joint of the arm so that the end effector or payload follow the commanded trajectory. The algorithms output these rate demands within limits defined according to arm and individual joint loading conditions present at the time of computation. The rate demands are passed to the joint servos via GPC-to-MCIU and MCIU-to-Arm Based Electronics (ABE) data busses.

The control algorithms supply the joint rate demands necessary to control either end effector translational and rotational rates or end effector position (rate or position control). The control algorithms obtain feedback on joint angles from high precision position encoders within the joint drive trains.

SERVO CONTROL

Classical servo loop compensation techniques are employed to ensure good stability over a wide dynamic operating range, as well as good steady state system performance. Feedback is obtained from digital and analogue tachometer data combined in a complementary fashion, and from high precision encoders providing joint position data, as shown in Figure 11-4.

SRMS CONTROL MODES

The SRMS may be controlled in the following modes:

- Manual Augmented Control Mode
- Automatic Mode
- Single Joint Control Mode
- Direct Drive Control Mode
- Backup Drive

96

The Manual Augmented mode of control enables the Operator to direct the end-point of the manipulator arm (or point of resolution in the payload) using the two three-degrees-of-freedom hand controllers to provide end effector (or payload) translation and rotation rate demands. The control algorithms process the hand controller signals into a rate demand to each joint of the system.

The automatic mode of control enables the operator to move the end point of the manipulator arm using a mission-keyboard entered trajectory (operator commanded auto-trajectory) or a pre-programmed trajectory. Any four pre-programmed automatic trajectories out of a total of twenty loaded in software may be active on the D&C panel. Storage is provided for up to two hundred positions and orientations in these automatic sequences.

The Single Joint Drive Mode enables the operator to move the arm on a joint-by-joint basis with full GPC support. The operator supplies a fixed drive signal to the control algorithms via a toggle switch on the D&C panel. In response, the algorithms supply joint rate demands to drive the selected joint while maintaining joint position on the remaining, unselected joints.

Direct Drive is a contingency drive mode, by-passing the MCIU, GPC and data busses and servo control loop by enabling the operator to provide a direct drive command to the MDA via hardwires. During operation in Direct Drive, brakes are automatically applied to all uncommanded joits. SRMS status information may be available to the operator via the D&C subsystem in this mode.

The Backup Drive Mode is a contingency drive mode used when no prime channel drive modes are available, enabling joint-by-joint performance. Backup drive is designed to fulfill the failsafe requirement of the SRMS by using only the electro-mechanical drive train of the selected joints, by-passing the rest of the system. No status information is available to the Operator through the D&C subsystem in this mode.

OPERATOR COORDINATE SYSTEMS

There are four Manual Augmented control operating modes available to the operator and selectable via a mode switch on the D&C panel, each of which refers point of resolution control to one (or more) of four different operator coordinate systems. The operating modes and associated operator coordinate systems are identified below.

Operating Mode (Manual Augmented Control)	Point of Resolution (POR)	Control Action Referred To
Orbiter Unloaded	Tip of End Effector	Orbiter Body Axis System for POR translations. rbiter Rotation Axis System for POR rotations.
End Effector	Tip of End Effector	End Effector Operating System.

Operating Mode (Manual Augmented Control)	Point of Resolution (POR)	Control Action Referred To
Orbiter Loaded	Pre-determined point within payload	Orbiter Body Axis System for POR translations. Orbiter Rotation Axis System for POR rotations.
Payload	Pre-determined point within payload	Payload Operating System.

Details of the coordinate systems are given in Figure II-5.

The operating modes and associated coordinate systems are chosen on the basis of providing for the Operator the most natural response to his controls during various critical task phases, so as to reduce his workload in making mental transformations as the SRMS takes on different configurations.

III THE SIMFAC FACILITY

Figure III-1 is a block diagram of SIMFAC showing the modular approach adopted in the design of the facility. The major subsystems are:

- the Simulation Subsystem
- the Scene Generation Subsystem
- the Operator Complex
- the Master Control Complex

THE SIMULATION SUBSYSTEM

The Simulation Subsystem is a self-contained computer complex for the manipulator mathematical model, control algorithms, servo software modules and data update to the Scene Generation Subsystem.

The Simulation Subsystem computer complex is shown in Figure III-2. Two TI-980B minicomputers, each with an associated floating point processor, are used in a master-slave configuration. The computers are augmented by an array processor in which the matrix calculations are performed.

Software is divided into three categories: the operating system, applications and service software.

The operating system software capabilities include:

- a real-time executive to perform synchronous and asynchronous task scheduling,
- interrupt processing and data transfer,
- foreground/background operation
- comprehensive disc file management,
- interactive operator communications,
- diagnostics

The Applications Software includes the models of the SRMS, payload and the orbiter.

The orbiter model includes mass properties and rotational dynamics (pitch, yaw and roll degrees-of-freedom). Orbiter stabilization can be established in either the inertial attitude mode, or earth pointing mode.

A number of payload model options have been configured, including the maximum envelope payload (a 15 ft. diameter, 60 ft. long cylinder) with weights 32,000 lb. (design case) and 65,000 lb. (design maximum). Each payload is fitted with a simulated grapple fixture and a sighting target to aid the operator in the tracking and "capturing" of payloads using the television camera on the SRMS wrist.

The SRMS model is subdivided into:

o   configuration and mass properties,
o   arm dynamics,
o   joint servo, gearbox and drive models,
o   arm control laws

The configuration and mass properties of the SRMS established during design and development testing provide the basic software data base used in the arm dynamics software.

The dynamics of the manipulator system are represented by a complex set of non-linear equations whose characteristic modes of motion exhibit wide variations by virtue of the large range of mass properties of the payloads handled and the various geometric configurations of the manipulator arm attainable within the reach envelope. As an example, the period of the fundamental structural bending mode for the straight arm configuration varies from approximately 2 seconds for the unloaded arm to about 50 seconds when a 65,000 lb. payload is attached. Similarly, the characteristic frequencies change by about 100% when the elbow moves through its range with a massive payload attached. In view of these wide dynamic ranges and of the fact that fine tuning of the integration step size to each condition (to maintain accuracy and avoid numerical instabilities) is not possible with a real-time simulation facility, a compromise between accuracy and speed of solution is necessary. In the case of SIMFAC, the compromise is affected by modelling the manipulator arm as a 23 degree-of-freedom system which includes the first six structural flexibility modes of motion (Table III-1) and by partitioning the equations into various loops which have solution update intervals of 2, 10 or 50 milliseconds.

The servo-mechanisms for the six SRMS joints are similar in configuration and, therefore, since they are not coupled (except through arm/payload dynamics), are simulated using the same basic software modules. Each module is made up of the models which represent the main servo hardware and electronic units, such as the motor, tachometer (analogue/digital) brakes, gearbox and position encoder.

The control algorithms provide the operator with control of the End Effector trajectory. They also respond to the attainment of limits of travel (reach limits) of any joint and to the occurance of predetermined computational singularities, where a controlled degree-of-freedom is lost through the

99

particular relative alignments of certain joints. These SRMS control algorithms are reproduced in the SIMFAC Applications Software, as are all of the SRMS control modes available to the Operator in the real system .

The service software processes all displays and control inputs and outputs. It also communicates with the Application Software via a data base comprising action flags, inter-module communications, invariant parameters and initialization parameters.

THE SCENE GENERATION SUBSYSTEM

The Scene Generation Subsystem is a three-computer complex augmented by an array processor which receives updated data from the simulation subsystem and, through a series of transformations, produces the four visual images that are used by the operator. Figure III-3 is a block diagram of the Scene Generation Subsystem showing the interconnections between the major units.

Two identical IDIIOM graphics generators are used, each generating two of the images. Graphics #1 produces direct (window view) images and #2 produces CCTV images. The graphics systems are of the vector type in which the images are formed by line drawings. Up to 2000 vectors per graphics system can be generated, of which 1300 are dynamic.

THE OPERATOR COMPLEX

The Operator Complex is an enclosed flight-like crew station patterned after the Orbiter aft flight deck, with all necessary man-machine interface elements including·

- o   Displays and Controls Panel,
- o   Hand controllers,
- o   Systems monitors and keyboard for engineering data and parameter changes,
- o   CCTV camera controls, and
- o   Four monitors, providing the window and CCTV views

The Displays and Controls Panel enables the operator to select the control modes. Displays on the panel provide for warnings and for the status of selected parameters.

The two direct view images look aft (into cargo bay) and upwards, the monitor CRT faces being placed against the windows. The direct view perspective is adjusted to a specified viewpoint in the Operator Complex and a lens system is incorporated which effectively places the image at infinity, thereby creating the illusion of depth to the Operator.

THE MASTER CONTROL COMPLEX

The Master Control Complex includes work stations for the Test Conductor and Systems Engineer and provides for full interactive control and monitoring of tests and communication with the Operator Complex.

The Test Conductor Panel, contains timers, CCTV controls, recorder controls and communications, and the the Systems Engineers anel contains a duplicate set of operation controls, arm parameter displays and system monitors,

A portable interactive terminal and a CRT monitor and keyboard are included in the complex.

Tasks may be frozen and restarted, or, if desired, re-initialized.

The Test Conductor can monitor engineering data on a CRT display system, by calling specified CRT "pages". Hard copy of a displayed page is available.

Simulated malfunctions may be inserted by the Test Conductor and/or cleared by keying-in an appropriate "malfunction number". Recording devices, selectable from the Master Control station, include 24 channels of pen recorders, audio (voice communication) recorder, video recorder, 9-track magnetic tape and a line printer.

IV   VALIDATION OF SIMFAC

Validation of the SIMFAC simulation model is achieved via an extensive set of performance comparisons with the comprehensive non-real-time SRMS simulation model, ASAD, developed by Spar for in-depth technical evaluations. ASAD is the most detailed and versatile model of the Orbiter-SRMS-Payload system currently available and, as such, is used as the Master Simulation model against which all other SRMS models are validated.

The ASAD program is modular in design, the principal modules being the SRMS Control Algorithms, Joint Servo and Gearbox, Manipulator Arm Dynamics and Orbiter Attitude Control System (ACS) modules. The program can accept an unlimited number of SRMS and Orbiter crew commands and can be used to analyze the effects on SRMS performance of up to seventy-six degrees-of-freedom.

Parameter changes in ASAD prior to a particular run may be implemented by the user to satisfy specific requirements. In particular, the integration step size, number of flexible modes retained when integrating the system differential equations, the updating period of system variables and "grid vector" used to suppress undesired degrees of freedom may be preselected as necessary to maximize simulation acuracy, minimize run time/cost, or achieve an acceptable compromise.

ASAD runs on a Control Data Computer system - a CDC 6600 - and operates typically at 30 times real time.

In view of the importance of ASAD as a detailed SRMS design, development and performance verification tool and as a basis for the validation of SIMFAC (and other SRMS simulation models), it has been necessary to apply considerable and detailed effort to the task of validating - and reconfirming the validity of - ASAD throughout the SRMS Program. This on-going work has involved:

o   validation by analysis;

o   validation by comparisons with SRMS unit and subsystem test performance (breadboard, engineering model, qualification and flight hardware);

o   validation by comparisons with other analysis and simulation programs - including SRMS applications of finite element programs, such as

101

"NASTRAN", "STARDYNE", together with other independent SRMS simulation models.

The primary aim of the SIMFAC validation against ASAD is to ensure that SIMFAC behaviour is consistent with that of ASAD within specified bounds. Emphasis is placed on validating the control algorithms and the arm dynamics model to establish the adequacy of SIMFAC to perform its primary function -- to provide an accurate visual representation of arm performance and behaviour to an operator such that the operator reactions to these displays will, in turn, be realistic.

Although the ASAD results have reflected the presence of the higher frequency flexible modes modelled, excellent correlation has been demonstrated at the lower frequencies which are controllable by the operator. The SIMFAC mathematical model is thus validated for the SRMS application.

V   PRINCIPAL SIMFAC STUDIES PERFORMED

Some of the major tasks carried out using SIMFAC are:

o   SRMS Parameter Sensitivity Evaluations,

     The Evaluation, Development and Verification of SRMS Operating
     Procedures,

o   Malfunction Simulations and Analysis of Malfunction Performance, and

o   Formal Simulations in Support of SRMS Performance Verification.

SRMS PARAMETER SENSITIVITY EVALUATIONS

A considerable number of parameter sensitivity studies have been performed throughout the SRMS Program. Based on the results of these studies, a "short list" of SRMS parameters which, under worst case tolerance conditions, might significantly influence the ability of the SRMS to meet performance requirements has been generated.

The SIMFAC parameter sensitivity study has addressed each of these parameters in turn, selected runs having been performed with the parameter value varied over a suitable range. A final set of sensitive SRMS parameters has thus been selected from which worst case combinations have been derived as a basis for system verification/certification simulations.

The sensitive parameters and the worst case combinations established from the SIMFAC parameter sensitivity study are identified in Table V-1.

It is significant to note that even through greater than expected sensitive parameter tolerances were used in these worst case combinations and quantitative differences between nominal and off-nominal performance were noted on ASAD, the operators were unable to detect any significant different in performance.

EVALUATION, DEVELOPMENT AND VERIFICATION OF OPERATING PROCEDURES

The development, evaluation and verification of SRMS operating guidelines, procedures and constraints has been achieved through a large number and range of

studies which have addressed all aspects of the SRMS design (mechanical, electrical, thermal, software and interfaces) and have examined the integrated Orbiter/SRMS mission requirements. From the results of the studies, operational requirements and limitations compatible with the SRMS design capability and anticipated on-orbit tasks have been identified and subsequently interpreted in terms of the appropriate SRMS operating procedures and constraints.

The purpose of the operating procedures and constraints is to provide the Operator with clear, detailed operating instructions for on-orbit preparation, checkout, operation, system management and shutdown of the SRMS, including SRMS software activation and initialization. Major SIMFAC studies have been conducted in which on-orbit tasks have been defined and carried out by NASA operators. Acceptability (and, ultimately, verification) of the procedures and appropriate constraints developed has been judged on the basis of:

o   task (or subtask) success,
o   operator workload,
o   time to completion
o   the operator's assessment of (and responses to) the characteristics encountered

The on-orbit tasks defined for the studies have all been carried out by the test operators under the control of a test conductor and have comprised:

o   full end-to-end payload deployments and retrievals.
o   automatic mode operation (addressing operator procedures for auto mode entry, monitoring, interrupt and exit).

o   Special subtasks for specific evaluations, involving, for example, maneuvering of the arm in the neighbourhood of singularities and reach limits, maneuvering of the arm in SINGLE JOINT, DIRECT DRIVE and BACKUP DRIVE modes.

These SIMFAC studies have confirmed that the SRMS operating procedures and constraints developed are realistic under flight-like conditions and that they provide for acceptable on-orbit task times and operator workload.

MALFUNCTION SIMULATIONS AND ANALYSIS OF MALFUNCTION PERFORMANCE

Extensive malfunction simulations and evaluations of malfunction performance have been carried out on SIMFAC. In one major study over five hundred data runs with malfunction insertion, were performed with the participation of nine test operators. Payload deployment and retrieval tasks were performed with payloads ranging from 1000 lb. to 65,000 lb. Malfunctions modelled in SIMFAC and evaluated in this study included the following:

o   Single axis and all-axis failure of the translational hand controller resulting in a sustained "hardover" maximum command,

o   Single and multi-joint worst-case runaway failures,

o   Seized, sluggish and joint free failures,

o   Joint position encoder failure,

103

All malfunctions were activated by the Test Conductor to coincide with high operator workload conditions and, where possible, difficult fault detection conditions during the SRMS task. Operators were not able to predict when in a run the malfunction would occur.

All of the malfunction studies carried out on SIMFAC have involved the accumulation and evaluation of comprehensive qualitative and quantitative data on the malfunction effects, in terms of SRMS uncommanded motions induced (and resulting hazard created), operator observations and responses and (where applicable) stopping distance following brake application.

Any loaded arm runs involving indicated contacts between the payload and the cargo bay have been analyzed using an off-line contact detection program which provides confirmation that a contact occurred and quantitative data on the contact velocity and kinetic energy.

The data from these SIMFAC malfunction studies have provided valuable insight into the effects of failures on man-in-the-loop performance and have provided major inputs for the development of formal SRMS malfunction procedures. In addition, the studies have identified clearly instances when, for a particular malfunction, occuring under worst case conditions, human operator responses (however fast) to the fault annunciations, alarm and/or visual cues were ineffective in preventing a payload/orbiter contact. Under such circumstances a design change (hardware and/or software) has been necessary to maintain failsafe SRMS performance. Confirmation that the design change has achieved this objective has been established from the results of repeat malfunction runs on SIMFAC with the design change incorporated.

A further major role played by SIMFAC has been in the evaluation of SRMS operational capabilities in the Direct Drive and Backup Drive modes after a malfunction has occurred. Studies have confirmed that the manipulator arm (with or without payload attached) can be safely and accurately maneuvered in these modes, demonstrating compliance with the SRMS failsafe requirement.

SRMS PERFORMANCE VERIFICATION

Amongst the most important and comprehensive man-in-the-loop simulations carried out to date on SIMFAC are those which support integrated SRMS performance verification and certification.

These indepth simulations take account of the effects of tolerances on "sensitive" system parameters by using chosen combinations which give worst case effects relative to specific performance characteristics (Reference Table V-1).

The objective of the simulations on SIMFAC is to verify SRMS compliance with specific performance requirements detailed in the SRMS Contact End Item (CEI) Specification. Each CEI specification requirement so addressed may be catagorized as either quantitative or qualitative.

Quantitative requirements specify numerical upper limits for either the magnitude of a variable of interest, or the magnitude of departure of a variable of interest from a specified command, or datum.

The verification criterion applicable to a quantitative CEI specification requirement is, therfore as follows:

Compliance is considered to be demonstrated - and verification with respect to the requirement achieved - when, under simulated worst-case conditions, the magnitude of the variable of interest, or its departure from the referenced command/datum, does not exceed the specified numerical upper limit.

Qualitative requirements are those which call up specific SRMS functional - or operational - capabilities, or design features not expressable in numerical terms.

The verification criterion applicable to a qualitative CEI specification requirement is dependent on the specific quality (SRMS functional/operational capabilty, or design feature) called up.

In general, it is necessary to establish, on the basis of worst-case simulation data, that the SRMS capability - or design feature - identified exists and adequately fulfills the objective(s) specified in the requirement. Adequacy in fulfilling the specified objective(s) is judged on the basis of factors which include speed and accuracy of task performance, safety and operator workload.

SRMS performance verification using SIMFAC involves the following steps:

o   Validate SIMFAC against the non-real-time simulation model ASAD

o   Prepare operating procedures and operating checklists for the verification runs

o   Perform complete checkout of all verification runs under data run conditions, including off-nominal parameter and malfunction runs

o   Conduct verification simulation readiness review

o   Carry out operator briefing and familiarization runs

o   Conduct verification data runs

o   Analyze results and generate verification report

A great many "flying" hours have been conducted on SIMFAC in support of SRMS performance verification and each CEI performance requirement has been rigorously addressed, the runs carried out having been selected to cover the impact of both off-nominal SRMS parameters and worst case configuration and maneuvering conditions.

By this means it has been possible to demonstrate convincingly that the SRMS design fulfill the performance objectives specified, which include·

-    full end-to-end payload deployment and retrieval capability,

-    fail-safe capability,

- operation in all control modes,

- rate and positioning accuracies for joints, end effector, payload point of resolution, and

- management of singularities and reach limits.

In performing this verification support role, SIMFAC has made (and is continuing to make) a major contribution in the process of formally establishing that the SRMS meets all design, performance and safety requirements.

VI CONCLUSIONS

The many major simulation studies performed on SIMFAC since the facility came into service in 1977 have demonstated repeatedly the importance of its role as a design, development and verification tool for the SRMS. SIMFAC has provided for the development of man-machine interfaces perator's primary hand controllers and displays and controls panel) and manipulator control software, the development of flightlike operating procedures, operating constraints and malfunctions procedures, an the verification of the SRMS performance with man-in-the-loop.

SIMFAC has shown clearly that the SRMS is capable of safely carrying out all of the on-orbit tasks for which it was designed and, as a result, has provided early confidence that the SRMS will perform successfully during tne forthcoming orbital flight tests.

SIMFAC is not, however, limited to studies within the SRMS program; the facility is, by design, extremely versatile and is capable of supporting the design and development of manipulator systems for non-space environments which are of high technical complexity.

ACKNOWLEDGEMENTS

REFERENCES

1.   J. MacNaughton, "International Cooperation in Space - A Canadian Viewpoint", presented at the Fourteenth Space Congress, Cocoa Beach, Florida, April 27-29, 1977.

2.   K.H. Doetsch, "The Remote Manipulator System for the Space Shuttle Orbiter", presented at the Deutsche Gesselschaft fur Luft-und Raumfahrt eV, Berlin, September 13-15, 1977.

3.   J.A. Stovman, C.G. Wagner-Bartak, K.H. Doetsch, "A Real-Time Simulation Facility for the development of Manipulator Systems with Man-In-The-Loop", Spar Aerospace Limited, Toronto, Ontario, Canada. K.H. Doetsch, National Research Council of Canada, Ottawa, Ontario, Canada.
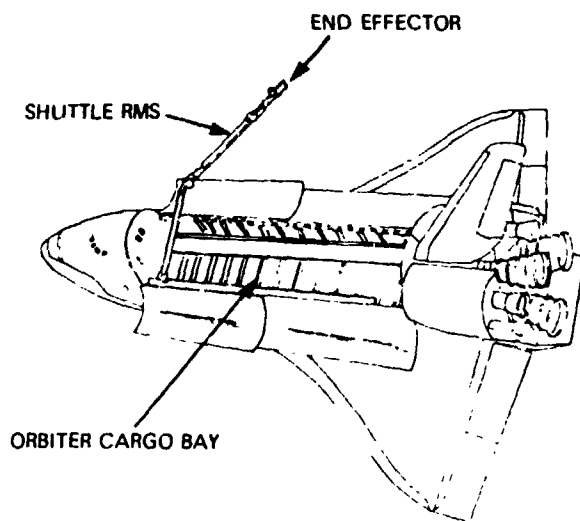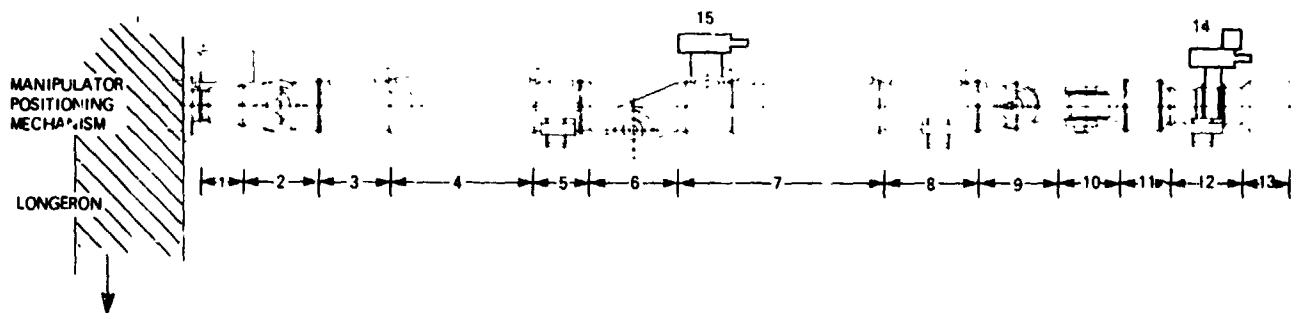
END EFFECTOR

SHUTTLE RMS

ORBITER CARGO BAY

FIG. II - 1   SHUTTLE RMS ON THE ORBITER

MANIPULATOR
POSITIONING
MECHANISM

LONGERON

COMPONENTS

1	SHOULDER YAW JOINT	8	WRIST FWD. ELECT. COMP.
2	SHOULDER PITCH	9	WRIST PITCH JOINT
3	SHOULDER ELECT. COMP.	10	WRIST YAW JOINT
4	UPPER ARM BOOM	11	WRIST AFT ELECT. COMP.
5	ELBOW ELECT. COMP.	12	WRIST ROLL
6	ELBOW JOINT	13	STANDARD END EFFECTOR
7	LOWER ARM BOOM	14	CCTV CAMERA & VIEWING LIGHT - WRIST LOCATION
		15	CCTV CAMERA WITH PAN/TILT UNIT – ELBOW LOCATION

(SHOULDER PITCH JOINT ROTATED THROUGH 90° FROM STOWED POSITION)
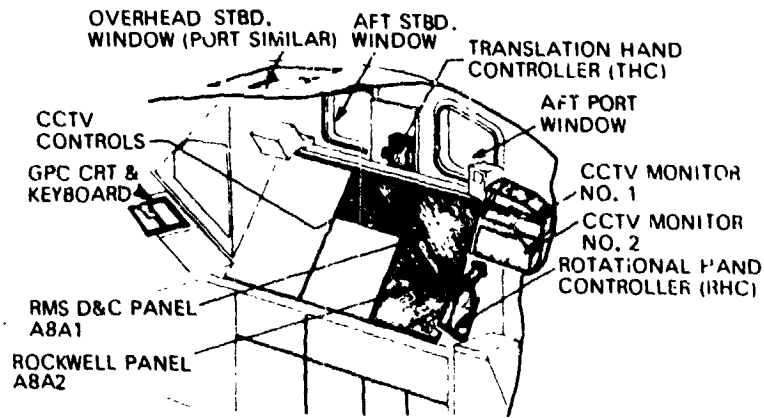
FIG. II - 2   MANIPULATOR ARM MECHANICAL ASSEMBLY
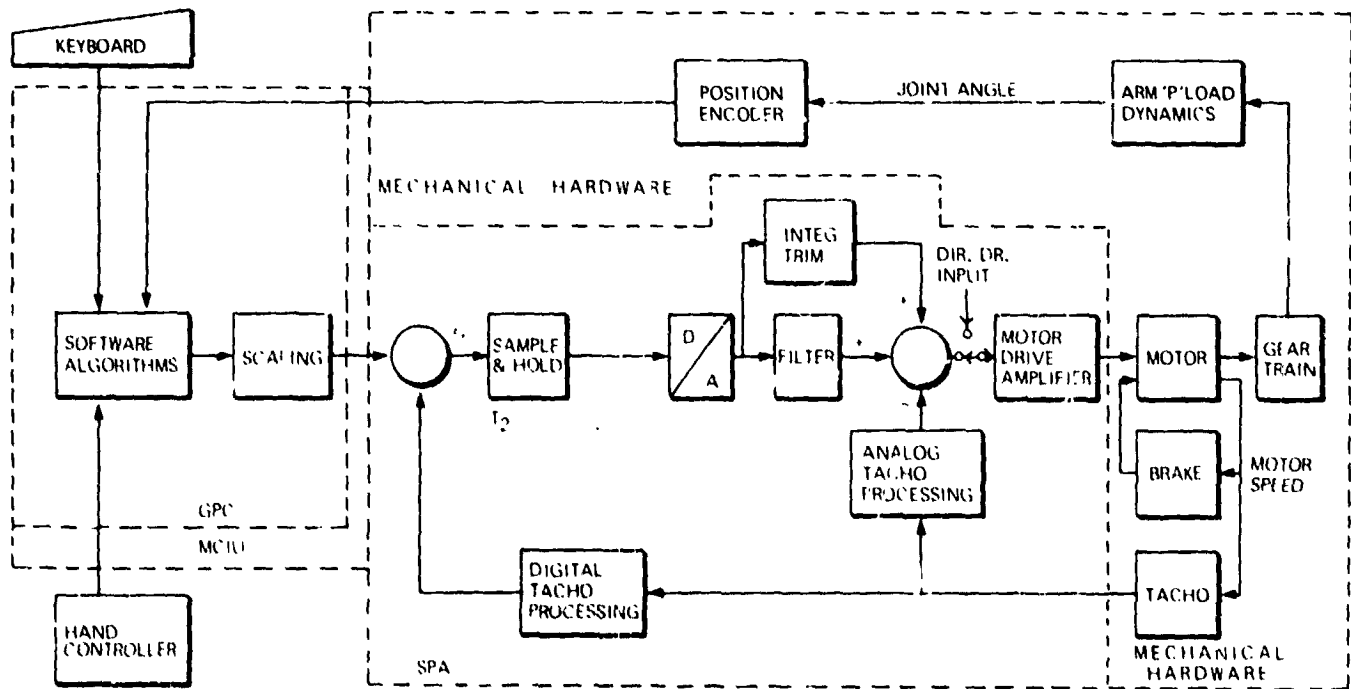
107

FIG. II - 3 RMS OPERATING STATION
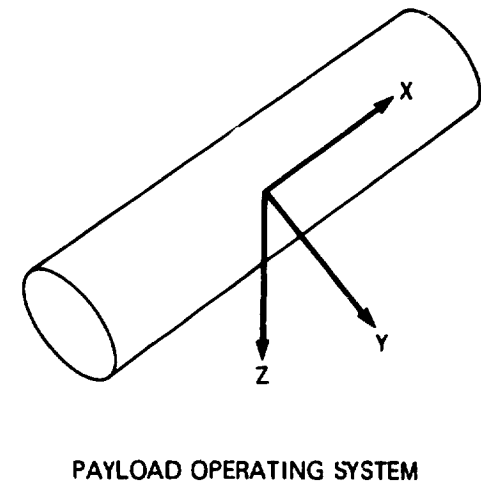

FIG. II - 4 JOINT SERVO CONTROL BLOCK DIAGRAM

236"

400"

X

Z

ORBITER BODY AXIS SYSTEM

END EFFECTOR
WRIST ROLL JOINT
WRIST YAW JOINT
WRIST PITCH JOINT
LOWER ARM

ELBOW PITCH JOINT

UPPER ARM

SHOULDER PITCH JOINT

0_1

X

Y

Z

END EFFECTOR OPERATING SYSTEM

$(0'' - 0')$

236"

400"

X

Y

0"

Z

ORBITER ROTATION AXIS SYSTEM

X

Y
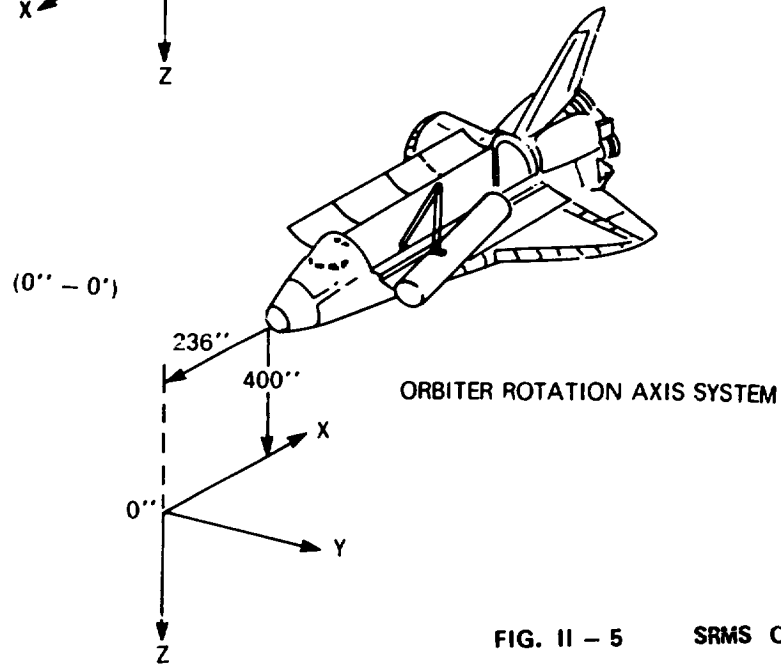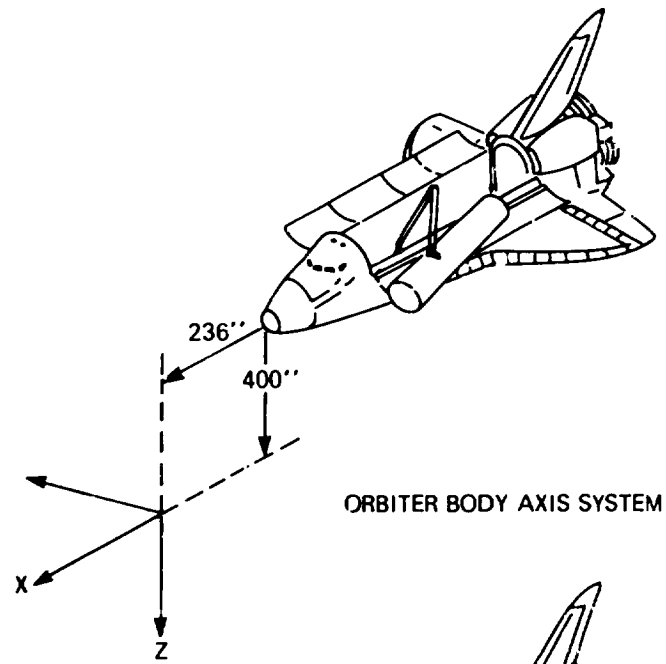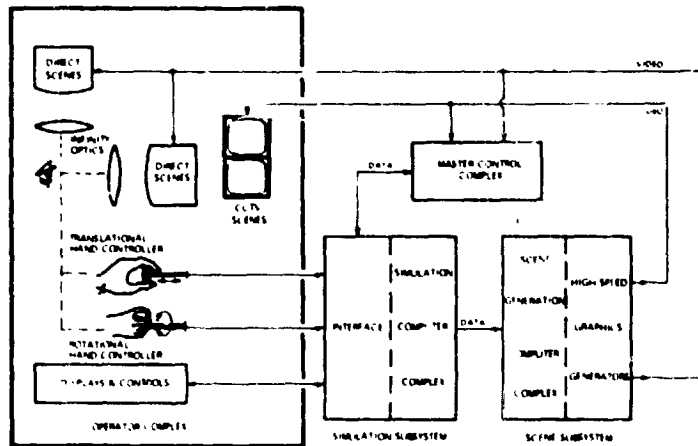
Z

PAYLOAD OPERATING SYSTEM
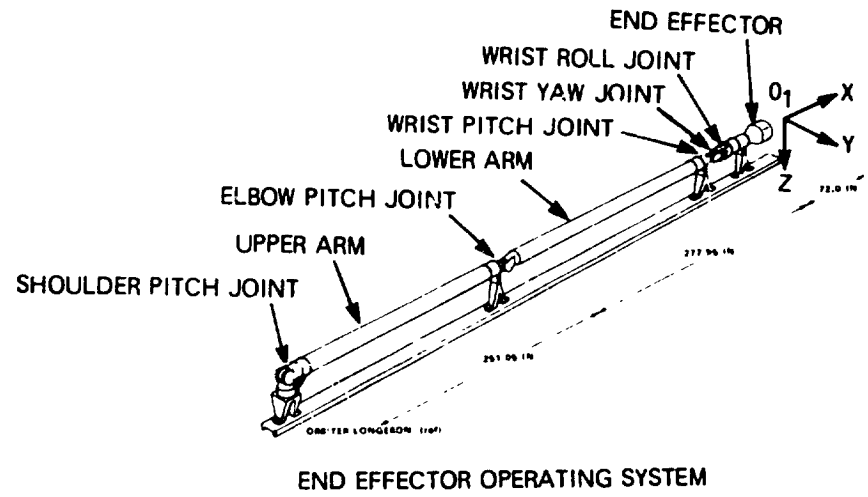
FIG. II – 5   SRMS CO-ORDINATE REFERENCE FRAMES

FIG. III - 1   SIMFAC BLOCK DIAGRAM
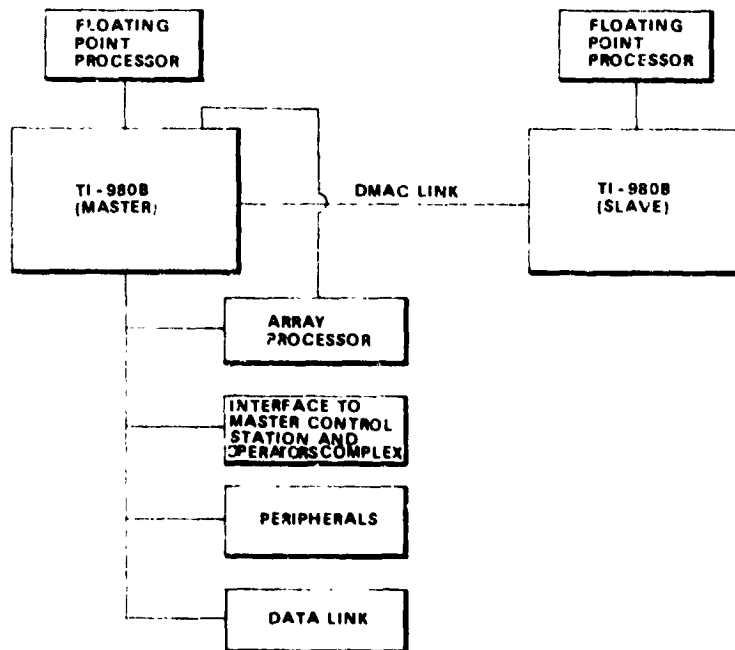
FIG. III - 2   SIMULATION SUBSYSTEM BLOCK DIAGRAM

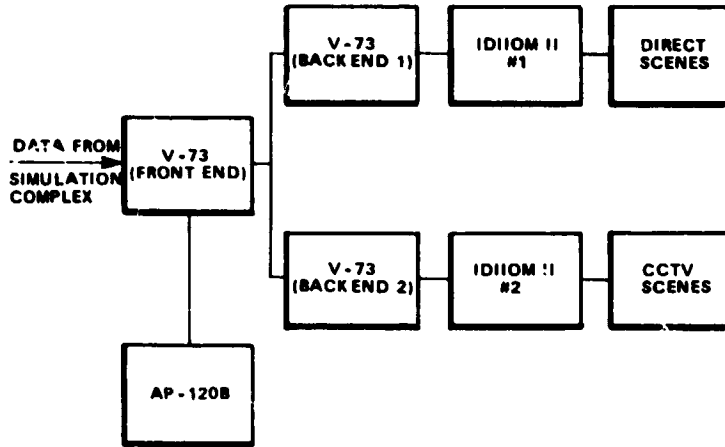| V-73
(BACK END 1) | IDIIOM II #1 | DIRECT SCENES |
V-73 (FRONT END)		
DATA FROM SIMULATION COMPLEX		
V-73 (BACK END 2)	IDIIOM II #2	CCTV SCENES
AP-120B		

FIG. III - 3   SCENE GENERATION SUBSYSTEM BLOCK DIAGRAM

DOF	NUMBER	TYPE
ORBITER ATTITUDE	3	ROLL, PITCH, YAW
CONTROLLED	6	ROLL, PITCH, YAW JOINTS
FREEPLAY	6	SHOULDER PITCH, ELBOW PITCH, WRIST ROLL
BENDING	8	SHOULDER PITCH, ELBOW PITCH
TOTAL	2.	

TABLE III - 1   ARM DEGREES OF FREEDOM (DOF) IN SIMFAC

111

TABLE V - 1   WORST CASE COMBINATIONS OF SENSITIVE PARAMETERS

PARAMETER	COMBINATION					
	1a	1b	2a	2b	3a	3b
GEARBOX EFFICIENCY	lo	hi	hi	lo	hi	lo
JOINT SERVO OUTER LOOP GAIN	lo	hi	lo	hi		
INTEGRAL TRIM LIMIT	lo	h.	lo	hi		
MOTOR CURRENT (TORQUE) LIMITS	lo	hi	lo	hi		
JOINT FRICTION	hi	lo	lo	hi	lo	hi
MOTOR FRICTION	hi	lo	lo	hi	lo	hi
BRAKE SLIP TORQUE					lo	hi
GEARBOX FULL RANGE STIFFNESS	lo	lo	lo	lo	lo	lo

SYSTEM CHARACTERISTICS

COMBINATION 1a GIVES — low drive torque/speed, sluggish response

1b GIVES — high drive torque/speed, rapid response

2a GIVES — low backdrive resistance

2b GIVES — high backdrive resistance

3a GIVES — low braking torque

3b GIVES — high braking torque.

112

SHUTTLE MISSION SIMULATOR

Charles Olasky

Abstract

The Shuttle Mission Simulator, located in Building 5 at the Johnson Space Center, is the primary training device for both Shuttle flight crew and Shuttle flight control personnel. The simulator was designed to provide real time simulation capability for all phases of the Shuttle Transportation System orbital missions including prelaunch, ascent, on-orbit operations, deorbit, entry, approach/landing, and roll-out. Full mission continuity is provided in transition between these mission phases. Dual fixed and motion base crew stations, instructor/operator stations, and computer systems allow parallel, simultaneous crew training with either complex capable of being individually integrated with the Mission Control Center. This integrated training capability allows flight control personnel training in the air/ground interface areas of tracking, telemetry (vehicle systems monitoring), uplink command control, and communications. With the exception of the simulated Data Processing System, which utilizes actual flight computers and associated flight software, all orbiter onboard systems are functionally simulated with extensive simulated malfunction capabilities. Additionally, Shuttle propulsion systems, vehicle dynamics, atmospheric/orbital environment, crew out-the-window visual scenes, and aural cues are rigorously simulated. The Motion Base Crew Station has the added feature of being mounted to a six-degree-of-freedom motion system that provides on-set and acceleration cues for launch and deorbit through landing training. The total SMS facility represents a major growth in simulator fidelity, sophistication, and capability over previous NASA mission simulators in support of manned spaceflight programs.

Introduction

Since the beginning of the Mercury Program the need of a spacecraft systems and mission procedures crew training device has been recognized by the NASA. Past program requirements have been satisfied by the Mercury Procedures Trainer, Gemini Mission Simulator, Apollo Command and Lunar Module Simulators, Skylab Simulator, and Orbiter Aeroflight Simulator. Today, in Building 5 at the Johnson Space Center, the Shuttle Mission Simulator (SMS) is operational and heavily involved in crew and flight control training for the first Shuttle Transportation System (STS) orbital flight.

After an extensive study and requirements definition phase, the SMS development contract was awarded to the Singer Company, Link Division, in January 1976. The contractual schedule article called for a phased/incremental delivery plan reflecting the following build-up in capabilities:

            Fixed Base Crew Station (FBCS) operational - May 1978
            Network Simulation System (NSS) operational - June 1978
            Motion Base Crew Station (MBCS) operational - August 1978
            Fixed Base Crew Station Update complete[1] - March 1980

[1]This deliverable consisted of the Orbiter Closed Circuit Television (CCTV) simulation, the Remote Manipulator System (RMS), and Payload Accommodation System (PAS) simulation, and the crew station aft and overhead window visual simulation.

The composite capability of these deliverables resulted in two separate standalone systems, the fixed and motion base crew station simulations and the simulation of the Ground Spaceflight Tracking and Data Network (GSTDN) interface to the Mission Control Center (MCC). Both crew station simulations can be run independently and simultaneously with capability for either to be integrated with the control center through the switchable NSS. These real time simulations provide generic and flight specific:

- Familiarization with Orbiter flight deck controls, displays, and related onboard systems.
- Training in nominal, contingency, and emergency crew and ground interface procedures.
- Familiarization of Orbiter handling characteristics supplemented with dynamic out-the-window visual scenes and vehicle motion cues.
- Training in the use of actual flight software and hardware for guidance, navigation, and redundancy management functions.
- Training for "end-to-end" inflight mission procedures and timelines including support of mission control center operations.

The FBCS is the larger of the two crew stations in that all flight deck work stations are simulated. These include:

- Forward commander work station
- Forward pilot work station
- Aft mission specialist work station
- Aft payload specialist work station
- Z-axis rendezvous work station
- Payload handling/RMS operator work station

The MBCS contains commander and pilot work stations with a "jump seat" instructor capability. This crew station is mounted to a six-degree-of-freedom motion system for acceleration and onset motion cues. The training emphasis for this crew station is directed toward ascent, entry, approach and landing mission phases.

The present STS mission schedule calls for the first manned orbital flight in late 1980 with follow-on flights increasing in frequency from several months interval to several weeks interval after the orbital flight test phase. The remaining sections of this paper will describe in more detail the in-place architecture and capabilities of the SMS that is fulfilling a major and demanding role in the preparation and execution of Shuttle program objectives.

Simulator Computer Complex

The SMS digital computer complex consists of: a Univac 1100 multiprocessor, functioning as a host computer; two strings (three minicomputers per string) of Perkin Elmer 8/32 computers, functioning as input-output intelligent controllers (IC's), six 8/32's within the Digital Image Generation (DIG) systems, and three 8/32's associated with the Network Simulation System (NSS). Additionally, there are five flight type General Purpose Computers (GPC's) assigned to each crew station simulation. Figure 1 diagrams the top level functional interfaces between these computers.

The Univac host computer complex is split into two separate systems, one each for the fixed and motion base simulations. One system is configured with 6 Command Arithmetic Units (CAU's) and 3 Input Output Arithmetic Units (IOAU's) while the other is configured with 4 CAU's and 2 IOAU's. A T-bar switching network allows either system to operate with either fixed or motion base simulation. Since each of the real time simulations are capable of running within a 4x2 configuration, the additional resources of the 6x3 configuration are applied to background/batch processing. Each of the host systems communicate with their respective intelligent controllers via data channels and special logic that interfaces the Univac 36 bit work format to the IC 32 bit work format. Both host computer real time simulation loads reside in seven 65K work memory modules of primary memory and two 131K word modules of extended memory. There are additional single 65K word primary and two 131K word extended memory modules available within one complex that are applied to background batch processing. Both local and remote terminals are available to initiate background processing.

Each of the fixed and motion base simulations contain three Perkin Elmer 8/32 computers that function as intelligent controllers which interface, format, control, and route data to and from the host and the major, functional, hardware elements of the SMS. These are categorized as the Crew/Instructor/ Operator Station (CIOS) interface, the Visual System interface, and the Simulation Interface Device (SID)/Flight Computer interface. The primary means of intracommunication within each set of associated IC's is through a common shared memory interface. All of the SMS 8/32 computers contain double precision floating point capability and have memory configurations that range in size from 25K bit to 512K bit (local memory) and 64K bit to 320K bit (shared memory). The capability to switch the NSS between fixed and motion base simulations is through shared memory.

Most of the SMS application software (Shuttle systems simulations) reside in the Univac host complex. Each real time simulation is structured into 13 frame jobs which are dispatched and executed in prescribed sequences. The basic frame time of each simulation is 40 milliseconds which allows the highest real time execution rate to be 25 iterations per second. Generally, this execution rate is applied to time critical (flight dynamics, flight software interfaces, (etc.) areas of the simulation. Other portions of the simulation are executed at lower execution rates. Dependencies between simulated vehicle systems are satisfied by ordering within frame jobs and by specifying the sequence of execution of specific frame jobs. Time critical simulation areas are synchronized and controlled through appropriate interfaces to the simulator Central Timing Equipment (CTE).

Crew Stations and Motion System

As previously mentioned, the FBCS contains all work positions of the Orbiter flight deck while the MBCS is limited to commander and pilot positions. Within this constraint both crew stations provide an accurate interior replication of the vehicle in all areas visible and accessible to flight crews. Both cockpits are presently in STS-1, Orbiter 102, mission configuration.

Ingress/egress for the FBCS is through flight deck floor hatch openings as in the actual Orbiter vehicle. Access to the MBCS is through a conventional door mounted at the aft bulkhead allowing a walk-in capability when the crew station is in a level attitude.

Both crew stations are supported by an aural cue system simulation. Sounds produced by the Shuttle vehicle that normally would be audible within the crew compartment, and characteristic of vehicle operational performance, are synthesized. Control of this simulation is from each respective instructor/operator station.

All FBCS and MBCS controls and displays, except for flight computer display and keyboard units, are interfaced through appropriate simulator signal conversion equipment (SCE), master controllers, and Crew/Instructor/Operator Station Intelligent Controllers, to the Univac host computing system--where the bulk of the onboard system simulations reside. Remaining simulated system sensor inputs/outputs are made available via the IC shared memory interface. The host to CIOS IC data channel interface also allows control for the MBCS motion system.

The MBCS motion system was specifically adapted for SMS use and features a unique tilt system in addition to the six-degree-of-freedom motion platform. These systems allow a composite 108 degree pitch-up hardware capability. For the normal liftoff, boost, and ascent mission phase an excursion to 90 degrees in pitch (80 degrees from the tilt mechanism and 10 degrees from the motion platform) has been programmed for the MBCS. This allows a sustained longitudinal acceleration cue by means of directable 1-g gravity vector through the backs of crew members. A maximum of 3-g real world axial acceleration is scaled and simulated for the launch/ascent phase. The motion system also provides acceleration cues for on-orbit, aeroflight and transition phases of orbital insertion, de-orbit, and abort. These onset cues are obtained through software filters for each of the six-degrees-of-freedom. Inputs to these filters are scaled vehicle translational accelerations and angular velocities which are output as proportional platform displacement commands in both position and attitude. Additional outputs by the motion software are vibration and buffet cues, for appropriate mission phases, as well as the necessary wash-out compensation to avoid reaching platform excursion limits (and to re-direct the earth's gravity vector to prevent its effect from resulting in false cues). Performance limits of the motion system are as shown in Table I.

Instructor Operator Stations

Two basic instructor operator stations (IOS's) are associated with the SMS. One station operates with the FBCS simulation and the other with the MBCS simulation with each functioning as the central controlling point for each respective simulation. In addition, there is an in-cockpit instructor/observer station within the aft section of the MBCS. Each of the two basic IOS's permit monitoring of all simulated vehicle systems, crew station panels and controls, and cockpit out-the-window visual scenes. Control and moding over all aspects of simulator operation is also provided for both training and checkout sessions. Procedurally, the operator stations are used to prepare the simulator for a training session and operate the simulation during the session. The instructor stations are manned to execute a specific training exercise including the, monitoring of simulated subsystem behavior, communication with the crew, and initiation of specific simulated malfunction cases or off nominal conditions. The primary interfacing medium at the IOS's are interactive alphanumeric CRT systems. Each station has CRT readout capability and keyboard/lightpen input capability. An extensive voice communications system allows coordination among all major elements of the SMS (crew stations, IOS's, NSS area, computer area, et cetera) as well as to the mission control center. The following console hardware exists at fixed and motion base IOS's:

116

Operator Station

- Two alphanumeric CRT displays
- Two keyboard/lightpen units
- Two graphic CRT displays
- Two visual monitors (CRTs)
- Two communication control panels

Shared Station Equipment

- Three 8-channel X-T recorders
- Two 2-channel X-Y recorders
- Two CRT hardcopy units

Instructor Station

- Nine alphanumeric CRT displays
- Four keyboard/lightpen units
- Five graphic CRT displays
- Two visual monitors (CRTs)
- Four flight computer display units
- One flight computer keyboard unit
- Six communication control panels

The motion base in-cockpit instructor/observer station is equipped with a single alphanumeric CRT and keyboard unit.

Visual System

The SMS visual system consists of two major functional areas, the image generation function and the image display function. Both SMS crew stations have identical forward window image generation and display configurations and capabilities. The FBCS has the additional Orbiter closed circuit television (CCTV) and aft/overhead window visual systems. Table II summarizes the visual scene content for each simulated mission phase of the SMS.

Each crew station simulation utilizes digital image generation (DIG) systems. The MBCS has a single system (forward windows) while the FBCS has three systems (forward windows, aft/overhead windows, and CCTV). All four DIG's are of the same basic configuration and differ only in data base (scene) content and in occlusion processing sophistication. Figure 2 illustrates a representative visual (single DIG) system interface for the SMS. The DIG controller 8/32 functions as the major data control center for a DIG. It receives simulated orbiter specific attitude, position, and dynamics data that is collected in the host computer then formatted and transmitted to visual shared memory by the visual intelligent controller. Relevant data base information is retrieved from disc storage by the DIG controller in response to these inputs from the intelligent controller. Formatted data and commands are then transmitted to the frame calculator.

The frame calculator performs coordinate transformations of received position and illumination vectors to an object coordinate system, accesses objects stored in the active data base via the DIG controller, and performs testing for visibility Data is then translated/rotated into a crew station window coordinate system reference where calculations of intensities as a function of illumination source and direction are performed. Data is limited (clipped) to only allow further processing of objects within the window field-of-view and converted into projected edges with associated display parameters in two dimensional coordinate form, for transmission to the scan line computer.

The scan line computer has double buffered memory that allows simultaneous writing of the present frame and reading of the next frame. An edge list function within the scan line computer, converts adjacent polygon boundaries to display edges, eliminates common edges, and sorts display edges by scan line. Occlusion calculations are performed to determine if the intersection of an

117

edge with a scan line is visible or occluded. Intensity, color, shading, and edge smoothing calculations are done for each visible intersection. This data is output to the appropriate video generator where digital to analog signal conversion provides signals suitable to drive the SMS display system.

Do to the potentially large number of real world moving objects associated with the Shuttle RMS and payload bay operations, the SMS CCTV and aft DIGS both contain a sophisticated occlusion system. This system processes defined lists of objects, within view from a specific eyepoint, and continuously calculates and provides ordering of occlusion priorities for these objects.

There are three different image display systems used on the SMS. Both crew stations contain a direct view TV, wide angle collimated light, forward window display system. This system allows simultaneous color presentations on any four of the six Orbiter forward windows. Field-of-view for each window is 40 degrees vertical by 45 degrees horizontal with 9 arc minutes of resolution. The fixed base crew station contains the orbiter 525 line CCTV simulation. This system contains two split screen monitors with a capability of viewing three different scenes simultaneously. Presentation is in black and white as in the real world vehicle. Video from the CCTV is available for downlink transmission to the mission control center as in actual Shuttle flight. The aft/overhead window displays for the FBCS consist of four liquid crystal light valve projection systems coupled with four tilted pancake window optical assemblies. Resultant field-of-view for each window is 70 degrees vertical by 93 degrees horizontal with 9.6 arc minutes of resolution. These windows presently provide monochromatic presentations. SMS interface and special effects electronics generate alphanumeric data to be displayed on the CCTV displays, and provide horizon layer, terminator effects, and cloud simulation for forward window displays.

Flight Computer Interface

Each of the two SMS real time simulations is interfaced to five flight-type Shuttle General Purpose Computers (GPC's) which use actual flight software. Figure 3 illustrate the SMS to GPC hardware interfaces which exist for both the FBCS and MBCS. These interfaces, consisting of the GPC's, Simulation Interface Device (SID), and SID Intelligent Controller, allow a simulation of the Shuttle Data Processing System (DPS). Functionally, this simulation includes Guidance, Navigation, and Control, Air-to-Ground Telemetry and Command Interface, Displays and Controls, Shuttle Systems Monitoring and Management, Payload Handling and Management, and Systems Sequencing. The SID IC facilities communication between the GPC's/SID and vehicle system modeling in the remainder of the SMS.

An individual GPC consists of a central processing unit, a memory, and an input/output processor (IOP). The IOP provides 24 buses (out of a total of 25) for interfacing to 10 types of Bus Terminal Units (BTU's). These BTU's are functionally categorized as:

- Multiplexer/Demultiplexer
- Mission Event Sequencing and Control
- Main Engine Interface Unit
- Mass Memory Unit
- Multifunction Crew Display System (consists of Display Electronics Unit, CRT display, and keyboard)

118

- Solid Rocket Boosters
- Launch Processing Unit
- Dedicated Display Unit

The remaining bus is for inter-computer communicat ns and is connected directly to the IOP's of each GPC.

The SMS SID was designed and developed specifically to interface the GPC's to Perkin Elmer 8/32 computers. It contains IOP interfacing hardware that emulates the front half (IOP side) of the BTU's. The remainder of the BTU's are functionally simulated on the SMS side of the SID interface. The SID also contains a modified IBM System 7 computer that functions as the Air/Ground Equipment (AGE) controller. It is programmed to interface with the GPC ACE connector interface and with the SID IC. It allows the SID IC to command GPC moding control functions, the processing of GPC in/out discretes, and the support of equipment real time synchronization. The AGE controller performs SID IC commanded functions and transmits appropriate feedback responses to the SID IC. Many of the AGE discrete interfaces are to the SMS crew station (via SCE) for panel switches and controls which have a direct GPC function.

Non-AGE, GPC input data flow consists of data collected from SMS subsystem programs (mainly residing in the host computer), processed to proper units and format by the SID IC, and placed on an GPC/IOP bus by the SID via the appropriate BTU model. GPC output data is commanded through an IOP data bus to the appropriate BTU simulation (SID), then to the SID IC for processing to proper units, and finally stored for access by the using SMS system programs.

There are a category of SMS crew station displays that are driven directly by GPC commands through the Dedicated Display Unit BTU. These are the Attitude Direction Indicator, Horizontal Situation Indicator, Alpha/Mach Indicator, Altitude/Vertical Velocity Indicator, and Surface Position Indicator. Additionally, the Multifunction Crew Display System has a direct crew station to GPC interface. This system of Display Electronic Units, CRT displays, and keyboards are the primary means of crew interaction and communication with the GPC's.

The SMS flight computer interface supports flight Mass Memory Units (MMU's) (tied to the SID via BTU simulated interface) as well as the capability of interfacing with simulated MMU's through the SID IC.

Shuttle Systems Simulation

The SMS contains mathematical modeling that simulates all Shuttle onboard systems that have crew and flight control (MCC) interfaces. Both of the FBCS and MBCS software loads execute in real time. Individual onboard systems are simulated to sufficient fidelity that crew station display and control responses and inputs are indistinguishable from those of the actual vehicle. Actual flight software is used and interfaced to simulated vehicle systems. Both hardware and software redundancy management features of the GPC/flight software are exercised. Reset/initialization points are provided throughout the various Shuttle mission phases that allow the simulation to be brought up with all systems fully synchronized relative to time. Over 3,800 individual simulated malfunctions have been preprogrammed within the application software and are menu selectable for activation from the instructor operator stations. Table III tabulates the major vehicle subsystems, as well as the environmental, visual, and MCC interface capabilities simulated within the SMS.

119

Network Simulation System

The Network Simulation System (NSS) simulates the real world Ground Space-flight Tracking and Data Network (GSTDN) and its associated interface with the Mission Control Center (MCC). The GSTDN is a world-wide network of stations, tied to the MCC through Goddard Space Flight Center (GSFC), which provides telemetry, tracking, and communication capability for manned spacecraft—including the Shuttle. These stations provide the RF links necessary for the reception of downlink telemetry data (incuding the stripping, conversion, and shipping of digitized voice data) the transmission of uplink command data, and the acquisition/computation of tracking data.

Figure 4 illustrates the NSS interfaces within the SMS. The NSS consists of three Perkin Elmer 8/32 computers, an instructor operator station, wideband and flight type recording equipment, special purpose synchronization and chan-nelization equipment, and modem input/output interface devices. The NSS can be switched to either FBCS or MBCS simulation and communicates through the IC shared memory interface that is accessable by the CIOS IC, the Visual IC, and the SID IC.

Shuttle downlink data consists of Operational Instrumentation (OI) data merged with GPC downlist and digitized voice data. The SMS simulates this process and the resultant simulated downlink stream is the same as the actual vehicle output. The NSS downlink system accounts for the transmission of telem-etry (real time and recorded) from the vehicle to the tracking sites, to GSFC, and then to the MCC. NSS downlink simulation functions include reception of formatted air-to-ground data; voice data stripping; remote site formatting, addition of header information, recording, site status message generation/routing, GSFC multiplexing, and routing to MCC. SMS CCTV video is also made available to the MCC in analog form.

The Shuttle uplink stream is used to send command and telemetry data to the Shuttle as well as acquisition data to the remote tracking sites. The NSS uplink function accounts for the GSFC reception of data from MCC and the con-version and routing of same to the sites. Simulated uplink site functions include data reception, validation, reformatting, recording, and transmission to the SMS via SMS IC shared memory.

The remaining NSS major function, Groundtrack, receives SMS generated Orbiter position, velocity, and communications systems status data to simulate the site function of vehicle tracking relative to site location. This includes calculations of Acquisition-of-Signal (AOS) and Loss-of-Signal (LOS) and signal strength as appropriate for the C-band and S-band site simulations. Formatters, upon proper simulated site moding control, place tracking data into an MCC com-patable format for transmission.

The NSS complex contains its own independent instructor operator station with both analog displays and controls as well as an interactive alphanumeric CRT system. CRT displays are constructed using both SMS available data and NSS internally generated data. Capability for simulation set-up, moding, systems monitoring, malfunction insertion, and voice communications are provided.

Conclusion

The SMS exemplifies numerous real time simulation advancements within one complex for flight crew training. Advancements have been realized in, utilization of computer image generation, interfacing of flight computers and associated software, completeness and sophistication of simulated systems, and computer system interfaces and software structuring. This facility will play a major role in execution of Space Shuttle program objectives for the remainder of the decade.

References

1. The Singer Company, SMS Digital Image Generator Operation and Maintenance Manual, JSC 11002-01, 1978.

2. IBM, SMS Interfaces and Capabilities, CDRL 007A2, 1978.

Table I

MBCS Motion System Dynamic Performance Units

ROTATION	EXCURSION (DEG)	VELOCITY (DEG/SEC)
PLATFORM PITCH	+28.0	
	-26.5	15.0
ADDITIVE EXTENDED		
PITCH	+0 to 80	42.1 UP
		43.0 DOWN
ROLL	+18.5	15.0
YAW	+23.0	15.0

DISPLACEMENT	EXCURSION (M)	VELOCITY (M/SEC)	ONSET ACCEL (G/SEC)
LONGITUDINAL	1.1	.61	+3
LATERAL	1.1	.61	+3
VERTICAL	0.9	.61	+3

Table II

SMS Visual Scene Content

FBCS and MBCS Forward Windows

- o Launch and Ascent Mission Phase
    - o Launch site area detail
    - o Low altitude earth Terminal Area Energy Management (TAEM) and landing area scene
    - o Solid rocket booster separation effects
    - o High altitude earth scene with horizon
    - o Star field
- o On-Orbit Mission Phase
    - o Day and night high altitude earth scene
    - o Star field, sun, and moon
    - o Rendezvous vehicle (mission dependent)
- o Entry and Landing Mission Phase
    - o Low altitude detailed earth scene
    - o Primary and contingency landing sites
    - o Runways, terrain features, landing site detail

FBCS Aft/Overhead Windows and CCTV Displays

- o On-Orbit Mission Phase
    - o Simplified earth
    - o Starfield, sun, and moon
    - o Orbiter ownship features
    - o Payload bay including doors, radiator panels, lights, and CCTV cameras with pan/tilt units
    - o Remote Manipulator System (RMS) arm including attached cameras and lights
    - o Payloads (mission dependent)

122

Table III
Shuttle Systems Simulation Content

- **COMMUNICATION, TRACKING AND INSTRUMENTATION**

  - OPERATIONAL INSTRUMENTATION SYSTEM
  - NETWORK SIGNAL PROCESSOR
  - MICROWAVE LANDING SYSTEM
  - RADAR ALTIMETER
  - MASTER TIMING UNIT
  - PULSE CODE MODULATION UNIT
  - PAYLOAD INSTRUMENTATION SYSTEM
  - INTERCOM AND UHF COMMUNICATIONS
  - S-BAND SYSTEM
  - TACAN
  - FLIGHT RECORDERS
  - CAUTION AND WARNING SYSTEM

- **DATA PROCESSING SYSTEM**

  - OPERATIONAL INSTRUMENTATION INTERFACE
  - FLIGHT COMPUTER INPUT/OUTPUT PROCESSING
  - MASTER EVENTS CONTROLLER
  - LAUNCH PROCESSING INTERFACE
  - PRIMARY AND BACKUP FLIGHT SOFTWARE
  - MAIN ENGINE INTERFACE
  - RMS MASTER CONTROL INTERFACE UNIT
  - FLIGHT COMPUTERS AND FLIGHT SOFTWARE

- **ELECTRICAL POWER**

  - POWER DISTRIBUTION AND CONTROL
  - FUEL CELLS
  - POWER REACTANTS STORAGE AND CONTROL

- **ENVIRONMENTAL CONTROL AND LIFE SUPPORT**

  - ATMOSPHERE CIRCULATION AND PURIFICATION
  - SPACE RADIATORS
  - FREON AND WATER COOLANT
  - GASEOUS SUPPLY

- **GUIDANCE, NAVIGATION, AND CONTROL**

  - THRUST VECTOR CONTROL
  - GN&C CONTROLS AND DISPLAYS
  - AERO SURFACE CONTROL
  - INERTIAL MEASUREMENT UNIT
  - STAR TRACKER
  - RATE GYROS AND ACCELEROMETERS
  - AIR DATA SYSTEM

- **MECHANICAL POWER**

  - AUXILIARY POWER UNIT
  - HYDRAULIC POWER SYSTEM

- **MECHANICAL SYSTEMS**

  - SEPARATION LOGIC
  - LANDING, BRAKING, GROUND CONTACT
  - EJECTION SEAT
  - UMBILICAL LOOKS

- **PAYLOAD ACCOMMODATION SYSTEMS**

  - REMOTE MANIPULATOR SYSTEM KINEMATI MODEL
  - END EFFECTOR AND SERVO SIMULATION
  - RMS ATTACHMENT INTERFACE AND PYRO
  - PAYLOAD RETENTION SYSTEM
  - PAYLOAD BAY DOORS
  - PAYLOAD BAY LIGHTING AND CCTV SELECTION AND CONTROL

- **PROPULSION**

  - MAIN ENGINE SYSTEM
  - MAIN ENGINE CONTROLLER
  - SOLID ROCKET BOOSTER SYSTEM
  - REACTION CONTROL SYSTEM
  - ORBITER MANEUVERING SYSTEM

- **VEHICLE DYNAMICS**

  - ORBITER AND TARGET EQUATIONS OF MOTION
  - AERODYNAMICS AND RCS/AERO INTERACTION
  - BODY BENDING AND FUEL SLOSH
  - MASS PROPERTIES

- **SHUTTLE ENVIRONMENT**

  - EPHEMERIS
  - ATMOSPHERE/GRAVITY/WINDS
  - AURAL CUES
  - MOTION

- **VISUAL SYSTEMS**

  - FORWARD WINDOW DIGITAL IMAGE GENERATION
  - CLOSED CIRCUIT TV DIGITAL IMAGE GENERATION
  - AFT/OVERHEAD WINDOW DIGITAL IMAGE GENERATION
  - VISUAL MODING, CONTROL AND FORMATTING
  - VISUAL SPECIAL EFFECTS
  - FORWARD WINDOWS DISPLAY SYSTEM
  - CLOSED CIRCUIT TV DISPLAY SYSTEM
  - AFT/OVERHEAD WINDOW PROJECTION AND DISPLAY SYSTEM

- **NETWORK SIMULATION SYSTEM**

  - UPLINK AND DOWNLINK TELEMETRY
  - TRACKING
  - DATA PROCESSING, FORMATTING, MODING, AND RECORDING
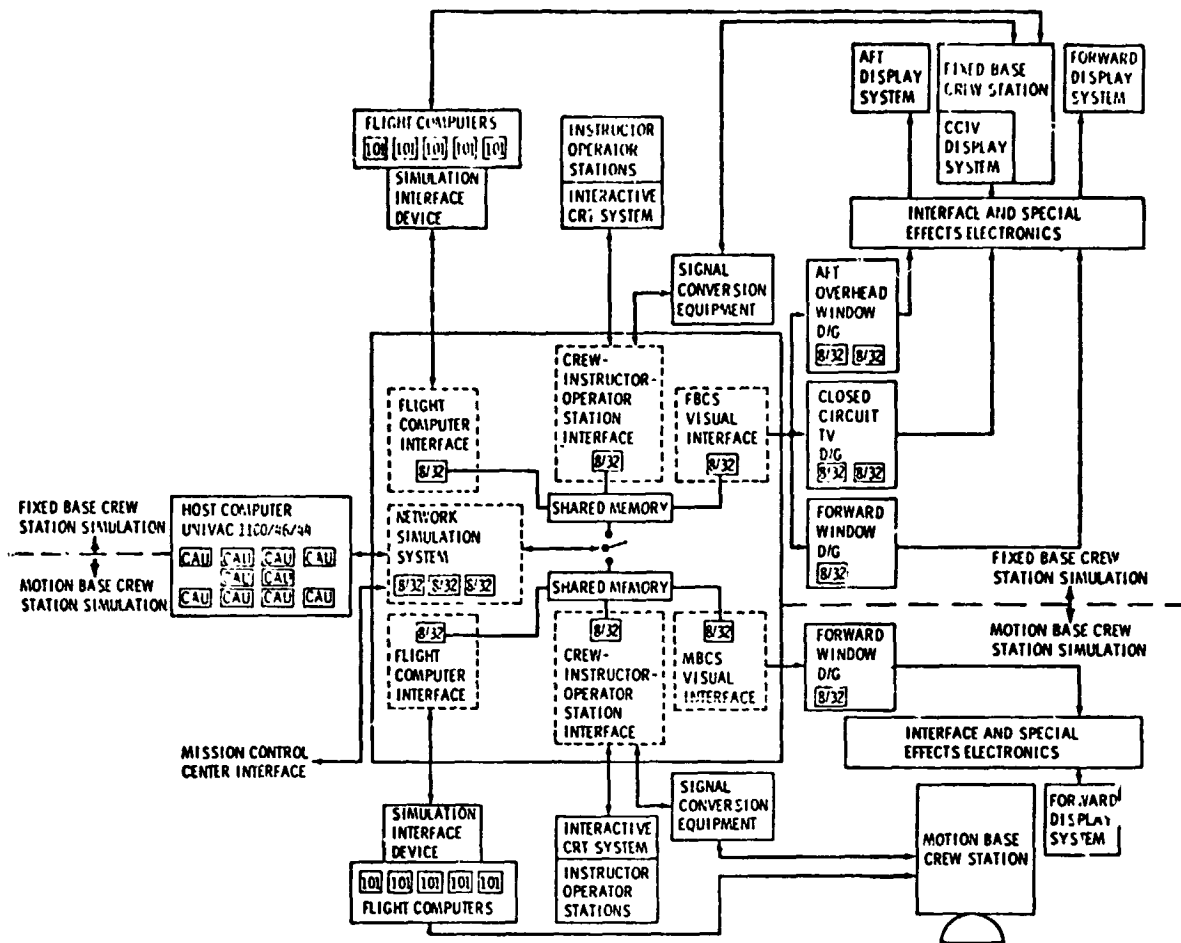 - COMMUNICATIONS
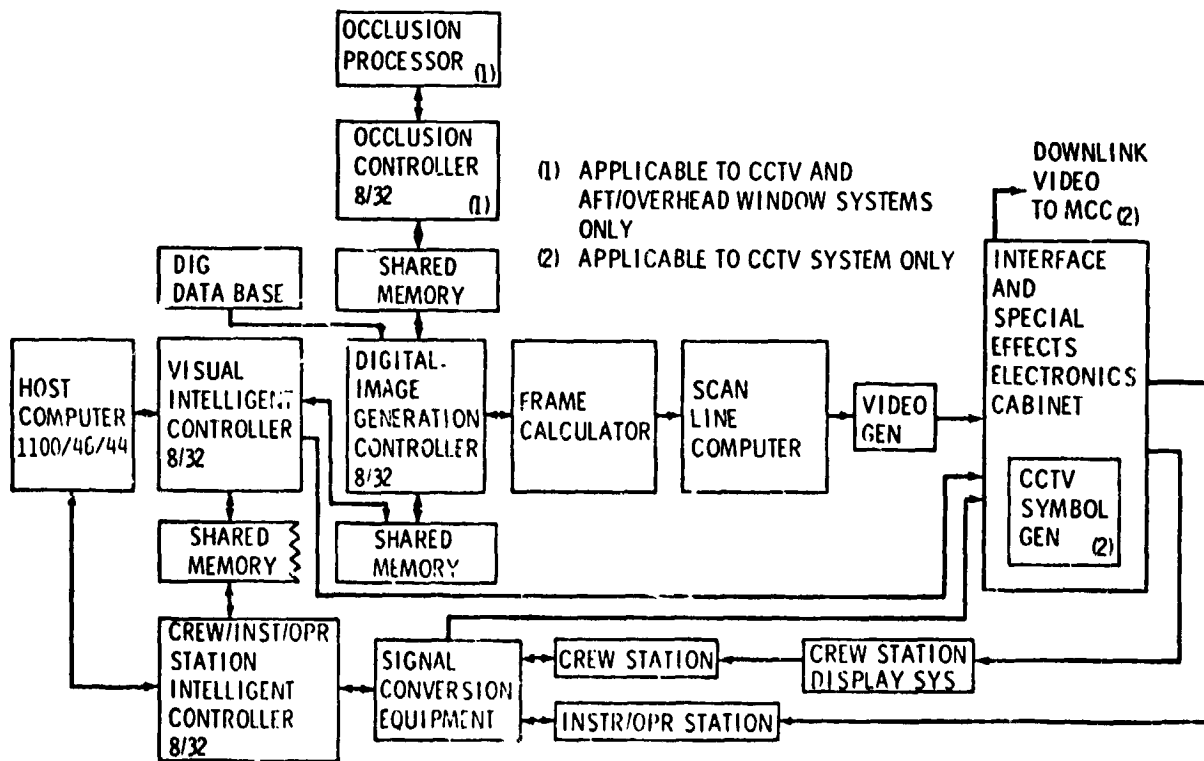 - MISSION CONTROL CENTER INTERFACE

Fig. 1 SMS top level block diagram.

(1) APPLICABLE TO CCTV AND AFT/OVERHEAD WINDOW SYSTEMS ONLY

(2) APPLICABLE TO CCTV SYSTEM ONLY
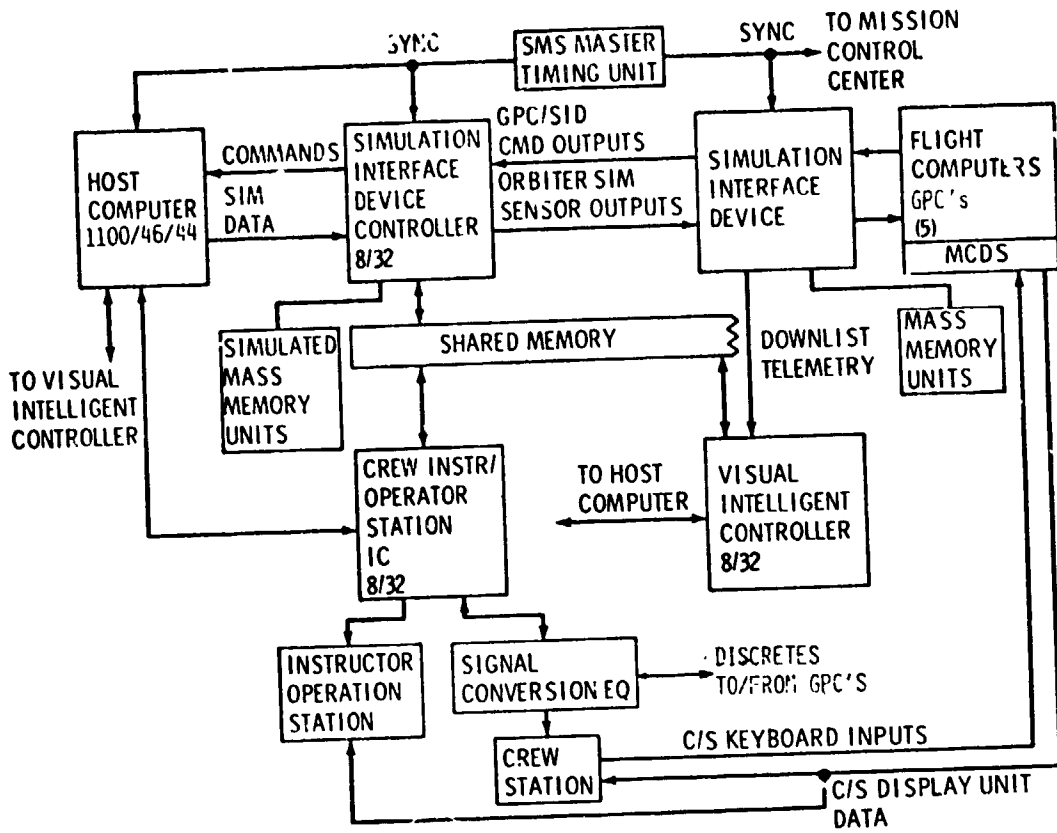
Fig. 2 SMS visual system interface.

124

Fig. 3 SMS/Flight computer interface.

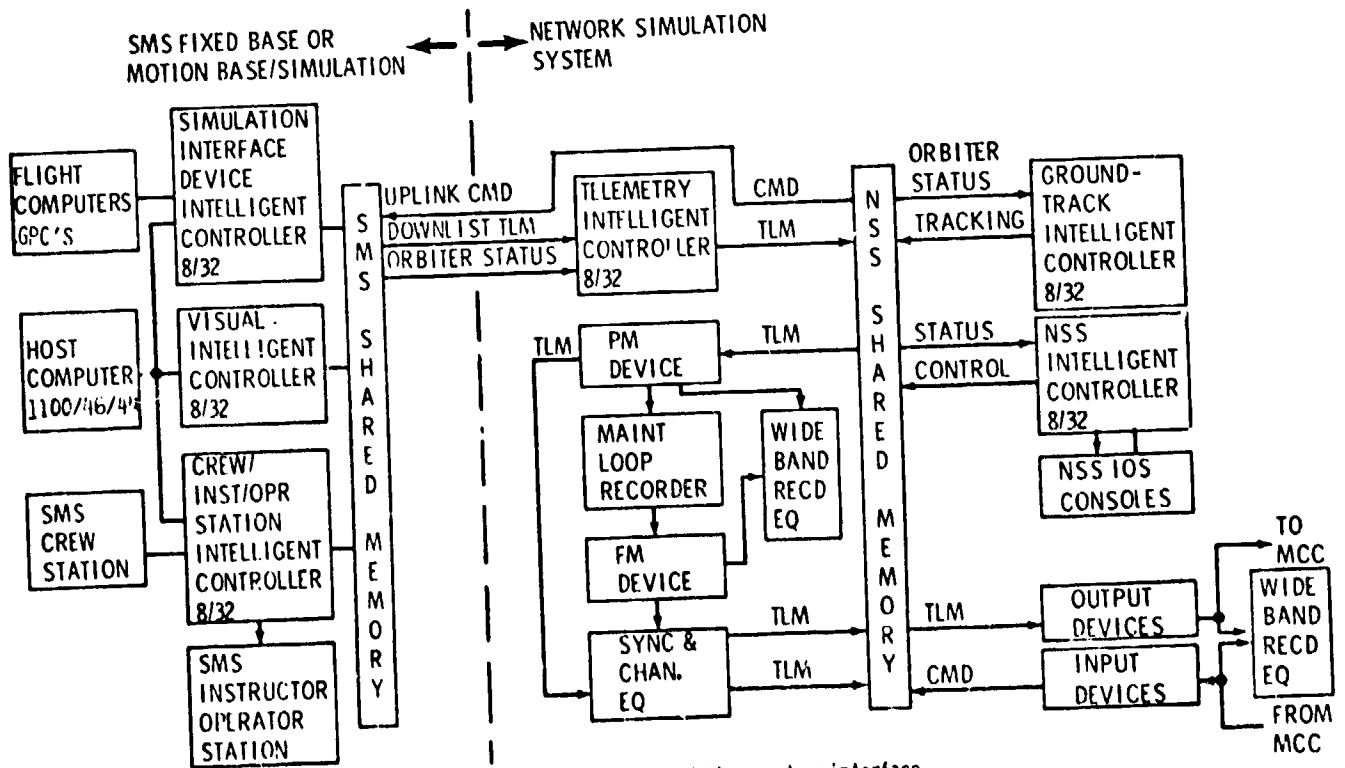Fig. 4 SMS, network simulation system interface.

125

A RADIANT HEATING TEST FACILITY FOR
SPACE SHUTTLE ORBITER THERMAL PROTECTION SYSTEM CERTIFICATION

William D. Sherborne and James D. Milhoan*

ABSTRACT

A large-scale Radiant Heating Test Facility has been constructed at
the NASA Lyndon B. Johnson Space Center so that thermal certification tests
can be performed on the new generation of thermal protection systems devel-
oped for the Space Shuttle Orbiter. This facility simulates surface ther-
mal gradients, onorbit cold-soak temperatures down to 200 K (-100° F),
entry heating temperatures to 1710 K (2620° F) in an oxidizing environment,
and the dynamic entry pressure environment. The capabilities of the facil-
ity and the development of new test equipment are presented.

INTRODUCTION

The Space Shuttle Orbiter has a lightweight reusable thermal protec-
tion system (TPS) that was developed to withstand the dynamic acoustic,
thermal, and load environments associated with launch, orbit, and atmos-
pheric entry. Although several thermal protection systems are used on the
Orbiter, the most demanding requirements apply to the leading edge struc-
tural subsystems (LESS), where maximum heating and the most severe thermal
gradients occur in the stagnation regions of the leading edges. A test
program is in progress at the NASA Lyndon B. Johnson Space Center (JSC)
to certify the LESS by subjecting full-scale test articles of the nose cap
and the wing leading edge (WLE), which make up the LESS, to sequential
tests that simulate launch acoustics, air loads, and entry heating. The
entry heating simulations, scheduled to begin in July 1980, are being
performed to verify thermal analyses used to design the LESS, to demon-
strate the LESS structural integrity under thermally induced stress, and
to evaluate the effects of oxidation on the LESS performance.

Because a new facility was required to accept items as large as the
LESS test articles, a large-scale Radiant Heating Test Facility (RHTF) was
constructed at JSC. The entry environments simulated in the RHTF include
peak temperatures to 1710 K (2620° F) in an oxidizing environment, severe
surface thermal gradients, cold-soak temperatures to 200 K (-100° F), and
dynamic pressure. The concurrent simulation of temperature and pressure
in an oxidizing environment is important because the LESS have reinforced
carbon-carbon (RCC) components whose oxidation characteristics, and there-
fore mission life, are sensitive to these factors. The RCC forms the
exterior surface of the LESS; simulation of severe surface thermal gradi-
ents on RCC is important to the structural behavior of the RCC and to the
indepth temperature response of the test article, which is dependent on

---

*NASA Lyndon B. Johnson Space Center, Houston, Texas.

cross radiation from the RCC. Simulation of cold-soak conditions that result from the orbital attitude of the vehicle relative to the Sun are required to demonstrate that the attach fittings have adequate allowance for thermal contraction and to precondition the test articles before heating because the thermal stresses are increased by this effect.

To accomplish the test objectives associated with simulation of oxidation effects and surface thermal gradients, the RHTF incorporates two unusual technical features: a new type of multizone large-scale heater that operates at high temperatures in an oxidizing environment over a wide pressure range, and a multichannel fiber optic pyrometer system that, in combination with a digital computer, controls the power to the heater.

Because the LESS test requirements dictated the design of the RHTF, these requirements are described in detail and used throughout the paper to illustrate the functions of the facility systems. However, the RHTF test capabilities are not restricted to the LESS tests because another objective was to construct a facility that could, with little or no modification, test other areas of the Orbiter TPS. The design and development of the RHTF to perform complex large-scale entry simulation tests on the Orbiter LESS is the subject of this paper.

TEST ARTICLES

The nose cap and WLE test articles (fig. 1) were fabricated from a variety of specialized components to form a strong lightweight assembly capable of withstanding the severe entry heating conditions in the Orbiter stagnation regions while limiting aluminum structure temperatures to less than 450 K (350° F). The higher temperature regions of the LESS are fabricated from RCC, a laminate of carbon cloth that is molded to the required shape and coated with silicon carbide to inhibit oxidation. The RCC is attached to the Orbiter primary structure with a complex set of high-temperature linkages that performs three important functions: (1) attaches the RCC to the structure, (2) allows differential expansion of the RCC components over a wide temperature range, and (3) thermally isolates the RCC from the primary structure. The attachment fittings are covered with flexible insulation to shield the structure from radiant heating at the attachment points. The area aft of the RCC is covered with high-temperature reusable surface insulation (HRSI), a lightweight silica insulation with a silicon tetraboride thermal emissivity coating that is bonded to the vehicle with a flexible strain isolation pad (SIP) and silicon rubber adhesive. A large section of the Orbiter primary structure (the forward fuselage area and bulkhead or the nose cap) and a portion of the wing spar and wing box (the WLE) are incorporated in both test articles to mount the RCC and HRSI and to ensure proper test boundary conditions.

127

TEST ENVIRONMENTS

To meet the objectives for LESS certification, the nose cap and WLE test articles must be subjected to environments that sim·late critical flight conditions. These environments are as follows.

1. Temperatures ranging from 240 to 200 K (-30° to -100° F) to simulate onorbit thermal conditions and the thermal gradients resulting from entry heating of the cold-soaked TPS.

2. Heating at specified rates from 200 to 1730 K (-100° to 2650° F) and cooling to near-ambient conditions over a period of 2000 seconds to simulate entry heating conditions from a 61-kilometer (200 000-foot) altitude to touchdown. Typical entry heating profiles are shown in figure 2.

3. Surface temperature gradients representative of the entry environments to evaluate the effects of thermally induced stresses within the nose cap and WLE systems. Gradients are produced by dividing the radiant heaters into a number of zones, then independently controlling each zone to a specified temperature profile. Several of these profiles for the nose cap are shown in figure 2 and the corresponding isotherms are shown in figure 3.

4. Control of the test article ambient pressure over a dynamic range from 0.013 to 101.3 kilopascals (0.1 to 760 torr) to simulate the entry altitude pressure environment. Degradation of RCC strength is expected to result from subsurface oxidation that occurs when microcracks in the protective silicon carbide coating of the RCC admit air. Because RCC oxidation effects and the thermal conductivity of LESS insulation depend on temperature and pressure, control of the pressure profile to within ±267 pascals (±2 torr) over the entire dynamic range and synchronization of the temperature and pressure profiles are essential.

TEST SEQUENCE

A typical test sequence begins by evacuating the chamber and repressurizing it to about 50 kilopascals (380 torr) to prevent condensation from forming during the cold soak of the test article. The test article is radiantly cooled in front of a cold shroud that is cooled by chilled methanol. When the cold-soak conditions have been achieved, the test article is moved to a position in front of the radiant heater, the nitrogen is pumped out of the chamber, and coordinated repressurization and heating profiles are begun. After peak temperature is achieved, progressively less power is applied to the heaters until they are no longer active. The test article is then returned to the cooling shroud so that heat stored in the heater elements will not delay the prescribed test article cool down. Before the test article is moved from the heater position, the cooling fluid circulating through the cold shroud is switched over to the cooling water circuit. The operation of these systems is described in more detail later.

RHTF SYSTEMS

The RHTF (fig. 4) is composed of several primary and support systems that provide the desired environments. The altitude simulation system consists of an altitude chamber, vacuum pumps, and a vacuum/repressurization control system. This system is central to the facility since all tests are conducted within the chamber. Figure 5 shows the altitude chamber with the WLE test article, the heater, and the cooling shroud installed. Because the altitude chamber can accommodate only one heater and one test article at a time, individual heaters for the nose cap and the WLE are assembled on carriages that roll on rails inside the chamber to facilitate rapid installation and removal. The heaters are controlled by a computerized feedback control system.

The coolant system is subdivided into several subsystems. The test coolant subsystem provides closed-loop water cooling for the heater reflectors and auxiliary shrouds to prevent overheating of the altitude chamber walls and instrumentation wiring. The refrigerated coolant subsystem circulates refrigerated methanol through the cold shrouds to simulate onorbit cold soak. A test article positioning subsystem with rails and an air-motor-powered chain drive is used to move the test article from the cold shroud to the heater position. A cryogenic subsystem supplies dry gaseous nitrogen to the altitude chamber to prevent condensation of atmospheric moisture on the surface of the test article and the cooling shroud during cold soak. The instrumentation and computer systems are used for test data acquisition and control and for critical measurement limit checks and automatic aborts. The computer provides real-time data output through cathode ray tube (CRT) terminals and a plotter for monitoring and quick-look evaluation of test data.

Heater System

The heaters have the most stringent requirements of any system in the RHTF; consequently, they received the most extensive design and development effort. These heaters must operate repeatedly at temperatures up to 1810 K (2800° F) in a low-pressure oxidizing environment without arcing while providing thermal gradients on the surface of the test articles.

Several heater concepts were considered, but the most promising used a resistance-heated graphite bar or plate as a heater element. Graphite heater elements can operate at high temperatures and can be readily machined to complex heater element geometries, thereby simplifying the assembly of compound curved arrays. The operating voltage of graphite heater elements can be limited to prevent arcing at low pressures by adjusting the cross-sectional area and selecting a graphite with the appropriate electrical resistivity.

WLE heater.- The WLE heater (fig. 6) is composed of 19 heater modules, 11.4 centimeters (4.5 inches) wide by 185 centimeters (73 inches) long, configured in a WLE array by a support structure that also serves as a manifold for supply and return of coolant to the heater modules. Each module (fig. 7) contains two "hairpin" graphite elements supported by power

electrodes at one end and a pivoted graphite support post at the other. This pivoted post allows the 1 centimeter (0.4 inch) of thermal expansion that the element experiences between 295 and 2035 K (70° and 3200° F) without overstressing the elements. The electrodes are water cooled and are supported by two rectangular tubes that also serve as the coolant manifolds for the module. Gold-plated base, side, and end reflectors are installed for maximum thermal efficiency and to limit the view factor of each module.

The modular construction serves two functions: each module can be independently controlled and the heater modules can be mounted on an alternate support to test flat articles up to 1.8 by 2.4 meters (6 by 8 feet) with 22 heater zones. If required, the center section of each module can be removed to make an array 1.2 meters (4 feet) wide for testing smaller articles.

The WLE heater was originally fabricated with bare graphite elements capable of reliable long-term operation at temperatures of 2035 K (3200° F) in a nitrogen atmosphere. However, because of the need to determine the effects of subsurface oxidation on the RCC, oxidation-inhibiting coatings were developed for the heater elements so that the heater could also be operated in an air environment. These coated heater elements were fabricated from graphites compatible with the coating but with relatively high electrical resistance. The increase in electrical resistance was compensated for by redesigning the heater element from a two-pass hairpin configuration to a shorter single-pass configuration. Four single-pass coated elements are installed in each heater module on new water-cooled electrodes. The electrodes at one end of the heater are fixed; those at the other end are mounted on electrically isolated ball bearing slides to accommodate the thermal expansion of the elements. The single-pass configuration offers another operational advantage by eliminating the high electrical potentials across the narrow gap at the electrode end of the double-pass elements, thereby reducing the probability of electrical arcing.

Nose cap heater.- The nose cap heater (fig. 8) forms a paraboloid of revolution that approximates the exterior surface contour of the nose cap test article. The heater is composed of 96 triangular and trapezoidal graphite elements arranged in 22 independent heating zones (fig. 9). The zones are arranged and sized to provide the desired gradients on the test article surface and to match the power capabilities of the heater control system as closely as possible.

The nose cap heater elements have serpentine current paths (fig. 10) to provide the proper resistance and evenly distribute the power over the surfaces of the elements. Element thickness is sized to provide the proper resistance and a wide current path so that a high ratio of heated-to-unheated surface area (approximately 70 percent) is maintained. This high ratio allows the heaters to operate only 83 K (150° F) hotter than the test article under peak temperature steady-state conditions. Also shown in figure 10 are the large-diameter electrodes that are capable of conducting high currents without encountering electrical contact problems resulting from excessive resistive heating.

130

A water-cooled stainless steel reflector is located approximately 15 centimeters (6 inches) behind the element surface to improve the efficiency of the heater and to shield the associated electrical connections and coolant hoses from excessive heat. The reflector and heater electrodes are mounted on a large stainless steel structure suspended from a carriage installed on rails in the chamber. The electrodes for the nose cap heater are rigidly mounted and thermal expansion is accommodated by element flexing.

Coated heater elements.- Concern over the effects of RCC subsurface oxidation led to the requirement to perform 100 mission simulations in an oxidizing environment. Studies conducted at JSC showed that bare graphite elements were capable of surviving a number of test cycles before becoming severely degraded but that they would compromise test results by depleting the oxygen available to the test article. An effort was therefore undertaken to develop an oxidation-inhibiting coating for graphite heater elements. Initial attempts at coating graphite centered around a silicon carbide pack cementation process used to coat the nose cap and the WLE. The results of these attempts were not encouraging because this coating was extremely rough and porous and the graphite substrate appeared to be eroded. The next attempt used a chemical vapor deposition (CVD) process that produced a silicon carbide coating rather than converting the surface of the graphite to silicon carbide as in the pack cementation process. The CVD coating produced a smooth dense uniform layer of silicon carbide.

Preproduction samples of CVD-coated heater elements have been evaluated during development tests. Entry simulation profiles for zones that have peak element temperatures below 1730 K (2650° F) can be repeated more than 40 times before elements in that zone exhibit coating loss. A transition to a higher coating loss rate occurs above 1785 K (2750° F) and temperatures approaching 1865 K (2900° F) reduce coating life to about four entry simulations. Although the oxidation of CVD-coated heater elements is fairly low (approximately equivalent to that of the test articles) for the LESS tests, it was believed that oxygen-depleted air could be produced within the region between the heater and the test article and ingested into the test article through gaps around the RCC components during repressurization of the chamber. This possible source of oxygen depletion is counteracted by the injection of a small amount of makeup air between the heater and the test article.

Heater Control System

The RHTF heater control system consists of (1) a set of temperature sensors to measure the surface temperature of the test article, (2) a computerized control subsystem that generates error signals proportional to the difference between the measured and the desired temperatures, (3) a set of 22 ignitron power controllers that control the voltage level at each heater zone in proportion to the error signal, (4) one 4:1 stepdown transformer for each power controller to reduce peak voltage from 480 to 120 V ac to prevent heater arcing at low-altitude chamber pressure, and (5) a set of water-cooled conductors that transmit power to the heaters. This system, when properly tuned and calibrated, is capable of controlling within

±5.6 K (±10° F) of a specified temperature under steady-state conditions and within ±27.8 K (±50° F) during transient conditions.

Infrared Pyrometers

Unique problems associated with the LESS test articles precluded the use of thermocouples as control sensors. Basically, the problems were threefold: (1) the silicon released from the RCC tended to form a eutectic with platinum/platinum-rhodium thermocouples, degrading them in a short time; (2) alternate thermocouple materials did not survive exposure in the high-temperature zones; and (3) attempts to use thermocouples with high-temperature inert sheaths resulted in a wide variability of measured data due to variations in thermal contact resistance where the thermocouples were bonded to the RCC. In addition, all thermocouples displayed extremely poor reliability after repeated cyclic tests and replacement/refurbishment was time consuming and costly. Because of these problems, alternate temperature sensors were researched.

The control sensors ultimately selected to replace the thermocouples are fiber optic infrared pyrometers (fig. 11). These pyrometers are used to monitor the temperatures of the control points on the test article opposite each heater zone and the temperatures of the heater elements to keep the elements below the operational temperature limit of the CVD coating. Each pyrometer is equipped with a lens assembly that gathers infrared energy over a very narrow view angle of 0.75° and focuses it on the end of a flexible fiber bundle, 1.83 meters (6 feet) long. The fibers transmit energy to a lead sulfide (PbS) detector cell located in a detector head assembly with signal conditioning electronics that amplify the signal before it is sent to the control room, where it is linearized and output to the computer control system. The transmission characteristics of the fibers and the spectral response of the lead sulfide cell make the pyrometer sensitive to a narrow wavelength band center around 2.2 micrometers. The narrow view angle permits the lens head to be mounted behind the heater reflector where it views the test article through slots in the heater elements. Use of the flexible fiber bundle allows the lens head to be mounted near heater electrodes, wiring buses, or the coolant line while the physically larger detector head can be positioned in a more protected location away from high-current fields that could induce electrical noise into the sensitive electronic amplifiers.

These pyrometers provide a useful output from 645 to 1920 K (700° to 3000° F). The lower output threshold is limited by the detector sensitivity and the small amount of energy that can be gathered by the narrow view angle. This threshold is acceptable for control purposes because the heaters are normally operating near full power level to achieve initial element warmup during the time the profile temperature rises from starting temperature to 645 K (700° F).

Initial trials of the pyrometers with RCC test articles produced poor results. The problem was traced to a defect in the lens head that caused the pyrometer to accept infrared radiation from a target area larger than desired. The manufacturer corrected the problem by adding additional light stops to the lens assemblies to block out light from outside the design

132

view angle. Other inaccuracies were traced to small nonlinearities in the linearization circuitry, which were corrected by performing a multipoint blackbody calibration.

Computer Control Subsystem

The output of the fiber optic pyrometers is fed into the RHTF computer control subsystem where it is processed by a control algorithm in the computer to provide an output error signal to the power controllers. The infrared pyrometer output is first converted to a temperature using blackbody calibration data and the first derivative of the response temperature. The response temperature is then algebraically summed with a temperature profile point generated by the computer using linear interpolation of a table of critical profile points. The resultant error signal is integrated and the response derivative, basic error signal, and integrated error signal are multiplied by their respective gain factors, which have been specified in a configuration card deck. The products of these three signals and their gain factors are then summed to provide a composite error signal.

Adding the response derivative to the basic error signal permits greater dynamic control accuracy by anticipating test article response, and adding the error signal integral results in an error signal to keep the heaters energized even when the basic error is zero. This composite error signal permits better steady-state control by compensating for test article thermal losses. The composite error signal is then processed to compensate for input nonlinearities in the ignitron power controllers, which results in linear input-to-output characteristics for the system.

Computer control offers several advantages over equivalent analog controllers. The gains can be input or changed to a precise level with the input of a computer card, whereas, with analog control, numerous potentiometers must be adjusted and input/output gains confirmed by physical measurements. Also, the computer system does not require the frequent realinement common to analog systems. The only potential disadvantages of computer control are that the gains must be determined empirically and the relatively short update interval can result in instabilities under rapidly changing conditions. Control checkout tests indicate that neither of these shortcomings is signficant.

Another advantage of computer control is the capability to select alternate control sensors rapidly if a primary sensor fails. The control algorithm automatically monitors control response and compares it to preset temperature and control rate-of-change limits. If either limit is exceeded for more than one computer cycle (1 second), the computer automatically selects a backup sensor for control. This sensor can be another infrared pyrometer, a thermocouple, or the heater input electrical power. Each backup sensor can be programed with its own profiles and gain factors to ensure optimum control. If the secondary sensor fails, the computer can be programed to select tertiary and then quaternary control sensors or to abort at a predetermined point in the backup selection.

133

The RHTF computer control subsystem provides control of up to 5 megawatts of power in 22 control zones with minimum operator input. It also detects out-of-limit conditions rapidly and immediately follows predetermined corrective actions or automatically aborts the test.

Altitude Simulation System

The altitude simulation system provides a controlled entry pressure environment and consists of an altitude chamber, a vacuum pumping unit, an altitude control subsystem, and an air replenishment subsystem. The stainless steel altitude chamber has penetrations for instrumentation and heater power lines and has an internal diameter and length of 3 and 6.1 meters (10 and 20 feet), respectively. An end bell can be removed from the chamber for installation and removal of test equipment, and four personnel doors provide entry for test article inspection and checkout. The vacuum pumping unit (a Stokes-type roughing vacuum pump in series with a Rootes blower) evacuates the altitude chamber at a rate of 0.47 m^3/sec (1000 ft^3/min) to an operational chamber pressure of 13.3 pascals (0.1 torr).

Altitude chamber pressure is controlled by modulating a ball valve in the vacuum line between the Rootes blower and the chamber and a valve in the repressurization line with a closed-loop feedback control system. Pressure profiles are generated by a microprocessor-based programer, and chamber pressure is measured with a capacitance manometer over a three-decade range from 1.3 to 133.3 kilopascals (10 to 1000 torr). Signals from the programer and the manometer are scaled, algebraically summed, and amplified to generate an error signal that drives the vacuum and repressurization control valves. Overshoot at points of inflection in the pressure profile is minimized by simultaneously operating these valves in opposition (as one valve opens, the other closes). Vacuum and repressurization amplifier gains are adjusted to optimize system response for different altitude pressure profiles. Dynamic entry pressure environments from 0.013 to 101.3 kilopascals (0.1 to 760 torr) are controlled to an accuracy ±267 pascals (±2 torr).

Cooling System

A closed-loop coolant system provides 0.06 m^3/sec (1000 gal/min) of cooling water for distribution to heater reflectors, heater electrodes, water-cooled conductors, auxiliary cooling shrouds used to protect instrumentation wiring and chamber walls, and other components that experience significant heating. The coolant transfers heat to a water-to-air exchanger that lowers inlet water temperature by 12.8 K (23° F) with a 4.2-megawatt heat load.

An emergency coolant subsystem is also installed to meet minimum cooling requirements in the event of a main pump failure. This subsystem provides a waterflow of about 0.03 m^3/sec (400 gal/min) from a potable waterline and is automatically activated by a drop in coolant supply pressure. A control panel and logic board permit manual activation and prevent inadvertent triggering during noncritical operations.

Refrigerated Coolant Subsystem

For selected tests, the test article must first be cooled to temperatures between 240 and 220 K (-30° and -100° F) to simulate orbital cold-soak conditions before entry heating simulation begins. The test article is positioned in front of a cooling shroud contoured to the approximate shape of the test article (for maximum cooling efficiency) and located at the opposite end of the chamber from the heater. The shroud is cooled by recirculating methanol coolant chilled to temperatures as low as 195 K (-105° F) by an 82-megajoule (78 000-Btu) refrigeration unit.

After orbital cold-soak and peak entry heating conditions have been simulated, the test article is repositioned in front of the cooling shroud to simulate cool-down rates between temperatures of 1030 and 295 K (1400° and 70° F). To prevent a potential fire hazard resulting from a methanol coolant leak in the vicinity of a hot test article, the shroud coolant is switched to circulating water from the test coolant subsystem by air-operated diverter valves before repositioning the test article in front of the cooling shroud.

Test Article Positioning Subsystem

The test article is transported between the heater and the cold shroud by a carriage drawn along a rail by an air-motor-driven chain. The nose cap test article is rotated 180° at a point midway between the two test positions by an air-motor-driven rotational drive incorporated in the test article carriage. The air motor drives are operated by a control system that senses the position of the test article within the altitude chamber and uses solid-state logic to automatically start, stop, and change speeds, thereby providing rapid precise positioning of the test article.

Data Acquisition System

The RHTF data acquisition system acquires, conditions, processes, records, and outputs in both tabular and plot formats data from 200 test article sensors and 56 facility sensors for engineering review and analysis. This system consists of an analog instrumentation and signal conditioning subsystem for acquiring raw data and a digital computer subsystem for processing and recording the data on magnetic tape.

The instrumentation subsystem acquires data from the sensors and performs preliminary signal conditioning before sending the data to the computer system for further processing. The system is prewired to accept inputs from the following sensors: (1) type K (chromel/alumel), type R (platinum/platinum-13-percent rhodium), and type T (copper/constantan) thermocouples; (2) bridge balance sensors, such as strain gages, strain-gage-based transducers, and resistance temperature devices; (3) fiber optic pyrometers; (4) heater voltage; (5) heater current; (6) altitude chamber pressure; and (7) other voltage output sensors, such as calorimeters. The data cables are routed through environmental feedthroughs

in the altitude chamber to a programmable patch panel that allows rapid instrumentation configuration changes between tests and facilitates frequent system calibration.

The channels selected for processing are routed to the analog input subsystem, which scans each channel 10 times per second, amplifies and digitizes the signal, and outputs the coded data to the central processing unit (CPU). The CPU performs all linearizations, zero offsets, and engineering unit conversions on the basis of previously input data and pretest calibration and displays the data on two CRT terminals in the RHTF control room.

Post-test data processing of the test data tapes is also accomplished with the computer subsystem. Tabular data can be retrieved in either sampled or averaged form for any timespan and interval specified, and data plots can be made with up to 6 measurements per page for any time interval specified.

CONCLUDING REMARKS

A large-scale Radiant Heating Test Facility has been constructed at JSC to perform certification tests on the Space Shuttle Orbiter TPS. Simulation of entry heating on full-scale test articles required development of innovative test techniques. One of these innovations was the development of silicon-carbide-coated graphite heater elements that make it possible to operate radiant heaters at temperatures up to about 1785 K (2750° F) in an oxidizing environment. Another innovation was combining a multichannel fiber optic pyrometer system with a digital computer system to control the power to each heater zone. Although the principal certification tests for which the facility was designed (the nose cap and wing leading edge structural subsystems) have not been completed, extensive tests to demonstrate the functional status of the facility systems have been performed. Nose cap and wing leading edge tests supporting the first flight are scheduled to be completed by the fall of 1980.

BIBLIOGRAPHY

Cox, B. G.; and Christensen, H. E.: Large Modular Graphite Radiant Heaters for Testing Space Shuttle Thermal Protection Systems, Eighth Conference on Space Simulations, Paper No. 16, NASA SP-379, 1975.

Suppanz, Murray J.; and Grimaud, John E.: Space Shuttle Orbiter Nose Cap and Wing Leading Edge Certification Test Program. Paper presented at Eleventh Space Simulation Conference, Sept. 23-25, 1980.
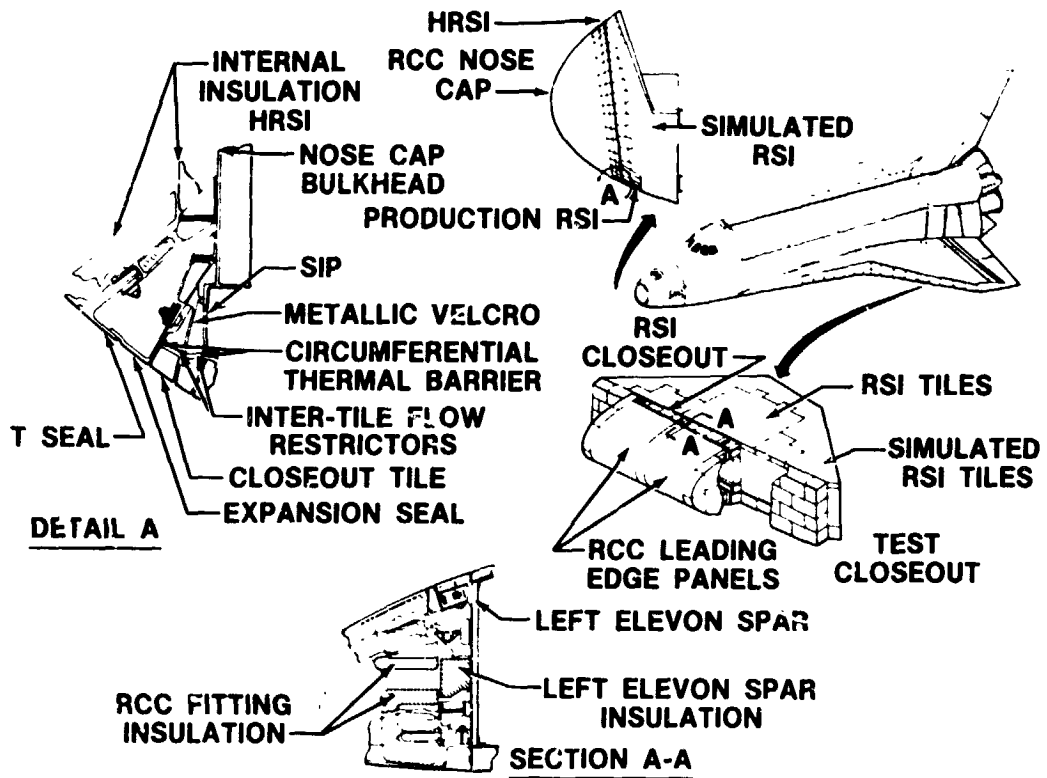
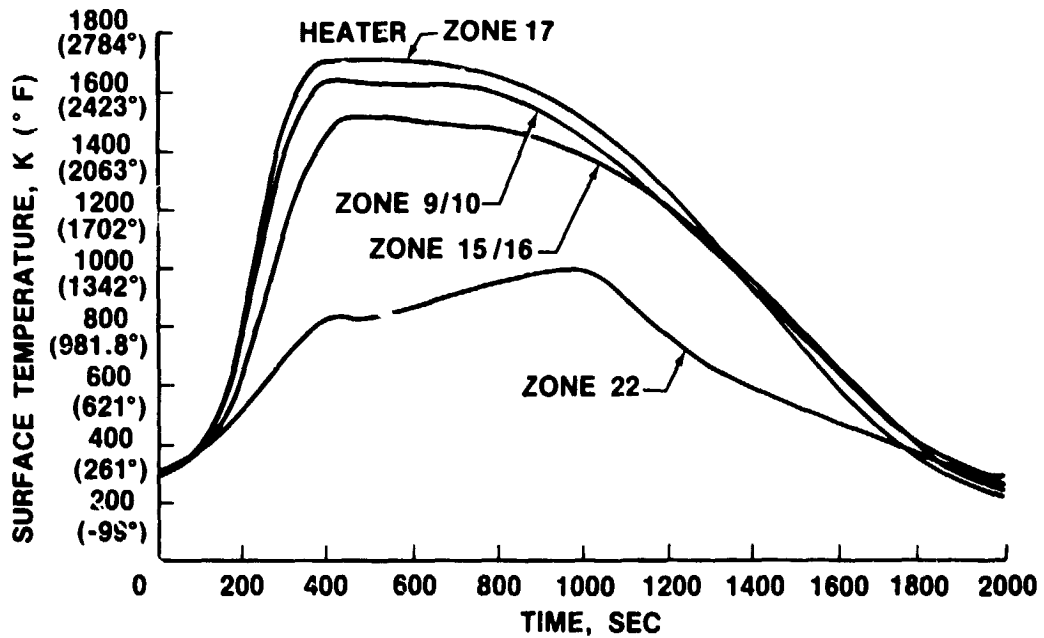Figure 1.- Leading edge structural subsystem test articles.

Figure 2.- Typical nose cap isotherms.

1 - 1254 K (1800°F)
2 - 1310 K (1900°F)
3 - 1365 K (2000°F)
4 - 1421 K (2100°F)
5 - 1476 K (2200°F)
6 - 1532 K (2300°F)
7 - 1587 K (2400°F)
8 - 1615 K (2450°F)
9 - 1629 K (2475°F)
10 - 1643 K (2500°F)

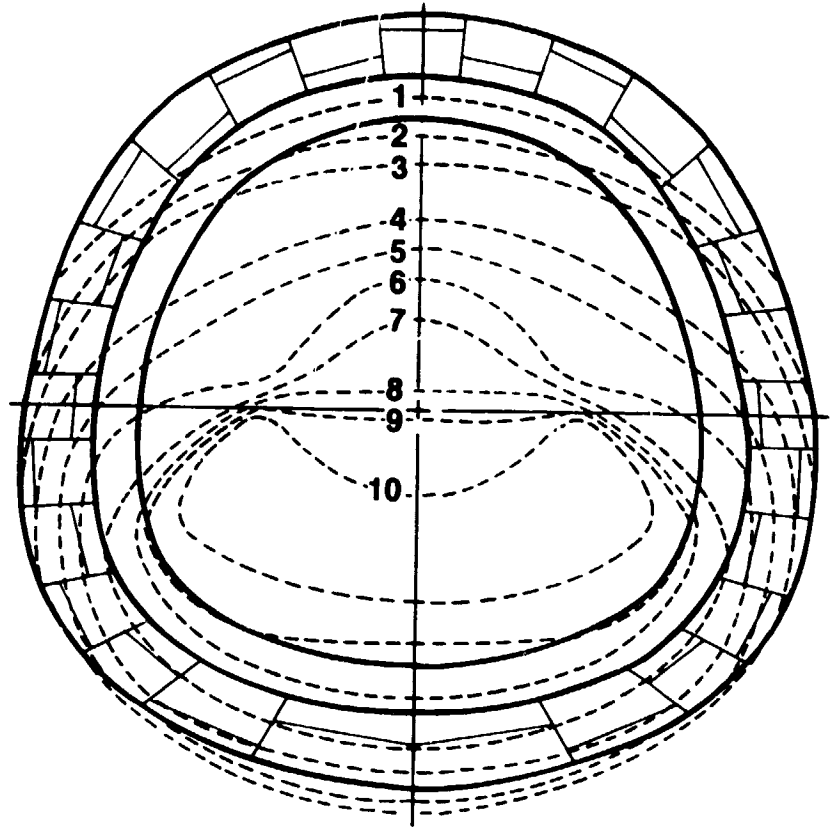Figure 3.- Typical nose cap entry temperature profiles.

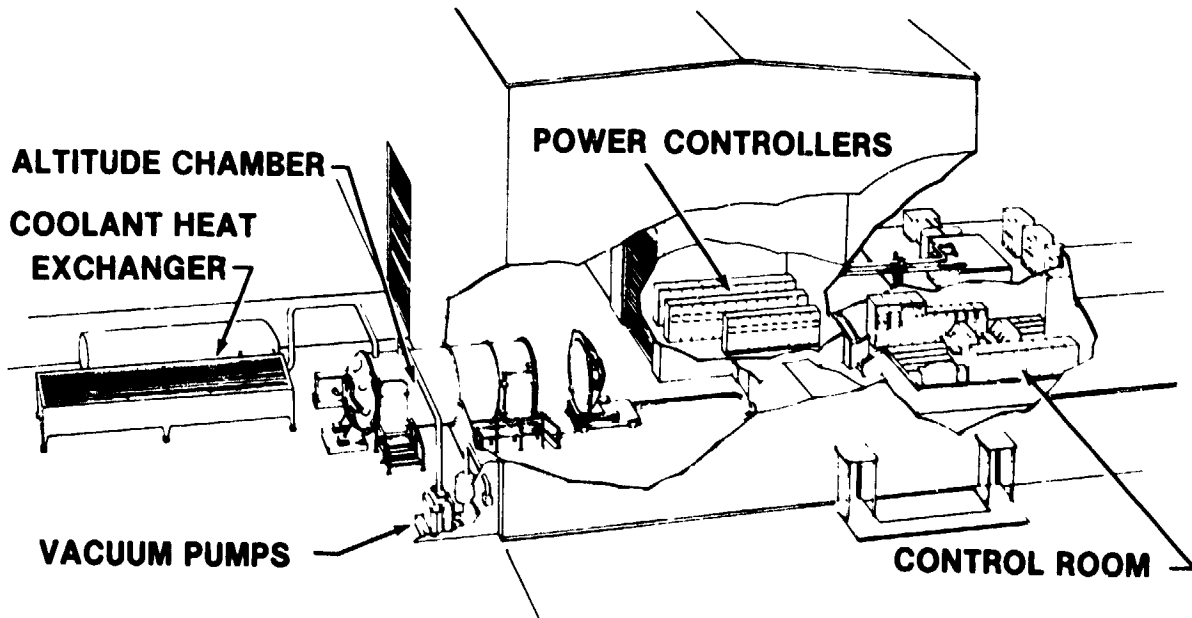Figure 4.- Radiant heating test facility.

WLE TEST ARTICLE
(HEATER POSITION)

WLE TEST ARTICLE
(CUSHION POSITION)

WLE
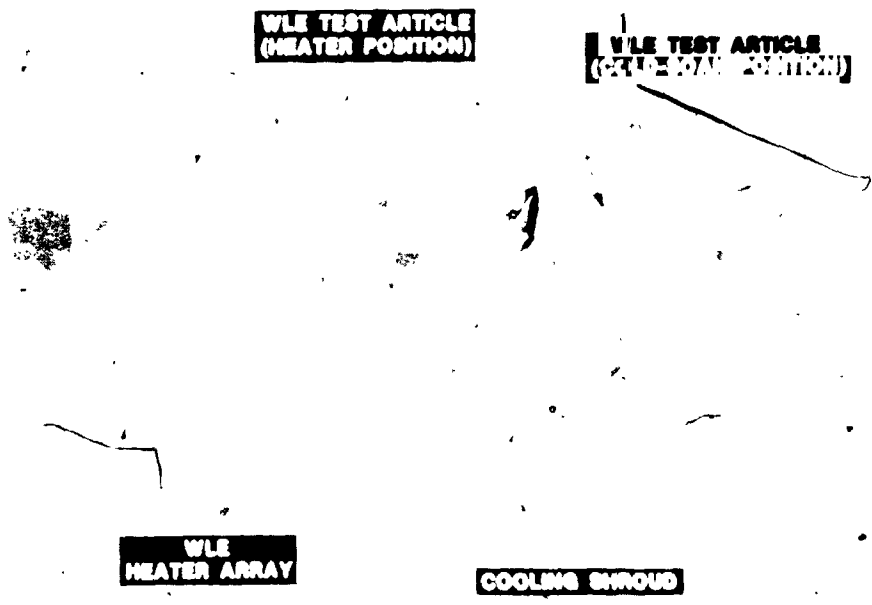HEATER ARRAY

COOLING SHROUD

Figure 5.- Wing leading edge test configuration. The test article
is shown in both the heater and the shroud positions for
illustrative purposes only.

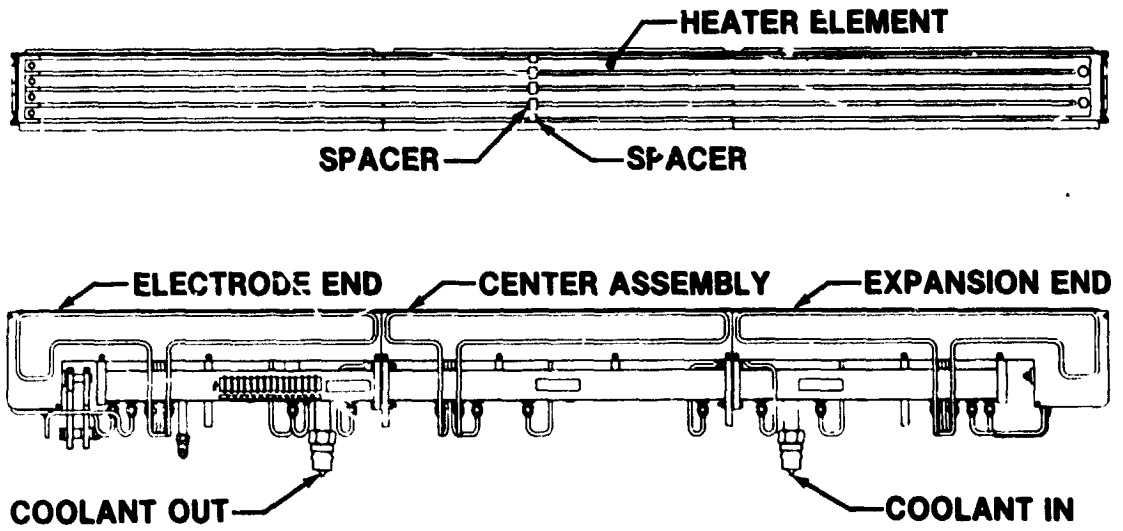Figure 6.- View of wing leading edge heater during test article fit check.
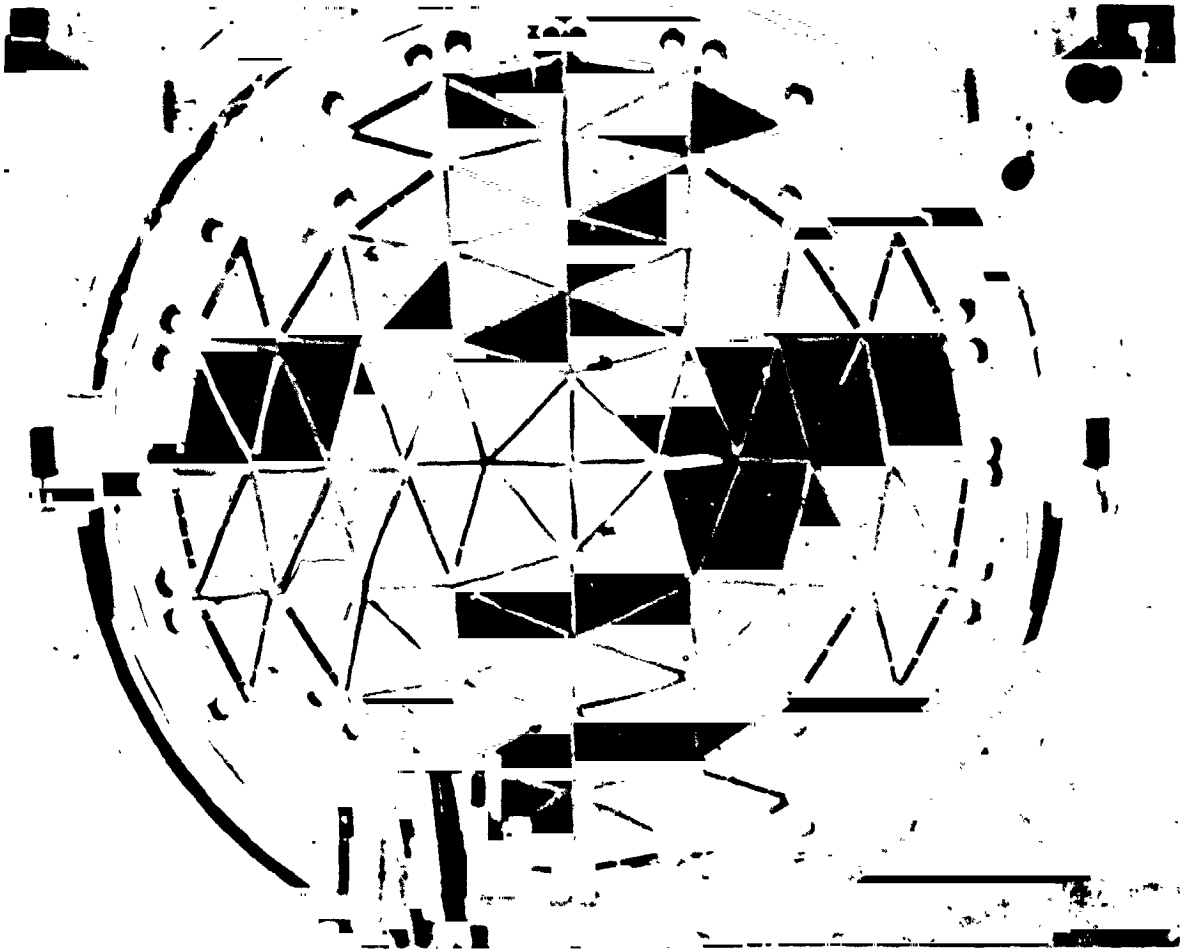
Figure 7.- Wing leading edge heater module.

Figure 8.- Nose cap heater.

140

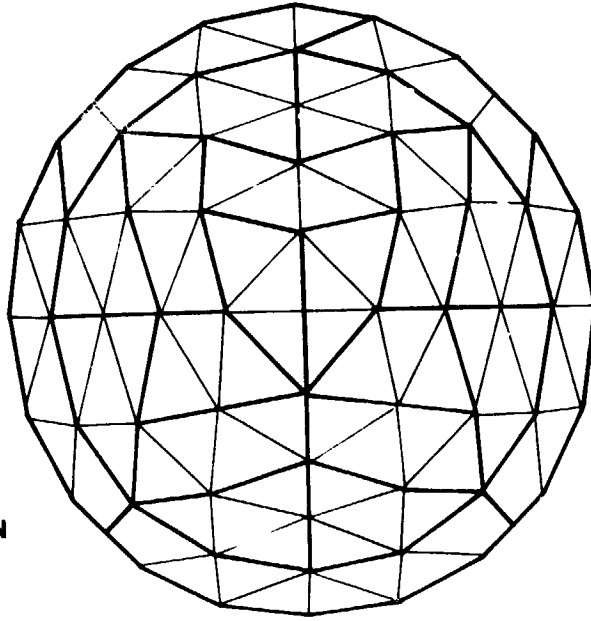MAJOR LINES
HEATER
ZONES

MINOR LINES
ELEMENT
CONFIGURATION

Figure 9.- Control zones and element configurations for nose cap heater.

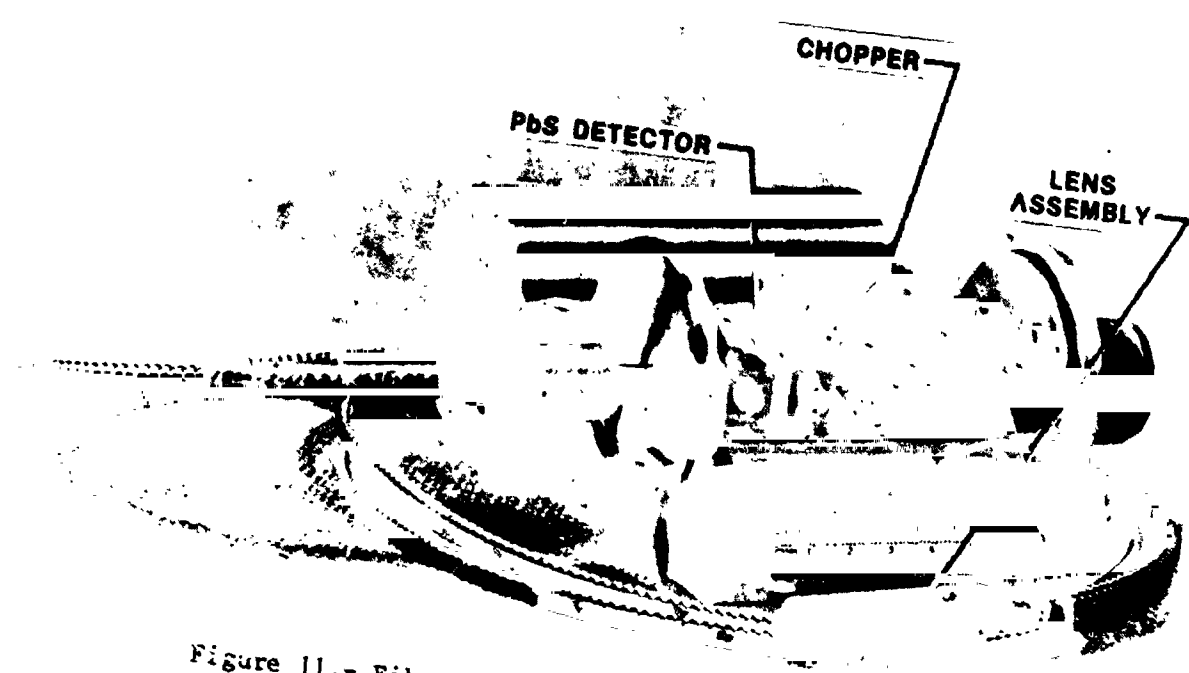Figure 10.- Typical nose cap heater elements.

141

Figure 11.- Fiber optic pyrometer detector head.

AN EFFECTIVE COMBINED ENVIRONMENT TEST FACILITY

Allen Deitch

ABSTRACT

A critical missile component required operational verification while subjected to combined environments within and beyond flight parameters. The testing schedule necessitated the design and fabrication of a test facility at the Re-entry Systems Division of the General Electric Company in order to provide the specified temperatures combined with humidity, altitude and vibration.

INTRODUCTION

A test facility was required that would provide the following environments in an established cyclic pattern; (See Figure 1)

1. Relative humidity up to 100%.
2. Cooling to -59°C (-75°F) and heating to +91°C (+195°F) at a rate of 5°-10°C (9°-18°F) per minute. Maintain temperature for four hours.
3. Altitudes up to 8.76 km (28,750 ft) during the cooling cycle.
4. Four hours of random vibration, 9.7g rms 10-2000 Hz, during the heating and cooling/altitude cycle.

Since a facility was not available to provide the above combined environments within the testing schedule constraints, one was designed and fabricated at the Re-entry Systems Division of the General Electric Company, Philadelphia, Pennsylvania. The facility became operational in October, 1979.

It was recognized that two unique objectives had to be accomplished concurrently;

1. Provide the capability of attaining cooling and heating rates of 5°-10°C (9°-18°F) per minute, and
2. Provide a vibration environment in conjunction with altitude simulation.

A test equipment configuration was designed to meet these objectives as shown in Figure 2. In order to achieve the relatively extreme temperature changes, it was determined that the heating and cooling sources should not only be isolated but located outside the test chamber. In this manner there would be no interaction between the two environments.

143

The only vibration exciter available for the test was an MB Model EL-250 which is not equipped for operation in a vacuum nor does it contain self-centering control for the 25 mm (1 in) displacement, double amplitude. Therefore, a special seal was required for the chamber-exciter interface.

CHAMBER CONSTRUCTION

The square-shaped exterior of the chamber was constructed of 10 mm (3/8-in) thick welded carbon steel plate and angle. The interior was insulated with a 76 mm (3 in) minimum thickness of fiberglass and covered with a protective liner of 3.2 mm (1/8-in) thick stainless steel sheet.

A 152 mm (6 in) diameter port was provided on each of the four sides of the chamber. One port furnishes the heat supply; the opposing port serves as the heat return. The two remaining ports are capped with removable penetration plates which contain electrical, pneumatic, hydraulic and cryogenic feedthroughs.

The chamber liner is octagonal in shape so that each port wall easily intersects the flat portion of the liner through a circular opening. The liner, by being almost circular, effectively utilizes the air flow pattern produced by the overhead circulating fan.

The 178 mm (7 in) diameter multi-blade fan is operated from an AC motor by means of a vertical ball bearing shaft assembly which penetrates the top of the chamber. The shaft was permitted to float thereby minimizing bearing loads due to changes in temperature. Quad rings which have a four-lobed cross section, as manufactured by the Minnesota Rubber Company, seal the rotating penetration for the altitude cycle which is accomplished by an external vacuum pump. The rings as well as the shaft bearings were lightly coated with silicone grease prior to assembly.

A multi-turn 13 mm (1/2-in) diameter by 1.3 mm (.049 in) thick wall copper coil supported from the liner encircles the test area. The coil receives electrically heated air to maintain temperature during the heat/humidity cycle and liquid nitrogen for maintaining the cold/altitude cycle. The clear dimensions (working volume) within the coil are 432 mm (17 in) diameter by 305 mm (12 in) high.

CHAMBER - EXCITER INTERFACE

The chamber is supported above a vertically positioned vibration exciter and sealed from room ambient and the exciter by means of a diaphragm placed between the chamber floor opening and the base of the vibration fixture.

Without self-centering, it was necessary that the maximum uplift of the exciter interface, caused by the pressure differential of the altitude cycle,

be limited to insure sufficient displacement for vibration testing. Therefore, the diaphragm was sized so that a maximum uplift of 6.4 mm (.25 in) occurred permitting the availability of ± 6.4 mm (.25 in) displacement for testing. In determining the diaphragm area, the weight of fixture, component and exciter armature were included as resisting the uplift.

The diaphragm, having an outside diameter of 127 mm (5 in), was fabricated from 3.2 mm (1/8-in) thick ethylene propylene rubber compounded for -68°C to +177°C (-90°F to +350°F) service.

ENVIRONMENTAL SOURCES

An existing portable heating unit containing a controller, blower and electrical heaters with capability up to 10 kw was consigned for use as the external heat source. The inlet and outlet of the unit were connected to the chamber ports with the existing 3 m (10 ft) long by 152 mm (6 in) diameter insulated flexible ducting. Valves were constructed to open and close the ducted ports as required. This obviated the need to remove and reinstall ducting during the test cycling. (Also capping and uncapping the ports.)

Two temperature controllers are used in the cycling process, the one included with the portable heating unit and one added for separate control of the cooling cycle. This permitted a manually operated diverter branch to be incorporated into the ducting system to allow operation of the heating unit with the chamber ports closed.

For measurement and control of humidity, a wet/dry bulb sensor was constructed using copper-constantan thermocouple wire. The pair of thermocouples were connected for direct readout of differential voltage on a digital voltmeter. Conversion to differential temperature established the relative humidity.

During the humidity cycle, the ports are closed in order to minimize moisture demand. A distilled water vaporizer furnishes humidity up to 100 per cent at 29°C (85°F). Heated air required during the humidity cycle is directed from the diverter to the chamber coil by means of a temperature controlled solenoid.

High temperatures are achieved by the flow of heated air from the external heating unit directly through the ducting to the chamber. The temperature rise rate is controlled by switch selection of up to five heaters rated at 2 kw each. Varying the opening of the port valves is an additional means of control.

For rapid cool-down Liquid Carbon Dioxide (LCO_2) is solenoid injected into the chamber with the ducted ports closed. The chilled gas displaces the heated air and is vented outside the test area. Without access to bulk LCO_2 22.7 kg (50 lb.) 5.5 MPa (800 psi) cylinders had to be used. To insure a sufficient supply of LCO_2 for meeting the cooling rate, two cylinders were piped in with one serving as standby.

Also, during the cool-down cycle, Liquid Nitrogen (LN$_2$) is circulated through the chamber coil and vibration fixture. When the chamber reaches the required low temperature, the LCO$_2$ is switched off and temperature control is shifted from the chamber to the test item. The LN$_2$ cools the test item to the specified temperature and then maintains the temperature in conjunction with the altitude-vibration cycle.

VIBRATION FIXTURE

The vibration fixture is basically a hollow cube constructed of 25 mm (1 in) thick aluminum walls. As shown in Figure 3, the flow of LN$_2$ through the vibration fixture is made possible by the use of 6 mm (1/4-in) Teflon hose reinforced with stainless steel wire braid. The hose, rated at -212°C (-350°F) and 10.3 MPa (1500 psi), adequately met the handling requirements of LN$_2$ while exposed to all the test environments.

The three components to be tested are mounted on the faces of the cube in such a manner that vibration occurs in each of the three mutually perpendicular axes. With the teflon hose attached to the fixture cross-axis vibration was verified at less than 100 per cent.

CONCLUSION

The facility performed the test successfully with over 200 hours of almost continual operation. In addition, no degradation of the selected materials was noticeable.

Prior to testing the flight components, the following design performance capabilities were verified by a systematic checkout of the facility:

Temperature Range	-73° to +121°C (-100° to +250°F)
Temperature Rate	up to + 20°C (35°F) per minute
Relative Humidity	up to 100%
Altitude	0 to 10 km (0 to 32,808 ft)
Vibration	5-2000 Hz, 12.5 mm (.50 in) D.A.
	13.34 kN (3000 lb force) sine
	28.05 kN (6300 lb force) random
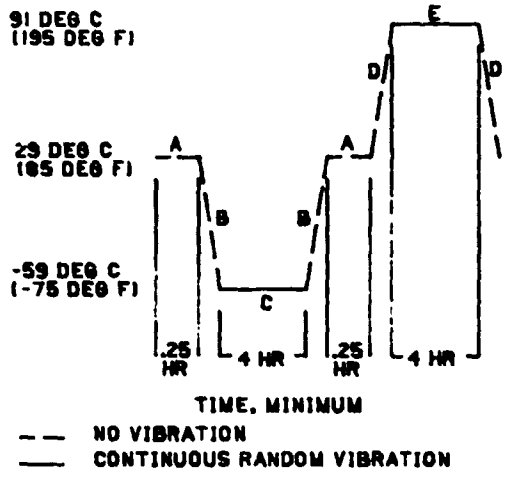
COMBINED ENVIRONMENT TEST CYCLE

FIGURE 1
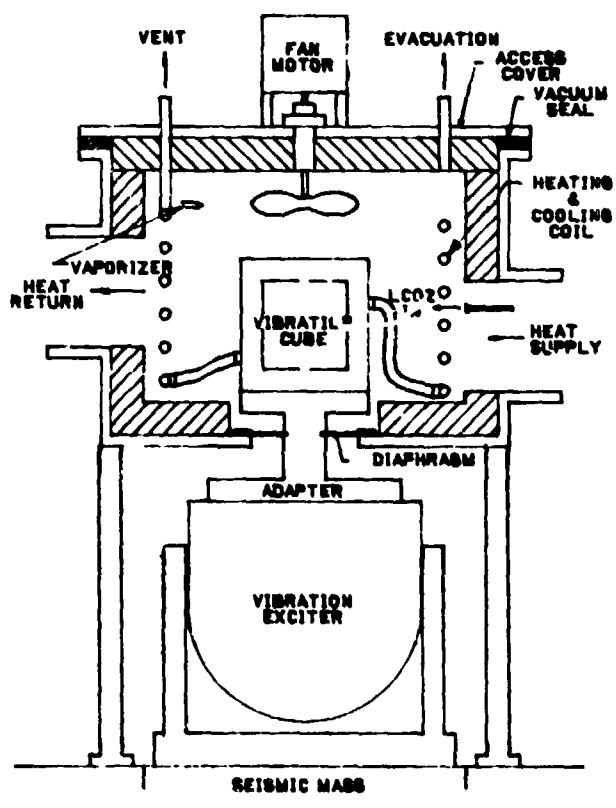
COMBINED ENVIRONMENT TEST FACILITY

FIGURE 2

Chamber interior (top cover removed) with three test
items mounted to the vibration fixture.
Figure 3

148

$\mathcal{D}_{13}$

AN INTEGRATIVE APPROACH TO SPACE-FLIGHT PHYSIOLOGY USING SYSTEMS ANALYSIS AND MATHEMATICAL SIMULATION

Joel I. Leonard*, Ronald J. White* and John A. Rummel**

ABSTRACT

An approach has been developed to aid in the integration of many of the biomedical findings of space flight, using systems analysis. The mathematical tools used in accomplishing this task include an automated data base, a biostatistical and data analysis system, and a wide variety of mathematical simulation models of physiological systems. A keystone of this effort was the evaluation of physiological hypotheses using the simulation models and the prediction of the consequences of these hypotheses on many physiological quantities, some of which were not amenable to direct measurement. This approach led to improvements in the model, refinements of the hypotheses, a tentative integrated hypothesis for adaptation to weightlessness, and specific recommendations for new flight experiments.

INTRODUCTION

The most complete set of observations on man's adaptation to weightlessness collected by the U.S. to date was obtained during the 28-day, 59-day, and 84-day missions of the Skylab program (Reference 1). The primary goal of the Skylab medical experiments was to define the changes which took place in the human body and, thus, achieve an understanding of the physiological responses which occur during extended exposure to the space-flight environment. Achieving a unified theory of adaptation to weightlessness was difficult because it required integration of a voluminous quantity of data obtained by many scientists from various disciplines. This task was further confounded by the need to consider supplementary results from a diverse spectrum of ground-based studies which mimic the hypogravic environment of space flight. It was clear that proper interpretation of all these data would require the unraveling of a complex network of feedback regulators involving many individual physiological subsystems. Therefore, a program was developed, based on an interdisciplinary systems analysis approach, to address this task. It was hoped that the systems analysis approach would be particularly suitable here because it would allow us to analyze and assimilate vast quantities of information, to understand the behavior of complex homeostatic systems, and to test scientific hypotheses explicitly and in as unambiguous a manner as possible.

Of the various techniques developed to satisfy these requirements, the tool which has proven most useful is a set of mathematical models capable of simulating a number of physiological systems. The benefits of using mathematical models are well known among those physiologists who employ them in their research studies. Formulating the model, when based on experimental evidence and known concepts, provides insight into the organization of the system elements, the processes within the elements, and the multiple pathways

---

connecting these elements. During simulation, the dynamic interaction between various subsystems and the relative importance of each element become more apparent through variation of the system's parameters. Once a model is validated, it is possible to predict quantitative responses of the human system that can be subjected to experimental verification. When experimental evidence is conflicting, difficult to interpret, or even difficult to obtain (as in the case of data obtained from space-flight studies), it is often possible to test the plausibility of an hypothesis by using an appropriate mathematical model. Also, models are an effective method of assembling knowledge about a physiological system. As this knowledge is organized, areas of missing information are revealed and the type of experiment needed to gather these missing data is suggested. In summary then, the simulation model can be considered a collection of integrated theories and empirical relationships against which a large portion of the space-flight data can be compared, evaluated, and tested for consistency.

Although mathematical modeling is now well established in the life sciences, this is the first time that a large array of models has been applied in a uniform manner to solve problems in space-flight physiology. This use of mathematical models was expected to complement the ongoing NASA program of employing ground-based experimental analogs of zero-g to provide additional insight into man's responses to weightlessness.

SYSTEMS ANALYSIS TECHNIQUES AND APPROACH

An important objective of the systems analysis project, at the outset, was to develop the mathematical and statistical techniques required to support an extensive integrative effort related to man's responses to weightlessness. It was apparent that data from all the major flight experiments of Skylab would need to be coupled with the appropriate analysis software in a single data base. Toward this end, a medical data analysis system was created which consisted of an automated data base, a software package of biostatistical and special purpose programs, and a set of simulation models of physiological systems (see Figure 1). Data from a wide variety of investigative areas were collected, including cardiopulmonary function, body fluids, biochemistry, nutrition and energy metabolism, musculoskeletal function, body composition, and hematology (see Table I). The total quantity of data contained in the data base is quite large in spite of the small number of astronaut subjects; information for approximately 900 man-days of space-flight study is provided by 80,000 measurement values representing over 900 independent parameters. Algorithms were provided to perform routine statistical tests, multivariate analysis, non-linear regression analysis, and autocorrelation analysis. Special purpose programs were prepared for rank correlations, factor analysis, and the integration of the metabolic balance data using models employing the conservation of mass, water, and energy. Figure 2 illustrates the data analysis system's for displaying data and visualizing computer generated model responses.
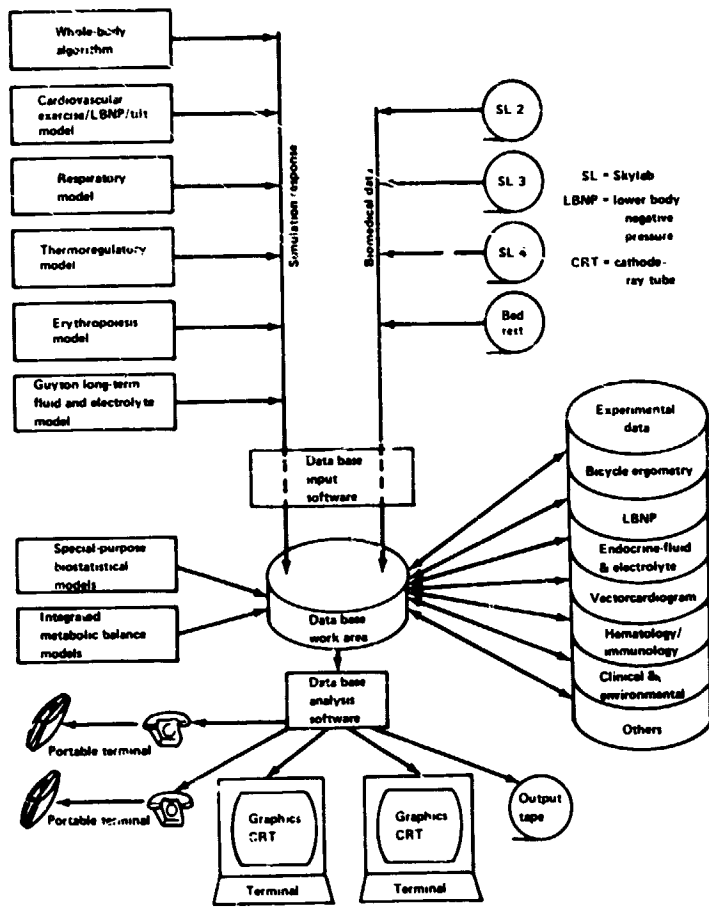
Figure 1: Skylab Integrated Medical Data Analysis System

TABLE 1

BIOMEDICAL EXPERIMENTS OF SKYLAB IN DATA BASE

Cardiovascular System

o Lower body negative pressure

o Submaximal exercise response

o Resting flows, pressures, heart rate

Pulmonary Function

o Respiratory function during rest and exercise

o Mechanical and metabolic efficiencies during exercise

Nutrition and Biochemical Metabolism

o Metabolic balances of water, nutrients and electrolytes

o Energy balance

o Body mass measurements

Musculoskeletal Function
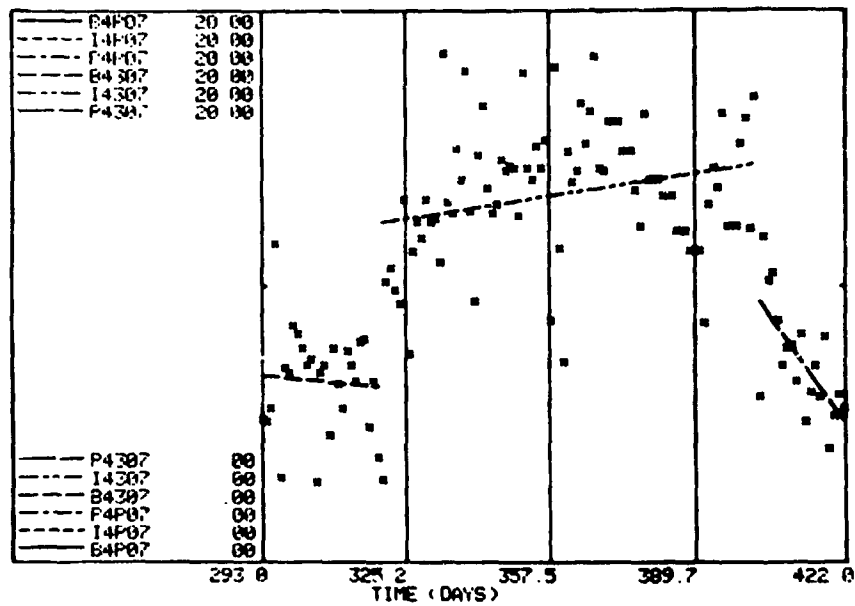
o Bone densitometry

o Calcium balance

o Strength tests

o Anthropometric measurements

o Lean body mass measurements

Body Fluids and Composition

o Body fluid volumes

o Composition of plasma, urine, and feces

o Hormones related to fluid-electrolyte balance and to stress

Hematology

o Red cell mass

o Blood volume

o Hemoglobin

o Indices of erythropoiesis

151

EXAMPLE OF CRT DISPLAY OF SKYLAB DATA WITH REGRESSION ANALYSIS

SHOWING URINARY CALCIUM FOR PREFLIGHT, INFLIGHT & POSTFLIGHT PHASES
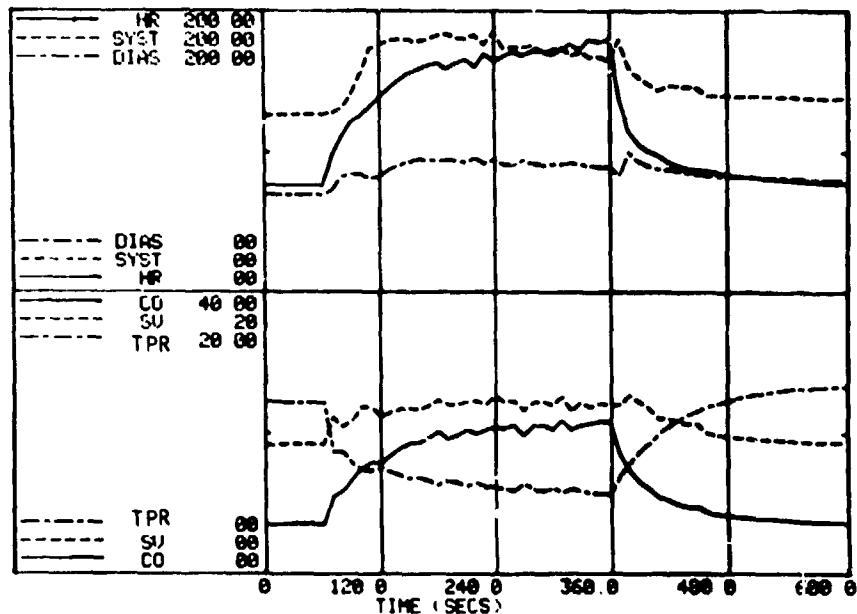
EXAMPLE OF CRT DISPLAY OF SIMULATION OUTPUT

SHOWING TRANSIENT RESPONSES TO EXERCISE (5 minutes @ 200 watts)

Figure 2:   Examples of Graphic Displays of Data Base Analysis System

In order to simulate short-term and long-term events, five basic models were employed in this project: a pulsatile cardiovascular model; a respiratory model; a thermoregulatory model; a circulatory, fluid and electrolyte balance model; and an erythropoiesis regulatory model (Figures 3 and 4). A major objective that was achieved early in the project was the integration of these subsystem models into a common framework termed the "whole-body algorithm." In addition to these six models, a model of calcium regulation is currently under development. All of the subsystem models are characterized by an active controlling system which regulates a relatively passive controlled system, and, taken together, these two components function as a negative feedback control system. The feedback variables for these

152

models include representations of many of the actual sensors present in the body, including temperature sensors, chemoreceptors, baroreceptors, oxygen sensors, and osmoreceptors. A majority of these models resulted from research directly assoc'ated with this project.

Exercise level ⟶
LBNP level ⟶
Tilt angle ⟶
150 input parameters ⟶

PULSATILE CARDIOVASCULAR MODEL

⟶ Blood flows
⟶ Blood volumes
⟶ Blood pressures
⟶ Heart function
⟶ 350 predicted variables

Inspire.' O_2 and CO_2 levels ⟶
Metabolic rate ⟶
30 input parameters ⟶

RESPIRATORY MODEL

⟶ Lung ventilation
⟶ Acid-base status
⟶ Cardi :c output
⟶ Arterial pO_2 and pCO_2
⟶ 80 predicted variables

Ambient temperature, pressure, and humidity ⟶
Metabolic rate ⟶
Clothing factor ⟶
330 input parameters ⟶

THERMOREGULATORY MODEL

⟶ Body temperature distribution
⟶ Evaporative water loss
⟶ Heat storage
⟶ Blood flows
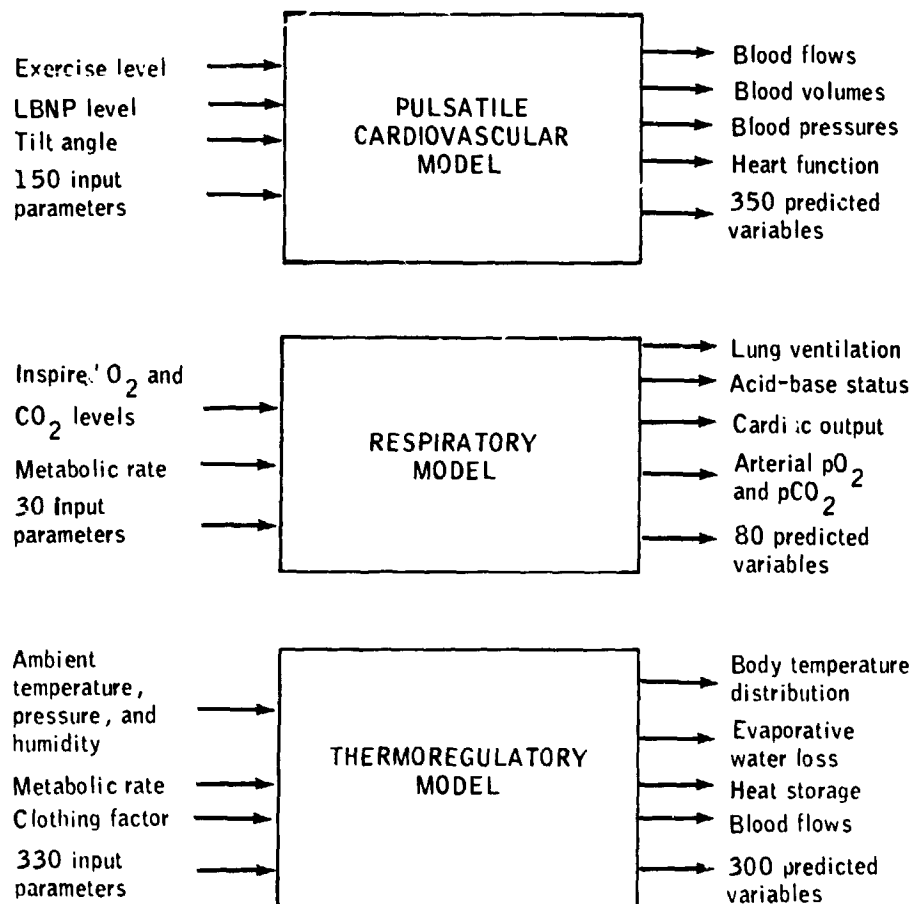⟶ 300 predicted variables

Figure 3: Models for Simulating Short-Term Events

Each of the models used in this project are deterministic and non-linear and are implemented using finite difference formulations. All models operate in an interactive time-sharing mode with the automated capability to display responses graphically and to compare data and model responses simultaneously. Most models were modified to include gravity dependent effects and to permit simulation of a human response to the stresses related to the space-flight program. In some instances, an alternative version of a model was developed to represent an animal species. Some of the experimental and clinical conditions for which the models were validated include hypogravic stresses, orthostatic stresses, metabolic stresses, environmental disturbances, and fluid shifts (Table II). Multiple stresses and sequential degrees of stress can be simulated just as in a real experimental protocol. Many hypotheses can be tested merely by adjusting the value of one or more of the fixed system parameters.
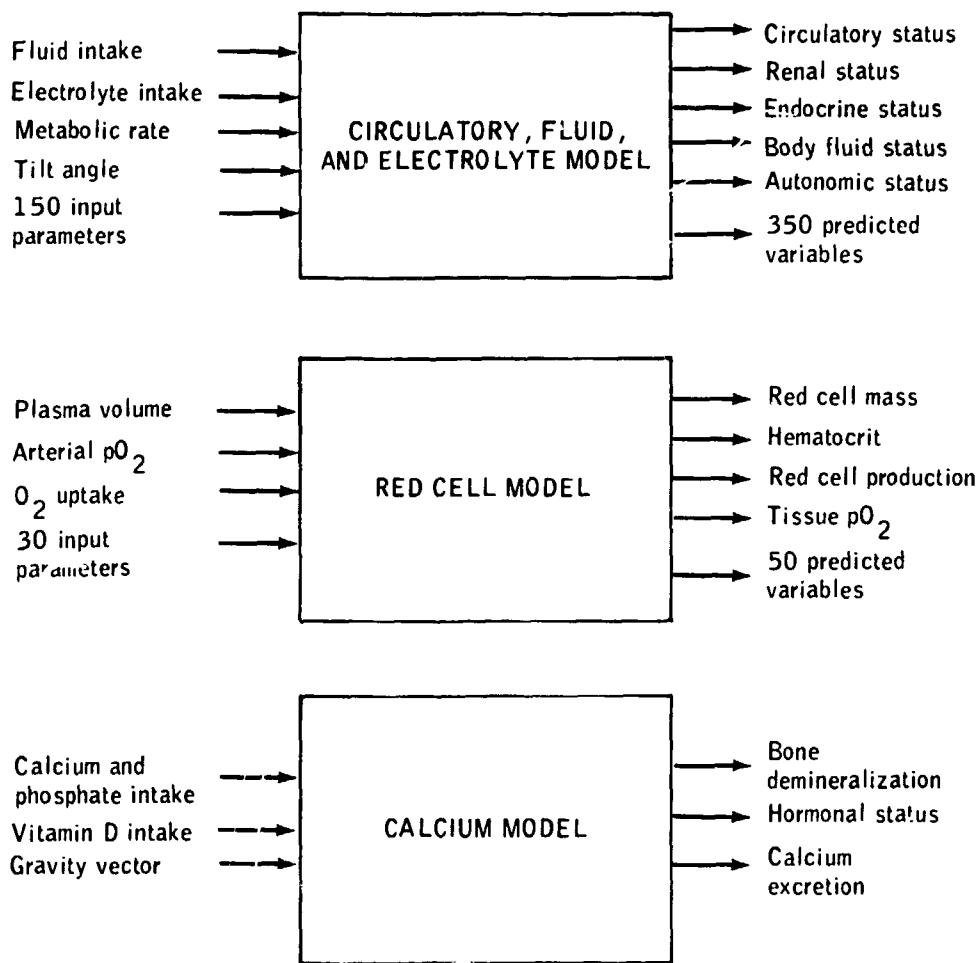
Figure 4: Models for Simulating Long-Term Events

The combinations of the data base analysis system with the group of simulation model formed the basis of the hypothesis testing approach that was used for integrating the Skylab findings (see Figure 5). The basic analysis systems permitted large arrays of space-flight data to be scanned rapidly, graphical visualization of correlations between variables, and statistical testing of hypotheses. This preliminary evaluation of space-flight data led naturally to qualitative examination of the mechanism involved in producing the observed responses. This procedure drew heavily upon the theory of physiological feedback regulating systems and often suggested hypotheses capable of being tested by using the predictive capabilities of the simulation models. The elements of the medical data analysis system (Figure 1) were designed to interact in either sequential or parallel fashion so that, for example, results from a data analysis could be employed as input forcing functions to a simulation model and the model's predicted responses could then be compared to additional data from the data base. While good agreement between model and data was desirable, it was not essential. The heuristic value of modeling is such that important objectives are often realized even when this agreement is poor. Such poor agreement often results in suggestions for additional data analysis, refinements of the mathematical models, changes in the hypothesis being considered, and suggestions for the design of new experiments to be performed either in space or on Earth. This is an interative process, as suggested by Figure 5, and is the heart of the systems analysis approach.

Table II

STRESSES RELATED TO SPACE FLIGHT THAT WERE STUDIED
USING SIMULATION MODELS

o HYPOGRAVIC STRESS

- Supine Bed Rest
- Head-down Bed Rest
- Water Immersion
- Space Flight

o ENVIRONMENTAL DISTURBANCES

- Hypoxia
- Hypercapnia
- Temperature
- Ambient Pressure

o ORTHOSTATIC STRESS

- LBNP
- Tilt Table
- Postural Change

o FLUID SHIFTS

- Hemorrhage
- Infusion
- Water and Salt Loading
- Dehydration

o METABOLIC STRESS

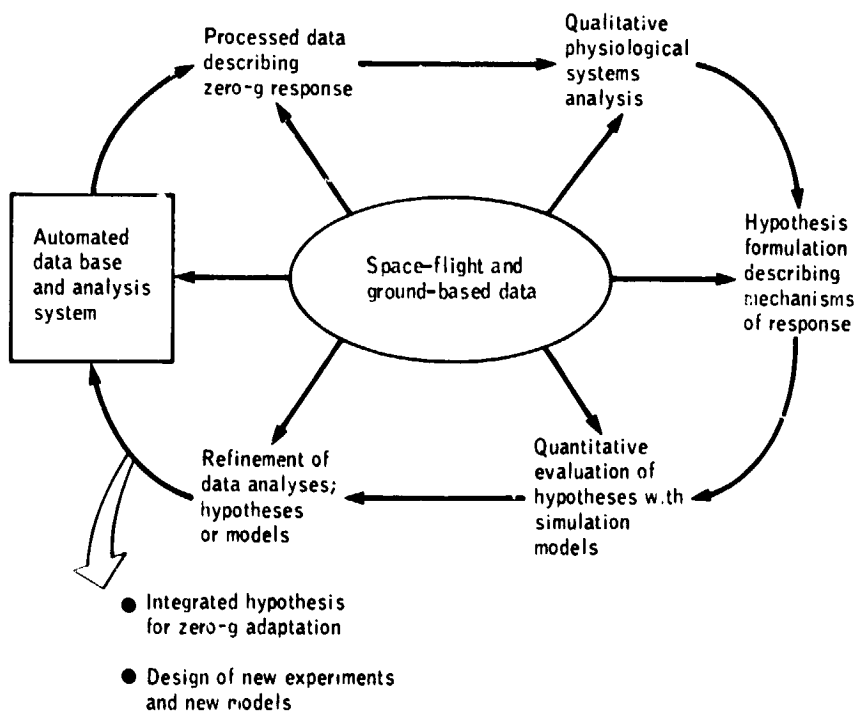- Exercise
- Diet Restriction

Figure 5:   Systems Analysis Approach for Evaluation of Space-flight Data

Statistical and modeling techniques naturally complement each other for integrating and correlating results from many different investigative areas. Predicting the consequences of hypotheses on unmeasured variables from many subsystems is within the capability of models such as the whole-body

algorithm, but is impossible if the testing of hypotheses is performed by traditional statistical approaches. As this simulation study progressed, it was possible to incorporate more and more diverse kinds of experimental results and hypotheses into a single model. While each hypothesis alone would not support a generalized theory, all of them taken together should converge toward a coherent picture of zero-g adaptation.

RESULTS AND DISCUSSION

This project encompasses a nine-year time period, and it has fostered many useful accomplishments. Several of these are discussed below.

Integrative Analysis

Systems analysis was valuable in performing various organization and integration functions that were not previously available to the space life sciences program on a systematic basis. These functions include:

a) integration of data from different investigative areas into a common data base to provide an interdisciplinary cross-correlation capability;

b) integration of physiological mechanisms relating to homeostatic control of a single functional system within the framework of a mathematical model;

c) integration of observed phenomena (experimental data) with simulated responses (theory) by simulating experimental conditions and comparing model and real-world behavior;

d) integration of diverse types of stresses acting on the same system to demonstrate common features of the regulatory processes;

e) integration of acute and long-term stress responses to hypogravity by systematic comparison of ground-based and space-flight studies;

f) integration of physiological subsystem models into a larger, more complex model to study theoretical interactive effects; and

g) integration of subsystem hypotheses related to zero-g adaptation into a unified theory showing overlapping and interactive effects between subsystems.

The last several items are of unusual importance and are therefore discussed in more detail below.

Whole-Body Algorithm

The physiological interaction of major body subsystems has been a subject of interest to researchers for some time. One objective in human system modeling is to produce not only reliable subsystem models but also an integrated model with each subsystem acting in concert with other subsystems to simulate the entire dynamic system of the body. However, efforts in this

156

direction have been quite limited. A contribution to this area was made with the development of a "whole-body algorithm" (Figure 6), which is envisioned as a mathematical model that can simulate the response of several major body regulatory systems to diverse, but specified stresses related to the space-flight environment (Table II). The approach selected for the construction of this model combined existing subsystem models that describe short-term stress responses (cardiovascular, respiratory, thermoregulatory models) with a model which described appropriate long-term responses (circulatory, fluid-electrolyte, endocrine, erythropoiesis models). The whole-body algorithm was designed so that the entire sequence of major physiological events for long-duration space flight could be simulated. This sequence included preflight experiments, acute physiological responses to zero g, changes in cabin environment, inflight responses to the experiments of interest (lower body negative pressure and exercise), acute reentry to one g, long duration readaptation to one g, and postflight experiment simulation.
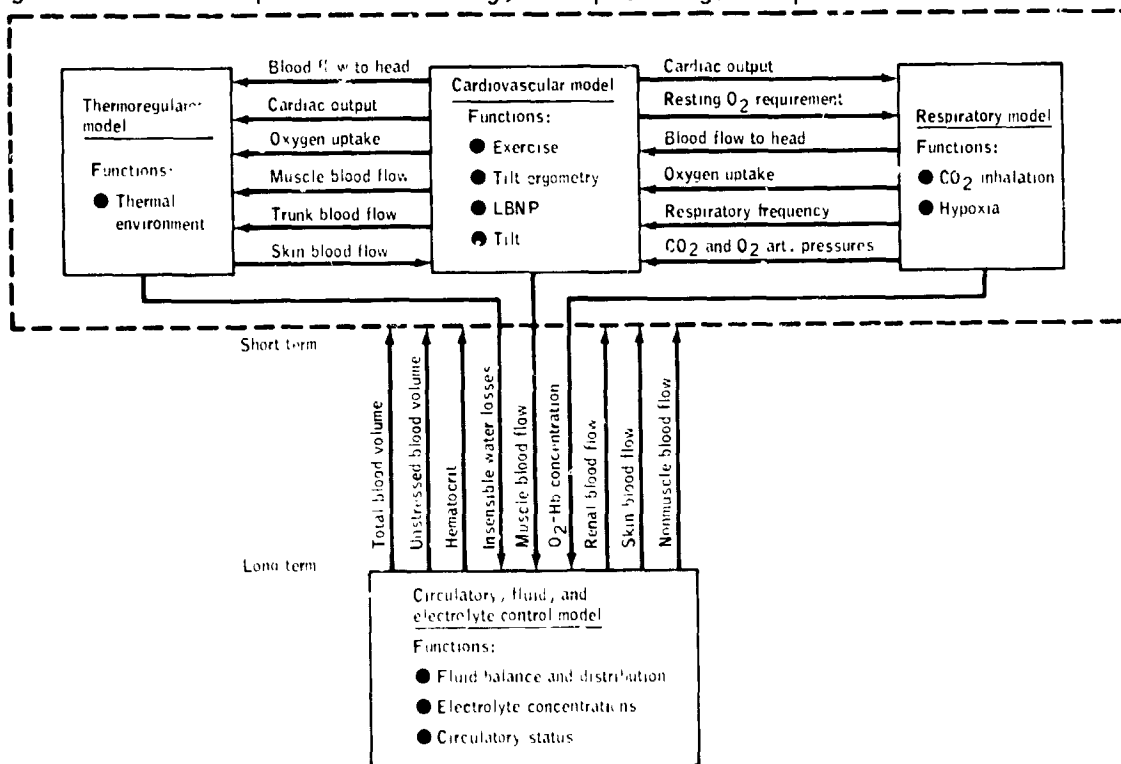
Figure 6: Whole-Body Algorithm

One advantage of using an approach which combines existing subsystem models is that each model considers various time lags, fast and slow controllers, and integration step sizes appropriate for its respective simulations. The model has a sufficiently flexible structure to permit changes to be made without totally disrupting the entire system. Such changes even include adding new subsystems or modifying existing subsystems. A model comprised of individual, well-defined subsystems also facilitates studying the interaction between the subsystems, and studying total system hypotheses, both important subjects in physiology today. An additional feature of the whole-body algorithm is its capability to simulate multiple and sequential stresses with little or no basic structural changes.

Sufficient testing was performed with the whole-body algorithm to demonstrate the basic capabilities of the model. Validations were performed for a number of single stresses as well as long-term bed rest accompanied by intermittent short-term stresses. Once model credibility was ascertained, it was possible to attempt simulations of entire space-) ght missions. Figure 7 illustrates one such simulation of a composite Skylab flight and demonstrates

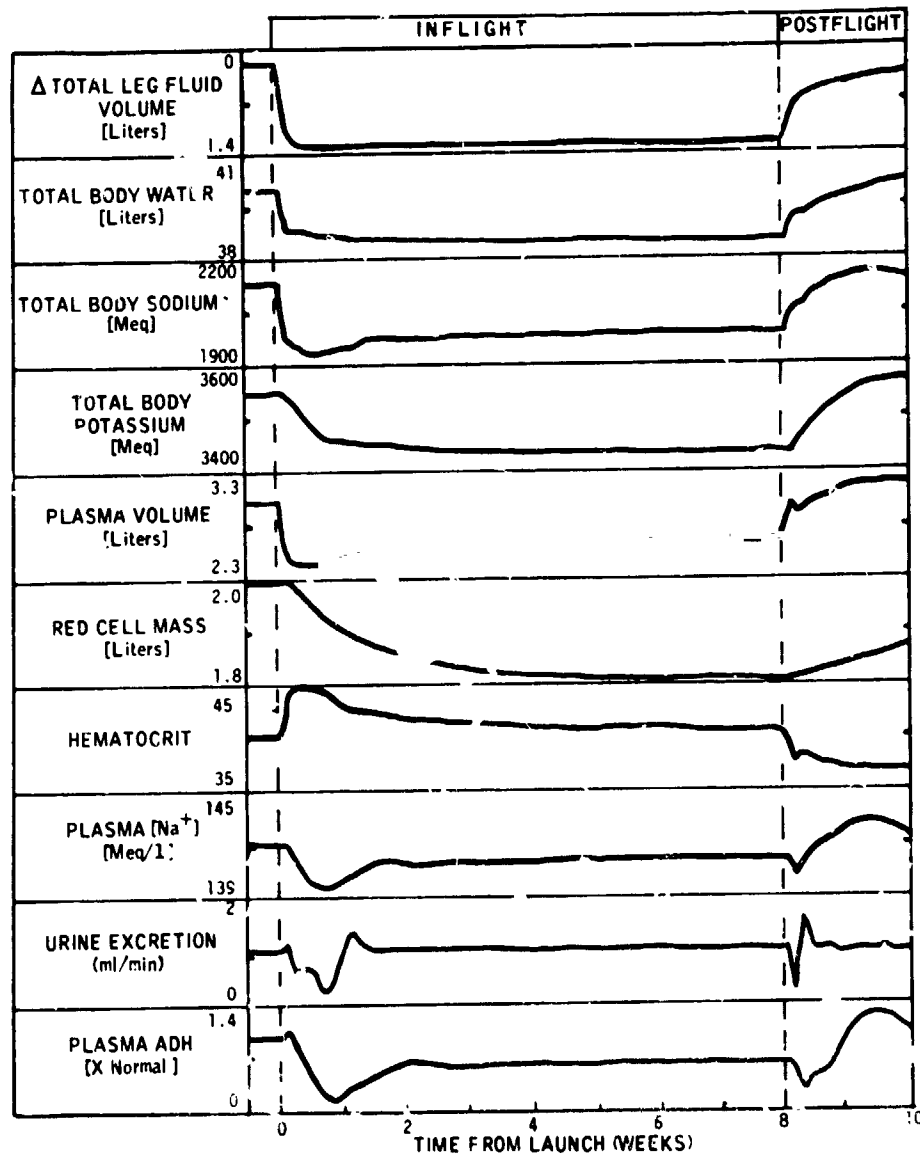Figure 7:   Simulation of Fluid-Electrolyte Regulatory Behavior During Composite Skylab Mission

reasonable predictions for a variety of fluid volume, electrolyte, endocrine, and renal responses. Nevertheless, many aspects and capabilities of the model have yet to be tested. One reason for this is that much of the data required to perform adequate validation of this large model have not yet been gathered. The whole-body algorithm has well over 1000 independent system variables, most of which correspond to physiological quantities. Unfortunately, in physiological research it is rare that more than a dozen parameters will be measured simultaneously during a single experiment. Therefore, data from multiple sources is required and, because identical biological conditions are not likely to be achieved, there is a risk in this approach. For these same reasons, the simulated responses to combined stresses have not been investigated. In a very real sense, this shortcoming is an opportunity to identify critical research areas related to measuring whole-body responses to combinations of environmental and metabolic disturbances. It should also be recognized that a model of this size is somewhat unwieldly and simulations take a relatively long time to perform. Therefore, most of the systems analysis performed in this program was accomplished with the individual subsystem models. The next phase of application will be to incorporate into the whole-body algorithm the candidate hypotheses for each subsystem that have shown promise in explaining the space-flight findings. When this is done, the whole-body algorithm will serve its main function as a central repository of a detailed integrated hypothesis of zero-g adaptation. In this way, the model should prove useful for supporting space-flight biomedical research programs, and for predicting indices of crew health.

Hypotheses of Zero-g Adaptation

The major application of these mathematical and data processing tools was directed toward achieving a better understanding of how humans adapt to long-term space flight. A detailed discussion of results in this area is out of the scope of this paper, but such a discussion will soon be available in book format (Reference 2). In terms of the several physiological systems studied, the following broad picture has emerged. Disturbances in the cardiovascular, fluid-electrolyte, erythropoietic, musculoskeletal, and metabolic systems, which are found during and after flights of various durations, appear to be attributed to two major effects of weightlessness (Figure 8). These are, first, the absence of hydrostatic forces, resulting in severe fluid shifts within the body, and second, the absence of deformation forces, resulting in disuse atrophy of normally load-bearing tissues. The first of these effects leads to a reduction in body fluids, most importantly, blood volume. The consequences of the second factor are reductions in bone and muscle mass. Whether disuse atrophy of musculoskeletal tissue can be prevented is still unresolved. In addition, a third factor, a long-term alteration of metabolic state, reflecting changes in dietary intake and exercise, was found to play an important role in aggravating the zero-g "deconditioning" processes of the space flight crews. However, it is doubtful at this time that these latter factors are beyond human intervention and correction on future missions. All of these events have both acute and long-term effects in the major physiological systems which lead to loss of weight and, upon return to a one-g environment, decreased tolerance for orthostasis and work.

159
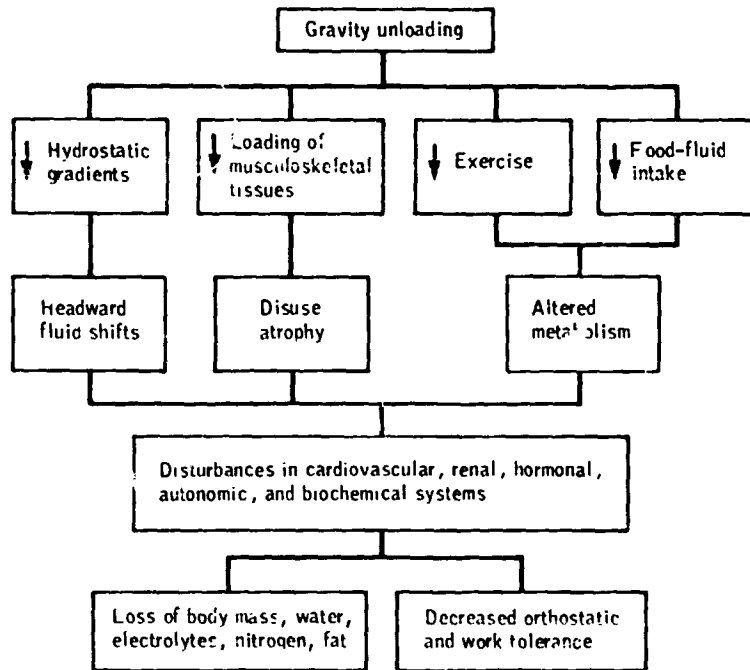
Figure 8: Physiological Effects of Exposure to Weightlessness

Our studies have been based on the belief that within the time span over which man has so far been studied in space, these responses to weightlessness are not pathological in nature; rather, they can be explained in terms of normal, although complex, feedback regulatory processes. Our simulation studies have supported this premise. Adaptation to weightlessness is said to occur when the body adjusts to these changes and reaches a new steady state (Figure 9). Each physiological system appears to have its own time course of adaptation. The rates of degradation and loss of such quantities as bone, muscle, fat, red cells, and water are all quite d fferent, depending upon the nature of the distu bance and on the time constant of the correcting homeostatic system. In Figure 9, the return to baseline reflects the establishment of a new homeostatic level appropriate to weightlessness.

The contribution of the simulation models was significant in developing a group of zero-g hypotheses. The utility of the models, however, extended beyond their important predictive capabilities discussed earlier. A benefit of the modeling process was related to the ways in which models shaped the data analysis effort. Quantitative modeling often required a new look at data which had already been analyzed by more traditional methods. The simulation approach required certain patterns of data in very specific forms. Satisfying

160
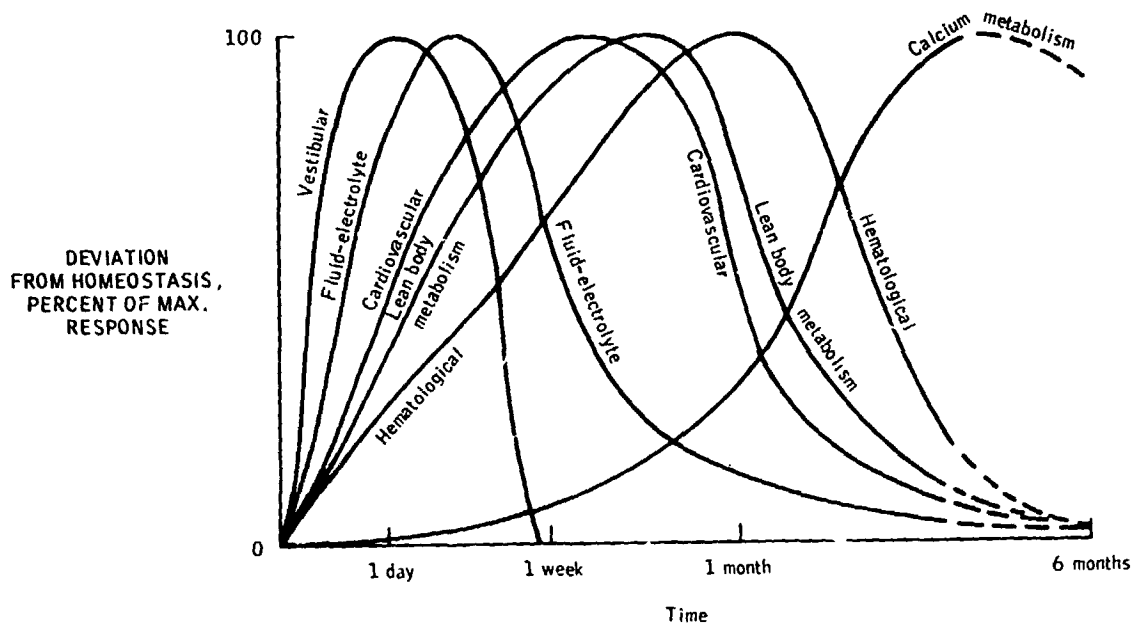
Figure 9: Approach Toward Homeostasis of Physiological Systems
During Space Flight

these model requirements led, in one instance, to an extensive metabolic
balance analysis for describing body composition changes during space flight.
Another benefit of modeling, at this stage of its application to space
physiology, was in forcing the analyst to think systematically,
comprehensively, and quantitatively about the system of interest. The
complexity of the models, reflecting the redundancy of the mechanisms in the
body, helped resolve some paradoxical findings by suggesting the involvement
of one or more competing pathways. Also, it was not always possible to
explain the long-term adaptation phase of space flight in terms of regulatory
feedback mechanisms more suited to corrective action of acute disturbances.
This suggested a logical division of the space-flight period into acute and
chronic segments for purposes of systems analysis. As a result, a
comprehensive analysis of acute ground-based studies was undertaken to enhance
our understanding of the immediate period following launch, an interval during
which few space-flight observations were made.

CONCLUSION

The effort described here has resulted in a more advanced analysis of space-flight data than was previously available. The accomplishments associated with this project include the following:

a) Establishment of a more definitive data analysis based on a composite picture of the nine crewmen from all flights;

b) Allowing estimation of quantities which could not be measured directly but could be derived from simple metabolic balance models or advanced simulation models;

c) Integration of data across disciplinary lines;

d) Quantitative evaluation of hypotheses by computer simulation and interpretation of data in terms of feedback control theory;

e) Reevaluation and reinterpretation of previously published Skylab data in the light of more recent findings from ground-based studies and Soviet missions.

This is not to imply that a definitive theory of space-flight adaptation was formulated. Rather, the fundamental contribution of the systems analysis effort has been to organize many of the major biomedical findings from space flight and correlate these findings with the scientific concepts that describe the requisite organ systems. Out of this effort has come an array of methods, tools, and techniques that have been essential for the handling, processing, and interpretation of experimental data in general and space-flight data in particular. Another benefit arising from this systems analysis project was an improved understanding of the physiological events which occur during human adaptation to weightlessness and the concomitant identification of critical areas ripe for future study. Recommendations for new experimental approaches generated by the current program have already contributed to the design of ground-based and future Spacelab investigations. Full potential of the systems analysis method will be realized only by maintaining an interative cycle between model developments and experimental research.

REFERENCES

1. Johnston, R.S. and L.F. Dietlein (Ed.) Biomedical Results from Skylab. National Aeronautics and Space Administration, Washington, D.C., SP-377, 1977.

2. Leonard, J.I., J.A. Rummel, and R.J. White (Ed.) An Integrated Analysis of the Physiological Effects of Space Flight. National Aeronautics and Space Administration, Washington, D.C. (in press).

ACKNOWLEDGEMENTS

A MULTIFREQUENCY EVALUATION OF ACTIVE AND PASSIVE
MICROWAVE SENSORS FOR OIL SPILL DETECTION AND ASSESSMENT

Richard G. Fenner
National Aeronautics and Space Administration
Lyndon B. Johnson Space Center
Houston, Texas

Stephen C. Reid and Charles H. Solie
Lockheed Engineering and Management Services Company, Inc.
Houston, Texas

ABSTRACT

During 1979, two major accidental oil spills occurred in the Gulf of Mexico. On June 3, 1979, the PEMEX well, Ixtoc I, suffered a blowout and was not capped until the spring of 1980. On November 1, 1979, the freighter Mimosa collided with the tanker Burma-Agate at the entrance to the Port of Galveston. Five to six of the Burma-Agate's tanks were ruptured. Fire resulting from the collision prevented them from being sealed, and several thousand barrels of crude oil were subsequently spilled into the Gulf. These spills presented a major ecological threat to the Texas Gulf Coast, but offered a unique opportunity to evaluate multiple-frequency microwave sensor data for oil-spill detection and assessment.

During the summer of 1979, the NASA/Lyndon B. Johnson Space Center was evaluating an X-band synthetic aperture radar (X-SAR) system on a NASA WB-57 high-altitude aircraft. Imagery of the Ixtoc I spill was obtained on June 3, 1979, in a flight over the Gulf of Mexico, east of Harlingen, Texas. In November, the NASA Earth Survey #2 C-130 aircraft was being made ready for a data-gathering mission. As part of the premission sensor evaluation, several runs were made over the Burma-Agate spill gathering active/passive microwave and multispectral scanner data. In January 1980, an additional C-130 aircraft active/passive microwave data flight was made over the Ixtoc I well oil spill. Supportive photographic data was taken on these C-130 flights.

This paper will present an evaluation of the data gathered on these flights with respect to how active and passive microwave sensors can best be used in oil-spill detection and assessment. Radar backscatter curves taken over oil spills will be presented and their effect on synthetic aperture radar (SAR) imagery will be discussed. Plots of microwave radiometric brightness variations over oil spills will be presented and discussed. Recommendations as to how to select the best combination of frequency, viewing angle, and sensor type for evaluation of various aspects of oil spills will also be discussed.

INTRODUCTION

Numerous studies[1-13] have been conducted which have firmly established the ability of remote sensors to define the presence of oil slicks, their aerial coverage, temporal development and spectral reflectance and emission characteristics.

The effect of oil spilled on the surface of the sea is to dampen the very short capillary waves that dominate microwave radar backscatter. Consequently, the use of radar for observing oil spills has been the subject of considerable experimental effort over the last several years. The oil-spill observation is ordinarily done with an aircraft-mounted imaging radar capable of displaying signals from the sea-surface wave patterns. A dark area on the image indicates the absence of capillary waves, and consequently, the presence of oil spills.

Since radar intrinsically possesses the all-weather, day/night capability and the large swath widths required for timely continuous monitoring of oil contamination of the ocean surface, an orbital radar system is a likely candidate for worldwide monitoring of oil spills.

Unfortunately, quantitative research into the amount of radar back-scatter suppression due to the phenomenon has been too little to adequately predict performance of operational radar oil-spill monitoring systems.

Early studies[14] conducted by the Naval Research Laboratory concluded that viewing angles greater than 45 degrees off nadir should be used to avoid specular returns and provide maximum swath widths for aircraft-mounted imaging radars.

Contrasted to the aircraft situation where incidence angle ranges of 45 degrees or greater are usually required to obtain reasonable swaths, a spacecraft incidence angle range of only a few degrees (Seasat case of five degrees at a 22-degree incidence angle) provides swaths of 100km or greater. This combined with allowable viewing angles and the ambiguity constraints of a spacecraft synthetic aperture radar (SAR) results in a need to well define the angular response of oilspill backscatter for various wavelengths to establish the system parameters for an orbital oilspill detection SAR.

K. Krishen[15] presented the analysis of 13.3 GHz scatterometer data gathered over a crude-oil spill off the Mi‹ ssippi River Delta in the Gulf oт Mexico. Krishen's results for a moderate sea state (wind speed of 18 knots) demonstrated that scatterometer systems can be used to detect oil spills at incidence angles less than 45 degrees off nadir and that the oil's smoothing of the sea results in a predictable decrease in the radar scattering coefficient.

This paper will present the results of analysis of the data taken on the previously mentioned aircraft flights. In analyzing the data, emphasis was placed on determining the optimum frequency and sensor for a spaceborne platform.

Before describing the results of this experiment, a brief review of the instrumentation and processing will be given to assist in the interpretation of the data presented in later sections of this paper.

INSTRUMENTATION

The NASA/JSC WB-57 and C-130 aircraft are operated as part of the Airborne Instrumentation Research Program (AIRP). They are used to gather

remote sensing data for Earth Resources Applications investigations. In addition to active microwave sensors, both aircraft carry Zeiss color and color-infrared photographic equipment and multispectral scanners. The C-130 aircraft is instrumented with passive microwave radiometer systems and four active microwave sensors called scatterometers. These systems are continuous wave radars that illuminate the surface in a fan beam from nadir to 50 degrees left of nadir along the flight path of the aircraft. The operating wavelengths are 75cm (400 MHz), 18.5cm (1.6 GHz), 6.3cm (4.75 GHz) and 2.3cm (13.3 GHz). The spatial resolutions are approximately 75mm x 180m, 40m x 120m, 40m x 60m, and 40m x 40m respectively. Tables I and II contain the system parameters of the C-130 microwave radiometer and scatterometer systems.

The WB-57 aircraft carries an X-band synthetic aperture radar (SAR) system. This system is a modified AN/APQ-102A military reconnaissance radar. Table III contains the performance parameters for this system.

The unique feature of this radar system is the ability to position the antenna to two different ranges of incidence angles. Figures 1 and 2 show these two modes of system operations.

DATA ACQUISITION

To obtain the signature of oil-covered surface and non oil-covered surface without changing the radar viewing direction with respect to the wind direction the aircraft was flown orthogonal to the oil slick flow direction. Two passes across each of the two oil slicks (Burma-Agate on 11/15/79 and Ixtoc I on 1/29/80) were made to obtain a sufficient number of independent samples for statistical analyses. The aircraft flew at an altitude of 1500 feet over the Burma-Agate spill and 2000 feet over the Ixtoc I spill. Figure 3 is an aerial photograph obtained with a Zeiss nine-inch camera over the Burma-Agate. Figure 4 is an aerial photograph obtained over the Ixtoc I well site.

Of the microwave sensor data acquired, only the 13.3 GHz scatterometer systems and the C-band radiometer acquired data over both spills. Additional scatterometer data at 4.75, 1.6, and 0.4 GHz was obtained over the Burma-Agate spill and additional radiometer data at 18 GHz, 22 GHz, and 37 GHz was obtained over the Ixtoc I spill.

Although no ground truth was taken at either site, onboard observations indicated a calm sea with low surface-wind conditions. In addition, an estimate of the sea state was made using the non oil-covered surface 13.3 GHz scatterometer backscatter coefficient measurements and data presented by Jones.[16] This estimate indicated wind velocities of less than two meters per second for the Burma-Agate flights and between four meters per second and six meters per second for the Ixtoc I flights.

SCATTEROMETER DATA ANALYSIS

By obtaining radar data across the oil slick, time histories of backscatter coefficient for each incidence angle of both oil-free and oil-covered surfaces provide measurements of the differences due to the presence of the oil. Figure 5 is a time history of 13.3 GHz 20-degree incidence angle backscatter coefficient for Run 2 of the Burma-Agate spill. The mean value of the non oil-covered surface is -8 dB while the mean value of the oil slick surface is -24 dB. Figure 6 is a time history of 13.3 GHz 20-degree incidence

angle backscatter coefficient for Run 3 of the Burma-Agate spill. The mean value of the non oil-covered surface is -9 dB while the mean value of the oil-slick surface is again -24 dB.

In both Figures 5 and 6, the radar return at 20-degrees incidence angle is decreased by about 16 dB due to the presence of the oil slick.

Figure 7 illustrates the angular and frequency dependence of this decrease in radar backscatter due to the presence of an oil slick on a smooth sea surface. The P-band (75cm) data is not included since the change in radar backscatter at the incidence angles being considered was negligible. The significant responses, greater than 6 dB due to the oil slick for 13.3 GHz and 4.75 GHz at 15- to 30-degrees incidence angles, are encouraging in that this range of angles has previously not been considered for oil slick detection.

Figure 8 is a time history of the 20-degrees incidence angle backscatter coefficient for the 13.3 GHz scatterometer and the microwave brightness temperature for the 18 GHz and 37 GHz radiometers for Run 2 of the Ixtoc I spill. Several significant features can be noted about the nature of this spill from Figure 8.

The higher value (-6 dB) of the backscatter coefficient at 20:55:20/27 is indicative of the return of non oil-covered surfaces with a surface wind speed estimated at six meters per second.[17] The decrease of the radar backscatter seen from 20:55:30 to 20:55:37 without a change in the radiometer brightness temperature is indicative of th. smoothing action of an oil sheen (thickness of less than 0.1mm).[18]

The further decrease in the radar backscatter and the increase in brightness temperature seen from 20:55:40 through 20:55:45 is indicative of an oil slick (thickness approximately 1mm).[19,20]

Figure 9 is a comparison of 13.3 GHz radar backscatter coefficient versus incidence angle for various wind speeds over open ocean and oil spills. The decreases in backscatter for incidence angles less than 30 degrees is seen to be less for higher wind speeds. The 2m/sec data is from the Burma-Agate spill, the 6m/sec from the Ixtoc I spill and the 30m/sec data is from an earlier spill reported by Krishen.[15]

RADIOMETER DATA DISCUSSION

Four radiometer data lines were selected because they highlight significant features of radio emission from an oil spill. Frequencies used in the data presented are C-, Ku-, and Ka-band (4.995 GHz, 18 GHz, and 37 GHz). Unfortunately, the 10.69 GHz scanner (Passive Microwave Imaging System) failed on the Ixtoc I mission and no data was obtained.

Figure 10 is a time history of C- and Ka-band brightness temperature from the Burma-Agate spill at incidence angles of 40 degrees. Both horizontal and vertical polarizations are shown. The Ka-band radiometer yielded the largest change in temperature. Review of the photographs from this flight line showed that the radiometers were turned on just as the aircraft started to pass over the oil slick. Immediately after the visible oil slick, there was an apparent clear area, then a small ship. The K-band radiometers, however, indicate that oil, though not visible to the camera was present, and clear water was not present until after the ship.

The next two Figures (11 and 12) are plots of data from the Ixtoc I spill with an incidence angle of 50 degrees. When looking at these figures, it should be noted that the C-band system looks ahead of the aircraft while the K-bands look behind the aircraft and thus a target appears in the K-bands approximately 20 seconds after it appears in the C-band. As in the Burma-Agate case, Figure 11 shows Ka-band data in which both the horizontal and vertical channels increase in brightness temperature. Ku- and K-band data (not shown) responded the same. Large quantities of oil were visible in a photograph of this area. Figure 12 shows the C-band results for the same area. At this incidence angle, the spill appears larger to the C-band radiometer's vertical channel. Part of this is possibly due to a larger antenna footprint for the C-band system.

However, the depression of the C-band horizontal channel is most interesting. It is believed that this is a function of wind velocity and the thickness of the oil on the surface.

Figure 13 is a plot of the data from three radiometers, C-, Ku-, and Ka-band made in the same area as the previous two figures, but at an incidence angle cf zero degrees. Large quantities of oil were visible in a photograph of this area. Notice the lack of a significant return in the C-band data while Ka-band rises almost 20 degrees Kelvin.

Although no attempt has been made to determine the thickness of the oil from this data, thickness measurements have been made at other frequencies.[20] Perhaps this data will aid others in deciding the relative importance of radiometric data and what frequencies should be used.

RADAR IMAGERY ANALYSIS

As stated previously, the radar imagery of the Ixtoc I spill was gathered as a part of the engineering evaluation of the system. Initial analysis of the data was more concerned with the ability of the radar systems to clutter-lock over water. The fact that the radar could image oil slicks was considered interesting, but radars had imaged oil slicks previously.

After analysis of the Burma-Agate and Ixtoc I scatterometer data produced the results shown in Figure 7, the radar imagery was again examined. This examination attempted to determine if the large decrease in backscatter at 20 degrees could be seen on the imagery.

Figure 14 is a radar image of the Ixtoc I slick taken in August 1979. This image was taken on a calm day. Winds in the area were five knots or less.

Plotted below the imagery are the quieting or decrease curves of Figure 7. Although the radar imagery was taken at X-band and the scatterometer data was taken at L-, C-, and Ku-band, it can reasonably be assumed that an X-band scatterometer would have produced a curve which would fall between the C-band and Ku-band curves.

Nadir is to the left of the image. The image spans a range of incidence angles from 14 degrees to 51 degrees. The brightness to the left of the image is typical of what happens to radar backscatter as you approach nadir. More and more energy is backscattered and less is forward scattered.

Note that the oil slicks still darken the image in this range, particularly around 20 degrees as predicted by the associated curves. The fact that the slicks are black indicates that the change is occurring over most of the grey scale of the film which is nominally 15 dB to 20 dB. This corresponds to the 10 dB to 15 dB quieting effect shown on the curve.

As noted previously, this imagery was taken on a relatively calm day. In discussing this imagery, NOAA representatives were quite surprised to see that the slicks could be seen on a calm sea. Their attempts to track the slicks with the U.S. Coast Guard AOSS system[6,7,13] had shown that at wind speeds less than five knots, slicks were not detectable.

This image and associated curves clearly show that the optimum range of incidence angles for oil-spill detection is in the 15 degrees to 25 degrees range. In this range, the larger surface return would place a less stringent power output requirement on the radar and the quieting effect of the oil is greatest for lower wind speeds.

CONCLUSIONS

The data set used to prepare this paper was gathered under target of opportunity circumstances, thus all sensors were not available for all flights. However some general conclusions can be drawn. These are as follows:

(1) The presence of an oil spill on a water surface can be detected by a microwave radar system at incidence angles less than 45 degrees. Higher radar frequencies produce greater contrast between surfaces with and without oil on the surface. In the incidence angle range of 15 degrees to 25 degrees, there is greater surface return and maximum quieting due to the oil, thus reducing power output requirements on the radar.

(2) Windspeed over the surface affects the magnitude of the difference between oil-covered and non oil-covered surfaces. The use of low ($<20°$) incidence angles at low microwave frequencies (L-band) provides less detectibility than higher microwave frequencies (Ku-band).

(3) An X- or Ku-band synthetic aperture radar (SAR) operating at orbital altitudes and incidence angles similar to Seasat would provide an effective means for detecting, monitoring, and tracking large oil spills.

(4) More study must be given to the effects of sea state on the active microwave oil-spill signature at incidence angles less than 45 degrees.

(5) Radiometers, while not having the resolution capability that SAR systems have, do have potential for determining oil thickness on the surface.

ACKNOWLEDGEMENTS

REFERENCES

1. Aukland, J. C., et al, 1971, Multi-sensor Oil Spill Detection: Proceedings Seventh International Symposium of Remote Sensing of Environment, pp 1045-1052.
2. Kennedy, J. M., Wermund, E. G., 1971, Oil Spills. Infrared and Microwave: Photogrammetric Engineering, pp 1235-1242.
3. Munday, J. C., MacIntyre, W. G., and Penney, M. E., 1971, Oil Slick Studies Using Photographic and Multispectral Scanner Data: Proceedings Seventh International Symposium of Remote Sensing of Environment, pp 1027-1043.
4. Aukland, J. C., Conway, W. H., and Sanders, N. K., 1969, Detection of Oil Slick Pollution on Water Surfaces with Microwave Radiometer Systems: Proceedings Sixth International Symposium of Remote Sensing of Environment, pp 789-796.
5. Thaman, R. R., Estes, J. E., Butler, R. W., and Ryerson, J. M., 1973, The Use of Airborne Imagery for the Estimation of Marine Oil Spills: An Operation Example: Proceedings Eighth International Symposium of Remote Sensing of Environment, pp 1093-1098.
6. Woolever, G. F., et al, 1975, Utilization of Remote Sensing Techniques for U.S. Coast Guard Missions: Proceedings Tenth International Symposium of Remote Sensing of Environment, pp 3-16.
7. Becker, R., 1972, Coast Guard Evaluates Oil Spill Detection Schemes, Microwave, May 1972, pp 12, 14.
8. Vizy, K. N., 1974, Detecting and Monitoring Oil Slicks with Aerial Photos: Photogrammetric Engineering, Vol. 40, pp 697-708.
9. Kotlarski, J. R., and Anderson, H. R., 1974, Oil Slick Detection by X-Band SAR: Proceedings Ninth International Symposium of Remote Sensing of Environment, pp 1775-1790.
10. Pilon, R. O., Purves, C. G., 1973, Radar Imagery of Oil Slicks: IEEE Transactions on Aerospace and Electronic Systems. Vol. AES-9, No. 5, September 1973, pp 630-636.
11. Kraus, S. P., et al, 1977, Radar Detection of Surface Oil Slicks: Photogrammetric Engineering and Remote Sensing, Vol. 43, No. 12, December 1977, pp 1523-1531.
12. Lund, T., 1978, Surveillance of Environmental Pollution and Resources by Electromagnetic Waves: D. Reidel Publishing Co., pp 309-318.
13. Maurer, A. T., Edgerton, A. T., and Meeks, D. C., 1977, U.S. Coast Guard Airborne Oil Surveillance System - Status Report: Proceedings Eleventh International Symposium of Remote Sensing of Environment, pp 1639-1640.
14. Guinard, N. W., 1971, The Remote Sensing of Oil Slicks: Proceedings Seventh International Symposium of Remote Sensing of Environment, pp 1005-1026.
15. Krishen, K., 1973, Detection of Oil Spills Using 13.3 GHz Scatterometer, Proceedings Eighth International Symposium of Remote Sensing of Environment, pp 1105-1119.
16. Jones, W. L., et al, 1977, Aircraft Measurements of the Microwave Scattering Signature of the Ocean: IEEE Transactions on Antennas and Propagation, January 1977, pp 52-61.

169

17. Moore, R. K., Fung, A. K., 1979, Radar Determination of Winds at Sea: Proceedings of IEEE, Vol. 67, No. 11, November 1979, pp 1504-1521.
18. Sabins, F. F., 1978, Remote Sensing, Freeman and Company, pp 334-342.
19. Smugge, T. J., 1979, The Use of Microwave Approaches in Hydrology: Proceedings of the American Society of Photogrammetry, pp 9-28.
20. Hollinger, J. P. and Mennella, R. A., 1973, Oil Spills - Measurements of Their Distributions and Volumes by Multifrequency Microwave Radiometery: Science Vol. 181, July 1973, pp 54-56.

TABLE I.- NASA/JSC C-13 AIRCRAFT MICROWAVE RADIOMETER SYSTEMS PARAMETERS

Parameter	Bands					
	L	Ku	K	Ka	C	X(PMIS)
Frequency (GHz)	1.4135	18	22.05	37	4.995	10.69
Bandwidth (MHz)	27	200	200	500	50	150
Sensitivity (degrees)	1	1	1	1	1	1
Integration Time (seconds)	0.1	0.1	0.1	0.1	0.1	Variable
Antenna Type	Phased Array	Horn	Horn	Horn	3-foot Dish	Phased Array (a)
Beam Width (3 dB)	16°	4°	4.5°	4°	5°	1.6° x 2.6°
Polarity	Either H or V	Sim. H & V	Sim. H & V	Sim. H & V	Sim. H & V	Sim. H & V
Incidence Angle (degrees)	0 - 50	0 - 50	0 - 50	0 - 50	0 - 50	49.5 (a)

(a) Scans constant incidence angle.

171

TABLE II.- NASA/JSC C-130 SCATTEROMETER SYSTEMS PARAMETERS

Parameter	Bands			
	Ku	C	L	P
Frequency (GHz)	13.3	4.75	1.6	0.4
Polarization	VV	VV or HH and CROSS	VV or HH and CROSS	VV or HH and CROSS
Along-track Resolutio (feet)	120	120	120	240
Cross-track Beamwidth (degrees)	2.5	4	8	16
Incidence Angles (degrees)	5-50	5-50	5-50	5-50
Nominal Bandwidth (Hz) ($\theta = 30°$ Vei = 150 kts)	400	150	50	12
Nominal Integration Time per Measurement (seconds)	0.16	0.32	0.64	1.0
Number of Measurements Averaged per Second	6	3	1.5	1.0
Precision of Measurement per Second of Spatial Data (dB) ($\theta = 30°$)	+0.36 -0.38	+0.57 -0.62	+1.0 -1.1	+2.0 -2.6

C-3

TABLE III.- X-BAND SIDE-LOOKING RADAR SYSTEM PARAMETERS

Transmit Frequency	9600 MHz
Transmit Output Power	50 KW
Transmit Polarization	Selectable Horizontal or Vertical
Pulse Width (half power)	0.90 Micro-second
Pulse Repetition Frequency (PRF)	Variable with Ground Speed (at 400 knots, PRF is 1352 PPS)
Pulse Spectrum Bandwidth	15 MHz
Antenna Stabilization Limits	Up 4.5°, Down 2.5° Azimuth ±6.75° Roll ±3°
Swath Coverage at 60,000 Feet	Mode I - 2.5 to 12.5 Miles Mode II - 10 to 20 Miles
Range Resolution	<50 Feet
Azimuth Resolution	<50 Feet
Azimuth Beamwidth	1.45° one way - half power
Receivers	One Vertical, One Horizontal (Hardwired to Recorder)
Recording Mode	Optical and Selected Digital
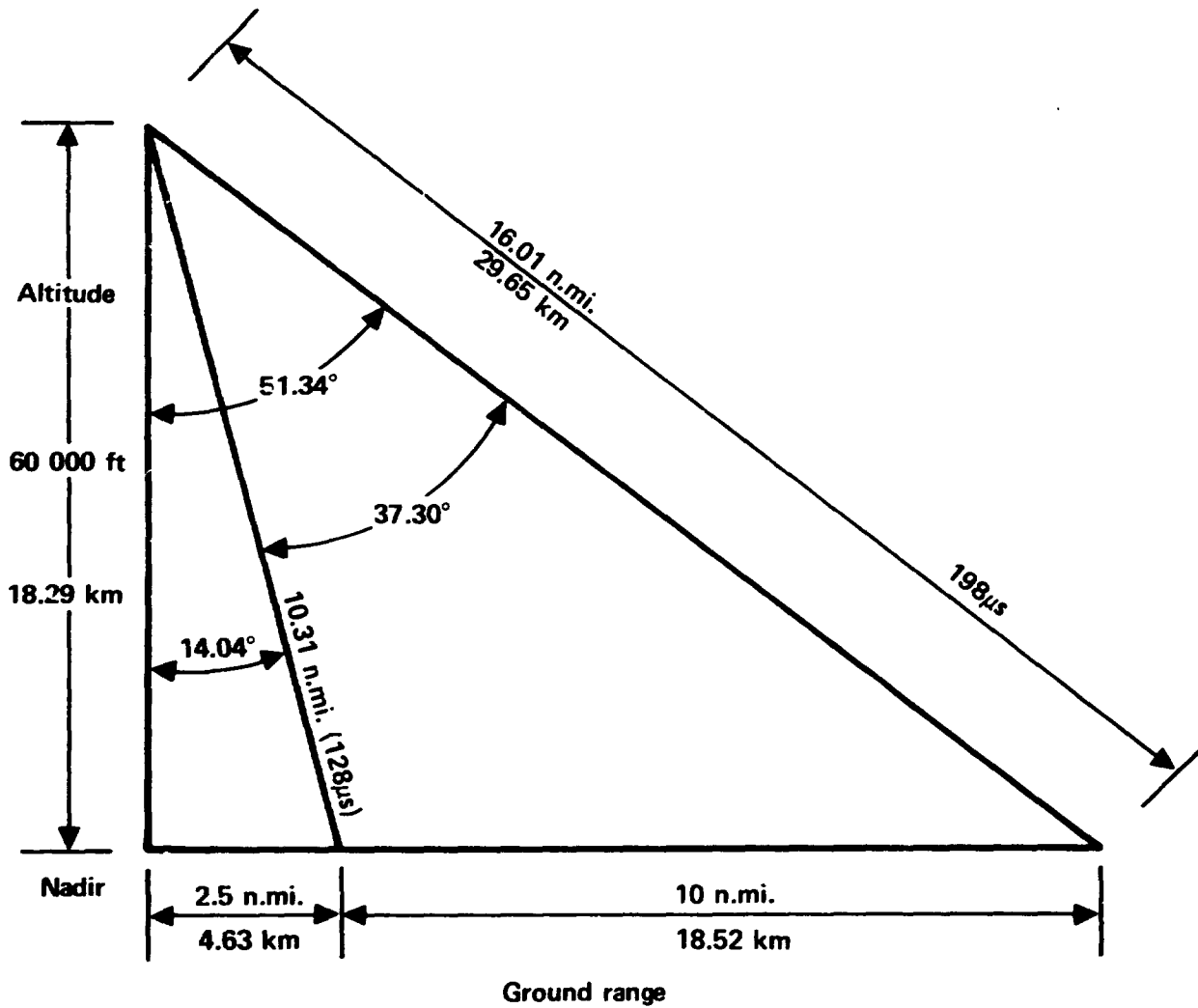
Figure 1.— Mode I, dual polarized X-SAR.
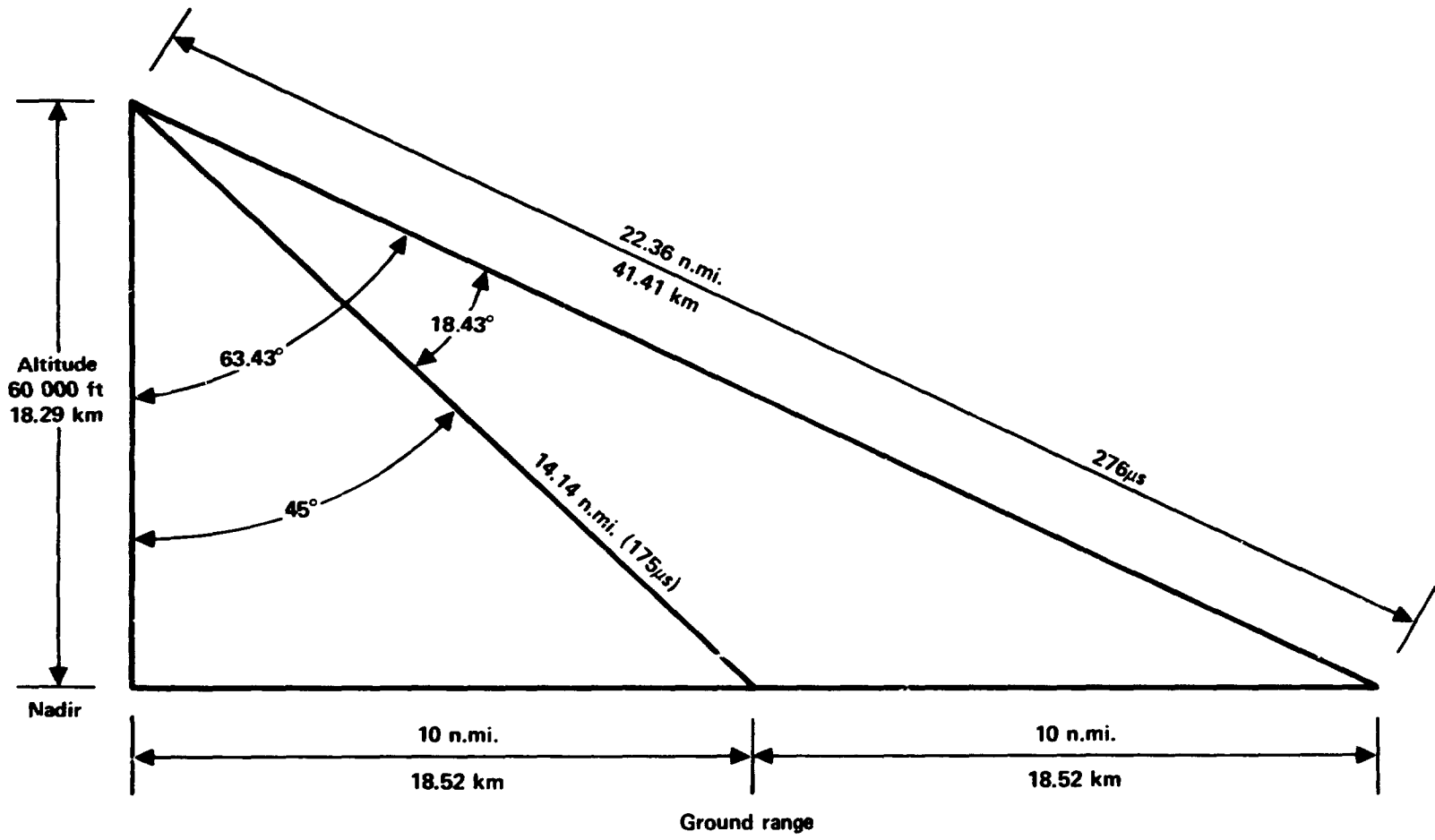
Figure 2.— Mode II dual polarized X-SAR.
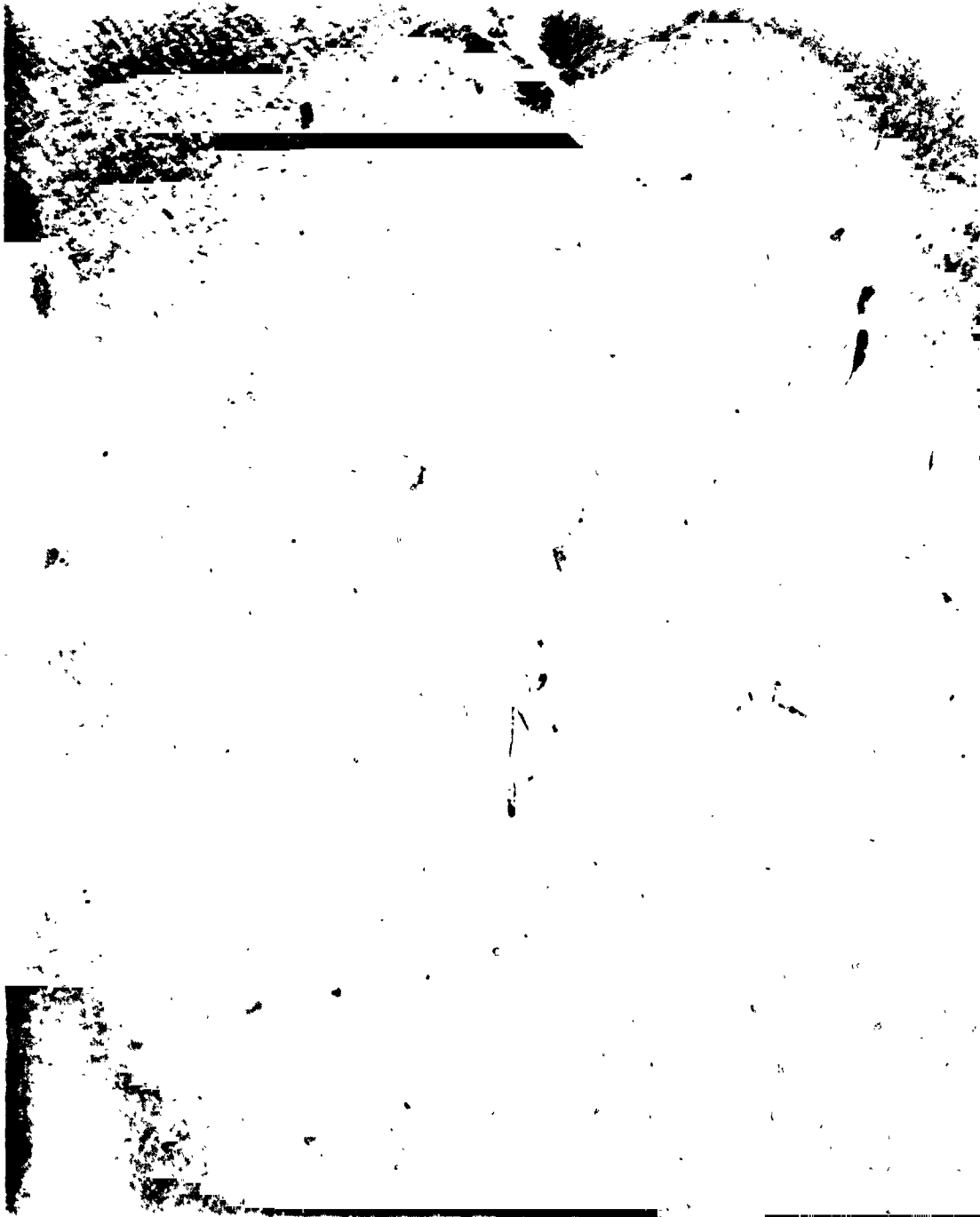
Figure 3.- Aerial photograph of the Burma-Agate.

176
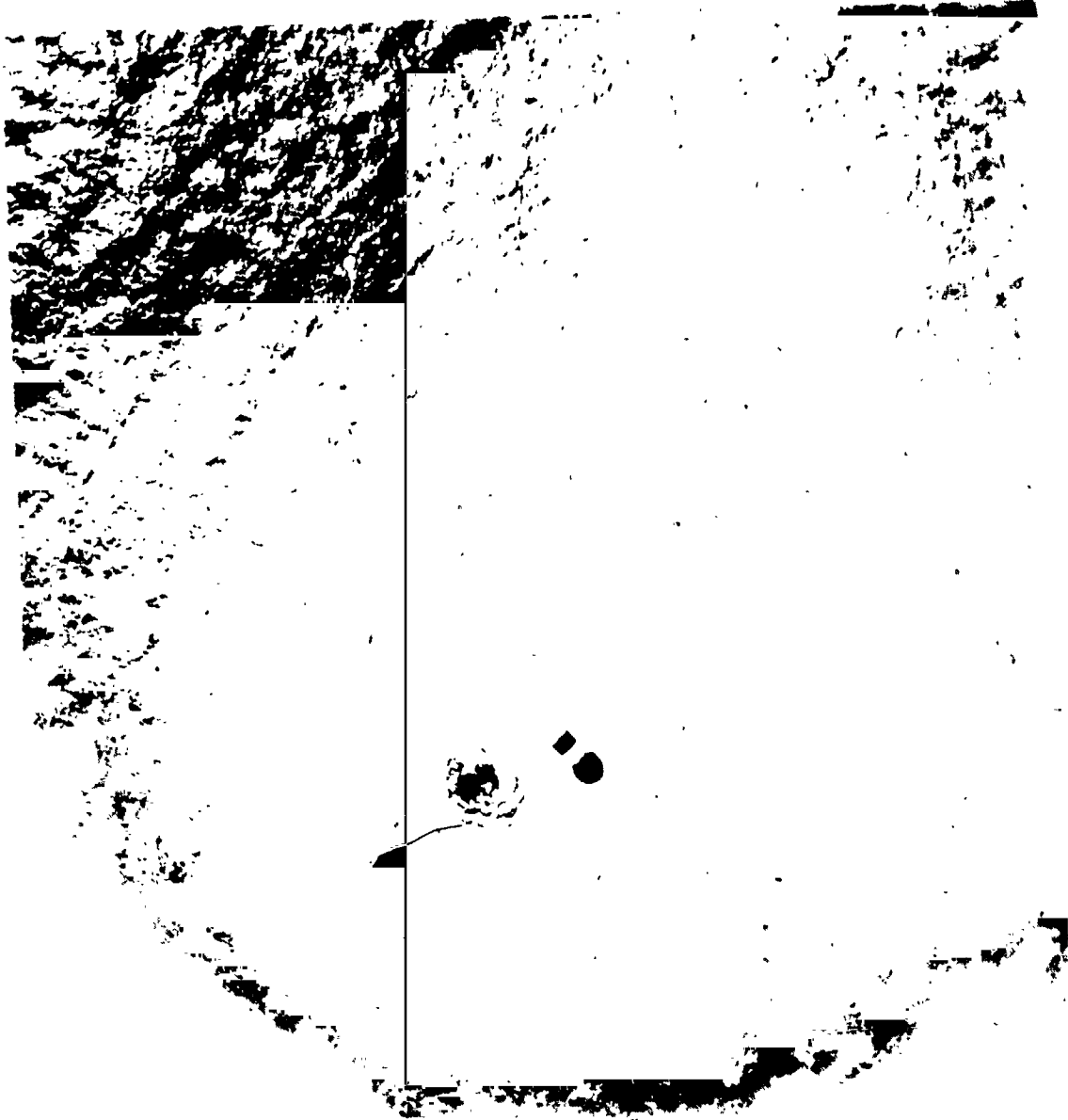
Figure 4.- Aerial photograph of the Ixtoc I well.
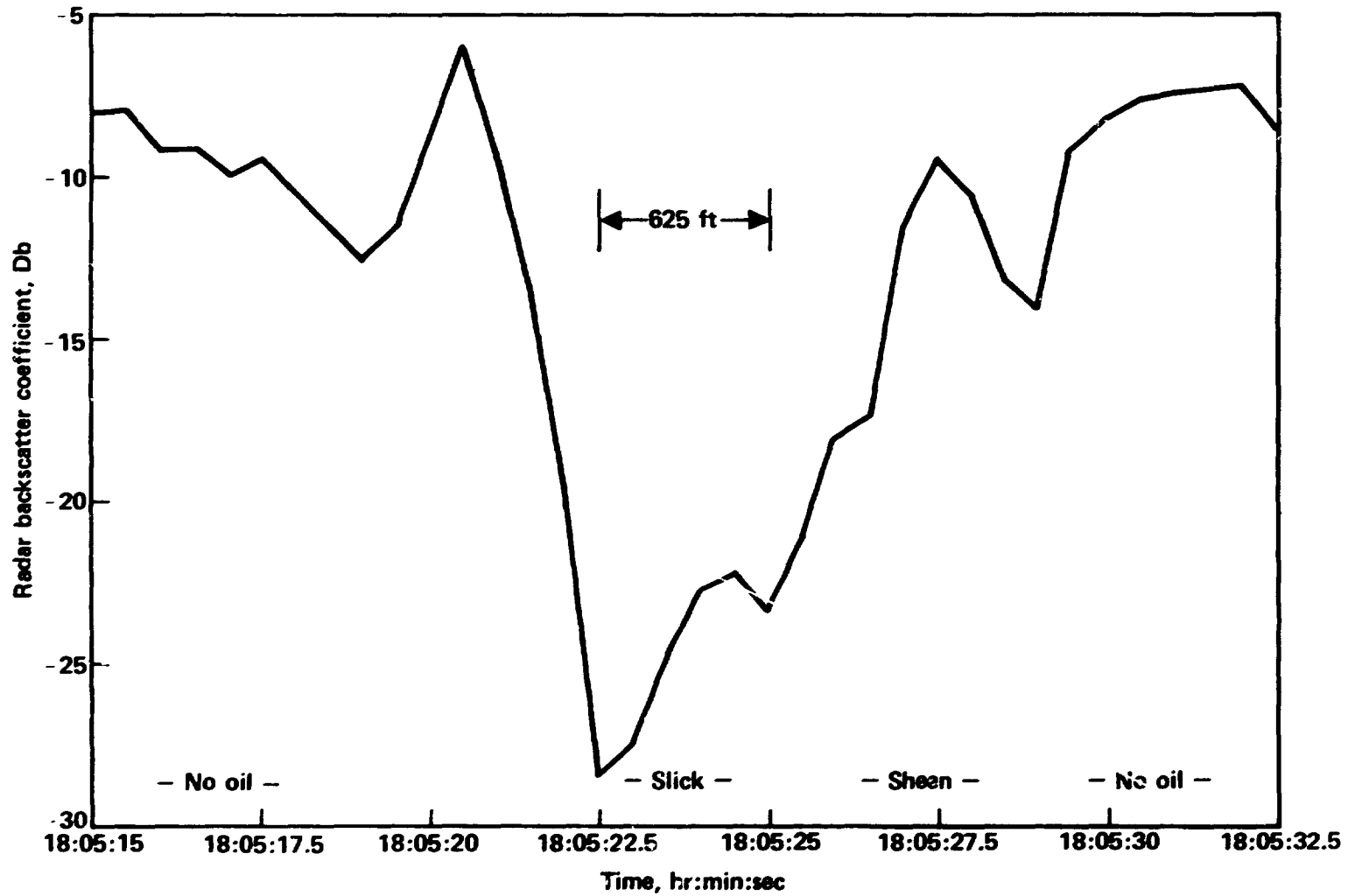
Figure 5.— Time history - 13.3-GHz scatterometer, 20° incidence angle backscatter
coefficient for run 2, Burma-Agate oil spill.
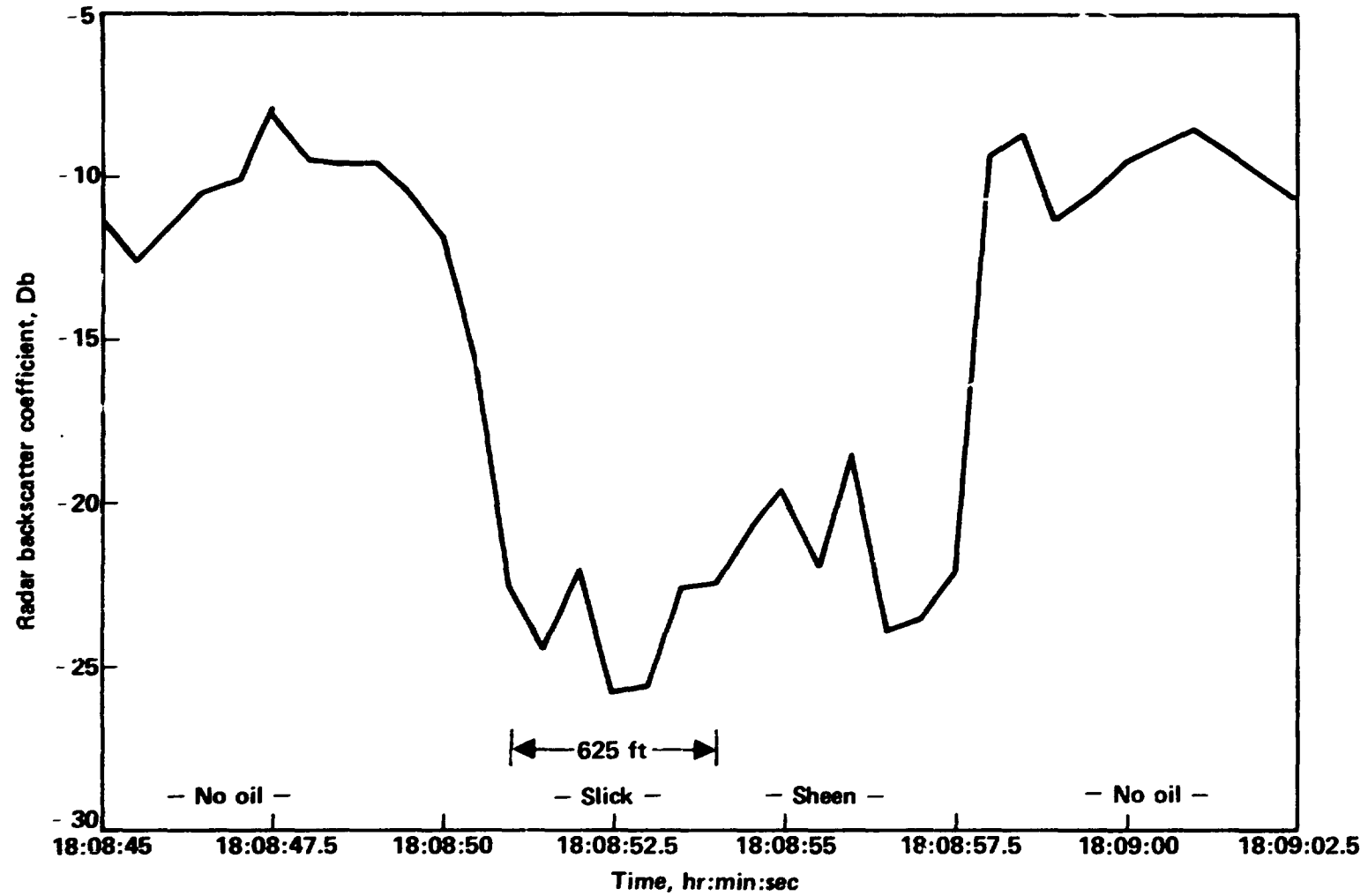
Figure 6.— Time history - 13.3-GHz scattercmeter, 20° incidence angle backscatter coefficient for run 3, Burma-Agate oil spill.
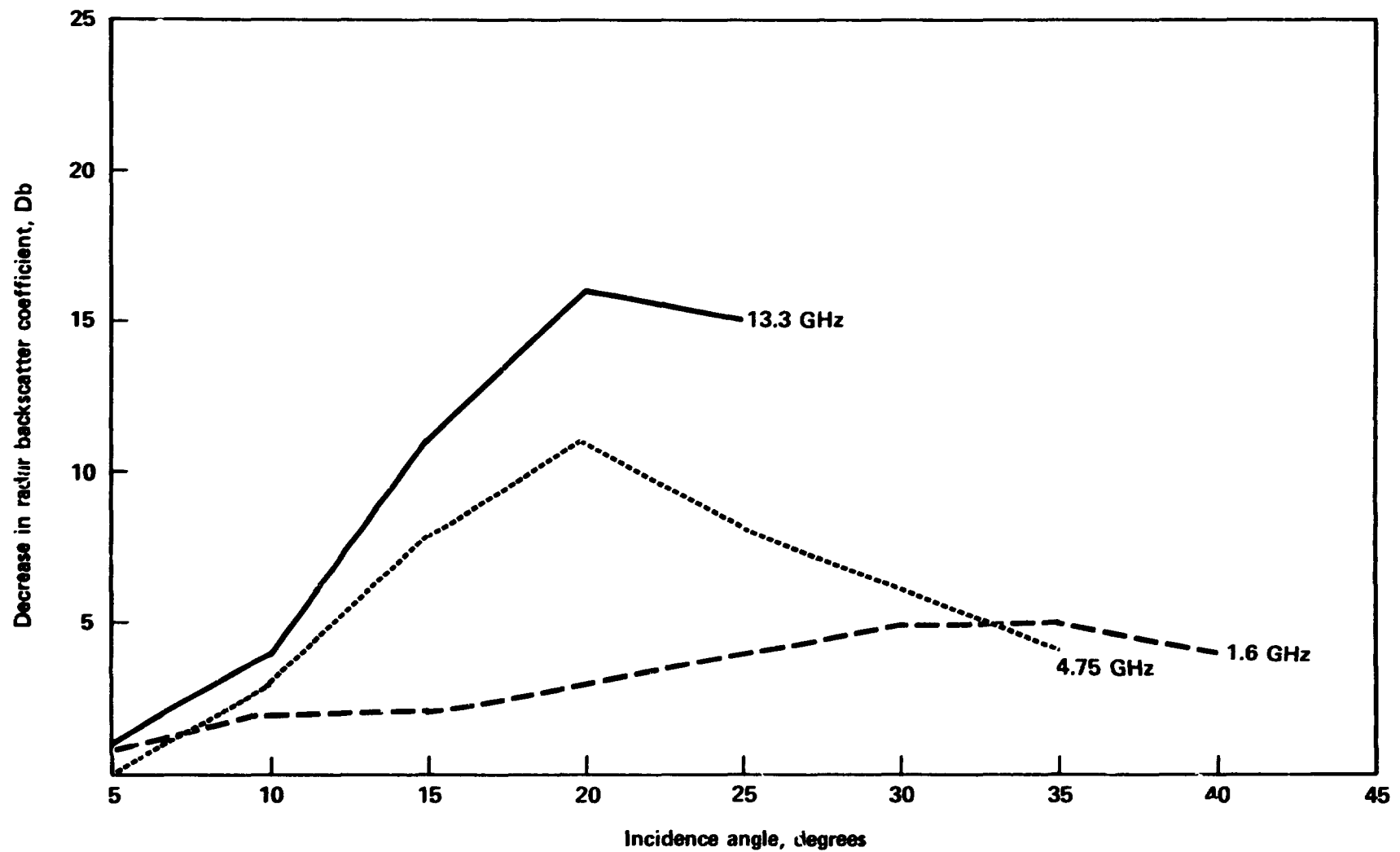
Figure 7.— Decrease in backscatter coefficient for 13.3-GHz, 4.75-GHz, 1.6-GHz scatterometer data versus incidence angle due to presence of oil slick on smooth sea surface, Burma-Agate oil spill, Runs 2 and 3.

180
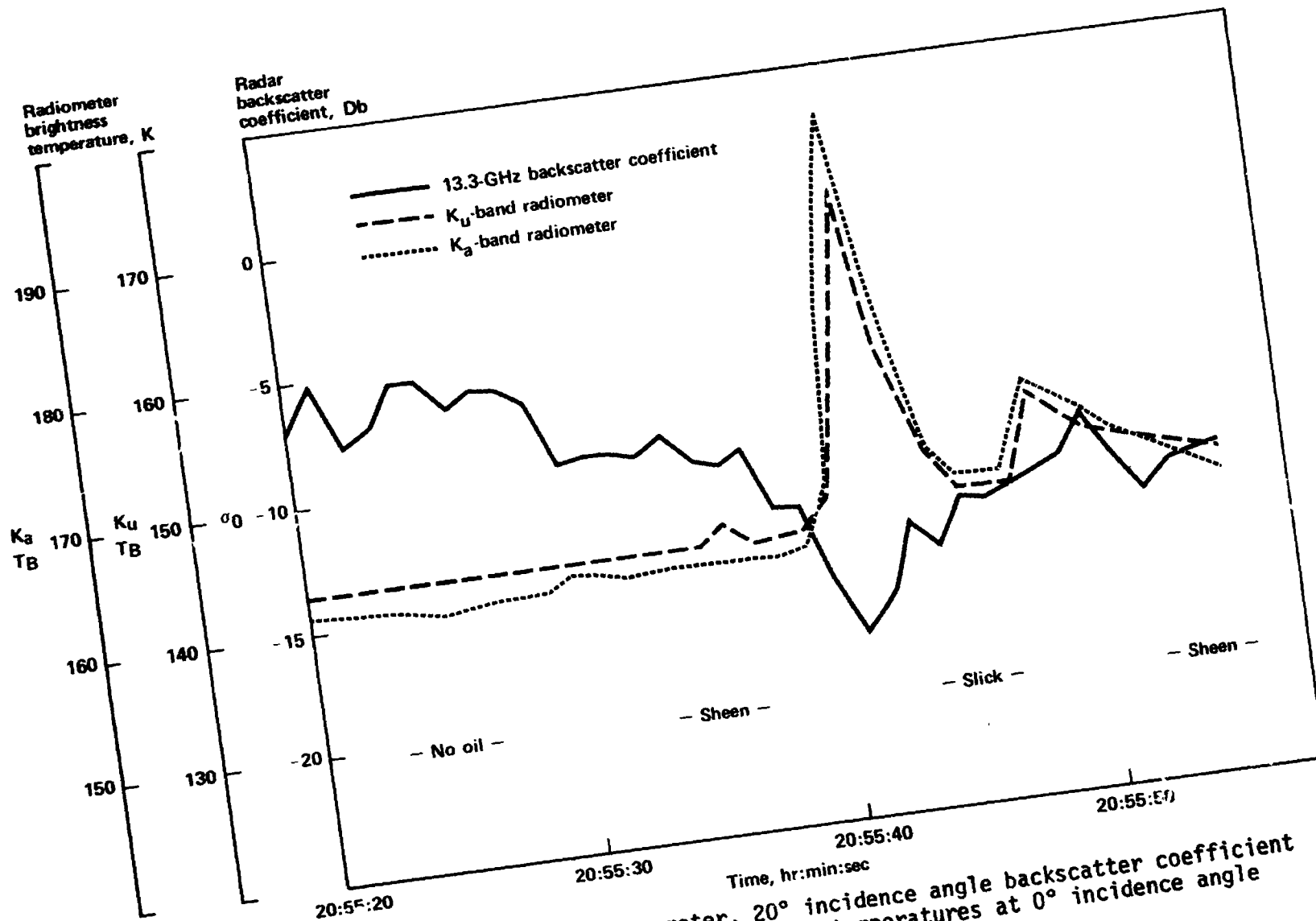
Figure 8.— Time history — 13.3-GHz scatterometer, 20° incidence angle backscatter coefficient and 18-GHz (K_u) and 37-GHz (K_a) radiometer brightness temperatures at 0° incidence angle for run 2, IXTOC I oil spill.

181
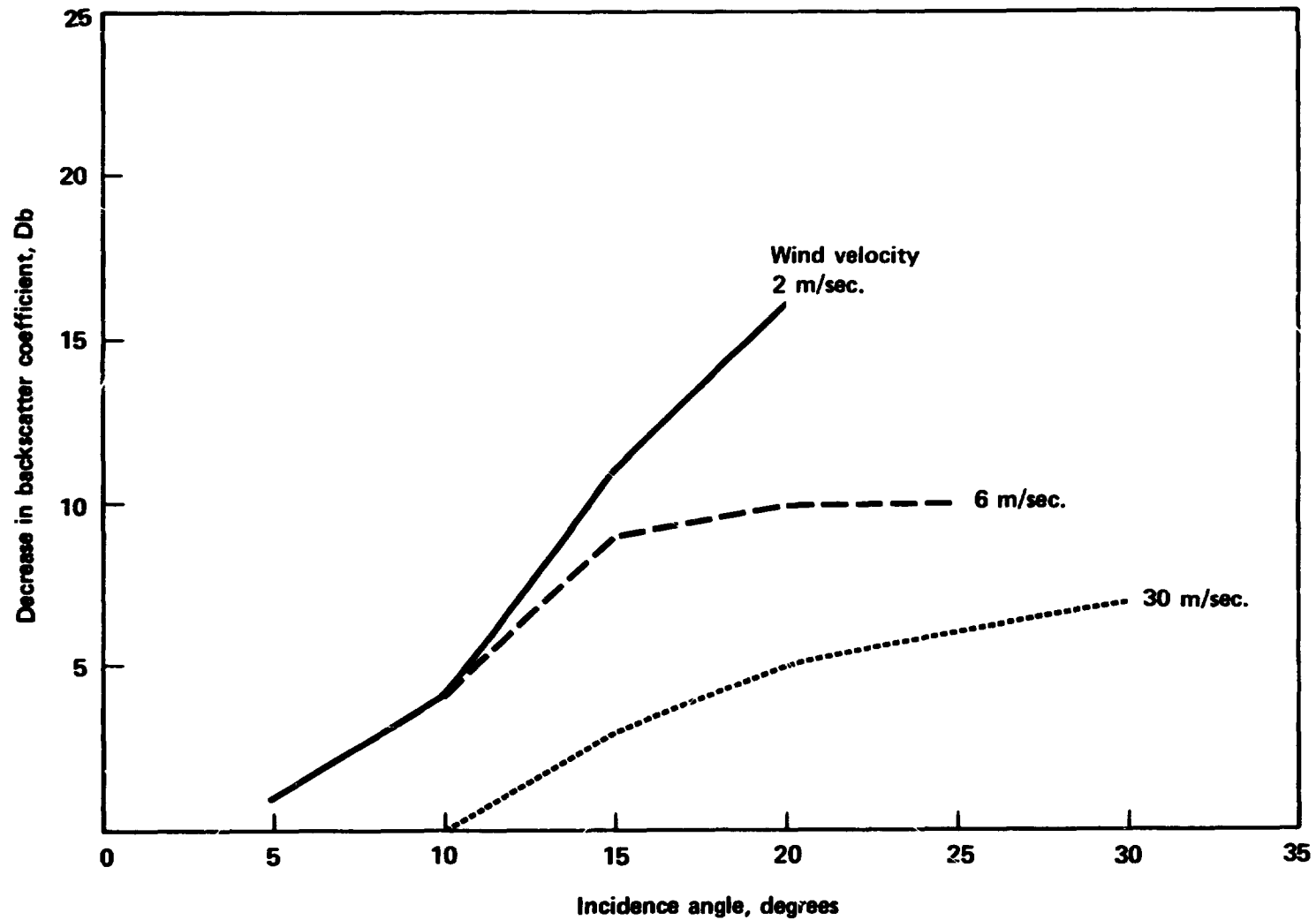
Figure 9.— Decrease in backscatter coefficient for 13.3-GHz scatterometer versus inciden
angle due to presence of oil slick for various windspeed conditions.
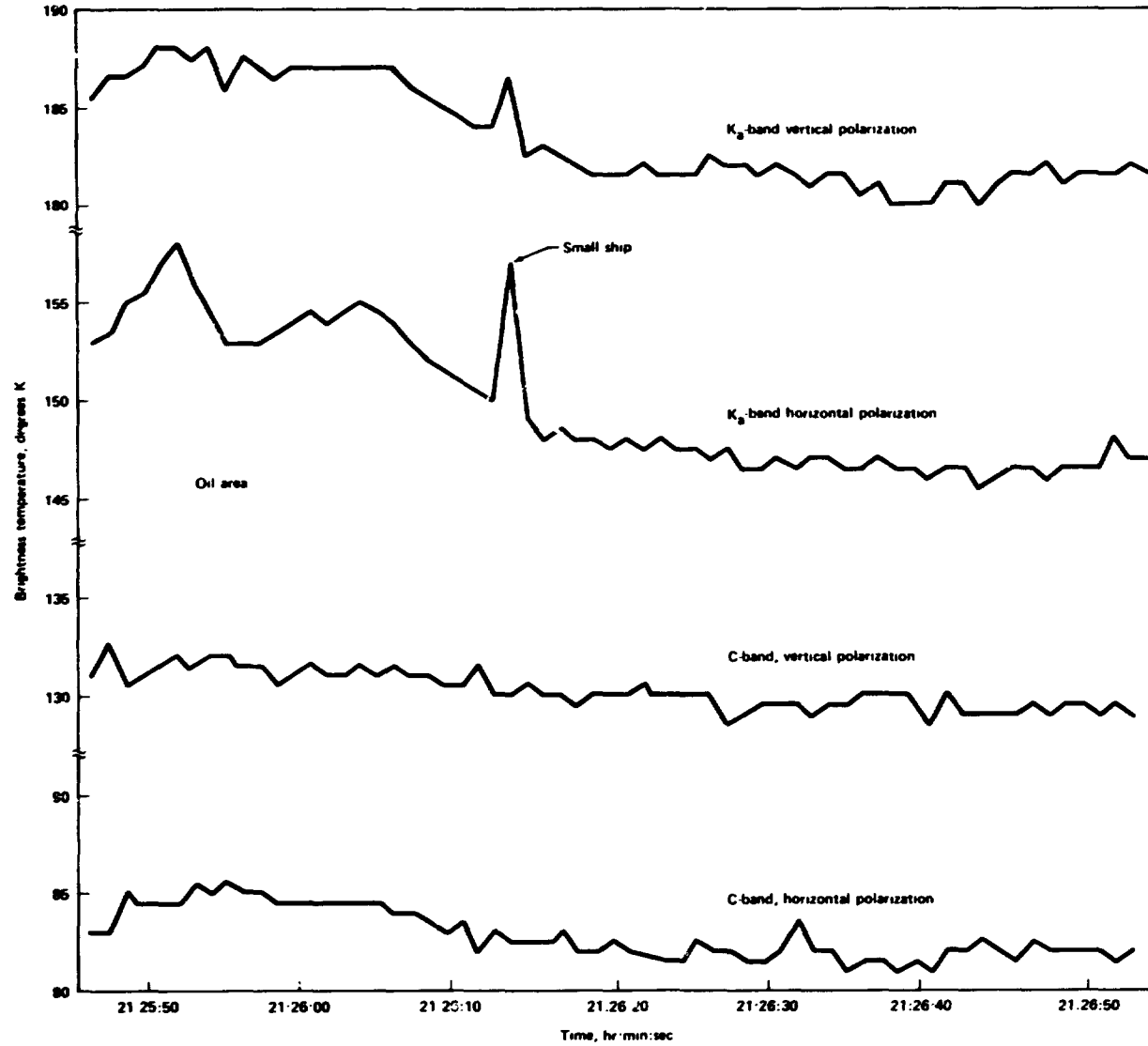
Figure 10.— Time history of C-band and K_a-band radiometer brightness temperature, 40° incidence angle, Burma Agate oil spill.
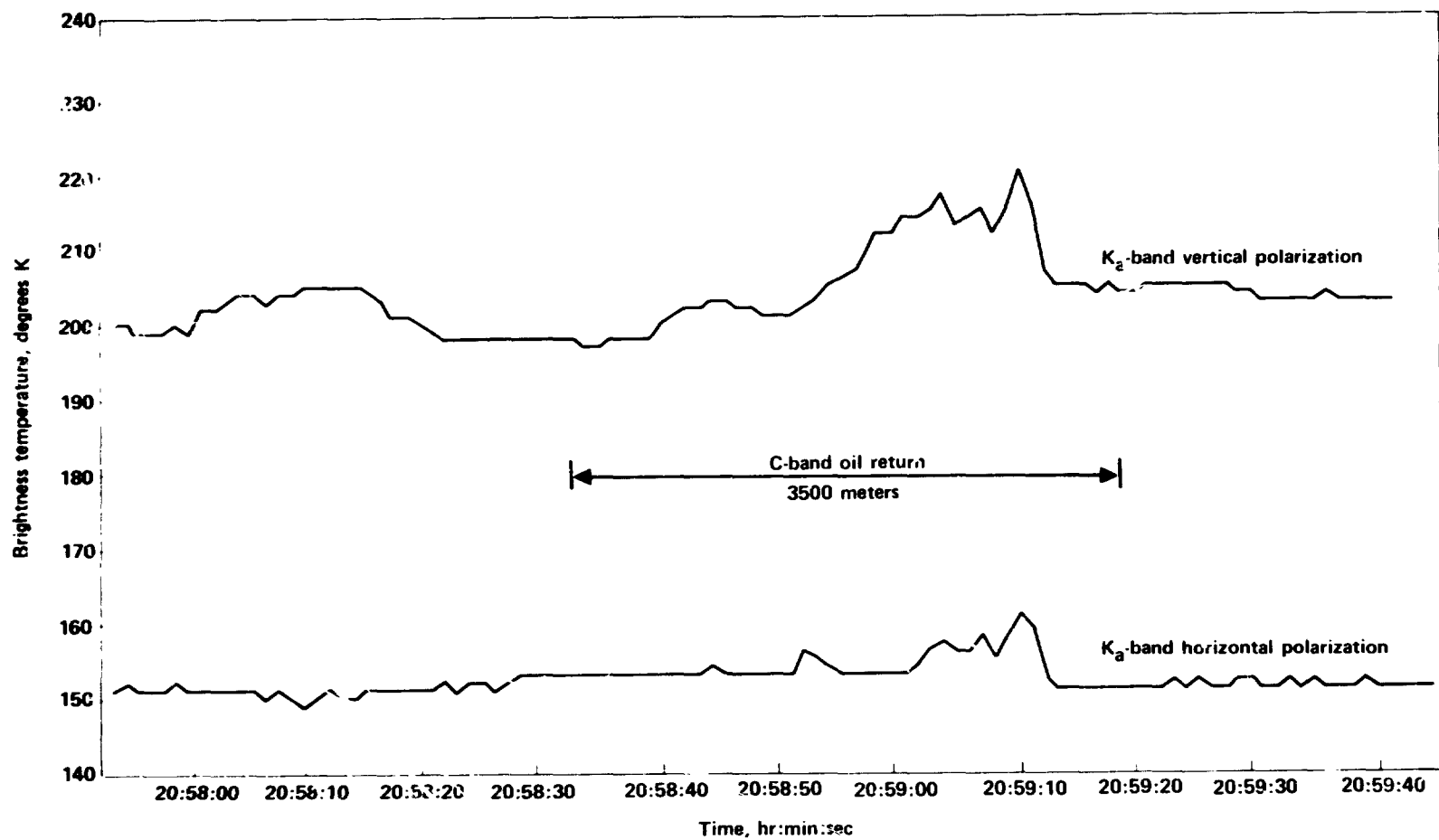
Figure 11.— Time history of K_a-band radiometer brightness temperature, 50° incidence angle, IXTOC I oil spill.
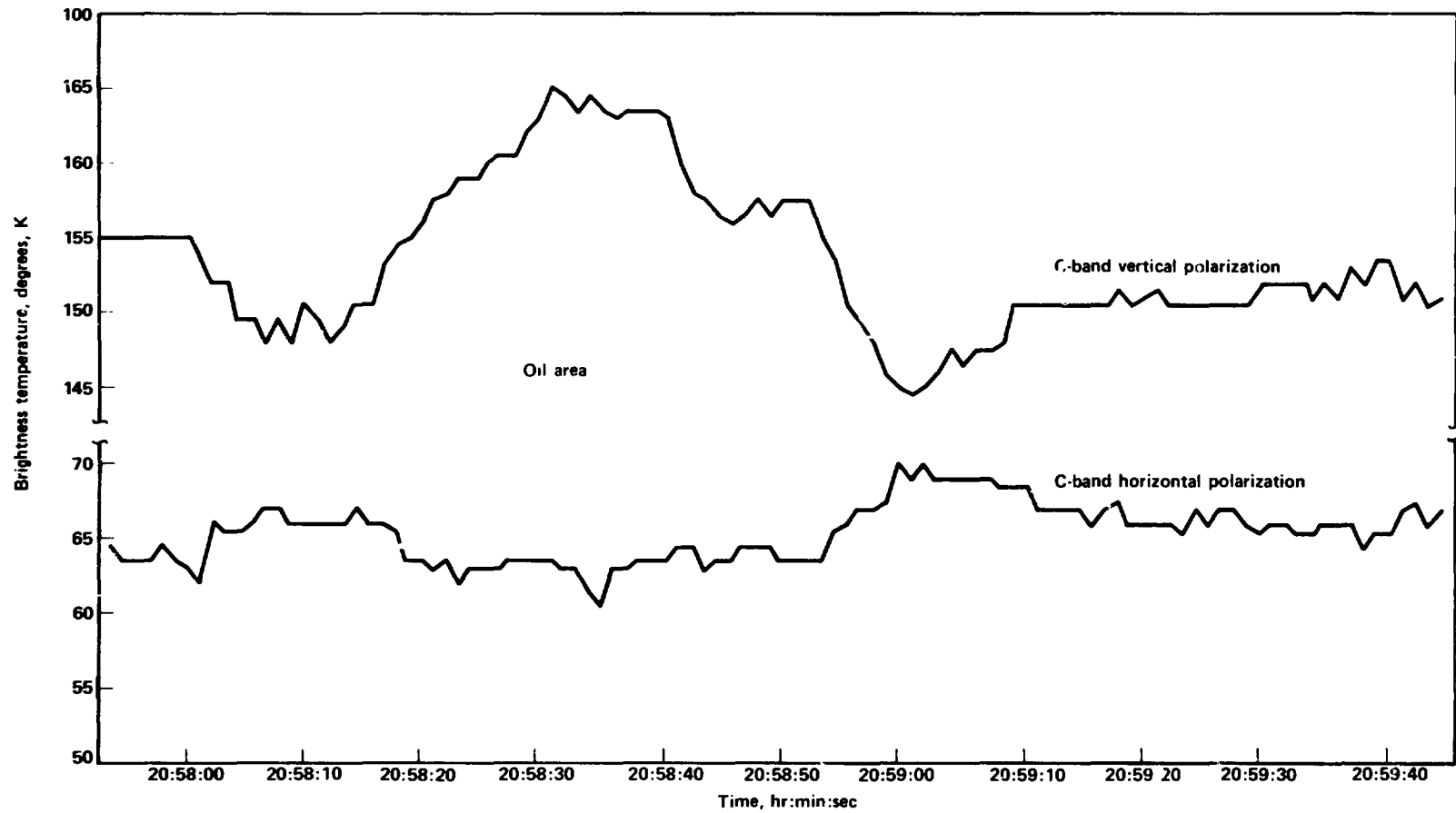
Figure 12.— Time history of C-band radiometer brightness temperature, 50° incidence angle, IXTOC I oil spill.
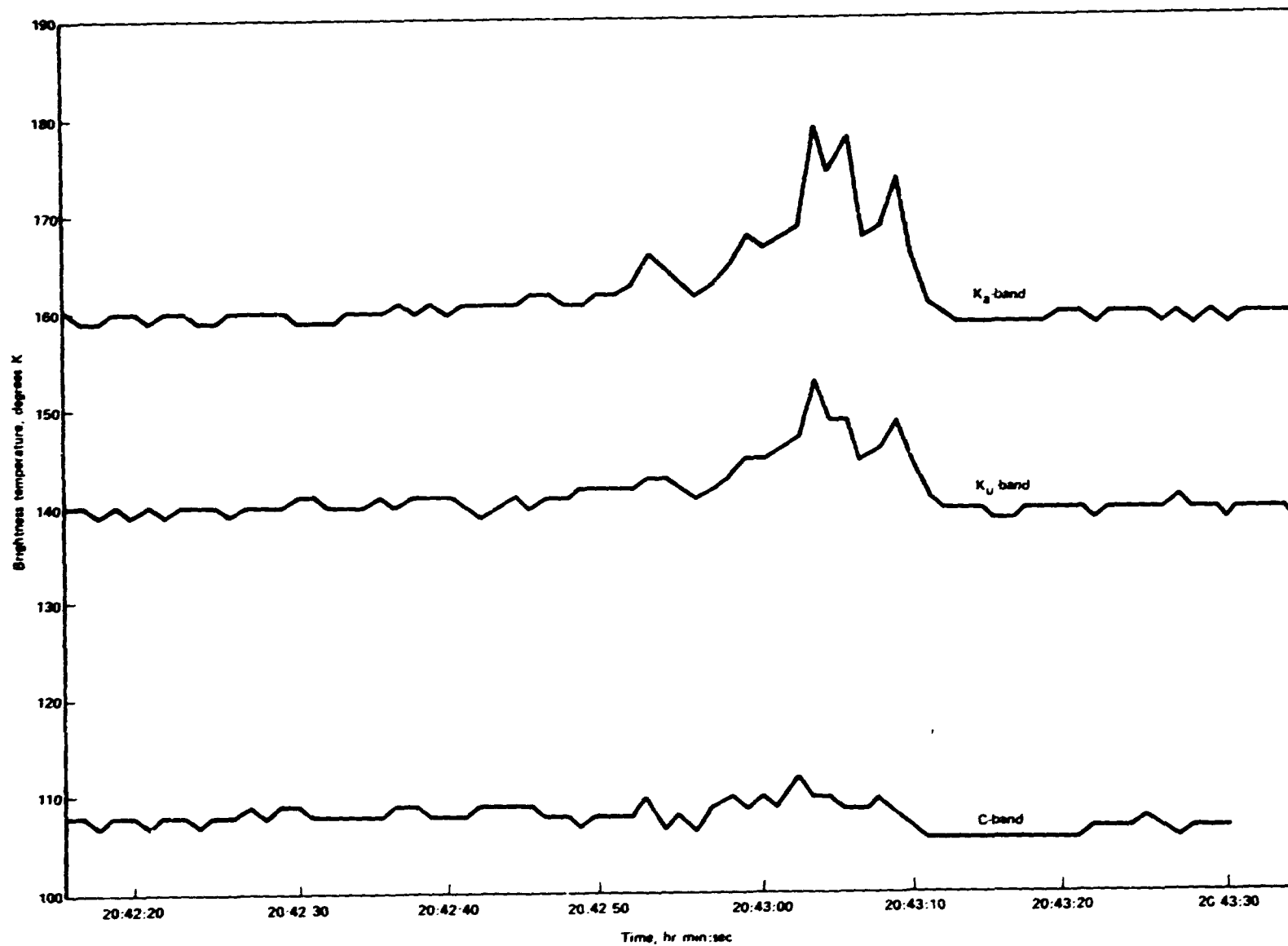
Figure 13.— Time history of C, K_a and K_u band radiometer brightness
temperature, 0° incidence angle, IXTOC I oil spill.
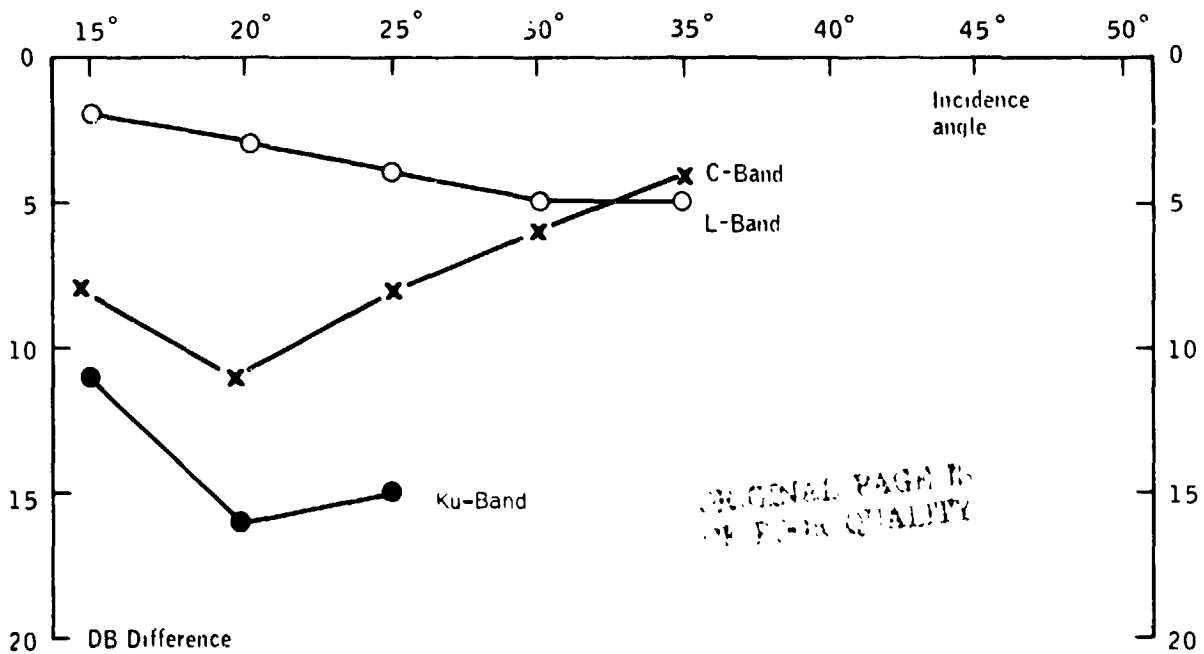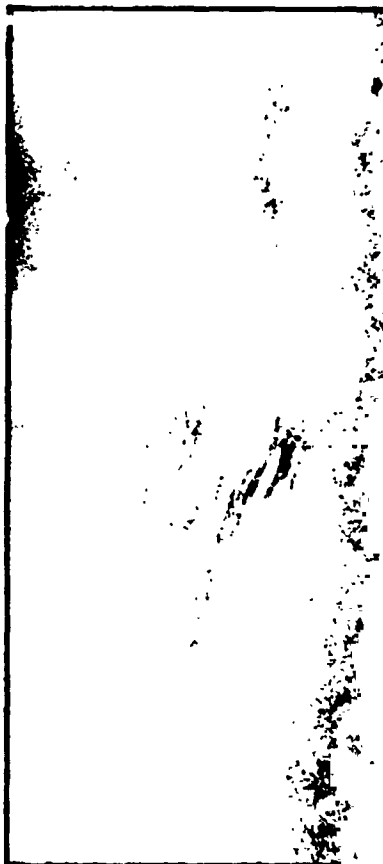
Figure 14.- Comparison of Radar Imagery and Decrease
in Scattering Coefficient Curves.

INTERACTIONS OF SURFACES WITH THE SOLAR PLASMA *

D. McKeown and C.R. Claysmith
Faraday Laboratories, La Jolla, CA

ABSTRACT

The induced environment is the main source of contamination on a spacecraft. The contamination of surfaces by Volatile Condensable Material (VCM) present on spacecraft is being studied by many investigators both in the laboratory and space. In addition to VCM, the space environment can also be a contributing factor in the contamination of surfaces. We have been investigating the effects of the interaction of the solar plasma with surfaces. Plasma particles impact at energies in the multikilovolt range and penetrate and become trapped in surfaces. Results show that protons can penetrate up to 600 monolayers into surfaces and reach saturation concentrations of 6%.

1.0 INTRODUCTION

Many investigators are conducting fundamental studies both in the laboratory[1,2,3] and space[4,5,6] on VCM contamination of surfaces as a function of temperature. Measurements are being made with the Temperature-Controlled Quartz Crystal Microbalance (TQCM) and include qualitative analysis of contaminant species, adsorption and desorption rates, sticking coefficients and changes in optical properties of surfaces. The TQCM[7] was developed in 1973 by Faraday Laboratories for NASA to monitor contamination between -60 and +100°C in space chambers. Recently, we completed construction of an extended temperature range TQCM system for space flight having higher mass sensitivity and ground command of temperature. Operating temperatures are attained either with radiative coolers or thermoelectric devices. The Air Force Materials Laboratory has a radiatively-cooled TQCM in flight on SCATHA[8] that was launched on January 30, 1979. JPL has a thermoelectrically controlled system ready for flight on a NOAA operational environmental satellite[9]. MSFC has both radiatively and thermoelectrically controlled systems awaiting flight on Shuttle[10]. The SCATHA system is shown in Fig. 1. It consists of a controller and two radiatively cooled sensor heads. The sensors are high mass sensitive 15-MHz optically-polished quartz crystals plated with aluminum.

The Principal Investigator for the SCATHA experiment is D.F. Hall. He has reported important data[4] on the measurement of surface contamination enhanced by spacecraft charging in the multikilovolt range[11]. In the

experiment, one TQCM views space. The other periodically views space and the sun at 1 rpm. Data from the sun viewing TQCM is significantly different from the TQCM pointed into space. The mass accumulation rate of the sun viewing TQCM is relatively insensitive to sensor temperatures between -34 and +58°C. The space viewing TQCM temperature showed mass accumulation only for temperatures below -30°C and mass desorption at higher temperatures. The most probable reason for the difference is solar UV radiation modifying the contamination and increasing its de- sorption energy[4]. Another effect that is independent of temperature and results in mass accumulation is the penetration and trapping of solar plasma into the aluminum surface plated onto the TQCM. We have been in- vestigating in the laboratory the effects impacts of protons and alpha particles present in the solar plasma have on surfaces.

2.0 LABORATORY MEASUREMENTS

A photograph of the plasma generator used for the measurements is shown in Fig. 2. A plasma is generated by first creating a narrow-energy ion beam. Gas is fed into a flat cylindrical chamber with circular aper- tures on the axis. Electrons from a filament are made to spiral along this axis by an axially directed magnetic field generated by a solenoid. The spiraling electrons collide with the neutral atoms to produce ioniza- tion. The ions are extracted from the chamber (anode), pass through the focusing system, a series of metal tubes separated with ceramic insula- tors, and accelerate towards the target (cathode). The target is an alu- minum plated 20 MHz quartz crystal for measuring mass gain or loss during bombardment. A 20 MHz crystal was used because of its high-mass sensi- tivity of $8.78 \times 10^{-10} g/cm^2 Hz$ needed to facilitate the measurements. The ion impact energy is controlled by varying the target potential.

Beam fluxes of about 10^{14} ions per second per cm^2 are easily ob- tained with any gas using this beam generator. In our experiments, only noble gas atoms were chosen as bombarding ions for the following reasons. Monatomic beams of singly charged ions of noble gases can readily be formed without mass analysis. They are available in pure quantities. The range of atomic number and weight of these gases is more than adequate for these investigations. They are inert so that reactions with surfaces are minimized. The generator is operated in a VacIon pumped chamber.

The effects of bombarding Al with 0.35 mA He^+ at 2.5 keV is shown in Fig. 3. During the first 35 min of impact the target increases in mass because the mass of He^+ trapped in the surface was greater than the mass of Al eroded by sputtering. For the next 15 min, the mass gained and lost is about equal, and the net mass change is approximately zero. After 50 min, the target became saturated with He. The mass loss rate is then equal to the sputtering yield of aluminum in He^+.

3.0 ION-SURFACE INTERACTIONS

3.1 Surface Mass Loading

The penetration and trapping of ions in a solid surface shown in Fig. 3 can be described by the mass rate of change per unit area,

dM/dt, of a target under bombardment.

$$dM/dt = \alpha m_1 i - \beta(t) m_1 - \mu m_2 i \qquad (1)$$

The absorption coefficient, α, is the fraction of incident particles that penetrate and become trapped in the target. The beam flux is i in ions/cm^2-s. The mass of the bombarding ion and of a target atom are, respectively, m_1 and m_2. The re-emission coefficient, $\beta(t)$ is the number of trapped particles re-emitted as succeeding layers of target atoms are sputtered. The sputtering yield, μ, is the number of target atoms ejected per incident ion. At $t = 0$, $\beta(t) = 0$, and as t becomes large, $\beta(t) \rightarrow \alpha i$. Once $\beta(t) = \alpha i$, the target will lose mass at a constant rate due to sputtering.

3.2 Ion Penetration into Surfaces

To penetrate beyond the first layer of atoms of a solid the inequality

$$\sigma n^{2/3} \geq 1 \qquad (2)$$

must hold, otherwise the particle will probably be reflected. The atomic number density of the solid is n, and $n^{2/3}$ represents the area number density seen by the incident particle with a total binary cross section, σ. This inequality is satisfied for protons and alpha particles in the solar plasma.

Although the cross sections at these low energies are not known accurately, Bohr[12] has shown a reasonable cross section to be

$$\sigma \approx \frac{2\pi a_0^2 E_R}{2.72} \frac{Z_1 Z_2}{(Z_1^{2/3} + Z_2^{2/3})^{1/2}} \frac{m_1 + m_2}{m_2} \frac{1}{E_1} \qquad (3)$$

which is replaced by

$$\sigma = \pi R^2 \qquad (4)$$

whenever $\sigma \gg \pi a_0^2 / (Z_1^{2/3} + Z_2^{2/3})$. At the lowest energies the binary collision cross section approaches the gas kinetic value. R is the distance of closest approach obtained as the solution of

$$R m_2 E / (m_1 + m_2) = 2 Z_1 Z_2 E_R a_0 \exp [-R(Z_1^{2/3} + Z_2^{2/3})^{1/2} / a_0] \qquad (5)$$

Subscripts 1 and 2 designate incident and target particles, respectively, with E the kinetic energy, m the mass, Z the atomic number, a_0 the Bohr radius and E_R the Tydberg energy.

To obtain the distribution of the penetrating ions it is necessary to consider their motion in the solid. Although the ions are probably neutralized upon entering the solid this is expected to be of no consequency since hard sphere type collisions are assumed to occur. For protons and alpha particles, $m_2/m_1 > 1$, large angle scattering occurs at each collision giving an erratic rectilinear path which resembles a diffusion process. In fact, the slowing down process is treated like that of neutrons where the particle slowing down density for a plane flux i is

$$q = \frac{i}{(4\pi R)^{1/2}} e^{\frac{-x^2}{4R}} \qquad (6)$$

where R is the "Fermi age." The density q represents the number of particles per cm^3 per second that slow down past an energy F at a given depth x in the solid. If $m_2/m_1 > 1$ the angular deflection of the incident particle from its direction of travel is small and the particle straggles about the penetration depth with an approximate Gaussian distribution.

Because the notion of range is complex, it is customary to define a linear, a vector and a projected range. The linear range is the total rectilinear path traversed by the particle to the point of stopping while the vector range is the vector distance from point of entry into the solid to the end point. Projection of the vector distance along a line normal to the surface gives the projected range. An approximate relation between the average linear range $[R_L]$ and the average projected range $[R_p]$ (or mean range) was developed by Linhard and Scharff[13] as

$$[R_L] \approx [R_p] \left(1 + \frac{1}{3}\frac{m_2}{m_1}\right) \qquad (7)$$

for an inverse square potential. For $m_2/m_1 \leq 1$, approximation (7) is quite accurate but, for $m_2/m_1 > 1$ the approximation has application to a portion of the low energy region only.

Scattering near the end point of the particle travel is probably a many-body collision problem and not the binary one assumed to obtain the distributions discussed in the previous section. If relation (2) is used as a necessary criterion for halting the motion of the incident particle, the cross section must be about the gas kinetic value,

$\sigma \approx 5 \times 10^{-16} \mathrm{cm}^2$; cross sections of these magnitudes correspond to energies the de Brolie wave length is comparable to the lattice separation indicating that more than one target atom contributes to a collision.

Andersen and Sigmund[14] have presented a model for non-binary scattering which is of importance at much higher energies than indicated by (2). It recognized the fact that, with such small mean free paths, correlations between successive collisions cannot be neglected in the low energy region. The model assumed involves a set of crystal lattice rows which are resolved into stacked symmetric rings of atoms. The incident particle moves along the symmetry axis of these rings with the projectile-ring interaction as the basic event with the ring presenting an effective potential field to the incident atom.

If the incident particle is aligned along the symmetry axis, close collisions become improbable because the field keeps the particle near the symmetry axis to produce channeling. For the interpretation of penetration distributions known in the literature as "supertails" it is important to investigate the low energy collisions to determine the density of vacancies, interstitials and self-interstitials created. From this, estimates of further projectile penetration by diffusion after the slowing down process can be made. Using a Born-Mayer potential for each lattice atom, a new reflecting (or stopping) energy replaces the one determined through (2) and is found to be

$$R_{refl} \approx p \ Ae^{-L/a} \qquad (8)$$

whenever $m_1 \gg m_2$. Constants p and L define the number of particles in the ring and radious of the ring element; A and a are the potential parameters. Reflection energies given by (8) are somewhat higher than that found through (2); for alpha particles in heavy materials, typical estimates are 5·10 eV.

3.3 Diffusion of Trapped Particles

Channeling explains the penetration to ranges of a few microns for particles in the keV range but "supertails" extend to depths of several microns. A possible explanation to these deep penetrations is the steady state diffusion approach of Sparks[15]. He assumes the diffusion of vacancies and self-interstitials created by the incident particles is unaffected by the relatively small number of implanted ions. With the bombarding particles forming substitutionals through the annihilation of vacancies two general forms of the integral penetration distributions, $n_s(x)$, result which may be expressed as

$$n_s(x) \approx \exp[-k(x-1)] \ ; \ x > 1 \qquad (9)$$

and

$$n_s(x) \approx \frac{d^{2+r}}{(x - 1 + d)^{2+r}} \; ; \; x > 1 \; . \tag{10}$$

The constant d depends upon the vacancy density interstitial density and the diffusion coefficient; 1 is located approximately at the edge of the stopping region. Distribution (10) normally occurs if vacancies and self-interstitials are created and annihilated in pairs. For distribution (9) to obtain the vacancies, the self-interstitials must be created at different rates which means that most of the interstitials must be of the bombarding particle type.

4.0 ION-BOMBARDMENT OF ALUMINUM

Laboratory measurements were made on aluminum to determine the effect the ions present in the solar plasma have on low atomic weight surfaces. The main constituents of the plasma are proton and alpha particles[16] having energies in the multikilovolt range. Heavier ions, such as iron, were not considered because their densities are too low to produce measurable effects.

Once the protons penetrate the surface, little will diffuse out because of the affinity of aluminum for hydrogen[17]. Any alpha particles that penetrate the surface will readily diffuse out because of the inert nature of helium. The principle effect of alpha impacts will be that of sputtering the surface.

To determine the saturation concentration of protons for aluminum, the distribution function q given by (6) can be used. The distribution is for the case $m_1 > m_2$. It has a maximum near the surface because of large angle scattering that occurs for the case in which the incident particle mass m_1 is less than the target atom mass m_2.

The mean penetration depth $[R_p]$ of the particles needed to scale the distribution function can be found from the $\rho - \epsilon$ relationship of Lindhard and Scharff,[18] which relates the range-energy of particles in solids:

$$\rho = R_m(1 - \frac{A_2}{3A_1}) \; \frac{166}{(z_1^{2/3} + z_2^{2/3})} \; \frac{A_1}{(A_1 + A_2)^2} \tag{11}$$

$$\epsilon = \frac{33}{z_1 z_2 (z_1^{2/3} + z_2^{2/3})^{1/2}} \; \frac{A_2}{A_1 + A_2} \; F_1 \tag{12}$$

where the subscripts 1 and 2 refer to the incident ion and the target atom, and E_1 is the energy of impact in keV.

Davie's group has shown that the ρ - ϵ relationship is accurate to about 20% for $\epsilon < 10$. Values for ρ, knowing ϵ, have been plotted by them for $0 < \epsilon < 10$ and $0 < \rho < 100$.[19]

The absorption coefficient α was found, experimentally, to be about 0.01.

The velocity ν at which the surface is sputtered was calculated using a yield, for Al in He$^+$ is the same as that for He^{++} (alpha particles). Experimentally, the yield for He$^+$ at 8 keV was found to be 0.3. The average erosion velocity of Al using these yields for He$^+$ and He^{++} is $\nu \approx 10^{-8}$cm/hr. By assuming that diffusion is zero, the saturation concentration of trapped hydrogen in aluminum was found.

The saturation distribution of hydrogen in aluminum, in hydrogen atoms per aluminum atom N_H/N_{Al}, is shown in Fig. 4.

5.0 CONCLUSIONS

A spacecraft traveling beyond the magnetosphere passes into the tenuous upper atmosphere of the sun known as the solar plasma. The plasma is composed mainly of electrons, protons, and alpha particles. Protons and alpha particles will impact at energies ranging up to 10 keV during periods of a quiet run and approximately 20 keV during solar activity.[16]

Low atomic weight metal surfaces will be damaged by the penetration and trapping of protons. Surface properties would be affected by the formation of hydrides in concentrations approaching 6%. It will take several years before surface properties would be significantly affected because of the low density of protons in the solar plasma. Damage would be accelerated during solar activity and for spacecraft passing near the sun.

Effects on nonconducting materials such as plastics, which are composed of large amounts of hydrogen, will be more pronounced because most of the plasma will be absorbed. For these materials, changes would become apparent in a few years. The protons and alpha particles that penetrated these surfaces will displace surface atoms. It takes about 25 eV to displace an atom from its lattice point[20]. In a year the plasma will produce about 10^{17} atomic displacements. In surface coatings, the displacements will produce discoloration through the creation of color centers and effect the solar absorptance.

6.0 REFERENCES

1. Muscari, J.A., and Jacobs, S., "Silver-Teflon Contamination UV Radiation Study", Proceedings USAF/NASA International Spacecraft Contamination Conference, AFML-TR-78-190, NASA-CD-2039 (1978) pp. 1112 - 1127.

2. Richmond, R.G. and Kelso, R.M., Effectiveness of Shuttle Orbiter Payload Bay Liner as a Barrier to Molecular Contamination from Hydraulic Fluids", Proceedings USAF/NASA International Spacecraft Contamination Conference, AFML-TR-78-190, NASA-CD-2039 (1978) pp. 846 - 862.

3. Visentine, J.T., Richmond, R.G., and Kelso, R.M., "Experiment to Measure Molecular Outgassing Rates from Shuttle Orbiter Flexible Reusable Surface Insulation (FRSI)", Progress in Astronautics and Aeronautics, Vol. 56, AIAA (1977) pp. 197 - 213.

4. Hall, D.F., "Flight Experiment to Measure Contamination Enhancement by Spacecraft Charging", Proceedings SPIE Conference, North Hollywood, CA (1980) Vol. 216 - 15.

5. Miller, F.R., "Shuttle Induced Environment Contamination Monitor", Proceedings USAF/NASA International Spacecraft Contamination Conference, AFML-TR-78-190, NASA-CD-2039 (1978) pp. 534 - 566.

6. Lynch, J.T., "Quartz Crystal Microbalance (QCM) Monitor of Contamination for LES-8/9", 9th Space Simulation Conference, NASA CP-2007 (1977) pp. 211 - 219.

7. McKeown, D., Corbin, W.E. Jr. and Naumann, R.J., "Thermoelectrically Cooled Quartz Crystal Microbalance", 7th Conference on Space Simulation, NASA SP-336 (1973) pp. 345 - 358.

8. McKeown, D., Claysmith, C.R., Breckenridge, W.T. Jr., Dummer, R.S., "Temperature Controlled Quartz Crystal Microbalance System", Report AFML-TR-77-83, AFML/MBE, Wright-Patterson AFB, OH (1977).

9. Maag, C.R., "NOAA-B Contamination Monitoring Instrumentation", Proceedings SPIE Conference, North Hollywood, CA (1980) Vol. 216 - 15.

10. McKeown, D. and Claysmith, C.R., "Quartz Crystal Microbalance Systems for Shuttle Contamination Measurements", Proceedings USAF/NASA International Spacecraft Contamination Conference, AFML-TR-78-190, NASA-CD-2039 (1978) pp. 605 - 629.

11. Kuch, G.A. and Holaday, B.H., "A Description of the Space Test Program P78-2 Spacecraft and Payloads" Report SAMSO TR-78-24 (1978).

12. Bohr, N., Penetration of Atomic Particles Through Matter, Det. Kgl. Dan. Vidensk, Selsk., Mat. - Frs. Medd., (1948).

13. Linhard, J., Scharff, M., and Schiott, H.E., Range Concepts and Heavy Ion Ranges, Dt. Kgl. Dan. Vidensk. Selsk., Mat. - Fys. Medd., Vol. 33, No. 14 (1963), pp. 643 - 721.

14. Andersen, H.H., and Sigmund, P., "Simple Non-Binary Scattering Model Applicable to Atomic Collisions and Crystals at Low Energies", Dt. Kgl. Dan. Vidensk. Selsk., Mat. - Fys. Medd., Vol. 4 (1966), pp. 723 - 752.

15. Sparks, M., "Theory of Supertails of Ions Bombarded into Crystals", Phys. Rev. Letters, Vol. 17, (1966), pp. 1247 - 1249.

16. Freeman, J.W., Van Allen, J.A., and Cahil, L.J., "Explorer 12 Observations of the Magnetospheric Boundary and the Associated Solar Plasma on Sept. 13, 1961", Beophys. Res., 68, (1963), pp. 2121 - 2130.

17. Bergstrom, I., Brown, F., Davies, J.A., Geiger, J.S., Graham, R.L., and Kelly, R., "On the Electromagnetic Separation Method of Preparing Radioactive Sources for Precision β - Spectroscopy", Nucl. Instr. Methods, 21, 249 (1963), pp. 249 - 261.

18. Lindhard, J., and Scharff, "Energy Dissipation by Ions in the keV Region", Phys. Rev., 124 (1961), pp. 124 - 132.

19. Davies, J.A., McIntyre, J.D., and Sims, G., "The Range of C^{137} Ions of keV Energies in Germanium", Can. Jour. Chem., 40, (1962), pp. 1605 - 1621.

20. Seitz, F., and Koehler, J.S., "Displacement of Atoms During Irradiation", Solid State Physics, (Academic Press, New York, 1956), pp. 307 - 448.
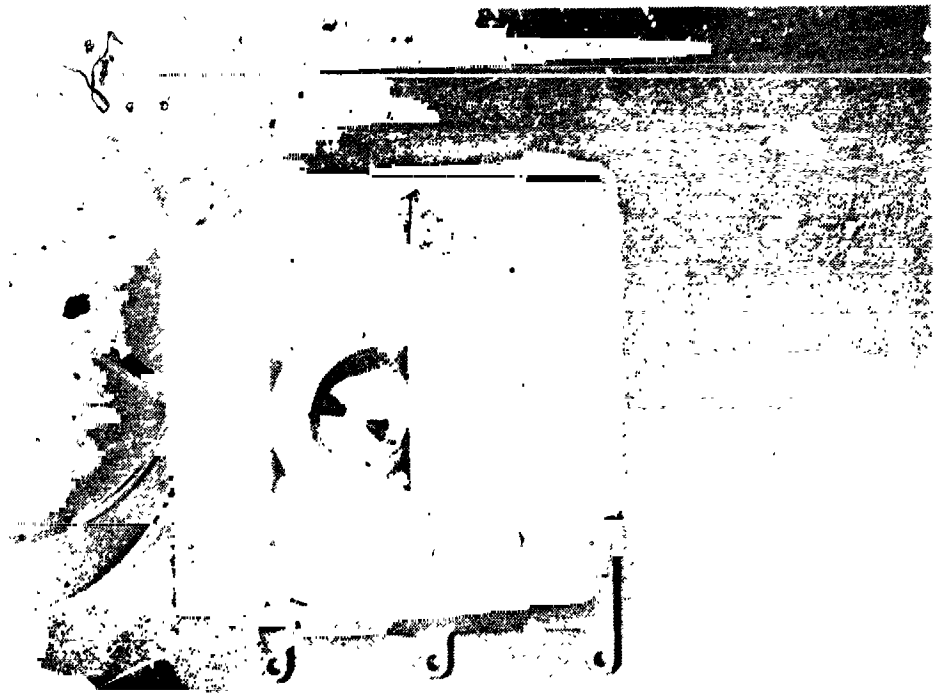
Fig. 1   SCATHA TQCM System without RPA Installed

197
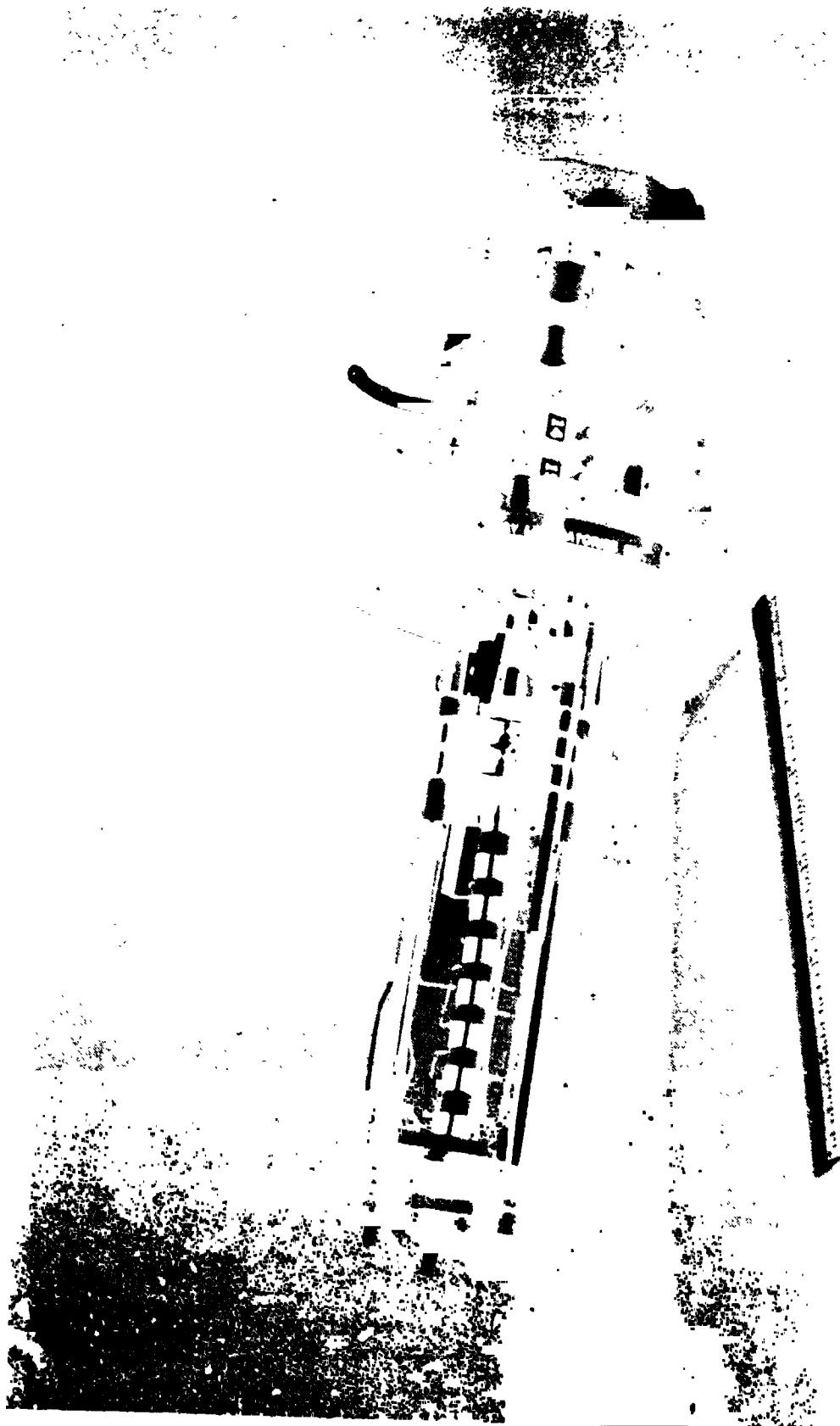
Fig. 2   Plasma Generator
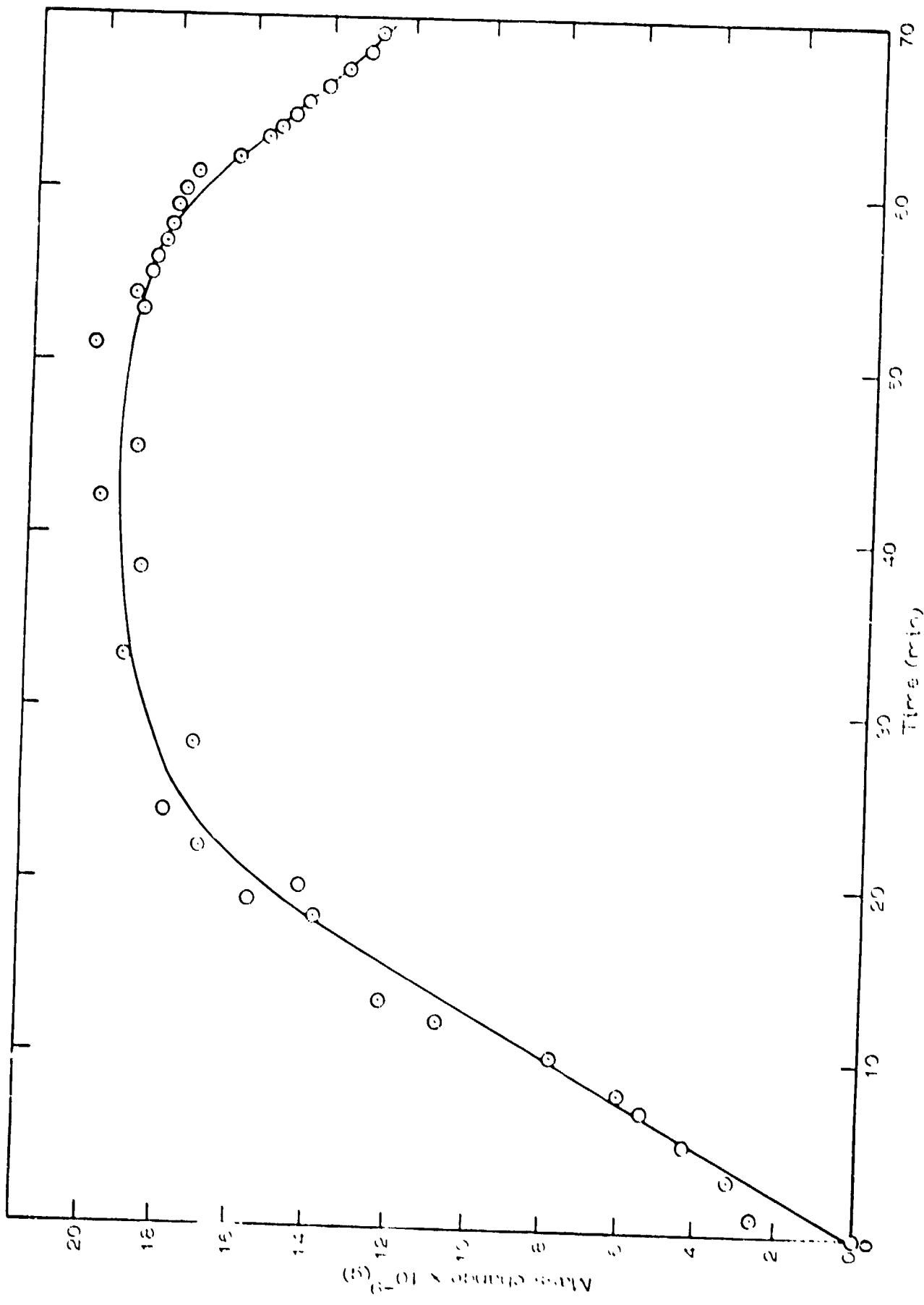
Fig. 3 Mass change of Al target under He$^+$ bombardment at 2.5 keV
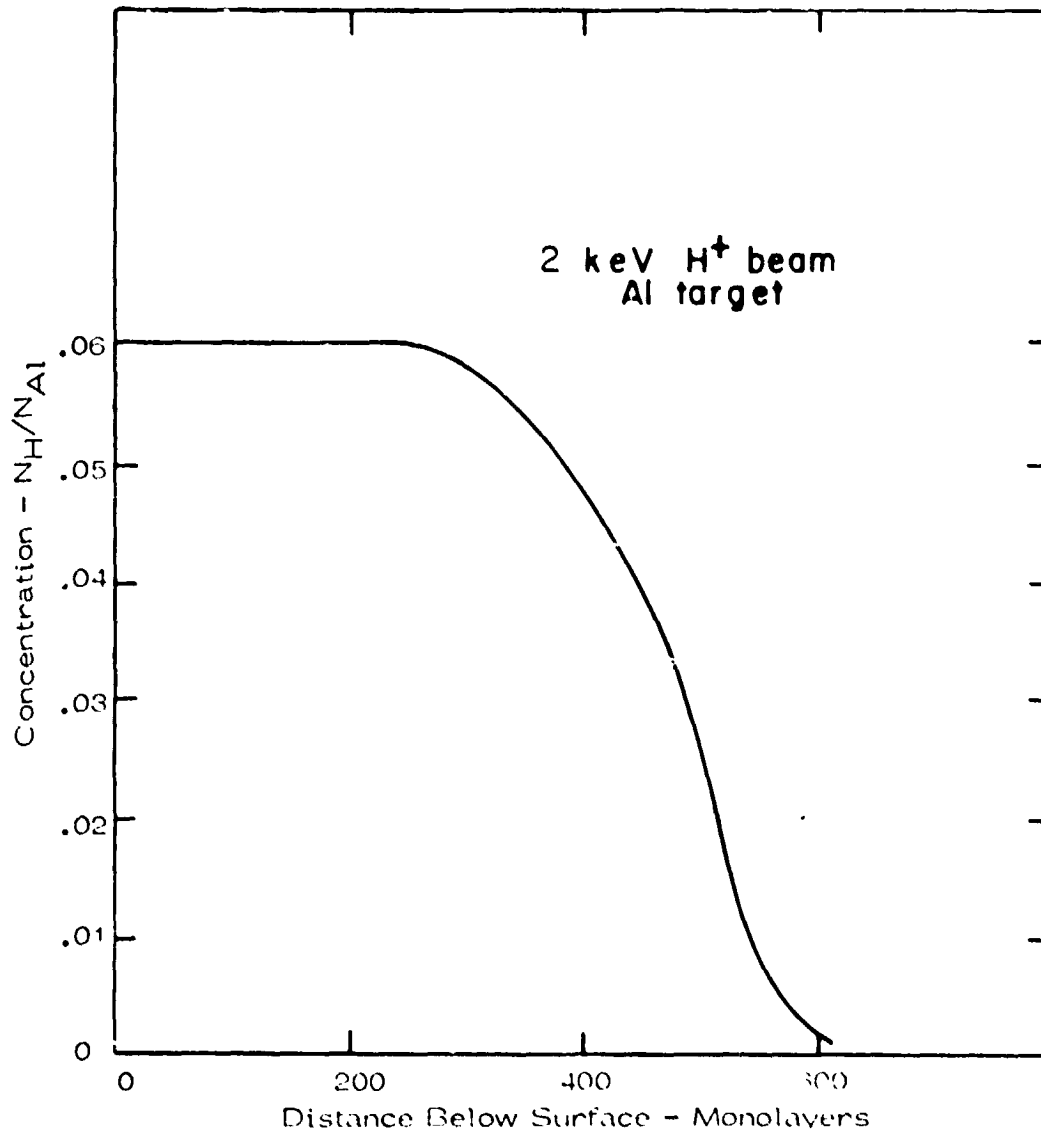
Fig. 4   Saturation concentration of hydrogen in aluminum

STS-1 MISSION CONTAMINATION EVALUATION APPROACH

Stephen Jacobs,* Dr. Horst Ehlers,* and Edgar R. Miller**

ABSTRACT

The Space Transportation System 1 mission will be the first opportunity to assess the induced environment of the Orbiter payload bay region. Two tools have been developed to aid in this assessment. The Shuttle Payload Contamination Evaluation computer program has been developed to provide an analytical tool for prediction of the induced molecular contamination environment of the Space Shuttle Orbiter during its onorbit operations. An Induced Environment Contamination Monitor has been constructed and tested to measure the Space Shuttle Orbiter contamination environment inside the payload bay during ascent and descent and inside and outside the payload bay during the onorbit phase. Measurements will be performed during the four Orbital Flight Test series. Measurements planned for the first flight have been described and predicted environmental data have been discussed in detail. The results indicate that the expected data are within the measurement range of the Induced Environment Contamination Monitor instruments evaluated for this paper, and therefore it is expected that useful contamination environmental data will be available after the first flight.

INTRODUCTION

Several aspects of the upcoming Space Transportation System 1 (STS-1) mission, which will be the initial launch, onorbit, and entry exposure of the Space Shuttle Orbiter to the space environment, are important to consider from a payload exposure standpoint. The Space Shuttle system was developed with the objective of providing a minimal contamination environment together with a versatile Earth-orbital payload delivery system and experimentation base. Many payloads already determined and many being considered for Shuttle-based operations are very sensitive to spacecraft-induced environmental contaminants. In addition, the multiple-reuse capability of the Space Shuttle necessitates unique considerations for payloads.

The induced environment of the Orbiter payload bay will be assessed for the STS-1 mission. Specific plans developed for the STS-1 mission are based on a multiphase approach philosophy that consists of (1) development of the contamination math model, (2) development of the contamination measurement instrumentation, (3) prediction of contamination, (4) measurement of contamination, (5) correlation of predictions and measurements, (6) update of the modeling process, and (7) application of the updated model to predict the induced contamination environment of future missions.

----

*NASA Lyndon B. Johnson Space Center, Houston, Texas.
**NASA Marshall Space Flight Center, Huntsville, Alabama.

This paper describes the contamination math model used in making preflight predictions and discusses predictions made for STS-1, describes the instrumentation that will be used in performing contamination measurements, and outlines the method for correlating predictions and measurements to assess overall mission contamination.

CONTAMINATION MODEL

Model Background

The Shuttle Payload Contamination Evaluation (SPACE) computer program was developed to provide an analytical tool with which to predict the external induced molecular contaminant environment of the Space Shuttle Orbiter during onorbit operations. It has been developed over a period of several years at Martin Marietta Aerospace, Denver Division, under contract to the NASA Lyndon B. Johnson Space Center (JSC). The SPACE program mathematically synthesizes the induced environment for the six major contaminant sources: (1) nonmetallic materials outgassing (i.e., the long-term bulk mass loss of material upon exposure to space vacuum), (2) early desorption from external surfaces (i.e., the initial high mass loss of absorbed and adsorbed volatiles, gases and liquids), (3) cabin atmosphere leakage from pressurized crew compartments, (4) two supplemental flash evaporator vent effluents, (5) thirty-eight 3.9-kilonewton (870-pound) reaction control system (RCS) thrusters, and (6) six C.1-kilonewton (25-pound) vernier control system (VCS) thrusters. Other sources can be easily added to the model.[1,2] The SPACE program predicts surface deposition and return flux (RF) on surfaces with up to 2π-steradian field-of-view molecular densities, and molecular number column densities (NCD) (which is the integrated density along a line of sight to infinity) for 17 lines of sight. Included in the model are a definition of Orbiter geometry (approximately 300 nodes); viewfactors between modeled surfaces and points along the 17 lines of sight; Orbiter source characteristics such as mass loss/emission rates, time and temperature dependence, and sticking coefficient; and effects such as surface reflection/re-emission, return flux/ambient scattering, return flux/ self-scattering and surface deposition.

Updating and Modeling for STS-1

The SPACE program has been updated in several areas to increase its capability for contamination assessment of STS-1. The first of these changes has encompassed surface contamination exchange in the payload bay; this update ultimately has taken the form of an "unlimited surface" multireflection capability with an approximate step solution. The model has also been updated to increase data handling and presentation; this update includes additions to the number of lines of sight from 17 to 25 in the far field as well as modification of the point matrix to include 50 lines of sight with 1.0 meter resolution in the near vicinity (<16 meters) of the Shuttle Orbiter. A special program has also been incorporated into SPACE to provide a variety of plotting capabilities.

In addition, the SPACE computer program has encompassed the modeling of the STS-1 configuration in the Orbiter payload bay, including the Induced Environment Contamination Monitor (IECM), the instrument package used to measure the contamination environment. Figure 1 shows the geometric modeling of the STS-1 payload configuration. This configuration is made up of the three development flight instrumentation (DFI) packages and the IECM package, which includes the quartz crystal microbalances (QCM's) and the mass spectrometer (MS) to be used for the STS-1 mission analysis. These instruments and others on the IECM will be discussed in more detail.

CONTAMINATION MEASUREMENT INSTRUMENTS

IECM System and Instruments

In this section, the IECM system and instruments are reviewed in outline form and the associated STS-1 operations are discussed. The IECM (fig. 2) is a self-contained (with the exception of Orbiter power and one astronaut-operated switch) minimum-interface payload. The instrument weighs 360 kilograms and is 124 centimeters long, 190 centimeters wide, and 79 centimeters high, corresponding to Orbiter X, Y, and Z axes, respectively. The extruded aluminum framework houses 10 STS-1 instruments, the data system, the tape recorder, the power distributor, the voltage regulator, and the batteries.

Thermal control of the IECM will be accomplished through a combination of passive and active means. The surfaces of the IECM will be passively cooled through radiation exchange from the 3/8-inch-thick aluminum baseplate and the aluminum side and bottom baffles. External panels are coated with S-13g LO. Ten 28-V dc electrical heaters are used to maintain thermal control during the cold case. Table I gives the physical and performance characteristics of the IECM instruments. In addition to standard instrument calibration, a special calibration using typical STS materials is being performed for the mass spectrometer at the University of Michigan, Space Physics Research Laboratories. The response of the IECM mass spectrometer to the outgassing of these materials will be compared to that of a laboratory mass spectrometer.

Each instrument and component was qualified and tested under vacuum conditions, individually and again with the system in the final configuration. The major system qualification tests consisted of temperature cycling, vibration, electromagnetic interference, thermal vacuum, and outgassing. Worst-case thermal vacuum testing was performed during September 1979 to confirm the thermal design. Included in these tests were hot-case onorbit, cold-case onorbit, and hot-case descent and postlanding. The IECM performed well during these tests after initial minor problems were corrected, without exceeding design temperature limits on critical components (i.e., batteries, data acquisition and control system, voltage regulator, and power distributor) or on the scientific instruments.

The IECM was designed to monitor payload-bay contamination at its location in the cargo bay during all phases of the STS-1 mission, including ground operations. The IECM will be operational before the STS-1 mission in the Orbiter Processing Facility (OPF) after final "cleanup" of the payload bay and before payload bay door closure. At least two sets of measurements will be made on the launch pad to obtain the integrated environmental effects of the Orbiter transfer from the OPF to the Vertical Assembly Building (VAB) and to the launch pad as well as to obtain environmental data on the pad facility itself. Other useful data will be taken by the IECM during this time frame coincidental with other checkouts and tests.

Ascent measurements begin with the IECM launch mode signal, which turns on the cascade impactor, the dewpoint hygrometer, the humidity monitor and the air sampler. Ascent measurements end with the onorbit signal to the IECM, at which time the onorbit-phase measurements begin. For the STS-1 mission, the mass spectrometer will scan from 1 to 150 amu (atomic mass units) in 300 seconds and then remain for an equal time period (300 seconds) on the water peak (18 amu). This operational mode was selected because of the importance of water as a potential contaminant. This cycle is repeated for the duration of the onorbit phase (more than 200 spectra). See figure 3.

The onorbit signal also begins the preprogramed temperature-controlled quartz crystal microbalance (TQCM) temperature cycling routine designed to obtain information on mass condensation at temperatures of 303, 273, 243, and 213 K (30°, 0°, -30°, and -60° C) for 90 minutes at each temperature with a 353 K (80° C) 30-minute cleanup cycle between each successive setting. At the end of the 213 K (-60° C) setting, the TQCM's are driven to 243, 273, and 303 K (-30°, 0°, and 30° C) at 30-minute intervals to measure discrete evaporation of condensed materials. The cycle is then repeated throughout the mission. Figure 4 shows one cycle of the TQCM temperature sequence.

In preparation for descent before payload bay door closure, the astronaut actuates the mass spectrometer switch, which turns the instrument off and mechanically seals the unit against repressurization. Upon receipt of the deorbit command, the IECM turns off the camera photometers and turns on the cascade impactor, dewpoint hygrometer, humidity monitor, and air sampler. The air pumps for the latter instruments are turned on at about an 18-kilometer altitude by timing from the deorbit signal.

This paper has, by design, been limited to discussing primarily the mass spectrometer and the QCM's. The other instrumentation is discussed in more detail in references 3 and 4. In addition, the IECM instruments previously mentioned and the operation of the IECM after landing are discussed. (The IECM continues to operate in the descent mode for about 1 hour after landing to obtain data on the postlanding environment.) Reference 4 also contains a discussion of the IECM systems and thermal design.

References 5 and 6 concern the TQCM, the cryogenic quartz crystal microbalance (CQCM), and the mass spectrometer, giving greater detail about these instruments for which the onorbit modeling validation will heavily depend.

CONTAMINATION ASSESSMENT

The SPACE math model (the contamination predictive tool) and the IECM instrumentation (the contamination measurement tool) have been described. In this section, the use of these primary tools to assess the STS-1 contamination levels will be discussed.

STS-1 Mission Conditions

There are various STS-1 parameters and assumptions that have been made for premission contamination predictions. The first series of these can be classified as operational flight requirements[7] and include

1. A 280-kilometer (150-nautical-mile) circular-orbit altitude

2. A launch inclination of between 32° and 42°

3. A 54-hour flight duration

4. A beta (Sun) angle not to exceed 60°

5. Payload bay to earth, which is referred to as Z local vertical (ZLV) and the main (X) axis perpendicular to the orbital plane (POP) except as required for operational or test activities

The STS-1 operational requirements lead to the establishment of certain conditions that have a significant influence on the amount of contamination detected by the IECM instruments.

1. The ambient atmospheric density is assumed to be the "medium" density at a 280-kilometer (150-nautical-mile) altitude. The return flux is due to collisions between induced contamination molecules and ambient environment molecules and is density dependent.

2. During the relatively long periods of ZLV attitude, the Orbiter thermal protection system (TPS) temperatures tend to level out, avoiding temperature extremes. As a result, outgassing rates for exterior surfaces are nominal. Also, Orbiter surfaces do not reach temperatures low enough for H_2O condensation (ice buildup) for any significant period of time; therefore, H_2O is readily reflected.

3. The ambient molecule velocity vector (V) is perpendicular to the Orbiter Z-axis during periods of Orbiter ZLV attitude. This case is of

special interest due to its relatively long duration during the flight.
The case of maximum return flux (V parallel to Orbiter Z-axis) is evaluated
for comparison (worst case).

In addition, there are other parameters that influence the measure-
ment and prediction of contamination levels. For example, IECM instrument
operation, performance, and output depend significantly on the position of
(1) payload bay doors and payload bay vent doors and (2) Orbiter elevon.

Open payload bay door conditions permit unrestricted onorbit instru-
ment operation. However, when the payload bay doors are closed even for a
short period of time, the gas pressure within the bay can rise to an unac-
ceptable level at which the IECM mass spectrometer characteristics are
changed and, possibly, to the point at which the mass spectrometer is dam-
aged. Even though the vent doors will remain open, the mass spectrometer
is not scheduled to be operational until after the early door closings.
The payload bay doors are open during the remainder of the onorbit period
except for the "deorbit rehearsal" period (fig. 3), when they will be
closed preparatory to potential re-entry. Since the vent doors will be
closed during this period, the mass spectrometer will be turned off to
prevent damage. The other IECM instruments will continue to operate in
nominal or orbit mode during this time.

The elevon, as a portion of the wing, contributes to the reflection
of molecules from the RCS/VCS engines and the flash evaporator plume. For
purposes of analytical prediction of the contamination environment for this
flight, the elevon is assumed to be in the nominal position ($0°$ angle).

To complete the definition of the parameters necessary for contamina-
tion predictions, the specific Orbiter sources and contamination measure-
ment instrumentation sensors valid for the STS-1 mission are discussed
briefly.

Table 3 lists the species, the effluent rate, the duration, and the
approximate time line for the major Orbiter contaminant sources of early
desorption, outgassing, cabin atmosphere leakage, the 3.9-kilonewton
(870-pound) RCS engines, the 1-kilonewton (25-pound) VCS engines, the
Orbiter maneuvering system (OMS) engines, and the primary water sources
(the flash evaporator vents, the potable (supply) water dump, and the
waste water dump).

The contamination measurement capability on the STS-1 consists of the
IECM mounted in the payload bay, as previously mentioned. The instruments
on the "top" surface of the IECM (fig. 2) are pointing in the Orbiter +Z
direction, which will be called line of sight one (LOS1). Depending on
the field of view, these instruments (except for the two camera photom-
eters) receive little or no direct contamination from the Orbiter and,
because of their location, are only exposed to what is referred to as
return flux. This flux results from collisions with other contamination
molecules/particles (self-scattering) or collisions with ambient molecules
(ambient scattering). The mass spectrometer, with its limited field of
view ($10°$ optimum), is operated at "low" bit rate and, as a result, cycles
through its mass range in about 10 minutes. The TQCM temperature varies
according to a 10-hour cycle (fig. 4). Therefore, the mass spectrometer

as well as the TQCM are sensitive to a particular contaminant species only at certain limited time periods during the mission. These times may not necessarily coincide with the brief contamination dumps.

The CQCM temperature depends on the Orbiter attitudes. Calculated cool-down temperatures for the CQCM show that about 10 to 15 hours are required in deep-space orientation to reach temperatures capable of condensing water. The STS-1 attitudes (primarily ZLV and short deep-space orientations) will not allow the condensation of water.

The TQCM's mounted on the sides of the IECM will receive direct contamination flux from Orbiter surfaces, particularly payload bay surfaces. Predictions of expected deposition rates are not yet available.

Predictions of the Induced Molecular Contamination Environment

The three standard indicators of the induced molecular contamination environment are density, molecular number column density, and return flux, as discussed previously. The goal is to predict as well as to measure these variables. Prediction is accomplished by math modeling using the SPACE computer program. Measurements obtained during the STS-1 mission by various instruments of the IECM will be restricted mainly to the determination of return flux. In addition to the return flux values, predicted values for number column density are provided. Some major induced molecular contamination environment contributors noted for duration of activity or relative high rate, or both, and for probability of detection are crew cabin leakage, outgassing/desorption, and the flash evaporator. Predictions for these sources have been summarized (table 4). In table 4, NCD and RF are shown for the total number of molecules. The outgassing data are based on a rate obtained after a lengthy period of 48 hours or more. Rates measured early in the mission may be one to two decades higher. The MS (RF) output is derived from RF (LOS1) data for two specific Orbiter attitudes (ZLV (XPOP) and RAM condition). The ZLV is the primary stable attitude during this mission and RAM represents the case of maximum return flux (i.e., with the payload bay pointing in the flight direction).

When the MS output is discussed, the specific expected spectra output for outgassing is not known. Therefore, to calculate meaningful sensor outputs, the highest mass peak in the predicted spectrum is assumed to correspond to approximately 10 percent of the total output. Although this percentage is somewhat arbitrary, the derived sensor outputs fall within the instrument sensitivity range.

The TQCM (RF) outputs are derived from RF (LOS1) data. The average mass is assumed to equal 100 for outgassing and the condensation coefficient at a crystal temperature of 213 K (-60° C) is equal to one. The deposition rate decreases with increasing crystal temperature (decreasing condensation coefficient). The flash evaporator and cabin leakage do not contribute to the deposition rate because sticking coefficients for the species are zero for the entire TQCM temperature range. The values listed in table 4 are within the normal measurement range of those instruments; however, to accumulate enough contamination on the TQCM sensing crystal to be counted will take some time. Other sources, such as supply and waste

water tanks, also contribute to the instrument output. These tanks are vented occasionally (table 3). The rates are high compared with the flash evaporator but are of relatively short duration. These H_2O dumps will be detected by the mass spectrometer, depending on the Orbiter attitude at the time of the dump since their duration exceeds the mass spectrometer cycle time.

A small fraction of the OMS, RCS, and VCS engine exhausts (namely, monomethyl hydrazine - nitrogen tetroxide) will accumulate on the TQCM during the mission. A few of the 80-millisecond bursts of gas species from engine firings may be measured by the mass spectrometer when spectral scan and exhaust time coincide. The same holds true for gases from sources such as the fuel cells and the auxiliary power unit.

These predictions (table 4) cover only part of the mission. It is expected that the instruments will show outputs during other portions of the mission, but lack of definition of the event time line and the randomness and short duration of the event preclude their prediction from a practical point of view. Therefore, a detailed evaluation of such events will be conducted postmission.

Inflight Monitoring

To obtain a time line of mission events not predicted premission and to take into account changes from premission to the actual time line, inflight monitoring is planned. The approach is as follows.

1. Significant Orbiter events are monitored real time during the mission to define the actual contamination event time line. This time line forms the basis for the assessment of IECM instrument output. These data are stored during flight on an onboard tape recorder. The parameters monitored define (a) the Orbiter characteristics and (b) the IECM status, as expressed by the IECM switch position (table 2), and the IECM power profile. The power profile provides indications of instrument operation cycles. Actual individual instrument output cannot be monitored.

2. IECM instrument outputs are surveyed to look for additional unexplained significant output characteristics. Attempts will then be made to correlate these outputs with any Orbiter-related events. All values of measured Orbiter parameters are recorded on tapes for later retrieval.

Postflight Data Reduction

Flight data concerning the contamination measurements will come from two different sources: the Orbiter and the IECM. Orbiter-related parameter data will be collected during the flight and reduced in detail after the flight at the NASA Marshall Space Flight Center (MSFC). Orbiter/IECM data analysis and assessment will be a joint JSC/MSFC effort, and the results will be published.

CONCLUDING REMARKS

An evaluation of the Orbiter-induced environment for the STS-1 mission has been performed. The evaluation approach consisted of developing a contamination model to predict the Orbiter-induced environment and developing an instrumentation package to measure the contamination environment. These tools will be applied for the first time on the STS-1 mission.

Based on this evaluation the following points can be made.

1. The STS-1 time line indicates that, for most of the mission, the Orbiter attitude varies frequently. Because the actual combination of attitude and source function for these periods is nknown, predictions of instrument output are impractical.

2. Two periods of the mission have stable (ZLV) attitudes and permit predictions of return flux for various Orbiter sources. For these attitudes, the predicted Orbiter-source return flux falls within the IECM instrument range and meaningful measured data are expected. For example, predictions of outgassing, flash evaporator output, and cabin leakage have been evaluated in detail.

3. For most periods of the mission, where attitude is variable, instruments of the IECM will continue to measure the contamination environment from Orbiter sources. Because no premission predictions will be available, these measured outputs will be correlated with the actual flight time line on a postmission basis.

4. Transient source events will, in some instances, be measured by several of the IECM instruments, depending on the instrument field of view and operating cycle. The evaluation of these data will also be performed postmission.

REFERENCES

1. Bareiss, L. E.; Hetrick, M. A.; Reiss, E. B.; and Strange Jenson, D. A.: Shuttle/Payload Contamination Evaluation Program, User's Manual. MCR-77-106, Martin Marietta Aerospace, April 28, 1977.

2. Reiss, E. B.; Hetrick, M. A.; Bareiss, L. E.; and Strange Jenson, D. A.: Shuttle/Payload Contamination Evaluation Program, User's Manual. Rev. A. MCR-77-104, Martin Marietta Aerospace, Sept. 30, 1977.

3. Miller, Edgar R.; and Decker, Rudolf, eds.: An Induced Environment Contamination Monitor for the Space Shuttle. NASA TM-73193, Aug. 1978.

4. Miller, Edgar R.: Shuttle Induced Environment Contamination Monitor. USAF/NASA International Spacecraft Contamination Conference, J. M. Jemiola, ed., NASA CP-2039, 1978, pp. 534-566.

5. McKeown, D.; and Claysmith, C. R.: Quartz Crystal Microbalance Systems for Shuttle Contamination Measurement USAF/NASA International Spacecraft Contamination Conference., J. M. Jemiola, ed., NASA CP-2039, 1978, pp. 605-628.

6. Ruff, R. C.; Taeusch, D. R.; Oran, W. A.; and Rathz, T.: USAF/NASA International Spacecraft Contamination Conference, J. M. Jemiola, ed., NASA CP-2039, 1978, pp. 567-604.

7. Flight Requirements Document, Space Shuttle Orbital Flight Test, Space Transportation System 1. Rev. D. JSC 10780, May 9, 1980.

TABLE I.- IECM INSTRUMENT CHARACTERISTICS AND MEASUREMENTS SUMMARY

Instrument (a)	Measurement	Operation (b)	Power Requirements, W	Field of view, deg	Sample rates	Resolution	Accuracy
Humidity monitor	Relative humidity, temperature	GPL, A, D, PL	4		6/min	±0.5%	±4%, typical ±2%, 273 to 343 K (0° to 70° C)
Dewpoint hygrometer	Dewpoint	GPL, A, D, PL	Normal: 5.5 Max. (transient) mode: 9		1/min	±0.5%	±1%, 266 to 300 K (-6.7° to 26.7° C)
Air sampler	Gaseous contaminants	GPL, A, D, PL	Operating mode: 28.6 Standby: 11.6			(d)	(d)
Cascade impactor	Particulate contamination of nonvolatile residue	GPL, A, O, D, PL	Operating mode: 10 Average standby: 3.0	c120	1/min GPL 6/min A, D, PL	±1.5 × 10⁻⁹ g	30 × 10⁻⁹ g
PSA	Optical degradation due to accumulated contamination	GPL, A, O, D, PL		150	(e)	(e)	(e)
OEM	Degradation of optics at 253.65 mm	GPL, O, D, PL	Operating mode: 41 Standby: 25	120	8 3 min/cycle	±0.8%	±1%
TQCM	Condensed molecular contamination at 213 to 303 K (-60° to +30° C)	GPL, A, O, D, PL	Operating mode: 73 (Max.) standby: 1.85	120	12/min/sensor A, D, PL 1 min/sensor GPL, O	±1.56 × 10⁻⁹ g ±1.65 × 10⁻⁹ g	1.5 × 10⁻⁸ g 1.5 × 10⁻⁸ g
CQCM	Condensed molecular contamination at 133 K (-140° C) to ambient	GPL, A, O, D, PL	Operating mode: 3.08 (Max.) standby: 1.33	120	12/min A, D, PL 1/min GPL, O		
Camera/ photometer	Particulate velocity, direction; photometry	O	Operating mode: 47.6/ camera (Max.) standby: 14.0/ camera	20	Film: 150 sec/exp Chopper: 1/ sec Photometer: 1/sec	20-µm particle at 1 m/sec	√ ±5 µm
Mass spectrometer	Molecular return flux	O	16	20	0.5/sec (slow scan) 5/sec (fast scan)	±1 count	0.2 to 0.4% for counting rate >512/sec

aPSA = passive sample array, OEM = optical effect module, TQCM = temperature-controlled quartz crystal microbalance, and CQCM = cryogenic quartz crystal microbalance.
b*GPL = ground prelaunch, A = ascent, O = onorbit, D = descent, and PL = postlanding.
cNonvolatile residue stage.
dSee table III.
eSamples for lab analysis.

TABLE II.- IECM SWITCH POSITION SEQUENCE

Event	IECM switch position	Function
Launch configuration	2	Mass spectrometer off: valve 1 closed valve 2 open (case 1)
1 to 2 hr after payload bay door opening on revolutions 1 and 2	1	Mass spectrometer on: both valves open (case 2)
15 to 45 min before payload bay door closure on rehearsal day	2	Mass spectrometer off: valves remain open (case 2)
30 to 90 min after payload bay door opening on rehearsal day	1	Mass spectrometer on: valves remain open (case 2)
15 to 45 min before payload bay door closure on entry day	2	Mass spectrometer off: valve 2 closed (case 3)

212

TABLE III.- MAJOR ORBITER CONTAMINATION SOURCES[a]

Source	Species	Effluent rate, g/sec	Duration	Time
Early desorption	H_2O, N_2, CO_2, O_2	[b]1×10^{-8} to 1×10^{-11}	Continuous	Continuous
Outgassing	H_2O, N_2, CO_2, O_2	[b]1×10^{-9} to 1×10^{-12}	Continuous	Continuous
Cabin atmosphere leakage	H_2O, N_2, CO_2, O_2	1.84×10^{-2}	Continuous	Continuous
3.9-kN (870-lb) RCS	H_2O, N_2, CO_2, O_2 and $MMH-N_2O_4$[c]	1420/engine	80 ms to 150 s	As required
0.1-kN (25-lb) VCS		40.8/engine	80 ms	As required
OMS		9798/engine	Variable	As required
Flash evaporator vents	H_2O	4.4	As required	$f(rad.\ T_{in},\ T_{out})$
Potable (supply) water dump	H_2O	[d]24.5	20 to 25 min	1/day
Waste water dump	H_2O	[d]24.5	10 to 15 min	1/day

[a]Minor Orbiter sources such as fuel cell vents (H_2, O_2) and auxiliary propulsion unit exhaust (NH_3) have low effluent rates and are of short duration.

[b]Units of $g/cm^2 \cdot sec$; rate is a function of material and surface temperatures.

[c]Monomethyl hydrazine – hydrogen tetroxide.

[d]Depends somewhat on flash evaporator usage. Clearing times are about 30 min.

TABLE IV.- MEASUREMENT PREDICTIONS

Source	NCD[a] (LOS1), molecules/cm^2	RF (LOS1), molecules/cm^2·sec·0.1 sr		MS (RF), counts/sec		TQCM (RF), Hz/sec·sr	
		ZLV	Maximum	ZLV	Maximum	ZLV	Maximum
Evaporator	6.6×10^{13}	7×10^{12}	6.3×10^{13}	1×10^5	1.3×10^6	-	-
Outgassing	1.0×10^{10}	1×10^9	2.5×10^{10}	[b]2	[b]50.0	2×10^{-2}	8.0×10^{-2}
Leak	2.0×10^{12}	8×10^{10}	2.4×10^{12}	[c]1×10^3	[c]3.6×10^4	-	-

[a]NCD = molecular number column density.

[b]Maximum peak, 10% of total.

[c]N_2, 76% of total.

STARBOARD

DFI 1

IECM

CQCM

+Z TQCM

X — AFT

MASS SPECTROMETER

DFI 2

DFI 3
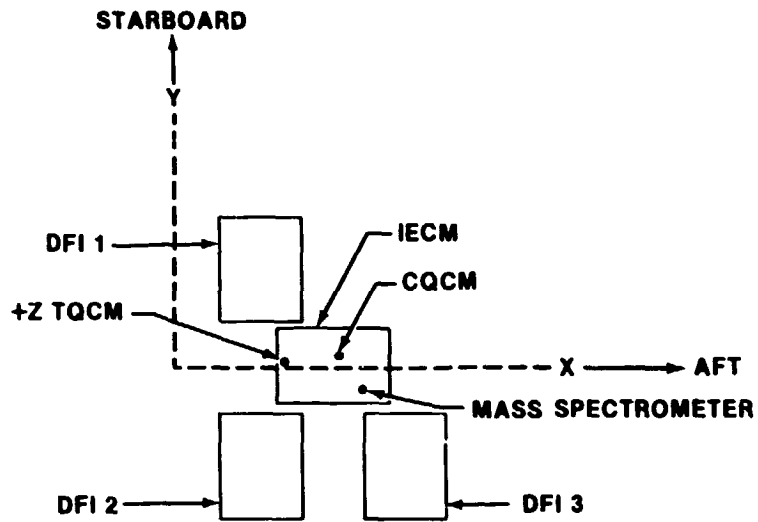
VIEW - Z-AXIS
TQCM - TEMPERATURE-CONTROLLED QUARTZ CRYSTAL MICROBALANCE
CQCM - CRYOGENIC QUARTZ CRYSTAL MICROBALANCE

Figure 1.- The IECM and the DFI for the Orbital Flight Test 1 payload
(looking downward into the payload bay).

AIR-SAMPLING SYSTEM

PASSIVE ARRAY

CASCADE
IMPACTOR

CQCM

DATA
SYSTEM

POWER DISTRIBUTOR

BATTERIES

CAMERA
PHOTOMETER

MASS SPECTROMETER

OPTICAL EFFECTS
MODULF

TQCM

VOLTAGE REGULATOR

TQCM
ELECTRONICS

Figure 2.- The IECM.

214
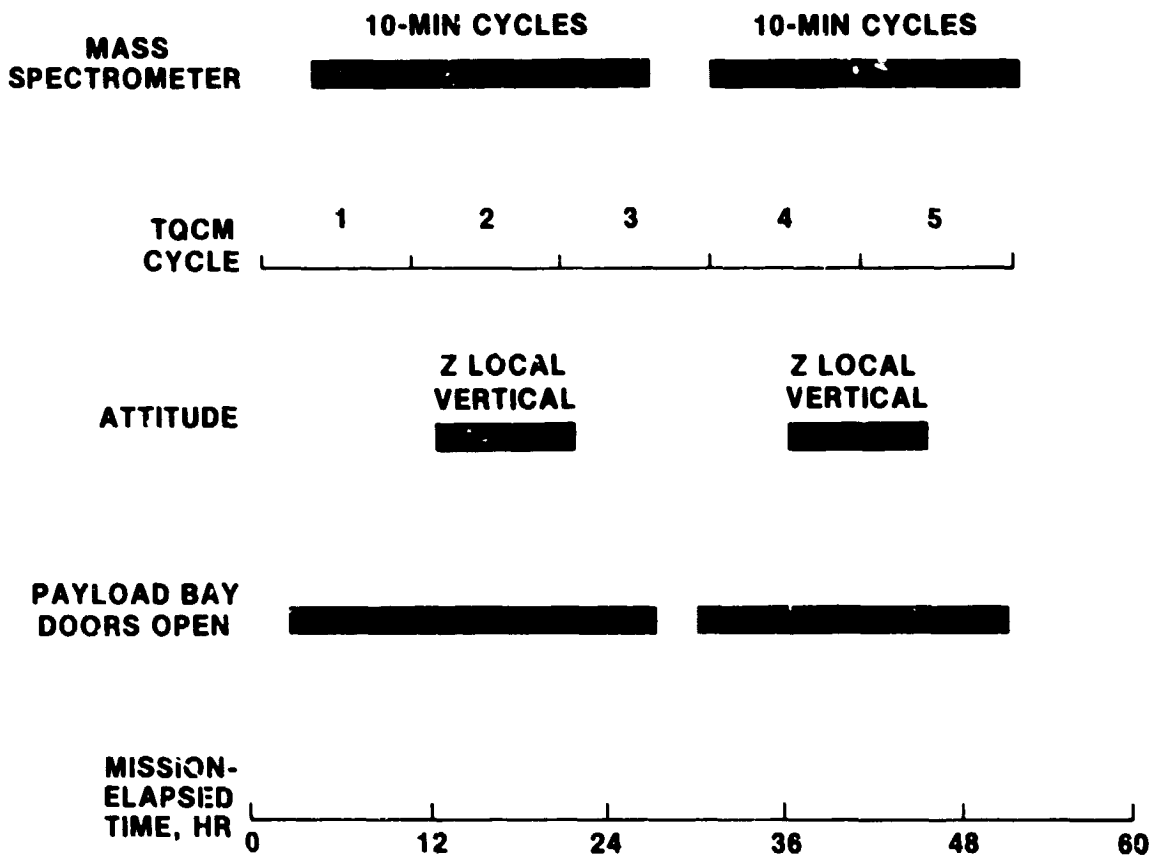
Figure 3.- The STS-1/IECM event time line.
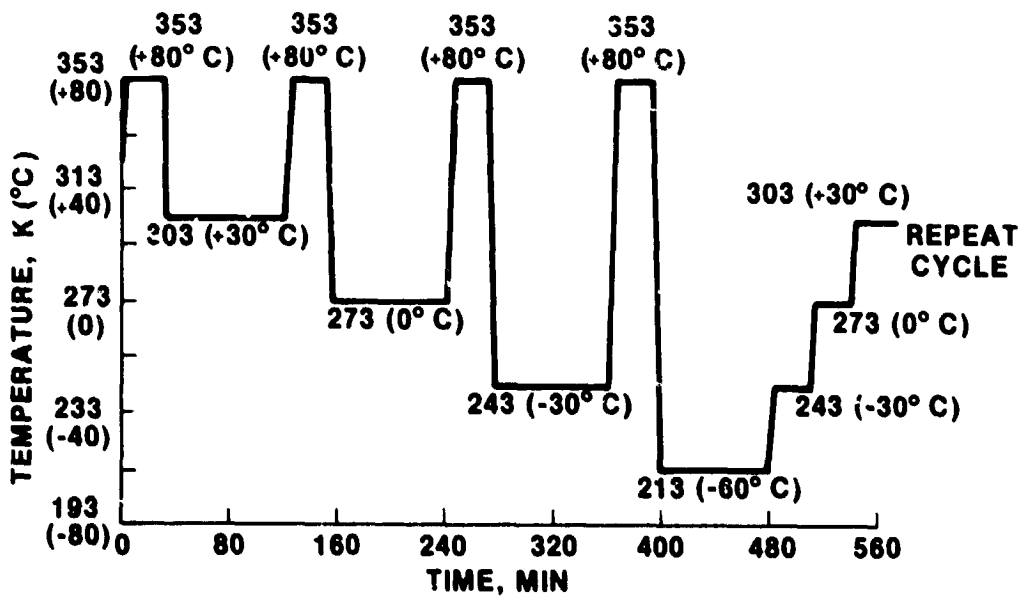
Figure 4.- The TQCM temperature sequence (one cycle).

215

EFFECTS OF THE SHUTTLE ORBITER FUSELAGE AND ELEVON

ON THE MOLECULAR DISTRIBUTION OF WATER VAPOR FROM THE

FLASH EVAPORATOR SYSTEM

by

Robert G. Richmond and Robert M. Kelso

ABSTRACT

A concern has arisen regarding the emissive distribution of water molecules from the Shuttle Orbiter Flash Evaporator System (FES). The role of the Orbiter fuselage and elevon in affecting molecular scattering distributions was unclear. An experiment was conducted at NASA-Johnson Space Center to evaluate the effect of these components. Molecular distributions of the water-vapor effluents from the FES were measured. These data are compared with analytically predicted values and the resulting implications are discussed.

INTRODUCTION

As spacecraft, payloads, and instrumentation have become more complex and mission durations increased, contamination of spaceborne optical systems has been shown to present significant problems (Ref. 1). With the emergence of the Space Shuttle program, more stringent cleanliness requirements in controlling contamination levels have been generated because: (1) the Shuttle is reusable and (2) payload experiments, in general, are expected to be more contamination-sensitive and utilize larger optical systems than previous spaceflights.

Recent investigations (Ref. 2) have identified several major Shuttle Orbiter on-orbit sources of contamination: (1) outgassing, (2) offgassing, (3) Shuttle Orbiter cabin atmosphere leakage, (4) supplemental flash-evaporator vents, (5) Vernier Control System (VCS) 25-lb. vernier engines, and (6) return flux (Figure 1). These sources, either steady state or transient in nature, represent the large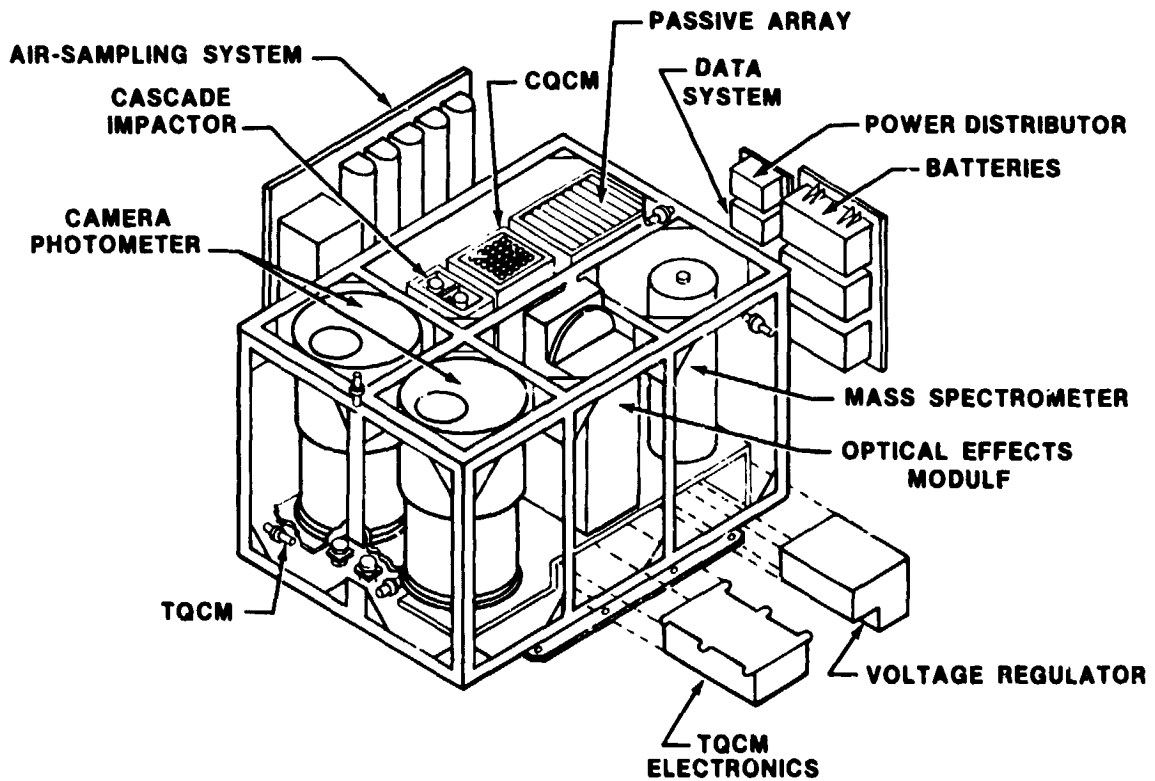st contributers to contamination levels on the Shuttle. Substances from these sources contribute to the on-orbit induced molecular and particulate environment in which scientific payloads will be operated. Exposure of payload experiments to this environment could result in the degradation of performance, e.g., increases in background brightness from scattering or emission of energy, or the condensation of reflectr. mol's on sensitive optical components and thermal-control coatings.

Experiments were conducted at the National Aeronautics and Space Administration, Johnson Space Center (NASA-JSC) to measure the distribution of water expelled through a specially-designed sonic nozzle into a thermal-vacuum environment. The nozzle was connected to an engineering model of the flight version of the flash evaporator system and the experiment was conducted in Chamber A of the Space Environment Simulation Laboratory. Water vapor was released into the chamber at various flow rates through the sonic nozzle and

the molecular fluxes of the resultant water-vapor plume were measured.

The primary objective of this series of experiments was to determine the directional characteristics of the nozzle as a function of elevon position and elevon/fuselage anticipated surface temperature extremes. These data are required to insure that excess fuel-cell water ejected overboard travels away from the Orbiter and does not reflect from spacecraft surfaces to produce an environment which could contaminate the payload experiments.

TECHNICAL BACKGROUND

The Flash Evaporator System (FES), one of four heat-rejection mechanisms integrated into the Shuttle Orbiter Active Thermal Control System (ATCS), is activated during on-orbit operation to provide two primary functions. The first function provides for ejection of excess fuel-cell water. The Shuttle Orbiter fuel-cell can generate over 650 kg/day of excess water during normal on-orbit operations. This excess fuel-cell water is ejected overboard the Orbiter by the flash evaporator through two non-propulsive, sonic nozzles at a variable frequency between 0-4 H_z (dependent on the Orbiter heat load) with a pulse width of 100ms. The second function of the flash evaporator is to provide supplemental heat rejection capability on an as-required basis when the Orbiter heat load exceeds the capability of the Shuttle radiator system. While the FES is comprised of two evaporator duct assemblies, the main evaporator, only the topping evaporator is used during payload operations because of molecular contamination considerations (Ref. 3).

Although the Flash Evaporator System assists in the reduction of the total weight of the vehicle as a result of evaporant dumping of fuel-cell water into space, subsequently reducing the size requirement of radiation panels, a major concern of the process is the increase in the contamination potential to the spacecraft and its payload experiments. Reflection of water from Shuttle wing surfaces during the evaporator operation could conceivably increase the particulate and molecular density of the induced environment of the Shuttle. Thus, it is necessary to determine the molecular flux and line-of-sight directions of the water molecules ejected by the flash evaporator.

THEORETICAL CONSIDERATIONS

A source-flow technique for modeling the spacecraft contamination in an on-orbit environment was developed for the NASA-Johnson Space Center (Ref. 4). This technique represented a reasonable approximation of the plume flow-fields and assisted in the final selection of location of plume sensors for the experiments.

The Shuttle Orbiter FES was considered as a point source in the model because at large distances from the evaporator nozzle the gas diverges radially as though it originated from a point source. The technique is primarily dependent on geometrical relationships between the angle (θ) as measured from the plume centerline of the nozzle and the distance (r) as measured from the source.

Predicted values for the molecular flux from the sonic nozzle were

determined by the relationship:

$$\Phi_1 = \frac{1.93 \cos^6 (0.608\ \theta)}{r^2} \quad g/cm^2.sec \qquad eq.\ (1)$$

for $0° \leq \theta \leq 148°$

and $\Phi_2 = 0 \qquad g/cm^2.sec \qquad eq.\ (2)$

for $148° \leq \theta \leq 180°$ (θ in radians)

Total flow rates for this function are 13.3 kg/hr (nominal average) and 31.7 kg/hr (maximum instantaneous). This function is shown graphically for normal-ized mass-flux in Figure 2.

Data from curves generated by equation (1), for variable evaporator flow rates, were used to predict the mass-flux rates for various locations in the plume flow field. These predictions were in turn used to determine where in Chamber A the plume measurement sensors should be placed.

EXPERIMENT CONFIGURATION

The general configuration for this series of experiments is shown photographically in Figure 3 and schematically in Figure 4. The basic configuration consists of four major elements: (1) the sonic nozzle, (2) the fuselage simulator, (3) the elevon simulator, and (4) the sensor and their location.

The sonic nozzle, some pertinent characteristics of which were discussed in Section III, was mounted 2.1 meters (7 feet) above the chamber floor and positioned to operate in a horizontal plane. The nozzle was installed flush with the front fact of a flat panel, 1.2m by 2.1m (4' x 7') which served as a simulator of the side fuselage of the Shuttle Orbiter. The fuselage simulator was equipped with heating elements to provide temperature control of the panel between -100°C and +40°C during test conditions.

A rotatable panel, representing a simulation of the wing elevon of the Shuttle Orbiter, was mounted normal to the fuselage simulator. The elevon simulator angle was varied with a motor drive assembly, thereby permitting changes in the plume profile due to pertubations attributable to the elevon to be assessed. All elevon angles were measured relative to the horizontal component of the nozzle centerline. The elevon simulator was also equipped with heaters to control temperatures between -100°C and +40°C. The nozzle, fuselage simulator and elevon simulator are shown in Figure 5.

Cryogenically-cooled quartz crystal microbalances were chosen for primary measurement of the molecular plume profile. The quartz crystal microbalance (QCM) has been a vital instrument in molecular flux measurements. The QCM has been used for several years in this laboratory to measure quantities of condensing contamination in a thermal-vacuum environment.

The QCM consists of a sensing crystal, reference crystal and associated electronics. With contamination condensing on the sensing crystal, a frequency difference, or beat frequency, is created. This beat frequency is proportional

218

to mass loading on the sensing crystal. Molecular flux (mass-flux) values can be established from the QCM sensitivity of 3.5×10^{-9} g/cm^2.Hz. Liquid nitrogen cooling adapters, Figure 6, were used in association with the QCM sensor to permit the QCM crystals to operate near cryogenic temperatures. The senor electronics were thermally isolated. Detailed operation of the QCM has been previously reported (Ref. 5,6) and will not be discussed here. Secondary (backup) measurements were provided by ionization gages, mass spectrometers and capacitance manometers.

General sensor location is shown in Figures 4 and 6. Figure 7 gives a closer view of the instrument. Five cryogenically-cooled QCM's were installed along the chamber wall at a distance of 10 meters from the nozzle. These five sensors, expected to measure molecular flux intensities in the range 10^{-6} to 10^{-8} g/cm^2.sec^1, were placed at angular locations of 0^0, 20^0, 30^0, 40^0, and 60^0 relative to the centerline of the flash evaporator nozzle. Only the primary QCM measurements will be reported here.

All of the molecular plume sensors were installed in the horizontal plane of the flash evaporator nozzle 2.1 meters above the chamber floor. This decision was based on math modeling predictions that the flow field was symmetrical around the plume centerline.

During those test points where the QCM's were not used to acquire data, specially constructed aluminized mylar curtains were lowered in front of the QCM's located at 0^0, 20^0, 30^0, and 40^0 relative to the centerline of the nozzle. Shown photographically in Figure 6, the curtains prevented line-of-sight transmission of water vapor from the evaporator to the cryogenically-cooled crystals of the QCM's during non-plume testing activities. At a chamber pressure of 10^{-6} torr the condensation coefficient for water at temperatures below -140^{0}C is approximately unity. This means that the impingment of water vapor molecules on surfaces of temperatures of lower value (near LN$_2$ temperatures), viz., the QCM crystal, will result in adherence of essentially all of the molecules. Thus, the mylar curtain prevented the QCM from becoming saturated by water vapor when they were not acquiring mass flux rates high enough to cause saturation of the instrument.

EXPERIMENTAL RESULTS AND DISCUSSION

A typical mass-flux distribution is shown in Figure 8. The data represent mass flux, g/cm^2.sec, as a function of angle relative to the nozzle centerline. These data are for the case where the elevon/fuselage assembly is cold (-100^{0}C), the elevon is positioned at the "nominal" 0^0 location, and a flow rate of about 16.5 kg/hr through the nozzle. The measured values compare quite well with those predicted by theory.

The effect of the elevon position on mass-flux distribution is shown in Figure 9. These data, representing the cold (-100^{0}C) elevon/fuselage, again agree quite well with predicted values with one exception--when the elevon is positioned in the "stowed" configuration. Considerably higher values of mass-flux were measured at the 30^0 and 40^0 angles than were anticipated, possibly indicating some scatter of the water-vapor molecules when the elevon is in the stowed position. Data from the QCM located 20^0 off the centerline of the nozzle was limited since the sensor became inoperative near the beginning of the experiment.

The effect of temperature of the elevon/fuselage assembly on mass-flux distribution was striking. Shown in graphical form in Figure 10, the "warm case" data indicates a narrowing of the molecular distribution from the nozzle. Although these data do not correlate well with the predicted values, they do suggest a more efficient dismissal of effluent from the nozzle, i.e., more molecules are directed away from the spacecraft. It is then apparent that the cold case data or the molecular distribution predicted by theory probably represent worst-case conditions of distribution of water-vapor molecules from the FES. The reasons for the differences in distributions directly attributable to spacecraft surface temperatures are unclear.

Each data point consisted of a set of 10-20 individual measurements utilizing nuclear instrumentation pulse-counting techniques. Each individual measurement represented an integration (pulse counting) time of 10 seconds. This approach permitted a precision or self-consistency of better than $\pm2\%$ between measurements. Measurements were reproducible after major configuration changes, e.g., elevon movement, elevon/fuselage temperature changes, and FES flow rate, to better than $\pm10\%$ for most measurements.

CONCLUSIONS

The directional characteristics of a specially designed, sonic nozzle for the dismissal of water-vapor effluents from the Shuttle Orbiter Flash Evaporator System have been measured for two specific cases. The specific cases include: (1) elevon position (simulated elevon) and (2) elevon/fuselage assembly surface temperature extremes, viz., -100°C and 40°C.

Cryogenically-cooled quartz crystal microbalances have been shown to be remarkably good sensors for measurement of water-vapor plume profiles in vacuo.

The theoretical source-flow technique for modeling the spacecraft contamination in an on-orbit environment and the corallary analytical function for molecular flow from a sonic nozzle are shown to agree closely with the cold-case data measured during this experiment.

Data from the warm (+40°C) elevon/fuselage simulator do not correlate well with predicted values. The reasons for poor correlation are not clear. The measured values from the warm case do suggest that the nozzle/surfaces combination is more efficient at directing the water molecules away from the spacecraft. It follows, then, that the cold case data or the molecular distributions predicted by theory probably represent worst-case distributions of water-vapor molecules from the flash evaporator system.

REFERENCES

1. Muscari, J. A. and Westcott, P., "Optical Contamination Evidence from Skylab and Gemini Flights," Applied Optics, Vol. 14, No. 12 (1975).

2. Rantanen, R. O. and Ress, E. B., "Payload/Orbiter Contamination Control Assessment Support, Final Report," Martin Marietta Aerospace, June 1975.

3. Jaax, J. R., 'Flash Evaporator Subsystem Hardware, Operational and Performance Description," October 1976.

4. Rantanen, R. O. and Jensen, Strange D. A., "Orbiter/Payload Contamination Control Assessment Support, Final Report," Martin Marietta Aerospace, April 1977.

5. Visentine, J. T. and Richmond, R. G. and Kelso, R. M., "Molecular Outgassing Measurements for an Element of the Shuttle Thermal-Protection System," Thermophysics of Spacecraft and Outer Planet Entry Probes, AIAA Vol. 56 (1977).

6. Richmond, R. G. and Kelso, R. M., "Effectiveness of the Shuttle Orbiter Payload Bay liner as a Barrier to Molecular Contamination from Hydraulic Fluids," Proceedings International Spacecraft Contamination Conference, Colorado Springs, CO, March 1978.

7. Visentine, J. T., Ehlers, H. K. F., and Roberts, B. B., "Determination of High-Velocity Water-Vapor Plume Profiles in a Thermal-Vacuum Environment," NASA SP-336, November 1975, page 727.

8. Santeler, D. J., Jones, D. W., Holkeboer, D. H., and Pagono, F., Vacuum Technology and Space Simulation, NASA SP-105, page 3.
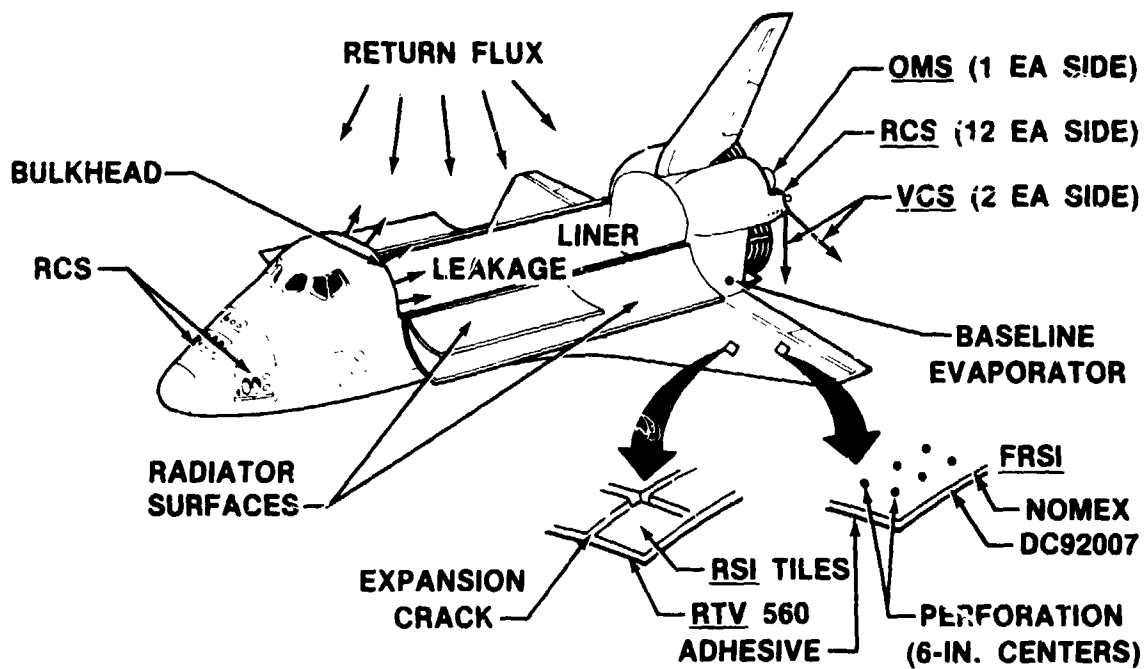
Figure 1.- Major shuttle orbiter
source locations.
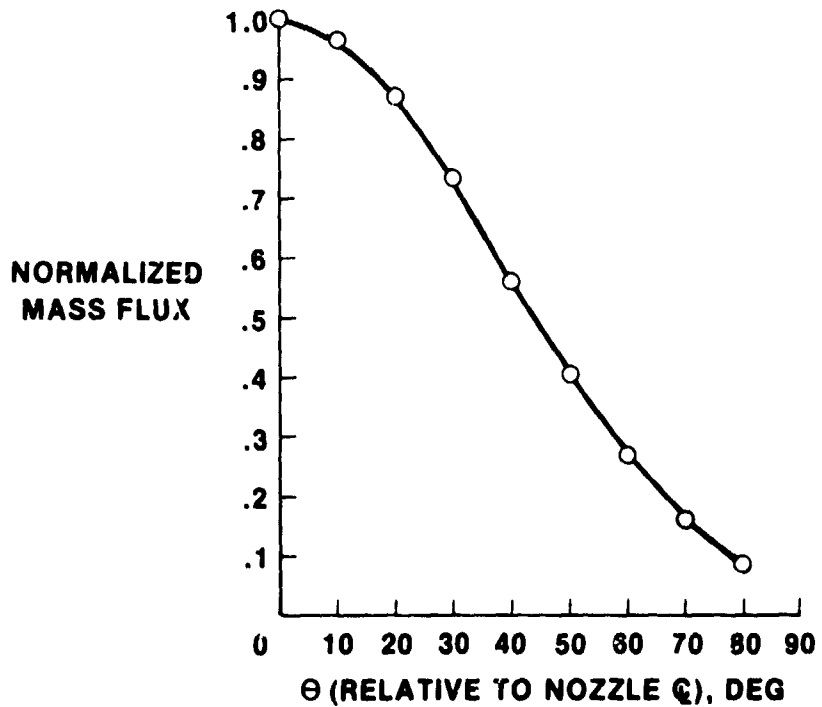
Figure 2.- Predicted normalized mass-flux distribution
after ref. 4.
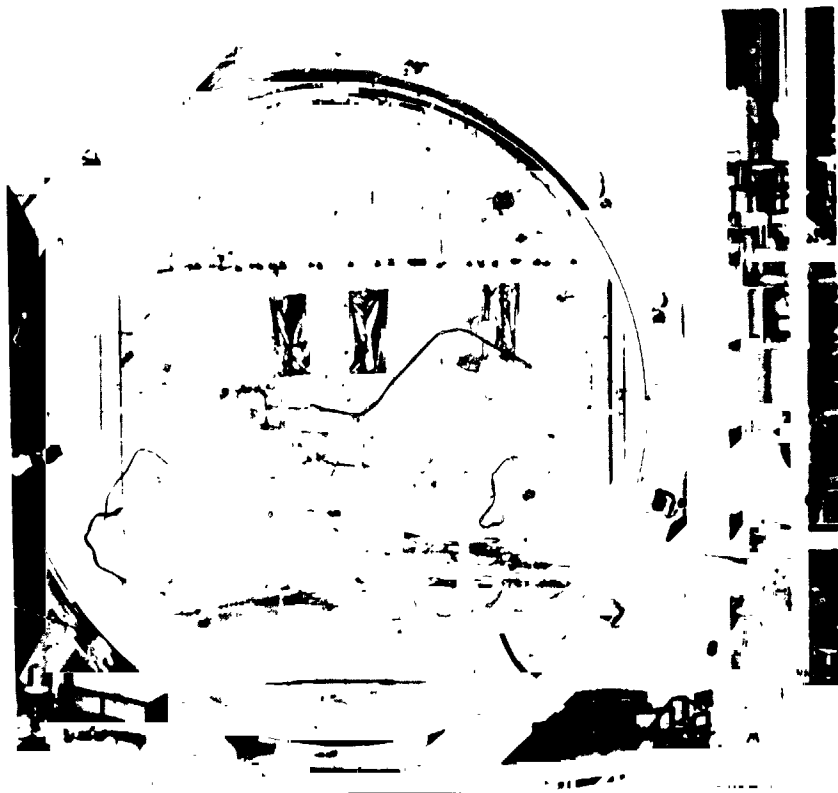
Figure 3.- Flash evaporator test setup in chamber A.
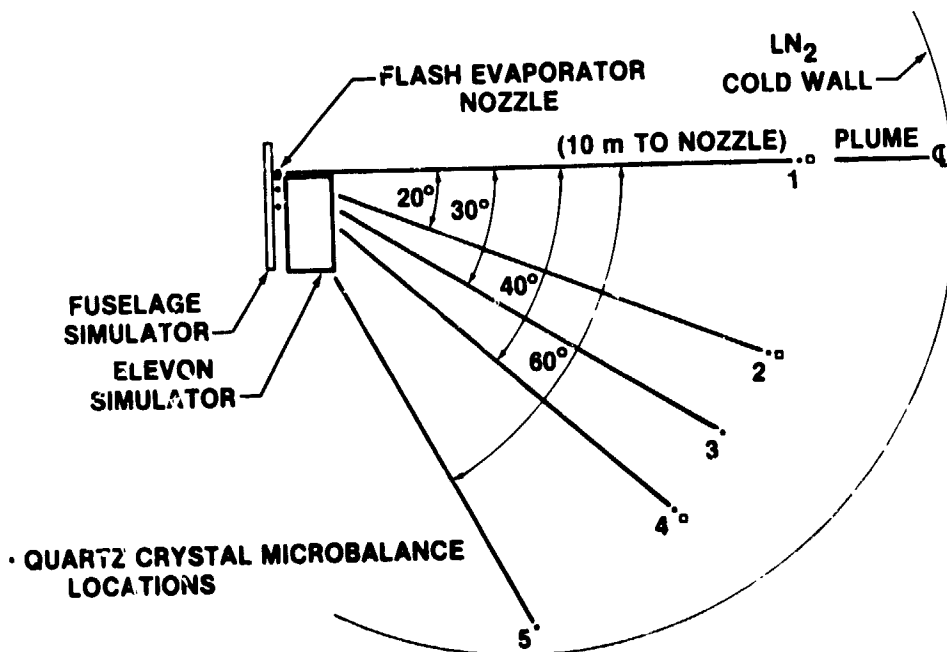
Figure 4.- Chamber A FES primary instrumentation.

223
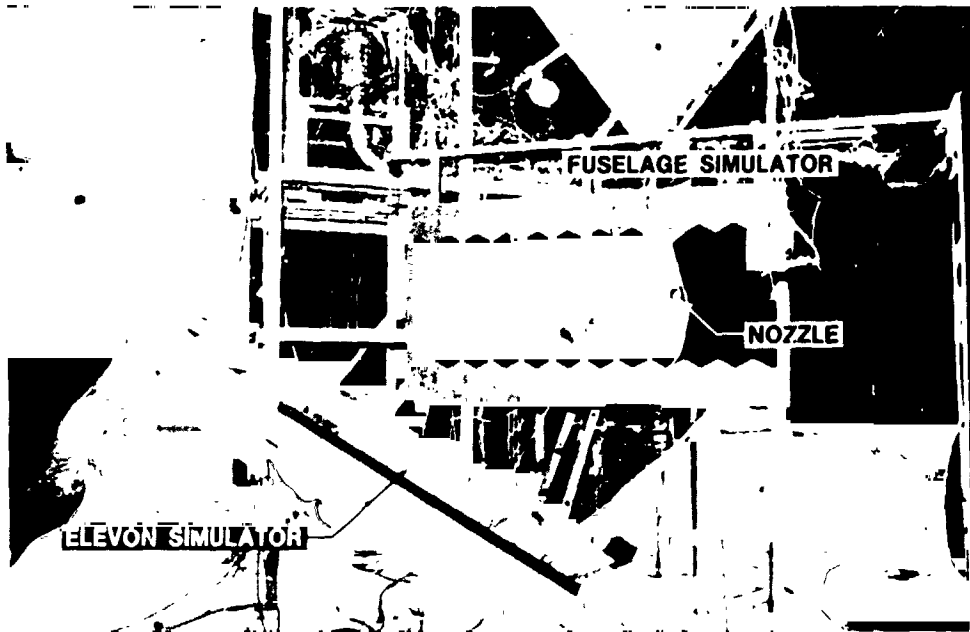
Figure 5.- Orbiter fuselage simulator, nozzle, and elevon simulator.
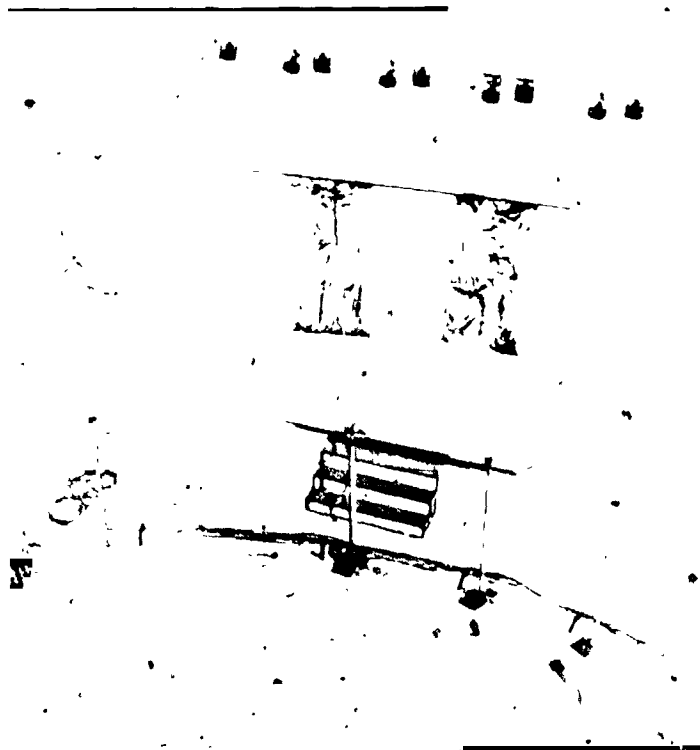
Figure 6.- Plume measurement locations.
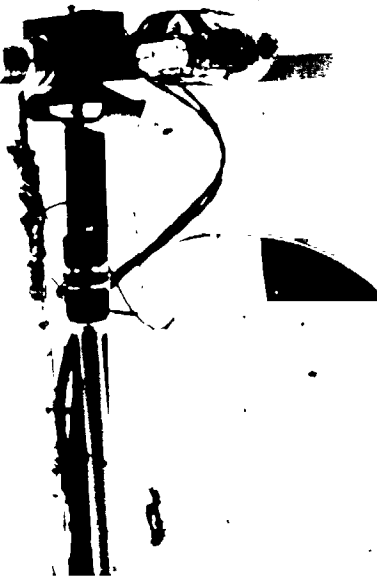
Figure 7.- Cryogenically-cooled
quartz crystal microbalance and
tubulated ionization gage.
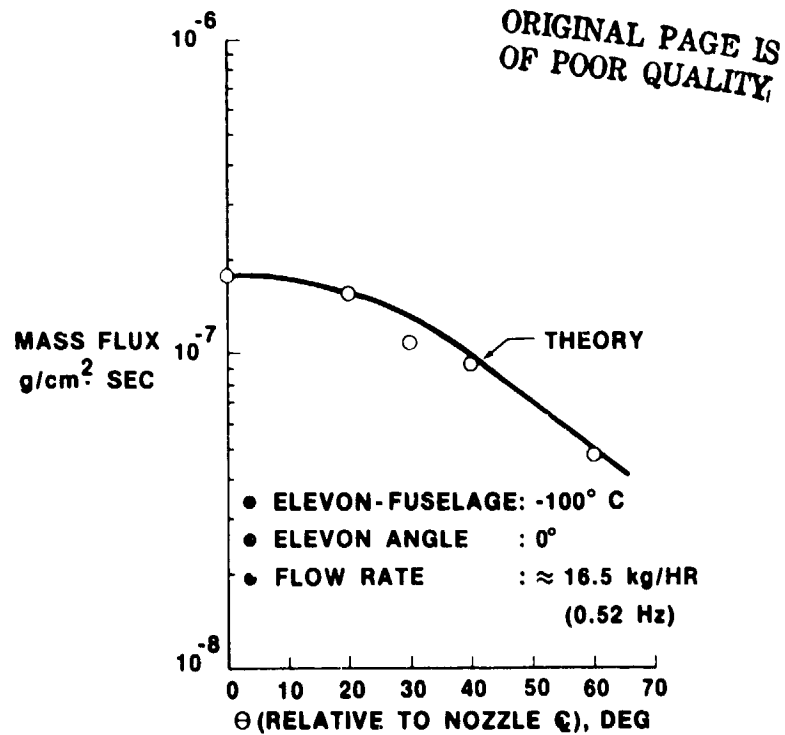
Figure 8.- Typical mass-flux distribution.

225
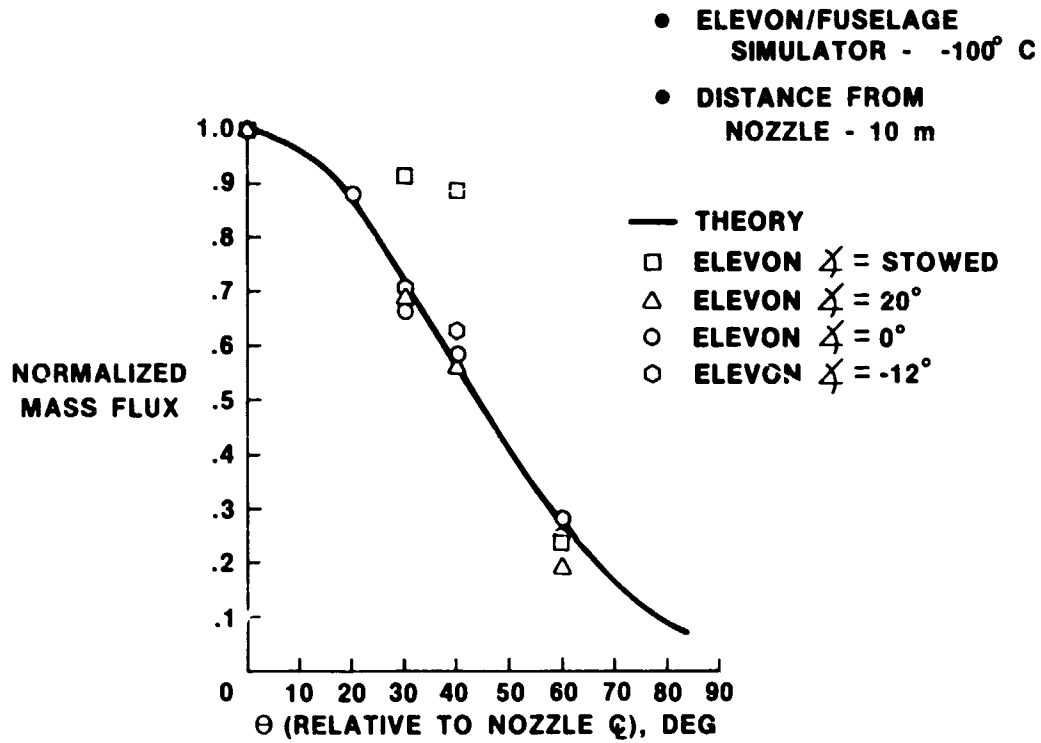
Figure 9.- Effect of elevon angle on mass-flux distribution.
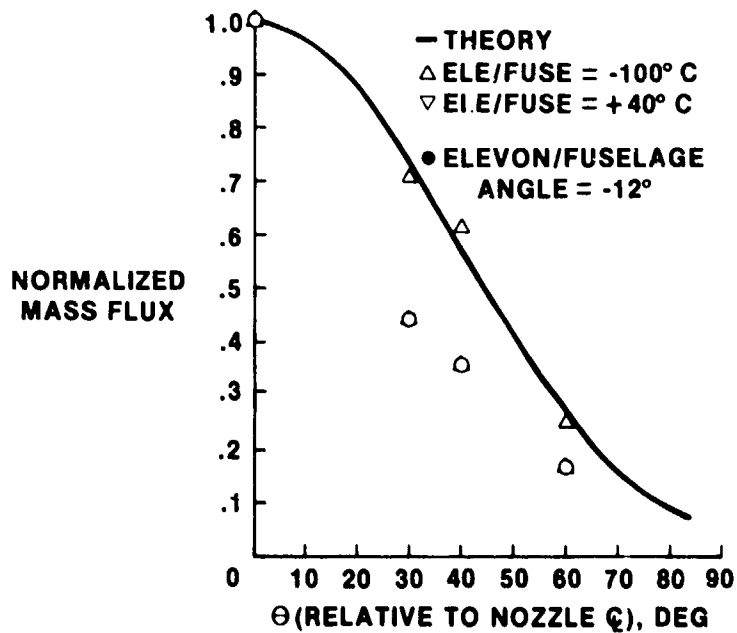
Figure 10.- Effect of elevon/fuselage
temperature on mass-flux distribution.

226

OUTGASSING TESTS ON IRAS SOLAR PANEL SAMPLES

G. Premat*   A. Zwaal*   N.H. Pennings**

1. INTRODUCTION

1.1 Purpose

The IRAS satellite (InfraRed Astronomical Satellite) is a joint venture between the Netherlands, United States and the United Kingdom to investigate the infrared sources in space by means of a telescope, which is cooled to superfluid helium temperature (about $\pm$ 2 - 10K).
Due to the low operation temperature the risks of contamination, particularly of the optical components, are high.
The efforts to diminish the contamination hazard to a minimum include selection of low outgassing materials, special treatment after manufacturing and special spacecraft handling procedures. All the constituting materials of the satellite are potential sources of contamination. Due to their location, their relatively high temperature and the many organic materials contained, the solar panels require special consideration.
At the request of Fokker, prime contractor for the IRAS project and manufacturer of the solar panels, the Materials Section of ESTEC carried out several outgassing tests on representative solar panel samples with a view to determining the extent of contamination that could be expected from this source.

1.2 Purpose of tests carried out in ESTEC

The materials for the construction of the solar panels have been selected as a result of contamination obtained in "Micro VCM" tests. This method is a "screening test" and gives only the "qualified" or "non-qualified" results according to criteria used by NASA as well as by ESA (1% TML and 0.1% CVCM).
This test method is intended to provide an accelerated means of determining the total mass loss of materials and their contamination attributes in exposure to vacuum ($<10^{-6}$ torr) at a temperature of 125°C. This method might give misleading results in case of those materials, whose outgassing kinetics at 125°C are different from those at the temperature of intended use.
The comparison of materials properties is only valid at 125°C. The measurement for collectors at 25°C with similar sticking coefficients. It is considered, however, that the method of using the defined screening operation is a conservative one. The risk is that a few materials which have acceptable properties (at the intended temperature of use) will be eliminated because their properties are not satisfactory at the test temperature of 125°C. It was, however, necessary to know the kinetics of outgassing (i.e. total mass loss of materials and

*ESTEC Noordwijk The Netherlands
**Fokker Space Division Schiphol The Netherlands
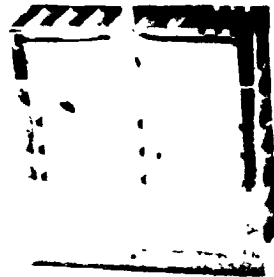
1a

1b

1c

1d
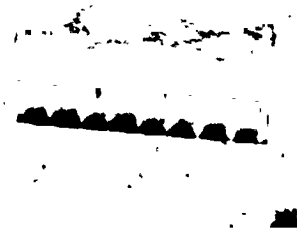
Figure 1

ccndensable volatile materials coming from selected products versus time, temperature of solar panels and different temperature configurations of telescope) to determine the contamination risks during the mission of the satellite.

2. DESCRIPTION OF SAMPLES

The six test samples have been manufactured like solar panels of a flight model (Figure 1).

3. DESCRIPTION OF TEST EQUIPMENT

The equipment developed at ESTEC to perform the outgassing measurements makes use of the advantages offered combining QCMs (Quartz Crystal Balance) with a conventional vacuum balance. This system (Figure 2) consists of a Sartorius 4201 vacuum balance with magnetically suspended sample hangers.

The balance has a sensitivity of 1×10^{-5} g, but due to the vibrations as well as temperature and humidity variations in laboratories, the accuracy is limited to 1×10^{-4} g. The maximum load of the balance is 25 g and the temperature is controlled by an oven containing the samples.

The three Celesco QCMs can measure the amount of materials condensed on the exposed crystal down to a few

VBQC-I OUTGASSING SYSTEM

- VACUUM BALANCE
- MAGNETIC SUSPENSION SYSTEM
- GLASS TUBE
- TO ION PUMPING SYSTEM
- TO MASS SPECTROMETER TO IONISATION GAUGE
- QUARTZ CRYSTALS
- COOLING TUBE
- COOLING TUBE
- COOLED CONDENSER PLATE
- HEATERS
- SAMPLE

Figure 2

time 10^{-8} g/cm^{-2} (sensitivity given by the manufacturer: 8.9×10^{-9} g/cm^{-2}/mV^{-1} output).
These QCMs can be cooled down from an ambient temperature to liquid nitrogen temperature.
The condensor plate (with holes in front of QCMs) is also controlled at the lowest QCM temperature and has a diameter of 146 mm (area $\pm$ 175 cm^{2})
The contaminants trapped on the plate can be collected for analysis (i.e. infrared spectroscopy).
The pumping system is a Varian VT102 ion pump system, equipped with a quadruple mass spectrometer permitting analysis of outgassing products which do not condense on the condensor plate (i.e. mainly water, solvents and atmospheric gases). Also pressures down to at least 10^{-9} torr can be obtained.
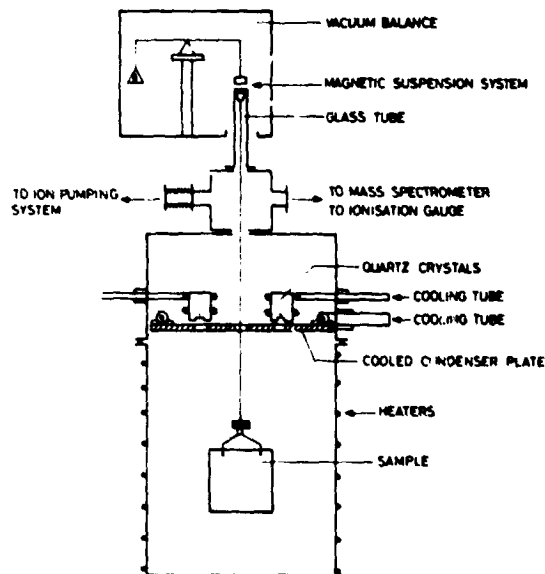
4. SAMPLE PREPARATION

Each sample has been conditioned for at least 24 hours at a standard temperature of $20^{\circ}C$ and a standard humidity of 65% before evacuating the test chamber and starting the test. This is similar to the conditioning used in the Micro VCM procedure (PSS-02T).

a. Clean the QCMs and cooled plate with a mixture of IPA and freon TF (50%-50%).
b. Mount the sample on vacuum balance and switch on.
c. Close the oven.
d. Pump down.
e. Cool the QCMs and cooled plate to the intended temperature when the pressure is about 10^{-4} torr.
f. When the QCMs and cooled plate temperatures are correct, start heating the oven.

In the normal sequence of operations, there was a minimum time between the actions; however, in some cases the time between the actions increased due to pumping failure, cooling failure, stabilization, etc. (see Table 1).
For the tests 1046/1047 and 1049 the cooling of the QCMs and heating of the sample have been started together under dry nitrogen at atmospheric pressures before pump down. The QCMs and the condensor plate are maintained at temperature as described in Table 2. Through the choice of these temperatures, a discrimination can be made between outgassing products with respect to their vapor pressure. The composition of the lightest fractions has been analyzed using a mass spectrometer in the pumping line.

5. MASS SPECTROMETER DATA

The analysis of gases coming out of samples has been carried out with a quadruple spectrometer (see Table 3). This analysis has only been carried out with the experiment 1042 (sample 3) because of failure of the spectrometer.

5.1 Infrared analysis of contaminants trapped on cooled plate

After each test the composition of the organic products condensed on the cooled plate have been analyzed by infrared spectrometry method. The results are shown in Table 4.

6. METHODS OF CALCULATION

The different parameters were collected continuously on six channels recorder and the recordings were analyzed by hand to measure the signal V.

a. In mV for the total mass loss versus time.
b. In mV for volatile condensables versus time.

The TML is calculated according to the following formula:

$$\% \text{ TML} = \frac{V(\text{atm} + V \text{ buoyancy effect} - Vt) \times S}{Mo} \times 100$$

where:

V atm = signal at atmospheric pressure

V = buoyancy effect[*]

Vt = signal during test versus time

S = sensitivity 10^{-4} g mV^{-1}

Mo = initial weight before testing.

The CVCM is calculated according to the formula:

$$\% \text{ CVCM} = \frac{(Vt - Vo) \times 8.86 \times 10^{-9} \times 175}{Mo} \times 100$$

where:

Vo = signal at time o[**]

Vt = signal during test versus time

8.86×10^{-9} g/cm^{-2}/mV^{-1} = sensitivity of QCMs (given by manufacturer)

175 cm^2 = area of condensor plate

Mo = initial weight of sample before test in grammes.

These data are listed and stored in the computer for calculations.

[*] buoyancy effect=buoyancy of balance + buoyancy of sample
(not including the air contained in the sample).

[**] Vc=the lowest signal observed after heating the sample.

The time zero has been taken from the heating of the sample for the
first four tests and at pump down time for the other three tests.
The zero value of the total mass loss has been measured from the
initial signal of vacuum balance as soon as the sample was mounted
corrected from the buoyancy effect measured after each test.
Due to vibrations of the vacuum balance during the mounting of the
sample and the pump down, the measurement of buoyancy effect is very
difficult and an error of a few mg can be done.
The zero value of the QCMs has been taken at the lowest value of
signal observed after cooling of the QCMs and heating of sample,
but this can be slightly overestimated because some contamination may
already have occurred during the cooling.
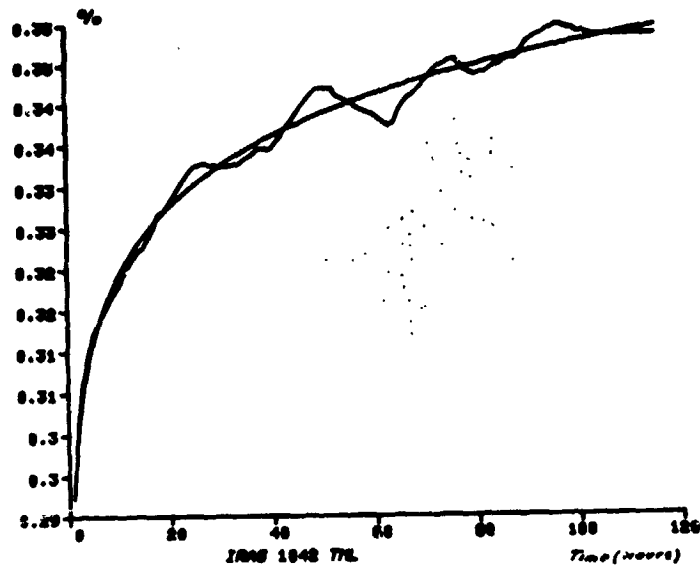
3a
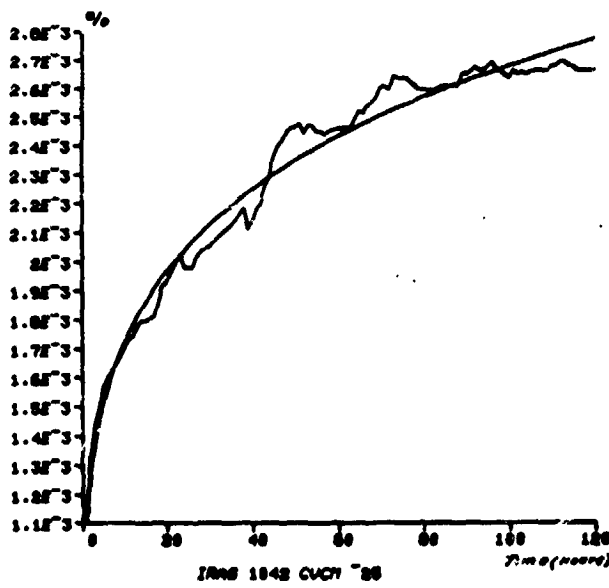
3b
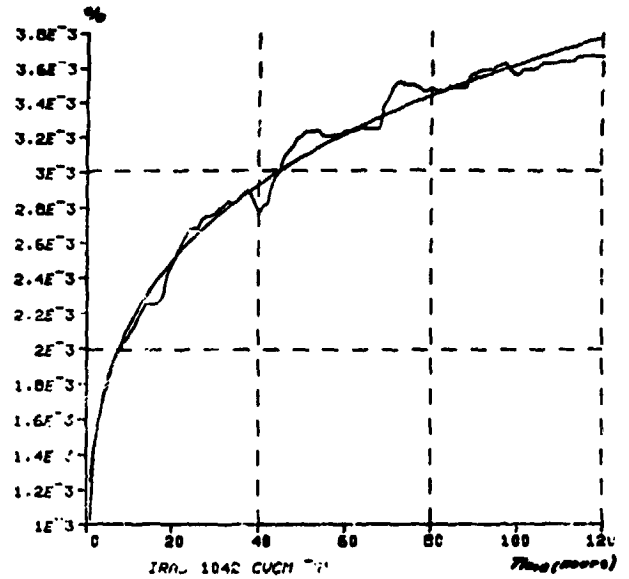
3c

Figure 3
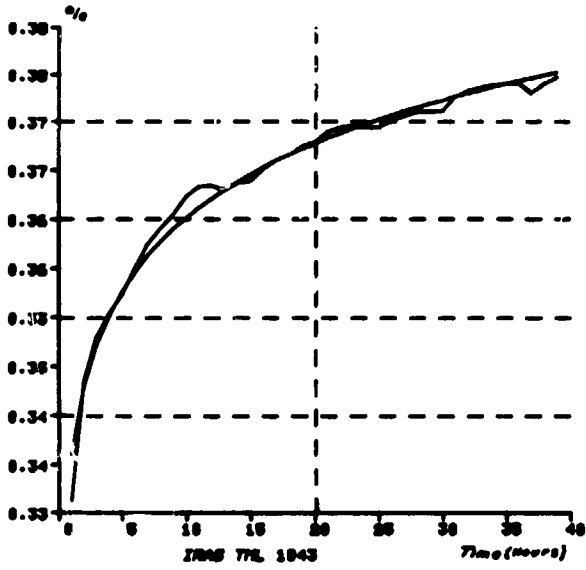
3d
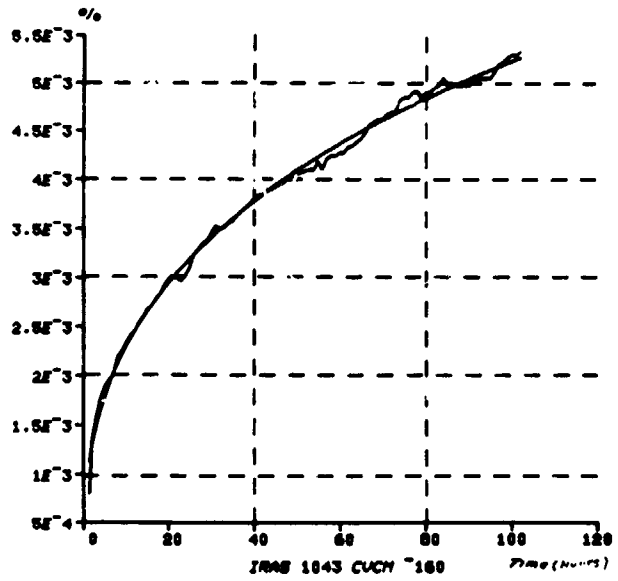
3e
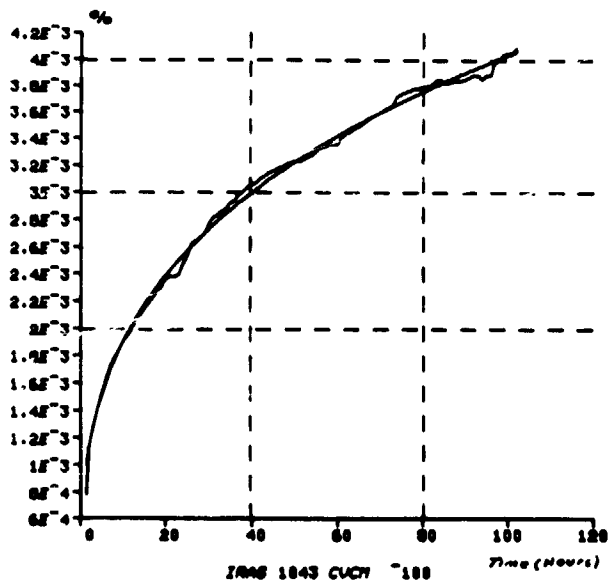
3f
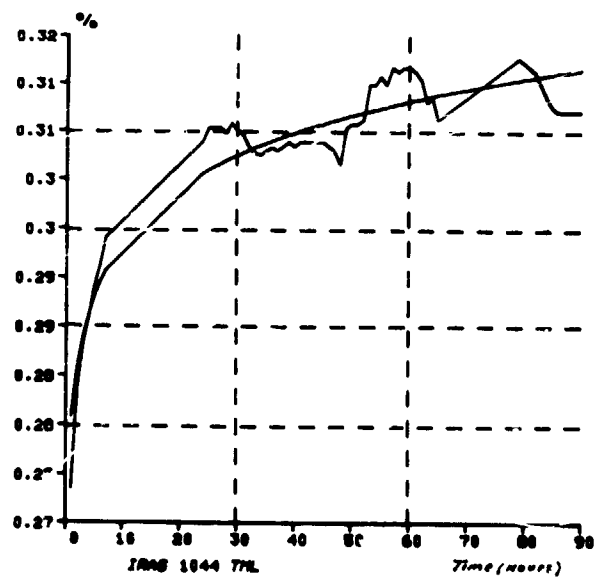
3g

Figure 3

3h

3i

3j

3k

Figure 3

234
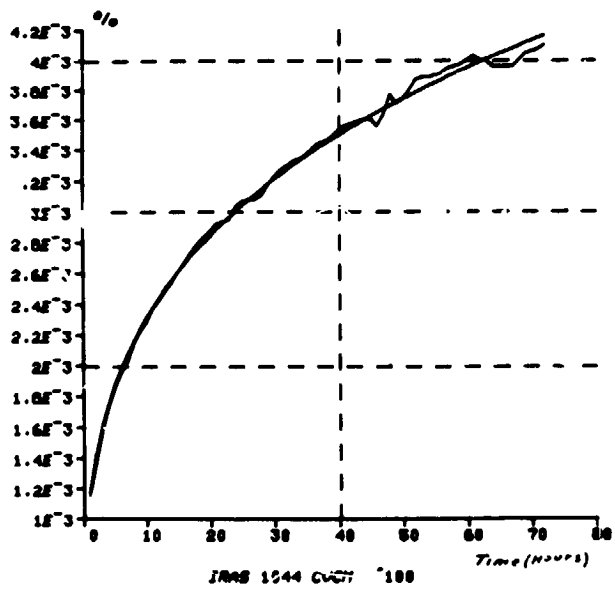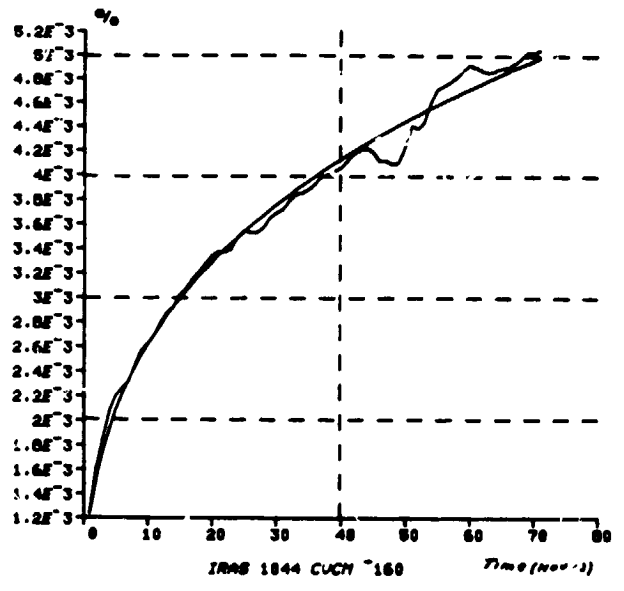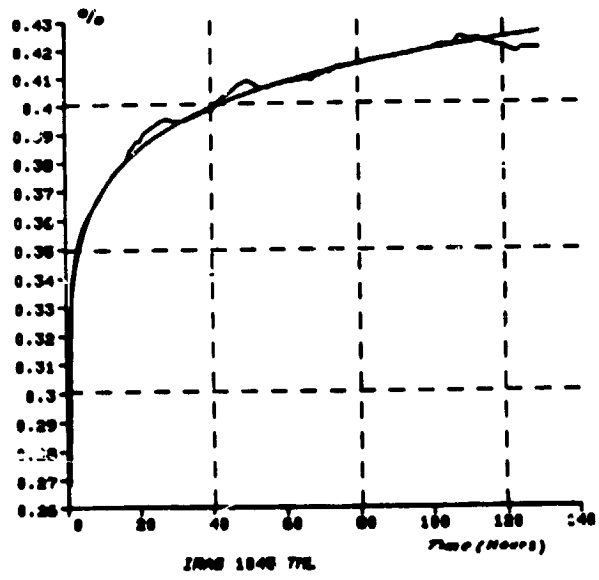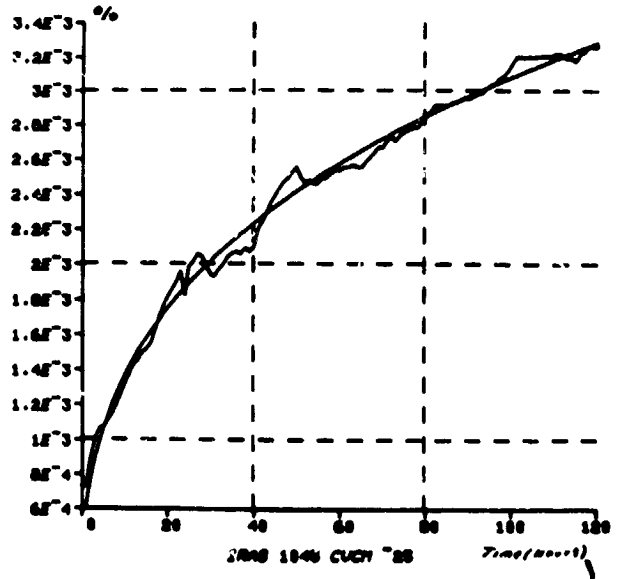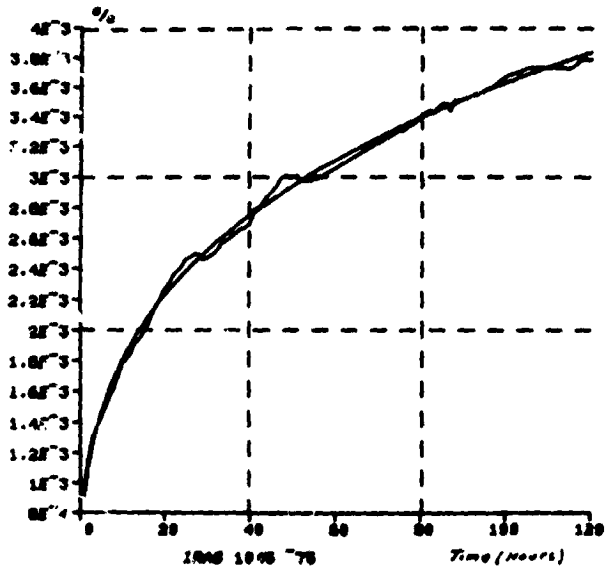
31
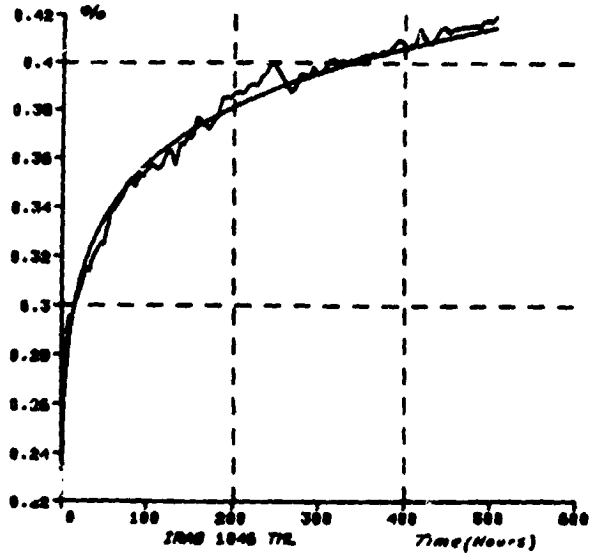
3m
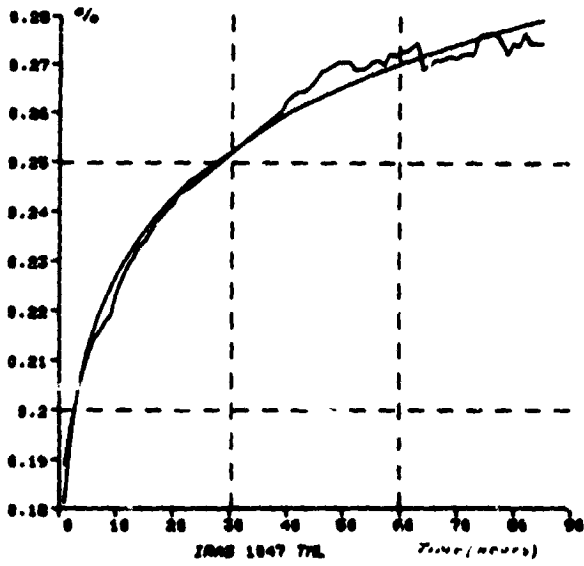
3n
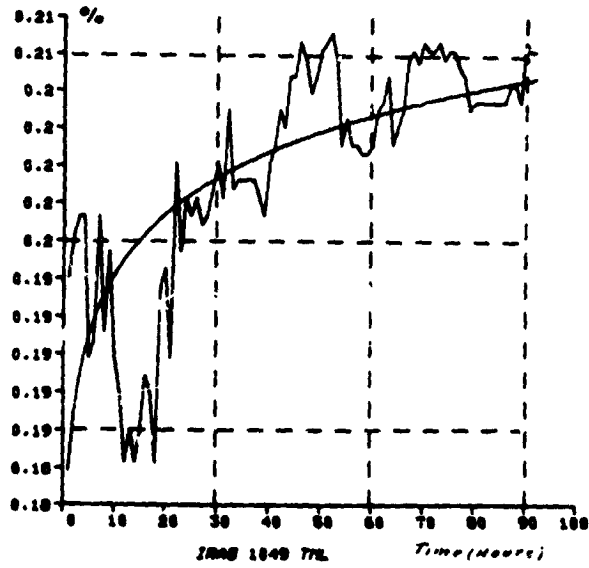
3o

Figure 3

7. COMPUTER CALCULATION METHOD

The method used is linear regression by equal increments. It is based on several tests of changes of variable, leading to a linear relation between the new variables and the necessary parameters by least square fit.

The calculation program is written in APL. It consists of a series of sub-programs corresponding to different equations, which are tested successively by comparison with experimental data, particularly the power function $Y = aT^b$ and the exponent function $y = ae^{bt}$.

Both equations are given; the correlation with the power function gives normally a better fit with experiment for durations not longer than 120 h.

This is the case for the IRAS tests.

7.1 The results are given as computer listing (see example of TML listing below)

```
------------------------------------------  -----

Y  =-0.2344280336 * Y (0.091627376635  (+/+)

------------------------------------------------
1930 / ANS     6 / MOIS    11 / JOURS   14 / HEURES  13 / /
REF  I 10750.1
POIDS    I  10750.1

----------  ------------------------------------------

TIME(H)   MES-           CALC.         ERR+/+        RATE
  1.0 I  2.6511E-1  --  2.3443E-1  --   11.574" --  8.1480E-2
  2.0 I  2.7349E-1  --  2.4980E-1  --    8.6605 --  1.1442E-2
  3.0 I  2.7907E-1  --  2.5926E-1  --    7.0992 --  7.9103F-3
  4.0 I  2.6279E-1  --  2.6610E-1  --    5.0726 --  6.8974E-3
  5.0 I  2.6651E-1  --  2.7160E-1  --    5.1761 --  4.9705E-3
  6.0 I  2.6995E-1  --  2.7626E-1  --    4.7233 --  4.2108E-3
  7.0 I  2.9209E-1  --  2.8019E-1  --    4.0750 --  3.6679E-3
  8.0 I  2.9395E-1  --  2.8463E-1  --    3.5096 --  3.2414E-3
  9.0 I  2.9405E-1  --  2.8671E-1  --    2.7703 --  2.9190E-3
 10.0 I  2.9601E-1  --  2.0949E-1  --    2.1350 --  2.6526E-3
 11.0 I  2.9501E-1  --  2.9203E-1  --    1.2774 --  2.4326E-3
 12.0 I  2.9501E-1  --  2.9437E-1  --    0.4072 --  2.2477E-3
 13.0 I  2.9074E-1  --  2.9654E-1  --    0.0609 --  2.0201E-3
 14.0 I  2.9060E-1  --  2.9096E-1  --   -0.0149 --  1.9540E-3
 15.0 I  3.0000E-1  --  3.0043E-1  --   -0.1512 --  1.0353E-3
 16.0 I  3.0093E-1  --  3.0223E-1  --   -0.4337 --  1.7380E-3
 17.0 I  3.0232E-1  --  3.0392E-1  --   -0.5271 --  1.6301E-3
 18.0 I  3.0320E-1  --  3.0581E-1  --   -0.7449 --  1.5532E-3
 19.0 I  3.0410E-1  --  3.0703E-1  --   -0.9357 --  1.4086E-3
 20.0 I  3.0550E-1  --  3.0040E-1  --   -0.9401 --  1.4132E-3
 21.0 I  3.0604E-1  --  3.0906E-1  --   -1.2163 --  1.3526E-3
 22.0 I  3.0697E-1  --  3.1118E-1  --   -1.3707 --  1.2950E-3
 23.0 I  3.0790E-1  --  3.1245E-1  --   -1.4769 --  1.2447E-3
 24.0 I  3.0603E-1  --  3.1367E-1  --   -1.5668 --  1.1973E-3
 25.0 I  3.1069E-1  --  3.1405E-1  --   -1.336, --  1.1539E-3
 26.0 I  3.1163E-1  --  3.1590E-1  --   -1.3973 --  1.1136E-3
 27.0 I  3.1349E-1  --  3.1708E-1  --   -1.1453 --  1.0760E-3
 28.0 I  3.1442E-1  --  3.1813E-1  --   -1.1887 --  1.0411E-3
 29.0 I  3.1516E-1  --  3.1916E-1  --   -1.2668 --  1.0004E-3
 30.0 I  3.1442E-1  --  3.2015E-1  --   -1.0243 --  9.7702E-4
 31.0 I  3.1440E-1  --  3.2111E-1  --   -2.1307 --  9.4913E-4
```

These listings give:

a. the power function from which the results were calculated.

b. the results:

    1. in column 1: time in hours
    2. in column 2: measured data (%)
    3. in column 3: data calculated from the equation (%)
    4. in column 4: difference between data calculated and measured
    5. in column 5: the rate in %/h

7.2 The different equations calculated for six tests are given in Tables 5 and 6.

We can see from these tables the differences which occur between equations corresponding to tests carried out at the same temperature. These differences and in some cases the absence of equation are due to technical incidents during tests (i.e. failure of oven, liquid nitrogen tank empty, high noise on the QCMs or failure of LN_2 regulation (LN_2 valves still open).

These incidents are the cause of variations in the data recorded (re-evaporation of contaminants from QCMs when the LN_2 is missing for example) and consequently of modification in the calculated equations. These incidents have been particularly frequent during the last three tests.

7.3 The curves measured and calculated (Figure 3) for TML and CVCM for each test indicate a fair correlation for the total mass loss, except for test 1049 (instabilities due to ice-drift on the vacuum balance), but are not conclusive in the case of CVCM.

8. PREDICTIONS

From the equations given in Tables 5 and 6, we calculated the % TML, % TML rate, % CVCM and % CVCM rate predictions from 1 to 10^5 hours. These predictions are shown in Tables 7, 8 and 9.

9. CONCLUSION

The results obtained show large discrepancies between them. These are mainly due to technical incidents during the tests and inaccurate zero during the analysis of recordings.

These differences influenced the equations used to carry out the calculations for the predictions.

Concerning the form of equation used to carry out the calculation, the power function is the best one that could be found at the moment to fit the experimental data, but it is not in agreement with any theory that this casts a doubt on the far away extrapolation. To validate a theory, a lot of long time duration tests (minimum three hundred hours for each sample without incident) should have been run. The predicted outgassing after 10^5 hours is, however, within a factor around 2 for TML and 10 for CVCM.

Notwithstanding their lack of accuracy, the results given in this paper should be sufficient to assess the contamination risk of the satellite with a reasonable confidence.

Action/failure	1042 time (h)	1043 time (h)	1044 time (h)	1045 time (h)	1046 time (h)	1047 time (h)	1049 time (h)
Mounting sample	-6	-27	-18	-5	-1	-1	-1
Pump down	-5	-26	-17	-4	0	0	0
Cooling QCMs	-3	-24	-15	-2			
Heating sample	0	0	0	0			
LN_2 failure					47th to 105 tank empty		
Oven failure					302 and 304 h 390 and 395 h		
Noise effects (unknown origin, probably electrical)					No data on QCMs. Too much noise	No data on QCMs. Too much noise	No data on QCMs. Too much noise
LN_2 valves frozen					Valves frozen	Valves frozen	Valves frozen

TABLE 1

0 : starting point of data

Test Number	Sample Number	TML T^oC sample + 125^oC	CVCM -25^oC	CVCM -75^oC	CVCM -100^oC	CVCM -160^oC	Observations
1042	3	* X 3h	* X 3h	* X 3h			* cooling time duration of QCMs before sample heating
1043	1	X			* X 24h	* X 24h	
1044	2				* X 15h	* X 15h	** long duratic test (400 h)
1045	4	X	* X 2h	* X 2h			
10~	**6	X T sample + 80^oC	X	X		X	*** two tests have been carried out. 1st: 24h at 100^oC 2nd: one week at 125^oC after recovering at 65% RH, 25^oC during m re than 48 h.
1047	***5	X T sample + 100^oC	X	X		X	
1049	5	X T sample + 125^oC	X	X		X	

TABLE 2

For the tests 1046 and 1047 the cooling of the QCM and heating of the sample have been started together under dry nitrogen at atmospheric pressure before pump dow..

238

m/e	$P=5\times10^{-7}$ torr $T?$ $(To+1)$ Amp	$P=2\times10^{-7}$ torr $T2$ $(To+15)$ Amp	$P=1.3\times10^{-7}$ torr $T3$ $(To+25)$ Amp	$P=1.5\times10^{-7}$ torr $T4$ $(To+38)$ Amp	$P=9\times10^{-8}$ torr $T5$ $(To+49)$ Amp	$P=?\times10^{-8}$ torr $T6$ $(To+73)$ Amp	$P=7\times1^{-8}$ torr $T7$ $(To+?7)$ Amp
1	6×10^{-11}	–	–	–	–	–	–
2	9.6×10^{-11}	3.2×10^{-12}	2.9×10^{-12}	1.7×10^{-12}	1.9×10^{-12}	1.4×10^{-12}	9×10^{-13}
12	1.5×10^{-11}	2.5×10^{-13}	–	–	–	–	–
13	–	–	–	–	–	–	–
14	6×10^{-11}	2.3×10^{-12}	2×10^{-12}	1.4×10^{-12}	1.5×10^{-12}	1.3×10^{-12}	9×10^{-13}
15	1.5×10^{-11}	–	–	–	–	–	–
16	9×10^{-11}	2.7×10^{-12}	2×10^{-12}	1.7×10^{-12}	1.5×10^{-12}	1.1×10^{-12}	5×10^{-13}
17	3×10^{-10}	7×10^{-11}	6.2×10^{-12}	4.2×10^{-12}	3.5×10^{-12}	2.8×10^{-12}	1.3×10^{-12}
18	1.3×10^{-9}	2.2×10^{-10}	1.4×10^{-10}	1.1×10^{-10}	8×10^{-11}	8×10^{-11}	4.9×10^{-12}
28	6.9×10^{-10}	3.4×10^{-10}	2.9×10^{-10}	2.3×10^{-10}	2.6×10^{-10}	1.7×10^{-10}	1.6×10^{-10}
32	1.2×10^{-10}	6×10^{-11}	8.9×10^{-12}	6.6×10^{-12}	8×10^{-12}	4×10^{-12}	3.5×10^{-12}
40	2.1×10^{-11}	2.5×10^{-12}	2.1×10^{-12}	1.9×10^{-12}	1.7×10^{-12}	1.1×10^{-12}	6.8×10^{-13}
44	1.5×10^{-10}	6×10^{-11}	4.2×10^{-12}	3×10^{-12}	2.2×10^{-12}	1.3×10^{-12}	9×10^{-13}
55	4×10^{-12}	–	–	–	–	–	–
57	4×10^{-12}	–	–	–	–	–	–
57	3×10^{-12}	–	–	–	–	–	–
69	3×10^{-12}	–	–	–	–	–	–
79	4×10^{-12}	–	–	–	–	–	–

TABLE 3

Note: To is the time of measurement of the pressure after the 2nd hour after pump down of the sample.

P is the pressure at the time when the recording has been carried out

Test Number	Sample Number	Results
1042	3	HC : 5.4×10^{-5} E : $\dfrac{3.1\times10^{-5}}{8.5\times10^{-5}}$ g
1043	1	HC : 2.5×10^{-5} E : $\dfrac{1.5\times10^{-5}}{4\times10^{-5}}$ g
1044	2	HC : 8.5×10^{-5} E : $\dfrac{2.6\times10^{-5}}{1.11\times10^{-4}}$ g
1045	4	HC : 1.25×10^{-4} E : $\dfrac{0.70\times10^{-4}}{1.95\times10^{-4}}$ g
1046	6	HC : 2.04×10^{-5} E : $\dfrac{8.90\times10^{-6}}{2.93\times10^{-5}}$ g
1047	5	HC : 2.89×10^{-5} E : $\dfrac{1.13\times10^{-5}}{4.02\times10^{-5}}$ g

TABLE 4

HC = hydrocarbon
E = ester

These results have been obtained according to document PSS-15/QRM-05T.

Test No.	% TML	Sample Temp.	Rate TML (%/h)
1042	0.03660 $0.2980(T)$	$125^{\circ}C$	$1.4567\times10^{-2}T^{-0.96340}$
1043	0.02976 $0.3409(T)$	$125^{\circ}C$	$1.0145\times10^{-2}T^{-0.97024}$
1044	0.02662 $0.280(T)$	$125^{\circ}C$	$7.4772\times10^{-3}T^{-0.97338}$
1045	0.5523 $0.3355(T)$	$125^{\circ}C$	$1.0529\times10^{-2}T^{-0.94477}$
1046	0.09162 $0.2344(T)$	$80^{\circ}C$	$2.1475\times10^{-2}T^{-0.90938}$
1047	0.09742 $0.1812(T)$	$100^{\circ}C$	$1.7648\times10^{-2}T^{-0.90260}$
1049	0.02330 $0.1873(T)$	$125^{\circ}C$	$4.375\times10^{-2}T^{-0.97670}$

TABLE 5

Test Number	% CVCM		Temp. °/C	Rate CVCM (%/h)	
1042	0.001107T	0.1916	-25	$2.1210 \times 10^{-4}T$	-0.6084
1042	0.001246T	0.2311	-75	$2.8795 \times 10^{-4}T$	-0.7689
1043	0.000904T	0.3256	-100	$2.9317 \times 10^{-4}T$	-0.6744
1043	0.001012T	0.3570	-160	$4.0286 \times 10^{-4}T$	-0.6430
1044	0.001161T	0.2987	-100	$.3.4679 \times 10^{-4}T$	-0.7013
1044	0.001232T	0.3276	-160	$4.0360 \times 10^{-4}T$	-0.6724
1045	0.000611T	0.3513	-25	$2.1464 \times 10^{-4}T$	-0.6487
1045	0.000899T	0.3026	-75	$2.7203 \times 10^{-4}T$	-0.6974
1046	ND		-75	ND	
1046	ND		-75	ND	
1047	ND		-25	ND	
1047	ND		-25	ND	
1049	ND			ND	
1049	ND			ND	

TABLE 6

Time	test 1042	test 1043	test 1044	test 1045	test 1	test 1047	test 1049
1	2.98×10^{-1}	3.45×10^{-1}	2.80×10^{-1}	2.96×10^{-1}	2.34×1	1.81×10^{-1}	1.88×10^{-1}
10	3.24×10^{-3}	3.65×10^{-1}	2.98×10^{-1}	3.81×10^{-1}	2.89×10	2.26×10^{-1}	1.98×10^{-1}
10^2	3.52×10^{-1}	3.91×10^{-1}	3.17×10^{-1}	4.32×10^{-1}	3.57×10^{-1}	2.83×10^{-1}	2.09×10^{-1}
10^3	3.83×10^{-1}	4.18×10^{-1}	3.37×10^{-1}	4.91×10^{-1}	4.13×10^{-1}	3.55×10^{-1}	2.21×10^{-1}
10^4	4.17×10^{-1}	4.48×10^{-1}	3.58×10^{-1}	5.58×10^{-1}	5.45×10^{-1}	4.44×10^{-1}	2.33×10^{-1}
10^5	4.54×10^{-1}	4.80×10^{-1}	3.81×10^{-1}	6.35×10^{-1}	6.73×10^{-1}	5.56×10^{-1}	2.46×10^{-1}

TABLE 7

Time	test 1042	test 1043	test 1044	test 1045	test 1046	** test 1047	*** test 1049
1	1.456×10^{-2}	1.014×10^{-2}	7.472×10^{-3}	1.853×10^{-2}	2.147×10^{-2}	1.764×10^{-2}	4.375×10^{-3}
10	1.585×10^{-3}	1.086×10^{-3}	7.944×10^{-4}	2.103×10^{-3}	2.651×10^{-3}	2.208×10^{-3}	4.016×10^{-4}
10^2	1.724×10^{-4}	1.163×10^{-4}	8.44×10^{-5}	2.38×10^{-4}	3.273×10^{-4}	2.764×10^{-4}	4.871×10^{-5}
10^3	1.875×10^{-5}	1.246×10^{-5}	9.981×10^{-6}	2.712×10^{-5}	4.042×10^{-5}	3.459×10^{-5}	5.140×10^{-6}
10^4	2.041×10^{-6}	1.334×10^{-6}	9.53×10^{-7}	3.080×10^{-6}	4.992×10^{-6}	4.329×10^{-6}	9.14×10^{-7}
10^5	2.22×10^{-7}	1.43×10^{-7}	1.02×10^{-8}	3.50×10^{-7}	6.16×10^{-7}	5.42×10^{-7}	5.7×10^{-8}

TABLE 8

**
*** see test conditions

Time (hrs)	test 1042 at -25 C % CVCM	test 1042 at -25°C %/h	test 1042 at -75°C % CVCM	test 1042 at -75°C %/h	test 1043 at -100°C % CVCM	test 1043 at -100°C %/h	test 1043 at -160°C % CVCM	test 1043 at -160°C %/h
1	1.11×10^{-3}	2.12×10^{-4}	1.25×10^{-3}	2.87×10^{-4}	9.00×10^{-4}	2.93×10^{-4}	1.01×10^{-3}	4.02×10^{-4}
10	1.72×10^{-3}	3.29×10^{-5}	2.12×10^{-3}	4.9×10^{-5}	1.9×10^{-3}	6.2×10^{-5}	2.30×10^{-3}	9.16×10^{-5}
10^2	2.67×10^{-3}	5.12×10^{-6}	3.61×10^{-3}	8.34×10^{-6}	4.03×10^{-3}	1.3×10^{-5}	5.23×10^{-3}	2.08×10^{-5}
10^3	4.16×10^{-3}	7.96×10^{-7}	6.14×10^{-3}	1.42×10^{-6}	8.53×10^{-3}	2.77×10^{-6}	1.19×10^{-2}	4.74×10^{-6}
10^4	6.46×10^{-3}	1.23×10^{-7}	1.05×10^{-2}	2.41×10^{-7}	1.80×10^{-2}	5.19×10^{-7}	2.71×10^{-2}	1.08×10^{-6}
10^5	1×10^{-2}	1.92×10^{-8}	1.78×10^{-2}	4.11×10^{-8}	3.82×10^{-2}	1.24×10^{-7}	6.16×10^{-2}	2.45×10^{-7}

Time (hrs)	test 1044 at -100°C % CVCM	test 1044 at -100°C %/h	test 1044 at -160°C % CVCM	test 1044 at -160°C %/h	test 1045 at -25°C % CVCM	test 1045 at -25°C %/h	test 1045 at -75°C % CVCM	test 1045 at -75°C %/h
1	1.16×10^{-3}	3.46×10^{-4}	1.23×10^{-3}	4.03×10^{-4}	6.11×10^{-4}	2.15×10^{-4}	9×10^{-4}	2.72×10^{-4}
10	2.31×10^{-3}	6.9×10^{-5}	2.62×10^{-3}	8.58×10^{-5}	1.37×10^{-3}	4.81×10^{-5}	1.8×10^{-3}	1.1×10^{-5}
10^2	4.6×10^{-3}	1.37×10^{-5}	5.57×10^{-3}	1.82×10^{-5}	3.08×10^{-3}	1.08×10^{-3}	3.62×10^{-3}	1.1×10^{-5}
10^3	9.13×10^{-3}	2.73×10^{-6}	1.18×10^{-2}	3.82×10^{-6}	6.9×10^{-3}	7.43×10^{-6}	7.27×10^{-3}	2.2×10^{-6}
10^4	1.91×10^{-2}	5.43×10^{-7}	2.51×10^{-2}	8.24×10^{-7}	1.55×10^{-2}	5.45×10^{-7}	1.46×10^{-2}	4.41×10^{-7}
10^5	3.61×10^{-2}	1.08×10^{-7}	5.35×10^{-2}	1.75×10^{-7}	3.48×10^{-2}	1.22×10^{-7}	2.93×10^{-2}	8.86×10^{-8}

TABLE 9

These results are plotted on the following curves.
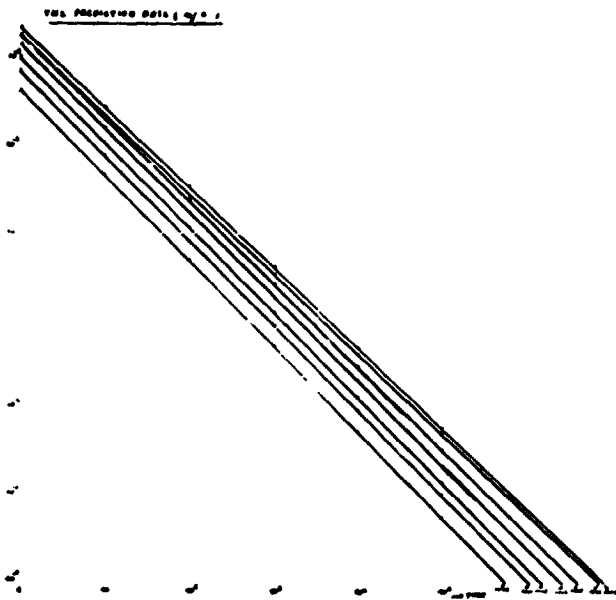
TML prediction rates
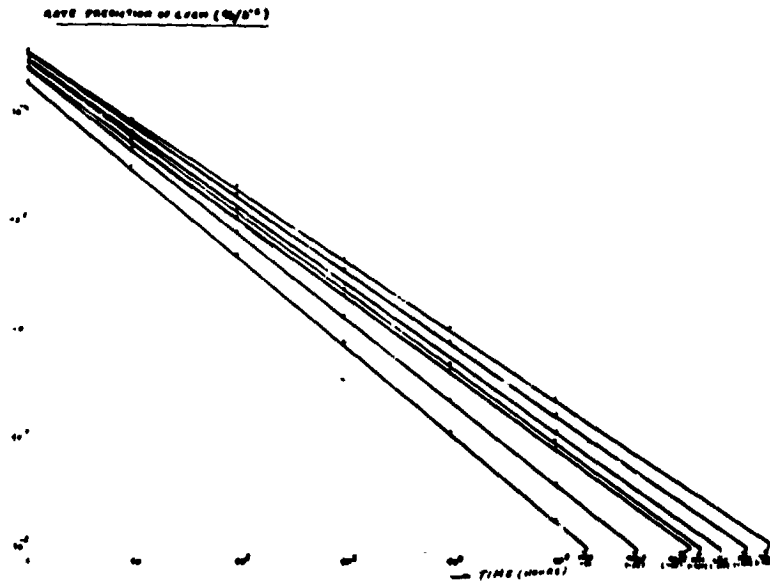
CVCM prediction rates

IUS SOLID ROCKET MOTOR CONTAMINATION
PREDICTION METHODS

C. R. Mullen* and J. H. Kearnes*

ABSTRACT

The Inertial Upper Stage (IUS) will provide transportation from low earth orbit to synchronous orbit or for interplanetary missions for many future spacecraft. The IUS Solid Rocket Motors represent a potential spacecraft contamination source which must be considered by spacecraft designers. A series of computer codes have been developed to predict solid rocket motor produced contamination to spacecraft sensitive surfaces. Subscale and flight test data have confirmed some of the analytical results. Application of the analysis tools to a typical spacecraft has provided early identification of potential spacecraft contamination problems and provided insight into their solution; e.g., flight plan modifications, plume or outgassing shields and/or contamination covers.

INTRODUCTION

A number of spacecraft with solid rocket motors (SRM's) have experienced degradation of thermal control with a resultant shortening of operational life, apparently due to contamination. Others have flown with calorimeters, reflectance gauges or quartz crystal microbalances and have measured various levels of contamination. The amount of instrumentation and locations have been limited on all spacecraft measurements, making it impossible to differentiate between sources of the apparent contamination.

In 1978, the Boeing Aerospace Company proceeded to develop analytical tools to predict contamination associated with the solid rocket motors of the Inertial Upper Stage (IUS). This effort resulted in a series of computer codes that defined the characteristics of exhaust flow fields, the chemical species generated and the resulting contamination.

Table I summarizes all sources of contamination experienced by a spacecraft from ground operations through the end of life (EOL) of the spacecraft and the currently-known mechanisms of transport of the contaminants from the source to the receiver. This paper discusses the SRM sources and transport mechanisms. It describes the analytical tools developed and the application of these tools to a typical spacecraft.

ANALYSIS TOOLS

A number of analytical tools have been developed to define the contamination from a solid rocket motor. The definition of the chemical species, thermodynamic and flow field properties of the motor exhaust were accomplished using existing computer codes which were modified for contamination prediction purposes. Figure 1 illustrates the analysis approach and shows the various computer codes (in parentheses) used for the different parts of the flow field. The following paragraphs describe in more detail each individual computer code or analytical approach.

*The Boeing Aerospace Company, Seattle, Washington

Combustion Chamber

In the combustion chamber and during the nozzle expansion, the chemical species and their thermodynamic properties were calculated using the CHEM program from the Plume Interference Prediction (PIP) computer codes (Reference 1). The chamber calculations are performed initially with the condensed species considered to obtain the proper combustion properties and to determine the percentage of condensed species in the flow. All condensed species are then removed from the list of possible products being considered. The chamber calculations and subsequent equilibrium chemistry expansion are then made with a gaseous-only composition. When the thermodynamic calculations are completed, the transport properties are calculated. A matrix of thermodynamic and transport properties are generated for various assumed levels of heat transfer between condensed species and the gas. This matrix then provides the data required in the nozzle expansion process to account for heat transfer and drag between particles and gas. The code has the option of equilibrium chemistry to the nozzle exit or chemistry can be frozen at a designated area ratio. The thermochemical data are then used as an input to PIP to define the nozzle exhaust flow field.

Nozzle Inviscid Flow Field

The nozzle inviscid flow field is calculated using the PIP computer code which uses a modified method of characteristics. The PIP computer program is designed to give detailed flow field information in the supersonic region of a reacting multiphase two-dimensional or axisymmetric flow field.

The flow of a gas/particle mixture is described by the equations for conservation of mass, momentum and energy. The code is fully coupled in that it considers the exchange of momentum and energy between the gas and particle phases. The equilibrium thermochemistry data were generated as described in the previous paragraph. In the gaseous phase the state variables pressure, density and temperature are related by the equation of state while for the particulate phase the equations are for the particle drag, particle heat balance and the particle equation of state.

A particle size distribution is input in the combustion chamber and the interactions of the particles with the gas (drag and heat transfer) define a radial mass distribution and limiting streamlines for the various size particles.

From the PIP code the nozzle exit plane inviscid thermodynamic and flow field properties are defined. The exit conditions must now be modified to include boundary layer effects.

Nozzle Boundary Layer

Earlier studies (Reference 2, 3, 4 and 5) have shown that nozzle boundary layers allow the flow field to expand to much greater angles than an inviscid solution. The Boundary Layer Integral Matrix Procedure (BLIMP) computer code computes nonsimilar chemically-reacting laminar or turbulent boundary layers for ablating, transpiration cooled or non-ablating internal flows (Reference 6). The program considers either local thermodynamic equilibrium or frozen composition for a general propellant gas. The code calculates both the subsonic and supersonic parts of the boundary layer and defines the velocity and

244

temperature profiles. It uses the axial pressure and velocity gradients along the nozzle wall as defined by the inviscid flow field calculation. Wall temperatures from full scale development motor tests are used as input to include heat transfer at the wall.

After calculating the boundary layer the PIP code exit plane conditions are modified near the nozzle wall to account for the boundary layer thickness and velocity profile.

Nozzle Exhaust Flow Field (Past Exit)

The exit plane conditions are modified to include boundary layer effects by superimposing the profiles calculated in BLIMP. The subsonic layer is simulated using the method of Cooper (Reference 5) where the subsonic portion is isentropically accelerated to conditions slightly above sonic conditions. With the nozzle exit properties modified to include viscous effects, the PIP code is restarted to calculate the exhaust plume.

A free molecular flow calculation has been provided as an option which permits treatment of the rarified regions of the plume. As the gas expands, the translational, vibrational and rotational modes freeze based on a Knudsen number of 10, 1.0 and 0.1 respectively. At freezing, the solution switches to an effective source solution. The streamlines are considered straight and the velocity constant. Conservation of mass then determines the density while other properties are found from the equation of state.

Molecular Flow Field

The CONSIM (Contamination Simulation) computer code was developed to predict the flux of molecules which have sufficient thermal energy to escape the plume in the direction of a critical spacecraft surface.

Conceptually, the program is very simple. A spacecraft geometry is constructed by building up simple shapes which can be defined mathematically; i.e., cylinders, spheres etc. The exhaust plume is likewise defined as a cone, which hereafter will be referred to as the emitting surface. The position of this emitting surface was chosen so that on one side the flow can be described by a continuum model, which implies small mean free paths or high collision frequencies, while on the other side of the surface the flow is in a free molecular regime with large mean free paths and low collision frequencies. The properties of mean flow velocity, Mach number, flow angle and gamma were calculated using the PIP computer code and input to CONSIM as constants. Density variations were also calculated externally and assumed to vary as $1/r^2$ along the emitting surface.

After the geometry and properties of the emitting surface have been defined, a Monte Carlo technique is employed to calculate the flux of molecules hitting any surface of the spacecraft. The basic procedure is to look at the percentage of molecules which have sufficient thermal energy to escape from a random point on the emitting surface in a random direction. After a number of points and directions have been investigated, a solution for the flux is converged on.

The program calculates a characteristic thermal speed (U_c) of the flow defined as the bulk velocity of the flow divided by the most probable velocity.

245

The most probable velocity for several species is plotted in Figure 2. By assuming the flow is in local thermodynamic equilibrium at the emission point implies that the thermal velocity is given by a Maxwell-Boltzmann distribution and that all directions of the velocity are equally probable. Figure 3 is the thermal velocity distribution for several species at a temperature of 200° K. From the equation in Figure 3 the shape of the curves are seen to be very dependant on this characteristic velocity.

Random thermal directions and velocities are chosen which are then vectorally added to the mean flow at the emission point. This resultant direction is then weighted by the fraction of molecules with this velocity and is then checked to see which, if any, spacecraft surfaces are hit. Tallies of the hits and misses for each surface are kept and after sufficient random directions and velocities are investigated, a converging solution for flux impinging on each surface is obtained.

Ambient Scattering

During SRM burns near low earth orbit, the ambient atmosphere is dense enough that exhaust products may be scattered by the oncoming ambient molecules and contaminate parts of the payload surface.

Exhaust products from the motor are scattered by collisions with the atmosphere which has a directed velocity V_{SC} (Figure 4) equal to the velocity of the spacecraft. Those exhaust particles in the volume element dV which are scattered into the solid angle Ω subtended at the volume element by the payload surface area A_{SC} will strike the payload and are assumed to stick. The model does not include self-scattering of the exhaust gas nor are multiple collisions with the ambient atmosphere considered. The amount of contamination in moleclues per unit area striking the payload surfaces is given by:

$$C = \int \frac{S(t,\theta)}{\rho^2} \frac{\nu(t,\phi)}{A_{SC}} \frac{\Omega(\rho,\theta)}{4\pi} dV \, dt \qquad (1)$$

where:

$\dfrac{S(t,\theta)}{\rho^2}$ is the source term which describes the density of exhaust-gas molecules as a function of time t, angle θ, and radial distance ρ.

$\dfrac{\nu(t,\phi)}{A_{SC}}$ is a term describing the collision frequency as a function of time and which also takes into account the angular ϕ dependence of the collision cross section of the exhaust molecules with the ambient gas. A_{SC} is the area of the payload.

$\dfrac{\Omega(\rho,\theta)}{4\pi}$ is a geometrical term representing the ratio of the solid angle subtended by the payload to the total solid angle 4π.

$\int dV \, dt$ represents integration over all appropriate volume and time.

Following burnout the exhaust flow field is assumed of the form:

$$\frac{S(t,\theta)}{\rho^2} = \frac{A(t)\cos\theta}{\rho^2} \qquad (2)$$

where A(t) is function of time as the internal insulation cools and outgassing slows.

The collision frequency term is given by (3)

$$\nu(t,\phi) = N(t)\,\sigma(\phi)\,V_{SC}(t)$$

$N(t)$ is the particle density of the ambient atmosphere and is a function of time because the spacecraft is changing altitude.

V_{SC} is the spacecraft velocity and $\sigma(\phi)$ is the cross section for collisions between the exhaust gas and the ambient atmosphere, and

$$\sigma(\phi) \simeq 4\cos\phi\,\sigma_{cm}\qquad(4)$$

where σ_{cm} is the cross section measured in the center of mass frame of the colliding particles.

By determining the solid angle subtended by the volume element and substituting for the volume element, the integral can be rewritten. During burnout when the vehicle may be pointing the outgassing nozzle into the wind, the integral is:

$$C = K \int_{t_{retrograde}}^{t_{posigrade}} A(t)\,V_{SC}(t)N(t)dt \int_{0}^{\pi/2} \int_{R_e}^{\infty} \frac{(X\cos\theta+1)\cos\theta\sin^2\theta\,X}{(X^2+1+2X\cos\theta)^2} dXd\theta \qquad(5)$$

where $K = \dfrac{2\sigma_{cm}}{d}$ and $X = \rho/d \quad \overline{d\sin\theta}$

Similarly, during main motor burn, an equivalent integral can be constructed by modifying the source term, geometry and integration limits.

Heat Soak Outgassing

During and after burnout of a solid rocket motor, heat from the combustion chamber conducts through the insulation to the motor case materials and heats them to temperatures which can significantly increase the case material outgassing rates resulting in severe contamination to spacecraft. The analysis approach is to use a one dimensional heat conduction equation to define temperatures vs. time on the external surface of the case. Test data are required to define the volatile condensible materials (VCM) which will emanate from the motor case at the predicted operational temperatures. Table II summarizes the information required and the assumptions for this analysis.

TYPICAL SPACECRAFT CONTAMINATION ANALYSIS

The analytical tools described in the previous paragraphs were applied to the IUS and a typical spacecraft as shown in Figure 5. Typical flight operations which affect contamination are the 111 second SRM1 burn, the 5 hour 10 minute coast with the SRM1 attached, SRM1 - 2 separation, SRM2 burn of 77 seconds and the contamination/collision avoidance maneuver occuring 55 minutes after SRM2 burnout. The following paragraphs describe the results of a steady state and transient analysis of the inter-molecular scattering in the SRM exhaust plume, ambient scattering during SRM operation in low earth orbit, ambient scatter of internal insulation during a possible retrograde maneuver and outgassing of the Kevlar epoxy motor case following SRM burnout and heat soak.

Steady State

The steady state analysis was made assuming the SRM operated at a constant 200 psia chamber pressure. The exhaust flow field was defined with and without a boundary layer in the nozzle as shown in Figure 6. The boundary layer thickness is approximately 0.1 inches thick. A boundary between free molecular flow and continuum flow was defined in the exhaust flow where the Knudsen number is ten. It was assumed that a majority of the molecules which would escape the exhaust plume would eminate from this location. Using the properties of the exhaust flow field along this surface and assuming an average gas molecular weight, the deposition of contamination along the vehicle surface is shown in Figure 5. This is equivalent to a molecular layer on approximately 0.000U5 percent of the surface area of the spacecraft. Since the exhaust flow field contains a large number of different molecules of various molecular weights, (Table III), and thermal molecular velocities are exponentially dependant on molecular weight, consideration was given to the effects of molecular weight on inter-molecular scattering. Hydrogen gas has the lowest molecular weight of the species and would (if the gas were to stick) put about 300 molecular layers of hydrogen on 100 percent of the surface. Assuming molecular carbon with a molecular weight of 12 is in the flow, an equivalent of one molecular layer over 0.005 percent of the surface area of the spacecraft results.

Transient Analysis

A simplified transient analysis was conducted because inter-molecular scattering increases exponentially with decreasing mean flow velocity during ignition and burnout transients. Steady flow fields were defined for transient chamber pressure conditions of 1, 30, 60, 100 and 200 psia. The ignition transient duration is approximately 0.15 seconds. The burnout transient, when considering the insulation outgassing after motor burnout, will last for four to five minutes (see Figure 7). This decay rate is defined using a combination of rubber insulation outgassing test data and analytical procedures as outlined in Reference 7. Inter-molecular scattering was defined for each of the chamber pressure conditions as shown in Figure 8 for SRM1 and 2. As the chamber pressure decreases a significant increase in molecular flux to the spacecraft is noted which peaks and begins to decline as the flow approaches a free molecular condition. SRM2 flux is small because of the smaller motor.

A summary of the ignition and burnout transients and the steady state flow field contamination is shown in Figure 9. It is evident that the transient burnout is the largest contributor to spacecraft contamination.

Ambient Scattering (Main Burn)

In the lower atmosphere (150-300 Km), the ambient environment is sufficiently dense to scatter the exhaust gas molecules in the backflow region during SRM1 operation. The ambient scattering model described earlier was used. Two atmospheric models were used, Reference 8, for the mean density atmosphere and Reference 9, for the maximum density atmosphere. Using a collision cross section of 5.0×10^{-15} cm^2, a molecular radius of two Angstroms and a typical trajectory, the ambient scattered molecules produce 1.51×10^{-5} microgram/cm^2 of contamination on the spacecraft.

Ambient Scattering (Retro-Grade Maneuver)

From a Titan Launch, the SRM1 boosts the IUS and typical spacecraft from low earth orbit toward synchronous orbit. Following SRM1 boost, a velocity vector correction may be required using the aft facing RCS pitch and yaw motors. If a reduction in velocity is required, the IUS will be rotated 180 degrees to point the RCS system to reduce spacecraft velocity. During this time, the SRM1 outgassing is decaying exponentially. The oncoming ambient molecules will impinge upon the outgassing molecules and some will be scattered toward the spacecraft. The amount of deposition of contaminant is strongly a function of both the motor outgassing rate and ambient density both of which are decaying rapidly with time. Figure 4 shows the ambient scattered contamination occuring during an SRM1 retrograde maneuver. It is evident that a delay in the retrograde maneuver can significantly reduce contamination. Currently a 180 second time delay is used for the IUS.

SRM Heat-Soak

The external surfaces of the Kevlar epoxy motor cases of the IUS SRM's are expected to reach temperatures of 500°F 25 to 30 minutes after motor burnout from heat being conducted from the inside surfaces of the motor case. Tests conducted on Kevlar epoxy materials heated to 400°F and 600°F have measured volatile condensible material (VCM) of 0.03 percent and 1.4 percent respectively. An interpolated value of 0.8 percent has been assumed for a 500°F external wall temperature. Table II summarizes the results of the analysis and the assumptions. Most of the outgassing will condense on cool internal surfaces of the interstage and equipment support ring with very little being vented overboard. The only outgassing which could reach the spacecraft would be through the interface connector bracket ' 's predicted to be 0.42 micrograms/cm² from the SRM2 motor case. SRM1 rem. the payload until synchronous orbit is reached which is approximately five hours after SRM1 burnout. Temperatures of the motor case at this time are predicted to be approximately 350°F which will produce only minor outgassing (VCM = 0.03%). Contamination deposition to the spacecraft from the SRM1 motor case following separation will be negligible since the temperatures have dropped significantly and the time between separation and SRM2 ignition is only three minutes.

Summary of Contamination Flux

Contamination to spacecraft results from ground operations through spacecraft end of life operations. This report has addressed potential sources of contamination from the IUS solid rocket motors during transfer orbit operations. Table IV shows a summary of the levels of contamination from the various SRM sources. Note that the retrograde maneuver is delayed 180 seconds to reduce contamination and the contamination/collision avoidance maneuver precludes contamination from the SRM outgassing after separation by not allowing the SRM nozzle to point in the direction of the spacecraft.

ANALYSIS VERIFICATION

The amount of ground or flight data useful for verification of analytical tools is very limited and incomplete. The following paragraphs describe Lockheed and AEDC ground test data and GSFC flight data which provides some verification of the analytical tools.

LMSC Test Data

Lockheed Missiles and Space Company conducted subscale solid propellant motor tests with aluminum loadings of 2, 10 and 15 percent at simulated altitudes of 50,000, 100,000 and 112,000 feet for comparison with analytical predictions using the PIP code. The tests were conducted in the High Reynolds Number Wind Tunnel Test Facility at the Marshall Space Flight Center. The details of the test and analyses are found in Reference 10 and an example of the comparison is shown in Figure 10. This figure shows that the computer code predicted a drop in the pitot pressure radial distribution with an increase in aluminum concentration which correlated with a measured drop in pitot pressure from the test program. It would indicate that the computer code is correctly accounting for the gas-particle interactions on total pressure loss.

AEDC Bi-Pr pellant Data

In March 1978, AEDC reported data (Reference 11) taken on a 5-lbf bi-propellant motor for g.. flux measurements in the plume backflow. The motor used mono-methyl hydrazine (MMH) and nitrogen tetroxide (N_2O_4) as the fuel and oxidizer, respecti ''. Many combinations of oxidizer/fuel ratio, nozzle expansion ratio, c. amber pressure, chamber geometry and duty cycle were investigated to determine their effects on the flux. A standard configuration was chosen which had oxidizer/fuel = 1.6, expansion ratio - 100, chamber pressure - 100 psia, 2-inch cylindrical combustion chamber and one percent duty cycle of 100 msec pulses. The baseline configuration was placed in the AEDC 10 ft. diameter by 20 ft. long cryogenic test chamber and the backflow fluxes were measured by eight quartz crystal microbalances (QCM's). The QCM's were cooled to $25^\circ K$ and were placed 26 to 147 degrees from the thrust axis and 39.4 to 155 cm. from the nozzle exit. Figure 11 shows the test data plotted against the flux calculat. ' using the gasdynamic codes described previously. Reasonable correlation is obtained between the analysis a 1 test data to approximately 135 degrees

GSFC Flight Data

The Anchore Interplanetary Monitoring Platform (AIMP-E) was launched in 1967 with a contamination monitor on the fourth stage near the THIOKOL TE-M-458 re o motor (Reference 12). The contamination monitor consisted of a light source, a reflectance plate and a solar cell sensor. The configuration is shown in Figure 12 along with the measurements made by the instrument. Approximately three minutes after fourth stage burnout, the contamination monitor indicated a change in the absorptivity which continued for 15 minutes. The absorptivity of the reflecting surface changed from 0.1 to 0.25 during this time. The decreasing absorptance at 9 hours and 30 minutes is not understood. The total deposit is known to have remained approximately two hours before the data recording was terminated.

A number of observations should be made: 1) no contamination was noted during solid rocket motor firing (25 seconds) which would indicate that the contamination was not associated with intermolecular self scattering during motor firing, 2) the motor case started to increase in temperature at about 3 minutes after burnout and peaked at 21 minutes after motor burnout, indicating the apparent contamination could be from materials outgassing outside the motor case (mylar insulation covered motor area) , and 3) the contamination accumulation 3 to 18 minutes after motor burnout is consistent with the transient analysis which predicts the majority of contamination from intermolecular interactions occurs after motor burnout.

CONCLUSIONS

1. Analytical tools have been developed to predict spacecraft contamination from solid rocket motors. Limited ground and flight data have confirmed some of the analysis tool results. LMSC subscale test pitot pressure data shows a reduced total pressure with increasing aluminum particle concentration which is confirmed by the analytical tools. Analytical predictions of mass flux in the plume back flow region correlate with AEDC experimental measurements. AIMP-E flight data indicates significant contamination on a contamination monitor after motor burnout which correlates with the analytical predictions.

2. Application of the analysis tools to a typical spacecraft on the IUS have produced the following conclusions:

   a. The outer surface of the IUS Kevlar epoxy motor case reaches $500^\circ F$ 25 to 30 minutes after motor burnout which allows 0.42 micrograms per cm^2 direct flux to the spacecraft through the interface electrical connector plate. The thermal blanket at the IUS/spacecraft interface prevents significantly more contamination to the spacecraft.

   b. A delay in retrograde maneuver of 180 seconds following SRM1 burn reduces the spacecraft contamination from 2.6 microgram/cm^2 to 0.015 micrograms/cm^2. This contamination results from ambient molecules scattering SRM1 outgassing products toward the spacecraft during a negative velocity correction maneuver. No delay is required in the retro maneuver for SRM2 since the ambient density in synchronous orbit produces negligible scattering.

   c. Intermolecular (self) scattering of exhaust products toward the spacecraft during or following SRM burns is negligible. The burnout outgassing phase produces 1×10^{-8} micrograms/cm^2 compared to 1×10^{-18} micrograms/cm^2 during steady state burn.

ACKNOWLEDGEMENTS

REFERENCES

1. Curtis, J. T. et al, "Plume Interference Prediction (PIP) Code Volume I, Users Manual and Test and Evaluation Report; Volume II, Maintenance Manual and Operator's Manual,"Calspan Report KC-5900-A-6 Volumes I and II, April 1977

2. Boynton, F. P., "Exhaust Plumes from Nozzles with Wall Boundary Layers," AIAA Journal of Spacecraft Vol. 5 No. 10, October 1968

3. Simons, G. A. "Effect of Nozzle Boundary Layers on Rocket Exhaust Plumes," AIAA Journal, Volume 10 No. 11, November 1972

4. Chirivella, J. E., "Molecular Flux Measurements in the Back Flow Region of a Nozzle Plume," 7th Plume Conference (Proc. ARE Conference) JANNAF 1973 CPIA Publication 234

5. Cooper, B. P. Jr. "A computational Scheme Usable for Calculating the Plume Backflow Region," McDonnell Douglas Astronautics Company Report MDAC, Paper WD 2899, August 1978

6. Evans, R. M. "Boundary La r Integral Matrix Procedure, BLIMP-J User's Manual," Aerotherm UM-. -64, July 1975

7. Kavanaugh, D. J., "IUS Solid Rocket Motors Post-Burn Outgassing Performance Prediction," Boeing Document D290-10499-1, Oct. 23, 1979

8. U. S. Standard Atmosphere, 1976, prepared under sponsorship of ESSA, NASA and USAF

9. U. S. Standard Atmosphere Supplements, 1966, prepared under sponsorship of ESSA, NASA and USAF

10. Tevepaugh, J. A., Smith, S. D. and Denny, M. M. "Assessment of Analytical Techniques for Predicting Solid Propellant Exhaust Plumes and Plume Impingement Environments," LMSC-HREC TR D497079, January 1977

11. Scott, H. E., Frazine, D. F. and Lund, Lt. E. G., "Bipropellant Engine Plume Contamination Study," USAF/NASA International Spacecraft Contamination Conference, USAF Academy, CO, March 7-9, 1978

12. Sheehy, R. N., "Contamination Monitor," NASA TMX-63279, January 1968

Table I: Contamination Sources

CONTAMINATION SOURCE	CONTAMINATION TRANSPORT PHENOMENA			
	DIRECT FLUX	AMBIENT SCATTERING	SELF SCATTERING	ELECTRO STATICS
o GROUND OPERATIONS				
o LAUNCH VEHICLE NON-METALLIC MATERIALS OUTGASSING				
o LAUNCH VEHICLE PROPULSION OPERATIONS AND CONTROL				
o SPACECRAFT NON-METALLIC MATERIALS OUTGASSING				
o IUS NON-METALLIC MATERIALS OUT-OUTGASSING				
o IUS SRM-1 AND -2 BURNS				
A IGNITION TRANSIENT	X	X	X	
B STEADY-STATE	X	X	X	
C BURNOUT TRANSIENT	X	X	X	
D SRM INTERNAL INSULATION OUTGASSING	X	X	X	
E SRM HEAT SOAKOUT MATERIALS OUTGASSING	X	X	X	
o IUS/RCS OPERATIONS				
o SPACECRAFT FREEFLIGHT				

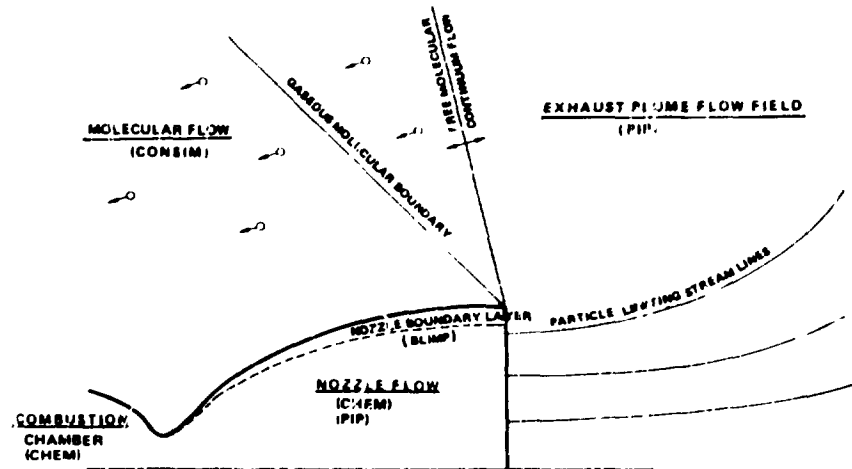X Indicates Contamination Sources Considered in this Paper
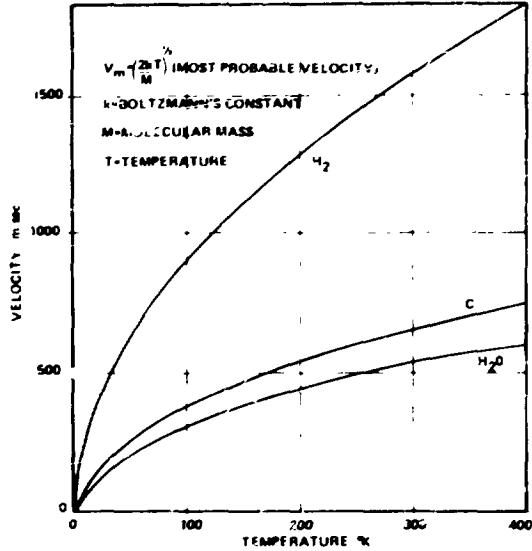

Figure 1: Analysis Approach

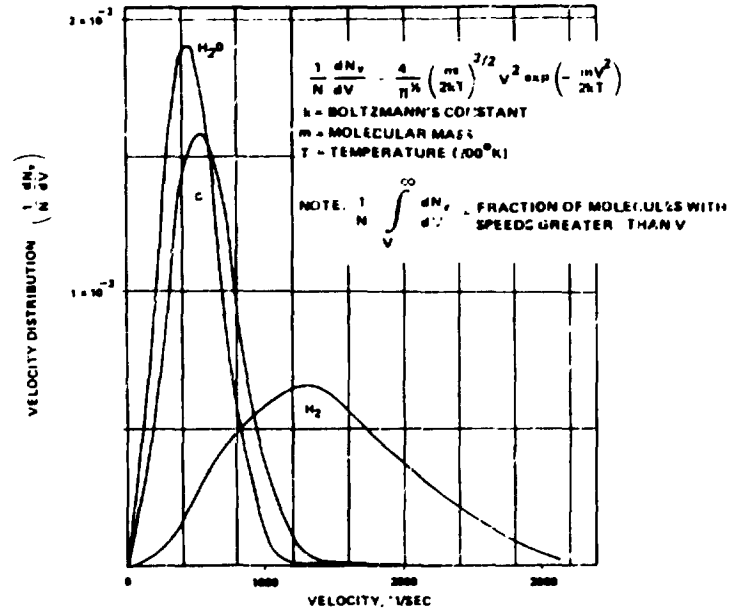Figure 2: Most Probable Thermal Velocity Versus Temperature

Figure 3: Thermal Velocity Distribution for Species
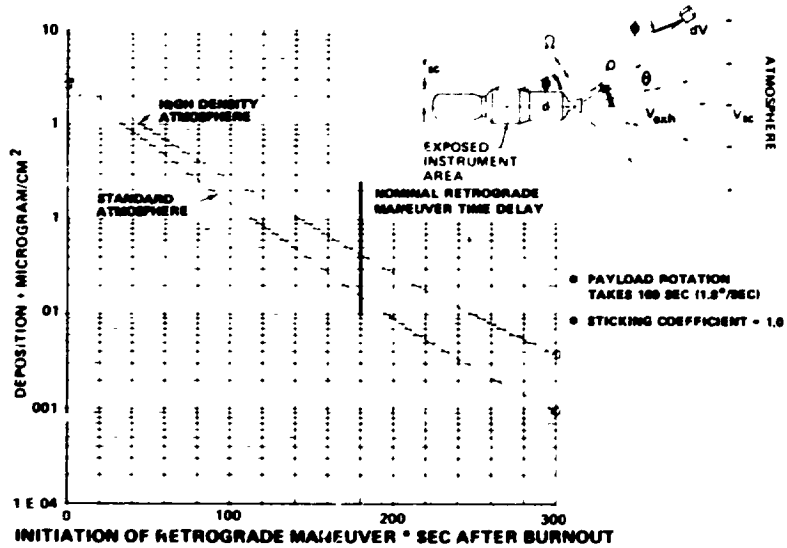
Figure 4: Contamination Deposition as a Function of Retrograde Maneuver Initiation Following SRM 1 Burnout

- PAYLOAD ROTATION TAKES 100 SEC (1.8°/SEC)
- STICKING COEFFICIENT - 1.0
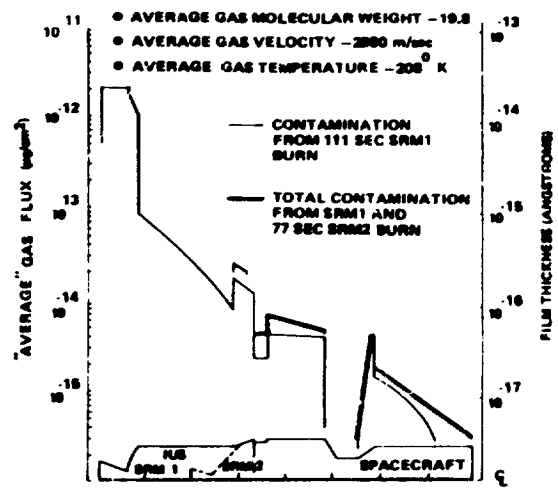
Figure 5: Average Exhaust Gas Molecular Deposition on IUS and Spacecraft

- AVERAGE GAS MOLECULAR WEIGHT - 19.8
- AVERAGE GAS VELOCITY - 2900 m/sec
- AVERAGE GAS TEMPERATURE - 208° K

Table II: VCM from SRM1 and 2 Kevlar Epoxy through Interface Bracket

STAGE	TOTAL WEIGHT LBS (GM)	VCM IN INTERSTAGE LBS (GM)	INTERSTAGE SURFACE AREA CM^2	INTERSTAGE SURFACE AREA TO ESS VENT AREA RATIO	ESS SURFACE AREA CM^2	INTERFACE BRACKET VENT AREA CM^2	VCM TO S/C Å
*SRM1	777.2 (3.53x10^5)	1.775 (805)	2.75x10^5	3.6x10^6	1.74x10^5	23.87	0604 (000006 GM)
SRM2	198.2 (8.99x10^5)	.6788 (308)			1.74x10^5	23.87	42 (021 GM)

*SRM1 CASE OUTGASSING CONDENSES ON INTERSTAGE AND ESS SURFACES.

ASSUMPTIONS

o 1/3 OF KEVLAR EPOXY VCM WILL OUTGAS INTO INTERSTAGE AREA FROM SRM1 HEATSOAK FOLLOWING MOTOR BURNOUT

o KEVLAR CASE OUTER SURFACES REACH 500°F TEMPERATURE

o ALL OUTGASSED MATERIAL GETS OUT OF MLI COVERING MOTOR CASE

o OUTGASSED MATERIAL WILL CONDENSE ON INTERSTAGE SURFACE (ASSUMING ITS TEMPERATURE IS APPROXI-MATELY 25°C)

o AMOUNT OF MATERIAL WHICH FLOWS THROUGH VENTS IS PROPORTIONAL TO THE FRACTION OF THE VENT AREA TO THE TOTAL COMPARTMENT SURFACE AREA

o 1/2 OF KEVLAR EPOXY MATERIAL WILL OUTGAS INTO ESS COMPARTMENT FROM SRM HEATSOAK FOLLOWING MOTOR BURNOUT

o 50% OF VCM IS EMITTED DURING FIRST 1/2 HOUR 99% AFTER 4 HOURS.

o VCM CONDENSES ON 50,670 CM^2 SURFACE AREA (BASED ON S/C DIAMETER)

o DENSITY OF VCM IS 1 GM/CM^3
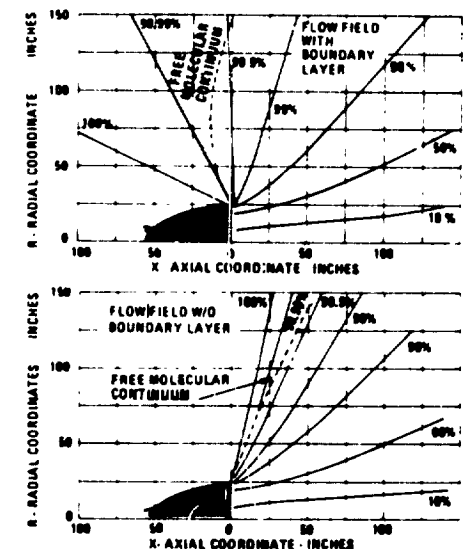
- PERCENT OF NOZZLE MASS FLOW
- GOOD FOR ALTITUDES ABOVE 100,000 FEET
- SRM EXPANDS 150° WITHOUT BOUNDARY LAYERS

Figure 6: SRM1 Exhaust Plume with and without Nozzle Boundary Layer

Table III: Potential Species in Backflow Region

SPECIES	MOLECULAR WEIGHT	$\dfrac{n_x^\circ}{n_{19.8}}$
H_2	2	4 36 E+18
C	12	4 04 E+08
NH_2	16	2 06 E+04
NH_3	17	1 71 E+03
H_2O	18	1 41 E+02
Average Gas	19 8	1 0
Na	23	5 15 E-04
HCN	27	2 16 E-08
CO	28	1 73 E-09
N_2	28	1 73 E-09
Cl	35 5	9 82 E-18
HCl	36 5	7 77 E-19
CO_2	44	4 09 E-27
AlOH	44	4 09 E-27
Fe	56	2 13 E-40
NaCl	58 5	3 60 E-43
AlO_2H	60	7 01 E-45
AlCl	62 5	1 32 E-47
Al_2O	70	6 19 E-56
KCl	74 5	6 19 E-61
AlOCl	78 5	1 13 E-62
FeCl	91 5	7 68 E-80
$Al Cl_2$	98	4 45 E-87
Al_2O_3	102	1 57 E-91
$Al Cl_3$	133.5	1 23 E-126

$$\frac{n_x^\circ}{n_{19.8}} = \frac{M_x}{M_{19.8}}^{3/2} \, e^{-(M_x-M_{19.8})\,V^2/2KT}$$

V = 2990 M/Sec (Flow Mean Velocity)
T = 208°K
M = Molecular weight
K = Boltzmann's constant
n = Number density
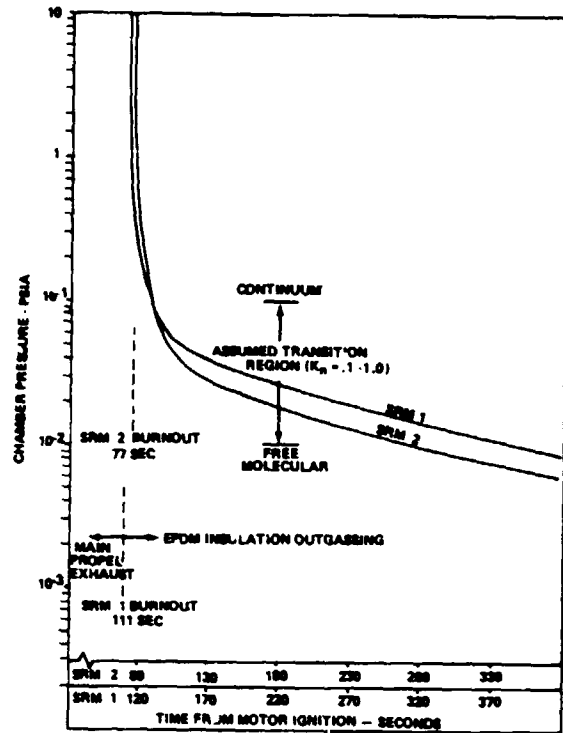
Figure 7: SRM1 & 2 Chamber Pressure Decay — Burnout Transient
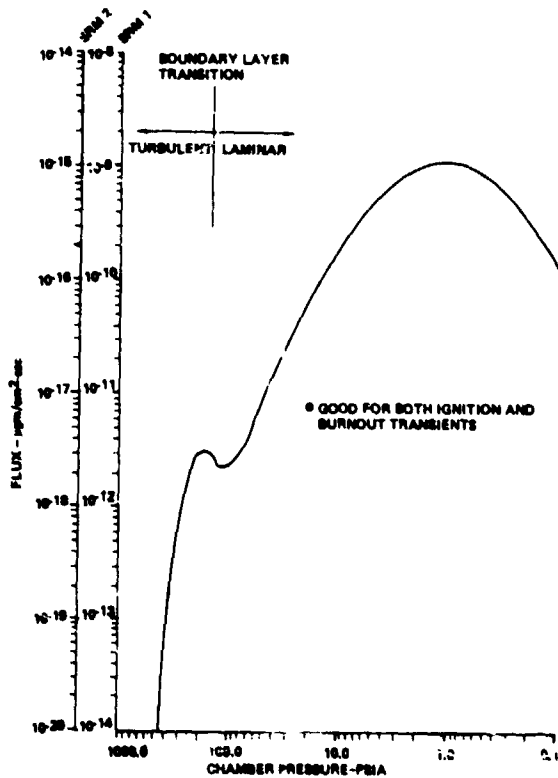
Figure 8: SRM Contamination Flux
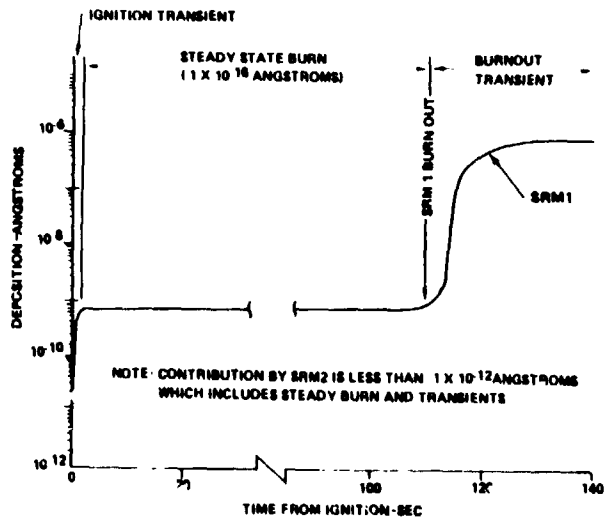
Figure 9: Contamination During Main Motor Burn

255

Table IV: Summary of Contamination to the Spacecraft During IUS Free Flight Deposition in Micrograms/cm^2

CONTAMINATION TRANSPORT \ FLIGHT OPERATION	SRM1 BURN	SRM1 RETRO-GRADE	SRM1 HEAT SOAK	SPM2 BURN	SMR2 RETRO GRADE	SRM2 HEAT SOAK	S/C IUS SEP	TOTAL
SELF-SCATTERING	1×10^{-8}	0	0	1×10^{-12}	0	0	0	1×10^{-8}
AMBIENT SCATTERING	7.5×10^{-6}	② 1.5×10^{-2}						1.5×10^{-2}
DIRECT FLUX	0	0	6×10^{-6}	0	0	① 4.2×10^{-1}	0	4.2×10^{-1}
TOTAL	7.51×10^{-6}	1.5×10^{-2}	6×10^{-6}	1×10^{-12}	0	4.2×10^{-1}	0	

① CONSERVATIVE ESTIMATE FROM KEVLAR-EPOXY MOTOR CASE WHEN HEATED TO 500°F 25 TO 30 MINUTES AFTER MOTOR BURNOUT.

② BASED ON 180 SEC. DELAY IN RETRO MANEUVER FOLLOWING SRM1 BURNOUT. NO DELAY WOULD PRODUCE 2.6 MICROGRAMS/CM².

RADIAL DISTRIBUTIONS OF NONDIMENSIONAL PITOT PRESSURE x/D$_{exit}$ ≈6 FOR 2 AND 15% AL PROPELLANTS AND A SIMULATED ALTITUDE OF 50,000 FT
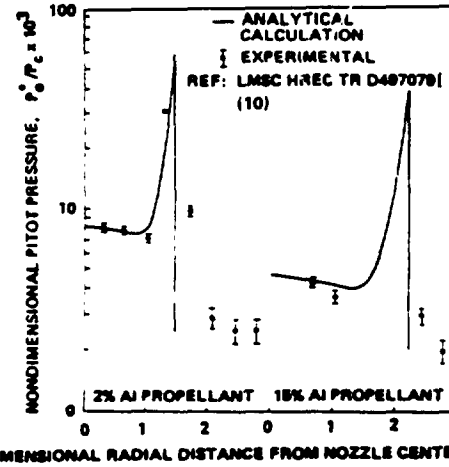
Figure 10: Pip Computer Code Verification — Pitot Pressures
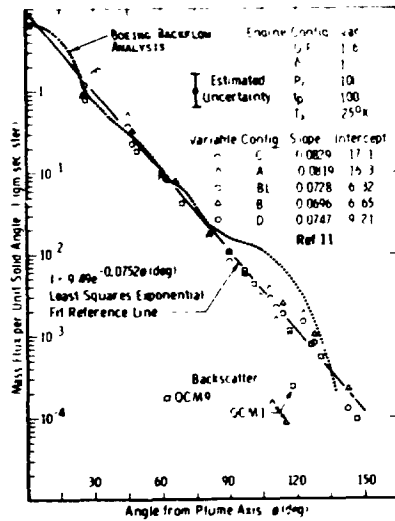
Figure 11: Boeing Backflow Prediction Correlation with Experimental Data (AEDC)
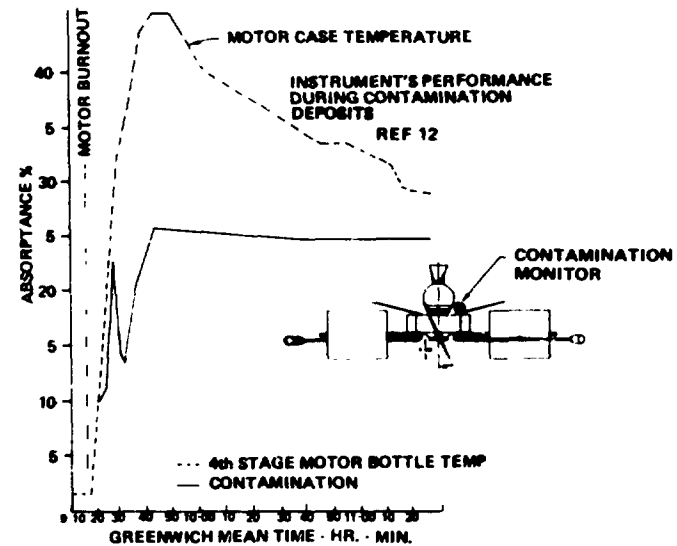
Figure 12: AIMP-E Satellite Flight Data

PERFORMANCE OF A FLIGHT QUALIFIED, THERMOELECTRICALLY
TEMPERATURE CONTROLLED QCM SENSOR WITH POWER SUPPLY,
THERMAL CONTROLLER AND SIGNAL PROCESSOR.

Donald A. Wallace*

ABSTRACT

A thermoelectrically temperature controlled quartz crystal
microbalance (QCM) system has been developed for the measure-
ment of ion thrustor generated mercury contamination on space-
craft. Meaningful flux rate measurements dictated an accurately
held sensing crystal temperature despite spacecraft surface temp-
erature variations from -35 °C to +60 °C. A thermal control
system was developed which held the sensing crystal at 25 °C ± 1 °C
over the flight temperature range.

An electronic control unit was developed with magnetic amp-
lifier transformer secondary power supply, thermal control elec-
tronics, crystal temperature analog conditioning and a multiplexed
16 bit frequency encoder.

INTRODUCTION

Operation of Ion Thrustors for spacecraft propulsion raises
the question of potential spacecraft surface contamination by
mercury from the thrustor beam. NASA Lewis Laboratories' Ion
Thrustor experiment on the P80-1 Space Shuttle program is con-
tracted to Hughes Aircraft Company which plans to monitor contam-
ination using QCMs (quartz crystal microbalances). Two QCMs
(operated by a single electronics control unit) will be placed at
right angles to the thrustor beam.

In order to make relatable contaminant flux rate measurements,
the collecting surface temperature, i.e. the QCM sensing crystal
temperature, must remain at a constant temperature. This temp-
erature was specified to be 25 °C ± 1 °C. The orbiting spacecraft
QCM attachment surfaces however are expected to vary between -35 °C
and +60 °C. This requirement led to a contract with Berkeley
Industries to develop a QCM sensor with an active thermal control
system which would accurately hold the 25 °C set point temperature,
would have minimal frequency temperature coefficient in the two
degree temperature region around the set point, would be operated
by an electronics unit with single point ground system power
supply, and would have crystal analog temperature outputs, a

* Berkeley Industries, Laguna Beach, California

multiplexed QCM 16 bit parallel frequency encoder and would not consume over 5 watts of power. This QCM system was developed, flight qualified and delivered to Hughes Aircraft Company in March 1980.

This paper presents some of the unique design problems encountered in this new QCM system, their solution and the system performance.

NOMENCLATURE

The following nomenclature is used in this paper:

T	Temperature - °C.
T_C	Sensing Crystal Temperature
T_{HS}	Heat Sink Temperature at QCM Attachment Point
I	Current - Amps
V	Voltage - Volts
PRT	Platinum Resistance Thermometer
R	Resistance - Ohms
R_T	PRT Resistance at Measuring Temperature
R_0	PRT Resistance at 0 °C
R_{100}	PRT Resistance at 100 °C
α, β, δ	Coefficients of Callendar-Van Dusen equation
k	Thermal Conductivity
L	Length
A	Area
f	Beat Frequency - Hertz
r	Time - Seconds
P	Power - Watts
Q	Heat Flux - Watts
m	Mass - Grams
C_p	Specific Heat - joules/gram - °K
SC	Solar Constant - 1353 w/m^2
TE	Thermoelectric Peltier Element

SYSTEM DESIGN

The contamination system, termed the Berkeley Industries MK 10 QCM System, consists of two thermoelectrically temperature controlled QCM sensors with a common electronics unit. The system is shown in Figure 1 and the functional schematic in Figure 2. The active elements of the QCM sensor include 10 MHz sensing and reference crystals, a platinum resistance (PRT) temperature sensing element, a thermoelectric heater/cooler and a dual oscillator/mixer hybrid chip element. The electronics unit has a power supply unit, a frequency encoder and a thermal control/temperature readout section. These various elements will be discussed separately.

Power Supply

The power supply is required to regulate the incoming 28 volt ±6 volt power, applying the proper EMI line filtering and to supply isolated secondary voltages for the QCM oscillator/mixer, the thermoelectric heater/coolers and the various signal processing electronic circuitry while using only 5 watts of power.

A magnetic amplifier transformer type secondary power supply with a 22 KHz oscillator was chosen after computer optimization studies. The high conversion efficiency and isolated secondary features were paramount factors in this choice. Thermoelectric elements have high amperage, low voltage operating characteristics which normally lead to very inefficient power converters. However, optimized mag-amplifier design can achieve 75 to 80% efficiency.

The secondary power supplied is ±11.5 volts, +10V and ±6 volts for the thermoelectric elements.

Frequency Encoder

The QCM beat frequency is digitally encoded using 16 bit counters and a quartz crystal clock to gate the frequency. The encoded parallel output is TTL/CMOS compatable. The QCM to be interrogated is selected by external signal, with a select verify signal returning. A count omplete signal terminates the frequency output cycle.

Thermal Control/Temperature Readout

The purpose of the thermal control system is to hold the absolute temperature of both QCM's sensing crystals at 25° ± 1°C. Conceptually, a platinum resistance element (PRT), thermally locked to the crystal, generates a voltage proportional to the crystal temperature. This voltage can be compared to a set point voltage (calculated for the desired 25°C) and either a positive or negative voltage supplied to the thermoelectric element which is thermally locked to the crystal and PRT. Thus the crystal is either heated or cooled until the setpoint is reached. The block diagram in Figure 2 illustrates the concept.

The dynamic thermal control elements in this system are the QCM crystal package, consisting of the sensing and reference crystals with the PRT sandwiched in between, the thermoelectric heater/cooler to which the crystal package is attached, and the electronic comparator circuit. Crucial to stable crystal temperature operation is the matching of the thermal time constants of the crystal package and the thermoelectric element and the dynamic response of the mag-amplifier/comparator circuit. As illustrated in Figure 3, the slope of the comparator response curve can be adjusted from a step change heating to cooling response

259

for a detected temperature error (the so called "bang-bang" response) to a very "soft" response. This response must be tailored to the thermal time constant of the crystal package. This time constant involves the mass of the sense crystal, reference crystal and PRT mount and the overall thermal conductivity (including joint resistance) from the TE element to the PRT and sense crystal.

If long time constants exist in the crystal package, temperature overshoot may result at the crystal before the correcting signal has time to respond. Uncontrolled temperature oscillations can then occur. Analysis and experiment determined stable operation to exist for short crystal package time constants and comparator response which delivered maximum current at the limits of allowable temperature excursion, i.e. ±1°C.

From

$$\frac{\Delta T}{\Delta r} = \frac{Q}{C_p \, m} \tag{1}$$

short time constants result from minimum mass and maximum positive or negative heat flow. Additionally, transient and steady state temperature gradients must be minimized if the PRT temperature is to represent crystal temperature. From

$$\Delta T = \frac{Q \, \Delta L}{k \, A} \tag{2}$$

the thermal conductivity of the assemblage must be high and length dimensions minimized for a low temperature gradient.

QCM Sensor Design

The QCM sensor assembly is shown schematically in Figure 4.

The thermoelectric heater/cooler is a 72 element low aspect ratio single stage unit designed for approximately 1/4 amp current at ±4 volts. The TE was soldered to the heat sink and the crystal package with high temperature eutectic solder. The low aspect ratio design gave the element greater shear strength for the vibrational launch environment.

The crystals are 10 MHz, AT cut optically polished 12.4mm diameter crystals with outward facing surfaces fully aluminum coated to reduce solar insolation effects. The crystal's aluminum electrode is overcoated with a quarter wave length thickness of magnesium fluride to avoid aluminum deterioation due to mercury yet at the same time optimize the surface reflectivity.

All metal parts, with the exception of the TE, are machined aluminum for high thermal conductivity. The aluminum is plated

with 1 μm of nickel eliminating mercury corrosional effects. The crystals are spring loaded into mounting rings which are bolted with high screw loading to the PRT mounting ring thus minimizing temperature gradients. The PRT unit is mounted in its mounting ring with high thermal conductivity epoxy.

Lead wires to the crystals and PRT are #30 Teflon coated Constantan wire for low heat leak to the TE.

The heat sink is designed for less than 1°C temperature gradient with maximum heat sink to crystal temperature differential.

QCM PERFORMANCE

Crystal Temperature Analog Output

The crystal temperature is determined from an analog voltage which is scaled for approximately 0 to 5 volts corresponding to -50° to +65 °C. The crystal temperature is assumed to be identical to the PRT temperature thus the emphasis in the sensor head design on structural features which minimize temperature gradients. The final accuracy of the temperature determination is actually a matter of voltage resolution in the telemetry signal and the linearity of the voltage-temperature curve. In this application, the linearity was specified to be ±1% of full scale or better.

The resistance-temperature characteristics of the PRTs was accurately determined at the temperatures of boiling and freezing points of distilled water (100 °C and 0 °C) and at liquid nitrogen boiling point (-196 °C). Points in between were measured with a calibrated thermocouple. A bridge circuit was used to minimize PRT selfheating. The resistance ratio curve, R_T/R_O was found to match very closely the NBS curve for pure, strain free platinum. The PRTs were then tested with the heat dissipation produced by the 0.973 ma circuit current and coefficients found for a best fit of the Callendar-Van Dusen equation,

$$\frac{R_T}{R_O} = 1 + \alpha \left[T - \delta (\frac{T}{100} - 1) \frac{T}{100} - \beta (\frac{T}{100} - 1)(\frac{T}{100})^3 \right] \qquad (3)$$

The coefficients are $\alpha = 0.003900$, $\beta = 0.09997$ and $\delta = 1.2031$. Minor differences are observed between these results and the values reported by Glassford (Ref. 1) for similar PRTs. These differences are due to the current flow in the PRT and evidently the availability of higher quality platinum.

Using Eqn 3, a reading accuracy of ±0.01 Ω PRT resistance results in ±0.02 °C accuracy in inferred temperature.

A test to determine the linearity of the analog voltage output with crystal temperature was performed in vacuum over a

temperature range of -45°C to 65°C. The analog voltage was measured with an accuracy of ±1 mv and the temperature to ±0.02°C using the PRT resistance. The resultant data is shown in Figure 5 for both QCM circuits. The data is seen to be well within the desired ±1% linearity requirement.

Crystal Temperature Control

The primary intent of this QCM system design was the maintenance of the crystal temperature at 25°C ± 1°C while the heat sink temperature varies from -20°C to +50°C (survive -35°C to +60°C). A test in vacuum was performed on the complete system, i.e. two QCMs and the Electronics Unit, over the survival temperature range, using the analog voltage output for crystal temperature indication and a separate PRT thermally attached to the QCM heat sink mounting plate for the heat sink temperature. The results shown in Figure 6 demonstrate the ability of the thermal control system to maintain the crystal temperatures well within the desired ±1°C range. The voltage outputs of the two QCMs were identical within the ±1 mv accuracy of the measuring instrument.

QCM Frequency Stability

The measurement of contaminant mass by a QCM assumes that frequency changes occur only as a result of mass deposited on the sensing crystal. In actuality, a small frequency shift may occur as a result of temperature gradients between the sensing and reference crystals. A crystallographic cut (35° 12') was chosen for the crystals in this program to reduce the frequency temperature coefficient to near zero. A test was performed in a vacuum bell-jar to confirm the clean crystal QCM stability with the thermal control system maintaining the crystals at 25°C ± 1°C as in Figure 6. The results, shown in Figure 7, indicate some minor thermal gradients do exist in the crystal package. However, considering the fact that a 30 Hz change in frequency is equivalent to a single monoloayer of mercury molecules, the QCM frequency stability is quite acceptable.

Solar Radiation Effect

During orbiting flight, the QCMs will at times be exposed directly to solar insolation which has been shown earlier in Reference 2 to have an effect on the sensing or exposed crystal's frequency. In the present QCM design, an effort was made to minimize this effect by limiting the radiant flux absorbed by the crystal and by using a zero temperature coefficient crystal unit. The results, shown in Figure 8, indicate that these efforts were only partially effective. The heat absorbed by the crystal which is not reradiated must either effect a rise in the bulk temperature of the crystal or create a heat flow and resultant temperature gradient in the quartz plate. Either effect would result in a frequency shift but for different reasons. The uniform bulk temperature rise would alter the frequency by the quartz temperature

coefficient relationship depending upon the crystal cut, while
a temperature gradient in the plate produces physical stresses
which result in a change in frequency. In this present QCM
design, the thermal locking of the PRT and the sensing crystal for
temperature reading accuracy resulted in a crystal mount design
in which it would be unlikely for the crystal bulk temperature
to change because of the high conductivity crystal edge mount but
would result in temperature gradient induced stress. The frequency
shift is quite repeatable and can be removed in the data reduction.

System Power Requirement

Tests in vacuum were performed to determine the required
system power which was specified to be less than 5 watts. The
power curve, shown in Figure 9, indicates that although the
specified maximum power was exceeded when the heat sink was at
$-20\,^{\circ}C$, the average power usage was considerably less than 5 watts.

CONCLUSIONS

A QCM system with thermoelectrically temperature controlled
contaminant flux sensing crystals has been developed and success-
fully flight qualified. The thermal control system is capable
of holding the mass sensing crystals at a precise temperature
($\pm\,1\,°C$) despite widely varying spacecraft temperatures.

ACKNOWLEDGEMENTS

This program was made more enjoyable by association with the
witty personality of George Thomas, Hughes Aircraft program
manager.

REFERENCES

1. Glassford, A.P.M., "An Analysis of the Accuracy of a Commercial
                      Quartz Crystal Microbalance", AlAA 11th
                      Thermophysics Conference, San Diego, Calif.,
                      July 14-16, 1976.

2. Wallace, D.A.,   "Transient Frequency Effects in Piezoelectric
                      Quartz Crystals Caused by Incident Thermal
                      Radiation" NASA SP-336, 7th Conference on
                      Space Simulation, November 12-14, 1973.
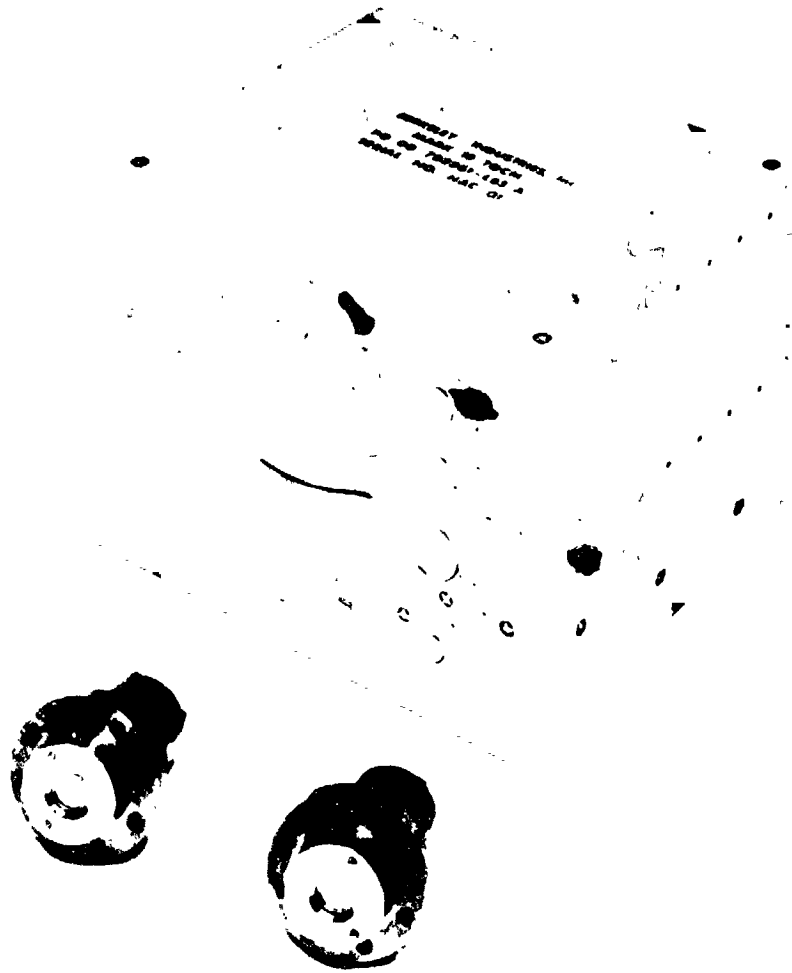
Figure 1   MK12 Thermoelectrically Temperature Controlled
             QCM Sensors and Electronics Unit
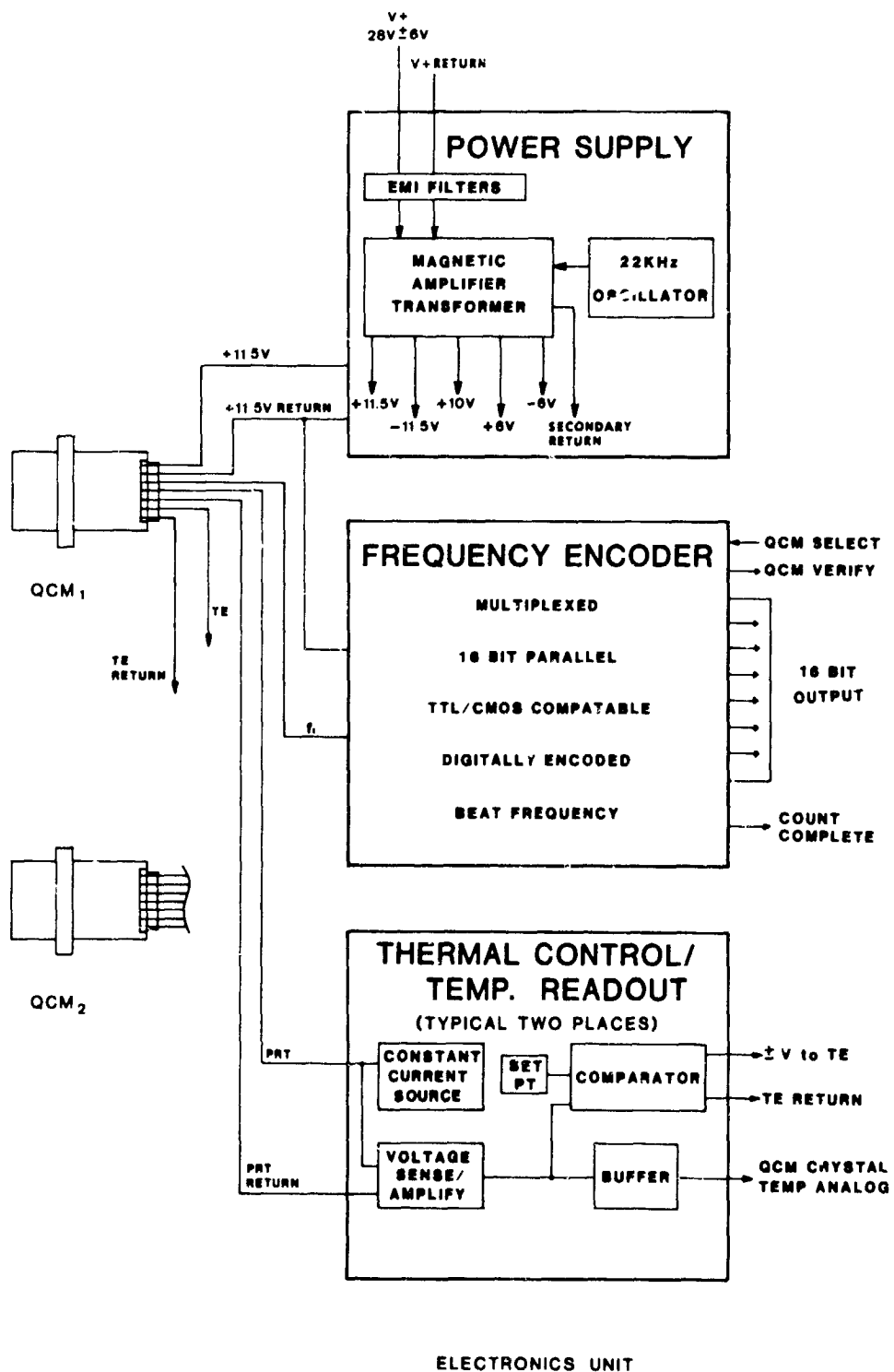
Figure 2   QCM System Functional Block Diagram

THERMOELECTRIC
ELEMENT
TE

SENSE
CRYSTAL

PRT

REFERENCE
CRYSTAL

HEAT SINK

I-current supplied to TE

DECREASING
DYNAMIC
RESPONSE

24°C   25°C   26°C

Tc

QCM   COMPARATOR
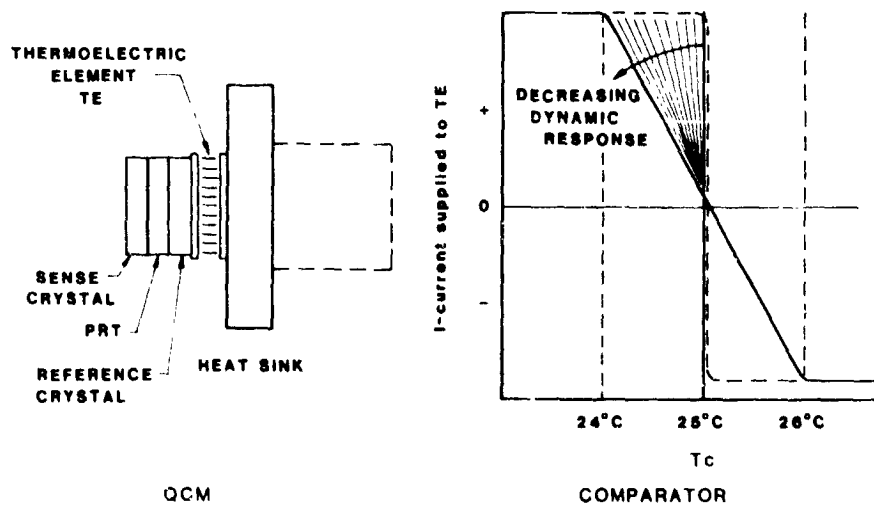
Figure 3   Dynamic Temperature Control Elements

CAP

CAP MOUNTING STUD

ELECTRICAL LEADS

SENSING CRYSTAL
IN MOUNT

PRT IN MOUNT

HEAT SINK/
MOUNTING FLANGE

REFERENCE CRYSTAL
IN MOUNT

THERMOELECTRIC
HEATER/COOLER

OSC/MIXER
HYBRID CHIP

ELECT. CONNECTOR

Figure 4   QCM Sensor Head

266

Figure 5   Crystal Temperature Analog Voltage

Figure 6   Crystal Temperature Control
at 25°C Set Point
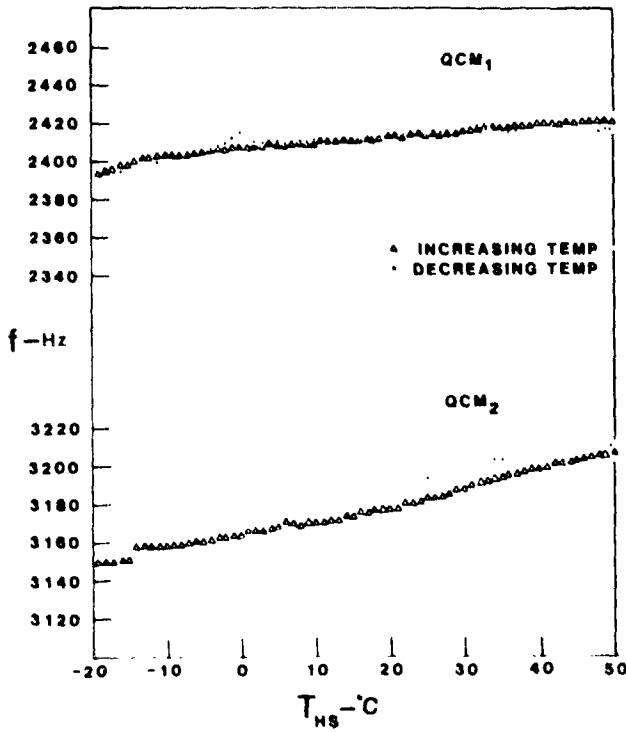
Figure 7   Crystal Frequency
            Stability with
            Thermal Control
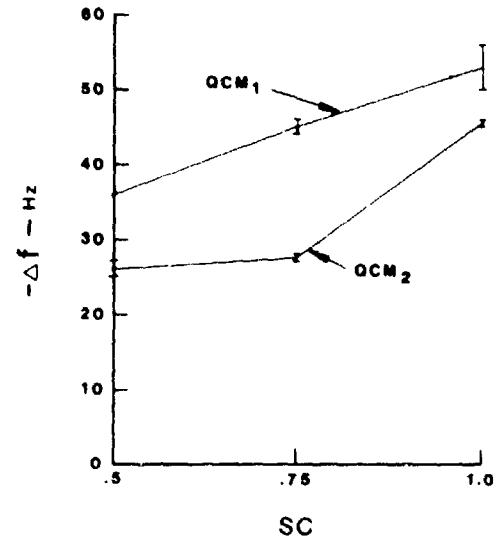
Figure 8   Solar Insolation
            Induced Frequency
            Effects
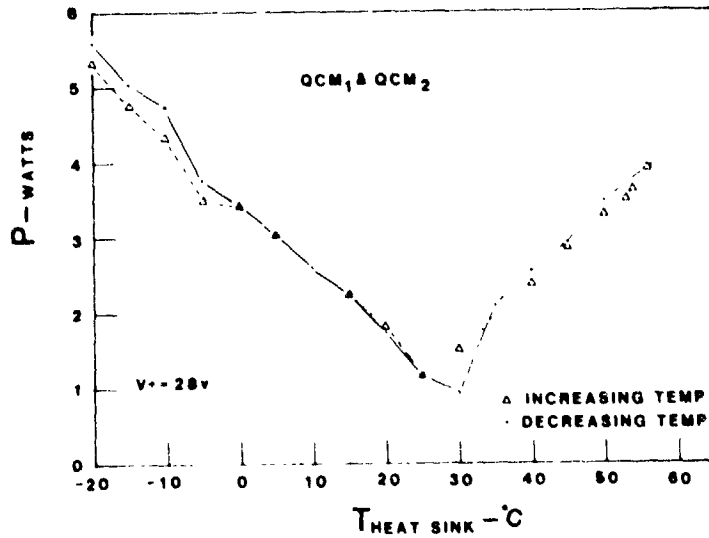
Figure 9   QCM System Power Requirement

WATER-DEUTERIUM OXIDE EXCHANGE IN POLYMERS USED IN SPACECRAFT APPLICATIONS

D. J. Carre[*]

ABSTRACT

The replacement of water (H_2O) by deuterium oxide (D_2O) and the exchange between atmospheric water and adsorbed or absorbed D_2O were investigated for the polymeric materials Kapton and Mylar using thermal gravimetric analysis (TGA) and infrared (IR) spectroscopy. Replacement of H_2O by D_2O is easily accomplished. However, exposure of D_2O samples to the ambient atmosphere or gases containing H_2O results in rapid proton and deuteron exchange between H_2O vapor and adsorbed D_2O. Replacement of H_2O by D_2O would not be a practical solution to alleviate spectral interferences that would result from water outgassing in spacecraft orbital environments. Maintaining the materials of interest in a dehydrated state is a more reasonable approach.

INTRODUCTION

Water ice formation on satellite optical surfaces has been suggested as a possible cause of decreased sensitivity of infrared sensing devices. For optimum performance, these devices rely on unattenuated signals in the infrared wavelength region where H_2O ice absorption occurs. It has been hypothe ized that the H_2O collects on the cryocooled optical surfaces after outgassing from materials in close proximity to the surfaces. The most likely sources of H_2O are polymeric insulation, such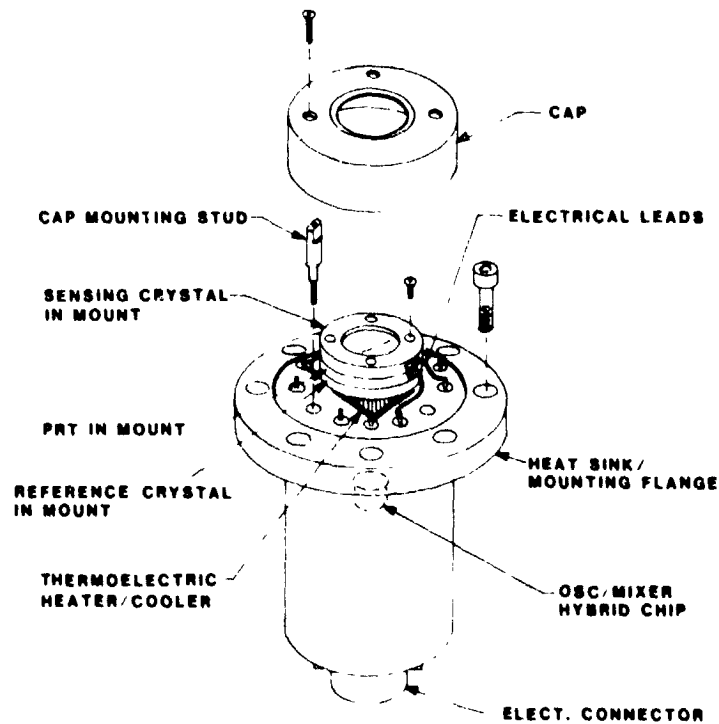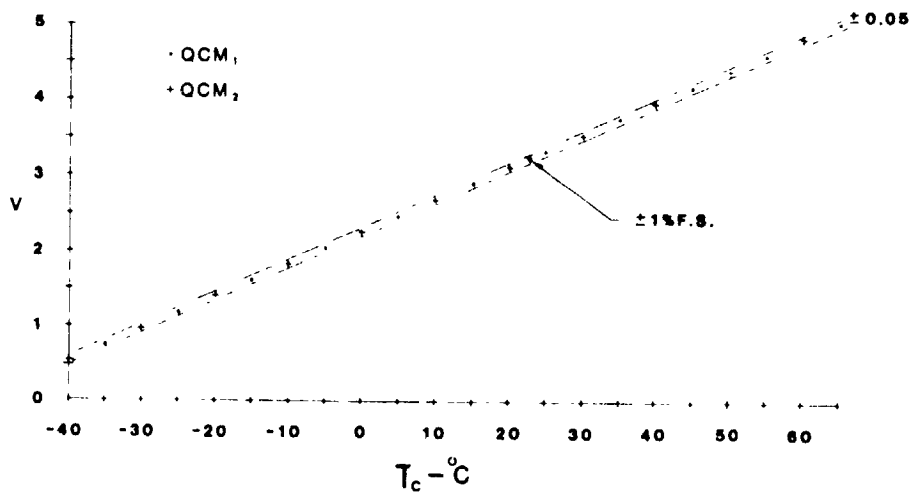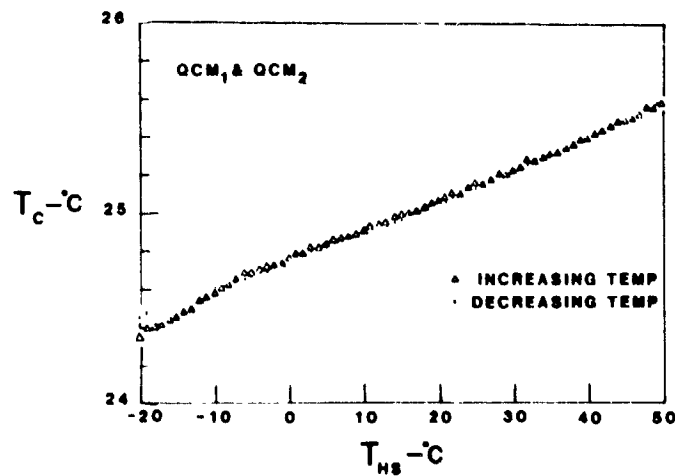 as Kapton, multilayer insulation (MLI), and aluminized Teflon. The suggestion has been made that replacement of associated H_2O with D_2O in the materials of interest would alleviate the problem by isotopically shifting the infrared ice absorption band out of the wavelength region of interest.

In order for the H_2O replacement to be considered a feasible solution to the problem, the following questions should be answered:

1. Is the H_2O-D_2O replacement accomplished easily, and what are the best methods?

2. Once the replacement is accomplished, how difficult is it to maintain the D_2O level?

3. How important are exchange processes between associated D_2O and ambient atmospheric H_2O?

The last question is the most critical. In the condensed phase, proton exchange between H_2O and D_2O occurs just below the diffusion-controlled limit and is, thus, very rapid (Refs. 1 and 2). In addition, the following rapidly established equilibrium is shifted toward the right at room temperature (K_{eq} = 3.94 at 20°C) (Ref. 3):

$$H_2O + D_2O \rightleftharpoons 2 HOD$$
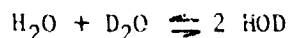
Both H_2O and HOD absorb infrared radiation in the wavelength region of interest. Because of the rapidity of proton exchange, the mixing phenomenon is expected to be limited by surface adsorption and bulk diffusion of water.

---
[*]The Aerospace Corporation, El Segundo, California

The D_2O-H_2O replacement phenomenon was investigated for Kapton, and to a lesser extent Mylar, by TGA and IR spectroscopy. In addition to atmospheric exposure, N_2 and Ar atmospheres were used to determine if gas adsorption would affect the exchange process significantly.

EXPERIMENTAL

The materials in the investigation were 0.005-in. Kapton and 0.003-in. Mylar sheets examined by means of IR and TGA, and aluminized-Mylar MLI, examined by means of TGA.

The TGAs were performed on a Perkin Elmer TGS-1 thermal balance in both the temperature programmed and isothermal modes of operation. Because of the restricted sample size, it was necessary to cut up the MLI into small pieces, which were then piled in the thermal balance weighing pan. The cutting disturbed the layered nature of the MLI and, as a result, the equilibrium H_2O content might be different from that in the layered configuration. The Kapton and Mylar sheets were simply cut to the appropriate size. The sample weights were generally on the order of 1 mg.

Infrared analyses were performed on a Perkin Elmer Model 467 infrared spectrophotometer. The IR spectra of Mylar and Kapton are shown in Figures 1 and 2. The spectral features in the presence and absence of H_2O and D_2O are included. The Mylar spectrum exhibits a rather small absorption because of the H_2O, and, as a result, only a limited number of experiments were performed. For Kapton, the amount of associated water is larger and, thus, more easily monitored. Despite the larger equilibrium water content, the spectrum of Kapton is complex in the wavelength regions of interest. In order to simplify the spectra, the reference beam of the double-beam spectrophotometer was passed through a sample of "dry" Kapton, which resulted in essentially the spectral features of H_2O and D_2O without interference from the spectral features of Kapton. Two approaches to obtaining these "difference" spectra were employed. In the early stages of the investigation, the "dry" reference sample was stored in an evacuated vacuum dessicator with phosphorous pentoxide as the dessicant. When spectra were obtained, the "dry" sample was placed in the reference beam. In the latter stages of the investigation, a more efficient method was used. A Kapton sample was mounted in a spectrometer gas cell with salt (NaCl) windows. The cell was evacuated to dehydrate the sample and was maintained at low pressure. By means of this approach, the reference sample could be kept in the "dry" state for long periods of time. Both approaches resulted in comparable spectra. Typical spectra obtained by means of the "difference" method are illustrated in Figure 3.

Two approaches were employed in examining the H_2O and D_2O contents of the polymers. In the early experiments in which pre-equilibrium with D_2O was required, the samples were first submerged in D_2O, then mounted in a "film" sample holder and exposed to the ambient atmosphere (relative humidity = 45 to 58%) for specified lengths of time. At the end of the exposure, IR spectra were obtained. It was found that the heating of the samples by the IR beam caused the samples to dehydrate. The rate of dehydration was measured, and the process was determined to have a half-life of approximately 7 min. As a result of this IR stimulated H_2O loss, it was necessary to adjust the experimental procedures to minimize errors. The length of time that the sample was in the IR beam was limited to approximately 2 min, and each data point followed re-equilibration with D_2O and exposure for specified times. By means of this approach, the spectral intensities were accurate to within 15%.

In later experiments in which other than ambient atmospheric exposure was required, the samples were mounted in a spectrometer cell with KRS-5 windows. Appropriate gases were purged through the cell for measured time intervals. The IR spectra were obtained by closing off the cell and placing it in the spectrometer only long enough to obtain the appropriate spectrum, 2 to 4 min. Minimizing IR exposure time and sealing off the cell minimized errors induced by IR stimulated water loss.

The gases used in the investigation were N_2 and Ar. They were both dried by passage through a drying cartridge containing molecular sieves. After drying, the gases were either admitted to the sample cell in the "dry" state or passed over H_2O or D_2O liquid prior to passage through the sample cell. The gas flow rates were approximately 30 ml/min for N_2 and approximately 40 ml/min for Ar. The D_2O was from Merck and Co. and had a deuterium content of 99.7 at% D.

RESULTS

Thermal Gravimetric Analysis

Mylar, MLI, and Kapton were analyzed in both temperature-programmed and isothermal modes of operation. The three materials exhibited two weight-loss processes, the first occurring in the temperature range 300 to 400°K, and the second at approximately 600°K. The first process is attributed to H_2O loss, whereas the second is consistent with sample thermal decomposition. The weight losses resulting from H_2O desorption were determined to be 0.93, 0.37, and 0.24% for Kapton, Mylar, and MLI, respectively.

Isothermal analysis was useful for the Kapton sample but not for Mylar and MLI. For the latter two, instrumental limitations on sample size coupled with low H_2O content resulted in isothermal-weight-loss profiles that did not permit detailed analysis, i.e., the signal-to-noise ratio was very low. For Kapton, isothermal desorption of water at 370°K resulted in a weight versus time profile (Figure 4) that could be analyzed. The curve is exponential with a half-life of 112 sec. The first-order behavior is illustrated in Figure 5. The observation of first-order kinetics is consistent with both bulk diffusion limited and surface desorption limited processes (Ref. 4). In addition, exponential behavior is consistent with just one process; two concurrent processes would give nonexponential results unless the two processes had identical relaxation times.

Infrared Analysis

The IR absorption maxima for H_2O associated with Kapton and Mylar occur at 3550 to 3620 cm^{-1} (2.76 to 2.82 µm) (Ref. 5). The shift to higher energy for the polymer samples implies that the H_2O is absorbed into the polymer matrix rather than being primarily present as physisorbed layers on the surface. Deuterium oxide exhibits a maximum absorption at 2600 to 2700 cm^{-1} (3.70 to 3.85 µm) in Kapton.

The analysis of the H_2O-D_2O exchange for Mylar was limited by the low-equilibrium H_2O content and, thus, small IR signal levels. However, some data were obtained for atmospheric H_2O exchange in a sample that was equilibrated with D_2O. These data are given in Figure 6. The IR absorption that results from the O-H stretching of H_2O and HOD increases with time and reaches approximately 95% of the maximum absorption in 60 min of exposure to the ambient atmosphere.

271

For Kapton, the larger equilibrium H_2O content permitted more extensive analysis. The change in the O-H and O-D vibration absorption amplitudes as a function of time for a sample that was equilibrated in D_2O and then exposed to the ambient atmosphere is shown in Figure 7. The shape of the O-H vibration absorption band appears to change with time. In addition, there appears to be a time-dependent shift in the absorption maximum wavelength. These changes can be attributed to differing relative amounts of H_2O and HOD as the D_2O is undergoing exchange. The O-H absorption reaches 75 to 80% of its maximum value in approximately 50 min and 90% of the maximum in approximately 90 min, which is nearly the same as that for Mylar.

The elimination of D_2O from a Kapton sample by "dry" N_2 gas was investigated. The spectral changes are shown in Figure 8. By purging the sample gas cell with N_2 gas, the D_2O is eliminated by means of an exponential process with a half-life of approximately 97 min.

Equilibration of a sample with "dry" gas followed by purging with the same gas passed over D_2O was investigated. The O-D absorption spectral changes are shown in Figures 9 and 10 for N_2 and Ar, respectively. The D_2O band grows in faster in the N_2 case, implying that Ar is more difficult to displace by D_2O than is N_2. The changes in optical density versus time for the data in Figures 8 through 10 are illustrated in Figure 11.

Equilibration of a Kapton sample in air followed by exposure to D_2O in N_2 gas resulted in isotopic exchange that occurred at essentially the same rate as equilibration in D_2O followed by air exposure.

DISCUSSION

The TGA and IR data indicate that H_2O is easily removed from the materials of interest by either heating or exposing to a "dry" atmosphere. In addition, once the material is dehydrated, D_2O can be readily introduced. The major problem that must be overcome is exchange between adsorbed D_2O and H_2O from the ambient atmosphere.

The exchange data indicate that exposure of D_2O equilibrated material to H_2O containing atmospheres must be strictly avoided. The reaction between D_2O and H_2O to yield HOD occurs rapidly and results in a mixture of H_2O, D_2O, and HOD. There should not be a significant isotope effect on diffusion and desorption. As a result, these three species would be expected to outgas with essentially the same rate. Oxygen-hydrogen bonds in both H_2O and HOD contribute to the interferences in the infrared region of interest. Thus, ice formation with significant amounts of HOD would cause IR signal attenuation.

It would be necessary to keep a constant D_2O-saturated atmosphere to maintain the D_2O levels in the materials in the prelaunch environment. A more reasonable approach would be to purge the materials with "dry" air or some inert gas. At the latest possible time, the system could be flushed with D_2O containing gas to equilibrate the materials with D_2O. Maintaining the materials at elevated temperatures, i.e., 50°C, during prelaunch would dehydrate the materials. As in the "dry" air purging, equilibration with D_2O prior to launch would be required.

CONCLUSION

Because of the rapidity of proton exchange reactions between H_2O and D_2O, it would be very difficult to maintain equilibrium D_2O levels in Kapton and

Mylar without employing very stringent controls pertaining to the exclusion of H_2O from the materials. The alternative methods of maintaining the materials in a "dehydrated" state by mild heating or purging the system with "dry" air would appear to be more feasible than maintaining D_2O equilibrium levels. These latter choices require either launching the system in a dehydrated state or equilibrating the material with D_2O prior to launch. Water exclusion measures would also be important for these methods. Although these methods appear to be reasonable a priori, the vigorous exclusion of water from critical spacecraft surfaces would be extremely difficult, if not impossible.

The investigations discussed herein were performed on thin sheet materials so that IR spectral analysis methods could be used.

ACKNOWLEDGMENT

REFERENCES

1. M. Eigen, "Proton Transfer, Acid-Base Catalysis, and Enzymatic Hydrolysis," Angew. Chem., Int. Eng. Ed., 3 (1964) 1.
2. J. E. Crooks, "Proton Transfer To and From Atoms Other Than Carbon," Compr. Chem. Kin., 8 (1977) 197.
3. V. Gold and C. Tomlinson, "The Disproportionation of HOD in the Liquid Phase," J. Chem. Soc. D. (1970) 472.
4. E. A. Zeiner, "A Multinodal Model for Surface Contamination Based upon the Boltzmann Equation of Transport," in Proceedings USAF/NASA International Spacecraft Contamination Conference, USAF Academy, Colorado, 7-9 March 1978.
5. D. J. Pasto and C. R. Johnson, Organic Structure Determination, Prentice-Hall, Inc., Englewood Cliffs, N.J., 1969.
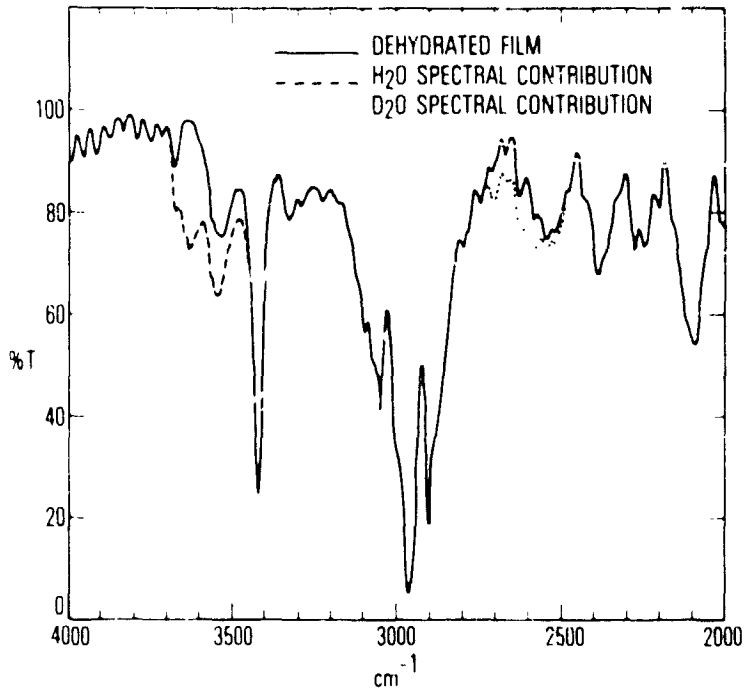
Figure 1.   IR Spectra ot 0.003-in. Mylar Film
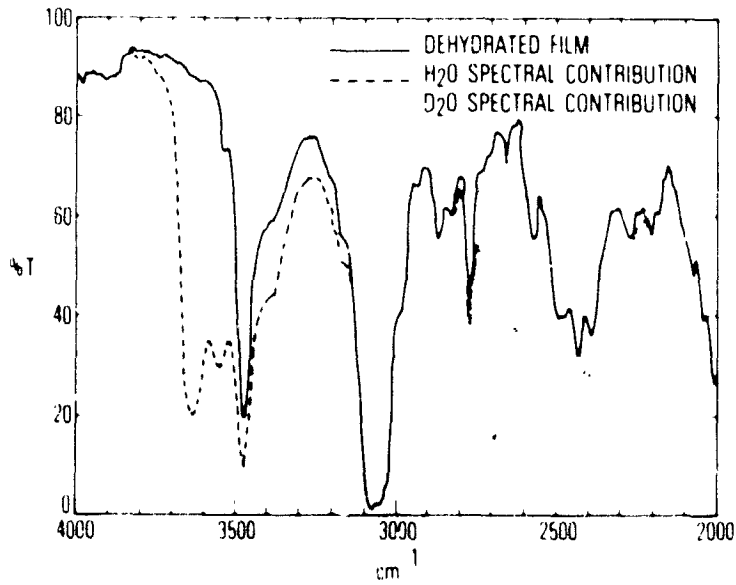
Figure 2.   IR Spectra of 0.005-in. Kapton Film
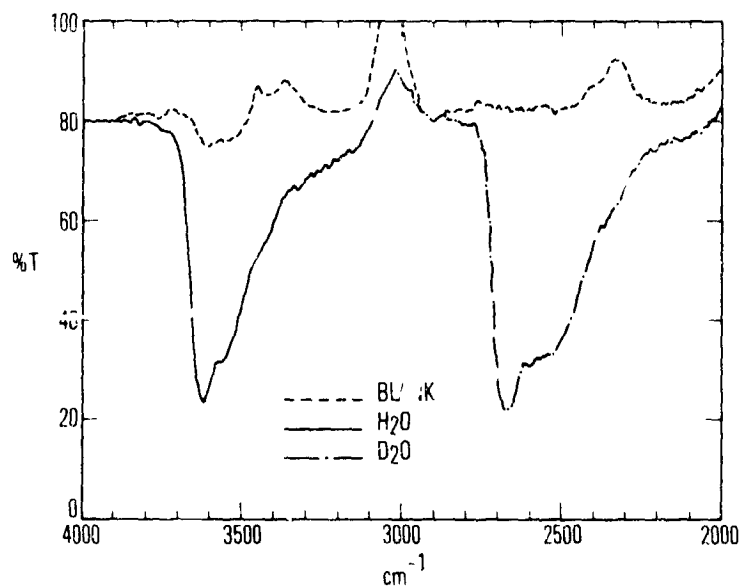
Figure 3.   IR Spectra of 0.005-in. Kapton Film
by Difference

0.01 mg (sample wt = 1.345 mg)
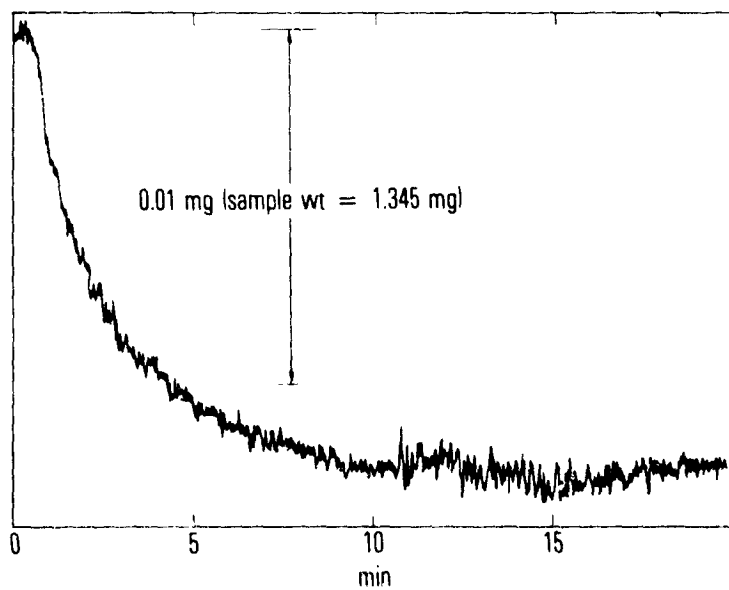
Figure 4.   0.005-in. Kapton Water Desorption at
370°K
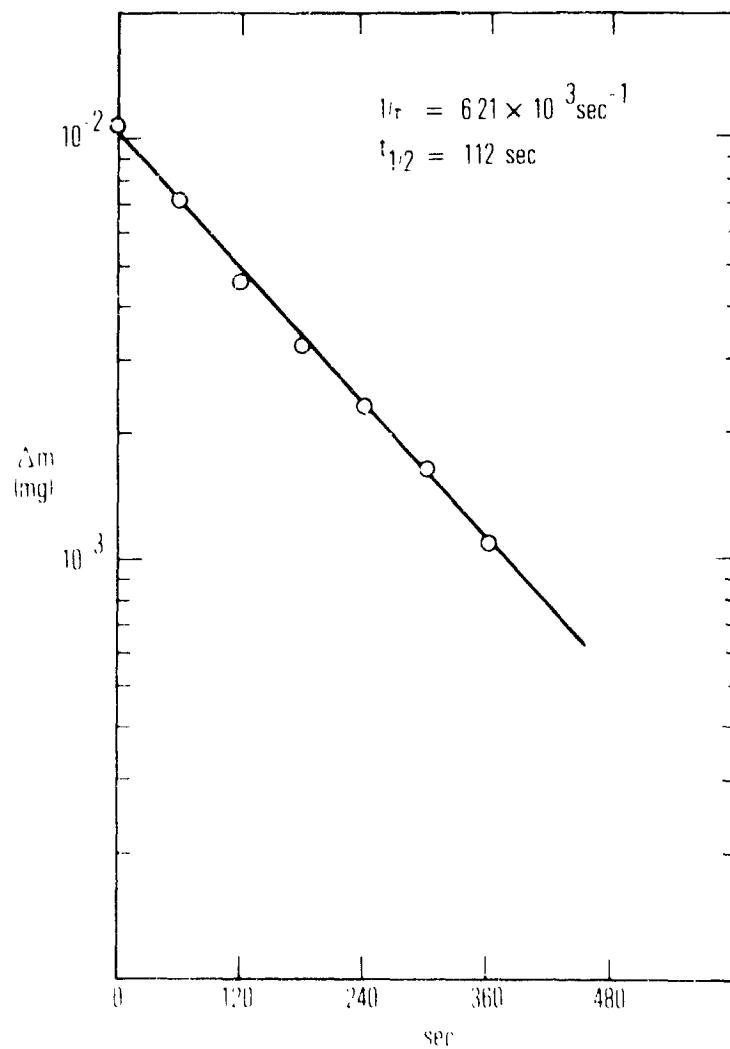
Figure 5.   0.005-in. Kapton Water Desorption at
370°K.   First order plot with
$1/\tau = 6.21 \times 10^{-3}$ sec^{-1}.
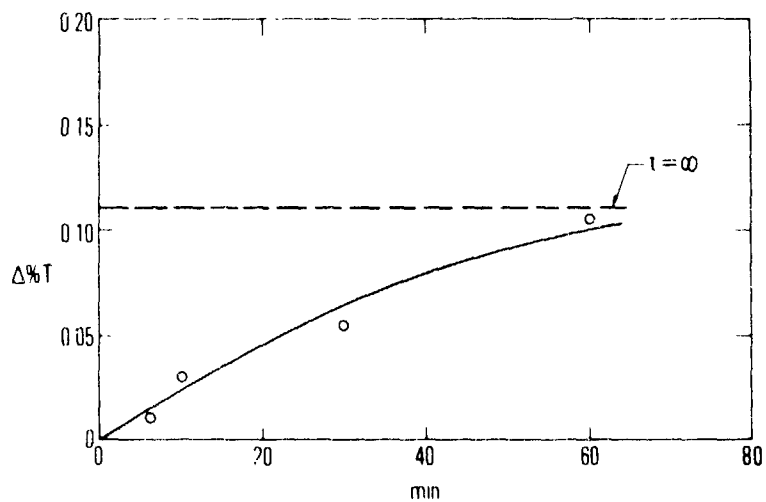
Figure 6. Exchange of Atmospheric H_2O for D_2O
in 0.003-in. Mylar Film. $\Delta\%$
transmittance versus time for
3620-cm^{-1} absorption.
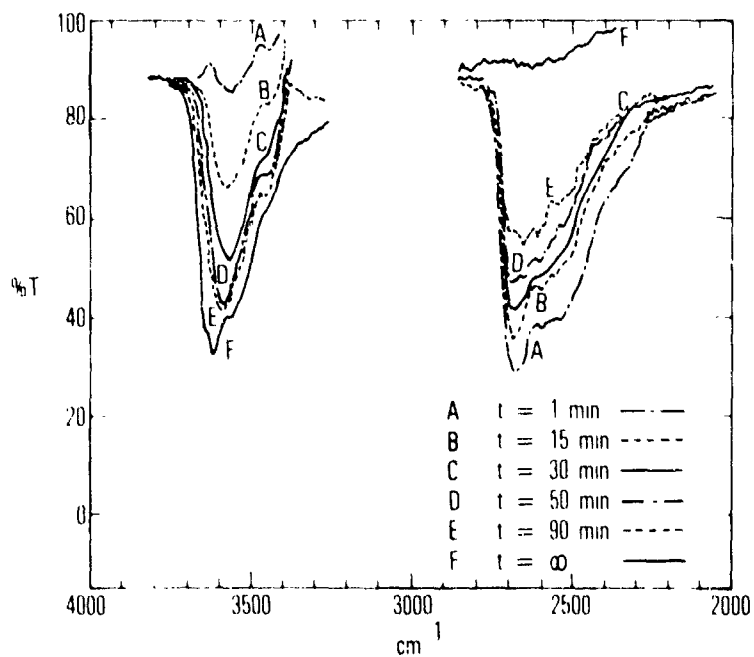
Figure 7. IR Spectra versus Time for Exchange
of Atmospheric H_2O for D_2O in
0.005-in. Kapton Film

277
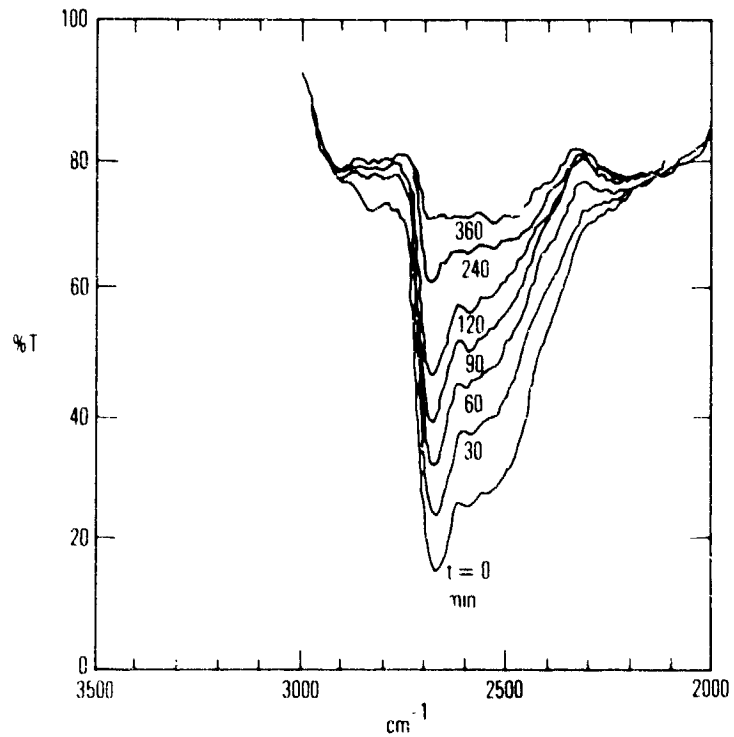
Figure 8.   IR Spectra versus Time for D_2O Removal from 0.005-in. Kapton Film with Dry Nitrogen.   Nitrogen flow Rate = 30 ml/min.
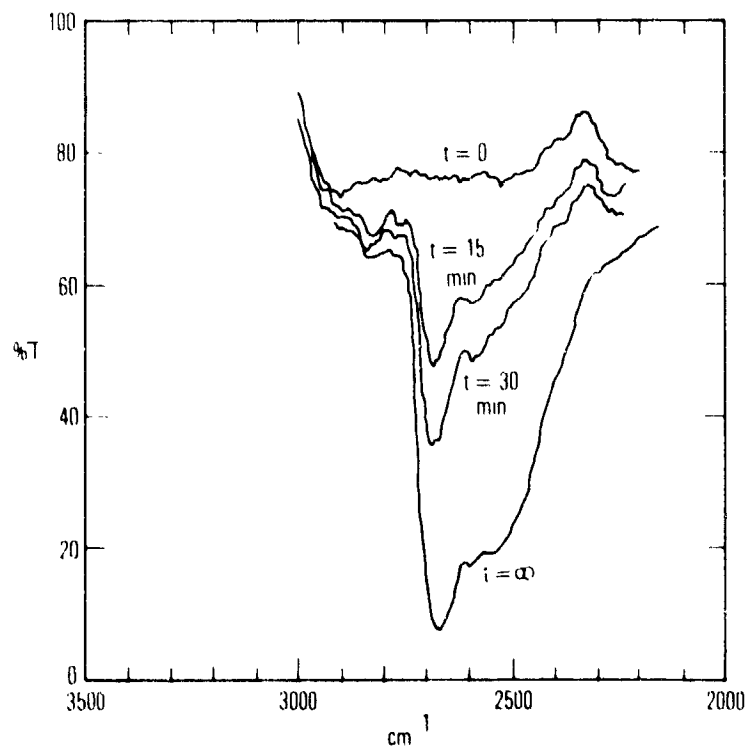
Figure 9.   IR Spectra versus Time for D_2O Uptake by 0.005-in. Kapton Film.   Nitrogen gas passed over D_2O at 30 ml/min flow rate.
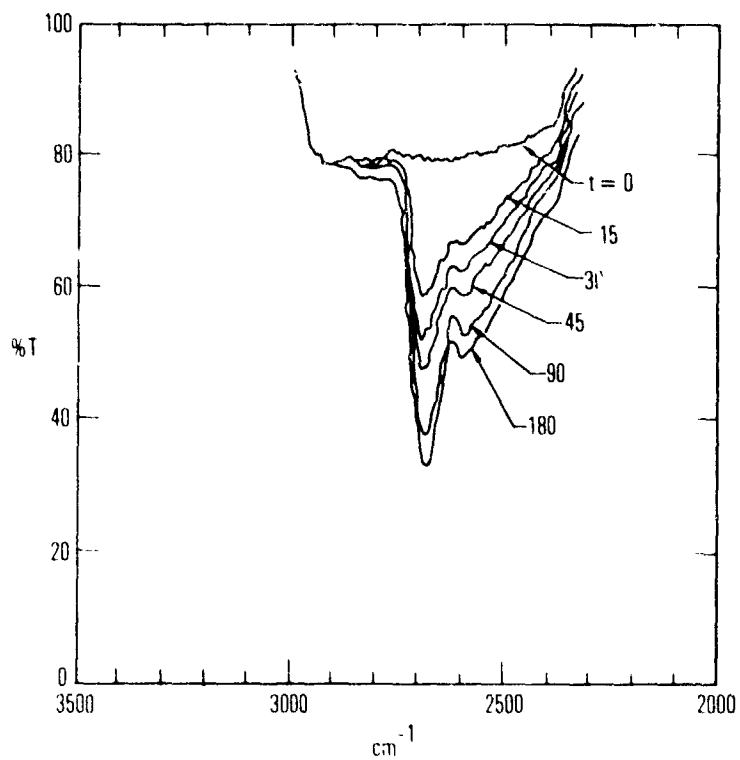
Figure 10.   IR Spectra versus Time for D_2O
Uptake by 0.005-in. Kapton
Film.   Argon gas passed over
D_2O at 40 ml/min flow rate.
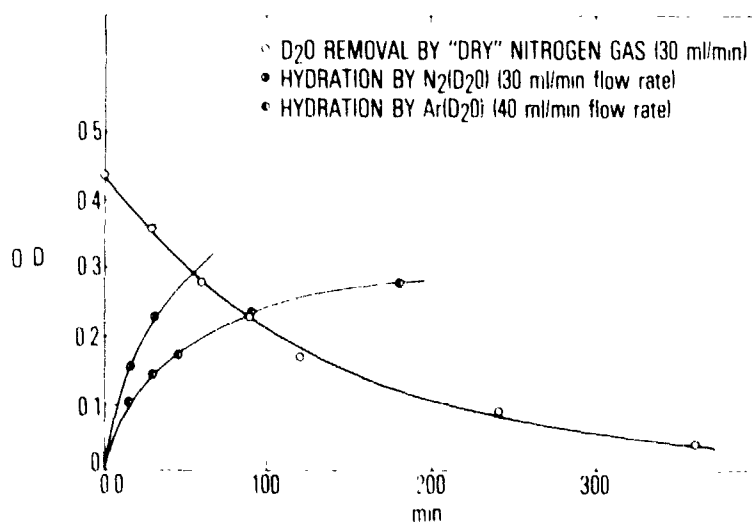
Figure 11.   Optical Density versus Time for
Dehydration and Hydration of
0.005-in. Kapton Film

279

THE IDENTIFICATION OF TRENDS IN OUTGASSING TECHNOLOGY

Joe A. Colony

ABSTRACT

A large amount of chemical analysis data involving identification of outgassing products from spacecraft, experiment modules, and support equipment has been accumulated at the Goddard Space Flight Center over the past ten years. In order to gain some insights into significant trends in the occurrence of outgassing problems and to assist in the implementation of meaningful materials selection policies, these data have been reduced to a computer compatible format and subjected to a variety of relevant program operations. From these data a list of the most troublesome outgassing species has been compiled and several useful and interesting materials' correlations have been developed.

INTRODUCTION

It has been recognized for a long time that outgassing of organic materials and subsequent condensation of the products on critical surfaces of flight hardware can be a serious problem. Detrimental effects include attenuation of optical signals in instrument systems, alterations of alpha/epsilon ratios of thermal control surfaces, corona discharge effects in high voltage electronics, and various detector malfunctions.

In order to guard against the occurrence of such problems, Goddard maintains a system of surveillance of outgassing levels in its thermal vacuum test facilities. This system involves operation of a liquid nitrogen-cooled cold finger to trap outgassed species in each vacuum facility during hardware testing. At the conclusion of each test, the condensed organic residues are washed from the cold finger and taken to the analytical organic chemistry laboratory for quantification and identification. These chemical analyses are performed using advanced instrumental methods including infra-red spectrophotometry and mass spectrometry. The results of these analyses are used routinely to indicate the acceptability of flight hardware or to flag down problem materials and track down outgassing sources.

In addition to this surveillance activity, an extensive materials' outgassing evaluation program has been conducted through the years by the Materials Control and Applications Branch. Through this effort, polymeric materials are subjected to a standard test condition (24 hours at 125°C in vacuum with a room temperature (25°C) collector plate) resulting in determination of total weight loss and total volatile condensable material (CVCM). This test has been accepted as ASTM-E-595-77, and thousands of materials have been evaluated. This information is being used as a basis for recommending materials for space flight use in order that the incidence of problems related to outgassing might be reduced. All spacecraft projects are required to include in their design requirements, a materials review, which contains an evaluation of outgassing potential. The effectiveness of this materials engineering effort can be shown both by the degree of success of our flight programs and by reductions in the occurrence of time and money-consuming

problems during the test and integration phase of spacecraft preparation.

An effort has now been made to develop more specific and technical information concerning the effectiveness of our programs by computerizing all of the analytical chemistry data accumulated over the last ten years of outgassing residue analysis. Pertinent data describing the test item, test facility, and the amount and composition of each sample were entered in the data bank. Computer operations were then developed and employed in order to generate data which might show significant events and trends in the occurrence of outgassing problems through the years. By finding specific changes in the frequency of occurrence of individual outgassed species and correlating them with known materials' usage practices, the impact of previous materials' decisions can be estimated. Also, an assist in making logical materials selections and establishing meaningful policies for future spacecraft projects may be obtained.

CHEMICAL ANALYSIS DATA

The scope of the analytical data used to form this study has been restricted somewhat in the hope of keeping it consistent and compatible. Analytical results of cold finger residues from thermal vacuum facilities at Goddard and some of its contractors have been included as well as witness mirror residues and wipe samples from various flight hardware which either had contamination problems or potential problems. However, analytical data from known materials, suspected sources, micro-CVCM tests, and contamination problems not related to outgassing have been excluded. The total number of analytical reports used was 1294 and covered the time period from 1970 through 1979.

Procedures for obtaining good analytical samples of thermal vacuum outgassing products have been developed and remained essentially unchanged throughout this period. The cold finger is a small cylindrical device (Figure 1) installed in the thermal vacuum facility and cooled with liquid nitrogen during part or all of a thermal vacuum operation in order to condense any volatile species which might be present. This scavenger process results in accumulation of sufficient sample for chemical analysis. The cold finger is warmed to room temperature during the back filling phase which results in maximum retention of condensables while avoiding condensation of water vapor from the air. The residue is then washed from the cold finger with spectrograde 2-propanol and the solution sent to the chemistry laboratory for analysis.

LIQUID NITROGEN OUTLET

COLD COLLECTING SURFACE

DRAIN FOR COLLECTING SOLVENT WASH SOLUTION

LIQUID NITROGEN INLET
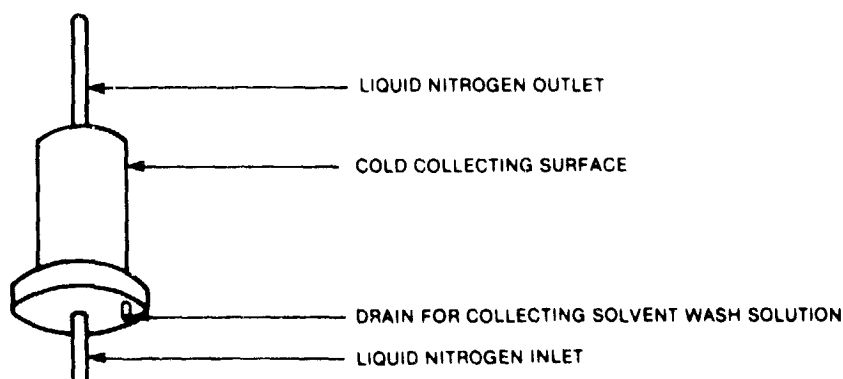
Figure 1 Diagram of Chamber Cold Finger

The cleanliness profile of spacecraft surfaces can be determined by taking wipe samples. The procedure involves the use of precleaned cotton swabs dampened with alcohol to wipe areas from 25 to 50 square inches. In order to obtain sufficiently clean cotton swabs, it is necessary to extract them in a Soxhlet extractor for 24 hours with chloroform followed by 24 hours with alcohol. This process removes all traces of wood resins, cotton seed oil, and adhesive which would interfer with the analysis. It is also important to make certain that the surfaces to be wiped are not affected by the alcohol solvent, ie., metallic sufaces, Kapton, Teflon, anodized, etc.

Although there have been a number of significant advances in our analytical technique and capability through the years, the basic procedure has been somewhat constant. The first step for a cold finger analysis is the gentle removal of the solvent by warming on the steam bath. The residue is weighed and is then ready for infra-red analysis. Wipe sample residues must be extracted from the swabs using hot alcohol and rinsing techniques and subsequent solvent removal on the steam bath.

The infra-red spectrum of one of these samples is most efficiently obtained using the technique called "cating a film". The sample is dissolved in a few drops of chloroform and applied to a polished potassium bromide (KBr) disc. Evaporation of the chloroform leaves a thin film of the sample. The fingerprint absorption spectrum is then obtained by scanning from $2\frac{1}{2}$ to 20 microns with a research grade IR spectrophotometer. Interpretation of IR data can provide good identification of homogenous samples, the prominent constituents of simple mixtures, and at least the more significant functional groups in complex mixtures.

When required, more specific identifications can be obtained using advanced mass spectrometric techniques. With this method the sample is ionized by electron bombardment in the mass spectrometer and the mass fragmentation pattern of the resultant positive ions is recorded. This pattern is very specific for each chemical species and results in unique chemical identification for each compound. Moreover, by the use of the combination gas chromatograph/mass spectrometer (GC/MS) a complex mixture can be separated and identification obtained for each of its components. Cold finger condensables are especially amenable to this technique since the very properties which allow mobility in a vacuum system also make the material suitable for chromatographic separation. If the GS/MS data does not account for all of the features shown by the infra-red scan, then a batch-type mass spectrum must be obtained using the direct insertion probe. Some of the materials which require this treatment are organic acids, amines, and higher molecular weight compounds.

A COMPUTER FORMAT FOR THF ANALYTICAL DATA

A computer format was developed to allow formation of a data bank containing the maximum amount of self-consistent information from chemical analysis reports from log books spanning a ten year period. These reports represent the work of different chemists using an evolving analytical capability and advancement in instrumentation and, therefore, contain some inherent inconsistencies. In addition, there have been some variations in thermal

vacuum facilities' operating procedures and policies. In spite of these possible sources of inconsistencies and the fact that the reports were never intended to be suitable for computerization, the data format shown below was established. Eighty-entry Fortran coding card were used-one for each analytical report-with the following number assignments:

TABLE I. CODING CARD FORMAT

	Column Numbers
Analysis report number	1-5
Analysis date	6-11
Job order number	12-14
Project name	15-19
Test Item name	20-29
Type of test	30-31
Facility Identification	32-34
Type of sample	35-36
Sample weight	37-39
Type of analysis	40
Materials identified	41-45, 46-50, 51-55, 56-60, 61-65, 66-70
Were there more?	71

Abbreviations and numbers were used where required in order to fit this format. The "Type of test" refers to the hardware testing program being monitored while the "Type of sample" refers to the method of sample collection, i.e., cold finger, wipe sample, etc. Facility identifications are the chamber numbers for the Goddard units and arbitrarily assigneu numbers for contractor facilities as shown in TABLE II. Sample weights are applicable only to cold finger samples and are listed in milligrams. The "Types of analysis" includes infra-red spectrophotometry, direct insertion mass spectrometry, and gas chromatography/mass spectrometry and combinations of these techniques which are number coded as shown in the table (TABLE II).

TABLE II. CODE NUMBERS AND ABBREVIATIONS

I Type of Analysis

	Number
Infra-red only (IR)	1
Mass Spectrometer · direct probe (MS)	1
Gas Chromatography/Mass Spectrometry (GC/MS)	3
IR + MS	4
IR + GC/MS	6
MS + GC/MS	7

II Facility Identification

	Number
Goddard Thermal Vacuum Chambers	236-245
Solar Environmental Simulator (GSFC)	290
University College London (UCL)	300
RCA Hightstown, N J	301
MSDS (England)	302
Jet Propulsion Laboratory (JPL), CA	303
Honeywell Radiation, Lexington, MA	304
Ford Aerospace, CA	305
ITT, Fort Wayne, IN	306
Fairchild, MD	307
Lewis Research Center, OH	308
General Electric, Valley Forge, PA	309
Gulton Ind, CA	310
..anta Barbara Research Center, CA	311
Cape Kennedy	312
RFI Clean Room (GSFC)	313
Wallops Island Flight Center, VA	314
Lockheed Missiles & Space, CA	315
Sperry Flight Systems, AZ	316

Computer operations on this data bank were designed to list data, sorting according to different categories such as test item, project, primary material, or frequency of occurrence of a material using various control parameters. Attempts were then made to illustrate interesting and informative materials' correlations, trends in types of occurrences, and technology areas in which improvement has been made or in which further study must be concentrated.

RESULTS AND DISCUSSION

In order to attempt to identify the kinds of materials which have most often been responsible for the observed outgassing problems at Goddard and significant trends in their rates of occurrence, programs for data sorting were written with the following kinds of parameters:
- -Count the number of times each material occurred as either the primary or secondary material.
- -List the count in quarter year increments.
- -Limit data to include only samples with ten or more milligrams weight.

Identification of Materials

From this listing, which disregards all samples where the amount of outgassing was less than 10 milligrams and includes only the predominant two species identified in each sample, a table of the most often reported problem materials was generated (TABLE III). It should be pointed out that many of these names used for identification are for generic classes and include large numbers of materials, for instance, aliphatic hydrocarbons, esters, and silicones, while others are for specific individual compounds such as di(2-ethyl hexyl)phthalate (DEHP or DOP), dibutyl phthalate (DBP), hydroxy methoxy benzophenones (HMBZP), and 2,6 ditertiary butyl p-cresol (BHT). Thus, we have shown that the most often found individual species is DEHP.

TABLE III. MATERIALS FOUND IN COLD FINGER RESIDUES

(Samples v 10 mg - April, 1970 Through December 1979)

Material Code	Number of Occurrences
1. ALHYD	196
2. MESIL	131
3. DEHP	118
4. ESTER	100
5. PHEST	29
6. DBP	27
7. ARMHY	23
8. MPHSI	19
9. HMBZP	19
10. UPETH	18
11. BH^T	16
12 DC704	16
13. RTV56	13
14. ORGAC	10
15. TCEPH	8
16. DEHAZ	6
17. TPP	6
18 DTAMQ	5
19. PCB	5
20 DEHAD	4

Trends in Occurrences of Generic Classes

In TABLE IV these individual materials have all been incorporated into the appropriate generic classes and the number of occurrences and their percentages calculated. This listing shows that esters (36%), aliphatic hydrocarbons (23%), and methyl silicones (16%) account for 75% of the outgassing problems observed during the last ten years of thermal vacuum testing at Goddard.

TABLE IV. PRINCIPLE MATERIALS BY GENERIC CATEGORIES

Category	Number of Occurrences	Percentage
1. All Esters	298	36
2. Aliphatic hydrocarbons	196	23
3. Methyl silicones	132	16
4. Aromatic silicones	48	5.7
5. Antioxidants	40	4.7
6. Aromatic hydrocarbons	23	2.8
7. Polyuretnane derivatives	18	2.2
8. Organic acids	10	1 1
9. Other materials	73	9

An attempt was made to show possible trends in the rates of occurrence of these classes of compounds by plotting the number of times they were found in samples over ten milligrams as a function of calendar year. Immediately it was discovered that the large differences in the numbers of reports issued from one year to the next resulted in discontinuities in all frequency curves for certain years. This was corrected by calculating a normalizing factor for each year (TABLE V) in order to weight results according to the total amount of analytical activity that year.

TABLE V. CALCULATION OF ANNUAL FREQUENCY NORMALIZATION FACTORS

Year	Total Number of Reports	Fraction of Average	Normalizing Factor
1970	29	129/29	4.4
1971	59	129/59	2.2
1972	164	129/164	0.79
1973	190	129/190	0 68
1974	115	129/115	1.12
1975	61	129/61	2.1
1976	184	129/184	0.70
1977	215	129/215	0 60
1978	102	129/102	1 3
1979	131	129/131	0 98
TOTAL	10 √1294		
AVERAGE	129		

Using these factors and the quarterly count data from the computer sorting, rate curves were plotted for the three major classes of contaminants, namely, esters, aliphatic hydrocarbons, and methyl silicones (Figure 2). From the curves it can be seen that real progress in reducing the instances of serious outgassing was made between 1970 and 1975. This time period correlates well with the initiation and acceptance of materials engineering practices dictating the incorporation of low outgassing materials only, into flight hardware. However, from 1975 to the present, little additional improvement
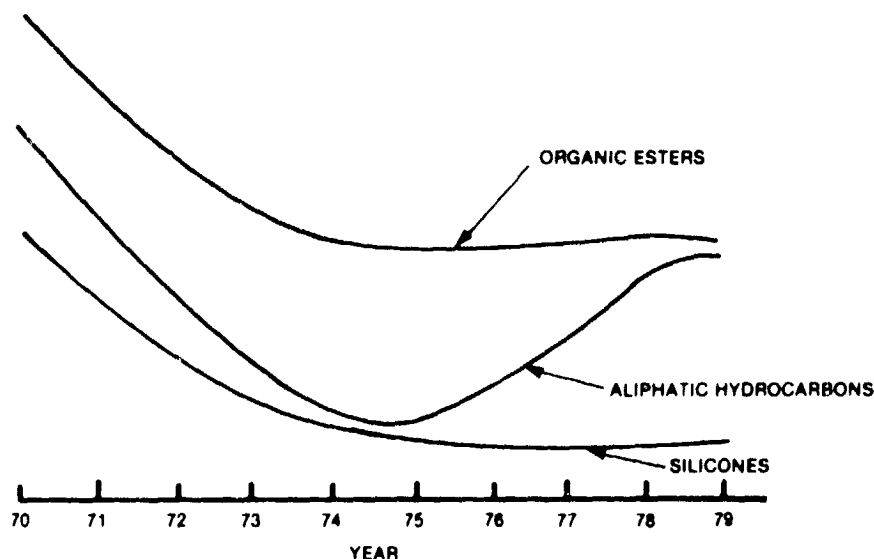
Figure 2 Normalized Frequency of Occurrence of Excessive Outgassing by Chemical Class

can be shown, and, in fact, the occurrence of serious outgassing due to aliphatic hydrocarbons has risen significantly. These facts indicate that increased research into possible sources and differentiation of outgassed aliphatic hydrocarbon species should be intitated and that schemes for more effective materials control and cleanliness procedures should be developed.

Outgassing from Solar Panels

A dramatic correlation between materials selection and outgassing was shown in the case of solar panel bakeouts. Historically, these have been one of the largest sources of condensable outgassing material and have resulted in excessive expenditures of time and money to perform repetitive thermal vacuum bakeouts in order to reduce the outgassing rates to acceptable levels. Some of the high outgassing solar cell adhesives used over the years have been Sylgard 182 and 184, RTV 511, and RTV 560/ RTV 580. TABLE VI shows the number of thermal vacuum tests performed on solar panels at Goddard for various projects along with the number of

TABLE VI OCCURRENCE OF SERIOUS OUTGASSING FROM SOLAR PANELS

Project	Test Year	Number Over 10 mg	Total Tests
RAE-B	1970	4	55
IMP-I	1970-73	8	8
SSS-A	1970-71	2	2
OAO	1970-72	10	10
IMP-J	1973	7	9
IEU	1974-75	12	2
ISEE-A	1976-77	1	11

286

these tests which resulted in cold finger residues over ten milligrams.
The dramatic improvement for ISEE-C, indicating only one bad outgassing
event out of eleven tests (9%) as compared to 91% bad for all previous
projects, is a direct result of changing from RTV 511 to RTV 566 solar
cell adhesive. Incidently, the one occurrence was not due to the cell
adhesive but was shown to be caused by the use of an improperly cured
polyurethane material used elsewhere on the panel.

Outgassing from Thermal Blankets

A similar improvement in outgassing performance has been shown for
thermal blankets (TABLE VII). In 1972-1974 eight out of nine thermal
blanket bakeouts resulted in excessive outgassing, whereas, in 1977-1979,
only three of twenty were in the excessive range. In this case, however,
no clear-cut materials' correlation could be found and it is likely that
the improvement can best be explained as due to the institution of better
cleanliness procedures during fabrication and handling.

TABLE VII OCCURRENCE OF SERIOUS OUTGASSING FROM THERMAL
BLANKETS

Project	Test Year	Number Over 10 mg	Total Tests
SAS-B	1972	5	5
ERTS	1972-73	2	3
ATS-F	1974	1	1
AEM-A	1977-78	1	3
IUE	1977	1	4
MMS	1978	1	4
SMM	1978-79	0	9

Antioxidant from Wire Insulation

The appearance of a unique material in many cold finger residues
since 1976 has caused an interesting and enlightening investigation. This
material, known as hydroxy, methoxy benzophenones, has originated from
certain electronics packages and a large number of cable bakeouts. Eighteen
out of twenty two samples where it was found were in the excessive range,
i.e., over ten milligrams. A little research has shown that this substituted
benzophenone is the antioxidant/uv stabilizer in Raychem "Spec 44" wiring
insulation. Our previous outgassing test data of Spec 44, done in 1976, showed
this material to be acceptable and repeat tests this year also support this
conclusion. However, it appears that the antioxidant is marginally condensable
and can be expected to cause problems only on surfaces cooled below room temp-
erature. The appearance of large amount of this material in cold finger
residues seems to be caused by the fact that there were very large amounts of
wire used and the borderline condensable material was collected on cold sur-
faces. For future space flight use, Raychem has agreed to produce their
"space grade" Spec 44 wire without this additive.

Miscellaneous Materials' Outgassing Trends

Other attempts to correlate materials' usage with outgassing results
have not been so unequivocal. For instance, tracking of the rate of occurrence

of four interesting specific compounds is shown in Figure 3.
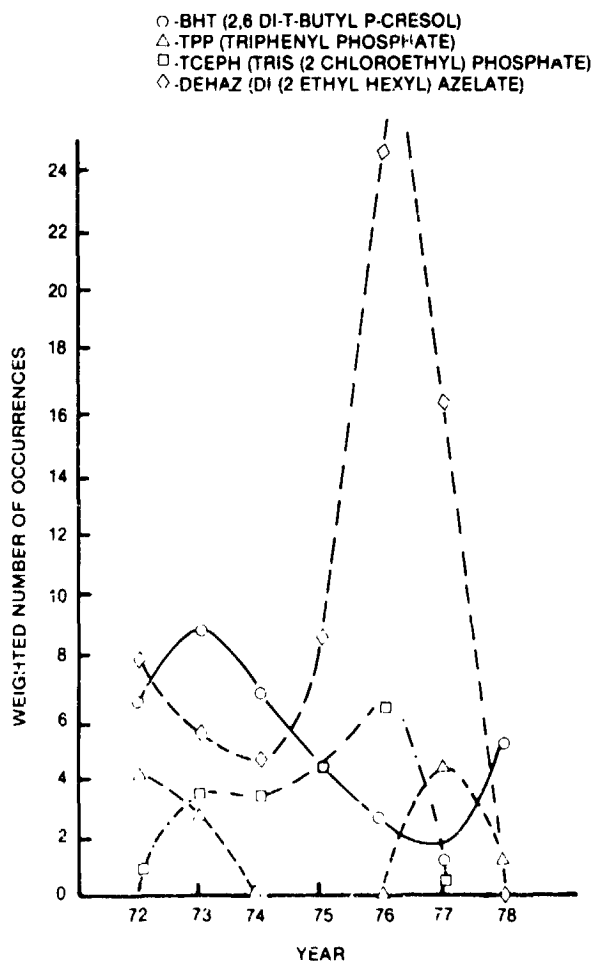
Figure 3   Normalized Rates of Occurrence of Some Unique Compounds

The appearance of the volatile antioxidant, BHT(2,6 ditertiary butyl
p-cresol), has declined somewhat in recent years, perhaps as a result of
better materials screening practices, but has not yet been eliminated.
This material is commonly used in synthetic rubbers and plastics, but its
specific sources in aerospace hardware are still uncertain.

The compound triphenyl phosphate, which is a fire retardant plasti-
cizer, was detected in 1972-1973 and then not again until 1977.   Studies
of the hardware and projects associated with the appearance of this material
were inconclusive with the only correlation being that it appeared mostly
in samples which also contained significant amounts of aliphatic esters
such as azelates and adipates.

The frequency of occurrence of another fire retardant, tris(2-chloro-
ethyl) phosphate, seems to have been more well-behaved.   Its occurrence,
which was associated with polyurethane foams, increased through 1976, and
since then has virtually disappeared from samples of collected outgassing

products. An even more dramatic shift in frequency, but again not well
explained, is the case of di(2-ethyl hexyl)azelate, a plasticizer used
for its low temperature effectiveness. The rate of appearance of this
compound increased radically in 1976 and 1977 and then, for no obvious
reason, dropped to almost nothing.

Thermal Vacuum Tests of Whole Spacecraft

Although there are not enough data from equivalent tests to provide any
accurate statistical trends, the outgassing results from whole spacecraft
are never-the-less of considerable interest and demonstrate some important
materials' correlations. Some of the results which can reasonably be com-
pared are presented in TABLE VIII.

TABLE VIII. OUTGASSING FROM THERMAL VACUUM TESTS OF WHOLE SPACECRAFT

Facility	Year	Spacecraft	Amount of Residue	Primary Products
238	1971	IMP-H	20 mg	Methyl silicones
238	1973	RAE-B	32 mg	DEHP/RTV-560
238	1978	AEM-A	1 mg	ALHYD
238	1978	AEM-A	1 mg	ALHYD
290	1975	CTS	38 mg	DBDAC (Anti-oxidant)
290	1975	CTS	2 mg	ALHYD
290	1975	NRL	9 mg	RTV-560
290	1975	NRL	6 mg	RTV-560
290	1977	ISEE-A	4 mg	ALHYD
290	1977	IUE	4 mg	ALHYD
290	1977	IUE	9 mg	ALHYD
290	1977	IUE	3 mg	ALHYD
290	1977	IUE	1 mg	ALHYD
290	1979	SMM	12 mg	ALHYD/DEHP
290	1979	SMM	1 mg	ALHYD

From facility 238, a dramatic reduction in amount of outgassed residue
was observed between the early 70's and the AEM-A(HCMM) tests which were
run in 1978 and resulted in only one milligram of collected material. For
the IMP-H in 1971, the large amount of outgassed residue (20 mg) was shown
to consist of methyl silicones from the solar cell adhesive (Sylgard). In
1973, excessive outgassing from the RAE-B(32 mg) was attributed to plast-
icized vinyl (probably wire insulation material) and to the solar cell adhesive
system, RTV-560/580. Both of these outgassing sources have now been elim-
inated from all flight hardware materials lists.

Tests conducted in the Solar Environment Simulator (SES), facility 290
provide less dramatic results because the collected cold finger residues
are always smaller due to the extremely unfavorable geometry (the facility
is gigantic compared to the cold finger surface area, and to the fact that
there is tremendous pumping capability, ie., high through-put per unit vol-
ume. However, there have been some notable occurrences such as in the case
of the CTS in 1975. The first thermal vacuum test resulted in 38 milli-
grams of collected condensable residue which was shown by mass spectrometry

to consist of a single chemical species with the ponderous chemical name of ditertiary butyl dimethylamino para-cresol. This material, also known as "Ethyl Antioxidant 703", is comparatively volatile and was completely absent from the subsequent cold finger sample where the amount of residue was only two milligrams.

Most of the other spacecraft tested in this facility have produced only moderate amounts of outgassing products. It has been demonstrated, especially in the case of the IUE, that continued thermal vacuum operation can be an effective _final_ clean-up technique. Thus, the last two cold finger amounts were about one milligram, which is the amount expected when the chamber is operated with no payload at all. The exact same sequence was observed with the SMM spacecraft in 1979.

CONCLUSIONS

Computerization of chemical analysis data has been used successfully to identify several important trends in the occurrence of outgassing problems in aerospace programs. The frequency of occurrence totals show that di (2-ethyl hexyl) phthalate (DEHP) is the most often found individual species in outgassing samples and that esters are tne leading generic class of compounds. The effectiveness of this data bank has been demonstrated by the good correlations between materials and their outgassing products for solar panel bakeouts and cable bakeouts. However, trends in frequency of occurrence of many compounds have been demonstrated where no correlation could be established. In the case of the class of compounds called aliphatic hydrocarbons, it was shown that the number of instances of significant outgassing due to these materials is increasing. If this trend is to be reversed, more knowledge concerning the sources and chemistry of the compounds included in this classification will have to be derived by intensified research in this area.

THE USE OF THE PRINCIPLE OF SUPERPOSITION IN MEASURING AND PREDICTING THE THERMAL CHARACTERISTICS OF AN ELECTRONIC EQUIPMENT OPERATED IN A SPACE ENVIRONMENT

Dr. Earl H. Gale*

ABSTRACT

This paper reviews the advantages and possible pitfalls of using a generalized method of measuring and, based on these measurements, predicting the transient or steady-state thermal response characteristics of an electronic equipment designed to operate in a space environment. The method requires generation of a set of thermal influence coefficients by test measurement in vacuo. A simplified thermal mockup is used in this test. Once this data set has been measured, temperatures resulting from arbitrary steady-state or time varying power profiles can be economically calculated with the aid of a digital computer.

INTRODUCTION

The two most common methods of predicting the thermal performance of an electronic equipment are to:

1) Make a thermal mathematical model and solve the resulting network equations using finite difference or finite element methods with the aid of a computer

2) Build a thermal mockup of the equipment which approximates the geometry and the dissipation profile of the equipment under design and directly measure the thermal performance in a simulated environment.

This paper describes a middle road to the above methods utilizing both measurements to initially thermally characterize an equipment and then a simple computer program to accurately and economically predict either the transient or steady-state thermal response of the equipment for any power versus time or steady-state profiles of interest. The method is of great value when the thermal performance with more than one power profile (duty cycle) is required.

The method requires the construction of a thermal mockup of similar configuration to the equipment under design with a unit power resistor attached within the equipment at each location of an electronic component having a significant heat dissipation. The unit resistors may be all of the same wattage rating and dissipation despite the fact they are located at positions where varying amounts of heat are to be dissipated. A thermocouple is installed in the vicinity of each of the unit resistors as well as at all other locations within the equipment at which temperature information is desired.

A single set of measurements in which each unit resistor is powered, one at a time, and the resulting temperature-time profiles at all points of interest are measured and recorded. This data bank allows the later prediction of temperatures using any power profile accurately, quickly and economically utilizing an easy to write computer program. This simple method is accurate only

---

*General Electric Company, Aircraft Equipment Division, Utica, New York.

in systems whose characteristic underlying differential equations are linear such as the equations describing the heat conduction within an equipment in a space (no air) environment.

This paper describes how the method was legitimately and successfully used to predict the steady-state thermal performance of an electronic equipment having various duty cycles despite the fact that the equipment case-to-surroundings heat transfer within a spacecraft was by thermal radiation, a mode of heat transfer described by nonlinear equations. A discussion of when it would be permissible to include such nonlinear surface heat transfer is presented.

NOMENCLATURE

A	radiating area of case
C	thermal capacity of conducting material
E	constant which is function of emissivities of equipment case finish and shroud finish in temperature-vacuum chamber
k	thermal conductivity
q''	heat flux per unit area
q'''	heat generation per unit time per unit volume
T	absolute temperature
w	specific weight of conductivity material
x,y,z	spatial coordinates
σ	Stefan-Boltzmann constant

Subscripts

c	cold
h	hot
i	index number of test measurement of temperature field resulting from single source
m	mean
t	total

THEORETICAL JUSTIFICATION OF METHOD

Heat transfer in electronic equipments used in space takes place by conduction and radiation. It is usual that the method of heat transfer internal to an equipment, that is, between heat dissipating components and the outer case of the equipment, is by conduction through structural paths with radiative heat transfer playing a negligible role. This usually happens by design as providing structural paths having high thermal conductances is necessary for good thermal management. Heat transfer from the outer equipment case may be by conduction through the equipment mounts, or thermal radiation from the case to the surroundings or a combination of both of these transfer mechanisms.

When heat transfer within the box is only by conduction, the resulting temperature field must satisfy the general heat conduction equation:

$$\frac{\partial^2 T}{\partial x^2} + \frac{\partial^2 T}{\partial y^2} + \frac{\partial^2 T}{\partial z^2} + \frac{q'''}{k} = \frac{1}{\alpha} \frac{\partial T}{\partial \theta} \qquad (1)$$

$$\alpha = \frac{k}{Cw} \qquad (2)$$

Since this governing equation is linear, the well-known principle of superposition can be used in the manner described in this report to predict the time varying or steady-state temperature field within the equipment. Reference 1 states: "The principle of superposition can be applied to all cases in which the effect of simultaneous superposed actions is the sum of the effects of each individual action. It can be applied, therefore, to linear system, i.e., to physical systems governed by linear differential or integral equations." Using this method to predict the thermal performance of a particular equipment will now be described.

IMPLEMENTATION OF METHOD

The particular equipment for which the author successfully used the analysis method described in this paper had the following characteristics:

1) In application, it was to be operated with a large number of different "duty cycles". Each duty cycle was defined by the power versus time history of each heat dissipating component within the equipment.

2) The equipment was radiatively cooled to its surroundings and, during the operation, the outer case temperature was approximately uniform.

3) Paths of high thermal conductance between heat dissipating components and the case were provided by design for heat management purposes; that is, the unit was designed for efficient internal conduction cooling.

TESTING PROCEDURE

The electronic equipment chassis that was later used in the construction of the engineering model was instrumented by the bonding of wire-wound resistors at locations at which there would later be significant thermal dissipations from individual electronic components. Thermocouples were attached at all component locations at which operating temperature information was required. In this particular test, a total of sixty thermocouples and forty resistors were used to characterize the thermal profile of the unit. A thermocouple was always mounted on the chassis structure adjacent to each wire-wound resistor.

A high vacuum, 10^{-5} Torr range, test chamber having a temperature controlled shroud was used in the test. The temperature of the shroud was held at that uniform temperature which had been specified for the design. Each resistor was activated, one at a time, and the resulting temperature-time history at all thermocouple locations was recorded.

The data was processed in the following manner. The temperature rise above shroud temperature for each location as a result of powering each resistor was recorded in a matrix format at the end of each ten-minute interval. Using the shroud temperature as the baseline or reference temperature meant that the nonlinear radiative equipment-to-surroundings (shroud) thermal resistance was included in the compilation of these thermal "influence coefficients". The error resulting from the inclusion of these radiative resistances will be discussed below where it will be shown to be:

1)   Small

2)   On the safe side, i.e., resulting in higher than actual predicted temperatures.

THE COMPUTER CODE

The concept for the computer code is obvious and simple. A program was written which simply added the temperature rises at each thermocouple location resulting from step infusions of heat at each resistor location at the end of incremental units of time. The process is one of summation of effects requiring the direct addition of temperature rises (a noniterative solution) and the computer time (cost) needed to analyze various duty cycles (power vs time) is very small.

Had the unit itself been conduction-cooled through its mounts, the above method would have been completely theoretically correct and the following section on estimating the upper bound of the error resulting from the nonlinearity of the radiative heat transfer path between the equipment case and the surroundings would not need to be considered.

UPPER BOUND OF NONLINEARITY ERROR

The upper bound of the error resulting from treating the radiative conductance from the case to the shroud as independent of temperature level will now be determined.

The basic equation describing radiative heat transfer from each region (node) of the equipment case to the shroud may be written in the following form:

$$q'' = EA\sigma(T_h^4 - T_c^4) \tag{3}$$

On factoring, equation (3) may be written:

$$q'' = EA\sigma(T_h^3 + T_h^2 T_c + T_h T_c^2 + T_c^3)(T_h - T_c) \tag{4}$$

References 2 and 3 show that if $T_h - T_c$ is small compared to $(T_h - T_c)/2 = T_m$, equation (4) may be replaced by:

$$q'' = 4EA\sigma T_m^3(T_h - T_c) \tag{5}$$

The criterion for the above approximation was always met when measurement with the individual unit resistors was taking place.

The formula describing the total heat transfer from any case region (or the entire case if the temperature is uniform) is of the same form as equation (3):

$$q''_T = EA\sigma(T_{ht}^4 - T_c^4) \tag{6}$$

Rewriting equation (6):

$$q''_T = EA\sigma(T_{ht}^2 + T_c^2)(T_{ht} + T_c)(T_{ht} - T_c) \tag{7}$$

Solving for $(T_{ht} - T_c)$ yields:

$$(T_{ht} - T_c) = \frac{q''_T}{EA\sigma(T_{ht}^2 + T_c^2)(T_{ht} + T_c)} \tag{8}$$

$(T_{ht} - T_c)$ found by summing (superposition) using equation (5) is:

$$(T_{ht} - T_c) = \sum_{i=1}^{n}(T_h - T_c) = \sum_{i=1}^{n}\frac{q''_i}{4EA\sigma T_m^3} = \frac{q''_t}{4EA\sigma T_m^3} \tag{9}$$

The ratio of $T_{ht} - T_c$ calculated by superposition using equation (9) to the exact total equation (8) has been calculated for a wide range of sink temperatures and temperature differences, and the results are presented in Figure 1.

It should be emphasized that this figure does not indicate the actual error but the upper bound of the actual error as during the unit resistor tests $T_m \approx T_c$ for each individual test. It should also be realized that this radiative resistance is never the total resistance between source and sink (i.e., component mounting location and shroud) but merely a series component. Thus, a 10-percent error in calculation of this quantity would result in a lesser total error.

If the possible upper error bound as shown in Figure 1 were too large to be acceptable, the absolute total error could be reduced by including in the computational program a temperature level correction factor, after equation (5), to correct the measured i^{th} case-to-shroud temperature difference to a case temperature more indicative of the case temperature during operation.

The form of this correction factor would be:

$$\frac{T_{mi}^3}{T_{mt}^3} \tag{10}$$

where T_{mi} was the mean absolute temperature resulting from the averaging of case and shroud temperature during the ith test and T_{mt} the temperature resulting from the averaging of case and shroud temperatures with the case temperature predicted using the total unit power.

CONCLUSION

The prediction method described in this paper can be an extremely useful and economical tool for predicting either the steady-state or transient thermal response. It is of particular value in each of the following situations:

1) Calculating the responses to equipment to be operated with many different duty cycles, i.e., power time profiles, where it would be impossible (due to time limitations) or uneconomical to run a multitude of tests using the actual power profiles

2) The procedure is also a valuable tool for checking the accuracy of finite element or finite difference programs in which internal thermal conductances have been determined by calculation rather than measurement and for which semi-empirical verification is desired.

REFERENCES

1. Theodore v. Karman and Maurice A. Biot, Mathematical Methods in Engineering, McGraw-Hill Book Company, Inc., 1940, p. 378.

2. Max Jakob, Heat Transfer, John Wiley, Volume I, 1955, p. 87.

3. Ibid., Volume II, 1957, p. 3.
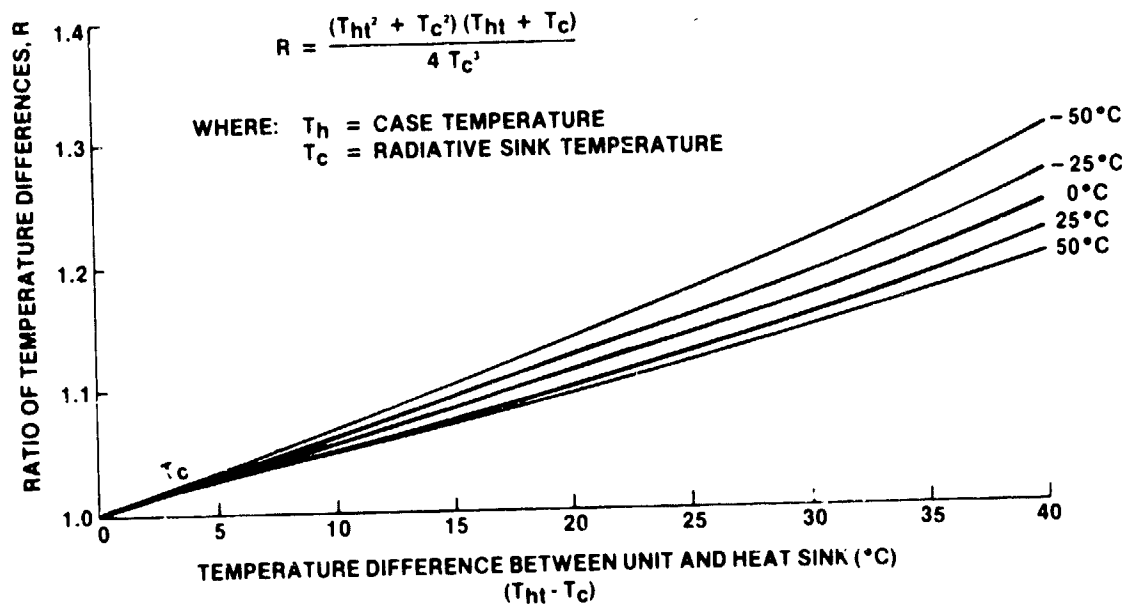
Figure 1. Ratio of Theoretical Maximum Sum of Surface-to-Sink
Temperatures to Actual Surface-to-Sink Temperature
Difference at the Same Total Unit Power

P78-2 (SCATHA) SATELLITE THERMAL BALANCE TEST
A LABORATORY TEST

Robert P. Parrish, Jr.*

ABSTRACT

Systems tests in Martin Marietta's Space Simulation Laboratory at Denver are now conducted with greater confidence. Planning and early systems checkout tend to preclude unpleasant surprises. Safety is part of the design and operation; examples are over-temperature kills, gimbal stops, and proven procedures and personnel. However, full-up thermal balance tests using the solar simulator, temperature control of infrared sources, the gimbal, a large number of thermocouples, and other requirements for a high fidelity thermal balance are still a challenge.

Add to this such things as several new members in the operating crew, combining development, qualification and acceptance testing in one test, exceeding the maximum design intensity of the solar simulator, an extremely tight test schedule impacting interface control and definition, a unique gimbal control requirement, and the test really becomes a challenge. This was the P78-2 (SCATHA) Satellite thermal balance test.

The lessons we learned in meeting this challenge is the subject of this paper.

The test was successfully conducted with minimal delays, and the P78-2 (SCATHA) Satellite was launched successfully.

INTRODUCTION

Surely another typical spacecraft thermal vacuum test report is repetitious! Yet, if it involves something new and different or is significant in some other way, the story should be told. No one thing about this test was new or particularly outstanding. However, so many things seemed to be working against a troublefree, successful test that weaknesses in our state of readiness and approach to the test became highly visible. Many tests have been conducted before and after this one. These involved few problems which were readily resolved. The high degree of success in conducting the subsequent tests has led us to believe that although problems will always be with us and accidents are not always prevented, their probability has been greatly reduced by the lessons learned in testing the P78-2 satellite. The satellite in the Space Simulation Laboratory (SSL) 29'x65' thermal vacuum chamber is shown in Figure 1.

---

* Martin Marietta Corporation, Denver Division

THE LABORATORY'S STATE-OF-READINESS

About two years had elapsed since the last major systems thermal vacuum test had been conducted. A skeleton staff had maintai d the facility during this period, but not adequately since most of their ti had been spent running component and subsystem tests. Enough of the remaining members of the staff were retained by being placed on other assignments to keep the capability of conducting a systems test. However, we all became rusty, and although we went through a retraining and recertification program, we still lacked the confidence that only several recent tests could provide.

The other aspect of readiness was the facility. It too did not have the advantage of recent use. To get it ready, a refurbish plan was developed and implemented. In fact, refurbishment of the solar simulator, which was known to be critical regarding maintenance and reliability, was started over a year before the first test requiring its use and about a year and a half before this test. It is shown in Figure 2 with some of its capabilities. The original performance characteristics of the system were attained, measured, and documented. Thirty-two kilowatt Xenon arc lamps were then obtained to replace the center seven twenty kilowatt lamps to reach the required intensity of 1.4 solar constants with a nominal fifteen percent margin. We ran a thermal vacuum test on an antenna and two brief development tests using the solar simulator and the chamber, and felt we were ready for the upcoming P78-2 tests, except for one item. This item was the programmable control system for the two-axis gimbal depicted in Figure 3. We started checking out the control system about a year before it was needed on this test. Our mistake here was in not fully recognizing the difficulty in repairing old one-of-a-kind digital control systems. With the suppliers' support, we started troubleshooting and continued on our own once he was not able to maintain his support due to other commitments.

By this time we were to the point where other requirements pertaining to the gimbal began competing with the repair of the control system for use of the gimbal. These requirements were a take-up reel, a partial gimbal shroud, and a safety stop for the gimbal. Limited access to the gimbal caused the these requirements and the controller repair to be delayed to the extent that their verification was not adequate due to schedule constraints. However, lack of good interface to establish its long-term reliability control was even more of a problem.

INTERFACE PROBLEMS

Though we had employed the established methods of interface control with a test plan, test procedures, fixture drawings, detailed schedules and other interface documents and meetings, we still fell far short of the needed interface control.

One interface problem that caused an overnight delay was an interference between the spacecraft and the partial shroud installed on the gimbal that precluded installation of the spacecraft on the gimbal. A design error caused in part by changing designers was not detected. Almost unbelievably, the identical dimensional error was made when dimensional checks were made to

verify proper clearances. Once the problem was detected when installing the spacecraft, the error was still difficult to find but could have been uncovered earlier had the interface dimensions been checked specifically by both the laboratory and the project as part of the design check

Reflections of the solar beam from flat surfaces of multilayer insulation (MLI) back up to the collimating mirror and back down to the spacecraft and monitoring radiometers were of much higher intensity than had been anticipated. See Figure 2 . This caused the electrical power to the solar simulator to be significantly less than normal for the intensities indicated by the radiometers. In spite of the fact that temperatures and other parameters from the spacecraft also indicated the solar intensity was slightly low, the correct decision to go with the radiometers was made. Flight data indicate the thermal environment simulation was quite close.

These are just two of the several interface problems encountered during this space simulation test program. They are, however, representative of two types of interface problems, one mechanical and the other environmental. One of the other interfaces we did not establish and work was the project to laboratory interface, especially before the test. No one laboratory engineer nor one program engineer was assigned as the primary one responsible for keeping both parties completely informed and making sure all interfaces were addressed and worked. The laboratory did have one person assigned but much was worked around him which made his task extremely difficult. Had the program and the laboratory provided primary points of contact, problems would have been resolved earlier.

The three aforementioned interface problems were those that were most significant for the laboratory. Others that the laboratory was sensitive to were:

   o Contamination monitoring
   o Instrumentation interfaces
   o Acceleration of satellite by gimbal
   o Quality Control involvement in laboratory operations
    & configuration
   o Safety responsibility - satellite and SSL
   o Access control
   o Lab schedule
   o Customer/Lab interface
   o Building humidity and temperature control requirements

This list is an example of considerations a laboratory must address.

Up to this point in time, we had not had a formal interface control document (ICD) for test programs. However, previous tests were either much more simple or like Viking, had much more extensive preparation including development and thermal models in which the interfaces could be developed and verified. A formal ICD will not eliminate all interface problems, but it will certainly focus attention on the interfaces.

LESSONS LEARNED

The length of time and intensity of training to retrain or train an experienced technician or engineer to be a competent member of the operating crew who can fill the positions for which he is certified with confidence has been underestimated. While no specific problems were attributed to lack of personnel capabilities, an overwhelming stress was placed on the few experienced members of the SSL staff to meet the needs of the test. A training program has been prepared and is being implemented to augment the on-the-job-training normally employed.

Perhaps even more difficult than the maintenance of skills is the maintenance of the facility. Keeping a facility of this type up to meeting the demands of today's test requirements with the available skills, time, and budget is indeed a challenge. Here again we felt we were refurbishing the facility to a like-new condition. However, a few months and tests later, a whole new set of failure modes began to appear requiring the utmost from the operating crews to keep the facility on-line and meeting the test parameters. A lot of statistical data is not available for these one- or few-of-a-kind system which makes needed maintenance budget and replacement frequency hard to estimate. The state-of-readiness of the laboratory must be maintained so programs come to a safe, reliable facility for space simulation tests. Redundancy, reliability, a good spare parts inventory, and a well maintained system are necessary to assure minimum risk to the item being tested and to the test program.

Given the space simulation facility and its staff are capable of preparing for and conducting successful tests, poor interface control can still lead to trouble. Even with the several problems of our crew and facility, we could have eliminated several problems in the P78-2 thermal balance test with better interface control. We certainly learned the need for a comprehensive ICD for all major systems test. We feel this is the most significant lesson learned from the P78-2 test.

A good communication interface both before and during the test is also critical. We found that the interface during the test has been more than sufficient but when the test requirements are being developed and transmitted to the laboratory, the interface can be quite inadequate. Subsequent test programs have gone very well due primarily to a strong communication link.

CONCLUSION

Space simulation test programs can be carried out with a high probability of being troublefree with a competent staff, a well-maintained test facility and attention to interfaces. The P78-2 (Scatha) satellite was successfully tested with one interruption and a four-day abbreviated retest to verify a modification. This was accomplished in spite of the new test crew, a facility beset with several operational problems, and marginal interface control. These problems have been addressed with very good results. Subsequent tests have been highly successful.
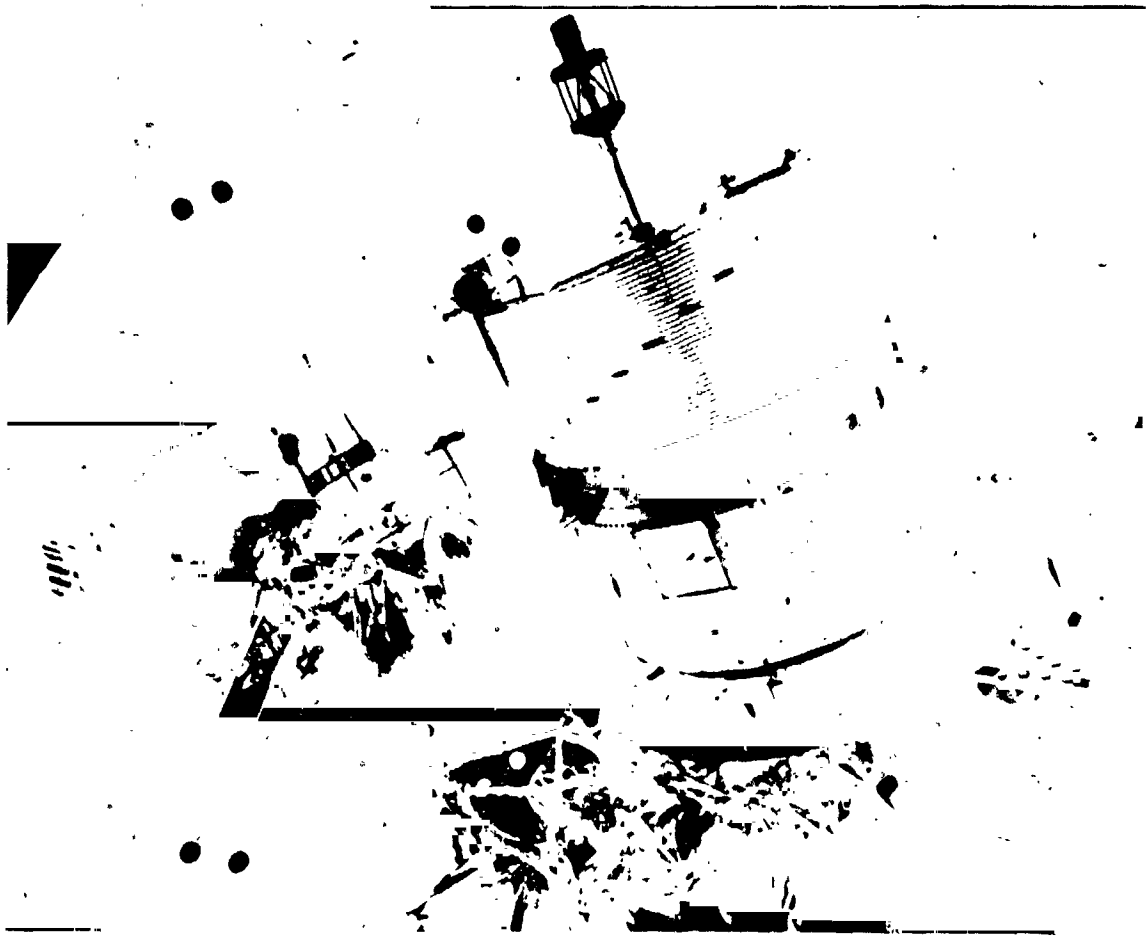
Figure 1. P78-2 Satellite In Chamber

Thermal Environment Simulation
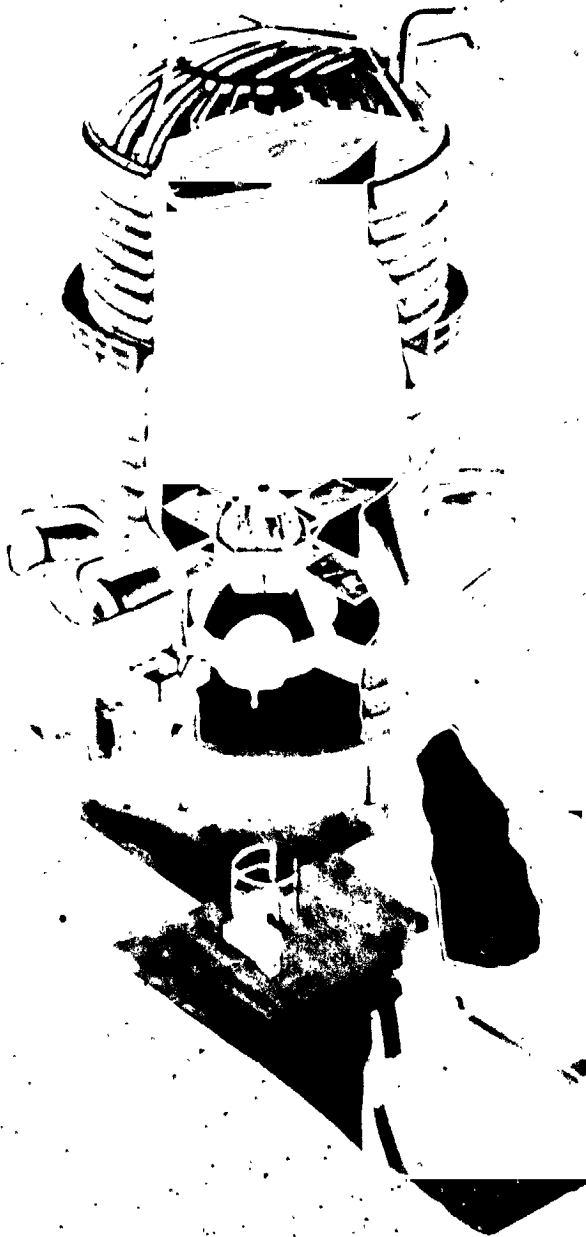
Maximum Test Specimen Size
   Vacuum 20 x 40 ft, Solar Vacuum 16 x 16 ft

Working Vacuum
   1 x 10⁻⁵ torr with Gas Load
   7 x 10⁻⁷ torr No Load

Cold Wall -320°F, LN₂ Cooled; Solar Collimating
Mirror, -60°F Cooled
   Simulates Uniform Free Space Background

Solar Simulation
   0.35 to 1.25 Solar Constants
   Close Spectral Match to NASA Curve

Infrared Simulation
   21 Separately Controlled IR Zones
   1,700,000 Btu/hr
   Simulates Heat from Sun & Planets

Pumping
   4 Mech. Pumps for Roughing Down to 10⁻⁴ torr &
   Diffusion Pumps as it is ~~~~~~~
   (36°K: 3 x 10⁵ liters/sec N₂)

Data
   1000 Channels Central Logging
   150 Auxiliary Channels
   50 Real-Time Display Channels
   10 Digital Display Channels

Figure 2. Basic Space Simulation Facility

303
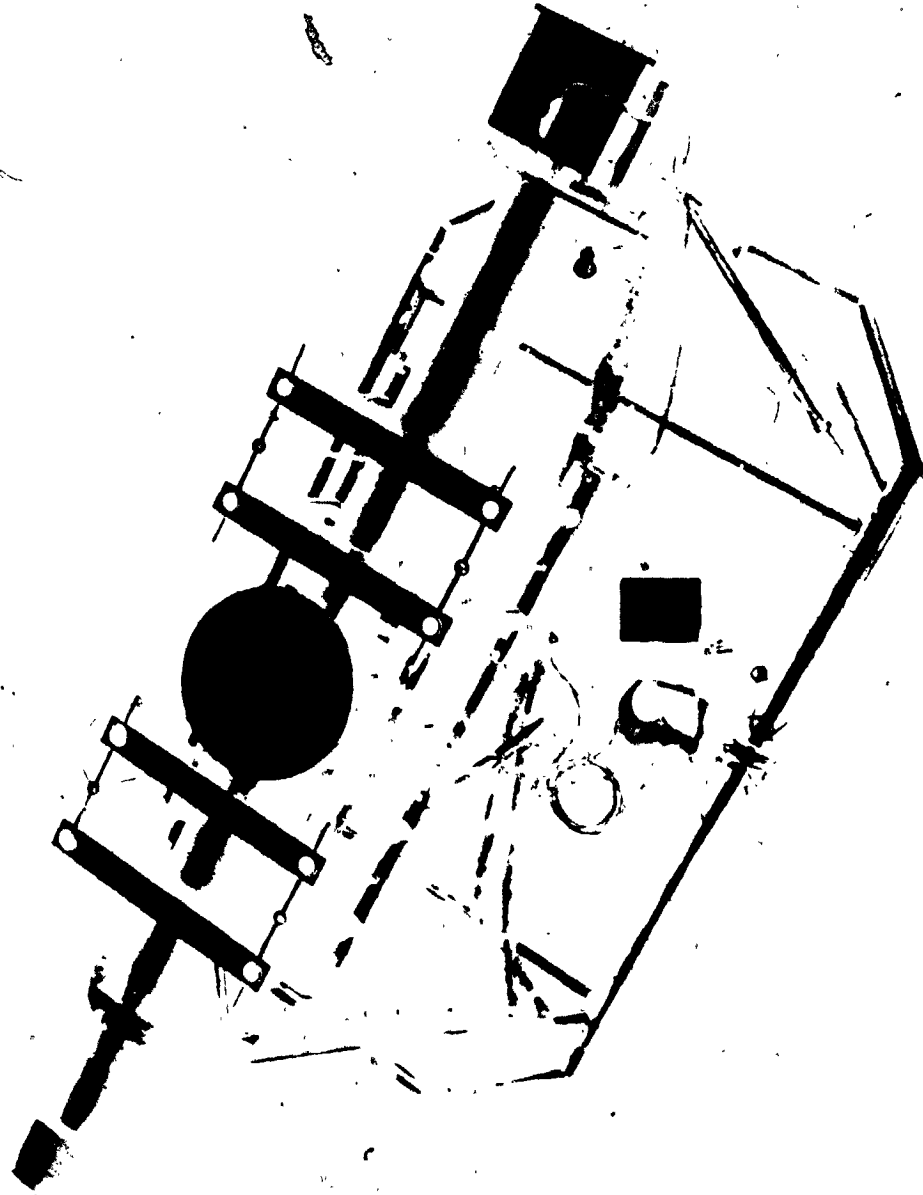
Figure 3.   Two Axis Gimbal

THERMAL VACUUM PERFORMANCE TESTING OF THE SPACE SHUTTLE ORBITER RADIATOR SYSTEM

Albert F. Behrend, Jr.*

Gorden D. Chandler**

Harold R. Howell+

ABSTRACT

The Space Shuttle Orbiter radiator system thermal vacuum performance test was conducted at NASA-Johnson Space Center in Chamber A of the Space Environment Simulation Laboratory in January-February 1979. The test objective was to verify the radiator system heat rejection performance capability utilizing two development and two flight radiator panels comprising one of the two Orbiter Freon-21 coolant loops. Radiator performance over the range of expected flight conditions was as predicted, and there was no degradation of performance after extended vacuum exposure.

INTRODUCTION

During on-orbit operations of the Space Shuttle Orbiter, heat rejection will be accomplished primarily by the space radiators. The radiators are located on the inside surface of the payload bay doors for protection during launch and reentry. On-orbit deployment is accomplished by opening the payload bay doors and exposing the radiators to the space environment. An optimum thermal coating and high radiation fin effectiveness are used to maximize the radiator heat rejection. However, the limited door area results in some vehicle attitude and heat load combinations which exceed the radiator capacity and prevents adequate cooling of the heat transport fluid, Freon-21. In those situations the topping flash evaporator is automatically activated to provide the additional cooling needed by boiling available excess fuel cell water. The Orbiter also will be constrained from those attitudes where the vehicle heat load results in the combined radiator and topping flash evaporator being unable to maintain the Freon-21 return temperature below the required $4.4^\circ C$ ($40^\circ F$).

To verify the Orbiter radiator system heat rejection performance capability for expected orbital attitudes a thermal vacuum performance test was conducted at NASA-Johnson Space Center on four radiator panels and their 'A (Flow Control Assembly), representing one of the two Orbiter coolant loops. The testing was performed in conjunction with the Orbiter integrated ATCS (Active Thermal Control System) test in Chamber A of the Space Environment Simulation Laboratory. A detailed description of the integrated system testing is provided in References 1 and 2.

*NASA-Johnson Space Center, Houston, Texas
**Rockwell International Corporation, Houston, Texas
+Vought Corporation, Dallas, Texas

SYSTEM/FACILITY DESCRIPTION

The ATCS, containing two independent flow loops, collects, transports and rejects waste heat from the Orbiter subsystems, equipment, and payloads from prelaunch through post landing for each mission. On-orbit heat rejection is accomplished by the use of space radiators. The baseline ATCS radiator system (Figure 1) has 6 radiator panels (3 in each flow loop) attached to the inside of the payload bay doors. Two additional radiator panels (one for each flow loop) can be mounted on the aft section of the payload bay doors for added heat rejection capability. The 3.1 m x 4.6 m (10 ft x 15 ft) panels which are contoured to the payload bay door to maximize the payload volume, consist of two basic designs - forward panels, which are deployed away from the payload bay door after the doors are opened on-orbit and reject heat from both sides of the panel; and aft panels, which are attached to the aft section of the doors and radiate from only the concave surface. The series-connected radiator panels contain parallel flow tubes and are constructed of a low density aluminum honeycomb bonded to thin aluminum face sheets and coated with a special silver Teflon coating. The silver Teflon provides a low absorptance of solar flux and a high thermal emittance. Coolant flow through each set of radiators is controlled by its FCA (one in each loop). The FCA's can be operated manually or automatically to control the radiator system outlet temperature to either 3.3°C (38°F - normal) or 13.9°C (57°F). The 13.9°C (57°F) control temperature is used to dump excess fuel cell generated water through the topping flash evaporator. A more detailed description of the ATCS is presented in Reference 3.

The test was conducted in Chamber A of the Space Environment Simulation Laboratory. Chamber A is the largest of the JSC thermal vacuum test facilities. The working volume of the chamber is 16.8 m (55 ft) in diameter and 27.4 m (90 ft) in height. The radiator system test article layout in conjunction with other ATCS test hardware is shown in Figure 2. Special test support elements supporting the test article were located on the first floor level outside the chamber. Cryogenic and diffusion pumping were used to obtain a chamber pressure of 1.3×10^{-4} N/M^2 (10^{-5} Torr). The chamber's entire liquid nitrogen shroud including the floor was cooled to liquid nitrogen temperatures to obtain the required environment for radiator system performance evaluation. Sublimation repressurization, using dry nitrogen and heaters to minimize water condensation on the radiator panels and insulated surfaces, was used to repressurize the chamber to sea level conditions. During chamber repressurization television and high voltage equipment (infrared simulators) operation was prohibited to prevent corona damage.

Two development and two "flight" radiator panels were installed in the configuration shown in Figure 2. To minimize gravity effects the aft panels were aligned with the plane formed by the panel edges tilted at an angle of 0.15 radians (8.75 degrees) with respect to horizontal with the outboard edge above the inboard edge. The forward panels were placed behind the aft panels with the plane formed by the panel edges in a horizontal position. A liquid nitrogen shroud was installed between the forward and aft panels to prevent radiant interchange between the upward tilted aft panels and the forward panels. The radiator panels were suspended by cables attached to the support structure. Payload bay door thermal simulators were installed below the two forward panels forming an angle of 0.62 radians (35.5 degrees) between the planes of the upper surface of the panels and doors, representing the deployed position of the panels during on-orbit operations. Heaters on the door simulators, simulating the infrared flux originating from the doors, were controlled from a power console located outside

the test chamber. The back side of the aft panels and the door simulators
were insulated with multilayer insulation to minimize heat leak from these
surfaces. Heaters also were installed under the back side insulation of
the aft radiator (panel 4) to prevent freezing during test points that
required isolation of panel 4 from the coolant loop.

Earth and solar environment simulation was provided by infrared lamps
capable of simulating both skewed and orbital cycle flux environments. Flux
from the lamps was input to the upper concave surface of the radiators by
an array of nine rows of lamps, each under separate computer control. Radio-
meters to measure heat flux were mounted flush with the upper surface of the
radiators in the plane of the radiator. Structure holding the environment
simulator and radiators was designed to minimize blockage thereby maximizing
radiator panel view to the chamber. Shutoff valves and a modified flight
type adapter tube to bypass the aft radiator panel were installed to allow
3-panel radiator system testing. Selection of either the 3- or 4-panel con-
figuration was made from a control panel in the facility control room.
Activation and mode selection for FCA operation was provided by a control
panel located in the facility control room.

TEST CONDITIONS/PROCEDURE

The tests for the Shuttle radiator subsystem were defined to provide
the performance envelope over a range of orbital environments and a range
of heat loads. A review of the expected Shuttle mission environments result-
ed in selection of 12 environments (Figure 3) for simulation in the test. The
heat load range tested was based on the ATCS coolant loop limits. The
selected radiator heat loads are indicated in Table I, which also gives the
environment used with each heat load. Tests were included to define radiator
performance for the 6 panel, baseline, configuration and the 8 panel, Space-
lab kit, configuration, as well as for both the normal 3.3^{o}C (38°F) and high
13.9^{o}C (57°F) radiator system outlet control temperatures.

Since analysis will be used to evaluate thermal perform ace in all
possible Shuttle attitudes, the test environments were selected to support
these future analyses. The test environments were based on both the range
of attitudes expected and the orbital transients. The attitude range includ-
ed both earth and solar orientations and extended from environment 4 (Figure
3), the coldest, to environment 3, the hottest. Environments 1, 2, and 5
simulated earth oriented orbits with fluxes nearly equally spaced between the
coldest and hottest. Two environments, 7 and 8, were required to simulate
the solar orientation, left side and right side, because only one side of the
radiator subsystem was used in the test. Correlation of the analytical models
to each of these environments will insure that future analytical predictions
for any Shuttle attitude will not be far removed from a test condition. This
should result in accurate and reliable performance predictions.

To further enhance the Shuttle radiator analysis, a solar attitude (6)
and an earth attitude (5) were each conducted for both the orbital transient
environment and at the steady-state orbital average environment. Environment
5 provided a maximum peak-to-peak orbital flux change, and environment 6 gave

307

a maximum flux change on the radiators at the earth's shadow penetration. Comparison of the test results for the transient environments to the results at the steady-state average environment provided a comparison that will allow evaluation of orbital transients using steady-state predictions.

Environment 9 was included in the radiator test to define radiator performance for the varying attitude of PTC (Passive Thermal Control). This attitude, a slow roll about the Shuttle longitudinal axis, is expected to be used frequently on most flights. It is a thermally benign Orbiter environment and nearly mid-way between the hottest and coldest radiator conditions. The remaining environments (10, 11, and 12) were included in the test because they were the reference conditions used in the radiator hardware design.

For each of the tests shown in Table I, the test procedure used was the same. The radiator system configuration was established by positioning the appropriate valves. The environment was controlled by adjusting the quartz lamp and heater intensities. The heat load was controlled by adjusting the supply Freon to the desired flow and temperature. Finally, the data was recorded when the radiator surface and fluid temperatures were stabilized.

Since the test chamber was maintained at vacuum (10^{-5} Torr), the various configurations were remotely controlled. A motor-driven valve was used to allow flow to all 4 panels or to bypass one panel for 3 panel testing. Another motor was used to remotely position the "mode valve" on the FCA to either the 6 or the 8 panel position. On the Shuttle, this valve is positioned manually during ground operations when the Spacelab kit panels are installed or removed. The high or normal radiator temperature control set point was controlled by a switch, similar to the Orbiter crew control, in the chamber control room. The motor-driven valves, and the set point switch had indicator lights to confirm their respective positions.

The desired heat load for each test was established by adjusting the ground coolant flow cart to supply the appropriate Freon flow and temperature at the flow control assembly inlet. Since there are no modulating valves except the radiator flow control valve in the ATCS coolant loop, the Shuttle loop flow should remain constant. The flow control valve was designed to provide a nearly constant flow resistance in any position. Thus, with relatively constant temperatures through the loop, the expected flow was predetermined and adjusted at the cart. With a fixed flow and controlled heat sink outlet temperature, the radiator inlet temperature could also be predetermined for each heat load independent of the environment. Therefore, the heat load was established by setting a predetermined inlet temperature and flow and holding the values constant for each test.

The environment settings were based on pretest calibrations and the radiometer and heater current indications. The total external radiator panel absorbed heat was calculated for each environment and input to the concave panel surface. External environmental flux normally incident on the surface of the forward panels was input on the concave surface during the test. The payload bay door absorbed heat also was calculated and input to the door simulator using electric heaters. From the known heater resistance, the heater current for each of six zones on the door was defined for each environment. For each test, the required heater current in each zone was adjusted and maintained to produce the correct thermal flux on the door simulator. The quartz lamps above the panels provided all the remaining environmental heat to both forward and aft radiator panels. Again, analysis was used to define the total panel absorbed heat, including earth emission,

308

albedo, and direct solar. Reflected solar energy from the door also was included. To provide direct correlation with the computer models, the calculated absorbed heats were defined for each of the five zones per panel as used in the models.

The nine rows of quartz lamps located above the panels had adjustable intensities in 1 bit settings to a maximum of 64 bits. Pretest calibration tests were made to define the affect of each row on the panel zones and facilitate adjustment of the absorbed heat profile across the panel. Unlike the other test settings, the quartz lamp intensities could not be predetermined. Radiometers located between the panels were used to define the final quartz lamp settings. They were positioned to represent the five computer model zones and coated with silver Teflon like the panels so as to read the same absorbed heat as the panels; one set for the forward panels and one set for the aft panels. This approach inherently adjusted for structure re-radiation and any chamber background flux. The radiometers recorded the total absorbed energy which, unfortunately, included that energy radiated from other parts of the curved panel that should not be included in the total external absorbed heat. To accurately represent the required environment, the radiometer indications were adjusted according to the panel temperature. The higher panel temperature required higher radiometer indications to represent the same external environment.

An approximation in the environment simulation that should be noted was the application of all external flux on only the top side of the forward panels. In actual Shuttle operation, a significant part of the absorbed heat will be to the cavity, or bottom side, of the forward panels. A pretest analysis confirmed evaluation of earlier test results and showed that the affect on performance could be neglected. The thermal conductivity across the 1-inch thick forward radiator panel was so high that absorbed heat on either surface had the same affect on the fluid outlet temperatures.

DATA ACQUISITION

A flexible data system using Hewlett-Packard 2112 and 2117 was the primary real time processor of the test data. Throughout the test, all data was recorded continuously on computer tape for subsequent printing in tabular or plotted form. However, it also was possible to observe the data on CRT's (cathode ray tube) in the control room and to activate a printer to obtain an immediate listing of selected data.

For steady-state test points, the CRT observations were used to verify the correct test article configuration, environment, and heat loads. The CRT's were also monitored to determine when steady-state was achieved. A printout of radiator data was obtained at stable conditions. To document and verify that conditions were steady, a second printout was obtained 900 seconds (15 minutes) later and compared to the first printout.

For the transient tests, the CRT's were monitored to verify initial conditions and abbreviated data was printed at 60-second (one-minute) intervals during the two-orbit environment transient. The radiometer readings were included in the 60-second data to insure that the correct environmental transient was applied.

TEST RESULTS

The radiator system test included a total of 49 steady-state and 6 orbital transient test points. Figures 4 and 5 summarize the complete three panel and four panel high load steady-state test results along with the analytical predictions. The test data and analysis results show good agreement. The small differences can be attributed to temperature, flow and heat flux instrumentation inaccuracies, and in some cases a true steady-state condition may not have been obtained due to test time limitations. The test data confirmation of the analysis provides a wide range of data for future radiator performance assessment. Figures 4 and 5 can be used to obtain radiator heat rejection for the twelve different orbit conditions. The highest orbital heat rejection was obtained for environment 4 which allows a radiator inlet temperature of 63°C (145°F) for a radiator return temperature of 3.3°C (38°F).

Six orbital transient test points were conducted to determine the effect of the use of orbital average steady environments in the performance assessment. Considerable peaking above the steady-state values (as much as 12°C (53.6°F) for environment 5) occurs during the sunlight portion of the orbit. Thus, the use of steady-state performance based on orbital average environments must be used with caution. For example, the radiator outlet should not be allowed to peak above approximately 15.6°C (60°F) to prevent overloading the flash evaporator. Therefore, evaluation of radiator peak outlet temperatures can only be inferred from the steady-state performance values.

The low load testing was conducted with environment 4 in which the aft panels view only deep space and the door centerline edge of the forward panels receive earth flux (convex side only). Analysis had indicated that the gravity effects would cause flow reversal in panel 4 before the low temperature limit of panel 1 was reached; i.e., the test low load limit would be dictated by gravity, whereas the flight low load would be limited by temperature. Reverse flow was evident in panel 4 in the lowest elevation tubes as expected. The tubes with reverse flow had inlet temperatures colder than the outlet and much colder temperatures than the other tube inlet temperatures. The coldest temperature observed was -42.4°C (-44.3°F) on panel 1 which is considerably above the freezing point of Freon-21, -135°C (-211°F). Extrapolation of the test data by analysis to the zero-gravity flight condition indicates that an inlet temperature of 5°C (41°F) is required to obtain a tube outlet of -135°C (-211°F). Thus a minimum heat load of approximately 4.7 joules/sec (4000 Btu/hr) could be allowed before fluid freezing occurs.

Fin temperature profiles measured throughout the test were used to calculate the radiator fin effectiveness. The overall average of 0.979 for the forward panels and 0.950 for the aft panels compared favorably with values of 0.975 and 0.944, respectively, from previously run single panel development tests with only cold wall environments.

The test was conducted over a 29 day period with seven chamber depressurization-pressurization cycles. During some re-pressurization sequences,

moisture condensation on the chamber cold walls caused "rain" in the chamber and some accumulation of water on the panel concave surfaces. Dust accumulation on the panels was also evident throughout the test. In order to verify that the test conditions of vacuum and temperature as well as the moisture and dust did not change the radiator performance, baseline performance data was taken throughout the test. The baseline data was taken with the lamp arrays off and the radiator flow control valve deactivated to obtain full Freon-21 flow through the panels. The following indicates that the change in radiator performance throughout the test is within the experimental accuracy.

TIME DAY:HR:MIN:SEC	INLET TEMP $^{\circ}$C ($^{\circ}$F)	OUTLET TEMP $^{\circ}$C ($^{\circ}$F)
25:15:23:23	48.4 (119.0)	-6.5 (20.4)
29:13:42:33	49.0 (120.1)	-8.2 (17.5)
54:06:04:54	48.8 (119.9)	-4.6 (23.6)

The data taken on day 29 shows a 4.3% improvement over the initial data (day 25) and the data at the end of the test (day 54) shows a 2.3% decrease from the initial values.

CONCLUSION

The testing verified the flight readiness of the Orbiter radiator system thermal performance. Radiator performance over the range of expected flight conditions was as expected and there was not degradation of performance during the test. Extrapolation of the single loop test data indicates that Orbiter hea loads ranging ^{f} · ヿ 17.46 joule/sec (15,000 Btu/hr) to 197.86 joule/sec (170,000 Btu/h. / . Icn a controlled 3.3°C (38°F) return temperature can be accommodated by the radiator system using 8 panels.

REFERENCES

1. Jaax, J. R., "Orbiter Active Thermal Control Subsystem Test," AIAA Paper, September 1980.

2. Jaax, J. R., "Integrated Active Thermal Control Subsystem Test Final Report," Crew Systems Division CSD-SH-143, Johnson Space Center JSC 14182, August 1979.

3. Jaax, J. R., "Orbiter Active Thermal Control Subsystem Description and Test History," Crew Systems Division CSD-SH-126, Johnson Space Center JSC 11295, July 20, 1978.

TABLE I
RADIATOR TEST POINT SUMMARY

HEAT LOAD	FCA SET POINT	ENVIRONMENT (REF. FIGURE 3)											
		1	2	3	4	5	6	7	8	9	10	11	12
MINIMUM – WITH NO PANEL TEMP. BELOW –123.3°C (–190°F)	NORM				X								
MINIMUM – WITH NO PANEL TEMP. BELOW –123.3°C (–190°F)	HIGH				X								
NOMINAL OFT HEAT LOAD	NORM	4*								4			
MAXIMUM FOR RFCA TO RETURN 3.3°C (38°F) MIXED OUTLET	NORM	X	X	X	X	X	X	X	X	X			
MAXIMUM FROM ORBITAL AVERAGE CASE – RUN W/TRANSIENT ENVIR.	NORM	X				X	X						
MAXIMUM FOR FES TO RETURN 3.9°C (39°F)	NORM	X	X	X	X			X	X	X			
MAXIMUM HEAT LOAD ALLOWED BY LOOP TEMPERATURE LIMITS	NORM	4		4									
FIXED RFCA INLET 4 PANEL 46°C (115°F) 3 PANEL 40.4°C (105°F)	NORM										X		
FIXED RFCA INLET 4 PANEL 44.8°C (113°F) 3 PANEL 39.4°C (103°F)	NORM											X	X
ACCEPTANCE TEST INLET TO RFCA	NORM				X								

*DENOTES 4 PANEL TEST ONLY

ON ORBIT CONFIGURATION

FLUID TEMPERATURE SENSOR
ELECTRONIC CONTROLLER
FLOW CONTROL ASSEMBLY

FCA SYSTEM
FLOW SCHEMATIC
(LEFT SIDE)
LOOP 1

NOTE:
RIGHT HAND PANELS ARE
NOTCHED FOR CLEARANCE
OF PAYLOAD BAY DOOR
LATCHES

RIGHT HAND
AFT PANEL

RIGHT HAND
MID-FWD
PANEL

RIGHT HAND
MID-AFT
PANEL

BYPASS
VALVE

FLOW CONTROL
VALVE

MODE CONTROL
VALVE

RIGHT HAND
FWD PANEL

3.2M

LOOP 2
STARBOARD SIDE

NO. 1 RH	NO. 2 RH	NO. 3 RH	NO. 4 RH

4.6M

NO. 1 LH	NO. 2 LH	NO. 3 LH	NO. 4 LH

AFT PANELS NO. 4 ARE REMOVABLE

FWD

CAVITY

DOOR

LOOP 1
PORT SIDE

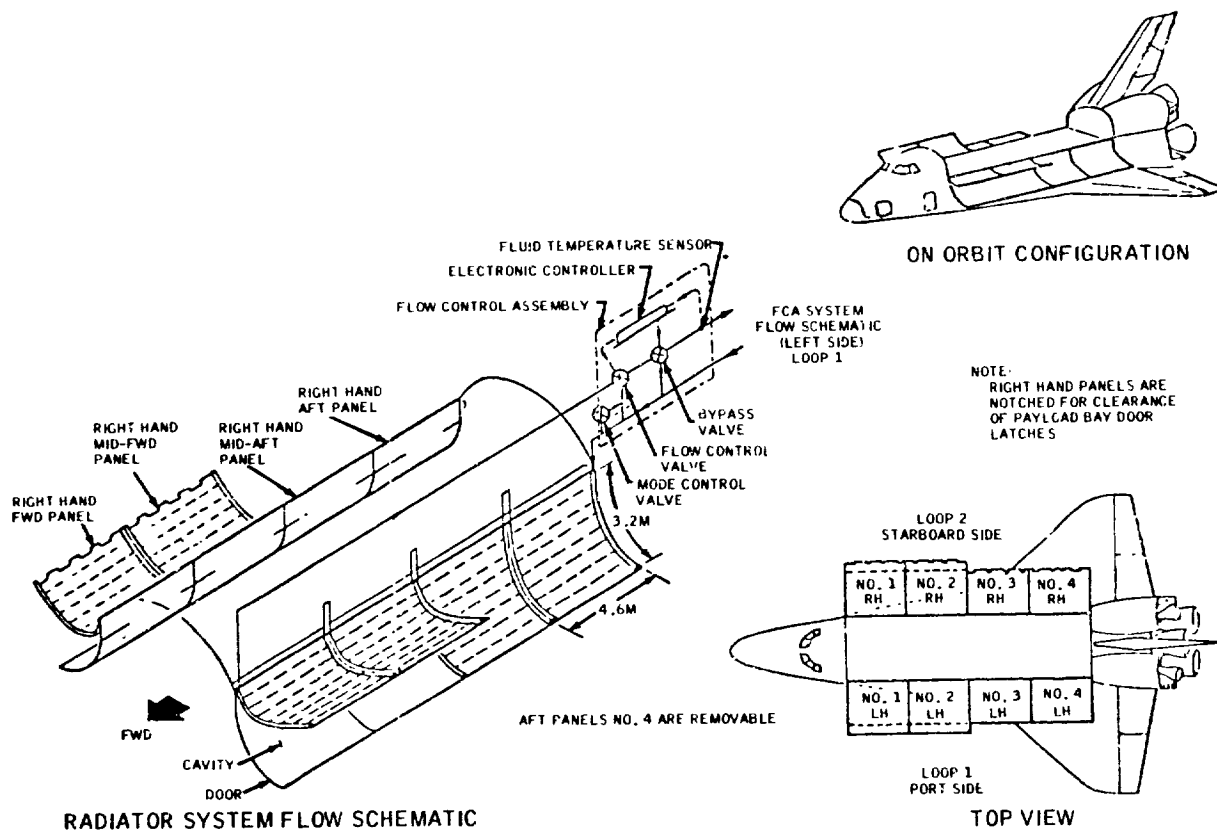RADIATOR SYSTEM FLOW SCHEMATIC

TOP VIEW

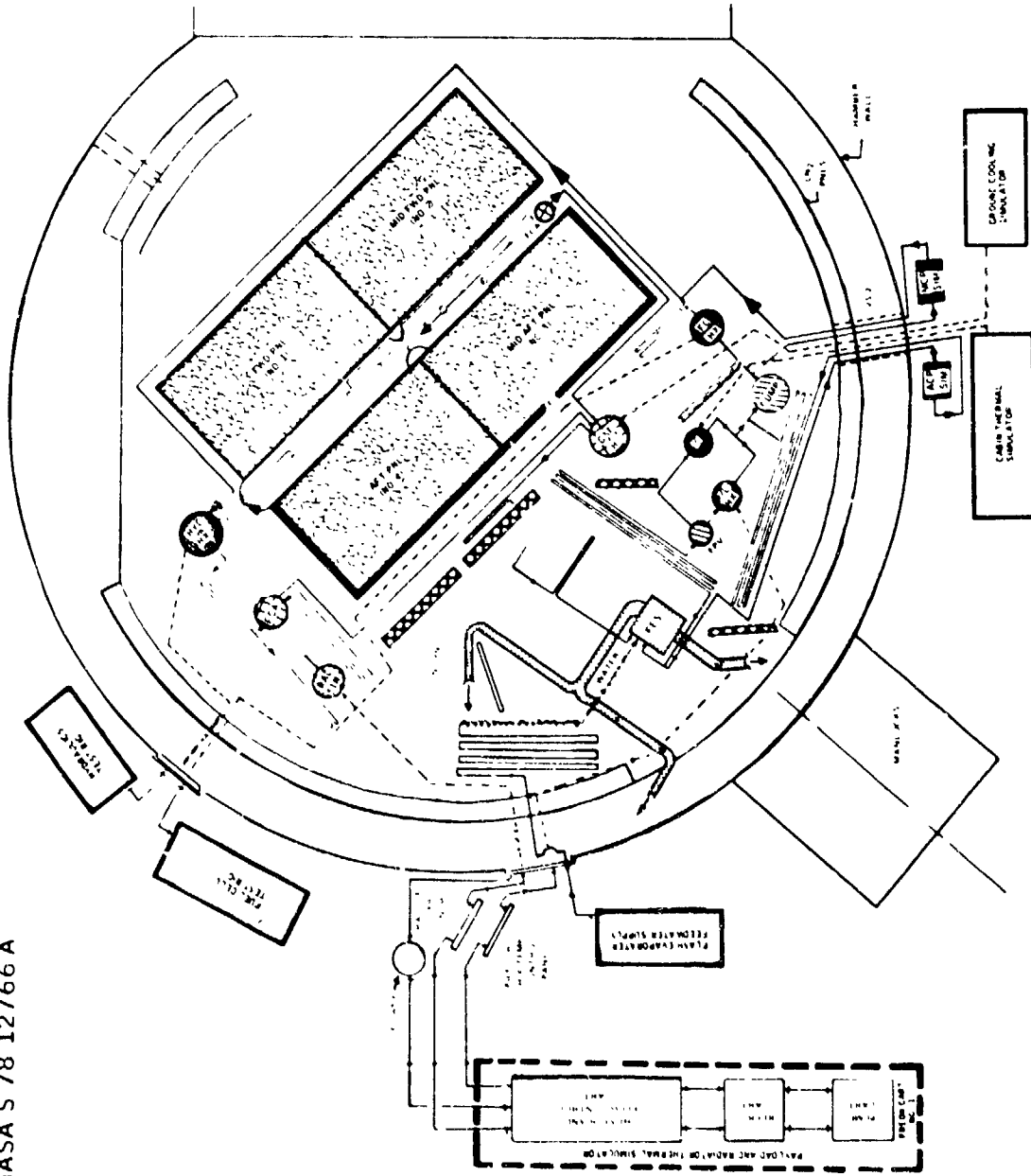FIGURE I.   ORBITER RADIATOR SYSTEM CONFIGURATION

FIGURE 2. INTEGRATED ATCS TEST LAYOUT
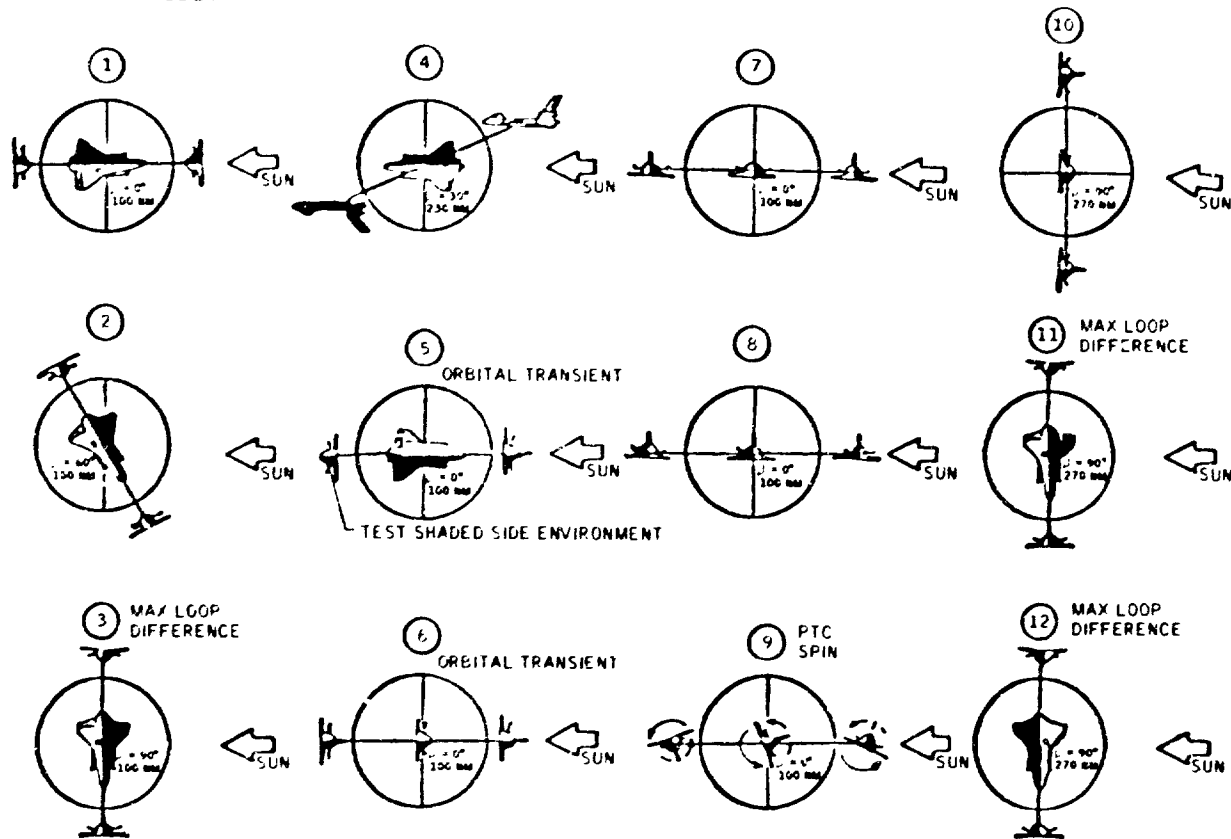
NASA-S-80-1527

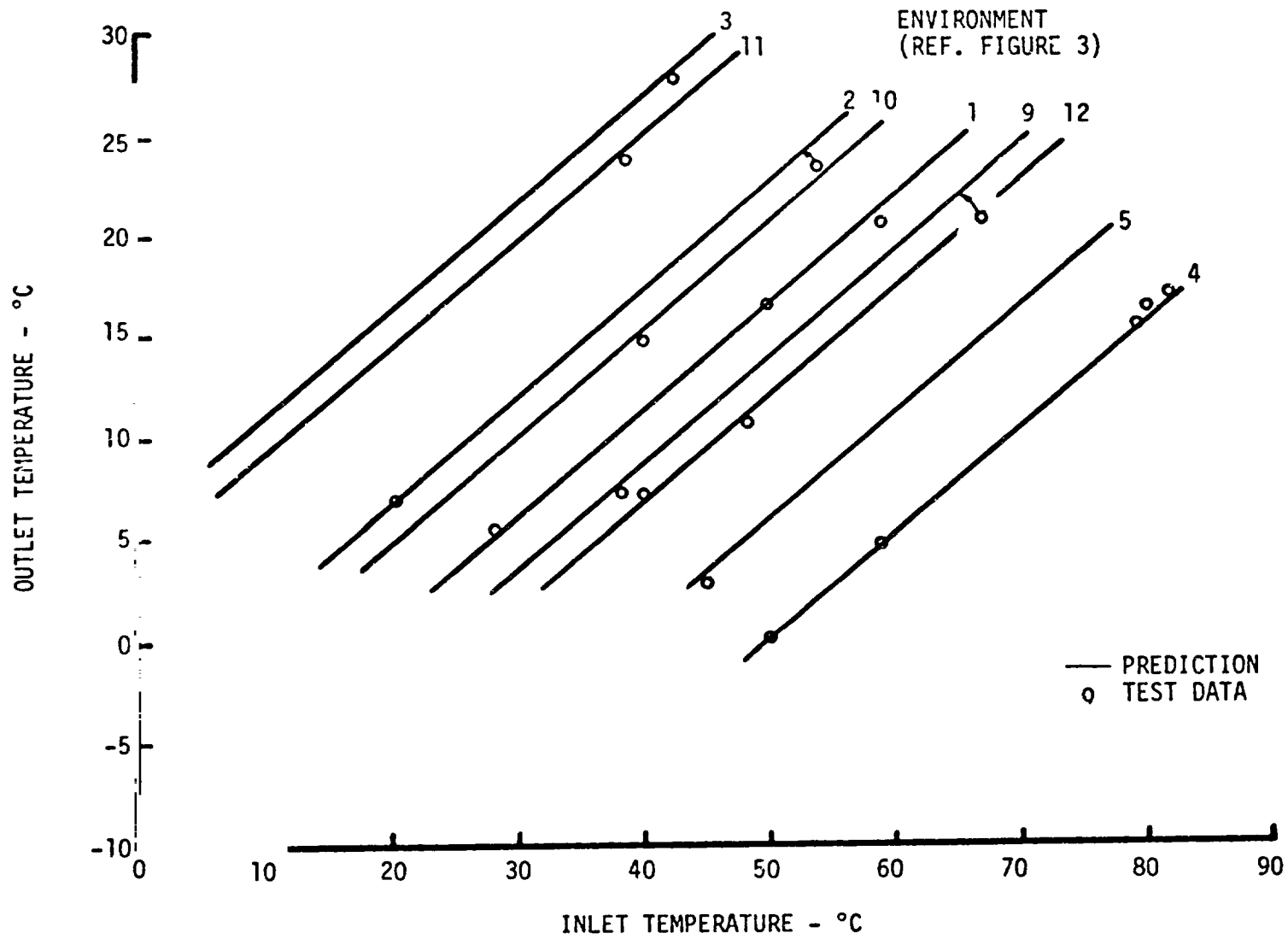FIGURE 3. ORBITER ATTITUDES FOR RADIATOR PERFORMANCE ASSESSMENT

FIGURE 4. COMPARISON OF ANALYSIS AND TEST DATA - 3 PANELS
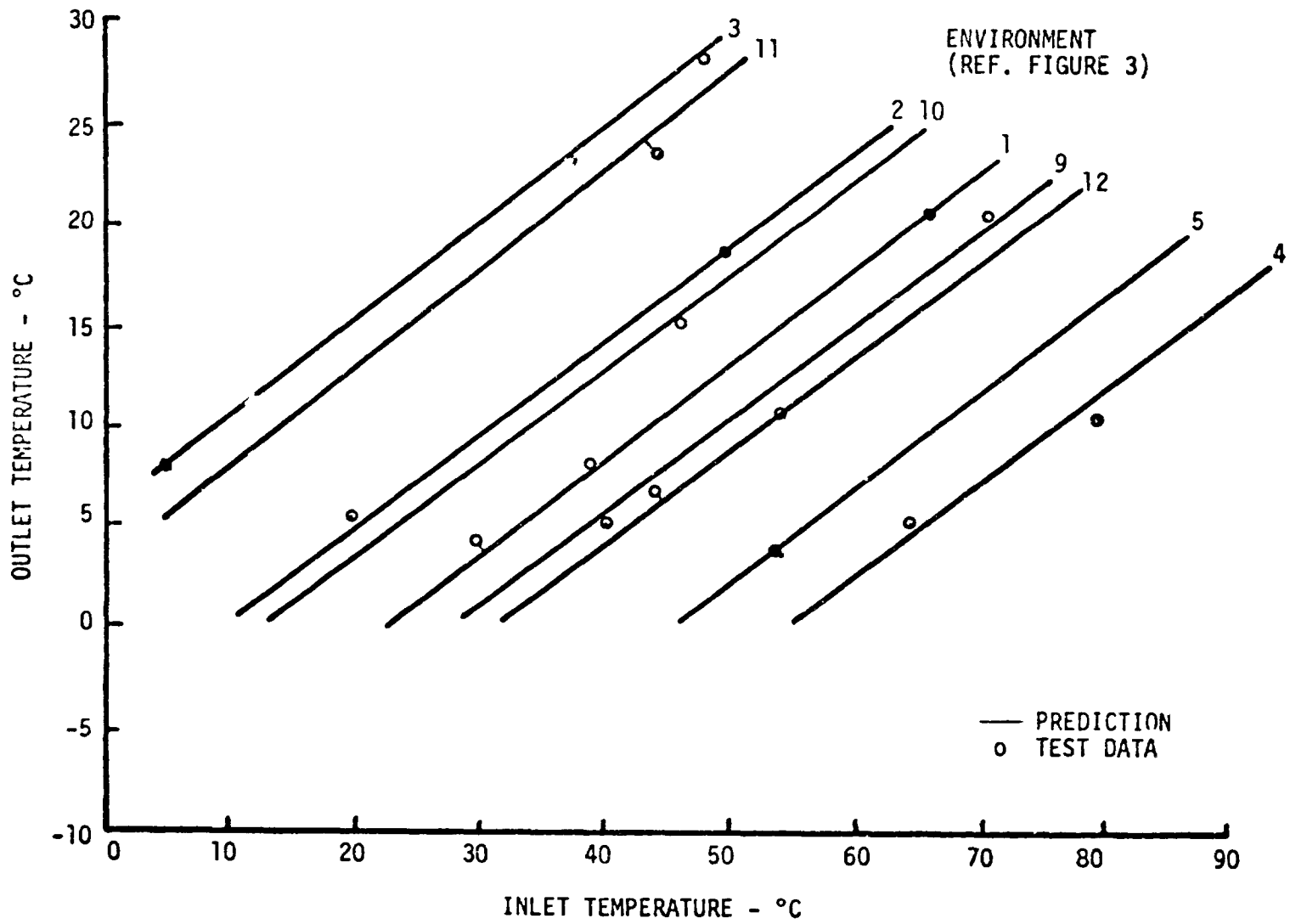
FIGURE 5.   COMPARISON OF ANALYSIS AND TEST DATA - 4 PANELS

317

SOLAR PANEL THERMAL CYCLING TESTING
BY SOLAR SIMULATION AND INFRARED RADIATION METHODS

Hubert E. Nuss*

ABSTRACT

For the solar panels of the European Space Agency (ESA) satellites OTS/MAROTS and ECS/MARECS the thermal cycling tests were performed by using solar simulation methods. The performance data of two different solar simulators used for these tests and the thermal test results are described. The solar simulation thermal cycling tests for the ECS/MARECS solar panels were carried out with the aid of a rotatable multipanel test rig by which simultaneous testing of three solar panels was possible. As an alternative thermal test method the capability of an infrared radiation method was studied and infrared simulation tests for the ultralight panel (ULP) and the INTELSAT V solar panels were performed. The setup and the characteristics of the infrared radiation unit using a quartz lamp array of approx. 15 m^2 and LN2-cooled shutter and the thermal test results are presented. The irradiation uniformity, the solar panel temperature distribution, temperature changing rates for both test methods are compared. The results indicate the infrared simulation is an effective solar panel thermal testing method.

INTRODUCTION

Thermal vacuum tests are required for qualification and acceptance of spacecraft subsystems. The purpose of qualification tests is to prove the subsystem design by checking its performance capability under thermal vacuum conditions more severe than predicted for orbit. The aim of the more severe temperature stress is to demonstrate design safety margin and to accelerate failure in marginal design. The objective of the acceptance tests is to demonstrate the performance of the subsystems of proven design in the temperature range expected in flight and to verify the workmanship according to flight standard quality. The cycling between temperature extremes is to induce temperature gradients in the subsystem thereby permitting observation of operation at other than stabilized conditions.

Thermal vacuum facilities are currently available with four distinct types of energy control: temperature controlled shrouds, solar simulators, infrared radiators, surface blanket heaters.

*Industrieanlagen-Betriebsgesellschaft mbH (IABG), Space Division, D 8012 Ottobrunn, West Germany.

The development of infrared simulators with tungsten fila-
ment quartz lamps (refs. 1 to 4) and other methods for infrared
simulation (carbon cloth heat post, fluid controlled panels,
thermal canister, electrical heaters) were described in several
papers (refs. 5 to 8). The application of the different methods
for thermal balance testing was investigated in these studies
and the performance data, testing philosophy, and cost effect-
iveness were compared (refs. 9 to 14).

For satellite programmes thermal vacuum tests have to be
performed for a number of units according to the same specific-
ation. It is especially true for acceptance testing of the
different solar panels of communication satellite's solar array.
The cost effectiveness of solar panel thermal testing can be im-
proved by testing simultaneously more than one panel. In this
paper the development of an infrared radiation unit for simul-
taneous testing of three solar panels is described. The per-
formance data and operational conditions of the infrared radiat-
or setup were studied.

Thermal cycling test results and cost effectiveness for
infrared simulation, for solar simulation for one solar panel,
and for multi-panel solar simulation are compared in the follow-
ing.

1. TEST REQUIREMENTS AND FACILITIES

Thermal vacuum testing of solar panels can be performed
by irradiating the panel front side by a solar simulation or an
infrared simulation setup. By radiation to LN2-cooled shrouds
the temperature gradients through the panel and the temperature
changing rates during the transient phases are similar to the
expected orbit conditions.

The main test requirements for solar panel thermal cycling
tests for different programmes are summarized in Table I. In
general the primary requirement for solar panel thermal testing
by solar simulation methods is the specification of the solar
irradiance to be simulated during test. For the ECS/MARECS
solar panel tests this irradiance was defined equivalent to a
definite value of the open voltage readout during the sunphases
of the thermal cycling test. For the infrared radiation methods
the equilibrium temperatures were specified and therefore the
power of the infrared radiators had to be adjusted to values to
achieve the temperatures required.

1.1 Solar Simulation Facility (Fig. 1 and 2)
The solar panel thermal cycling tests for the OTS/MAROTS
programme were performed in the 3m-space simulation facility of
IABG (ref. 16). The facility is equipped with an LN2-cooled
shroud of 3 m diameter and 7 m length. The solar simulator is
an off-axis system. The radiation is performed by four 25 kW
and five 6.5 kW Xenon Arc lamps. The light is collected in
elliptical mirrors, folded by a plane mirror system to a collim-
ation mirror which directs the radiation into the reference
plane. By means of a light integrator the radiation of the dif-
ferent light sources is superimposed, hence improving the uni-
formity in the reference plane.

319

The collimation mirror consists of about 1000 adjustable mosaic elements and was adjusted to irradiate a reference plane of 1.9 m diameter, which was sufficient for the dimensions of the solar panels with 1.31 m width and 1.45 m height. The uniformity measurements showed a maximum deviation from the mean value of radiation intensity in the reference plane of + 8 %. For simulation of the cold phases an LN2-cooled shutter between collimation mirror and test article shielded the simulated solar radiation.

The relatively low overall efficiency of the solar simulator was due to the fact that the solar simulator was in a modification phase which was not completed when the tests had to be performed.

The ECS/MARECS solar panel thermal cycling tests were carried out in the 3m-space simulation facility with the complete modified solar simulator implemented (Fig. 2). Compared to the original design the folding mirror system for the modified solar simulator could be deleted. The solar simulator was equipped with an integrator adjusted to the efficient operation of five 25 kW Xenon Arc lamps. The mosaic mirror was exchanged by a segment mirror consisting of 37 elements. Due to the optical system modification a solar beam diameter of 2.4 m in the reference plane and an overall efficiency of the solar simulator of approximately 10 % could be achieved. For the ECS/ MARECS solar panel thermal cycling tests the facility was equipped with a rotatable multipanel test rig of triangular shape (ref. 21). By this additional device the cost effective simultaneous testing of 3 solar panels was possible: one panel being irradiated by the solar simulator while for the other two a coldphase was simulated.

1.2 Infrared Radiation Facility
(Fig. 3, 4, 5)

The thermal vacuum tests for the INTELSAT V solar panels (dimensions 1.65 m width, 1.91 m height) were carried out in the thermal vacuum facility 3.5 m-TVA of IABG (ref. 18). The facility is equipped with a GN2-cooled shroud of 3.5 m diameter and 6.3 m height. For the infrared simulation thermal cycling tests the facility was furnished with an infrared radiation unit with quartz-line lamps and a liquid nitrogen-cooled, movable shutter (Fig. 3 and 4). The lamp array can be shielded during the coldphase by moving the LN2-cooled shutter in front of the lamp radiators. The infrared radiation unit consists of three lamp array modules with a total number of 300 quartz-line lamps (nominal power 500 W each). Fig. 3 shows a schematic sketch of two modules of the lamp array used for irradiating two solar panels. For the third solar panel a third lamp array module on the rear side of the two exhibited ones was used. In between the first two and the third lamp array module an LN2-cooled shroud is located to minimize the radiation of not LN2-cooled surfaces to the panels during coldphase. By 150 electrical control units and power supplies the 150 lamp pairs can be controlled separately.

320

For the thermal vacuum cycling tests of the ultralight panel (ULP, dimensions 1.1 m width and 3.22 m height) (ref. 19) two lamp array modules as shown in Fig. 3 were used.

The primary requirements for an infrared radiator setup to be applied for thermal cycling tests are optimum uniformity of irradience in the test plane and minimum blockage of cold shroud during the coldphases. The blockage of the shroud was reduced by the LN2-cooled shutter as shown in Fig. 4. By measuring the irradiance distribution before the test and adjusting the different control units the irradiance uniformity was optimized.

To monitor the irradiance distribution of the infrared lamp array modules a solarcell sensor of 16 cm^2 surface area was moved vertically and horizontally in the testplane. A typical readout of the sensor measured by scanning along a distance of approximately 5000 mm is shown in Fig. 5. The result of the evaluation of a total number of 765 measured extreme values for the three infrared lamp array modules is given in Table II. This Table indicates that for the testplane of 15 m^2 an irradiance uniformity of $\leq \pm 10$ % could be achieved with approx. 75 % of the measuring points within the range of $\leq \pm 5$ %.

2. TEST RESULTS

The temperature T_p of a solar panel in a space simulation facility is described by the following equation:

$$mc \frac{dT_p}{dt} = \alpha F I - \sigma e \varepsilon F (T_p^4 - T_{sh}^4) \tag{1}$$

mc : Thermal capacity of test article

$\frac{dT_p}{dt}$: Temperature change of test article with time

I, F : Irradiance and surface area, respectively

σ : Stefan-Boltzmann-Constant

e, T_{sh} : Viewfactor to shroud and shroud temperature, resp.

ε, α : Emissivity and absorptivity, respectively

The solar panel thermal equilibrium temperature T_E can be derived from equation 1:

$$T_E = \sqrt[4]{\frac{I \alpha}{2 \sigma \varepsilon} + T_{sh}^4} \tag{2}$$

From equation 2 the relative temperature change $\Delta T_E / T_E$ due to a relative intensity variation $\Delta I / I$ can be calculated (ref. 20):

$$\frac{\Delta T_E}{T_E} \approx \frac{1}{4} \cdot \frac{\Delta I}{I} \tag{3}$$

321

Taking into account the irradiation uniformity and the heat conductivity in the panel surface (characterized by the expression λF_{12}) the following expression for the temperature change ΔT_{E1} is found from equation 1:

$$\Delta T_{E1} = \frac{\alpha}{8 \sigma \varepsilon T_{E1}^{3} + \dfrac{\lambda F_{12}}{F}} \Delta I \qquad (4)$$

For the transition from warmphase to coldphase from equation 1 the ratio f of the slopes of the temperature - time - plotts for solar simulation and infrared simulation can be derived:

$$f = \frac{dT_p/dt \big|_{solar}}{dT_p/dt \big|_{IR}} = \frac{T_p^{4} - T_{sh1}^{4}}{T_p^{4} - T_{sh2}^{4} - \dfrac{\varepsilon_1 F_1 e_1}{2 \varepsilon F e} T_1^{4}} \qquad (5)$$

For the infrared radiation method surface parts of the lamp array which are not completely covered by the LN2-cooled shutter are taken into account by including an irradiance of an emissivity ε_1, of a viewing factor e_1, of an area F_1 and of a temperature T_1.

2.1 Solar Panel equilibrium Temperature Distribution
In Fig. 6 a typical transient phase for solar simulation thermal cycling is exhibited. The temperatures on the solar panel frontside were measured in the range $61 \pm 4^{\circ}C$. According to equation 2 an equilibrium temperature of $T_E = 60^{\circ}C$ can be calculated. By using equation 3 and a value of $\pm 8 \%$ for the irradiance uniformity a maximum temperature variation of $\pm 7^{\circ}C$ is estimated. The measured temperature uniformity of $\pm 4^{\circ}C$ can be interpreted by the effect of heat conductance in the panel surface as described by equation 4.
A typical transient phase for infrared simulation cycling tests with three solar panels is plotted in Fig. 7. The temperatures on the three solar panels were measured in the range $85 \pm 5^{\circ}C$. The lamp array modules with 300 radiators were operated with a total power of 39 kW on a surface area of 15 m^2. Using the given reflectivity of the lamp reflector and the viewing factor determined by geometry of the test setup an irradiance of $I = 1.83$ kW/m^2 is calculated. From equation 2 an equilibrium temperature of $T_E = 83^{\circ}C$ is determined in good agreement with the experimental results.
The panel temperature distribution at the end of the cold phases is measured in the range $-158 \pm 5^{\circ}C$ for solar simulation cycling tests with one and with three panels and for infrared simulation tests with one and with three panels.

2.2 Temperature Changing Rates

During transition from warmphase to coldphase the temperature changing rates $\Delta T_p/\Delta t$ for solar simulation and for infrared simulation were measured as indicated in Table III. There is no essential difference in the temperature changing rates of solar simulation and infrared simulation in the temperature range $T_p > 50^{\circ}C$ to $T_p = -50^{\circ}C$. For a panel temperature of $T_p = -150^{\circ}C$ the temperature changing rate for infrared simulation is by a factor of 2 lower than the rate for solar simulation. In this temperature range the influence of structure parts of the lamp array modules which are not completely covered by the shutter has to be considered.

2.3 Cost effectiveness

The primary test cost saving effect can be achieved by simultaneous testing of three instead of one solar panel. Using a solar simulation facility and a multipanel test rig for three solar panels the operational test costs per panel amount to approximately 40 % of the costs for single panel testing. With a setup of infrared lamp array modules for three panels the operational test costs per panel are about 38 % of the operational costs for single panel solar simulation testing.

3. CONCLUSIONS

The comparison of multipanel thermal testing data for solar simulation and infrared simulation with single panel testing data indicate that the essential thermal cycling test requirements can be fulfilled for the two multipanel testing methods.

During an operational time of approximately 1000 hours for the infrared lamp array modules including an LN2-cooled shutter no essential operational problems occurred and, therefore, the reliability of the system is promising.

In cases where no spectral match and no low collimation angle of the radiation are required infrared simulation thermal cycling of solar panels is advantageous because of cost effectiveness of multiple panel testing, high efficiency of infrared radiation setups and high life time of radiators.

REFERENCES

1. Skinner,D.J.; Wallin,S.P.; Wolff,C.M.: The Design and Application of an Infrared Simulator for Thermal Vacuum Testing, NASA SP-298, 1972, p. 197.

2. Dewey,R.L.: Control of an Artificial Infrared Environment to Simulate Complex, Time-Varying Orbital Conditions, NASA SP-298, 1972, p. 217.

3. Nelson,L.A.; Levine,M.B.: Development of a Heater Post and Spotlight Array for Thermal Vacuum Testing of the INTELSAT V Communication Satellite, NASA SP-336, 1973, p. 663.

4. Williams,F.U.: Analysis of Radiative Sources with Both Specular and Diffuse Characteristics in the Visible and Infrared Spectrum, NASA SP-379, 1975, p. 355.

5. Levine,M.B.; Nelson,L.A.: Development of a Carbon Cloth
    Heat Post Module for Thermal Vacuum Testing of a Spinning
    Spacecraft, NASA SP-298, 1972, p. 555.

6. Skinner,D.J.; Breiby,J.E.: The Design and Operation of an
    Infrared Simulator for Testing of the Shuttle Radiator Sys-
    tem, NASA SP-336, 1973, p. 679.

7. Gülpen,J.; Lorenz,W.: Infrared Test Techniques Developed
    for the Helios Spacecraft, ESA SP-95, 1973, p. 301.

8. Esposti,P.L.D.; Strom,B.: Experimental Comparison between
    Infrared and Solar Simulation Test Philosophies in the
    Light of the Tests carried out on the Sirio Thermal Model,
    ESA SP-95, 1973, p. 263.

9. Arnoult,J.F.; Rollier,P.: Thermal Design Verification,
    Qualification and Acceptance Testing Concept for Future
    Large Space Objects, ESA-CR 3255/NL/77/HP(SC), 1977.

10. Prian,V.D.; Calimbas,A.T.; La Blanc,E.A.: Space Thermal
    Simulation for Satellite Heat Transfer Design Evaluation,
    Proc.5th Internat.Conf.Heat Transfer, Soc.of Heat Transfer
    of Japan, 1974, p. 267.

11. Ziermann,C.A.: A Comparison of Solar Beam and Infrared
    Simulation During Spacecraft Thermal Vacuum Testing, Proc.
    IES, 3rd Aerospace Testing Seminar, 1976, p. 67.

12. Schmidt,W.F.: A Comparison of Test Philosophies for Space-
    craft Thermal Vacuum Testing, Proc.IES, 3rd Aerospace Test-
    ing Seminar, 1976, p. 73.

13. Weydandt,J.; Schwarz,B: Study of Thermal Design Verificat-
    ion, Qualification and Acceptance Testing Concept for Fut-
    ure Large Space Objects, ESA-CR 3199/NL/77/HP(SC), 1977.

14. Brinkmann,P.W.; Shickle,W.A.; Walker,J.B.: Economic Use of
    Facilities for Thermal Testing of Large Satellites and Sub-
    systems, ESA SP-139, 1978, p. 387.

15. Schneider,K.: OTS Solar Array, ESA-SP 140, 1978, p. 193.

16. Nuss,H.: Calibration and Characteristic Measurements of a
    Solar Simulator Facility for Thermal Balance Tests, ESA SP-
    95, 1973, p. 137.

17. Brodersen,H.; Rizos,I.: INTELSAT V Solar Array, ESA SP-140,
    1978, p. 209.

18. Reimann,J.: Facility for High Intensity, Thermal Balance
    Testing Using the Infrared Canister Method, ESA SP-95, 1973,
    p. 335.

19. Schneider,K.: Development and Testing of ULP Solar Array,
    ESA SP-140, 1978, p. 231.

20. Nuss, H.: Thermal Vacuum Testing of Solar Panels by Solar
    Simulation and Infrared Simulation, Proceedings IES of the
    25th Technical Annual Meeting, Seattle, 1979, p. 188.

21. Brinkmann,P.W.; Reimann,J.: Efficient Thermal Cycling of
    Solar Panels in Solar Simulation Facilities with a Multi-
    Panel Test Rig, ESA/DFVLR, Second European Symposium on
    Photovoltaic Generators in Space, 15-17 April 1980.

22. Fokker-VFW, Space Division, Document ECS/057/PRO/0028/FOK
    and ECS/057/PRO/0034/FOK.

Table I: Test Requirements for Solar Panel Thermal Cycling Tests (ref. 15, 17, 19, 22)

Programme	Test Method	$\frac{P}{mbar}$	$\frac{I}{SC}$	$\frac{T_w}{°C}$	$\frac{T_c}{°C}$	n_c	$\frac{t_w}{min}$	$\frac{t_c}{min}$	n_p	Additional Requirements
OTS/MAROTS										Equilibrium criterion: $\Delta T/\Delta t \leq 3°C/hour$
Qualification	Solar Simulation	$1\cdot10^{-5}$	1 ± 0.03			50	93	117	1	
Acceptance		$1\cdot10^{-5}$	1 ± 0.03			10	93	117	1	
ECS/MARECS										Adjust solar irradiance to a value I equivalent to an open voltage of 64.1 ± 0.5 V
Qualification	Solar Simulation	$1\cdot10^{-4}$	1.26 ± 0.04		appr.-17°	50	30	150	1	
Acceptance		$1\cdot10^{-4}$	1.08 ± 0.04		appr.-170	10	30 ± 3	90 ± 3	3	
ULP	Infrared Simulation	$1\cdot10^{-5}$		70 ± 10	-170 ± 10	20	80	250	1	Transition coldphase to warmphase: $\Delta T/\Delta t \leq 10°C/min$
Qualification										
INTELSAT V										Equilibrium criterion for mean value of reference thermocouples
Qualification	Infrared Simulation	$1\cdot10^{-5}$		90 ± 5	-170 ± 5	35	100	188	1	
Acceptance		$1\cdot10^{-5}$		85 ± 5	-170 ± 5	7	100	188	3	

P : Chamber pressure

I : Irradiance of solar simulator in testplane

T_w, T_c : Equilibrium temperature of panels during warmphase and coldphase, respectively

t_w, t_c : Duration of warmphase and coldphase, respectively

n_c : Number of cycles

n_p : Number of panels per test

325
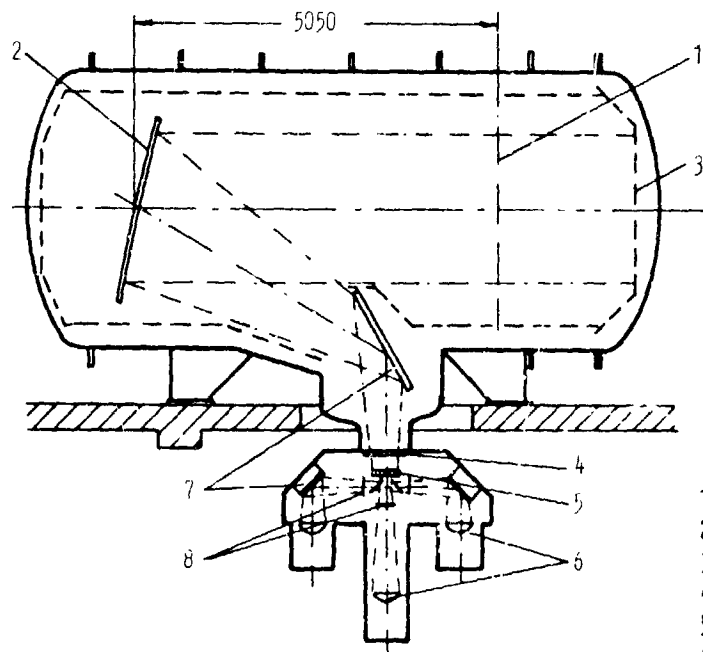
Fig. 1: 3m-Space Simulation Facility
with Solar Simulator

1 Reference plane
2 Collimating mirror
3 Cold shroud
4 Quartz window
5 Integrator
6 Collector with high pressure
   Xenon lamp
7 Folding mirrors
8 Filters

Measures in mm
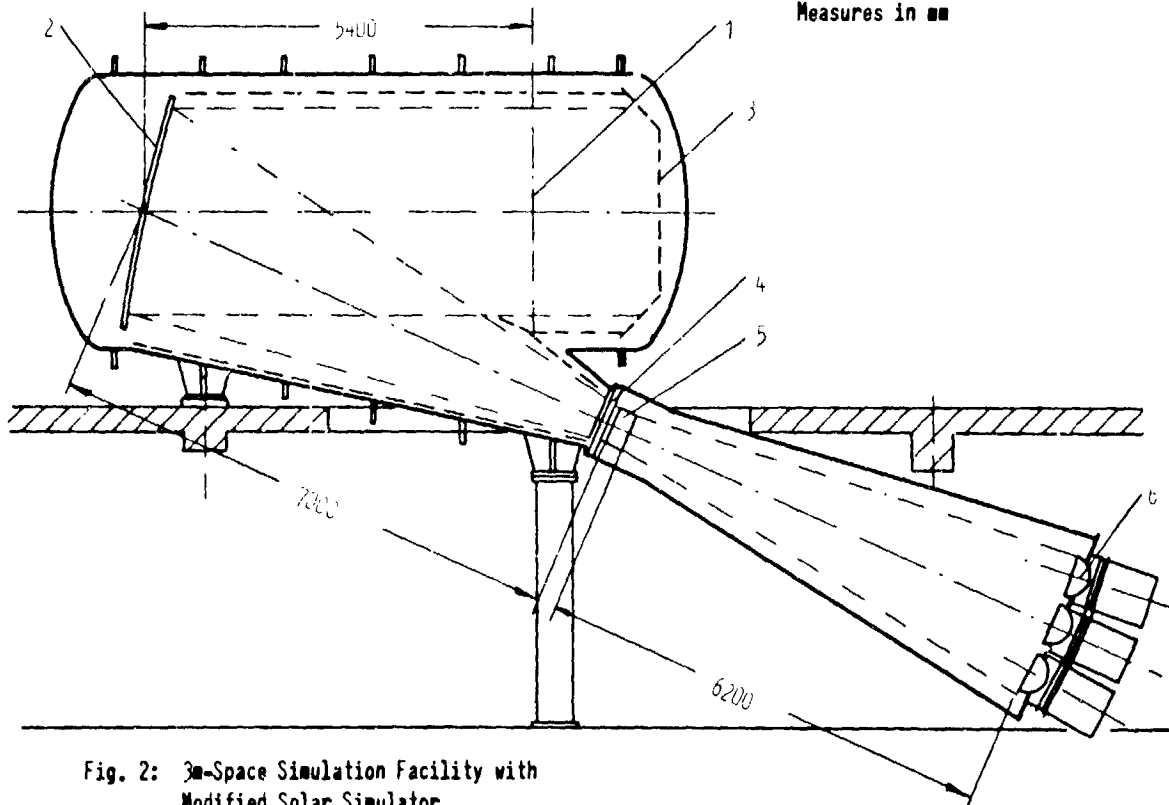
Fig. 2: 3m-Space Simulation Facility with
Modified Solar Simulator
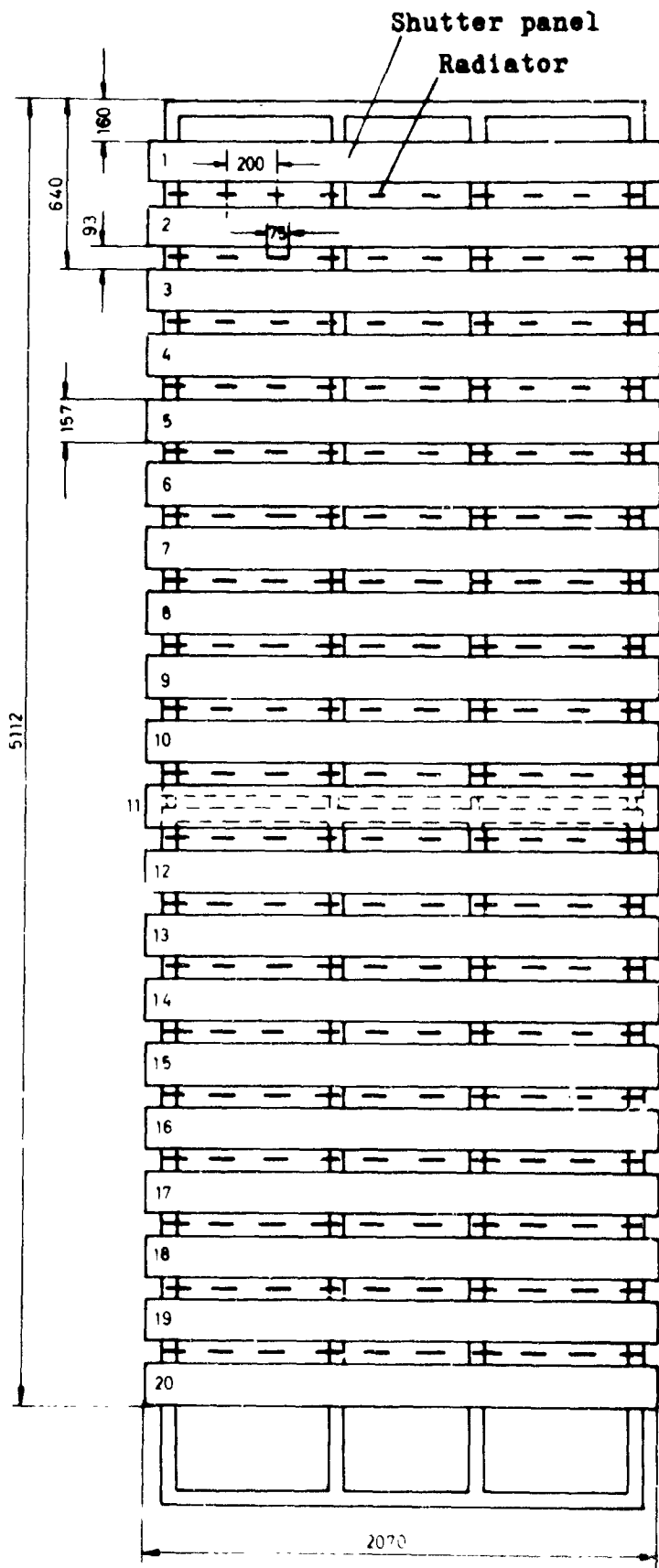
Fig. 3: Two Infrared Lamp Array Modules with Shutter Panels

Table II:

Number of extreme values n_e which show deviations from the mean value of

$$100 \ \frac{I_i - I_M}{I_M}$$

I_i : local irradiance,

I_M : mean value of irradiance

n_e	$100 \ \dfrac{I_i - I_M}{I_M}$
568	$\pm\, 0\,\%$ to $\pm\, 5\,\%$
144	$>\pm\, 5\,\%$ to $\pm\, 7\,\%$
53	$>\pm\, 7\,\%$ to $\pm\, 10\,\%$

327

Fig. 5: Typical Irradiance Distribution

Fig. 4: Shutter Position during Warm- and Coldphase

328
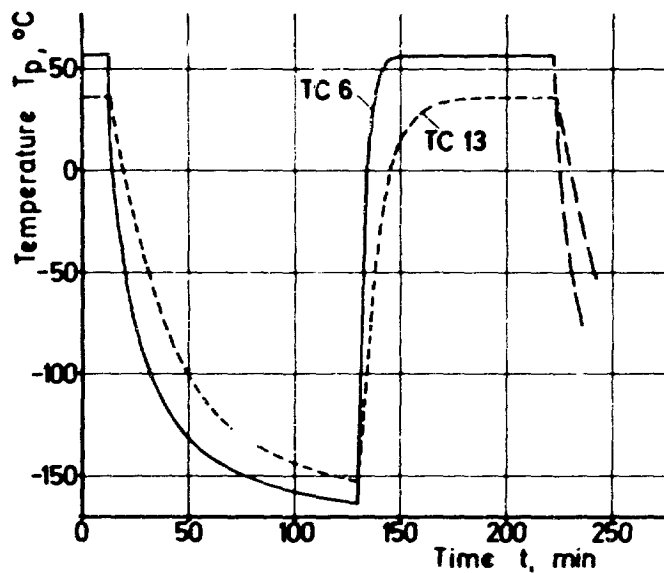
Fig.6: Typical Transient Phase of Solar Simulation Cycling.
TC 6: Frontside Thermocouple; TC13: Rear Side Thermocouple

Fig.7: Typical Transient Phase of Infrared Simulation Cycling
of Three Solarpanels.

Table III: Temperature changing rates

f_m: ratio measured

f_c: ratio calculated
(equation 5)

T_p, °C	$\dfrac{\Delta T_p}{\Delta t}$ °C $\overline{\text{min}}$		f_m	f_c
	IR	Sol. Sim.		
− 50	6.5	7	1.08	1
− 100	1.9	2.3	1.21	1.1
− 150	0.2	0.4	2	2
− 155	0.03	0.3	10	10.4

THERMAL PROTECTION OF
REENTRY VEHICLES BY ACTIVELY COOLED NOSETIPS

R. E. Walker*
J. W. Hidahl**

ABSTRACT

This paper presents recent analytical modeling efforts and clear-air ground test results of a transpiration-cooled nosetip (TCNT) design. The discrete water injection platelet TCNT described was conceived and created by the Aerojet Liquid Rocket Company to achieve the performance requirements for severe reentry vehicle trajectories. Nosetip ground test data are presented from the Air Force Systems Command's Arnold Engineering Development Center (AEDC) hyperballistic Track G test facility in varying clear-air environments. Thermal performance computer modeling techniques, combining both local heat blockage and boundary layer recovery enthalpy reduction are outlined.

INTRODUCTION

During the last several years test programs and analyses have been conducted to define the mechanisms and limits involved in using a liquid coolant (water) to provide thermal protection for reentry vehicle nose cones. Impetus for the work was the need to increase the reliability of the reentry vehicle under conditions of high aeroheating and adverse weather encounter. In the last two years much progress has been made in understanding the mechanisms and defining operating limits involved in cooling nosetips. The purpose of this paper is to document the current status of the work. Although advancements have been made in both the aeroheating and weather survivability areas, this paper deals with the aeroheating thermal protection aspects of the work.

Although primarily related to reentry nose cones the aeroheating thermal protection of reentry vehicles has application to many problems of current interest, both for military and civilian use, such as:

1. Leading edge coolant for shuttle type reentries to increase reliability and perhaps reduce weight.

2. Leading edge cooling of evader type powered aircraft.

3. Use in wake seeding and/or electronic attenuation/clarification application.

* Senior Engineering Specialist, Aerojet Liquid Rocket Company
**Senior Engineer, Aerojet Services Company

4.   The use in high speed weapons intercept or attack systems.

Most of the recent pertinent test data were from tests conducted in the hypervelocity range at Air Force Systems Command's Arnold Engineering Development Center (AEDC). From July 1978 through July 1979 twenty five tests were conducted in the 1000 foot long test cell "G" with launch velocities in the range of 16,000 to 18,000 feet per second and at cell pressures of 100 to 500 mm Hg, equivalent to altitudes of 47,000 to 11,000 feet. Of these 25 tests, 10 were in clear air and 15 were through varying ice field densities. For the clear air tests considered, the nosetip coolant flow rates and distributions over the nosetip surface were the primary variables. Data acquisition consisted of inflight coolant flow rate and surface temperature measurements and inflight laser photographs of the nosetip surface. In addition, post test inspections of the test piece were used to define overall nosetip surface conditions.

NOMENCLATURE

A	=	$h_1/(G\ Cp\ T)$
B	=	$h_1/(K\ T)$
C	-	Diffusion coefficient
C_D	=	Drag Coefficient
c_n	-	Slot equivalent
f		Blowing ratio, $(\rho V)_c/(\rho V)_e$
	=	Mass Flow Rate
h_1	=	Liquid side film coefficient
K	=	Conductivity
M	=	Mach Number
Nu	=	Heat transfer Nussult Number
Nu_m	=	Mass Transfer Nussult Number
P	-	Pressure
q_{net}	-	Net heat flux to surface of fin
q_D	=	Total heat to droplet
r_m		Mean droplet radius
Re	-	Droplet Reynolds Number, $2\ r_m\ (V_e-V_c)\ \rho_g$
	-	Liquid Reynolds Number in coolant slot, $\rho_c\ V_c\ c_0$
r		$-A/2 + \sqrt{A^2/4 + B}$
	-	Schmidt Number
S_t	=	Stanton Number
T	=	Temperature
t	=	Time
V	=	Velocity
$\dot{V}$	=	Vaporization rate
	-	Weber Number, $V_e^2\ \rho_e/\rho$

ρ	=	Density
σ	=	Surface Tension
μ	--	Viscosity

SUBSCRIPTS

c	-	Coolant property
d		Droplet property
e		Edge property
s		Surface property
g		Gas property
v		Vapor property
o		Without blowing

332

NOSETIP CONFIGURATION

The ten clear air tests in the AEDC Track G hypersonic facility were conducted during performance of the Advanced Ballistic Reentry Program (ABRV) (Reference (1)) using nosetips of one basic design; although internal coolant flow metering differences were designed into the nosetips.

All the nosetips tested were hemispherical (R_N = 0.65 inches), with base half angles of approximately 17° (overall length = 0.5 inches) The nosetips were fabricated from thin sheets (.0007 to .002 inch) of 347 stainless steel which were diffusion bonded to form a monolithic structure with the mechanical properties of the parent material. The flow passages needed for flow metering and surface distribution were chemically etched in the individual sheets or platelets prior to diffusion bonding. Coolant flow distribution over the nosetip surface was characterized by collecting and measuring the flow rate from 15 independent hydraulic sections which were aligned axially down the nosetip. The surface of the nosetips was cooled by approximately 4400 individual coolant exit slots which occupied approximately one half of the nosetip surface area. Flow metering within the nosetip was tailored to provide different coolant distributions for specific thermal protection applications.

A photograph of the nosetip external configuration is shown on Figure 1. Typical flow metering paths within the nosetip are shown on Figure 2. It is this in-depth flow metering which allowed the surface coolant distribution to be tailored to provide test data over a range of local coolant mass fluxes. Coolant distributions for three of the tested nosetips are shown on Figure 3.

TRACK OPERATING CONDITIONS AND INSTRUMENTATION

The independent track operating parameters were the nosetip launch velocity, pressure and temperature within the 1000 foot long cell. Detailed descriptions of the Track G facility are contained in Reference (2). For the series of clear air nosetip tests under consideration the launch velocities were 17 to 17.5 KFPS while cell pressure produced altitudes equivalent to 11,000 to 20,000 feet. These conditions provided excellent simulation of actual reentry environments. The resulting heat flux distributions over the nosetip for the range of test conditions are shown on Figure 4. Cell temperature was near ambient, 539°R, for all tests and the resulting enthalpy ranged from 6500 Btu/lbm at range entrance to 3800 Btu/lbm at range exit. The velocity degradation with flight distance accounts for most of this variation.

A major factor in the success of the test series was the data acquisition available at the facility. The data consisted of coolant flow rate measurements, nosetip surface temperature plots, and laser photographs. Coolant total flow rates were calculated from x-ray photographs of the displacement of the piston in the coolant cylinder. A drawing of the nosetip and model holder containing the coolant system is shown on Figure 5. When coupled with the nosetip hydraulic data and design computer code the total coolant flow rate could be used to accurately determine the coolant mass flux distribution

within approximately 5%. A photograph of the nosetip in flight near the mid-range location is shown on Figure 6. The coolant water droplets and nosetip surface pattern may be seen on the photograph.

Thermal mapping of the nosetip surface was accomplished through the use of image converter cameras. Two systems were used, one with a temperature range of 2250°R to 8100°R and the other with a range of 2850°R to 8100°R. Measurement uncertainty for both systems is approximately ± 200°R. The maximum measurable temperature for either system in these tests was defined by the nosetip material melt temperature (3000°R). The main limitation to the otherwise excellent data system was the rather high lower limit on temperature sensitivity. The nosetip design temperature was 2260°R, only 10°R higher than the lower sensitivity limit of the best IC camera. Consequently, a large amount of valuable thermal information was not available for analysis. Improvements in the temperature sensitivity range appear possible in the near future.

NOSETIP OPERATING CONDITIONS AND DATA TRENDS

The data contained in Table I summarize the nosetip and track operating conditions for the 10 clear-air tests. Thermal data from these tests were available at up to 4 stations on each test. However, at some stations, temperatures were below the IC camera sensing levels, and on some tests, shock cap or after-body flare masked the data. There was sufficient data from the first test series, however, to allow the data to be used to design the coolant distribution flow profile for the second test series. A plot of these data along with the design mass flux profiles is shown on Figure 7.

Although the data available from the two test series was not complete enough to provide a solid basis for a comprehensive empirical model, it did provide an excellent base from which to correlate the engineering analytical model. This basic model formulation was supported by both the thermal data trends and the appearance of the liquid coolant mantle surrounding the nosetip which was observed from the inflight laser photographs. Before proceeding to the description of the analytical model some additional comments relating to the empirically observed nosetip behavior will be discussed.

The most interesting of these observations, and perhaps the most unexpected, is the apparent "self healing" aspect of the thermal protection phenomena associated with stagnation point blunting and "dimpling". The blunting is caused by melting and/or erosion as the nosetip stagnation region approached the material melt temperature.

The concave depression or "dimple" has been a characteristic of all nosetip testing performed in the facility. The dimpling is slight, 10 to 30 mils deep and 30 to 50 mils in diameter. However, it appears that this dimpling constitutes a significant self-healing aspect of the nosetip. Since the stagnation point has generally been undercooled, either by design or through fabrication anomalies, it has tended to get hot. This results in melting and/or increased erosion. The formation of the dimple is a natural protective occurrence which reduces local heating and establishes an equilibrium between delivered and required coolant flow rates. The data

presented on Figure 8 show the influence of stagnation point mass flux on observed surface temperature. These data show a substantial decrease in coolant required for a given surface temperature as dimpli ̄g occurs.

A second observation of significance is the apparent insensitivity of coolant requirements to nosetip roughness. An untested nosetip has an effective surface roughness estimated to be approximately 5 mils. After repeated tests, particularly in a weather environment, the roughness approaches 25 to 30 mils. No differences have been found in the coolant flow/surface temperature relationship for the two cases. It should be noted that the smooth wall boundary layer momentum thickness at the base of the nosetip is typically on the order of 1.5-2.0 mils.

A third observation, which led to the formulation of the coolant vaporization modeling improvements, was the presence of a mantle of liquid droplets surrounding the nosetip during flight. Coupled with this observation is the fact that the nosetip cooling models which existed at the time the test program was initiated considered only the influences of local coolant injection and could not adequately predict the observed thermal behavior (low surface temperature) in the downstream portions of the nosetip. These observations from the first test series led to the development of the present downstream cooling model which uses coolant droplet atomization, drag and vaporization to predict distributed thermal energy exchange in the nosetip boundary layer.

NOSETIP MODELING TECHNIQUE

The objective of this work was to establish analytical procedures for predicting the performance of the Aerojet discrete injection cooled nosetip. These procedures considered not only the local blockage and internal heat transfer phenomena but also the influences of coolant carryover from upstream injection slots. In addition to the development of the analytical model, an initial calibration of the model using existing test data was accomplished.

The current Aerojet nosetip concept utilizes film cooling as a major means of protection against reentry heating. The coolant, which is injected from discrete slots as a mixture of liquid and vapor, provides protection through two mechanisms. Some local heat transfer blockage, caused by local injection, occurs just downstream of each slot. Also, as the heated injected liquid is entrained in the boundary layer and flows along the surface of the body, it absorbs energy directly from the hot gases and vaporizes, thereby cooling the downstream region. This process also alters the boundary layer development compared to that for a non-blowing surface.

Analysis procedures which have been developed in the past have only included local effects. No upstream injection cooling has been considered. This overly conservative approach has resulted in unrealistically high predicted coolant requirements. Also, the previous model did not allow accurate predictions of the coolant requirements in the downstream region of the nosetip and, thus, was of little value in designing a flight experiment where accurate predictions of surface temperatures over the entire tip are desirable.

335

Considerable experimental data has been recently obtained on the ABRV program. These data indicate that the downstream cooling effects are a significant contributor to total nosetip coolant requirements, and may reduce coolant requirements by as much as 50 percent. This data provided an excellent base for the initial formulation of a downstream cooling model; however more detailed data are desirable to better model the individual downstream cooling and blockage phenomena.

ANALYTICAL MODEL DESCRIPTION

The nosetip aerodynamic environment is characterized using the ABRES Shape Change Code (ASCC). Included in the code are the influences of surface roughness and heat flux augmentation at the stagnation point. This code generates the baseline non-blowing heat flux and pressure distributions and the boundary layer thickness and edge properties. Relevant data are put on mass storage data files for use by the downstream cooling and design codes. Coolant atomization, vaporization and boundary layer enthalpy reduction are calculated within the downstream cooling program to provide a reduced surface heat flux distribution. The program uses this reduced heat flux together with the pressure and enthalpy distribution, the nosetip hydraulic input and the particle environment (if any) to compute surface heating and erosion.

The heat transfer mechanisms which influence nosetip performance predictions and coolant requirements, i.e., the internal heat transfer, the local boundary layer heat blockage, and the downstream cooling will be discussed in more detail in the following paragraphs.

Internal Heat Transfer

A schematic diagram of the thermal model for the internal nosetip cooling is shown below. The nosetip surface is considered to be composed of platelets which form fins which are "2t" thick and having coolant channels between which are "D" deep. The coolant enters the channels at $X=0$ at a temperature T_{co} and at a rate G per unit cooled wall surface area. At the end of the platelets, $X=L$, the platelets are exposed to a hot gas at temperature T_g with a surface film coefficient h_g.

336
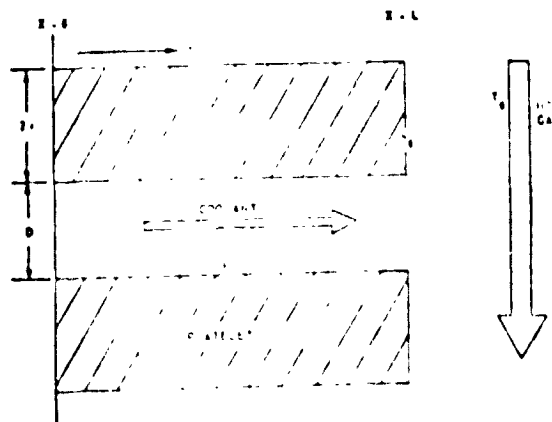
It is assumed that the heat conduction in the platelets is one-dimensional and that the platelet material and coolant properties are not temperature dependent.

The resulting form of the fin equation as used in the internal cooling model (Reference (3)) is:

$$T_w = T_{co} + Q_{net}/(K\ r_1) \tag{i}$$

Mass Transfer Blockage

Two mass transfer blockage models were examined during the ABRV Program. Originally, a correlation based on the work of Bartle and Leadon, Reference 4, was used. However, during the analyses of the ground test results, the model was found to yield much lower stagnation point temperatures than were measured. A blockage correlation based on the work done on the Nosetip Cooling Technology Program (NCT), Reference 5, was found to yield better correlation with the test data.

A comparison of the blockage ratios, q/q_o, predicted by the two models is shown on Figure 9 as a function of the blowing parameter, B'. The forms of the two correlations are similar. The Bartle and Leadon model is based on a correlation which relates the blockage ratio, q/q_o, to the mainstream specific heat ratios $C_p{}^*$, the blowing ratio, F, and the unblown Staton number, ST_o:

$$q/q_o = \frac{\dfrac{FC_p{}^*}{ST_o}}{\left[1 + F\ \dfrac{C_p{}^*}{3\ ST_o}\right]^3 - 1} \tag{2}$$

The NCT model relates the blockage to these same parameters but takes the form

$$q/q_o = \frac{1}{(1 + FM\ \dfrac{C_p{}^*}{St_o}\ F)^3} \tag{3}$$

Where FM characterizes the blockage as a function of land position. FM takes the form:

$$FM = .03 + .14\ e^{-2.8\ X/L} \tag{4}$$

Where X/L is the relative land position.

Downstream Cooling Model

The analyses of the test data gathered on the ABRV Program, as well as test data presented on previous programs, have indicated the need to include

337

downstream cooling effects in the nosetip analytical model. Initial formulation and development of this model was completed during the ABRV Program. In addition some correlation of the model with the existing test data was accomplished. As more of the recent test data are evaluated and the empirical trends are identified, these data will be used to further refine the model.

The downstream cooling model was formulated based on boundary layer energy balance considerations. The enthalpy in the boundary layer is reduced as a result of vaporization of coolant injected upstream. The phenomena considered include droplet atomization, acceleration, heat transfer, mass transfer and boundary layer thermal dilution. Equations relating to these processes were based on the work of Ingebo (Reference (6)) and Priem (Reference (7)) and may be found in the Appendix. These processes are shown schematically on Figure 10. The coolant is atomized at the slot exit and enters the gas stream as a series of droplets. The droplets are accelerated by the gas stream and vaporized as they proceed downstream. The vaporizing droplets exchange energy with the boundary layer gases resulting in a reduced boundary layer enthalpy. In addition, the coolant injection changes the boundary layer temperature and velocity profiles compared to the non-blowing case.

COPRELATION OF MODEL WITH TEST DATA

Nosetip surface temperature measurements resulting from the two test series were used to correlate the engineering analytical model. Preliminary correlation results of the new model are displayed in Figure 11 as solid lines for four tests. The measured temperature data are indicated on the plot by the circle-line combination. The dashed lines demonstrate the previous model (no downstream cooling influence) predictions for the same test conditions. As can be seen from the figures, the current revised model results in an improved predictive capability at body angles of greater than 20°.

Improvements in the stagnation region modeling which will include an improved modeling of stagnation region heat flux and inclusion of the affects of blunting and dimpling are currently being evaluated.

CONCLUSIONS

Based on the test program and subsequent analytical model development several conclusions have been drawn. These include:

1. Excellent test data were obtained from 10 clear air tests at flight environmental conditions during two test series. Data from the first test series were used to design the coolant flow distribution for test series 2 and data from both series were used to develop and provide initial calibration for a nosetip cooling model.

2. The nosetip cooling model provides predictions of coolant requirements which significantly improved accuracy compared to previous models. The model includes characteristics of the three cooling mechanisms.

Internal cooling has been modeled using a fin equation with constant heat
transfer coefficient. Local boundary layer blockage is computed using a
correlation derived from tests which were expressly designed to provide
blockage data for discrete injection nosetips. The downstream cooling
routine considers atomization of the injected coolant; acceleration of the
droplets; drop vaporization and mixing of the vapor with the boundary
layer gas; and the reduction in boundary layer enthalpy and heat transfer
which results from this mixing.

3.   Good correlation to the clear air track test data was obtained
using the analytical model.

4.   Further model development and verification testing to better
define the various cooling mechanisms involved in downstream cooling is
justified and recommended. These tests should include:

      (a)   Cold flow tests to better characterize coolant penetration
           and atomization.

      (b)   Hot gas tests (T $\sim$ 1500°F) to characterize coolant vaporiza-
           tion.

      (c)   Aeroheating tests with instrumented nosetips in a plasma
           arc environment to provide the necessary nosetip temperature
           data for further model calibration.

REFERENCES

(1)   "Advanced Ballistic Reentry Vehicle (ABRV) TCNT Development Program
     Final Report," Report 290770-004-001, ASC to AVCO-SD, April, 1980.

(2)   Trimble, M.H., Smith, k.T. and Matthews, R.K., "AEDC High Temperature
     Testing Capabilities," AEDC-TR-78-3, April 1978.

(3)   "ALRC - TCNT Subsystem ABRV, Phase II, Flight Test," Proposal No.
     LR 947768, ALRC to AVCO-SD, August, 1977.

(4)   Bartle, R.E. and Leadon, B.M., "The Effectiveness as a Universal
     Measurement of Mass Transfer Cooling in a Turbulent Boundary Layer,"
     Proceedings of the 1962 Heat Transfer and Fluid Mechanics Institute.

(5)   Jaffe, N.A., et al., "Final Technical Report, Nosetip Cooling Tech-
     nology (NCT) Program Investigation of Discrete Injection Cooling,"
     Aerotherm Division/Acurex Corporation Technical Report. SAMSO TR
     73-380, October, 1973.

(6)   Ingebo, R.P. and Foster, N.H., "Drop Size Distribution for Cross
     Breakup of Liquid Tests in Airstreams," NASA TN 4087, October, 1957.

(7)   Priem, R.J. and Heidmann, M.F., "Propellant Vaporization as a Design
     Criterion for Rocket Engine Combustion Chambers," NASA TR R-67, 1960.

TABLE I. AEDC TRACK G CLEAR AIR TESTS

Nosetip S/N	Test No.	Cell Press. (Torr)	Launch Vel. kfps	Range Entrance Stagnation Point Heat Flux,Btu/ft^2	Stag. Press. (psia)	Mid-Range Flow Rate Ratio	Max Temp. (^{o}R)	Loc.	Comments
Test Series No. 1:									
G-1	5046	350	17.7	24,700	2180	.69	3000	30°	Many Spots
G-1	5049	350	17.6	24,200	2160	.64	3000	0°-2°	Stag Pt Dimpled
G-1	5057	350	16.9	21,100	1990	.92	2400	0°-2°	-
G-2	5058	350	17.6	24,200	2160	.54	3000	0°-2°, 30°-35°	-
G-1	5060	350	17.6	24,200	2160	1.0/.2*	3000	0°-10°	Flow Leak
Test Series No. 2:									
G-4	5249	350	17.0	21,500	2010	.51	?	-	-
G-7	5252	-··	1 9	21,100	1990	.45	3000	0°-10°	-
G-7	5254	35	16.9	23,200	1990	.38	2880	0°-5°	-
G-7	5258	350	16.9	23,200	1990	.32	3000	15°-30°	•
G-5	5259	500	16.9	23,200	2830	.62	≤3000	0°-90°	•

*Actual fl rate through nosetip estimated to be this low due to massive coolant leak.

Figure 1. AEROJET NOSETIP
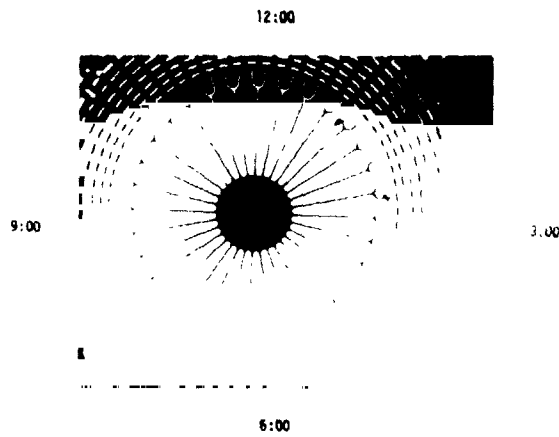
Figure 2. TYPICAL METERING PLATELET
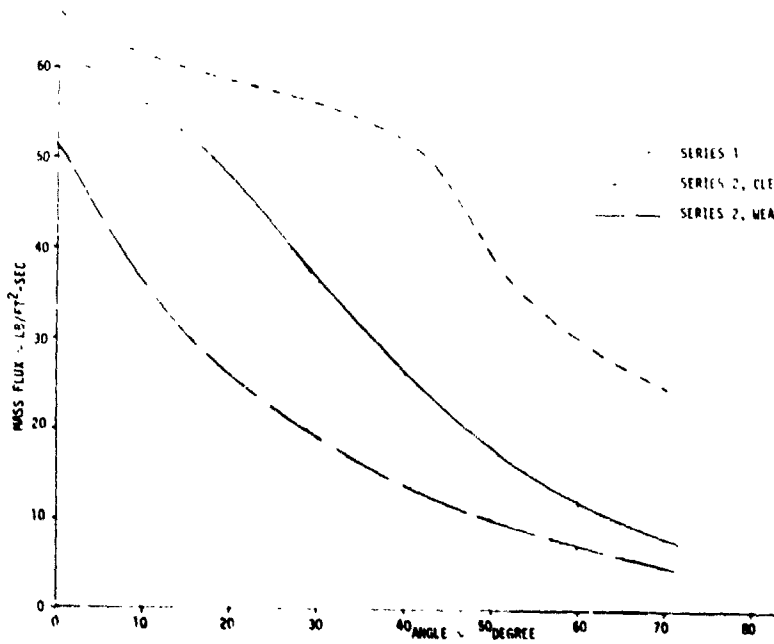
Figure 3. MASS FLUX DISTRIBUTION

TRACK G HEAT FLUX DISTRIBUTIONS (ASCC CODE,
R_n = 0.65 IN, SMOOTH WALL)

350 Torr Sta. 20 (Mid Range)

500 Torr, Sta 20 (Mid Range)

350 Torr, Sta 40 (Exit Station)

Heat Flux, Unblocked, Btu/ft^2-sec

Surface Distance, in.

Body Angle

Figure 4.

GRAPHITE/EPOXY

NOSETIP

LEXAN BASE

PROPELLANT

PRIMER

1.25

FIRING PIN

SHEAR PIN

ALUMINUM

PISTON
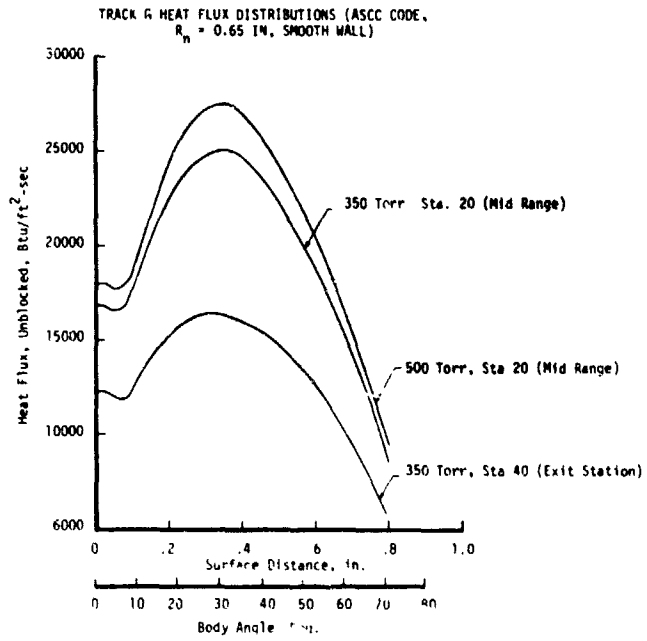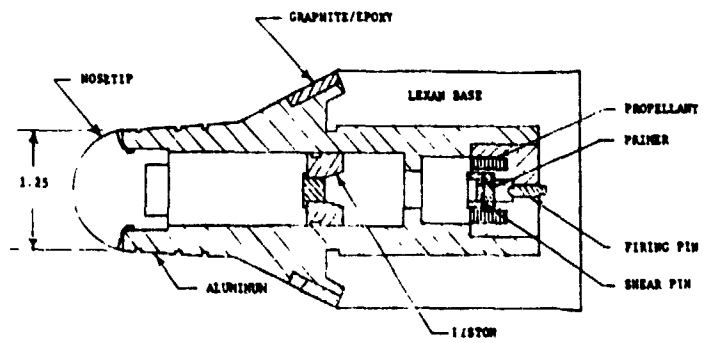
Figure 5.   NOSETIP AND MODEL HOLDER

Figure 6. NOSETIP IN FLIGHT
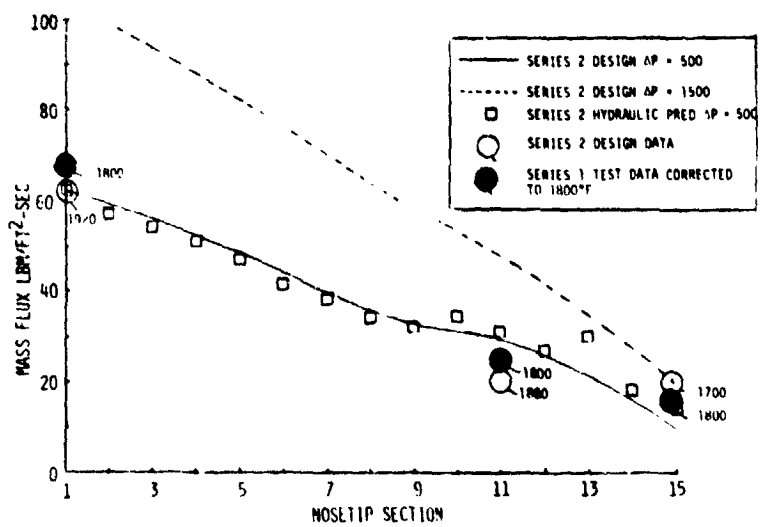
Figure 7. COMPARISON OF SERIES 1 and 2
FLOW DISTRIBUTION WITH TEST DATA

350 TORR
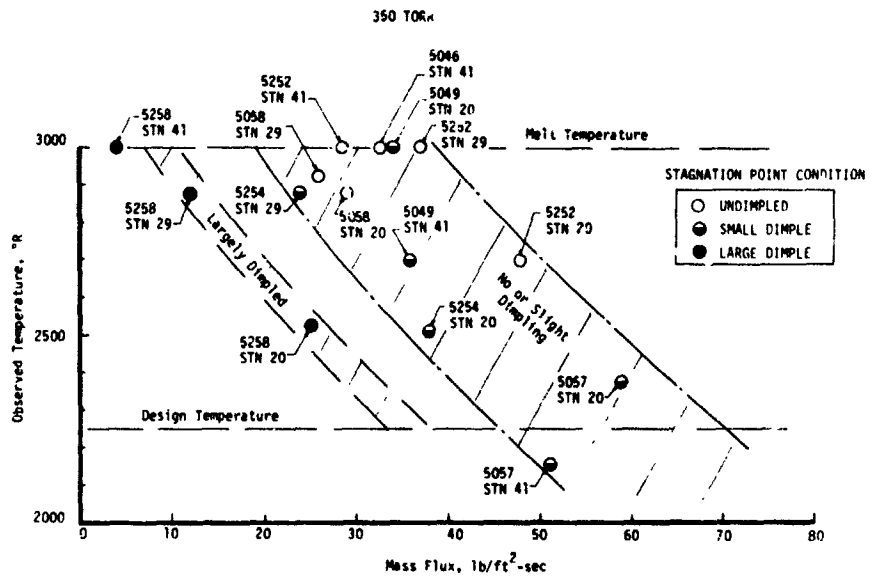
Figure 8. TRACK G CLEAR AIR STAGNATION
POINT TEST DATA
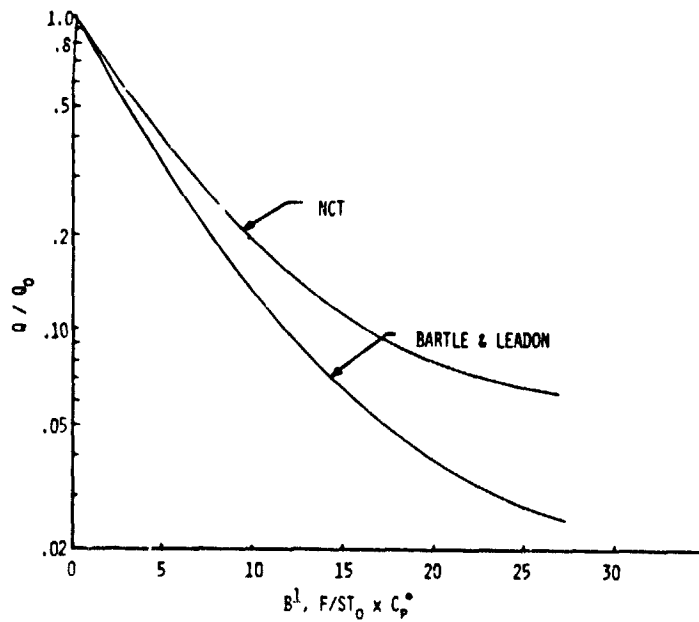
Figure 9. BLOCKAGE CORRELATION COMPARISONS

344
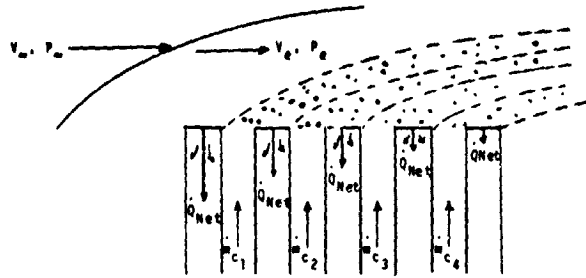
COOLANT ATOMIZATION AT SLOT EXIT = F (SLOT DIM, $(\rho V)_c$, $(\rho V)_e$, COOLANT PROPERTIES)

COOLANT VAPORIZATION = f (COOLANT PROPERTIES, GAS PROPERTIES, ΔV, DROP $_{DIA}$)

DROPLET/JET TRAJECTORY = f ($(\rho V^2)_c$, $(\rho V^2)_e$, DROP $_{DIA}$)

ENTHALPY REDUCTION = f (m VAPORIZED UPSTREAM)

HEAT FLUX REDUCTION = f (ENTHALPY REDUCTION)

Figure 10. DOWNSTREAM COOLING PROCESSES
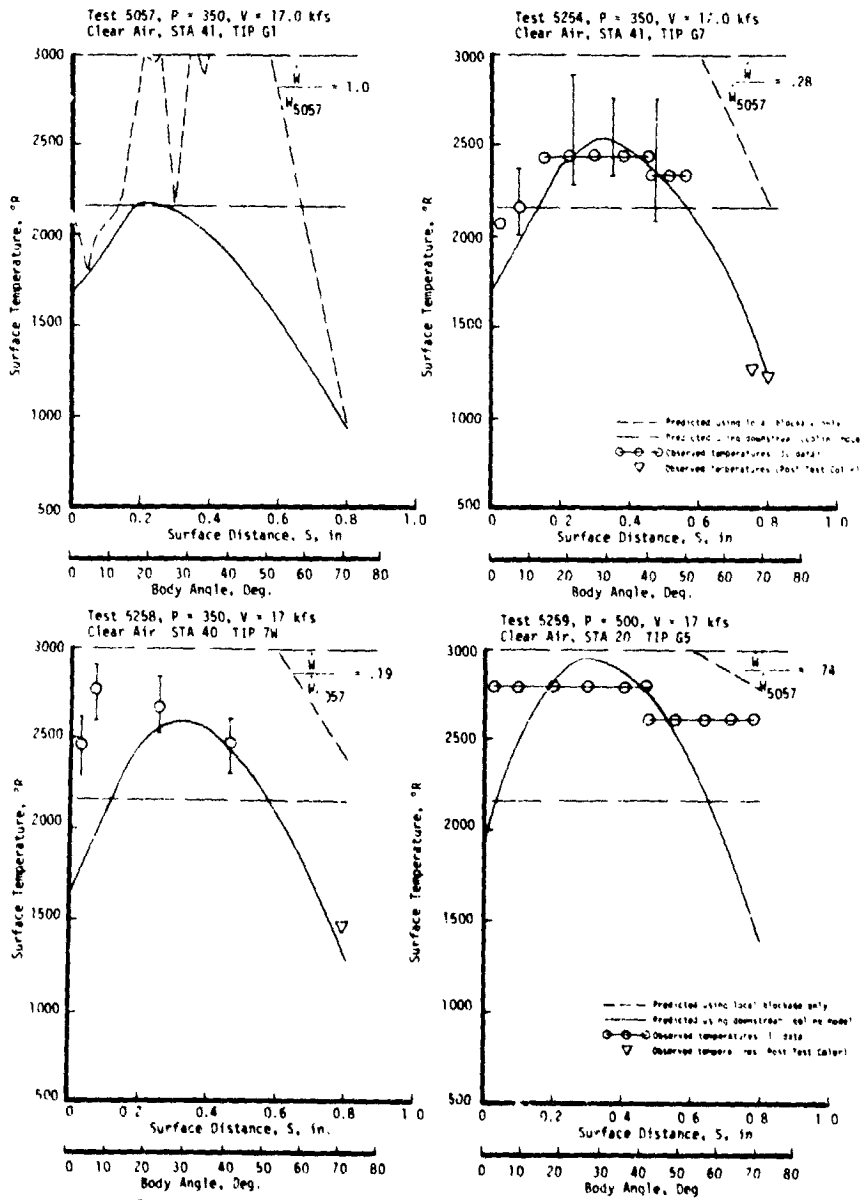
Figure 11. COMPARISON OF MODEL PREDICTIONS
WITH TRACK G DATA

345

APPENDIX

EQUATIONS USED IN DOWNSTREAM COOLING MODEL

I.   DROPLET ATOMIZATION (REFERENCE (6))

$$r_m = 1.95 \ (WE * REY * V_e/V_c)^{-0.25} \ D_o$$

II.   DROPLET DRAG/ACCELERATION (REFERENCE (7))

$$\frac{\Delta V_d}{\Delta t} = -0.375 \ C_D \ \frac{\rho_g}{\rho_c} \ \left[\frac{V_e - V_c}{r_m}\right]^2$$

$$C_D = 27 \ (R_e)^{-0.84} \qquad (M \leq 0.5)$$

$$C_D = f \ (M)* \qquad (M > 0.5)$$

III.   DROPLET HEAT TRANSFER

$$Q_D = 2 \ \Pi \ r_m \ K \ N_u \ (T_g - T_c) \ Z$$

$$N_u = 2 + .6 \ P_r^{.33} \ R_e^{.5}$$

$$Z = \frac{y}{e^{y-1}}$$

$$y = \frac{\dot{W}_v \ C_p}{2 \ K \ r_m \ N_u}$$

IV.   DROPLET MASS TRANSFER (REFERENCE (7))

$$W = 2 \ \pi \ C \ \frac{MW_g \ r_m \ N_{um} \ P_v \ \alpha}{RT}$$

$$\alpha = P_s/P_v \ \ell n \ (P_s/(P_s - P_v))$$

$$N_{um} = 2 + 0.6 \ S_c^{.33} \ R_e^{.5}$$

---

*From "Compressible Fluid Flow", by A. H. Shapiro, The Ronald Press Company, New York, 1953

NEW METHODS TO DETECT PARTICLE VELOCITY
AND MASS FLUX IN ARC-HEATED ABLATION/EROSION FACILITIES

D. B. Brayton, B. W. Bomar, B. L. Seiber, and P. D. Elrod
ARO, Inc., AEDC Division
A Sverdrup Corporation Company
Arnold Air Force Station, Tennessee 37389

ABSTRACT

Arc-heated flow facilities with injected particles are used at the Arnold Engineering Development Center (AEDC) to simulate the erosive and ablative/erosive environments encountered by spacecraft re-entry through fog, clouds, thermo-nuclear explosions, etc. Two newly developed particle diagnostic techniques used to calibrate these facilities are discussed. One technique measures particle velocity and is based on the detection of thermal radiation and/or chemiluminescense from the hot seed particles in a model ablation/erosion facility. The second technique measures a local particle rate, which is proportional to local particle mass flux, in a dust erosion facility by photodetecting and counting the interruptions of a focused laser beam by individual particles.

INTRODUCTION

Arc-heated particle-injected (seeded) flow facilities are used at Arnold Engineering Development Center (AEDC) to test nose cone materials and geometries by simulating the erosive and ablative/erosive environments of spacecraft re-entry. The two high-enthalpy, ablation testing (HEAT) facilities at AEDC each employ a seeded arc jet exiting into a low-expansion-ratio nozzle with relatively high static pressure (1 atm) to generate a high velocity (1500 msec^{-1}), high temperature (2000 to 4000°K), and high number density (a few particles per cm^3) duet cloud entrained in hot (2000 to 5000°K) gas that produces both erosion and ablation of models. The Dust Erosion Tunnel (DET) facility at AEDC employs a seeded arc jet exiting into a high-expansion-ratio nozzle with low static pressure (much less than 1 atmosphere) to generate a high velocity (1000 to 3000 msec^{-1}), low temperature (a few hundred °K), and low number density (1000 to 2000 per m^3) dust cloud entrained in a low-density, cool exitus gas that causes model erosion.

It is required that these facilities be calibrated regarding particle field characteristics. To this end two newly developed calibration instruments are described. One, the thermal emission velocimeter (TEV) measures the velocity of high-temperature particles in the HEAT facilities. Individual particle velocities are measured by collecting and photodetecting light self-radiated by a particle crossing two small, spatially separated, and separately photodetected regions in the flow. The two photodetected pulses then gate an electronic counter, thereby quantizing the time interval between pulses and providing the time versus distance measurement of velocity. Data is sequentially recorded, thereby providing a time-history of particle velocity at a point. The second instrument measures a local particle rate, which is proportional to local particle mass flux, in the DET facility by photodetecting interruptions or blockages of a laser beam as individual particles pass through the beam near its focus. Individual photodetected events are counted over fixed time intervals and recorded, thereby monitoring particle rate.

Measurements of both particle velocity and rate using these electro-optical techniques have been developed to the point that they are now effective, reliable diagnostic tools.

The remainder of this paper is concerned with the design and application of these instruments.

NOMENCLATURE

AEDC	Arnold Engineering Development Center
A_p	Cross-sectional area of particle; $\pi D_p^2/4$ for a spherical particle (m^2)
$\bar{A}_p$	Mean or average value of A_p (m^2)
ARO	Arnold Research Organization
ASA	American Standard speed (or exposure index) of a photographic emulsion (-)
A_v	Probe-volume virtual-aperture area or maximum cross-sectional area of the high detectivity region of the probe volume (m^2)
bit	Binary number (0 or 1) (-)
byte	Eight bits (-)
CRT	Cathode ray tube
DET	Dust Erosion Tunnel
D_f	Diameter of fiber optic (m)
D_ℓ	Diameter of lens or lens system aperture (m)
D_p	Diameter of particle (m)
D_v	Diameter of the probe-volume virtual aperture or diameter of the high-detectivity region of the probe volume (m)
Δf	Electronic bandwidth (Hz)
GPIB	General purpose interface bus
HEAT	High-enthalpy ablation testing
IEEE	Institute of Electrical and Electronic Engineers
k	Kilo or 1000
LV	Laser velocimeter
L_v	Effective probe volume length dimension (m)
micron	Micrometer or 10^{-6} meter
N_p	Total number of particles in the particle field (-)
$\overset{o}{N}_{ph}$	Average or mean photon arrival rate (Hz)
N_λ, $N_\lambda(T)$	Spectral radiant intensity in the normal direction $(W \cdot m^{-3} \cdot sr^{-1})$
$\bar{N}_\lambda(T)$	Value of $N_\lambda(T)$ averaged over the wavelength interval $\Delta\lambda = \lambda_2 - \lambda_1$ $(W \cdot m^{-3} \cdot sr)$

348

N_λ'	Spectral radiant intensity at an angle β relative to the surface normal $(W \cdot m^{-3} \cdot sr^{-1})$
n	Number of photons received over some time interval; number of (photocathode electron) events detected as one thermal particle passes through one probe volume (-)
$\bar{n}$	Average or mean value of n (-)
n_p	Number of particles per unit volume (m^{-3})
PMT	Photomultiplier tube
$P_{(n,\tau)}$	Probability of n events over a time period τ with a Poisson distribution (-)
p	Total cone beam power (W)
P_b	Power radiated by the backdrop (background surface) in-line with both the virtual aperture and the aperture of the collecting lens system (so as to be collected and detected) (W)
P_p	Power radiated by the particle that is incident onto the detector (W)
RM	Rate monitor
SNR	Inherent signal-to-noise ratio of the photoelectron signal burst generated by a single particle (-)
SNR_{ph}	Inherent signal-to-noise ratio of the collected photon signal burst from a single particle (-)
s_f	Distance of object (fiber optic) from imaging lens system (m)
s_v	Distance of probe volume from imaging lens system (m)
T	Absolute temperature (^oK)
TEM_{oo}	Propagating electromagnetic wave with transverse electric and magnetic (TEM) fields and Gaussian intensity distribution
TEV	Thermal emission velocimeter
V1, V_1	Upstream probe volume region
V2, V_2	Downstream probe volume region
V_v	Volume of the principal or high collection efficiency region of the probe volume assuming $s_v \gg D_\ell \gg D_v$; detection volume or volume within which a particle must be to be detected (m^3)
v_p	Velocity of particle $(m \cdot s^{-1})$
x_{pf}	x-axis or depth dimension of particle field (m)
x_{vb}	Distance between the probe volume and the backdrop surface (m)
$x^\sim$	Normalized x-axis coordinate of a single probe-volume-region coordinate system (-)
ZCD	Zero-crossing detector
Δz, Δz_v	Particle displacement distance corresponding to duration of TEV signal for one probe volume (m); z-axis probe-volume dimension (m)

z''	Normalized z-axis coordinate of a single probe-volume-region coordinate system (-)
z_{12}	z-axis distance between the upstream and the downstream probe volume (m)
α_b	Emissivity of backdrop surface (-)
$(1 - \alpha_b)$	Diffuse reflection coefficient of backdrop surface (-)
α_p	Emissivity of particle (-)
$\bar{\alpha}_p$	Detection-interval $(\Delta\lambda)$-averaged α_p (-)
β	PMT cathode photoelectron yield per joule of incident energy (j^{-1})
γ	Relative value of the beam power trigger level setting (of maximum value 1) (-)
η	Quantum efficiency (photocathode electrons per photon) (-)
θ	Divergence angle of radiation cone of Fig. 13 (r)
$\theta_{1,2}$	Angle between the probe volume axes (r)
θ_c	Angle of radiation collection; same as θ_v (r)
θ_v	Angle of a probe volume high-detectivity region; same as θ_c (r)
λ	Wavelength of thermal emission (m)
$\Delta\lambda = \lambda_2 - \lambda_1$	Wavelength band for which detection efficiency is 50 percent or greater (m)
λ_1	Lower wavelength limit for which detection efficiency is 50 percent or greater (m)
λ_2	Upper wavelength limit for which detection efficiency is 50 percent or greater (m)
λ_{T-MAX}	Wavelength corresponding to the peak (maximum) value of $N_\lambda(T)$ (m)
σ_{ph}^2	Variance in n (-)
τ	Signal period; time period (s)
Ω_c	Solid angle of radiation collection; $\pi\theta_c^2/4$ (sr)
Ω_c'	Relative radiation collection efficiency (of maximum value 1) (-)

THERMAL EMISSION VELOCIMETER

As previously mentioned, the HEAT facilities produce both an ablative and an erosive testing environment. Gas temperature and velocity are nominally 2000 to 5000°K and 1000 to 2000 msec^{-1}, respectively, and the small injected particles (of nominally 100 to 200-µm-diameter carbon material) are heated, ablated, and accelerated in the nozzle to temperatures, sizes, and velocities that are generally unknown until measured.

Streak photography using a high-speed camera, laser velocimetry, pulsed laser holography[1] and thermal emission velocimetry[2] have all been applied to measure the dust cloud parameters. Photographing the hot particles with a high-speed camera produced streak image recordings from which particle

velocity could be measured with ±15 to ±20 percent accuracy; such a technique has been used over the entire range of the fa llity operating conditions. A laser velocimeter (LV) that utilized four interference fringes, a 30-deg forward scattering angle, a high-power argon-ion laser, and a narrow bandwidth [1.0 nanometer (nm)] spectral filter (to reject the thermally emitted signal), produced good signals at low working gas temperatures (up to 2700°K). However, very little particle velocity data could be recorded -- signal processing/recording instrumentation applicable to low-cycle-count LV signals was not then available. However, such an LV potentially can provide ±10 percent accuracy velocity data over all HEAT facility operating conditions if proper signal processing and narrower bandwidth spectral filtering are employed. The pulsed laser holographic recording technique,[1] using the HEAT arc jet as an optical diffuser and recording holograms on the jet far side, produced reconstructed particle images of marginal quality. More recently, the thermal emission velocimeter (TEV) technique[2] was employed to measure particle velocity through essentially the entire operating range of the HEAT facilities and with ±5 percent accuracy. The TEV was much simpler to build, operate, and maintain in comparison to the proposed LV system and produced similar results. It is now thought that the TEV technique can be expanded or a multiple-laser-beam technique (similar in principle to that of the particle rate monitor discussed herein) can be developed to permit total particle field parameter measurements to be made in the HEAT facility in the near future; such an effort is currently underway at AEDC.

TEV OPERATING PRINCIPLES

The thermal emissive velocimeter measures the velocity of hot particles by detecting the thermal radiation emitted by a particle when its trajectory carries it through each of two spatially separated probe volumes.

The TEV detection system shown in Figure 1 defines two regions or volumes in space, V1 and V2, that (1) are regions of maximum light collection (and detection) efficiency (Appendix A discusses light collection efficiency) and (2) are spatially separated by a known distance. That is, the electro-optical detection systems to the left in Figure 1 will detect a point source of light with high relative collection efficiency only when it lies within one of the two detection regions V1 and V2. Thus a hot particle moving along the z axis of Figure 1 through these regions while emitting thermal radiation will generate photodetected signal amplitudes versus particle spatial position as indicated in Figure 2. Knowledge of the spatial distance between the two detection volumes and the transit time between the two signal maxima permits a calculation of particle velocity.

Throughout the remainder of this article it will be assumed, unless otherwise stated, that the probe volumes and/or the particle number density are sufficiently small such that only one particle at a time is detected.

TEV OPTICAL DESIGN

The most common TEV optical design employed at the AEDC is illustrated in Figure 1, with an exception that many times only one photomultiplier tube (PMT) detector was employed to detect both optical signals (with both fiber-optic components directed to the common PMT). Two achromatic collimating lenses were employed back-to-back to first collect and collimate the radiated

signals, and then to focus the collimated signals onto the ends of two optical
fibers. The fiber ends served as limiting apertures. The fiber optics col-
lected the signals and transmitted them to the control room, at which point
they were photodetected. Plastic fibers were used in the detector head where
short radius bends were required, and glass fibers of high transmission effi-
ciency were employed to transmit the signals to the detector(s). All of the
fiber-optic components were single, continuous elements of 250-μm diameter.
Th. high noise level of arc-current-induced electromagnetic radiation emitted
by the HEAT facilities suggested that the photodetectors and other electronic
instrumentation be located in the shielded environment of the control room,
located 30 m from the arc heater.

The wavelength selectivity of the optical system components caused the
overall system radiation detection efficiency to be very low, but, neverthe-
less, adequate for detection purposes. Even though the transmission bandwidth
of the lenses and optical fil·~s (of nominally 400 to 1100 nm) approximately
coincided with the peak of the spectral emission band of the thermal radiation
(from the nominally 2000 to 4000°K particles, see Appendix A), the thermal emis-
sion bandwidth was approximately a factor of 4 larger than the transmission
bandwidth of the optics. Furthermore, the bandwidth of the PMT detectors em-
ployed (which were existing detectors and not specially selected for the appli-
cation) was very narrow (320 to 530 nm) and further reduced the optical system
effective bandwidth by an additional factor of 8. Wide bandwidth PMT de-
tectors are generally available with gallium arsenide photocathode material
that has high responsivity over a 240- to 880-nm bandwidth.

TEV PROBE VOLUME GEOMETRY

The three-dimensional geometry of the probe volume can be scaled up or
down by changing the diameter of the virtual aperture, D_v, through the equation
$D_v = s_v s_f^{-1} D_f$, where the quantities in this equation are defined in Figures 1
and 11. If conventional spherical surface lenses are used with a circular
aperture in axial symmetry, for $s_v \gg P_\ell \gg D_v$ (Figure 1) the volume of the
'pal or high-collection efficiency region of the probe volume (the shaded
region of Figure 1) is

$$V_v \approx \frac{\pi D_v^3}{6 \, \theta_c} \tag{1}$$

A TEV optical design that provides both the smallest probe region maxi-
mum (or length) dimension and minimal systematic measurement error is shown in
Figure 3. Note that the probe volumes are not totally in line along the flow
direction. Time periods would be measured as particles traversed between the
two probe volumes as with the normal TEV. However, at the signal period
$\tau = D_v v_p^{-1}$ there would occur an accumulat of signal data above the baseline
data because of particles intercepting both probe volumes, thereby generating
effective probe volumes of much smaller maximum dimension. The maximum length
of the effective probe volumes is given by (see Figure 3)

$$L_v \approx \frac{\eta_v}{\sin \left[(\theta_{1,2} + \theta_v)/2 \right]} \tag{2}$$

Note also that the probe volume centerlines are both parallel to the x' - y plane and therefore the normal (though usually small) systematic error associated with a nonuniform distance between the probe volumes is eliminated.

The concept that a relatively simple optical system (consisting of an imaging lens system and the single opening of an aperture) will collect point source radiation with high efficiency from only a small, definable region in space is fundamental to the design of a TEV and is outlined in Appendix B. Statement (2) of Appendix B, which identifies which rays will be collected, can be used to determine the probe volume geometry by way of collection efficiency contours. For the case of a circular aperture stop at the fiber optic and a circular lens system aperture stop, the single-probe-volume collection efficiency contours are x-axis symmetric as indicated in Figure 4a, which is a two-dimensional plot of contours of constant radiation-collection efficiency.

Two important probe volume geometries result when either one of the single-probe-volume aperture stops is changed from a circle to a narrow slit as illustrated in Figures 4b and c. Both are important to TEV design since they can be advantageously utilized as follows: (1) a reduction in the z-axis width of the aperture of the imaging lens system reduces the single-probe-volume signal duration for remote (or non-central) particle trajectories to correspond to $\Delta z \cong D_p + D_v$ particle displacement;* (see Figure 4b with particle trajectory parallel to the z-axis); (2) a reduction in the z-axis width of the aperture of the fiber optic reduces the single-probe-volume signal duration for central particle trajectories to correspond to $\Delta z \cong D_p$ particle displacement, assuming $\Delta z_v << D_p$.

Case (1) above, which can be used to reduce the z-axis widths of the remote regions of the two TEV probe volumes, represents the TEV geometry that is most often employed at AEDC. However, in one employment where much lower than usual accelerating gas temperature (and particle temperature) was expected, this slit aperture was not used, allowing the full circular collecting lens aperture to gather light and produce maximum signal amplitude. Signal broadened data, from the remote probe volume regions, were minimized by choosing only the particular data samples that resulted from the employment of relatively large trigger level settings on the electronic signal processor; (see the subsection "Computer Controlled Counter Method" of the section "TEV SIGNAL CONDITIONING AND DATA ACQUISITION" in this paper).

Case (2) above, which reduces the z-axis width of the central region of the probe volume, has not been utilized to date. However, such an employment can potentially be used in conjunction with a TEV to measure the z-axis dimension of a translating particle and may be used for this purpose some time in the future at AEDC. It is not difficult to envision a TEV-based system that simultaneously measures the velocity and two orthogonal dimensions of a translating particle.

---

*For very remote particle trajectories with finite (nonzero) lens aperture slit width, the signal duration slowly increases so that $\Delta z \cong D_p + D_v$ is not satisfied; in fact, $\Delta z >> D_p + D_v$ is satisfied. However, signals from such very remote probe volume positions are relatively very weak and therefore are usually ignored by an electronic signal processor.

Cases (1) and (2) above can be effectively used in conjunction, i.e., deployed in the same single-probe-volume optical system, to simultaneously achieve the benefits of both. However, it must be remembered that both cases contribute to a reduction of the total number of signal photons detected from a translating particle.

TEV EXTRANEOUS RADIATION SOURCES

Extraneous, noise-contributing radiations not received from the hot signal particles in the TEV probe volumes can be categorized as either (1) direct, line-of-sight radiation components from remote particles, from a radiating accelerating gas, and from a hot radiating backdrop surface (via rays through the detection volume virtual aperture in line with the collection aperture, see Appendix 3), or (2) indirect radiation components (from particle field, accelerating gas, cell lights, or whatever) scattered off the backdrop and then through the same high-detectivity region of the probe volume in line with the detector optics aperture. The direct component that results from particles located in the remote, low-detectivity regions of the probe volume can be substantial to the point of obscuring the signal. Substantial obscuration would result, for example, if the particle field were dense enough such that because of particle blockage the detector could not see through to the relatively low-emittance backdrop. This condition would frequently occur without a particle being located in the high-detectivity region of the probe volume if

$n_p \pi D_v^3 (6\theta_c)^{-1} < 1$ and $\exp(-x_{pf} n_p A_p) \ll 1$ where $\pi D_v^3 (6\theta_c)^{-1}$ is the assumed approximate volume of the high-detectivity region of the probe volume and $(n_p A_p)^{-1}$ is the mean free path of a light ray propagating through the particle field.

The indirect components of detected radiation result from radiation being scattered off the (assumed) diffusely reflecting backdrop. These components cannot usually be eliminated by reducing the diffuse scattering coefficient of the backdrop to a negligible value as (1) most low-scatter, high-absorbing optical surfaces, such as flat black paint or black optical felt, will diffusely scatter at least a few percent of the incident radiation and (2) a high spectral reflectivity or mirror surface, which will scatter typically a few tenths of one percent, only reflects or deviates the line of sight of the detector package to another backdrop surface, and does not by itself provide a solution.

The relative detection of a particular extraneous radiation component is governed, in part, by the position in space from which it originated; the collection efficiency analysis of Appendix B can be used to determine the relative contribution versus spatial position of any component. For example, it can be shown that if the number of particles that illuminate the backdrop originate from a relatively small (in comparison to x_{vb}) bounded region, then the radiated particle field component that is diffusely reflected off the backdrop is negligible (relative to signal) if[2]

$$x_{vb}^2 \gg A_v (1 - \alpha_b) N_p / \pi \tag{3}$$

In this equation, x_{vb} is the distance between the probe volume and the backdrop surface, A_v is the probe-volume virtual-aperture area, $(1 - \alpha_b)$ is the

(assumed) diffuse reflection coefficient at the backdrop, and N_p is the total number of particles in the particle field (radiating at the backdrop).

Detection Conditions

For a TEV system employing a high-responsivity photomultiplier tube and a time-interval counter type of signal processor to effectively extract data, the following conditions must be met: (1) the detected thermal radiation quantum number (photons) resulting from a single particle traversing the high-detectivity region of a probe volume, assuming no background radiations are present, must be great enough to produce large inherent signal-to-noise ratio (or SNR, see Appendix C); (2) the mean detected level of background radiation (photons/second), assuming no principal particle is present, must be significantly less than the detection level when a principal particle is present, and (3) the particle number density, n_p (assumed uniform over a depth x_{pf}), must be low enough such that $n_p << V_v^{-1} + (\bar{A}_p x_{pf})^{-1}$, where V_v is the volume of detection** of a single TEV-probed region, $\bar{A}_p$ is the mean particle cross-sectional area, and x_{pf} is the x-dimension or depth of the particle field.

If the above detection conditions are not met, it is doubtful that a time-interval counter (signal processor) can be effectively employed; however, in some cases, other signal-processing means, more capable of extracting periodic data from noisy environments, may possibly be used. For example, if condition 1 is not met but the inherent single particle SNR is low and of approximate value SNR $\cong$ 1, then a correlation type of signal processor would provide a good opportunity to extract data from the near side of a particle field, regardless of conditions 2 and 3. For condition 1 with SNR << 1, conditions 2 and 3 must be approximately met for even a correlator type to extract data in a reasonable time.

TEV SIGNAL CONDITIONING AND DATA ACQUISITION

Moving Pictures of Oscilloscope Method

The initial means of processing and acquiring TEV data was to take movie pictures of the signal displayed on an oscilloscope. The optical signals from the two probe volumes were detected on a common photomultiplier tube (PMT) detector. A very sensitive movie film (ASA 400 color film, push processed to ASA 800), a movie camera optimized for low light level, and an oscilloscope designed to record high-speed, single-swept events were used to record TEV data. The scope was operated in a single horizontal (time) sweep mode with the (normally manually controlled) horizontal sweep reset command signal being automatically delivered by, and synchronized to, the movie camera. To accomplish the latter, a circuit was developed that automatically rearmed the oscilloscope horizontal sweep immediately upon each opening of the movie camera shutter. After each rearming, the first signal (if any) meeting the qualifications of the oscilloscope trigger circuit would be displayed on the CRT and recorded on film. Utilizing this method, individual TEV signal events were recorded at the frame rate of the movie camera, nominally 15 to 75 frames per second.

**The detection volume or probe volume is the volume within which a particle must be to be detected.

Computer-Controlled Counter Method

The final choice of a TEV signal-processing and data-acquisition system consisted basically of a 20-picosecond resolution programmable electronic counter, a crystal-controlled general purpose lectronic timer, a flexible disk magnetic storage device, and a graphics display terminal, all interfaced to a microcomputer. The counter was operated in the time interval measurement mode to process TEV signals and its start-stop channel trigger levels were programmed by the microcomputer. The timer was started at the beginning of a data run to correlate acquired data with time.

Such a system provided the major benefits of (1) automatic progression during a run through a range of trigger levels sufficient to obtain TEV data under most tunnel conditions, (2) acquisition and storage of data at high rates, and (3) automatic reduction and plotting of data following the run. The computer was programmed to stop and acquire data at each trigger level for a time that was sufficient (e.g., 0.1 sec) to obtain a large data sample. The typical HEAT facility run time was only a few seconds. Without automatic, step-by-step ranging of the trigger levels during a run, a few (unnecessary) preliminary runs would be required to establish trigger levels for each new set of arc heater conditions.

A microcomputer with 28k 16-bit words of memory was used to control the counter trigger levels and to acquire, store, and display the counter and timer data (Figure 5). TEV time-interval-counter data and timer data were stored on the magnetic flexible disk for permanent retention and were later reduced, displayed, and copied in a velocity histogram format.

Figure 6 is a flow chart of the computer program used to control trigger levels and acquire TEV data. A combination of Fortran and assembly language programming was used to implement this flow chart. Trigger levels are changed by factors of two (40 mV, 80 mV, 160 mV, etc.) every 100 msec during a run. Each time a new trigger level is selected, information on the memory location where data from the previous trigger level was stored is maintained so that data can later be analyzed by trigger level. After seven levels have been programmed (700 msec), the sequence of trigger levels repeats. This sequencing allows at least some data to be recorded throughout the run regardless of signal level variations. Following an initial data run to establish the range of pulse heights, the number and range of trigger levels programmed may be reduced.

Data from the TEV time-interval counter was rounded to the nearest nanosecond and stored in computer memory as a 16-bit unsigned integer in the range 0 to 65535 nsec. The value of run time from the general purpose timer was stored to a resolution of 10 msec as another 16-bit integer. However, to conserve memory, run time was only stored with every tenth TEV reading. The average time required to read and store a single TEV reading was 600 μsec, which permitted in excess of 100 readings to be obtained at each programmed trigger level provided the rate of TEV pulses was adequate. Data were stored in computer memory until either the maximum run time programmed had elapsed or until 15,000 TEV readings (memory capacity) had been acquired. The TEV data were then recorded onto flexible disk and, if desired, read back and processed for display by trigger level. A typical TEV velocity histogram is shown in Figure 7.

PARTICLE RATE MONITOR

The Dust Erosion Tunnel (DET) generates a high-velocity (1000 to 3000 $msec^{-1}$) dust cloud of large cross-section (0.1- to 0.4-m diameter) and low number density (resulting from 100 $gm \cdot sec^{-1}$ maximum, particle mass injection). The mean particle size ranges from a few tenths of a millimeter to one millimeter average dimension (the particle shape is irregular, nonspherical). Optical access to the test section is provided by pairs of opposing windows viewing transversely through the dust cloud jet with one window on each side of the test section.

Over the years, various optical instrumentation techniques have been used to calibrate the DET particle fields. A pulsed laser holographic technique[1,3] was employed to measure particle size, velocity, and number density; a laser velocimeter[4] measured particle velocity; and an optical fiber-optic technique[5] was used to measure particle size. Much of this data is summarized in a report describing the DET facility and its calibration.[6] More recently, an optical particle rate (number/time) monitor (or RM) was employed that measured the instantaneous local particle rate throughout a run by photodetecting and counting the number of beam power reductions as particles intercepted a small laser beam. This instrument provided data for a nominally 3:1 particle size range, and it is believed that two of these instruments would provide data over the full 10:1 range of mean particle size that is characteristic of the DET facility operation. Furthermore, recent results indicate that by separately photodetecting the interruptions of many closely spaced, small laser beams by individual particles, size and velocity as well as relative contribution to rate per unit area can be measured. The particle rate monitor instrumentation will now be described.

RATE MONITOR OPERATING PRINCIPLE

The particle rate monitor employs a laser beam of special geometry that is transmitted through the DET particle field. Individual particles of the low-number-density particle field intercept the beam and produce transient reductions of beam power. These are detected and counted using a photomultiplier tube (PMT), a special pulse-discriminator circuit, and an electronic counter operating in the event-counting mode. Individual particle interruptions are counted over fixed intervals of time, and accumulated count data and time data are periodically recorded on the magnetic tape of a microprocessor-based graphic display unit.

RATE MONITOR PERFORMANCE CHARACTERISTICS

The optical geometry of the particle rate monitor beam is shown in Figure 8. A truncated-cone-geometry laser beam (see Appendix D for particle rate monitor optics) converges to a minimum diameter disk slightly smaller than the smallest particle size to be detected. The beam then diverges symmetrically about the minimum diameter. The point of minimum cone diameter is positioned in front of a model being tested. The detection cross section, or the area through which a particle center must pass to be detected, is based on a particle blocking a specific minimum fraction (50 percent or more, for example) of the laser beam; the detection cross section of both a small and a large spherical particle is indicated in the figure. For a particle to be detected,

the center of the (assumed spherical) particle must intercept the detection cross section or detecting area.

It is advantageous that the detection cross section increases as particle size increases. This is because particles of larger (mass weighted) mean size can be injected only at lower (number per second) rates and therefore require a larger detection cross-section to accumulate a large data sample in a given time. Also, one beam geometry can be effectively employed for a range of particle sizes. To date for the DET application a 500-μm, or micron, cone minimum diameter has been used to detect chiefly in the 400- to 1000-micron range.

For design purposes it is necessary that the cone minimum diameter be an appreciable fraction of the (mass-weighted) mean particle size so that the many small particles usually present in a sample having a large mean particle size will be discriminated out and not detected. Otherwise the possibility would exist that the accumulated count data would not be representative of the large particles that dominate the model erosion process.

The convergence-divergence angle of the cone beam is also important. First it determines, in part, the detection cross section that must be large enough to obtain a large number of particle counts per sampling interval. It should be noted that the relative (reduction in beam power) trigger level also determines the detection cross section. Secondly, a significant cone angle limits the longitudinal dimension of the detection cross section, permitting monitoring of particle rate in an area of flow more representative of an immersed test model than the entire flow area.

Inherent Signal-to-Noise Ratio

Assuming that the detected level of background radiation is negligible relative to the RM beam power, then accurate RM count data are obtained if the RM beam power at detection, γp, produces a high inherent signal-to-noise ratio (SNR >> 1). The effective detection time interval is determined by the electronic bandwidth, Δf, of the threshold trigger circuit of the electronic counter. The intrinsic or inherent SNR is thus (see Appendix C)

$$SNR = (\gamma p \beta / \Delta f)^{\frac{1}{2}} \tag{4}$$

where γ is the beam power trigger level setting relative to the total cone beam power p, and β is the PMT cathode photoelectron yield (photoelectrons per joule). For example, an SNR of 20 is generated with a 50-percent trigger level ($\gamma = 0.5$) of a $P = 10^{-5}$ watt beam with $\Delta f = 10^8$ Hz and $\beta = 10^{16}$ per joule.

RATE MONITOR SIGNAL CONDITIONING AND DATA ACQUISITION

Initially, to acquire data with the particle rate monitor system, a zero-crossing detector (ZCD) was used to compare the instantaneous PMT signal voltage to a fixed-reference voltage; the ZCD outputted a level change when the two voltages became equal. ZCD output level changes were electronically counted over fixed time intervals to produce rate monitor data. A commercially available, IEEE-488 bus-compatible, electronic counter operating in an event-counting mode was employed. However this initial system was not satisfactory as it produced inconsistent data.

The cause of the data inconsistency was due to two undesirable character-
istics in the PMT detector output signal. These were (1) included broadband
electrical noise attributable in part to the moderate signal-to-noise ratio of
the detected optical signal (quantum noise) and in part to the included elec-
trical noise induced by the nearby 5-MW arc heater (generating the facility
flow) and (2) the problem of window contamination buildup, which resulted in
attenuation of the signal beam and a slow decrease of the mean signal level de-
tected during a run. It was necessary that both problems be compensated for in
order to extract optimum usable information.

The tunnel windows, which provided optical access to the test cell, slowly
became contaminated during the run. The rate of this contamination was not
necessarily constant, resulting in a detected beam power that continually de-
creased in an unpredictable manner, often to only 25 percent or so of the
original pre-run values. Since the events to be detected were also character-
ized by a partial beam blockage and a corresponding detection level change,
some means to discriminate between the two events had to be developed. A char-
acteristic of the events that differed significantly between the two was the
relative time duration of each, the drop in signal caused by a particle block-
age occurring over a much shorter time than the gradual attenuation of the sig-
nal attributable to window contamination. A circuit was therefore developed to
supply to the ZCD a varying threshold or reference voltage equal in amplitude
to a percentage (corresponding to beam blockage by a spherical particle of a
given size or larger) of the time-averaged, low-pass-filtered signal level.
This effectively caused the attenuation of the beam caused by window contamina-
tion to be invisible to the ZCD's.

The other undesirable characteristic, that of a moderate level of broad-
band noise on the signal attributable chiefly to the low optical power of the
signal beam in the early prototype RM system, was dealt with by employing lens
L1 of Figure 13 and by adding variable hysteresis to the ZCD circuitry. The
relative amount of hysteresis, again as a percentage of the variable low-pass-
filtered PMT signal level, was selectable by setting two 10-turn potentiom-
eters.

The data acquisition system for the particle rate monitor consisted of a
graphic microcomputer system and two electronic counters operated in an event-
counting mode, interconnected by an IEEE-488 bus. One counter was connected to
the signal-conditioning electronics and maintained a running total of valid
events (particles blocking a predetermined percentage of the beam). The second
counter had as its input a 10-MHz clock and functioned as a time reference.
The microcomputer read the contents of both counters approximately four times
per second and stored the information on magnetic tape.

Typical rate monitor data is shown in Figure 9. Note that the dust was
turned on and off periodically during a run as different models were injected
into the test region. The RM data showing large fluctuations in dust rate from
model to model have correlated well with net model erosion measurements taken
after a run.

APPENDICES

A. Thermal Emission and TEV Signal

The characteristics of the thermal radiation emitted by a blackbody will be briefly outlined. The results will be applied in a subsequent section to define the thermal signal and thermal noise components.

Thermally emitted blackbody radiation is characterized by a Lambertian or cosine distribution of power versus angle between the radiation direction and the surface normal, i.e.,

$$N_\lambda' = N_\lambda \cos \beta \tag{5}$$

where β is the angle between the radiation N_λ' and the surface normal. N_λ (power $\cdot$ area^{-1} $\cdot$ wavelength^{-1} $\cdot$ solid angle^{-1}, or W $\cdot$ m^{-3} $\cdot$ sr^{-1}) is the monochromatic thermal radiation intensity in the normal direction, given by Planck's law

$$N_\lambda = C_1 \lambda^{-5} \left(\exp \frac{C_2}{\lambda T} - 1 \right)^{-1} \tag{6}$$

where T ($^\circ$K) is the absolute temperature, λ (cm) the monochromatic wavelength, $C_1 = 1.190 \times 10^{-12}$ watt $\cdot$ cm^2, and $C_2 = 1.439$ cm $\cdot$ $^\circ$K. Equation (6) is plotted in Figure 10.

With the aid of Equation (5) it can be shown that a small radiating elemental area observed at an oblique angle β is equivalent to a reduced (by a factor cos β) projected area emitting along its surface normal. Therefore, for example, a small spherical blackbody (for example, a TEV thermal particle) will radiate as if it were a blackbody disk of the same diameter as the sphere and with the normal-to-the-disk surface parallel to the observation direction.

For a particle in the high radiation-collection-efficiency region of a probe volume (see Appendix B), the thermal signal power incident on the detector is given by, assuming $D_p \lesssim D_v$ (see Figure 11),

$$P_p = \Omega_c A_p \int_0^\infty \alpha_p N_\lambda(T_p) \, d\lambda \cong \Omega_c A_p \int_{\lambda_1}^{\lambda_2} \alpha_p N_\lambda(T_p) \, d\lambda \cong \Omega_c A_p \bar{\alpha}_p \bar{N}_\lambda(T_p) \Delta\lambda \tag{7}$$

where $\Omega_c \cong \pi \theta_c^2/4$ is the solid collection angle of the detector optics, A_p is the cross-section or projected area of radiation of the particle ($A_p = \pi D_p^2/4$ for a spherical particle), α_p is the particle emissivity, $N_\lambda(T_p)$ is the particle monochromatic thermal radiation intensity in the normal direction, λ_1 and λ_2 ($\lambda_2 > \lambda_1$) are the wavelengths at which the overall detection efficiency (or product of detector quantum efficiency and optical system transmission coefficient) of the TEV drops below 50 percent, $\Delta\lambda = \lambda_2 - \lambda_1$, and the raised bar notation denotes average value over the wavelength interval $\Delta\lambda = \lambda_2 - \lambda_1$.

B. Radiation Collection Efficiency

The purpose of this appendix is to review, very briefly, the radiation-collection efficiency of an imaging lens pair followed by a circular transmission aperture such as a fiber-optic component. More thorough reviews can be found elsewhere.

The optical system to be discussed is shown in Figure 11. A pair of positive lenses, of the achromatic point source collimating type, will be used to represent a simple form of a general type of high spatial resolution, achromatic, imaging system. Assume that points 1, 2, 3, and 4 to the right of the imaging lenses are point sources of light; these will image then to points 1´, 2´, 3´, and 4´ to the left of the lenses such that all (of the infinity of) rays from point 2, for example, that intercept the aperture of lens L1 will be directed by the lenses to pass through point 2´. Ray traces such as these can be employed to show the following: (1) that points within the shaded region 1, 2, 3, 4 image to points within the shaded region 1´, 2´, 3´, 4´ such that the former region is a region of high (point source) radiation-collection efficiency, so high in fact that all rays from a point within this region that also intercept the aperture of lens L1, will pass through aperture A´ and be collected; (2) any ray, directed from right to left, that is in-line with the (virtual hole in the) virtual aperture A and the aperture of lens L1, will be redirected by the lenses to pass through the real aperture A´ and be collected; any right-to-left ray that does not meet these criterion will intercept the opaque (non-hole) portion of aperture A´ and therefore will not be collected.

A thorough comprehension of these statements, in conjunction with elementary ray-tracing techniques, will permit one to compute surfaces of constant radiation-collection efficiency for the region to the right of the lenses. A quadrant of such a contour diagram is illustrated in Figure 12 for the case of circular (x-axis symmetric) optical components and assuming $s_v \gg D_\ell \gg D_v$, which is typical of many geometries. For $s_v \gg D_\ell \gg D_v$ the contour plot is symmetric also about the z-axis, and therefore all four quadrants would plot identically. The coordinates of Figure 12 are normalized such that

$$x^{\sim} = \frac{D_\ell}{D_v s_v} \ x \quad \text{and} \quad z^{\sim} = \frac{2}{D_v} \ z \tag{8}$$

The relative radiation collection efficiency, $\Omega_c^{'}$, plotted in Figure 12 is related to the actual effective radiation-collection solid angle, Ω_c, by

$$\Omega_c^{'} = \frac{4 \ s_v^2}{\pi D_\ell^2} \Omega_c \tag{9}$$

again assuming $s_v \gg D_\ell \gg D_v$.

C. Inherent Signal-to-Noise Ratio (SNR)

Because of the statistical nature of the number of photons detected during the passage of a thermal particle through a TEV probe volume, for example, the TEV signal amplitude is inherently uncertain and noisy. The relative magnitude of such inherent noise will now be discussed.

For the TEV, the photon flux impinging on the PMT photocathode originates from a thermal broadband source and the photons can be assumed to be emitted at random time intervals. Under such conditions the probability that n photons will strike the photocathode in a time interval τ is given by a Poisson distribution as follows:[7]

$$P_{(n,\tau)} = \frac{(\overset{o}{N}_{ph} \tau)^n}{n!} \exp(-\overset{o}{N}_{ph} \tau) \tag{10}$$

where $\overset{o}{N}_{ph}$ is the average photon-arrival rate. The average value for n and the variance in n, σ^2_{ph}, can be obtained directly from $P(n,\tau)$ as:[7]

$$\overline{n} = \overset{o}{N}_{ph} \tau \tag{11}$$

$$\sigma^2_{ph} = \overset{o}{N}_{ph} \tau = \overline{n} \tag{12}$$

The inherent photon flux signal-to-noise ratio, $\overline{n}/\sigma_{ph}$, is given by

$$SNR_{ph} = (\overset{o}{N}_{ph} \tau)^{\frac{1}{2}} \tag{13}$$

and the inherent cathode photoelectron SNR for a single TEV particle pulse is given by

$$SNR = (\eta \overset{o}{N}_{ph} \tau)^{\frac{1}{2}} = \left[\beta N_\lambda(T_p) \alpha_p A_p \Omega_c \Delta\lambda (D_p + D_v) v_p^{-1} \right]^{\frac{1}{2}} \tag{14}$$

where η (dimensionless) is the photocathode quantum efficiency, $N_\lambda(T_p)$ ($W \cdot m^{-3} \cdot sr^{-1}$) is the monochromatic blackbody radiation intensity discussed in Appendix A, A_p (m^{-2}) is the particle cross-section or projected area of radiation ($A_p = \pi D_p^2/4$ for a spherical particle), Ω_c (sr) is the solid collection angle, $\Delta\lambda$ (m) is the spectral detection bandwidth of the optics and detector, and $\tau = (D_p + D_v) v_p^{-1}$ is the time duration of the TEV signal pulse for a particle of diameter D_p and velocity v_p passing through a high detectivity probe volume region of diameter D_v.

The amplification or multiplication of the cathode photoelectron current in the PMT dynode chain is essentially noise-free. The use of high-gain PMT in conjunction with a low-pass filter of bandwidth $\tau^{-1} = (D_p + D_v)^{-1} v_p$ and a low-noise amplifier (if necessary)[†] ensures that the cathode photoelectron SNR is preserved to within a factor of two at the filter (or amplifier) output.[7] During the occurrence of the signal pulse (with the particle approximately centered in the probe volume for SNR >> 1) the filter (or amplifier) output voltage level will achieve a mean peak value and an average variance of the peak that provide a voltage ratio SNR that is within a factor of two of the

---

[†]A signal amplifier is usually necessary with low photoelectron SNR (SNR < 10) depending on the input voltage level requirements of the signal processor.

charge ratio SNR that appeared in the PMT cathode and plate electron currents. Thus, the quantum nature of the photon flux from a detected TEV particle causes an inherent photon flux SNR; this SNR is then reduced by a factor $\eta \, v$, on photodetection and then approximately preserved through the electron multiplication, electronic amplification, and low-pass-filtering processes.

D. Particle Rate Monitor Optics

The particle rate monitor optical system that generated and detected the cone beam is shown in Figure 13. A 0.005-w helium-neon laser source (S) of 0.6328-μm wavelength, emitted a TEM_{00}, approxim ely collimated, continuous-wave laser beam of nominally 0.6-mm diameter. The laser illuminated, by way of lens L1, a piece of light-diffusing tape, D. The diffusing tape was Scotch®† tape No. 810, the commonly used office type that could be written upon. The tape scattered and absorbed all of the incident light with approximately 0.4 percent (20 μw) scattered into a principal low-divergence, forward-scatter cone of approximately $\theta = 0.2$-radian divergence angle. This then intercepted a 100-μm diameter, centered circular aperture A1. It should be noted that the lens L1 focused the gaussian laser beam to a spot diameter that was smaller than the aperture A1 (to the focus point 2 of Figure 13), and that the distance between L1 and the diffuser-aperture (D-A1) combination was varied so that the aperture diameter was fully illuminated with approximately 40 percent of the power scattered forward in the principal lobe intercepting the aperture A1. The aperture A1, in conjunction with the very closely located diffuser tape D, effectively created a disk of point sources that was imaged by way of lens L2 and aperture A2 (which controlled the cone convergence-divergence angle), out into the test section to a 500-micron disk (of focused or imaged point sources). Lens L3 reimaged the cone beam onto a photomultiplier tube. Aperture A3 and the laser line (spectral) filter LLF were employed to reject radiation from test cell camera lights.

REFERENCES

1. Belz, R. A. and Menzel, R. W. "Particle Field Holography at Arnold Engineering Development Center," Optical Engineering, Vol. 18, No. 3, May-June 1979.

2. Brayton, D. B. "Velocimetry of Hot Particles by Detection of Thermal Emission," presented at the 25th International Instrumentation Symposium on Aerospace Test Measurements, sponsored by the Instrument Society of America, May 7-10, 1979. (Paper did not appear in the published proceedings; however, copies were made available to conference attendees).

3. Trolinger, J. D. and Belz, R. A. "Holography in Dust Erosion Facilities," AEDC-TR-73-160 (AD766420), September 1973.

4. Cline, V. A., Jr. "Dust Particle Velocity Measurements Using a Laser Velocimeter," AEDC-TR-72-159 (AD752225), December 1972.

5. Bentley, H. T., III "Fiber Optics Particle Sizing System," AEDC-TR-73-111 (AD766647), September 1973.

---

†Registered trade mark of the Minnesota Mining and Manufacturing Co.

6. Lewis, H. F., et al., "Description and Calibration Results of the AEDC Dust Erosion Tunnel," AEDC-TR-73-74 (AD910291L), May 1973.

7. Photomultiplier Manual, Theory, Design, Application, Technical Series PT-61, RCA Corporation, Harrison, N. J. 07029, September 1970, p. 56-76.
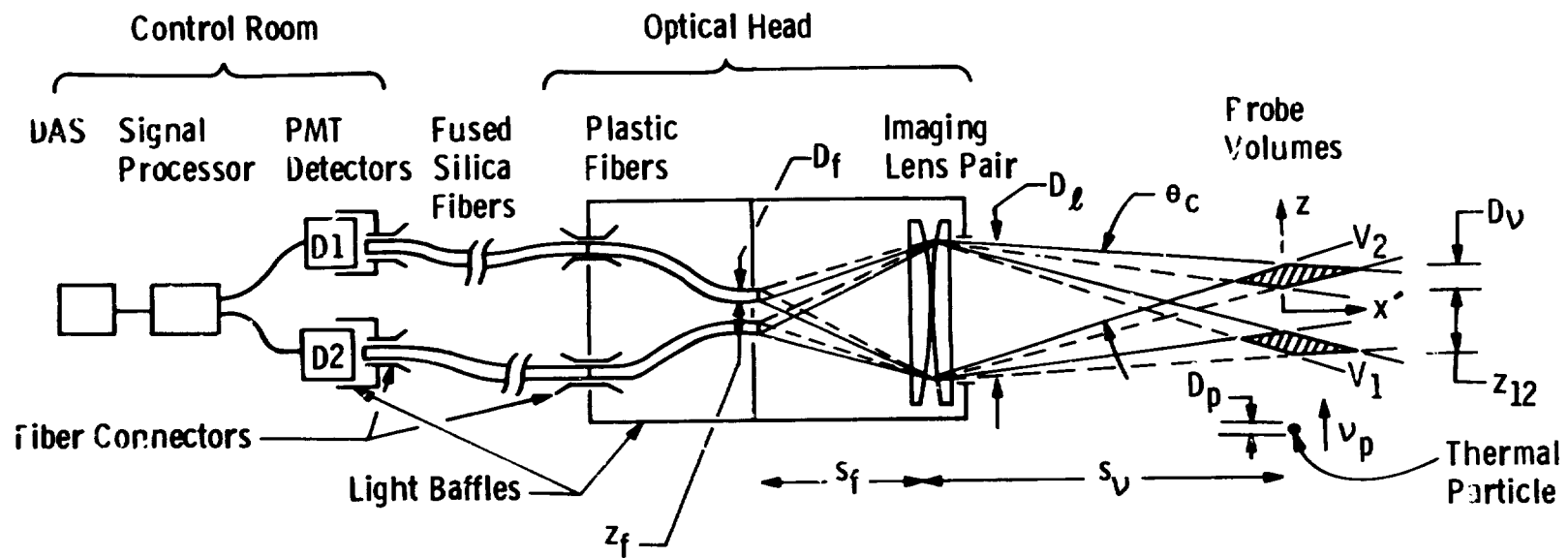
Control Room

Optical Head

DAS Signal PMT Fused Plastic Imaging Probe
Processor Detectors Silica Fibers Lens Pair Volumes
Fibers

D_f

D_ℓ

θ_c

z

D_ν

V_2

x'

V_1

z_{12}

D1

D2

D_p

ν_p

Fiber Connectors

Light Baffles

z_f

S_f

S_ν

Thermal
Particle

Figure 1. Thermal Emission Velocimeter
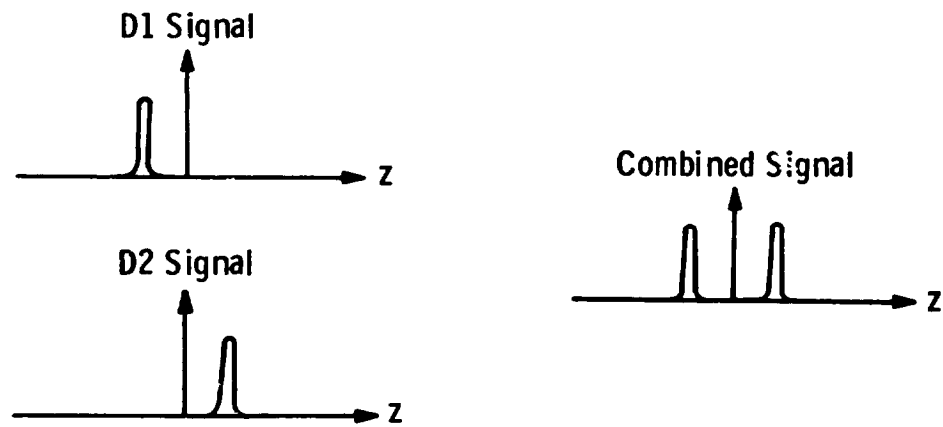
D1 Signal

D2 Signal

Combined Signal

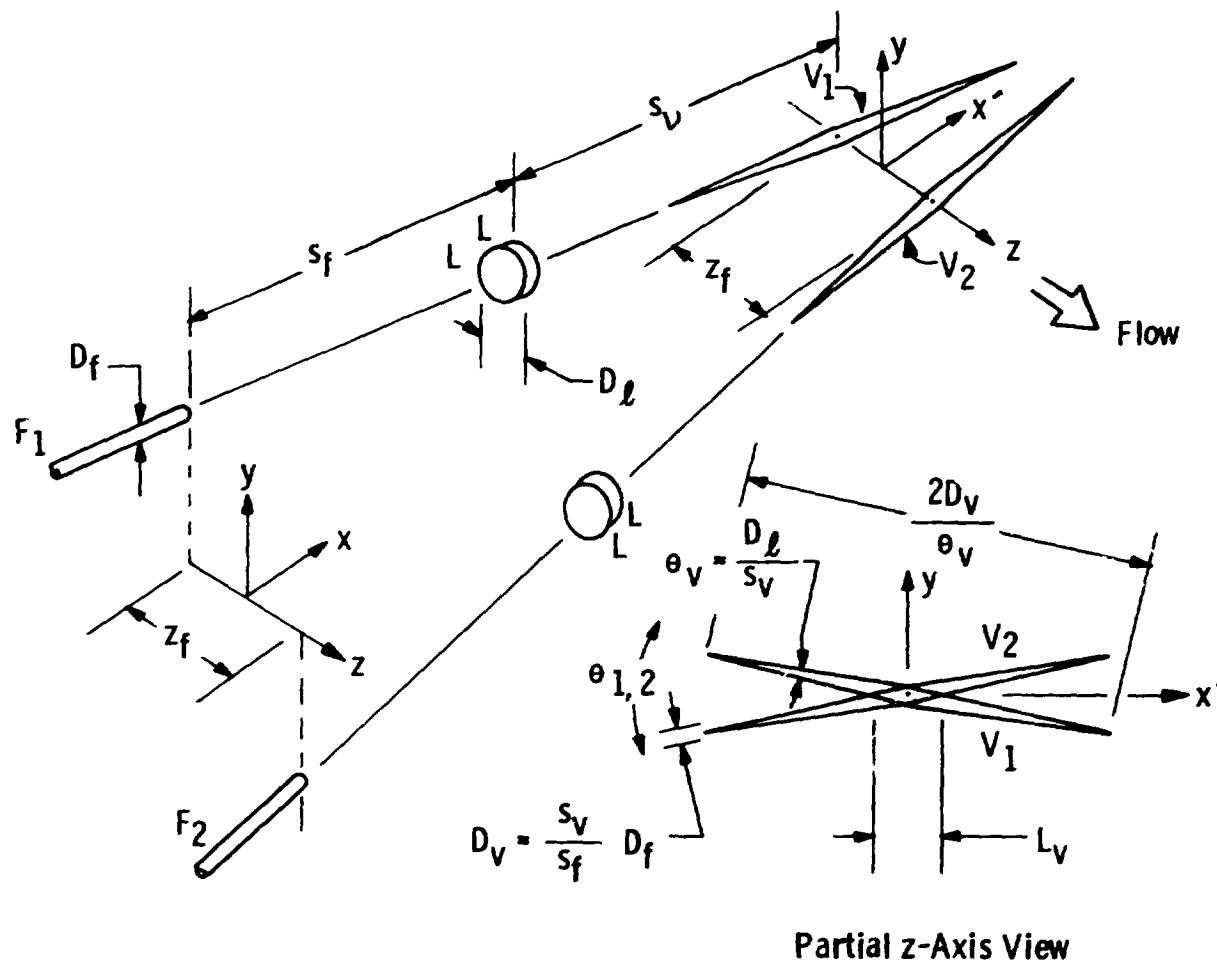Figure 2.   Detected Signal Amplitudes versus Particle Position

Figure 3. TEV Geometry Configured for Small Probe Volume
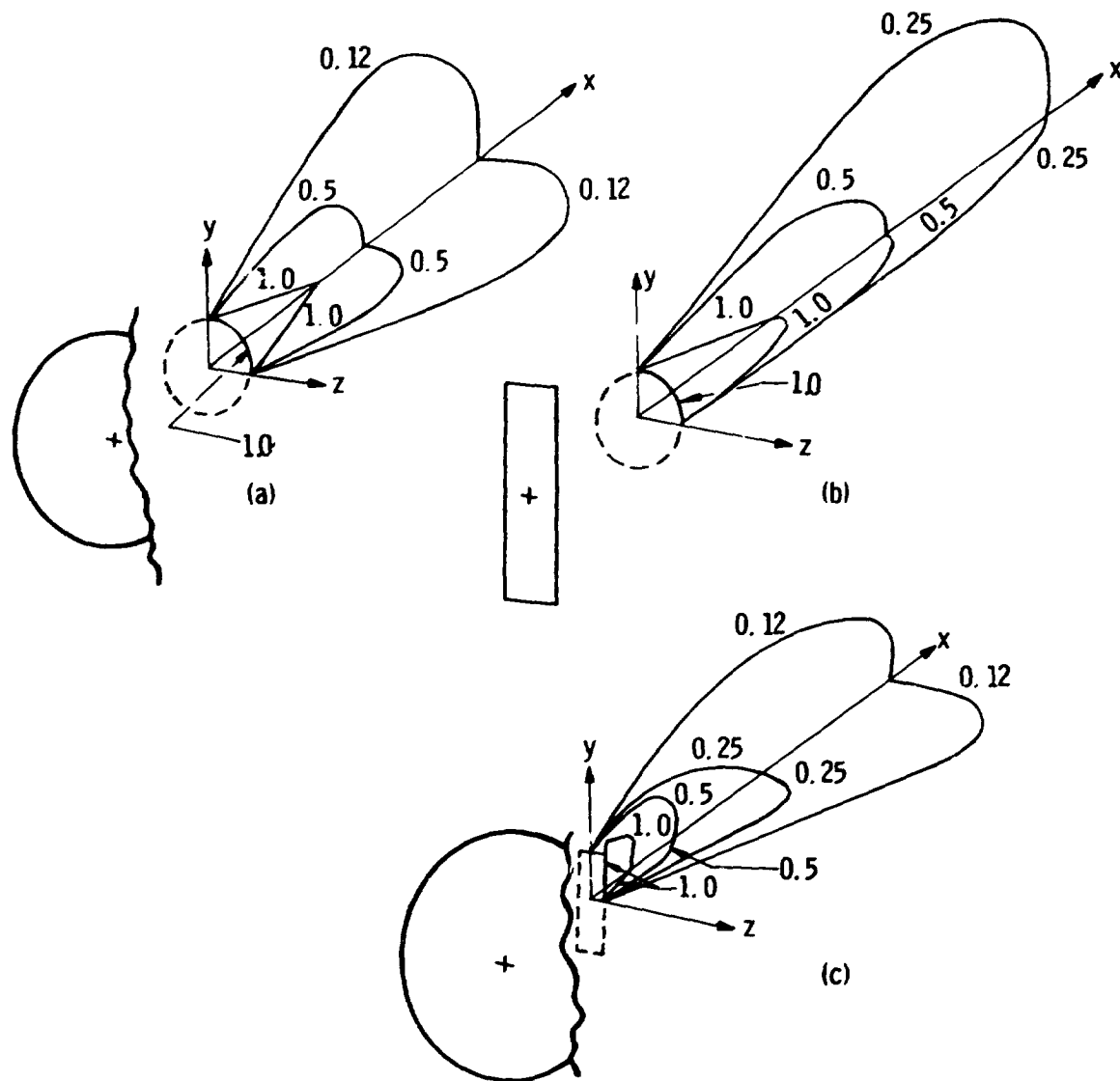Length and Minimal Systematic Measurement Error

Figure 4. Approximate Radiation Collection Efficiency Contour
Plots for Three Different Geometries of Collecting
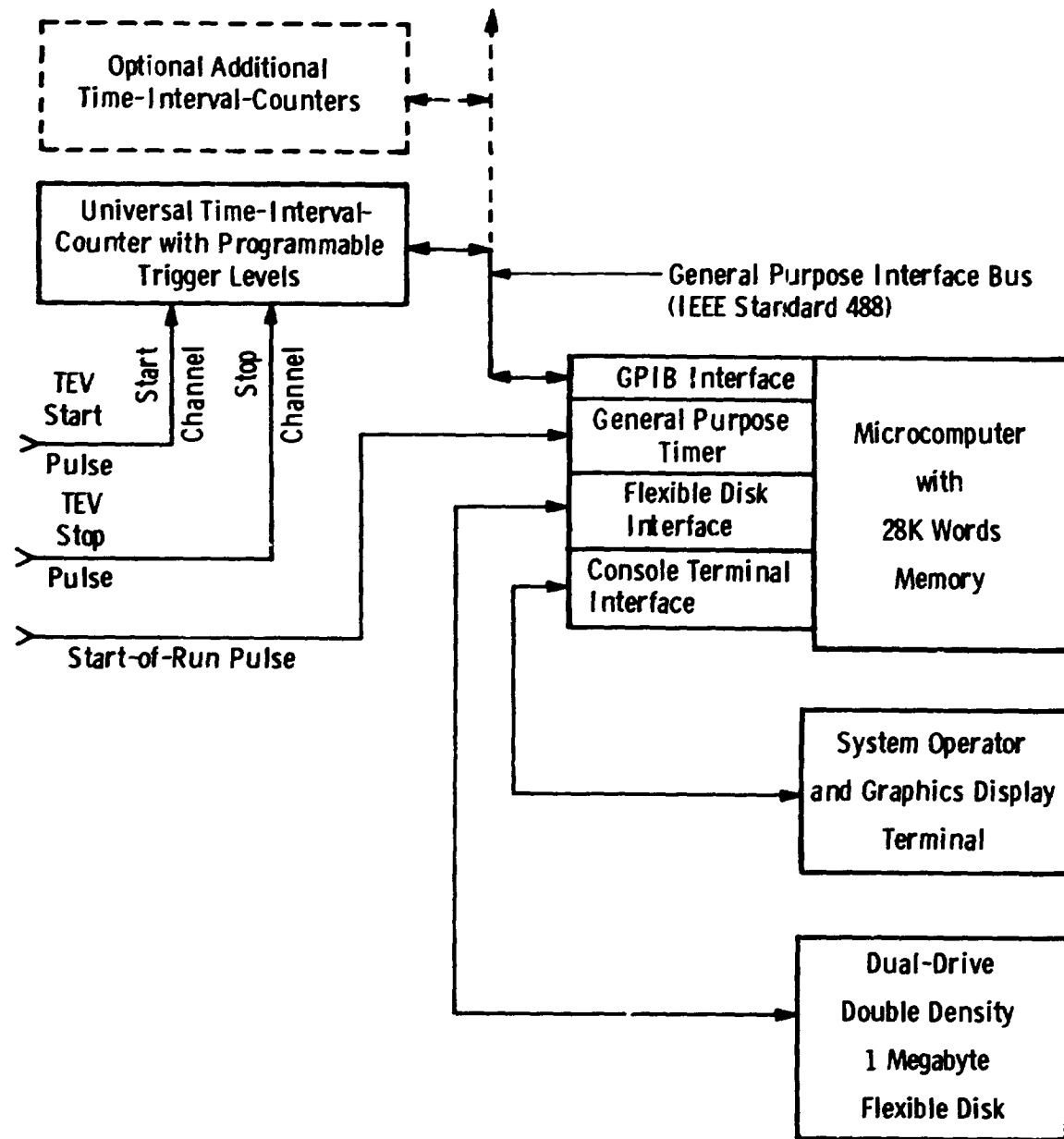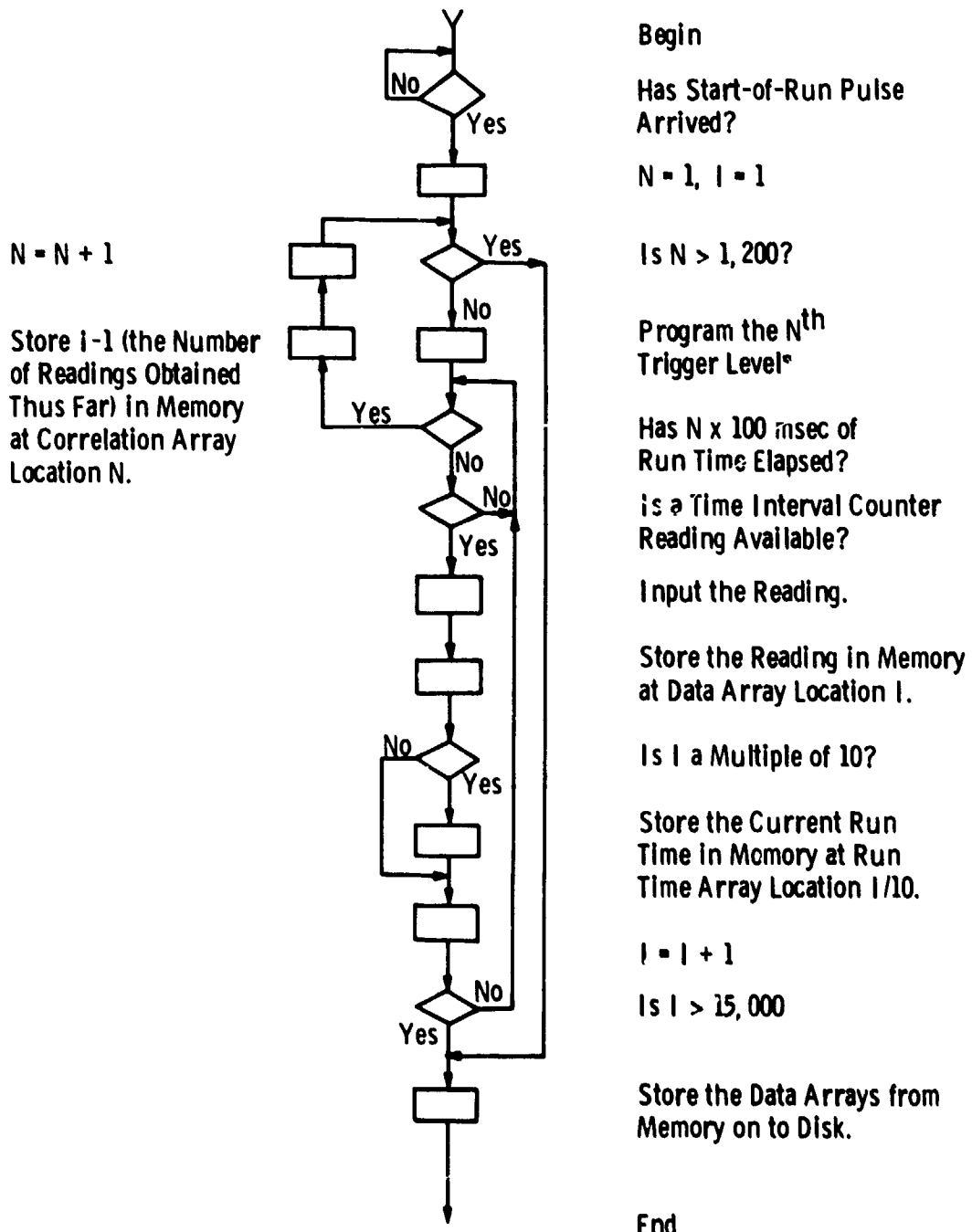Lens Aperture and Virtual Aperture

Figure 5. Data Acquisition System

Begin

Has Start-of-Run Pulse
Arrived?

N = 1, I = 1

N = N + 1

Is N > 1,200?

Store i-1 (the Number
of Readings Obtained
Thus Far) in Memory
at Correlation Array
Location N.

Program the Nth
Trigger Level*

Has N x 100 msec of
Run Time Elapsed?

is a Time Interval Counter
Reading Available?

Input the Reading.

Store the Reading in Memory
at Data Array Location I.

Is I a Multiple of 10?

Store the Current Run
Time in Memory at Run
Time Array Location I/10.

I = I + 1

Is I > 15,000

Store the Data Arrays from
Memory on to Disk.

End

*Trigger Levels Repeat in Cycles of 7.

Figure 6.   TEV Data Acquisition Program Flow Chart

370
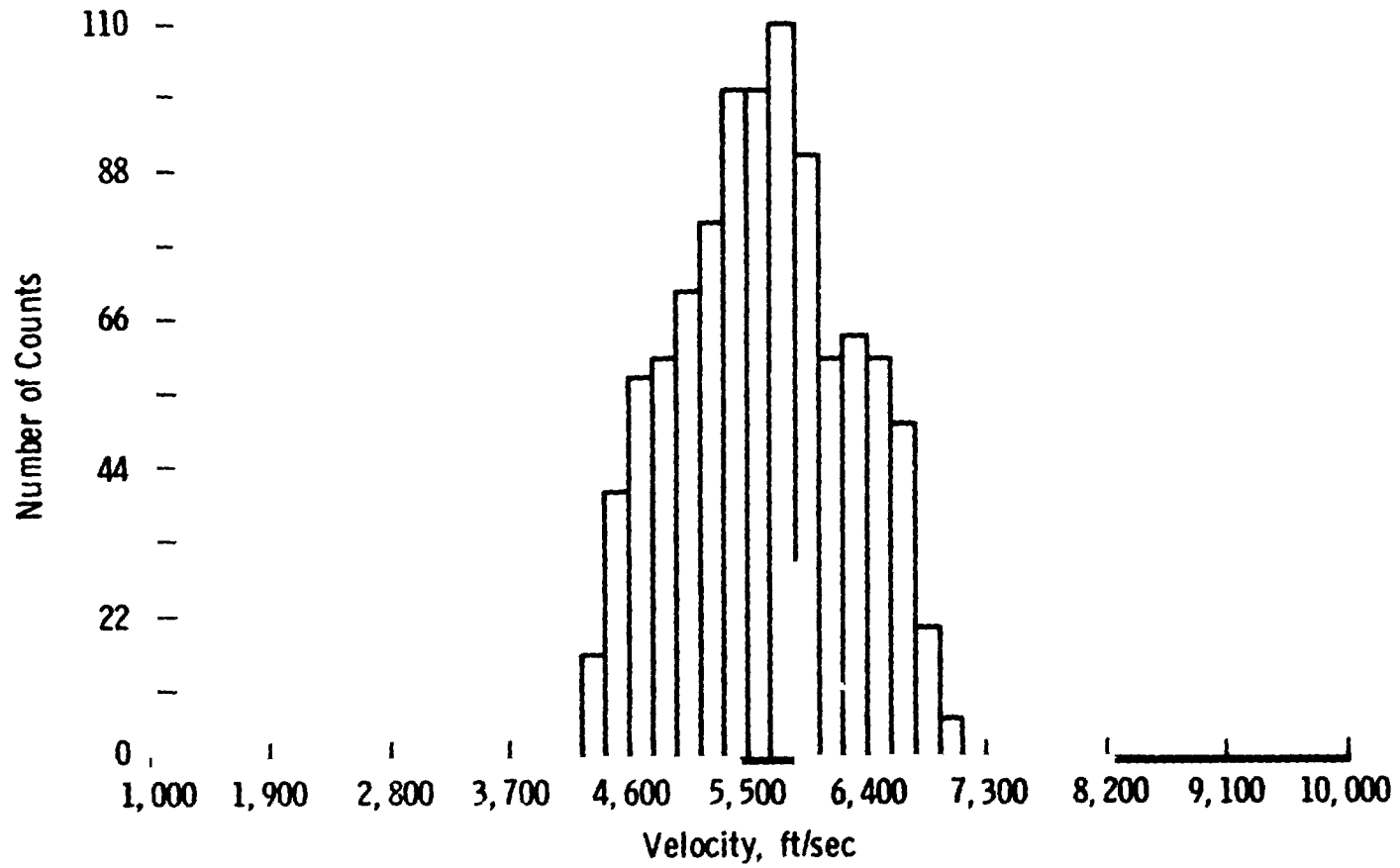
Figure 7. Typical TEV Data

Flow

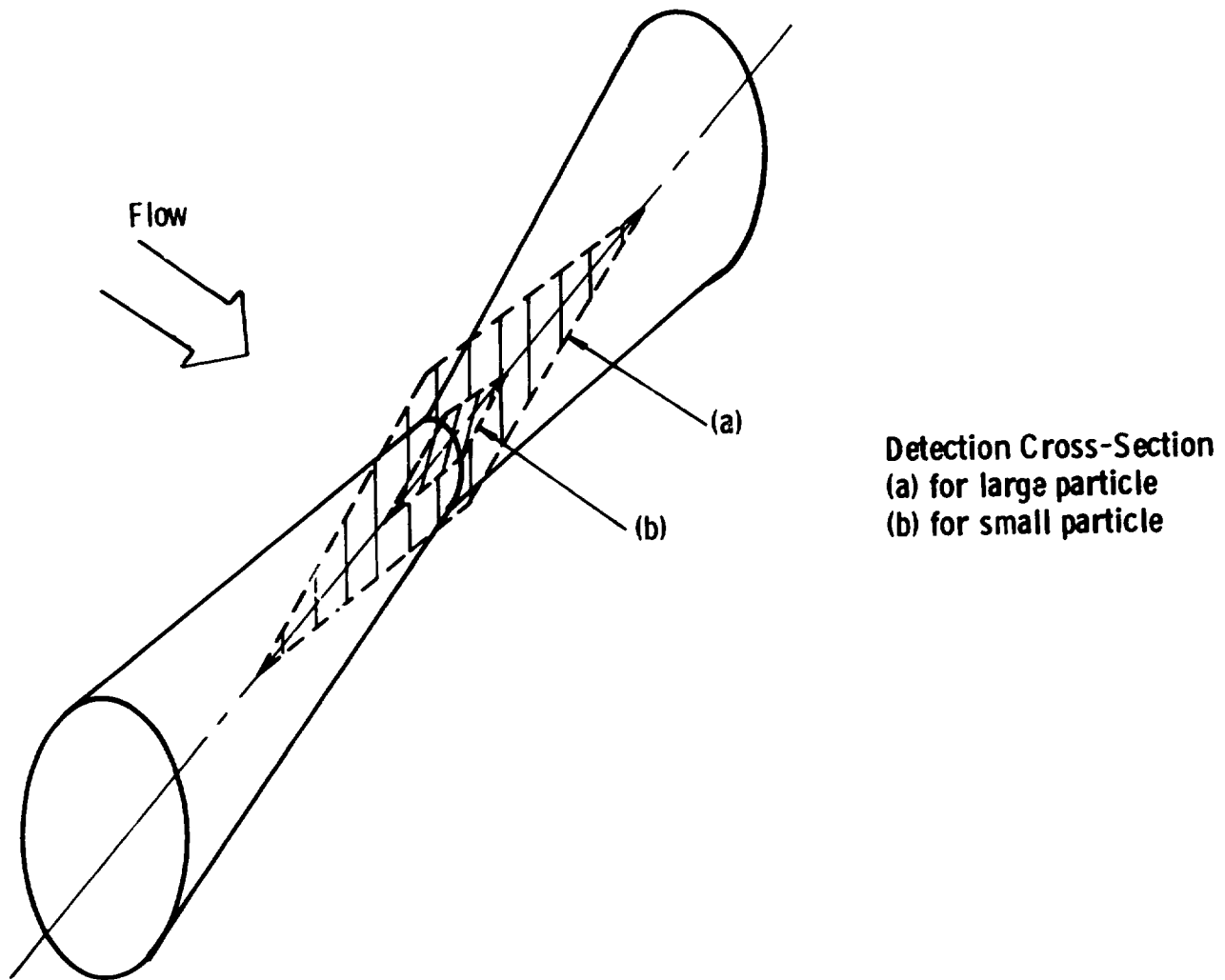Detection Cross-Section
(a) for large particle
(b) for small particle

Figure 8. Particle Rate Monitor Beam
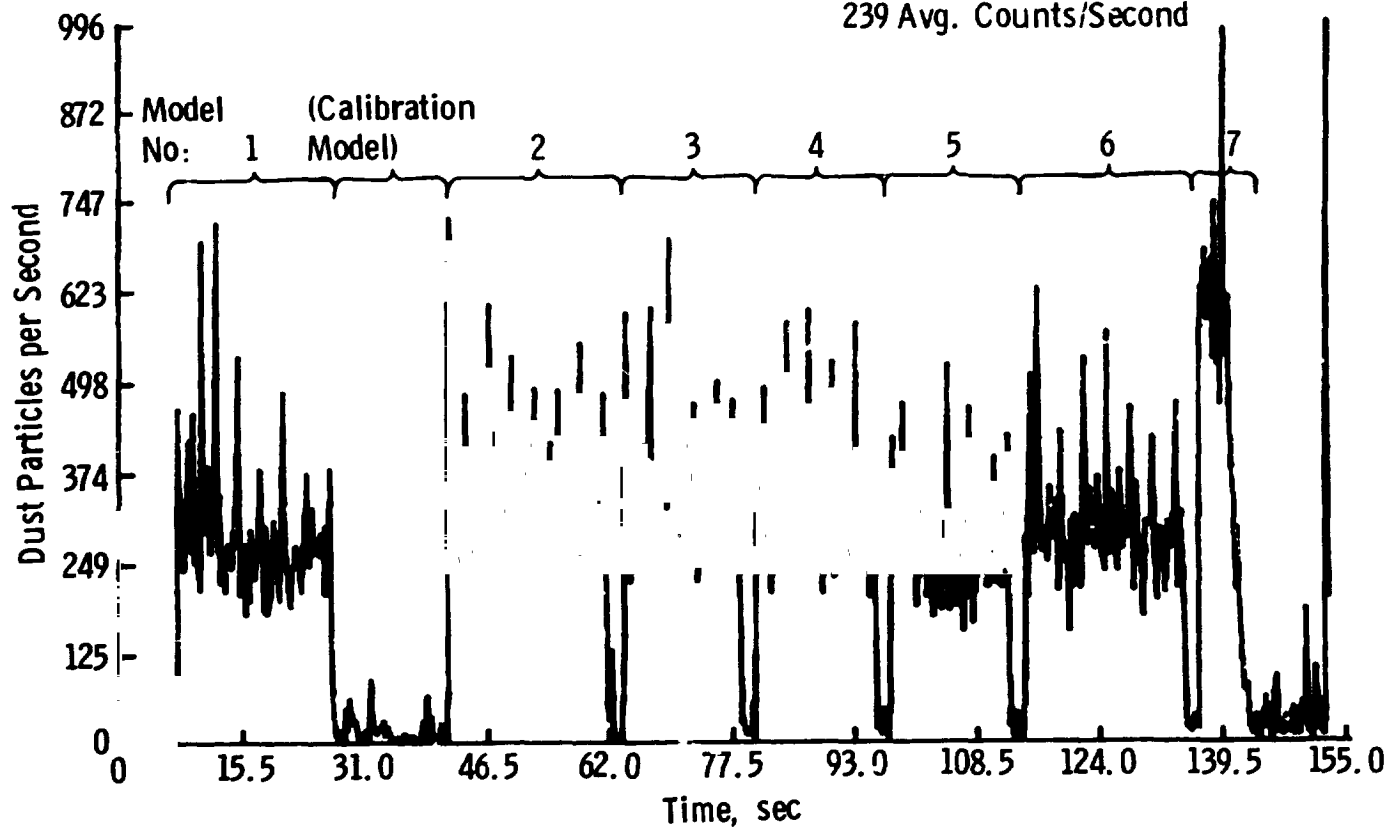
Figure 9. Typical Rate Monitor Data
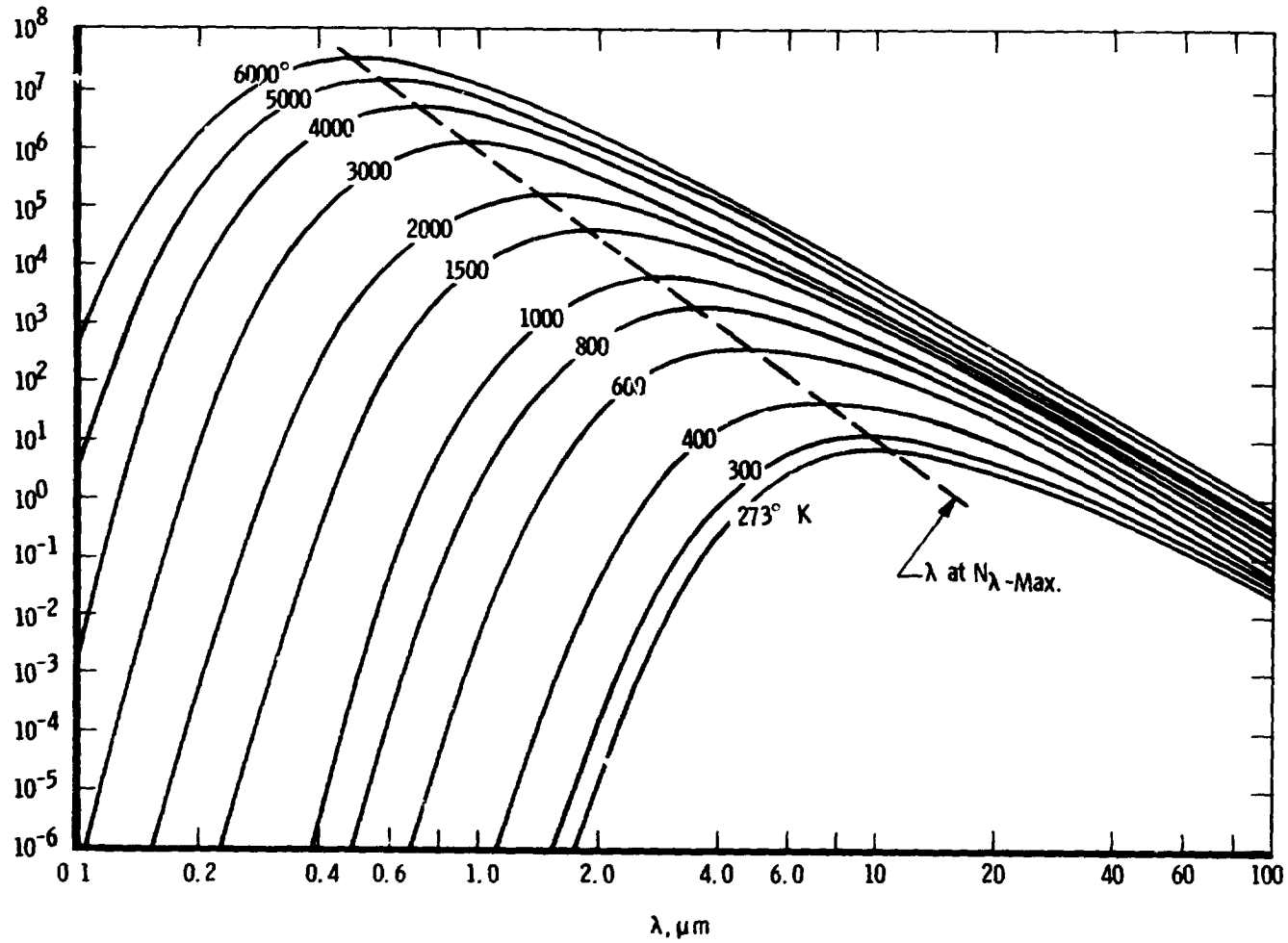
Figure 10. Normal Component of Spectral Radiant Intensity,
N_λ, (watt·m^{-2}·sr^{-1}·µm^{-1}) for a Blackbody as a
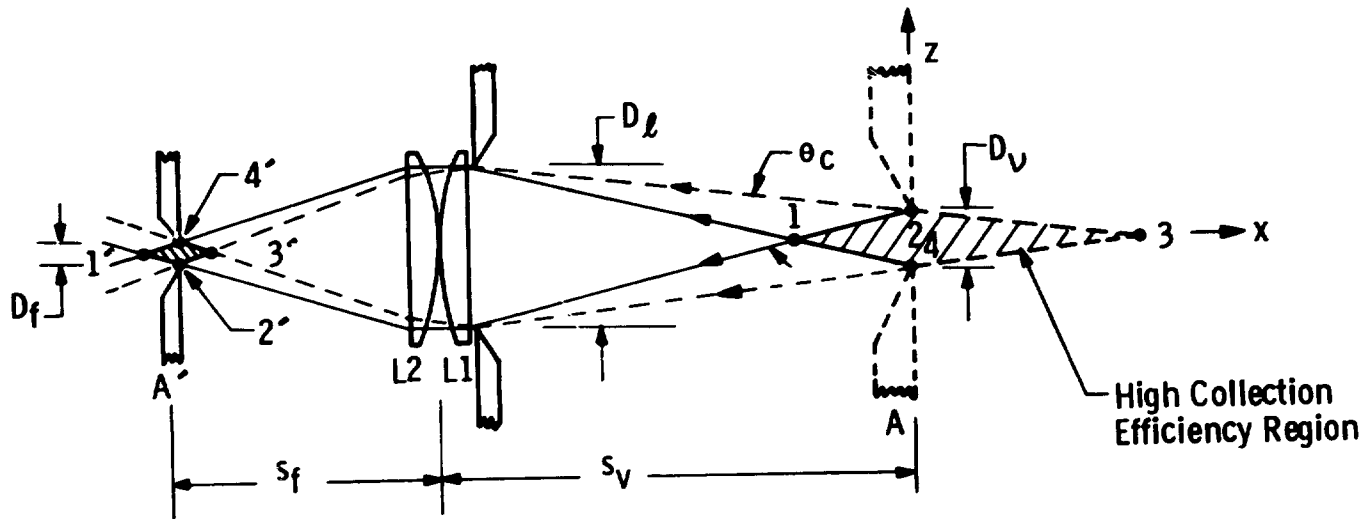Function of Temperature and Wavelength

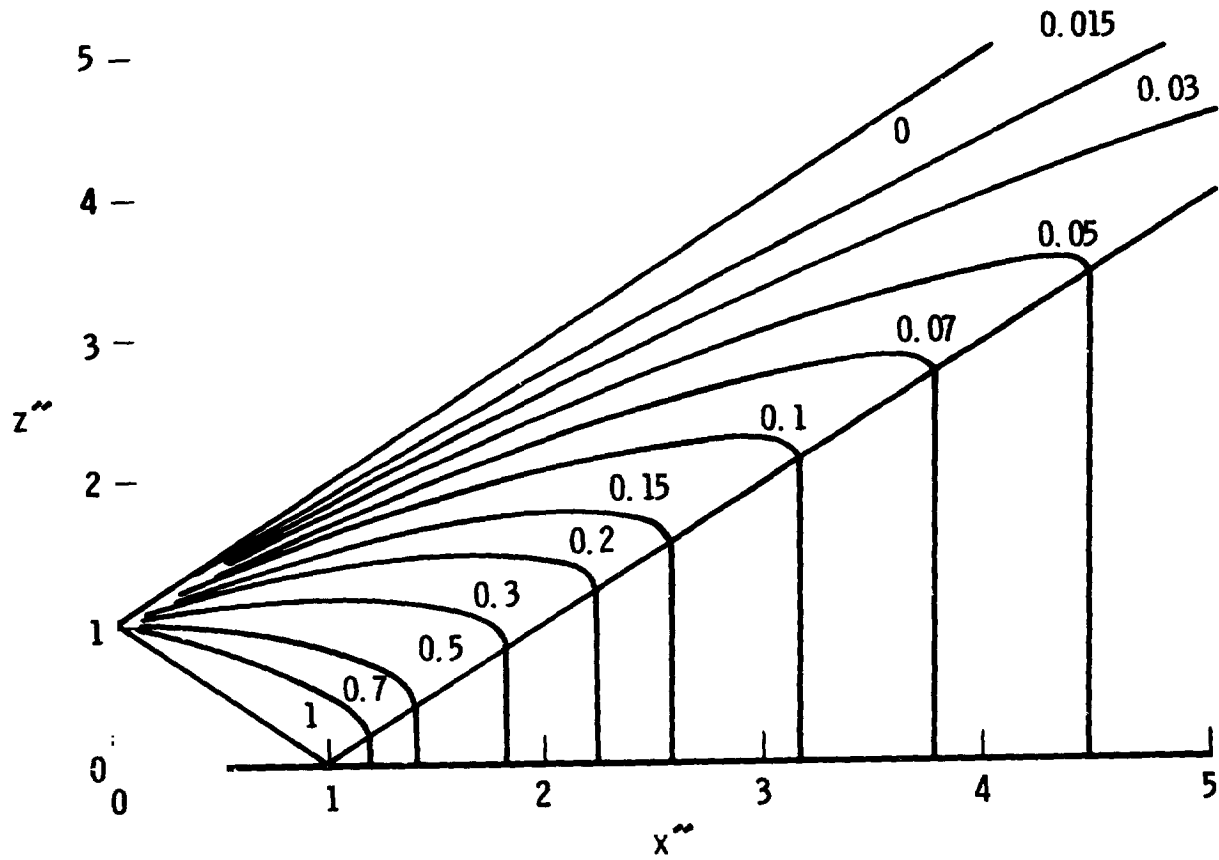Figure 11. Aperture Lens-Pair Radiation Collection Diagram

Figure 12. Contour Plot of Relative Radiation Collection
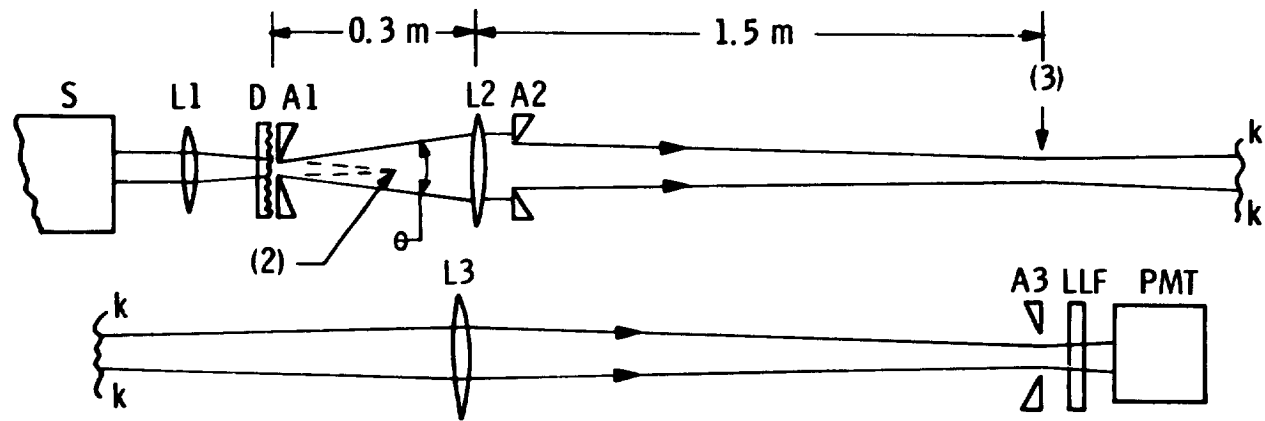Efficiency for the Optical System of Figure 9

376

Figure 13. Particle Rate Monitor Optics

THERMAL STRESS RESPONSE OF GENERAL PURPOSE
HEAT SOURCE (GPHS) AEROSHELL MATERIAL

I. M. Grinberg*, L. E. Hulbert*,
and R. G. Luce*

ABSTRACT

A thermal stress test was conducted to determine the ability of the GPHS aeroshell 3-D FWPF material to maintain physical integrity when exposed to a severe heat flux such as would occur from prompt reentry of GPHS modules. The test was performed in the Giant Planetary Facility at NASA's Ames Research Center. Good agreement was obtained between the theor. .cal and experimental results for both temperature and strain time histories. No physical damage was observed in the test specimen. These results provide initial corroboration both of the analysis techniques used and that the GPHS reentry member will survive the reentry thermal stress levels expectrd.

INTRODUCTION

The General Purpose Heat Source (GPHS) is a radioisotope-fueled heat source to be used to provide electric power for the International Solar Polar Mission (ISPM) - Radioisotope Thermoelectric Generator (RTG). Modular in design, the GPHS consists of a series of modules stacked in sufficient quantity to meet the converter power requirements. Each heat source module contains four 62.5 W (thermal) PuO_2 fuel pellets and is rectangular parallelepiped in shape, as shown in the Figure 1 schematic.

The generator is designed to break apart during reentry into the earth's atmosphere, either following end-of-life or from a launch abort, exposing the stacked heat source modules to the environment. In turn, the stacked modules will separate due to aerodynamic forces such that the individual heat source modules will reenter the earth's environment. Release of the fuel during reentry and at earth impact is prevented by a combination of metal post-impact shell, carbon-based impact shell, and 3-D fine weave pierced fabric (FWPF) carbon-carbon aeroshell, and specific design characteristics selected on the basis of tests and analyses.

An accurate prediction of the thermal stress response of the GPHS module aeroshell is an important aspect of the overall heat source design. Many factors must be accurately accounted for in the analysis of material response, including material properties, heat flux distribution, and design features. Unfortunately, there is no adequate criterion available to predict the thermal stress failure of 3-D carbon-car' .n, and relatively little experience and data base have been developed for the thermal stress resistance of the FWPF C/L

---

* Battelle, Columbus Laboratories, Columbus, Ohio.

material in accident environments that could result from applications of the GPHS. Thus, a meaningful comparison of thermal stress predictions with experimental data cannot be made without the generation of new data for the specific material of interest.

To overcome this lack of experience, a thermal stress test was designed and conducted on 3-D FWPF C/C to determine the ability of the aeroshell material to maintain physical and mechanical integrity when exposed to a severe heat flux environment such as would occur from prompt (steep angle) reentry of GPHS modules. Thermal and thermal stress analyses were performed to design the test model, select instrumentation, and determine the required environmental test conditions. The thermal stress test was conducted in the Giant Planetary Facility (GPF) at NASA's Ames Research Center (ARC).

ENVIRONMENTAL CONDITIONS

Reentry Environment

Test conditions were selected based on duplicating the peak tensile stress and strain levels in the GPHS module aeroshell that would result from prompt reentry of the GPHS modules. Initial conditions for this trajectory are reentry angle -89.9 degrees at an altitude of 121.9 km (400 kft) with a corresponding velocity of 10.97 kmps (36 kfps). Breakup of the generator and separation of the heat source modules are assumed to occur at 61 km (200 kft), an altitude sufficiently high to provide the peak aeroheating that would occur on this trajectory.

Reentry heating and pressure histories, along with freestream Reynolds number and Mach number histories, are shown in Figure 2 as a function of altitude. The stagnation point heating rate has been normalized to a 2.54 cm (1 in.) radius hemisphere. Reentry parameters for broad face stable and side face stable hypersonic modes are shown in Figure 2. The maximum aeroheating rate expected for the heat source module for this trajectory is approximately 47.7 MW/m^2 (4200 Btu/ft^2-sec) for the side on stable reentry mode.

Test Facility Selection

The NASA Ames 70 MW Giant Planetary Facility (GPF) was selected for the thermal stress test because this facility can provide the desired heating rates and can readily accommodate the test model configuration and size anticipated.

The arc heater in the GPF is capable of operating at a maximum electrical power input of 70 MW. A mixture of hydrogen and helium or hydrogen and nitrogen is used as the test gas. The nozzle used has a circular cross-section geometry and an exit diameter of 6.99 cm (2-3/4 in.). Based on previous thermal stress test experience with this nozzle, a flat faced, right circular cylindrical geometry test specimen was designed, with maximum model dimensions not to exceed 4.128 cm (1-5/8 in.) diameter and 8.57 cm (3-3/8 in.) length. With this test model geometry and size, an electrical power input of approximately 25 to 30 MW is required to achieve a stagnation point heat transfer rate on the test

model corresponding to peak heating conditions for the GPHS module during prompt reentry (side on stable hypersonic mode).

THERMAL STRESS TEST MODEL DESIGN

The thermal stress test model design is shown in Figure 3. This design is based on analyses conducted to determine the heat transfer rate for selected test facility operating conditions and the thermal and thermal stress response of the material. The flat face cylinder-flare configuration is consistent with thermal stress test experience at NASA Ames, and the overall size of the test specimen can be easily accommodated within the GPF facility. The axisymmetric configuration provides for symmetric external and internal boundary conditions and facilitates the thermal and thermal stress analyses. The specific wall thickness, 0.51 cm (0.2 in.), was selected to yield peak tensile stress and strain levels on the inside flat face surface of the FWPF C/C identical to the peak values expected during prompt reentry of the heat source module for the side on stable mode.

The flat inner surface of the front face allows for the application of both a thermocouple and an extensometer for measuring the back face temperature and strain history of the specimen.

The cylindrical portion and the integral tapered skirt were machined from a single block of Avco FWPF C/C material with the Z-fiber direction parallel to the axis of symmetry as shown in Figure 3. From the nominal diameter of 4.128 cm (1-5/8 in.), a Teflon flare is used to increase the overall diameter of the model assembly to 7.62 cm (3 in.) in a total assembled length of 8.57 cm (3-3/8 in.). The size of the aft-cone flare was selected so that the instrumentation package could be fit into the model assembly. Teflon was used for the cone-flare section in order to electrically insulate the C/C test model from the model sting. Threaded phenolic pieces are used to join the Teflon flare section to the C/C test model and the model assembly to the steel sting. The phenolic also serves to electrically insulate the model assembly from the sting. A 1.27 cm (1/2-in.) diameter hole is provided through the phenolic pieces to house components of the strain measuring instrumentation and to serve as a passage for electrical instrumentation wires.

Figure 4 shows the major components of the thermal stress test model. Shown in Figure 4 is the FWPF flat-faced cylinder flare, the Teflon flare with the forward phenolic connector, and other components which are identified and discussed in the following paragraphs.

The extensometer and back face thermocouple instrumentation assemblies for the thermal stress test models were specially developed and built to fit in the test specimen. Figure 5 is a schematic of the instrumentation package which fits into the 1.27 cm diameter hole in the pheonlic threaded pieces previously shown in Figure 3.

The main support bar is approximately 1.27 cm diameter and 4.45 cm (1-3/4-in.) long. Holes were drilled into the main support bar to (1) attach the 0.32 cm (1/8-in.) diameter tungsten forks (center-line distance between forks is

0.64 cm [1/4 in.]), (2) accommodate the thermocouple spring and alumina tube (approximately 0.32 cm diameter hole), (3) run the thermocouple leads through the main support (0.16 cm [1/16-in.] diameter hole), and (4) run the strain gage leads through the main support bar (0.32 cm-diameter hole). An electrical terminal was fastened to the face of the main support bar using epoxy cement in order to make the strain gage connections. The main support assembly is held in position using a spring which maintains the forks and thermocouple in contact with the back face of the C/C model.

Flat spots were gound on the tungsten forks where the four strain gages (Micro-Measurement Company, Model No. WK-06-0628P-350) were bonded to the forks using BR-G10 high temperature (260 C [500 F]) cement. The strain gages were used to measure bending strains in the forks. The ends of the forks were ground to a point with a total included cone angle of 60 degrees.

A 30 gage Pt-Pt/10 percent Rh thermocouple was used to measure the back face temperature of the C/C specimen. The thermocouple bead was ground to maximize its surface contact area with the back face of the C/C model (see detail, Figure 5). The bead was left rounded where it contacts the alumina tube in order to maintain a small contact area at this material interface. This bead geometry is commonly used to increase measuring accuracy. The contact area between the thermocouple bead and the C/C model was estimated to be approximately 400 times greater than the contact area at the alumina oxide tube interface.

SUPPORTING DESIGN ANALYSES

Thermal and thermal stress analyses were performed to determine the response of the FWPF C/C material to ensure that reentry stress levels would be achieved in the test model at arc heater conditions within the GPF operating envelope.

Thermal Analyses

Thermal analyses were performed to predict transient temperature distributions through the 3-D C/C test specimen as a function of specimen dimensions and GPF test conditions. A two-dimensional, transient heat-transfer computer program used to perform the reentry thermal and ablation analyses were used to perform the thermal analyses.

Table I shows the GPF operating conditions used in determining the thermal response of the 3-D C/C test model, corresponding to peak heating associated with a prompt GPHS reentry. At this arc heater operating condition, the stagnation point cold wall heat flux to the thermal stress test model is approximately 51.9 MW/m^2 (4570 Btu/ft^2-sec).

The nodal temperature-time history obtained from the thermal analysis was used as input for the thermal stress analysis.

Thermal Stress Analysis

Development of an axisymmetric thermal stress model allowed the application of computer program DOASIS to calculate the thermal stresses and strains for the test model configuration. This program has been well tested both for elastic and elastic-plastic strains.

A finite element model was developed for the test specimen using the two-dimensional model generation capability of the INGEN program developed by LASL.[1] This finite element model is shown in Figure 6. Temperatures were obtained for input into the DOASIS program by interpolation from the temperatures previously calculated using the finite difference code.

Elastic and elastic-plastic stress analyses were conducted to determine the suitability of the test model geometry and wall thickness using available elastic-plastic material property data. These analyses were made at various time intervals by inputting the specimen temperature distribution into the DOASIS computer program and iterating to obtain the elastic-plastic stresses. Although this procedure does not account for the time-dependent temperature history, the analyses are believed to be sufficiently accurate to demonstrate the stress relief obtained when the C/C composite undergoes compressive plastic flow at the front face surface.

Table II shows the results of the DOASIS analyses at various specimen exposure times. The DOASIS-calculated peak reentry tensile stress calculated using elastic-plastic property data is 103.4 $M_1 \cdot n^2$ (15 ksi). From Table II, it can be seen that this stress level is predicted to occur at approximately 1 sec into the test.

Deformations of the test specimen were also predicted as part of the thermal stress analyses. Radial deformations computed at the forward inner cavity surface are compared with the measured deformations later in this paper.

INSTRUMENTATION CALIBRATION
AND TEST PROCEDURES

Instrumentation used to measure the back face strain was calibrated prior to the conduct of the thermal stress test in the Ames GPF. Also a thermal analysis was conducted to determine the error in the back face temperature due to contact resistance at the FWPF C/C-thermocouple interface. Results of these activities are summarized as follows.

The strain gage extensometer used to measure the C/C specimen strain was calibrated after the strain gages and lead wires were attached. The sensitivity of the strain gage beam system was found to be 4184 $\mu\varepsilon$/MV/volt excitation.

Effects of temperature on the extensometer transducer's electrical output were checked by exposing the transducer to various temperature levels using a constant temperature oven.

Thermal analyses were conducted to determine the potential error in the temperature measurement that could result from poor contact between the thermocouple bead and the back face of the C/C test model. Although positive contact between the thermocouple bead and the C/C test model back face was maintained using a spring, there existed a thermal contact resistance at this interface. Based on information available for the contact conductance between tungsten and graphite[2] and a contact pressure of approximately 2.1 MN/m^2 (300 psi) at the thermocouple-C/C interface (cold pretrial measurement), a room temperature contact conductance of approximately 5674 W/m^{2}K (1000 Btu/hr-ft^2-F) was predicted between the thermocouple bead and the C/C material. During the test, there is a decrease in this conductance due to stress relaxation of the spring.

Results of this thermal analysis are presented in Figure 7 for the nominal heating rate conditions. The indicated thermocouple temperature reading is presented as a function of the actual back face temperature and contact conductance. For a contact conductance of 5674 W/m^{2}K (1000 Btu/hr-ft^2-F), the maximum difference between the indicated and actual back face temperatures is estimated to be approximately 121 to 149 C (250 to 300 F) over the test duration. Also shown in Figure 7 are the corrections that should be made to the indicated thermocouple reading for lower (1418, 2837 W/m^{2}K) and higher (28372 W/m^{2}K) contact conductances. For the latter value, there is practically no difference between the indicated and actual back face C/C temperature.

The effect of mechanical injection loads on the extensometer was evaluated by installing the test model in the holder and operating the sting which inserts the test model into the gas stream. The model was installed with the tungsten forks of the extensometer oriented in a direction perpendicular to the traversing direction of the sting. Placing the forks in this orientation minimizes the deceleration loads on the forks in the direction in which the strain would be measured.

Calibration tests were performed prior to testing of the FWPF test sample in order to determine the heater operating conditions required to achieve the desired nominal heating rate. A calorimeter model was used to measure the stagnation point heating rate.

Prior to inserting the FWPF test model into the arc-heated gas, the calorimeter model was inserted to ensure that the arc heater was functioning properly and the nominal heating rate of approximately 51 MW/m^2 was achieved.

The test model was inserted into the gas stream for approximately 3 seconds. During insertion, the model was protected by a nylon sabot which covered the cylindrical nose portion of the test sample. The two piece sabot was held in place around the test specimen using fine wires. The wires usually melt in approximately 200 to 500 msec, depending on the arc heater operating conditions, and the sabot is forced away from the model by the high dynamic pressures associated with the gas stream. The elapsed time associated with the removal of the sabot after the retainer wires are melted is of the order of a millisecond. Thus, the test model is subjected to a step-like change in environment.

An optical pyrometer was used to measure the front face stagnation point temperature history.

TEST RESULTS

The oscillograph measurement of back face temperature and strain are shown in Figure 8 along with the predicted back face temperature and strain histories. A corrected back face temperature history is also shown in Figure 8 using the measured temperatures and a FWPF C/C-thermocouple contact conductance of 2837 W/m^2K.

It can be seen that there is good agreement between the predicted and measured temperature history (based on contact conductance of 2837 W/m^2K), and that the predicted strain levels are in good agreement with the measured values. The slopes of the predicted and measured strain histories are practically identical to each other with a difference in strain of approximately 200 $\mu m/m$. The predicted strain values are based on the back face temperature history using a contact conductance of 2837 $W/m2K$.

No cracks or other physical damage was observed in the test specimen even though the tensile stresses and strains reached those levels expected during reentry of the GPHS module. This provides initial corroboration that the GPHS reentry member will survive reentry thermal stresses.

CONCLUSIONS

The thermal stress test conducted in the NASA Ames Giant Planetary Facility (GPF) demonstrated that the Avco FWPF C/C composite can withstand GPHS prompt reentry heat flux, stress, and strain levels without suffering noticeable damage or loss of physical integrity.

The predictive techniques used to calculate the thermal and thermal stress response of the FWPF C/C aeroshell material were found to be in good agreement with the measured values following appropriate corrections for contact resistance between the specimen back face and the thermocouple bead. Although this comparison is based only on one test, the agreement lends credence to the theoretical methods being used in predicting temperatures and strains of FWPF C/C.

It was demonstrated that the strain/deformation developed by FWPF C/C, when subjected to severe reentry environment heat flux levels, could be successfully measured through proper design and calibration of a newly-conceived instrumented system.

For further corroboration of the theoretical methods, as well as obtaining further proof of the durability of the C/C composite, additional FWPF C/C specimen tests are needed at various heat flux levels characteristic of GPHS prompt reentry conditions such that the failure stress/strain levels can be determined and associated with specific initial reentry trajectory conditions.

REFERENCES

(1) Cook, William A. "INGEN, A General Purpose Mesh Generator for Finite
Element Codes", Los Alamos Information Report LA-7135-MS, March, 1978,
19 pp and appendices.

(2) Rohsenow, W. M., and Hartnett, J. P., "Handbook of Heat Transfer",
McGraw-Hill Book Company, New York, 1973, Chapter 3.

TABLES

TABLE I.   INPUT VALUES FOR THERMAL ANALYSIS
OF THERMAL STRESS MODEL

| Enthalpy MJ/kg | Stagnation Values | | Free-Stream Conditions | | Cold Wall Stagnation Point Heating Rate to 2.54 cm Radius Hemisphere, MW/m^2 |
	Model Impact Pressure, N/m^2	GPHS Heating Rate (Cold Wall), MW/m^2	Mach Number	Velocity, m/sec	
81.4	1.5 x 10^5	51.9	1.7	2,591	79.2

TABLE II.   ELASTIC AND ELASTIC-PLASTIC THERMAL STRESSES

| Time, Sec | Maximum Tensile Stress, MN/m^2 | | Maximum Compressive Stress, MN/m^2 | |
	Elastic	Elastic-Plastic	Elastic	Elastic-Plastic
	Nominal Heating Rate			
0.25	69	55	-200	-145
0.51	97	76	-159	-124
0.75	110	90	-138	-124
0.94	117	103	-131	-117
1.28	117	117	-117	-117

FUEL PELLET

POST IMPACT SHELL

GRAPHITE
IMPACT SHELL (GIS)

FLOATING
MEMBER

GIS CAP

CBCF

LOCK MEMBER

AEROSHELL
CAP

STANDOFF
RING

GIS

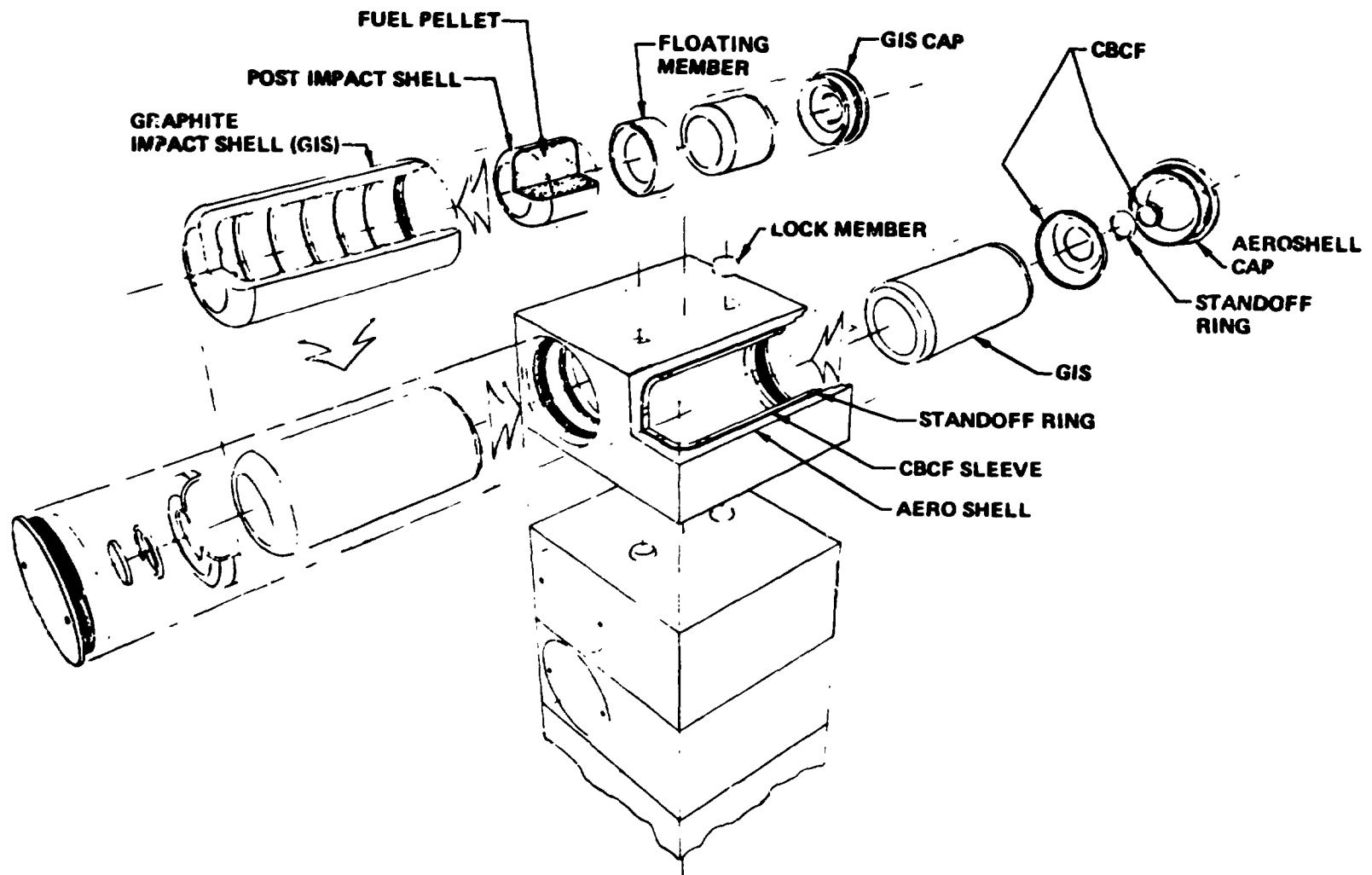STANDOFF RING

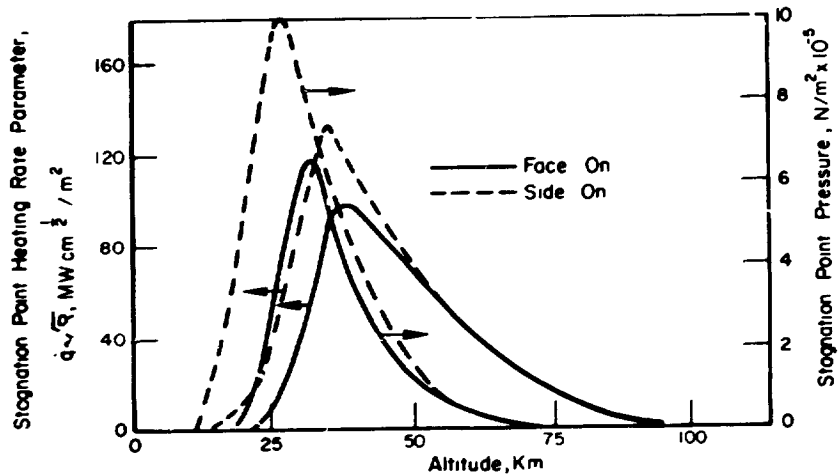CBCF SLEEVE

AERO SHELL

Figure 1.   GPHS Module Schematic

Figure 2a. Reentry Heating and Stagnation Pressure
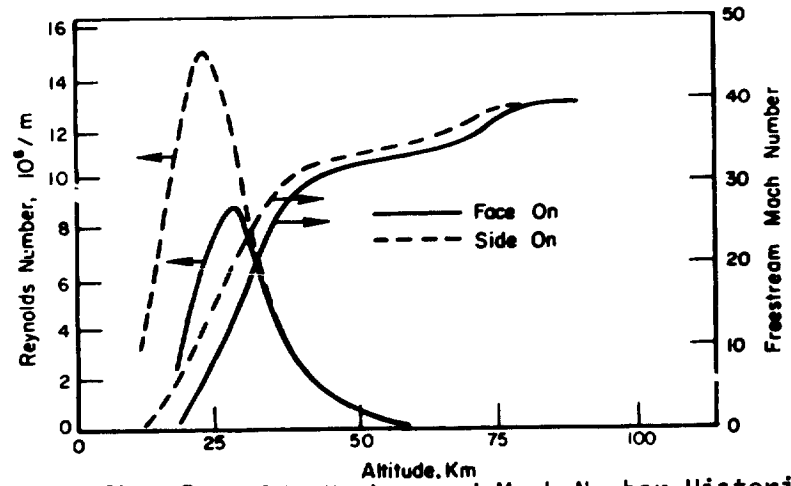
Figure 2b. Reynolds Number and Mach Number Histories

Figure 2. Prompt Angle Reentry Parameters
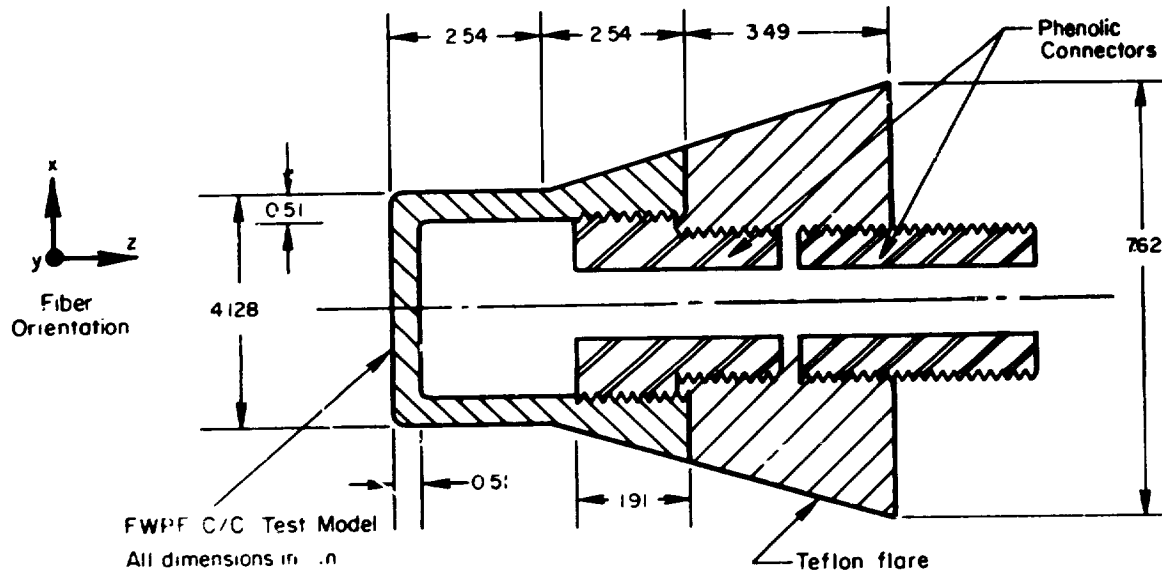
Figure 3. Cross-Sectional Drawing of Thermal Stress Model

Figure 4. Photograph of Thermal Stress
Model Components

Thermocouple

Al₂O₃ Tube

Hole for Strain Gage
Bridge Leads

Terminal for Connecting
Strain Gage Leads

Strain Gages

Tungsten Forks

Hole for Thermocouple
Leads

Hole for Thermocouple
Assembly

Main Support Bar for Instrumentation

Thermocouple Spring

Al₂O₃ Tube

Figure 5. Schematic of Instrumentation Package for
the Thermal Stress Tests

Figure 6.   Finite Element Model of the
Thermal Stress Test Model

Figure 7.   Back Face Thermocouple Response
As a Function of Back Face
Temperature and Contact Conductance

Figure 8.   Thermal Stress Test, Comparison of
Experiment and Analysis

SPACE SHUTTLE ORBITER NOSE CAP AND WING LEADING EDGE
CERTIFICATION TEST PROGRAM

Murray J. Suppanz*
John E. Grimaud**

ABSTRACT

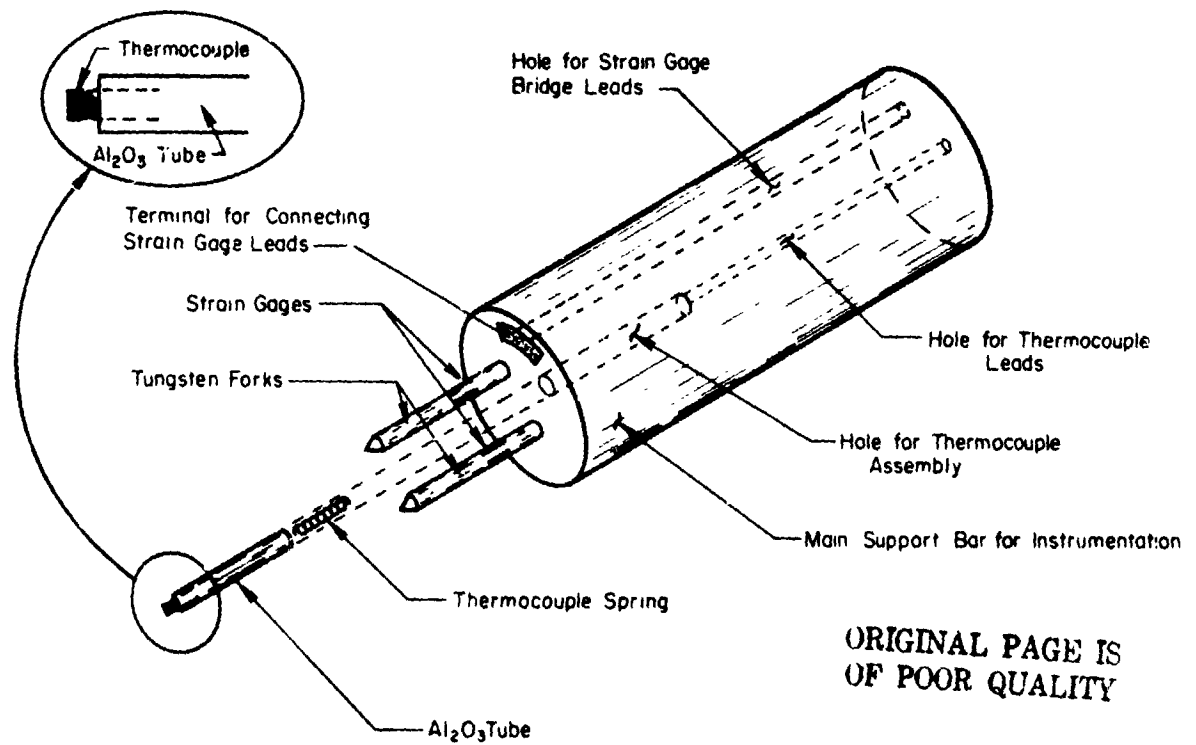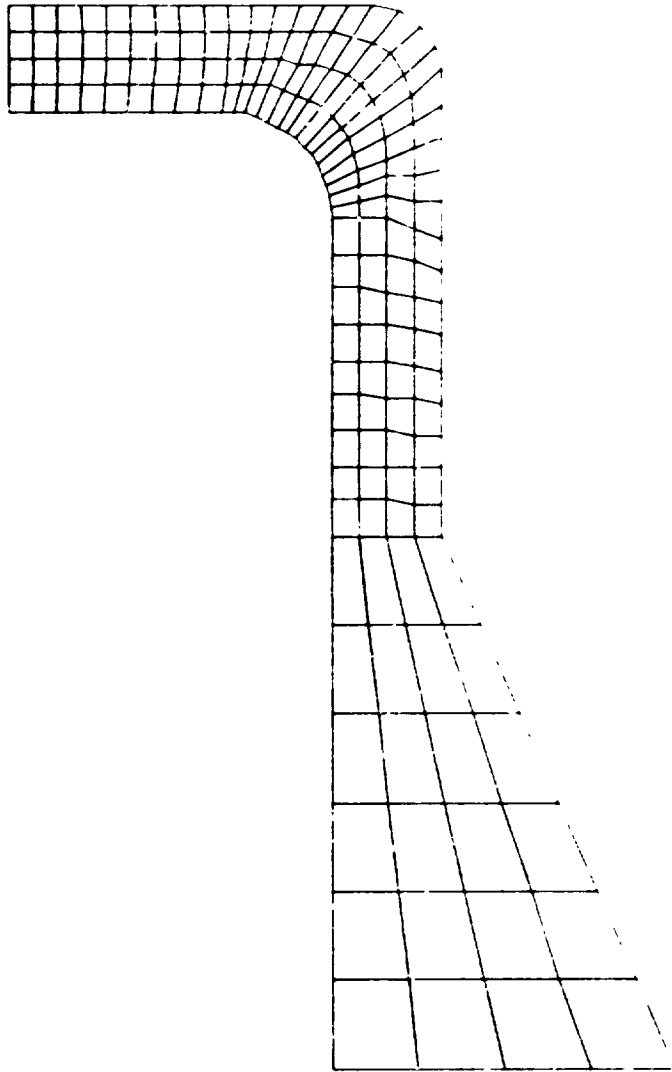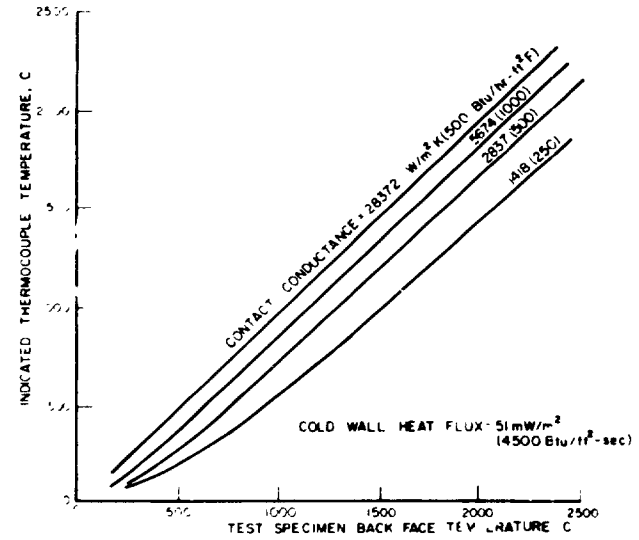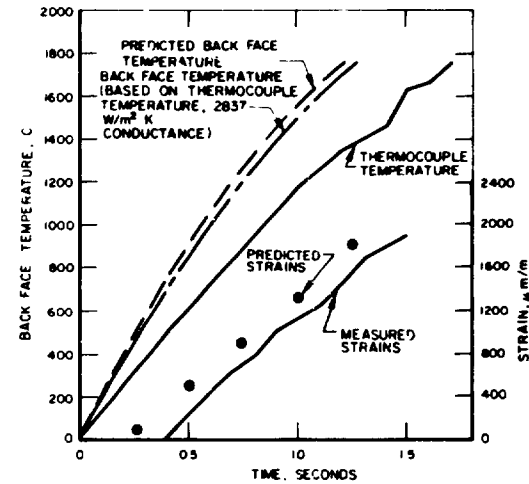A reinforced carbon-carbon thermal protection system is used on the Space Shuttle orbiter vehicle's nose cap and wing leading edge regions where temperatures reach 1538°C (2800°F). To verify the analyses used to certify reinforced carbon-carbon for the first flight and operational missions, a unique multi-environment incremental test program was developed and implemented through the combined efforts of Rockwell International and the National Aeronautics and Space Administration. Three separate facilities at the Johnson Space Center were used to subject full-scale nose cap and wing leading edge test articles to simulated critical launch, on-orbit, and atmospheric entry environments.

INTRODUCTION

During atmospheric entry, the Space Shuttle orbiter vehicle's external surfaces will reach temperatures up to 1538°C (2800°F) in regions of highest aerodynamic heating. Unlike the Apollo spacecraft, which was designed for a single-mission life and employed a nonreusable charring ablator thermal protection system (TPS) to protect the structure from aerodynamic heating during entry, the orbiter was designed to be reusable for up to 100 missions with minimal refurbishment between flights. Therefore, the orbiter TPS must be able to withstand fatigue loading.

The orbiter TPS consists of four different material configurations (Figure 1), each optimized for a specific maximum temperature range of operation. The vehicle surfaces that will encounter the highest temperatures are protected by reinforced carbon-carbon (RCC), which can withstand thermal and structural loads generated by the flight environment of the orbiter. The remainder of the vehicle's surface is covered with various forms of reusable surface insulation (RSI). The RCC components (including their internal insulation, supporting structure, support links, and attachment fittings), and the tiles and seals at the interface of the RCC and RSI make up the orbiter's leading edge structural subsystem (LESS). The LESS components, consisting of the nose cap and wing leading edges, were designed on the basis of thermal and structural analysis

---

*Space Systems Group, Rockwell International, Downey, California
**Lyndon B. Johnson Space Center, National Aeronautics and Space
  Administration, Houston, Texas

programs that predicted the reaction of these components . . theoretical flight environments. However, because of the complexity of the LESS design, the types of materials involved, and the range of environmental conditions the LESS must withstand, extensive testing was required to verify these analyses.

The required testing involved a unique test program and facilities that could simulate the critical environments of launch, earth orbit, and entry into the earth's atmosphere. Through the combined efforts of Rockwell International and the National Aeronautics and Space Administration (NASA), a comprehensive test program was developed in three facilities at the Johnson Space Center (JSC), where the nose cap (NC) and wing leading edge (WLE) test articles were sequentially exposed to simulated critical portions of flight.

These test articles (Figure 2)—designed to duplicate the thermal, dynamic, and structural qualities of the orbiter—were manufactured according to production procedures. The NC test article consisted of RCC components, structural attachments, internal high-temperature thermal insulation blankets, a portion of the forward fuselage interface containing HRSI TPS tiles, thermal barriers, and related thermal control system (TCS) multilayer insulation blankets. The WLE test article consisted of a 7-foot section of the wing box and front spar, two RCC panels with a T-seal interface and structural attachments, high-temperature spar insulation blankets, interface and wing HRSI and LRSI TPS tiles, and related thermal barriers. These articles, with their hundreds of instrumentation sensors, were exposed sequentially to acoustic excitation, structural airloads, on-orbit cold soak, and atmospheric entry thermal conditions to simulate the critical flight environments of a typical mission.

The goal of this test program was to support certification of the LESS for 100 missions by experimental verification of the design analyses. This paper provides an overview of the orbiter TPS and describes in detail the LESS NC and WLE test articles, test program philosophy, test environments, facility considerations, and results of completed tests that support certification of the orbiter LESS for the first orbital flight.

TPS REQUIREMENTS

The TPS associated with the Space Shuttle orbiter vehicle must attenuate aerothermal heating, which results in temperatures up to 1538°C (2800°F) on the vehicle's external surfaces, to protect the aluminum structure from exceeding its design limit temperature of 176°C (350°F) during any phase of the Shuttle mission. The TPS must also sustain acoustic and structural loads and deflections, as well as natural environments such as salt spray, fog, and rain. In addition, the system must provide an acceptably smooth aerodynamic surface, be reusable with minimal refurbishment over a 00-mission life, and be weight efficient without imposing unrealistic manufacturing, installation, or flight constraints. The TPS must also perform efficiently as an element of the thermal control system, whose purpose is to keep the temperature of the structure and vehicle subsystems within limits during earth orbit.

TPS DESIGN

The TPS consists of both active and passive elements. Active elements include movable seals and flow barriers associated with the aerodynamic control surfaces (i.e., elevons, rudder, and body flap). Passive elements comprise the different TPS materials covering the entire external surface of the vehicle.

The passive TPS consists of four different material configurations (Figure 1), each optimized for a specific operational temperature range. One, fabricated RCC, is used in the areas of highest heating on the vehicle—the NC and the WLE—where temperatures generally exceed 1260°C (2300°F). The material construction is a multilayer graphite laminate with an oxidation-resistant coating, molded to the desired shape, and mechanically attached by Inconel fittings to a forward bulkhead or wing spar. The RCC is also designed to withstand aerodynamic loads and serves as an extension of the aluminum primary structure. Because RCC is not a good insulator, the adjacent aluminum structure and Inconel attachment fittings must be protected from exceeding design temperature limits by internal insulation.

The remaining three material configurations are broadly characterized as reusable surface insulation. Only two are used on the WLE and NC test articles, but a description of each follows to provide an overview of the entire orbiter TPS.

High-temperature reusable surface insulation (HRSI) tiles are used in areas where temperatures are generally below 1260°C (2300°F) and above 648°C (1200°F). These tiles are nominally squares 15.24 by 15.24 centimeters (6 by 6 inches) made from low-density, high-purity silica fibers. The top and sides are covered with a tetrasilicide-borosilicate glass coating that provides a surface emittance of 0.85 and a solar absorptance of 0.85. In addition, the tiles are waterproofed with a silicone resin. HRSI tiles weigh either 144 or 352 kilograms per cubic meter (9 to 22 pounds per cubic foot) depending on the area of application, and they vary in thickness from 2.54 to 12 centimeters (1 to 5 inches). Approximately 20,000 HRSI tiles are used on the orbiter vehicle.

Low-temperature reusable surface insulation (LRSI) tiles are used in areas where temperatures are generally below 648° (1200°F) and above 371°C (700°F). LRSI is of the same material construction as HRSI except that the tiles are 20 by 20 centimeters (8 by 8 inches) square and contain a white moisture-resistant coating with a surface emittance of 0.8 and a solar absorptance of 0.32. LRSI tiles range in thickness from 0.5 to 3.5 centimeters (0.2 to 1.4 inches). Approximately 7000 LRSI tiles are used on the orbiter vehicle.

Coated Nomex felt reusable surface insulation (FRSI) is used in areas where temperatures are lower than 371°C (700°F) during entry and 398°C (750°F) during ascent. FRSI, which is constructed of basic Nomex (Aramid) fiber, varies in thickness from 0.4 to 1.0 centimeter (0.16 to 0.4 inch) and is applied in 0.9- by 1.2-meter (3- by 4-foot) sheets that are coated with a silicone elastomer, providing an emittance of 0.8 and a solar absorptance of 0.32. FRSI covers approximately 50 percent of the orbiter's upper surface.

REINFORCED CARBON-CARBON

RCC for use on the orbiter NC and WLE is currently manufactured by the Vought Corporation. Fabrication begins with a rayon cloth that is treated with graphite and impregnated with a phenolic resin. This impregnated cloth is layed up as a laminate of 19 to 38 plies and cured in an autoclave. After cure, the laminate is pyrolized at high temperature to convert the resin to carbon. The part is then impregnated with furfuryl alcohol in a vacuum chamber, cured, and again pyrolized to convert the furfuryl alcohol to carbon. To obtain an oxidation-resistant coating, the material is packed in a retort with a mixture of alumina, silicon, and silicon-carbide, and placed in a furnace with an argon atmosphere at a temperature of 1760°C (3200°F). A diffusion reaction occurs that converts the outer carbon-carbon layers to silicon-carbide with no thickness increase. Oxidation resistance is then enhanced by impregnating the coated RCC part with tetraethyl-orthosilicate (TEOS). Together, the silicon-carbide and TEOS protect the internal layers of carbon-carbon from oxidation during entry into the earth's atmosphere.

The advantages of RCC are its good high-temperature mechanical properties and high resistance to fatigue loading. The primary disadvantage of RCC is associated with loss of strength due to subsurface oxidation, which is greatest at intermediate operating temperatures around 870°C (1600°F).

The maximum size of individual RCC components is limited, from a practical sense, by the deflections of the structure and the linear growth that can be accommodated conveniently in the design as the material expands at high temperature. The WLE is made up of 44 RCC panels (22 for each wing) whereas the nose cap is one piece. The RCC panels are mechanically attached to the wing with a series of floating joints to reduce loading on the panels caused by wing deflections and differential thermal expansion. The seals between wing leading edge panels, referred to as "T-seals," are made of RCC. They allow lateral motion for thermal expansion between the RCC and wing structure, and prevent the direct flow of hot boundary-layer gases into the WLE cavity during entry.

Inconel 718, A-286, and titanium fittings are bolted to flanges on the RCC components and attached to the aluminum wing spars and nose bulkhead. Inconel-covered Dynaflex insulation protects the metallic attach fittings and spar from the heat emitted by the inside surface of the RCC wing panels. Inside the NC is a blanket made from ceramic fibers and filled with silica fibers and HRSI tiles to protect the forward fuselage from the heat emitted by the hot inside surface of the RCC.

In both the NC and WLE, internal heat is transferred primarily through radiation from the backside of the RCC components. Peak aerodynamic limit loading is on the order of 34.5 kilopascals (5 pounds per square inch) on the NC and 23.4 kilopascals (3.4 pounds per square inch) for the wing.

TEST PHILOSOPHY

Testing required to develop the RCC system can be categorized in three general areas: (1) materials characterization tests, (2) design evaluation tests, and (3) system design verification tests. Material characterization tests were conducted to develop basic thermal physical property data, optimize mechanical strength, and study degradation processes. Design evaluation tests were performed on full-scale RCC components to verify analytical strength predictions, thermal performance, and design methods. System design verification tests were performed to verify not only RCC components but all of the elements and components that compose the total NC and WLE edge portions of the vehicle. Material characterization and design evaluation tests were primarily the responsibility of the RCC manufacturer, Vought Corporation, which was under contract to Rockwell. Rockwell was responsible for defining the system design verification tests.

The LESS test objectives to support flight certification fall into four principal categories: (1) to validate analytical modeling techniques, (2) to verify the mission life of hardware elements, (3) to verify structural integrity, and (4) to demonstrate the ability of floating mechanical joints to allow for expansion and contraction of RCC components.

VERIFICATION TEST REQUIREMENTS

In fulfilling the design and development responsibilities for the Shuttle orbiter, Rockwell is responsible for defining the various environmental conditions to which the orbiter will be exposed during its mission cycle. The simulation parameters of interest for the verification of the NC and WLE include critical environments of ascent, earth orbit, and atmospheric entry. The various environmental conditions and their respective mission time lines were studied to determine the critical factors and their principal degrading effects. These studies indicated that three different environmental tests were required to simulate the most critical flight mission exposure: acoustic excitation, structural airloads, and thermal conditions of earth orbit and atmospheric entry. No single facility can produce all of the desired environmental conditions. However, it was considered technically justifiable and experimentally expedient to expose the system components to the three environments sequentially in different test facilities to accumulate valid damage effects.

Basically, the requirement was to apply the three environments in their order of occurrence during the mission—i.e., launch acoustics, orbit and entry temperatures, followed by landing airloads. Upon development of the detailed test plans, however, it was considered prudent to perform all airload tests before the orbit and entry thermal exposure to minimize instrumentation refurbishment requirements during the three environmental exposures. In addition to instrumentation considerations, it was desirable to certify the hardware systems incrementally on a flight-by-flight basis. This approach, in addition to its overall schedule advantages, was more conservative and able to accommodate anomalies that might develop during the test program. The final decision

394

was to expose each article incrementally to simulated acoustic, airload, and thermal environments in four test phases—Phase A being equivalent to 8 missions, B to 16, C to 24, and D to an additional 52 mission cycles (Table 1).

TEST ARTICLE DESCRIPTION

The NC and WLE certification test articles (Figures 3 and 4) were designed to encompass all structural, mechanical, and thermal boundaries essential to proper evaluation of the related RCC components. The NC article consisted of the complete RCC nose cap assembly: forward shell, T-seal, expansion seal, internal insulation blankets, and fuselage closeout system, plus a section of the forward fuselage structure, closeout HRSI tile, and acreage tile. The WLE test article consisted of two RCC panels (No. 16 and 17) of the right-hand wing and interconnecting T-seal, all RCC attach fittings, wing front spar thermal insulation, attach fitting insulation, and a section of wing structure.

The NC and WLE were the selected test article configurations because they comprise the fewest component parts yet represent all of the mechanical, structural, and thermal boundaries required to evaluate the system's performance. Additional simulated or RCC panels were required on both sides of RCC Panels 16 and 17 to provide realistic structural closeout during acoustic testing.

There are some differences between the test article configurations and the actual NC and WLE of the orbiter vehicle scheduled for the first orbital flight as a result of ongoing design changes that were judged to have minimal effect on the system evaluation and could be accounted for by analytical procedures. The NC test article has a modified RCC T-seal on the lower side whereas the current design is segmented with a designed aerodynamic overlapping joggle. The test strip was simply cut before coating to allow for the equivalent expansion freedom. Acreage tile was obtained from production rejects. The aft sections of the WLE upper and lower surfaces were also covered with rejected tiles for structural protection in the thermal test and for dynamic influence on the structure in the acoustic tests. The WLE test article was fabricated from a dedicated test article identified as WA-19, originally built for the acoustic fatigue test program. The NC test article was designed and fabricated uniquely for the RCC verification program and required only instrumentation changes for different environments. The thermal configuration of the WLE employed insulating closeout panels at each end of RCC Panels 16 and 17, plus additional insulation on the remaining portions of the front spar. The acoustic configuration, as noted earlier, used a fiberglass panel (No. 18) plus supplemental fiberglass closeouts at the ends of Panels 16 and 18. The airload test configuration was the least complex, not requiring any special structural closeouts at the ends of the RCC panels.

FACILITIES AND TESTING

Facility considerations and test methodology were based on meeting Shuttle acoustic, airload, and thermal requirements.

Acoustics

An acoustic facility capable of meeting the NC and WLE test requirements was nonexistent at the inception of the Shuttle program. However, the vibration and acoustic test facility (VATF) at NASA's Johnson Space Center (JSC), originally constructed to support the Apollo program, was upgraded early in the Shuttle program to develop the high acoustic levels needed to simulate the orbiter's flight regime. For the acoustic tests, the NC and WLE articles were placed in acoustic reverberation rooms. The setup for the NC test is shown in Figure 5. The acoustic test levels and spectra are shown in Figures 6 and 7.

Before the NC and WLE were acoustically excited, structural modal tests were performed. A small shaker was used to excite the structure dynamically while accelerometers mounted at preselected locations on the outer surface of the RCC were monitored. Results of the modal tests were used to determine areas most responsive to acoustic excitation so that instrumentation locations could be optimized. Appropriate acoustic closeouts were provided to prevent direct test-level sound impingement upon internal areas of the test article. The average of ten surface-mounted microphones was used to establish the acoustic test environments. Additional microphones were used to measure the sound field at locations inside the test articles.

The test article responses were sensed by accelerometers and strain gages. The reverberant rooms were large enough—12.2 by 5.8 by 4.9 meters and 14.3 by 11.6 by 9.8 meters (40 by 19 by 16 feet and 47 by 38 by 32 feet)—to provide many resonance frequencies and good sound-field quality in all one-third octave bands at and above 50 hertz. In addition to the reverberant environment, a 100-hertz "hot-spot" horn was placed 10 centimeters (4 inches) from the surface of the NC to generate an 88- to 112-hertz sine-sweep acoustic field simultaneously with the application of the aerodynamic field.

Airloads

Special simulated airload structural test systems were required to meet the RCC test objectives. Limited airload simulation as well as acoustic and thermal testing techniques had been developed at the Vought Corporation during early RCC shell development tests. Even though the specific Vought testing techniques were not used for the NC and WLE system test programs, the Vought experience served as the basis for many of the final systems and facilities that were developed for the system test program.

The airloads tests were conducted in the JSC structures test laboratory (STL). The test setups and loading systems (Figure 8) were designed especially to fit the specific size and test requirements of the NC and WLE articles. The basic structural test system design approach was to surround each article completely with a self-contained reaction loading fixture. Each fixture contained hydraulic load application jacks, strategically located to apply loads normal to the test surface. Because of the varying pressure distribution, 54 load pads and 39 load jacks were required on the NC test article; 61 load pads and 22 load jacks were required on the WLE test article. Metal pads applied loads uniformly through 2.5-centimeter (1-inch) foam pads, as shown in Figures 9 and 10.

The test conditions for the NC were relatively simple: all loads were compressive with the design limit and fatigue load levels of the same sign and magnitude (Figure 11). The design limit loading for the WLE, however, included both compression and tension loads, and required different and complex loading for the fatigue test series. The WLE fatigue load spectrum consisted of three different up loads and three different down loads, all of varying sign and magnitude, as shown in Figure 12.

Initially, the NC appeared to have a buckling instability condition, which resulted in a special requirement to design an NC load application system that allowed buckling freedom. The system design used 54 compartment air bags that corresponded to the load pad geometry and separate free-standing support frames to isolate movement of the deflection transducers from that of the reaction frame.

The hydraulic load application system presented another special and unique design issue. Although the requirements could have been met through the use of a servocontrolled load system, the relatively large quantity of load channels rendered such a system cost and schedule prohibitive. From several conventional hydraulic load maintainers available from earlier test programs, a system of automatic valves and timers was used to design and fabricate the desired test mechanism. Mechanical load limiters were combined with an automatic load abort capability from the computerized data acquisition systems to provide test article safety from inadvertent overload or underload conditions.

Temperature

During the thermal tests, the NC and WLE articles had to be subjected simultaneously to the local temperature distributions and the temperatures and pressures to be experienced by the orbiter during atmospheric entry to simulate the thermally induced TPS and structural deflections and stresses, as well as the degradation of RCC components due to subsurface oxidation.

The facility requirements to fulfill these objectives included (1) multichannel radiant heating systems capable of accommodating the NC and WLE test article geometries, providing the required temperature distributions and histories, and operating in an oxidizing atmosphere (e.g., air), (2) cooling systems for cold-soaking the test articles to on-orbit temperatures before initiation of the entry heating, (3) systems to alternate the test articles between the radiant heaters and cooling shrouds, (4) a vacuum chamber large enough to accommodate the test articles, radiant heaters, cooling shrouds, and translation hardware, (5) a vacuum pumping system of sufficient capacity to provide altitude simulation, and (6) a computer system for data acquisition, real-time data display, annunciation, abort of out-of-limit test or control parameters, and feedback control of individual heater zones to achieve prescribed temperature profiles by monitoring local test article surface temperatures.

Because no NASA or industrial facility could meet all of these requirements, a capability was established at NASA JSC where the other sequential environmental simulation tests (acoustic and airloads) were to be conducted on the NC and WLE to minimize problems associated with test article logistics, handling damage, inspections, and instrumentation refurbishment.

The thermal facility (Figure 13), known as the JSC 5-megawatt radiant heating test facility (RHTF), consists of a vacuum chamber 3.3 meters (10 feet) in diameter and 6 meters (20 feet) long; a vacuum pumping system that can simulate altitude pressure within ±1 torr over a range of 0.07 to 760 torr; cryogenic shrouds cooled with liquid nitrogen, glycol, or methanol refrigerants that can cool the test articles to a temperature of -129°C (-200°F); test article translation and rotation systems; a 256-channel data acquisition and feedback control system with annunciation and abort limit checking of all channels; and modular heater systems tailored to the NC and WLE test articles.

The radiant heater systems developed for the NC and WLE thermal certification tests are unique. The NC heater (Figure 14) consists of 96 triangular and trapezoidal graphite elements configured to the NC geometry and grouped into 22 individual control zones to simulate the temperature distributions to be experienced by the NC during entry. The WLE heater (Figure 15) consists of nine heater modules, each containing four 1.8-meter (72-inch) graphite elements. The modules are configured to the WLE geometry and are individually controlled to simulate the temperature distributions experienced on the WLE during entry. The heater and overall test system are shown in Figures 15 and 16.

The initial tests (Phase A) required to certify the orbiter for its first flight will use uncoated graphite heater elements in an inert (nitrogen) atmosphere. Subsequent tests (Phases B, C, and D) will use silicon-carbide-coated graphite heater elements, developed to operate in an oxidizing (air) atmosphere. A silicon-carbide coating is required on the heater elements for the same reason it is used on the RCC—to inhibit oxidation and prolong element life. In addition, silicon-carbide elements must be used with a prescribed air bleed rate to ensure that the partial pressure of oxygen is representative of flight. If the mission-life certification tests (Phases B, C, and D) were conducted with uncoated heater elements, the test objectives could not be attained because the altitude control system's vacuum unit can handle only limited air flows and the available oxygen would react much more readily with the bare elements than with the test articles, resulting in an inadequate simulation of RCC subsurface oxidation.

Because of the poor reliability of thermocouples at the peak temperatures required for these tests, fiber-optic infrared pyrometers were purchased for noncontact monitoring of test article surface temperatures and providing a signal for feedback computer control of each heater control zone. The fiber-optic lens system views the test article surface through a hole in the heater reflector and between heater elements.

RESULTS AND DISCUSSION

Phase A WLE acoustic fatigue testing was completed in May 1978 as part of the acoustic fatigue test program, which used the WA-19 WLE test article configuration. The WLE WA-19 test article was then returned to Rockwell for refurbishment and upgrading to the latest design configuration; it was returned to JSC in December 1979. The Phase A WLE airload tests were completed in March 1980, whereupon the test article was disassembled, inspected, and equipped with thermal instrumentation in preparation for the Phase A thermal tests scheduled for July and August 1980.

The NC test article was delivered to the JSC vibration and acoustic test facility, where Phase A acoustic tests were completed in January 1979. The Phase A NC airload tests were completed in February 1980. However, inspection, disassembly, and refurbishment in preparation for the Phase A thermal tests revealed that the internal high-temperature insulation blankets required redesign and replacement. This necessitates repeating the acoustic exposure before the thermal tests are conducted. The retest of the Phase A NC acoustic test is scheduled for June 1980, and the Phase A NC thermal tests are planned for August and September 1980.

Completion of the Phase A NC and WLE testing, presently scheduled for September 1980, will support certification of the orbiter LESS for the first orbital flight. The Phase B, C, and D testing will then continue until the NC and WLE test articles undergo 100 mission exposures to each environment—sometime in February 1982.

CONCLUDING REMARKS

A unique multienvironment, incremental test program was developed and implemented through the combined efforts of Rockwell and NASA JSC to support certification of the orbiter LESS for a 100-mission life. Three facilities at JSC (VATF, STL, and RHTF) were used to expose full-scale NC and WLE test articles sequentially to acoustic excitation, structural airloads, and on-orbit cold soak and entry temperatures to simulate critical flight environments.

TABLE I. TEST SEQUENCE

Test Phase	Sequence	Tests	Test Duration Equivalent Missions	Supports Certification for Flights
A	1	Acoustics	32	1 - 2
A	2	Airloads (design limit) (fatigue spectrum)	1 32	1 - 2
A	3	Thermal (nonoxidizing)	8	
B	4	Thermal (oxidizing)	16	
B	5	Airloads (fatigue spectrum)	64	3 - 6
B	6	Acoustics	64	
C	7	Thermal (oxidizing)	24	
C	8	Airloads (fatigue spectrum)	96	7 - 12
C	9	Acoustics	96	
D	10	Thermal (oxidizing)	52	
D	11	Airloads (fatigue spectrum)	208	13 - 100
D	12	Acoustics	208	
D	13	Airloads (ultimate loads)	1	

400
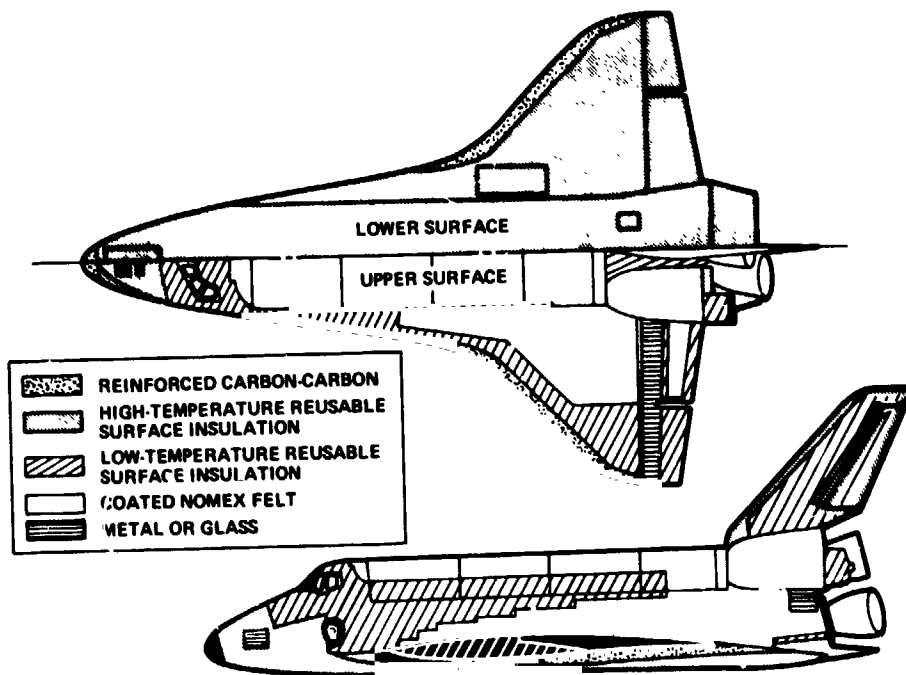
Figure 1. Orbiter Thermal Protection System

Legend:
- REINFORCED CARBON-CARBON
- HIGH-TEMPERATURE REUSABLE SURFACE INSULATION
- LOW-TEMPERATURE REUSABLE SURFACE INSULATION
- COATED NOMEX FELT
- METAL OR GLASS
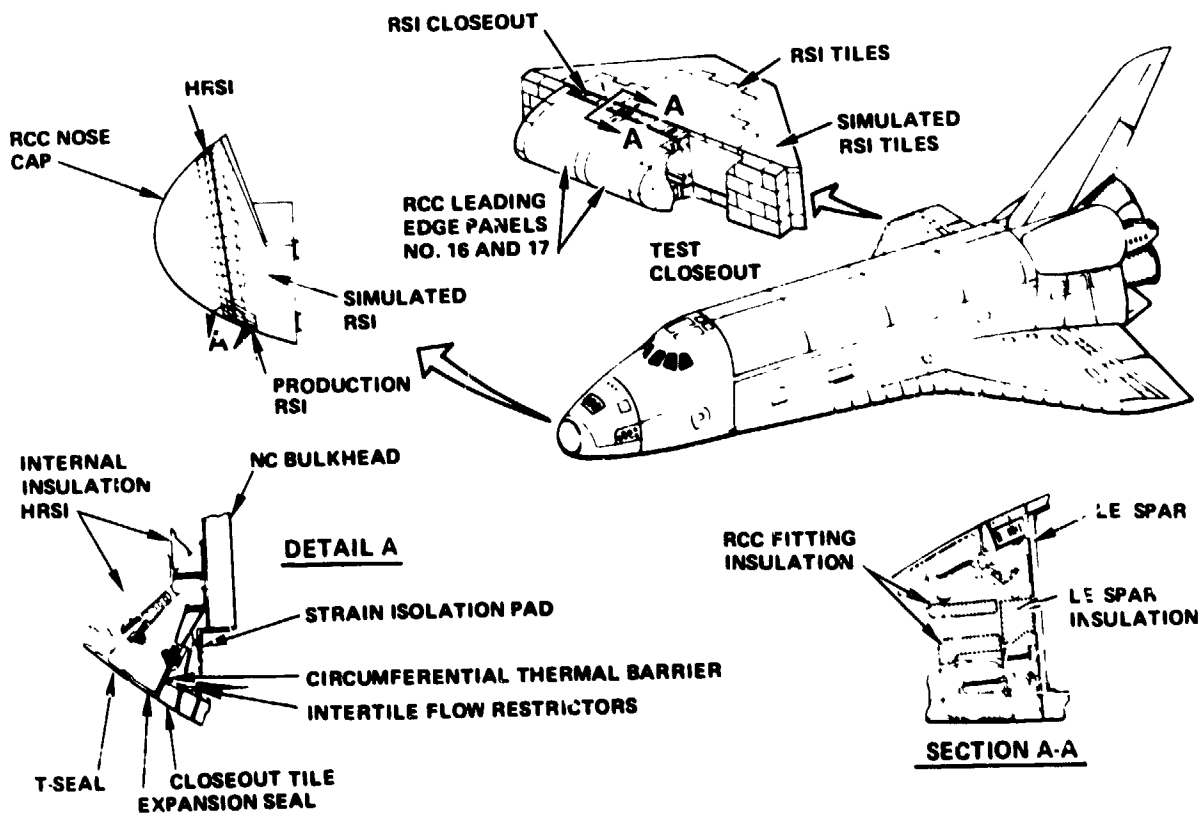
Figure 2. Nose Cap and Wing Leading Edge Test Articles
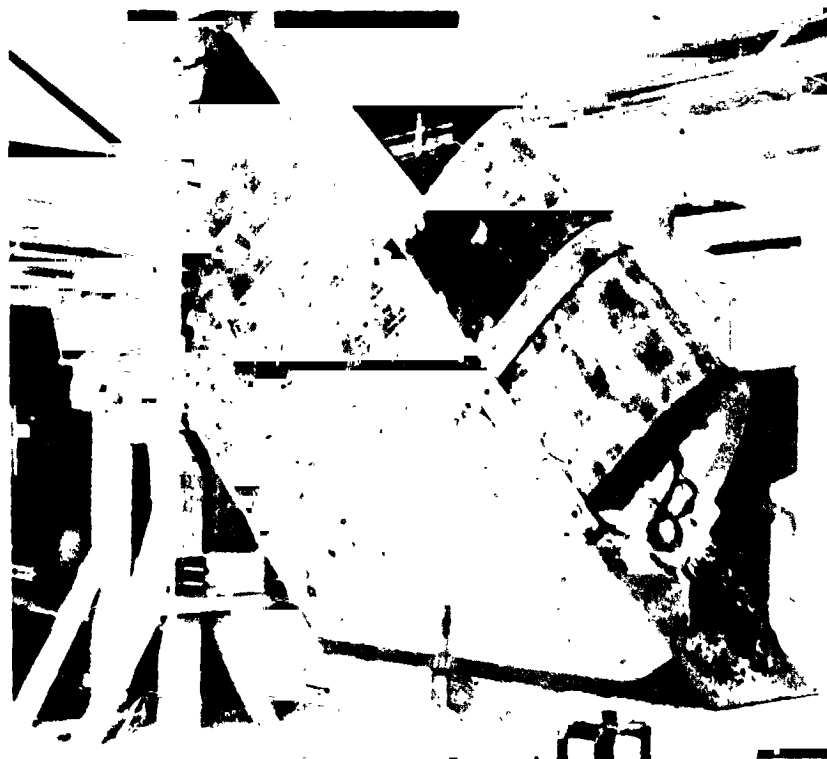
Figure 3. Nose Cap Test Article

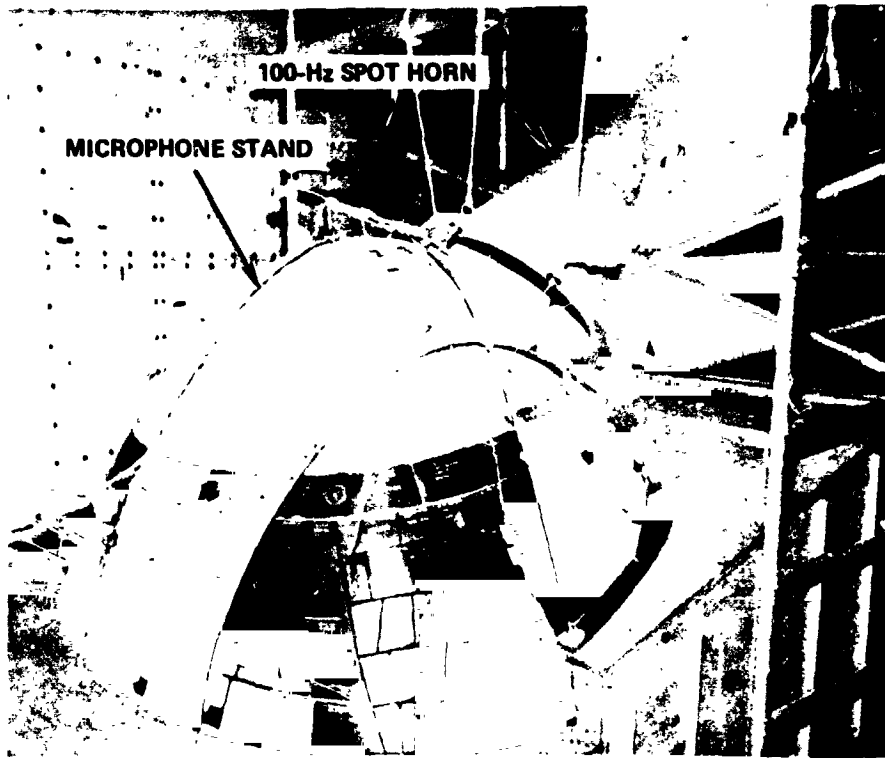F . re 4. Wing Leading Edge Test Article

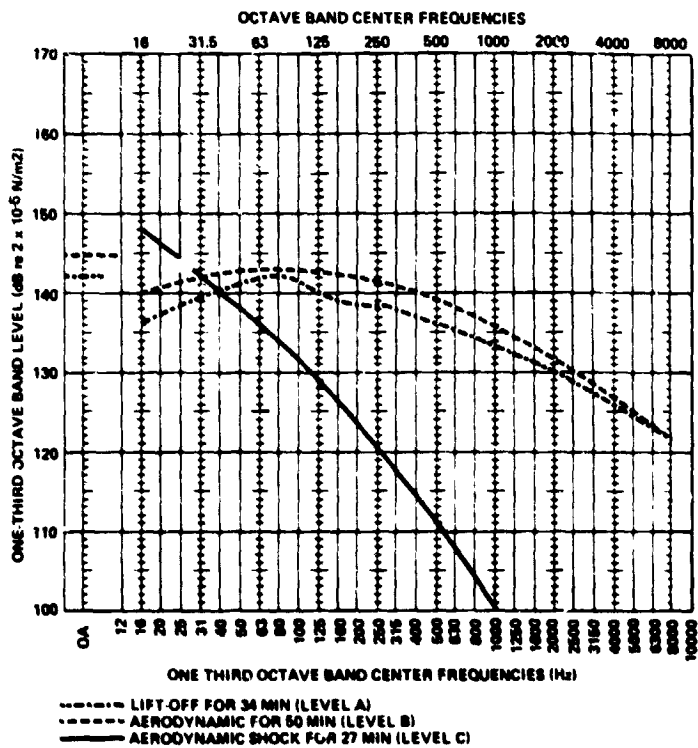Figure 5. Nose Cap Acoustic Test Setup

Figure 6. Acoustic Test Environment for Nose Cap

403
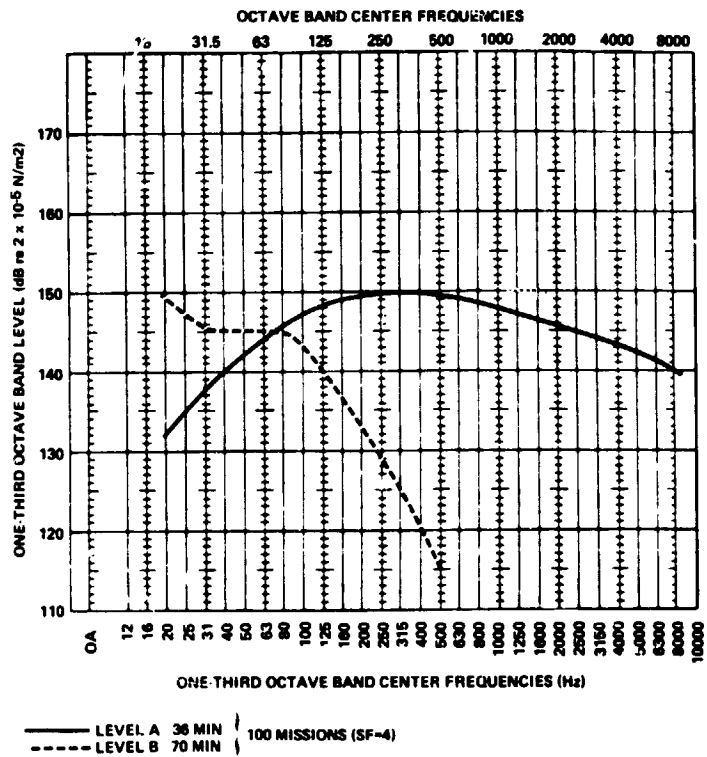
Figure 7. Acoustic Test Environment for Wing Leading Edge
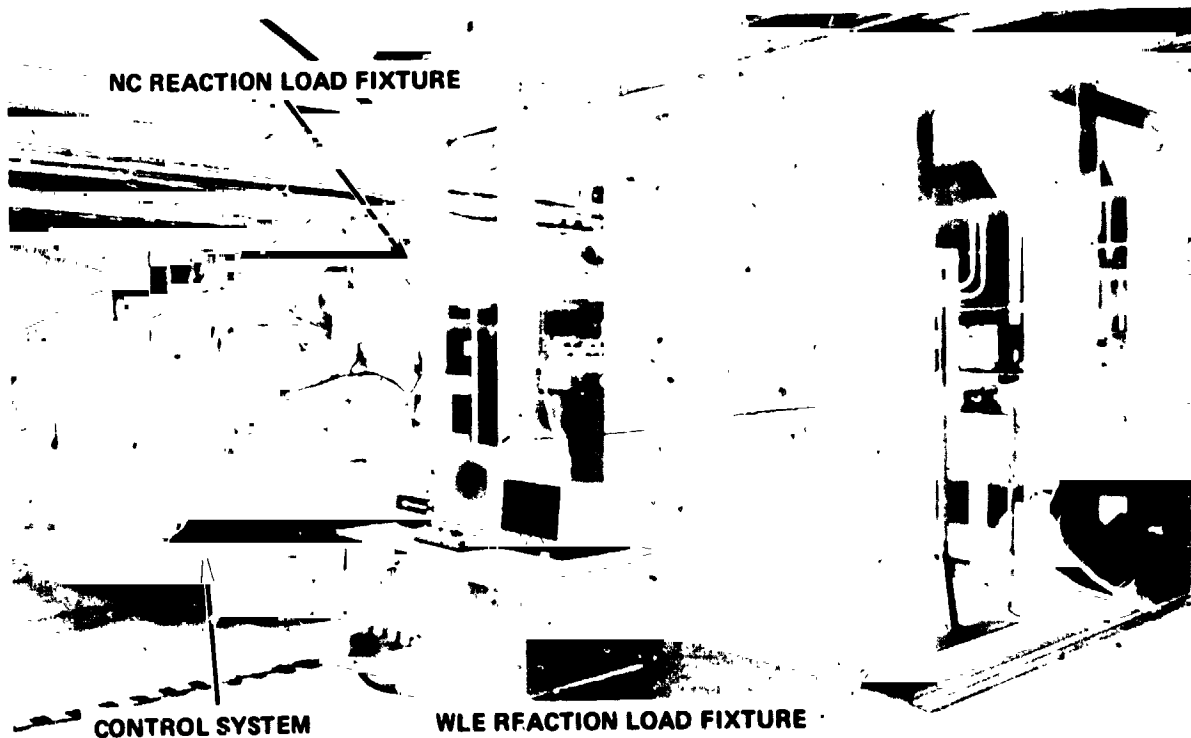
Figure 8. Airloads Test Setup
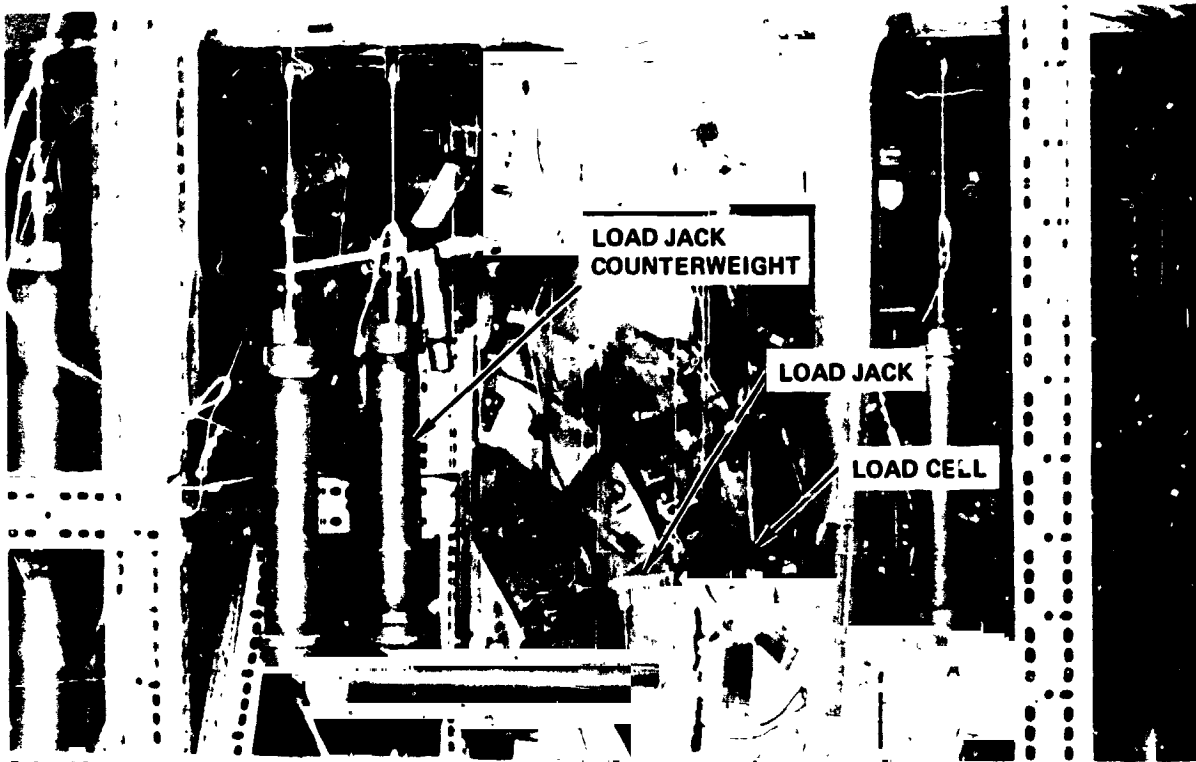
Figure 9. Nose Cap Airloads Test Setup
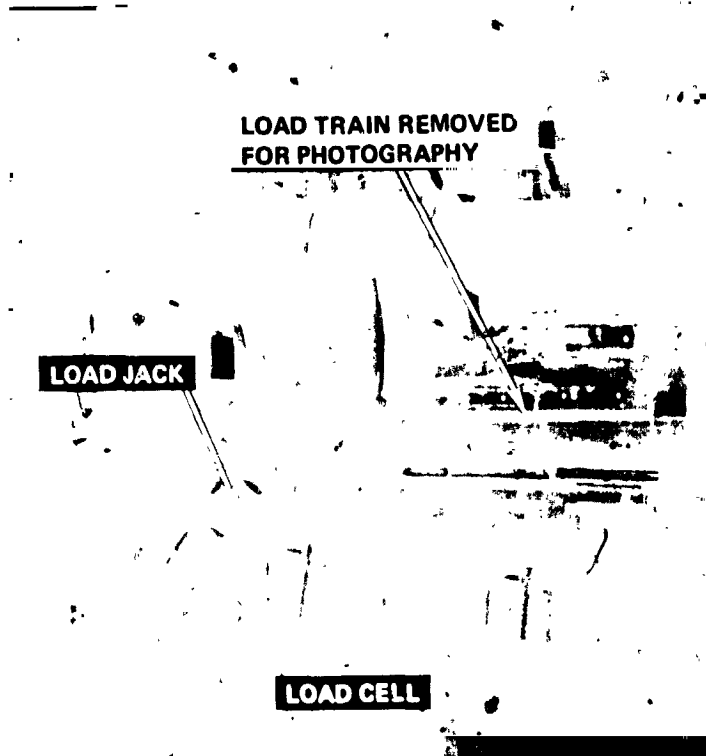
Figure 10. Wing Leading Edge Airloads Test Setup

ORIGINAL PAGE IS
OF POOR QUALITY

BODY STATION (IN.)	PRESSURE (PSIA)					
	$\phi = 0^\circ$	$\phi = 20^\circ$	$\phi = 40^\circ$	$\phi = 55^\circ$	$\phi = 70^\circ$	$\phi = 90^\circ$
236.00	11.190	11.190	11.190	11.190	11.190	11.190
236.65	11.045	11.032	11.019	11.008	10.999	10.985
246.32	8.898	8.688	8.477	8.307	8.158	7.947
265.67	6.035	6.177	6.787	7.074	7.183	7.274

	$\phi = 105^\circ$	$\phi = 120^\circ$	$\phi = 135^\circ$	$\phi = 150^\circ$	$\phi = 165^\circ$	$\phi = 180^\circ$
236.00	11.190	11.190	11.190	11.190	11.190	11.190
236.65	11.020	11.054	11.098	11.122	11.156	11.190
246.32	7.990	8.032	8.075	8.118	8.160	8.203
265.67	7.327	7.358	7.333	7.283	7.208	7.132

- LOADS ARE SYMMETRICAL ABOUT VERTICAL AXIS.
- INTERMEDIATE VALUES DETERMINED BY LINEAR INTERPOLATION RELATIVE TO BODY STATION AND ϕ.
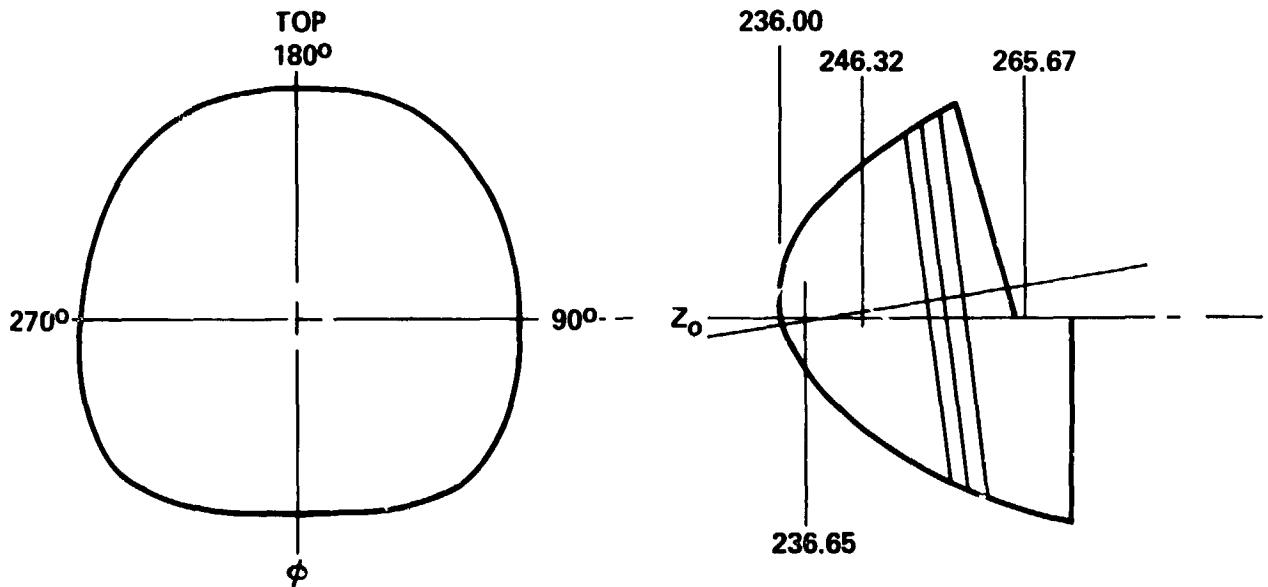
Figure 11. Nose Cap Design Limit Loads

406
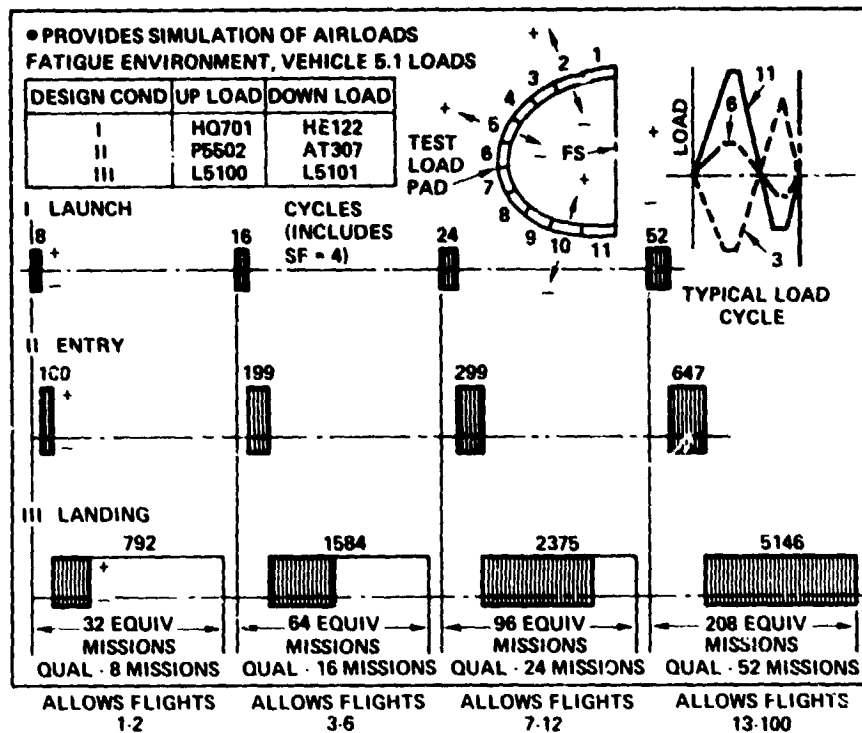
Figure 12. Wing Leading Edge Airloads Spectrum
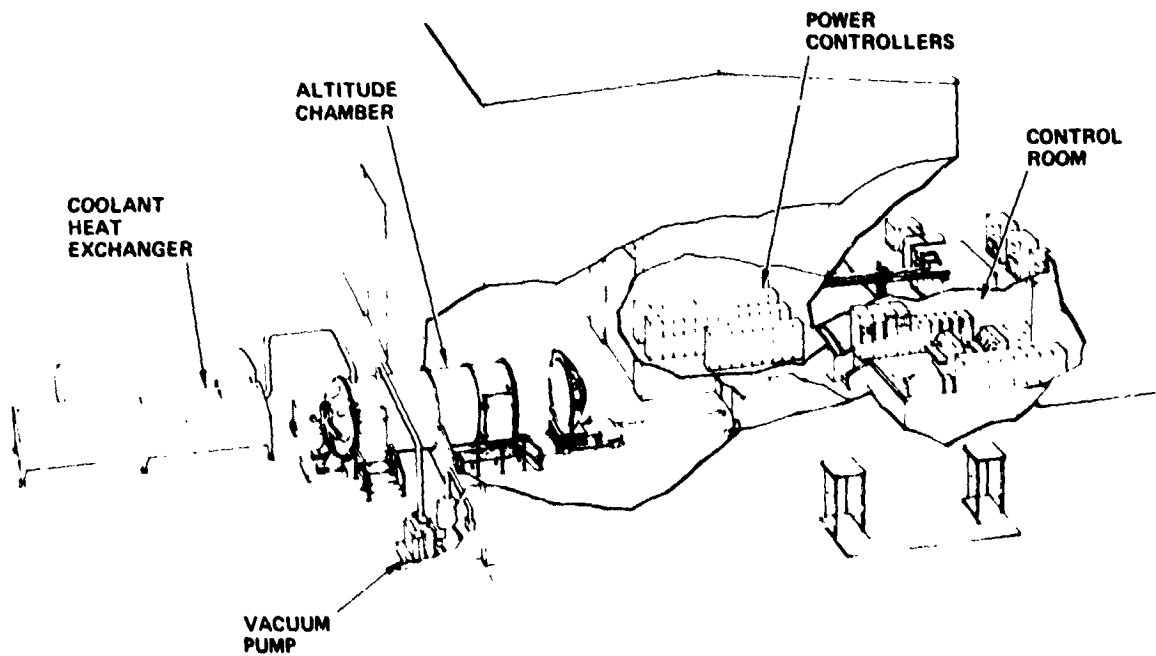
Figure 13. Radiant Heating Test Facility

407
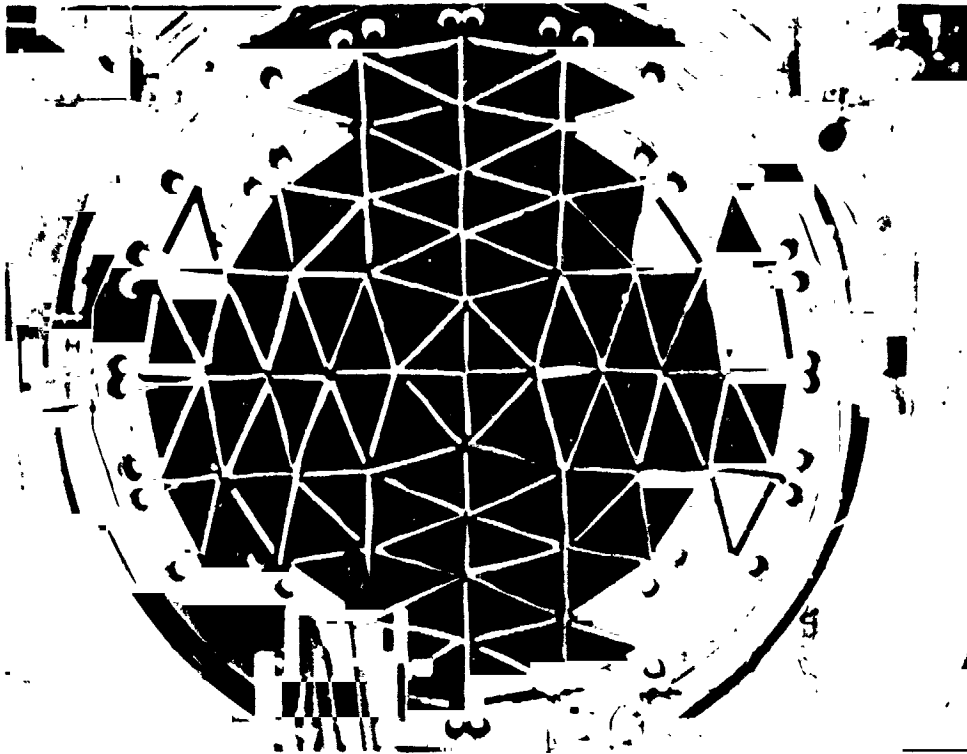
Figure 14. Nose Cap Heater
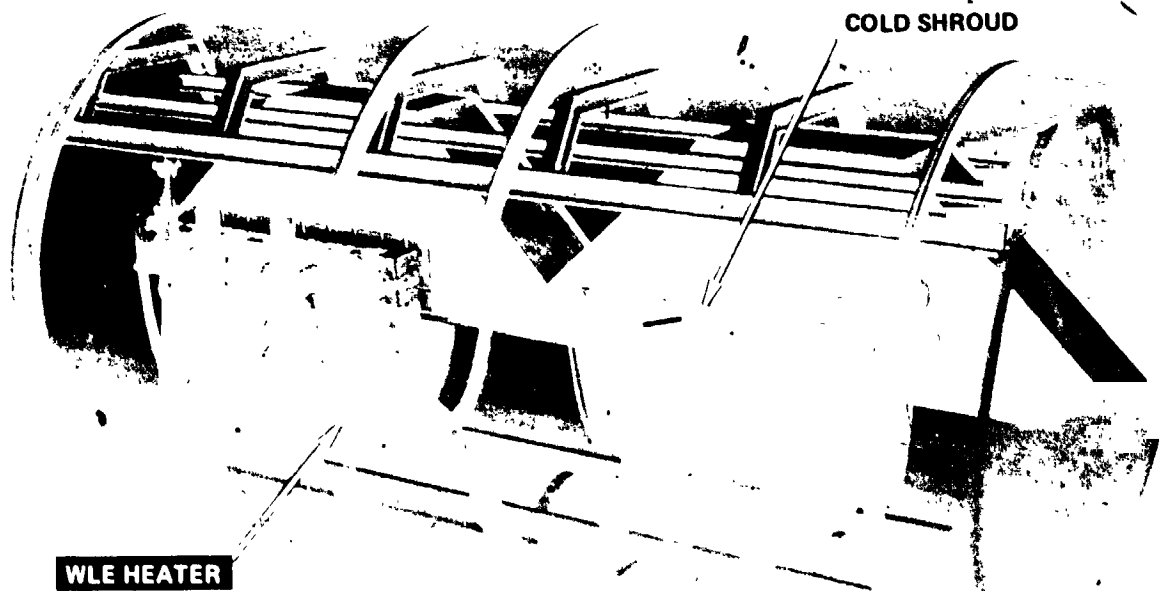
Figure 15. Artist's Concept of Wing Leading Edge Test System (Test Article Shown in Both the High- and Low-Temperature Positions)

Figure 16. Wing Leading Edge Test Setup

HEATSHIELD MATERIAL SELECTION FOR ADVANCED BALLISTIC REENTRY VEHICLES

P. J. Legendre,[*] T. Holtz[*] and J. C. Sikra[**]

ABSTRACT

This paper presents a review of the available ground test data obtained in support of the Air Force Systems Command Space and Missile Systems Organization (presently Ballistic Missile Office) efforts to evaluate the roll torque and thermodynamic performance of recently flown, tape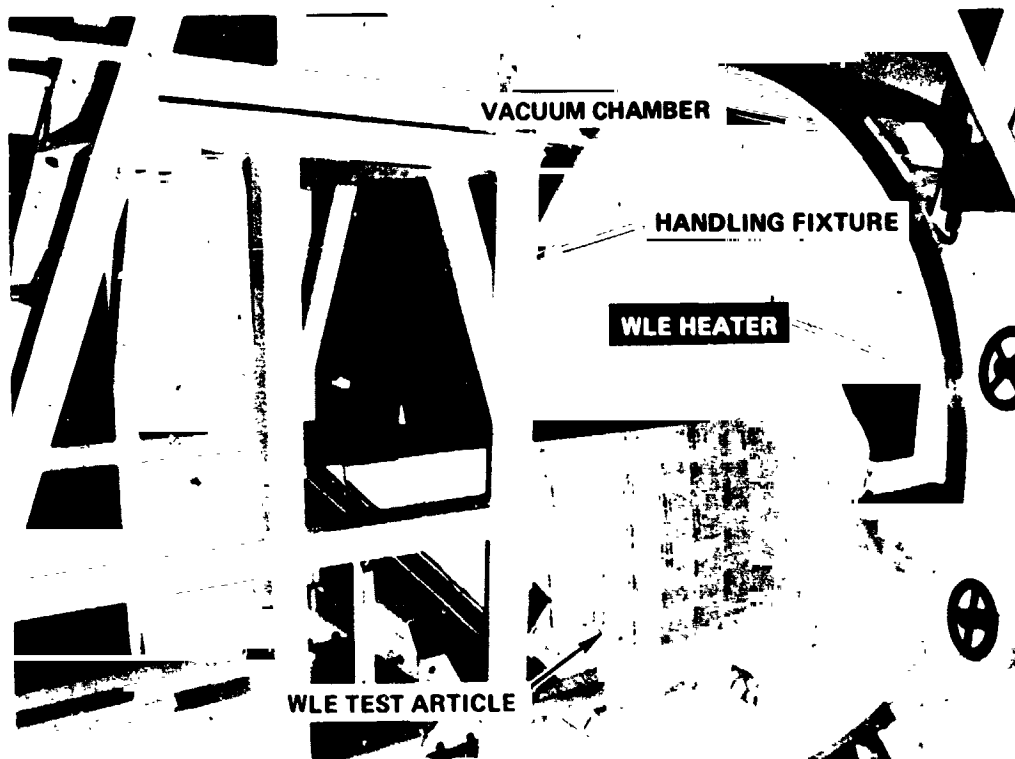-wrapped carbon phenolic heatshield materials in order to select a material for future flight tests. These efforts evaluated the performance of staple rayon fiber and AVTEX continuous rayon fiber as precursor materials for heatshields. The materials studied were referenced to the IRC FM5055A heatshield materials flown during the past decade. Three different arc jet facilities were used to simulate portions of the reentry environment in this study.

The paper specifically addresses the comparison of the IRC FM5055A and the AVTEX FM5055G, both continuous rayon fiber woven materials having the phenolic impregnant filled with carbon particles. The AVTEX continuous fiber, unfilled material FM5822A was also examined to a limited extent. Test results showed that the AVTEX FM5055G material provided a close substitute for the IRC FM5055A material both in terms of thermal protection and roll torque performance.

INTRODUCTION

During the past few years, a number of heatshield materials were developed to replace the International Rayon Corporation (IRC) rayon-based FM5055A carbon phenolic heatshield material for reentry vehicles. This replacement was necessitated when IRC stopped the production of continuous fiber rayon. The carbon phenolic heatshields based on this material have performed satisfactorily with respect to roll torque and thermal protection. Current· , the continuous fiber rayon cloth is being produced by AVTEX, Inc. For a while, however, the supply of continuous fiber rayon cloth was non-existent or in doubt, so that the Air Force Space and Missile Systems Organization (SAMSO) developed carbon phenolic heatshield materials manufactured from rayon cloth woven from staple rayon fibers.

In the discussions to follow, the flight heatshields and ground test heat-shield specimens using the continuous fiber cloth manufactured by IRC will be referred to as IRC. This cloth is impregnated with phenolic resin filled with carbon particles and is designated FM5055A. Similarly, the same items manu-factured from the AVTEX continuous rayon fiber cloth will be referred to as AVTEX. The AVTEX carbon phenolic heatshields come in two variations. In one, the phenolic with which the rayon cloth is impregnated is loaded with carbon particles. This combination is called AVTEX filled [AVTEX(F)] with the

---

designation FM5055G. The other is AVTEX rayon cloth impregnated with phenolic resin without carbon particles. This is called AVTEX unfilled [AVTEX(U)] with the designation FM5822A. Similarly, heatshields fabricated from staple rayon cloth and impregnated with resin with and without carbon particles are known as filled staple, FM5829A, and unfilled staple, FM5832A, respectively.

Finally, there are three manufacturers who are qualified to manufacture reentry heatshields to Air Force specifications: HITCO, Haveg-Reinhold, Inc., and Kaiser Industries. Table I summarizes the known differences in the manufacturing techniques of the three heatshield manufacturers. If, for example, a test specimen is referred to as an AVTEX(F)/HITCO, then the heatshield is made from continuous rayon cloth produced by AVTEX, the impregnating phenolic is loaded with carbon particles, and the heatshield was processed per the HITCO process outlined in Table I.

A number of the heatshields flown during the past two years were produced from new heatshield materials. Unfortunately, some vehicles with heatshield mid-sections fabricated from the unfilled staple rayon cloth and manufactured by the HITCO process (FM5832A, Process A) exhibited unacceptable levels of roll torque on recent flight tests. Vehicles with mid-sections fabricated from the unfilled staple rayon cloth and manufactured by the Kaiser process (FM5832A, Process B) exhibited satisfactory roll torque characteristics. Finally, a vehicle with a filled staple heatshield manufactured by the HITCO process (FM5829A, Process A) also exhibited unsatisfactory roll torque characteristics.

In a continuation of the program described here, the Air Force Systems Command Ballistic Missile Office is currently evaluating heatshield material and fabrication options to make a heatshield which will produce more desirable vehicle roll behavior. The leading candidate is a carbon phenolic made from the AVTEX continuous rayon fiber carbonized cloth and impregnated with the carbon filled resin (FM5055G). The process selection in this evaluation was open.

It was the prime objective of the study reported herein to review the available ground test data and based on these results make an interim recommendation for a candidate material and process for future heatshields. The present study thus encompasses principally the comparison of IRC FM5055A material to the AVTEX(F) FM5055G and the processes by which both have been manufactured.

NOMENCLATURE

M_e	Edge Mach Number
H_e	Edge Enthalpy, Btu/lb
P_e	Edge Pressure, atm
$\dot{q}_{cw}$	Cold Wall Heat Flux at the edge, Btu/sq ft sec
τ_w	Boundary Layer Shear at the wall, lbs/sq ft (psf)
QA	Quality Assurance

HT   Height

1 inch   =   2.54 cm

1 mil   =   0.00254 cm

1 foot   =   30.5 cm

1 pound (lb) = 0.454 kg

1 atm = 760 mm Hg

3413 Btu = 1 kw-hr

1 Btu = 1054 joules

°R = 0.555°K

DESCRIPTION OF TESTS

A general test matrix of all of the ground tests reported in this paper is presented in Table II. Note in this table that heatshield specimens were tested other than those made from FM5055A, FM5055G and FM5822A. These other specimens, from material designated FM5832A, were made from staple rayon cloth which was found to contribute to unsatisfactory heatshield roll torque performance in these and previous tests. Therefore, this study focused on (1) comparing the performance of FM5055G and FM5822A materials with the old FM5055A, and (2) investigating the reasons for the poor performance of the FM5832A materials.

As shown in Table II, three different arc jet facilities were used to obtain the ground test data: the Air Force Flight Dynamics Laboratory (AFFDL) 50-megawatt arc jet, the General Electric Company (GE) Hy-Arc facility, and the Avco Corporation 10-megawatt arc jet. Each facility accommodated a different test specimen configuration, had different instrumentation, and provided a somewhat different test environment. Thus the tests supplemented each other in the information obtained. Table III summarizes the test environments.

AFFDL 50 MW Tests

SAMSO sponsored a series of roll torque manufacturing comparison tests in the AFFDL arc jet facility. Prototype Development Associates (PDA), Inc. was the test conductor. Of a total of 25 heatshield specimens tested, five were AVTEX(F) FM5055G models, three fabricated with right-hand (RH) splices and two fabricated with left-hand (LH) splices. There were eight IRC FM5055A models, five with right-hand splices and three with left-hand splices. Haveg was the fabricator of all 25 models and simulated the constructions of the other manufacturers, as required. A detailed test matrix is presented in Table IV (Reference 1), and the test technique is described in References 2 and 3.

The results from these tests were very interesting. As own in Figure 1, all of FM5055G LH and RH spliced models rolled in the same . (negative)

direction. This indicated that the overwrap helix angle, which was left-handed for all the models, was a significant parameter in producing roll torque and, in fact, dominated here over the splice direction. The rate of change of roll rate for the RH splice model, AF-4, was greater than either (AL-1 and AL-2) LH splice models. Two of the RH splice models, AF-1 and AF-5, did not start rolling for 3 and 4 seconds, respectively.

A review of the test films showed that models AL-1 and -2 spun smoothly in the predicted direction.

When AF-4 was reviewed, it was noted that minor lands formed on the heatshield along with minor pock marks. Cross hatching was not noted until later in the test. On the other hand, AF-5 exhibited minute pits at first. No lands were observed. The surface was noted as being mottled in appearance with a uniform distribution of pocks. It is not known if the delay in the spin for AF-5 was due to a bearing problem or to the absence of lands on the model early in the test.

All three of the AVTEX(U) FM5822A RH splice models (AU-1, -3 and -4) hardly rotated. Their surfaces in the 50 MW tests tended to degrade late in the tests with some char peeling noted.

Several of the SAMSO IRC FM5055A baseline models exhibited a somewhat random roll behavior (Figure 1), with even some roll reversals experienced by the FB-3 and FB-1 models.

In conclusion, the two FM5055G LH splice models produced the most consistent roll torque performance. The FM5055G RH splice models were consistent in roll direction only, and the reasons for the delayed roll onset of AF-1 and -5 are not known. The observations from the test films indicate that development of local surface features, such as lands, during the ablation process may be related to the roll torque performance.

Prior to these roll torque manufacturing comparison tests, SAMSO sponsored a development roll torque screening test series in October 1978. Over 30 models were tested and some of the test results are applicable to this study. A summary of results is presented in Table V.

A total of 12 data points were obtained from the screening tests and the roll torque manufacturing comparison tests for the IRC FM5055A model, with a left-hand helix, left-hand splice, and externally cured. It has been designated B-, SB- and RB- in the two test series. Eleven of the 12 FM5055A models gave regular, repeatable roll performance. (The fabrication of the twelfth, Model B-2, is in question.)

In the October 1978 test series (Table V), three FM5055A models (FM-1, -2 and -3) were fabricated similarly to the RB Reference models listed in Table IV, except for the cure. These three models were cured in a female mold (internal bag). As shown in Table V, these internally bagged models (FM serial nos.) performed comparably to the externally bagged models (B serial nos.). Thus, type of cure did not appear to be a principal variable affecting performance.

413

GE HY-ARC Tests

From Table II, 35 models were tested in the GE HY-ARC facility. Of these, five were fabricated of AVTEX(F) FM5055G and six of IRC FM5055A. Many of these models were instrumented with thermocouples, and as indicated by Table II, several had other special thermal and ablation instrumentation.

Both the FM5055A and the FM5055G materials exhibited similar recession rates, 0.0085 and 0.0089 inch per second, respectively. As shown by Figure 2, their temperature histories follow the prediction identically. The thermo-couple response times for the materials are tabulated in Table VI. The fore-going data are taken from Reference 4.

The post-test examinations showed considerable differences between the char profiles for the FM5055A and FM5055G materials. A sample of FM5055A exhibited a narrow, densified region near the model surface with large interior voids. This interior structure has heretofore not been modeled in thermal analyses. The FM5055G maximum surface roughness was much smaller than the FM5055A (Table VII, Reference 4). In fact, the FM5055G material had a 0.70 mil maximum roughness height whereas the FM5055A and the FM5822A had maximum roughness heights of 1.10 and 1.30 mils, respectively. Since the mean or nominal roughness data are all comparable (Table VII), the differences in maxima indicate that FM5055G has the most uniform surface characteristics.

The problem was noted that thermal expansion of carbon phenolics is not adequately predicted. This expansion could be facility or material peculiar, or could be a real phenomenon; further study is required. In either or both cases, this expansion will have to be factored into the reentry vehicle charring ablator computer programs.

Sufficient testing was not performed in this series to differentiate between most of the process variables, e.g., bagging effects, splice effects, etc.

Avco 10 MW Tests

A series of tests was performed in the Avco 10 MW arc jet facility (Table II) to obtain a detailed evaluation of the ablative response of candidate staple-fiber materials. Twenty-nine models were tested in this series, including three AVTEX(F) FM5055G specimens.

The ablative performance of the heatshield materials is summarized in Table VIII, taken from Reference 5. The recession rates for the three FM5055G models varied from 0.00209 to 0.00252 inch per second, whereas the FM5055A recession rates varied from 0.00211 to 0.00624 inch per second. The thermo-dynamic test conditions were within 2.5% for all parameters for the five valid FM5055G and FM5055A test runs.

The 10 MW arc jet test conductor, Avco, presented a very detailed post-test description of the models. Two of the FM5055A models exhibited hard black charred surfaces, with stepped regions of material removal and interlaminar separation. Surface char appeared to be susceptible to fabric layer separation. From the movies, it was noted that a small surface anomaly was present at the beginning of the high heat pulse with little effect on

414

total ablation. Erosion patterns started near the leading edge. Interlaminar separations began about 11.1 sec into the test. Material progressive delamination was evident. One FM5055A test was compromised due to overexposure of the film. However, surface expansion of 0.029 inch was noted in one area of the test sample.

The three FM5055G models exhibited a hard black charred surface with a stepped transition region 0.8 inch from the leading edge. The film review showed some small surface "spots" at the start of the high heat flux cycle, and the surface had some brightness variations over its entirety. An ablation/erosion pattern developed near the leading edge and progressed slowly downstream. Limited ply delamination occurred. The FM5055G material had a lesser tendency to delaminate than FM5055A.

The FM5055A and FM5055G centerline surface recession profiles are presented in Figures 3 and 4, respectively (Reference 5). As these figures show, the profiles for both materials are fairly consistent.

The 10 MW temperature history data for FM5055A, FM5055G, FM5832A and FM5822A were approximately equivalent. This means that all of the candidate heatshield materials may give equal thermal protection, including the staple fiber materials.

Some overall general observations noted in Reference 5 follow:

1. All models except the FM5832A material manufactured by Kaiser exhibited poor interlaminar integrity, resulting in ply lifting and loss of material en masse when exposed to a high heating environment. The FM5055G rated the best of the materials with respect to interlaminar integrity except, of course, the FM5832A Kaiser staple fiber. This material exhibited relatively smooth ablation for all three test models.

2. The FM5832A Kaiser staple material temperature gradient was different from the other materials tested, but the reason is not known at this time. This material exhibited a pure linear temperature distribution through the test sample.

3. Reversal of the cloth lay-up angle to the flow had no obvious effect in suppressing the ply separation.

4. Again, as in the 50 MW tests, no clear correlation with bagging effects was noted. An additional data point relative to bagging effects on FM5055A was obtained from detailed photographic time histories of two specimens cut from heatshields made by the standard HITCO process. However, one was internally bagged and the other externally bagged. No clear performance difference were observed here.

Results

The results of this study show:

1. The FM5055A and the AVTEX FM5055G materials have comparable thermodynamic performance in the three facilities utilized by SAMSO for testing. Mass loss and recession rates are virtually the same. In-depth density and temperature profiles exhibit some minor differences, believed to be of little operational significance. The FM5822A unfilled material shows greater mass loss and recession than either the FM5055A or the FM5055G filled materials.

2. The FM5055G material generally exhibits a smoother, more regular appearance with less evidence of local delamination after ablation tests than does the FM5055A material. Consistent with this, the maximum measured surface micro-roughness of FM5055G is less than that of the FM5055A, although the nominal roughness heights are the same. The FM5822A material has a more irregular gross appearance, more evidence of delamination, and both a larger maximum and larger nominal surface micro-roughness than either of the filled materials.

3. The roll performance of the 50 MW test specimens from the 1978-79 tests can be summarized as follows:

   a. Eleven out of 12 IRC FM5055A models with left-hand splices and left-hand helices, externally bagged, gave regular, repeatable roll performance. (The construction of the remaining model is in question.)

   b. Two out of three IRC FM5055A models with left-hand splices, internally bagged, performed comparably to the externally bagged models. The third model has a smooth roll history but about one-half the torque of the others.

   c. Two out of two AVTEX FM5055G models with left-hand splices and left-hand helices, internally bagged, exhibited smooth torque production at the lower level of the singular model described in b. above.

   d. Out of five IRC FM5055A models with right-hand splices and left-hand helices, internally bagged, two showed smooth torque comparable to the higher level of previously described models, one had smooth torque comparable to the lower level of previous models, but in the opposite direction, and two showed somewhat irregular torque production.

   e. Out of three AVTEX FM5055G models with right-hand splices, internally bagged, one exhibited smooth torque of high magnitude, and the remaining two showed apparently smooth torque but of uncertain magnitude because of delayed roll initiation.

   f. Three AVTEX FM5822A models with right-hand splices and internally bagged exhibited very low, almost neutral, torques.

416

4. The only data available at the time of this study for comparison of bagging effects is on FM5055A. In general, the 50 MW arc jet in-situ ablation movies show that the externally bagged specimens have a slightly more regular surface with fewer local spots of delamination than the internally bagged specimens. These differences are subtly qualitative and hence subjective. As enumerated in 3. above there are no clear differences in 50 MW roll performance due to bagging. In-situ closeup still pictures of one pair of 10 MW runs giving a bagging comparison show no surface feature differences.

CONCLUSIONS

The AVTEX filled FM5055G material provides a close substitute for the IRC filled FM5055A in terms of both thermal protection and roll torque performance.

Pure bagging effects, isolated from tapelap and tapewrap differences, are difficult to discern from the ground tests, where bagging appears to be a secondary parameter at most. If uniformity in surface appearance during ablation is indicative of predictable roll performance, as was indicated by the ground test experience with staple rayon, then external bagging may be preferable to internal bagging.

In all 50 MW arc jet tests and in some staple rayon flight tests, the tapewrap helix angle appears to dominate roll torque behavior. Although other mechanisms may dominate on continuous fiber heatshields in most flight regimes, the wrap helix mechanism is still present. It was recommended that a right-hand wrap helix be selected for future flight test vehicles to preclude the possibility of helix-induced negative (left-hand) torque in any flight interval.

REFERENCES

1. L. Groener, Final Data Report for Roll Torque Manufacturing Comparison Tests -- AFFDL 50 MW Arc Jet Facility, PDA TR 1353-39-29, 12 February 1979.

2. J. Stetson, et al., "Technique for In-Situ Roll Torque Measurements," Paper presented at the 26th ISA Int. Inst. Sym., 5-8 May 1980, Seattle, WA.

3. L. S. Groener, et al., "Ground and Flight Test Investigations of Reentry Vehicle Heatshield Roll Torque," AIAA Paper 80-0447, March 1980.

4. J. W. Metzger, "Thermal Shield Study--HY-ARC Channel Flow Tests," GE-AEDM-79-001, 13 March 1979.

5. H. E. Hoercher, et al., Avco Ten Megawatt Arc Facility Staple Fiber Material Test Results, Avco Report AVSD-0005-79-CR, 9 February 1979.

TABLE I. ALTERNATE FABRICATION PROCESSES

Supplier	Process A HITCO	Process B Kaiser	Process C HAVEG
Tape orientation	Fill side in	Fill side in	Fill side in
Bias cut	Parallel to warp	Parallel to w.	Parallel to warp
Direction of winding[a]	LH Helix	RH Helix	LH Helix
Tape splice orientation	RH	RH	RH
Splice facing direction	FWD facing	AFT facing	FWD facing
Cure	Internal bag	External bag	External bag
Finish machine	Grind	Grind	Single - point
Debulk cycles[b]	Two max.	None	None
Cure cycle	Per GE spec.	Per GE spec.	Per GE spec.

[a]A left-hand (LH) wrap is def{· , by feeding the tape onto the mandrel from the right side (looking forward). A right-hand (RH) wrap is defined by feeding the tape from the left side (looking forward).
[b]Staple rayon only

TABLE II. ARC JET TEST MATRIX

AFFDL 50 MW	GE HY-ARC	AVCO 10 MW
FM 5055A (5)	FM 5055A (4)	FM 5055A Calibration (1)
FM 5055A LH Splice (ext) (3)	FM 5055A Special instrum. (2)	FM 5055A (HITCO) (3)
FM 5832A Lot 00186 (3)	FM 5832A Lot 00186 (6)	FM 5832A Lot 00166 (3)
FM 5832A (HITCO) Lot 00422 (3)	FM 5832A Lot 00422 (6)	FM 5832A Lot 00186 (3) (No pre-heat)
FM 5832A (Kaiser) Lot 00422 (3)	FM 5832A Lot 00079 (3)	FM 5832A (HITCO) Lot 00422 (3)
FM 5822A (3)	FM 5832A Special config. (3)	FM 5832A (HITCO) Lot 00422 (3) (No pre-heat)
FM 5055G (3)	FM 5832A Special instrum. (3)	FM 5832A (Kaiser) Lot 00422 (3)
FM 5055G LH Splice (2)	FM 5822A (3)	FM 5832A Lot 00079 (3)
	FM 5055G (4)	FM 5829A Calibration (1)
	FM 5055G Special instrum. (1)	FM 5822A (3)
		FM 5055G (3)
25 models	35 models	29 models

TABLE III. COMPARISON OF GROUND AND FLIGHT TEST ENVIRONMENTS

		M_e	H_e	P_e	q_{cw}	τ_w
Flight	Alt. (ft)	--	1000 BTU/lb	ATM	1000 BTU/ ft^2-sec.	PSF
	60K	8.2	9.0	1.3	2.5	150
	30K	5.8	4.5	2.9	2.1	170
Ground Facilities						
AFFDL 50MW		2.2	2.4	4.5	2.4	120
AVCO 10MW		1.5	7.0	1 5	1.1	47
GE-HYARC		0.8	9.7	6.0	1.1	17

TABLE IV. 50 MW ·OLL TORQUE MANUFACTURING COMPARISON TEST MATRIX

50 MW Run No.	Strut	Model S/N (Exp. Ref.)	Heatshield Variation	Part No. SK43173-	Rationale/ Remarks
RTN 109-1	1	RB-1	FM5055A(IRC) LH splices	-29	Reference Baseline
	2	FB-1	FM5055A(IRC) RH splices	-35	Female Baseline
	3	S16-1	FM5832A, Lot C018G	-31	STM 16 Material
	4	S17-1	FM5832A, Lot C0422	-31	STM 17 Material
	5	PV-1	FM5832A, Process B	-31	Process Variation- Alternate Fabricator
RTN 109-2	1	FB-2	FM5055A, RH splices	-35	Female Baseline
	2	PV-2	FM5832A, Process B	-31	Replicate
	3	S16-2	FM5832A, Lot C0186	-31	Replicate
	4	S17-2	FM5832A, Lot C0422	-31	Replicate
	5	RB-2	FM5055A, LH splices	-29	Reference Baseline
RTN 109-3	1	FB-3	FM5055A, RH splices	-35	Female Baseline
	2	RB-3	FM5055A, LH splices	-29	Reference Baseline
	3	S17-3	FM5832A, Lot C0422	-31	Replicate
	4	S16-3	FM5832A, Lot C0186	-31	Replicate
	5	PV-3	FM5832A, Process B	-31	Replicate
RTN 109-4	1	AF-1	FM5055G, (Avtex Filled)	-35	Alternate Material
	2	FB-5	FM5055A, RH splices	-34R	Female Baseline
	3	AU-3	FM5822A, (Avtex Unfilled)	-33	Alternate Material
	4	AL-1	FM5055G, LH splices	-34L	Splice/Wrap Effects
	5	AL-2	FM5055G, LH splices	-34L	Replicate
RTN 109-5	1	FB-6	FM5055A, RH splices	-35	Female Baseline
	2	AF-4	FM5055G, (Avtex Filled)	-34R	Replicate
	3	AU-1	FM5822A, (Avtex Unfilled)	-33	Replicate
	4	AF-5	FM5055G, (Avtex Filled)	-34R	Replicate
	5	AU-4	FM5822A, (Avtex Unfilled)	-33	Replicate

419

TABLE V. SUMMARY OF 50 MW ROLL TORQUE MEASUREMENTS, ABRES TESTS

Model S/N	SK43173 P/N	Heatshield	Lot No.	Manuf. Date	Condition	Run No.	Strut	Air Bearing S/N	Final Rpm[b]	Measured Torque In-lb	Torque Corrected For Roll Damping In-lb
B-1	-1D	Standard Baseline	CO295	3/23/78		103-8	1	5	-6000	-.35	-.475
B-2	-1D	(LH splices male	CO295	4/07/78		7	3	4	+1600[a]	+.13	+.13
B-3	-1D	cure)	CO295	3/23/78		6	1	2	Jammed --		--
B-4	-1E		CO295	6/15/78		8	3	3	-10,000	-.65	-.85
B-5	-1E		CO295	6/15/78		9	1	5	-11,500	-.55	-.75
B-6	-1G		CO295	8/25/78	HI Residual Volatiles	12	5	5	-3200	-.24	-.34
B-7	-1G		CO295	8/25/78	Moderate bunching	13	5	5	-2900	-.29	-.38
B-8	-1G		CO295	8/25/78	Some bunching	14	1	1	-7500	-.58	-.72
R-1	-2D	RH splices, male	CO295	3/23/78	Heavy bunching	6	3	4	Jammed --		--
R-2	-2D	cure	CO295	3/23/78	Heavy bunching	8	4	4	-600	~ 0	-.06
R-3	-2E		CO295	6/15/78	Heavy bunching	9	3	3	-4500	-.425	-.5
D-1	-3D	Isotropic Dixiecup	CO295	3/23/78		8	2	1	0	0	--
D-2	-3D		CO295	3/23/78		7	4	F	Non rotating		--
D-3	-3D		CO295	3/23/78		6	2	3	Jammed		--
D-4	-3D		CO295	3/23/78		6	4	F	Non rotating		--
D-5	-3E	0-180 Dixiecup	CO325	6 16/78		9	2	1	+2800	+.2	+.18
D-6	-3E		CO325	6/15/78		9	4	4	+200	~ 0	--
D-7	-3G	Isotropic Dixiecup	CO424	9/15/78		13	2	2	0	0	--
D-8	-3G		CO424	9/15/78		14	3	3	+1400	+.12	+.10
AFJ-1	-19G	LH splices, Aft	CO295	8/25/78		103-10	3	5	-6000	-.375	-.52
AFJ-2	-19G	Facing Joints	CO295	8/25/78		10	4	4	-6800	-.48	-.63
AFJ-3	-19G		CO295	8/25/78		12	4	4	-1500	-.12	-.14
SB-1	-29G	Short configura-	CO295	8/25/78		11	3	5	-5900	-.32	-.41
SB-2	-29G	tion Baseline	CO295	8/25/78		12	1	1	-7500	-.75	-.90
FM-1	-7G	LH splices,	CO295	8/25/78	As molded	11	4	4	-4500	-.28	-.39
FM-2	-7G	Female mold,	CO295	8/25/78	As molded	12	2	2	-1100	-.18	-.26
FM-3	-7G	Short Configura- tion	CO295	8/25/78	As molded	12	3	3	-4200	-.28	-.36
LRS-1	-28G	Unfilled Staple,	CO422	9/15/78	Mod bunching	13	4	4	<20	0	-.05
LRS-2	-28G	FM 5832A, LH	CO422	9/15/78	Mod bunching	14	2	2	<20	0	-.05
LRS-3	-28G		CO422	9/29/78	Little bunching	14	4	4	<20	0	-.05
LHF-1	-30G	Fill direction	CO407	9/15/78		13	1	1	-30,000	-1.7	-2.1
LHF-2	-30G	splices, LH	CO407	9/15/78		13	3	3	-30,000	-1.9	-2.4

[a]All heatshields IRC FM5055A, External bag cured, with LH forward facing splice joints except where noted.
[b]At end of nominal 5 second exposure (except as noted).
[c]4 second exposure.

420

TABLE VI.   THERMOCOUPLE RESPONSE TIMES, HY-ARC TESTS

T = 2000°F

Run No.	Material	Time to 2000°F, sec	Depth, in.
40	FM5055A	14.7	0.113
41		15.3	0.105
42	↓	12.6	0.093
43	FM5832A, Lot C0186	(19.8)P	0.250
44		17.0	0.141
45		-	-
46	↓	-	-
71	FM5055G	(14.6)P	0.045
72	↓	(15.8)P	0.093
84	FM5832A, Lot C0422	(17.0)P	0.139
85		15.0	0.134
86	↓	15.1	0.138
87	FM5832A-QA	12.1	0.108
88	FM5055A	15.0	0.098
89	FM5832A-QA	15.1	0.106
90	↓	(14.0)P	0.118
96	FM5832A, Lot C0186	13.4	0.120
97	↓	14.4	0.131
98	FM5822A	13.9	0.110
99		12.7	0.110
100		13.7	0.125
101	FM5055A	14.2	0.103
102	FM5055G	13.2	0.105
103		13.3	0.106
105	↓	13.5	0.112

P = Projected intercept value

TABLE VII.   COMPARISON OF SURFACE ROUGHNESS, HY-ARC CHANNEL FLOW

Material	Max HT, mils	Frequency, Fraction of Sample Length	Nominal HT, mils
IRC FM5055A			
HITCO	1.10	0.09	0.35
HAVEG	1.10	0.07	0.30
FM5832A			
Lot C0186	0.85	0.03	0.25
Lot C0422	0.90	0.05	0.35
QA SHIELD	0.95	0.13	0.25
AVTEX			
FM5055G	0.70	0.06	0.30
FM5822A	1.30	0.02	0.40

421

TABLE VIII.   SUMMARY OF ABLATIVE PERFORMANCE OF HEATSHIELD MATERIALS,
10 MW ARC JET TESTS

Run. No.	Sample Description*	Weight[a] Grams			Thickness[b] Inches			Peak Surface Brightness[c] Temperature, °R	Recession Rate[d] $\dot{S}$, in/sec
		Pre	Post	Loss	Pre	Post	Loss	T_b	
11,848	FM5055A	35.2	29.2	6.0	0.600	0.574	0.026	2710-6120	f
11,849	FM5829A	24.4	17.3	7.1	0.420	0.398	0.022	3040-6210	0.00330
11,850	FM5832A Lot C0186 (No pre-heat)	29.9	22.8	7.1	0.500	0.410	0.090	6340	f
11,851	FM5832A Lot C0186 (No pre-heat)	29.7	22.6	7.1	0.500	0.407	0.093	6270	f
11,852	FM5832A Lot C0186 (No pre-heat)	29.8	22.8	7.0	0.499	0.408	0.091	6382	0.00160[g]
11,855	FM5832A Lot C0186	29.3	21.3	8.0	0.500	0.417	0.083	2970-6250	0.02094[g]
11,856	FM5832A Lot C0186	29.6	22.1	7.5	0.499	0.412	0.087	3030-6060	0.00666[g]
11,857	FM5832A Lot C0186	29.7	22.5	7.2	0.500	0.422	0.078	3100-6110	0.00323
11,858	FM5832A Lot C0422 (No pre-heat)	28.5	21.8	6.7	0.500	0.468	0.032	5970	0.00252
11,859	FM5832A Lot C0422 (No pre-heat)	28.4	21.3	7.1	0.500	0.425	0.075	6370	0.00242
11,860	FM5832A Lot C0422 (No pre-heat)	28.3	21.1	7.2	0.500	0.410	0.090	6300	0.00209
11,861	FM5832A Lot C0422	28.6	21.4	7.2	0.500	0.450	0.050	~3200[e] -6070	0.00367
11,862	FM5832A Lot C0422	28.6	21.1	7.5	0.501	0.444	0.057	3180-6170	0.00360
11,863	FM5832A Lot C0422	28.4	21.1	7.3	0.500	0.441	0.059	3160-6100	0.00411
11,864	FM5055A	30.5	23.9	6.6	0.491	0.463	0.028	2890-6150	0.00264
11,865	FM5055A	31.0	24.5	6.5	0.501	0.479	0.022	2800-6190	0.00297

TABLE VIII. SUMMARY OF ABLATIVE PERFORMANCE OF HEATSHIELD MATERIALS
10 MW ARC JET TESTS (Continued)

Run. No.	Sample Description*	Weight[a] Grams			Thickness[b] Inches			Peak Surface Brightness[c] Temperature, °R T_b	Recession Rate[d] $\dot{S}$, in/sec
		Pre	Post	Loss	Pre	Post	Loss		
11,866	FM5055A	31.0	24.8	6.2	0.500	0.475	0.025	2730-6220	0.00211
11,867	FM5832A (Kaiser) Lot C0422	27.4	20.3	7.1	0.466	0.419	0.047	3020-5930	0.00306
11,868	FM5832A (Kaiser) Lot C0422	27.5	20.2	7.3	0.468	0.468	0.048	3030-5930	0.00333
11,869	FM5832A (Kaiser) Lot C0422	27.5	20.2	7.3	0.469	0.416	0.053	~3110[+e]-5930	0.00232
11,870	FM5055C	25.5	18.9	6.6	0.406	0.377	0.029	2840-6070	0.00252
11,871	FM5055C	25.5	19.0	6.5	0.406	0.379	0.027	2790-6000	0.00216
11,872	FM5055C	25.5	19.2	6.3	0.406	0.384	0.022	2770-6010	0.00209
11,873	FM5822A	24.4	17.2	7.2	0.402	0.375	0.027	32.00[+e]-6460	0.00106[g]
11,874	FM5822A	24.4	17.4	7.0	0.402	0.355	0.047	3310-6180	0.00287
11,875	FM5822A	24.4	17.4	7.0	0.402	0.367	0.035	3280-6240	0.00260
11,876	FM5832A Lot C0079	30.0	22.2	7.8	0.501	0.441	0.060	3310-6320	0.00353
11,877	FM5032A Lot C0079	30.0	22.3	7.7	0.500	0.427	0.073	3270-6420	0.00193
11,878	FM5832A Lot C0079	30.0	22.5	7.5	0.500	0.456	0.044	3260-6270	0.00228

*All specimens are HITCO process unless otherwise noted.

[a]Total weight including thermocouple wires and adhesive.

[b]Centerline location 1.125 inches from test surface leading edge.

[c]Measurement taken by a high resolution Thermodot Recording Pyrometer sensitive to radiation at 0.8 microns. This unit was focused 1.125 inches from the specimen's leading edge, along the centerline and covered a 0.176 inch spot diameter.

[d]Estimate from Nikon film profile camera.

[e]Scale change, reading did not peak.

[f]NO ESTIMATE. Considerable data scatter as a result of surface expansion.

[g]Questionable estimates.
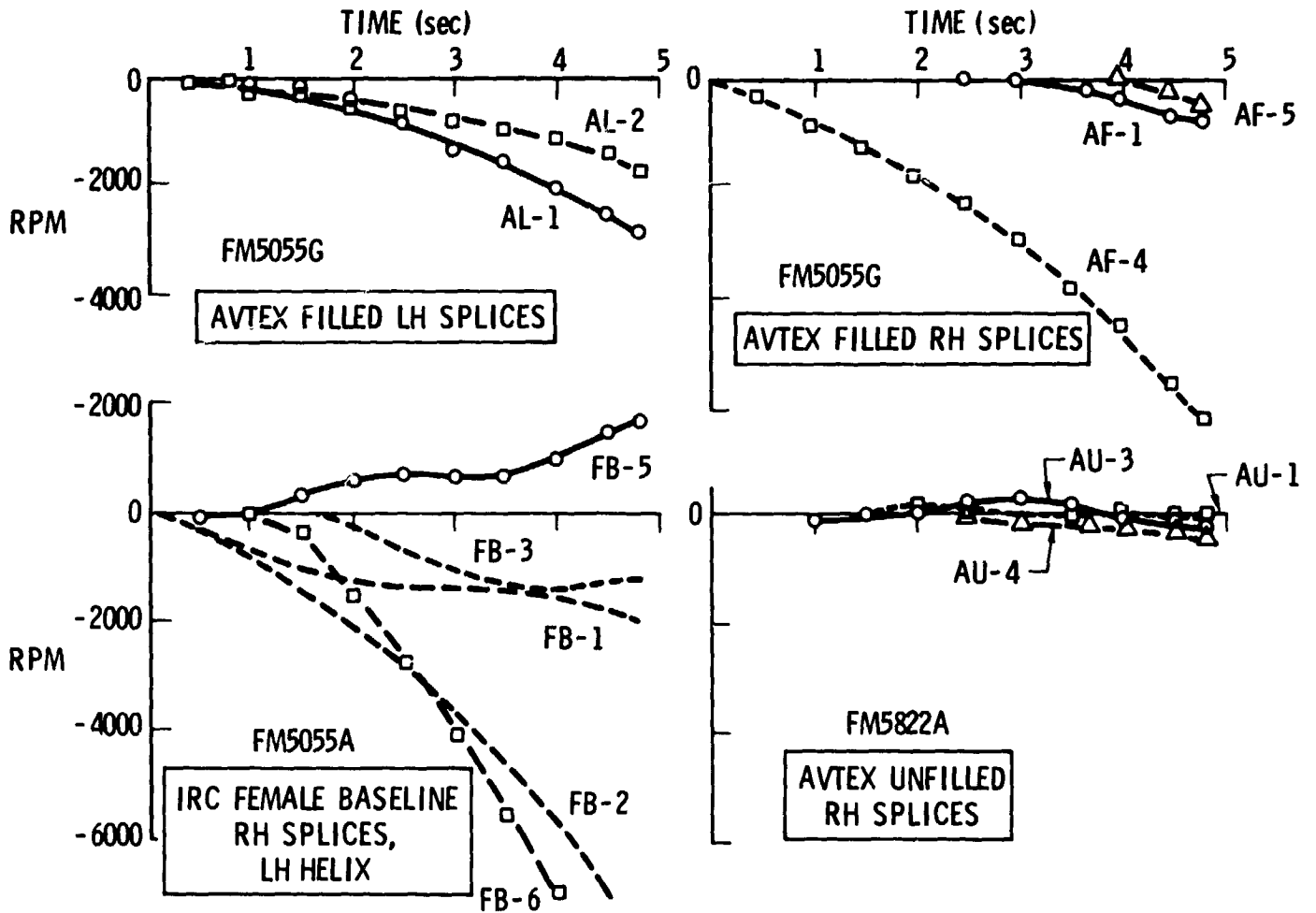
Fig. 1. Roll Rate Histories, Runs 109-4 and 109-5

Legend (on plot):
- ○ AVTEX (F) FM5055G RUN 105
- □ IRC FM5055A RUN 41

Axis labels:
- TEMPERATURE, °F x 10^{-2}
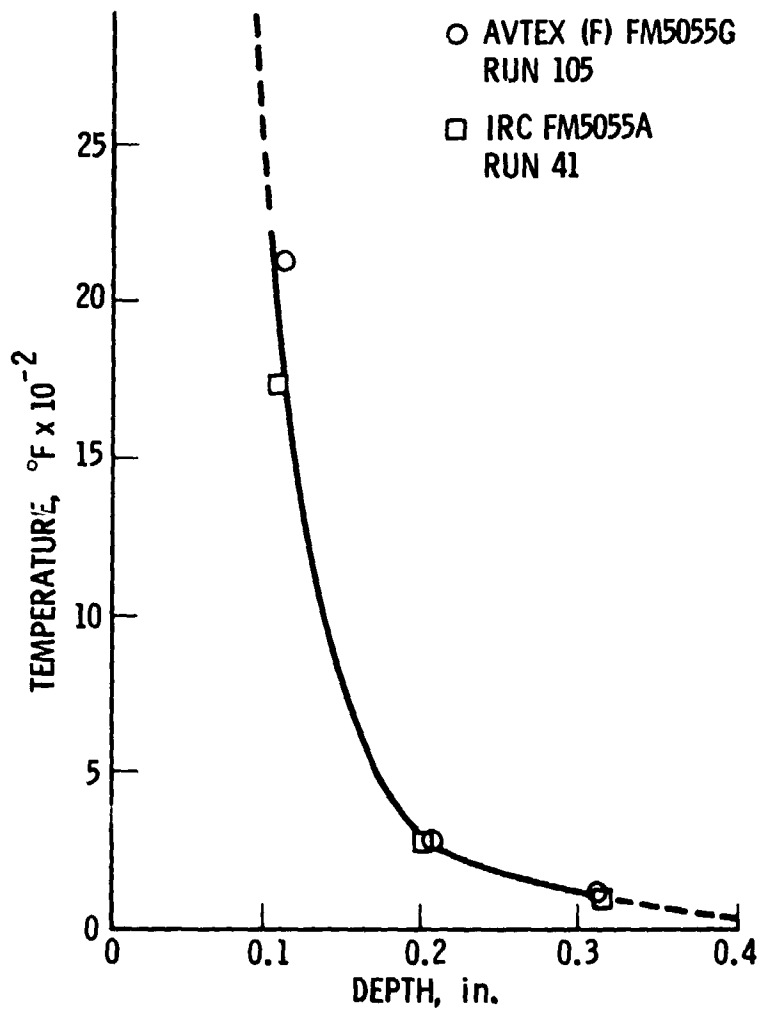- DEPTH, in.

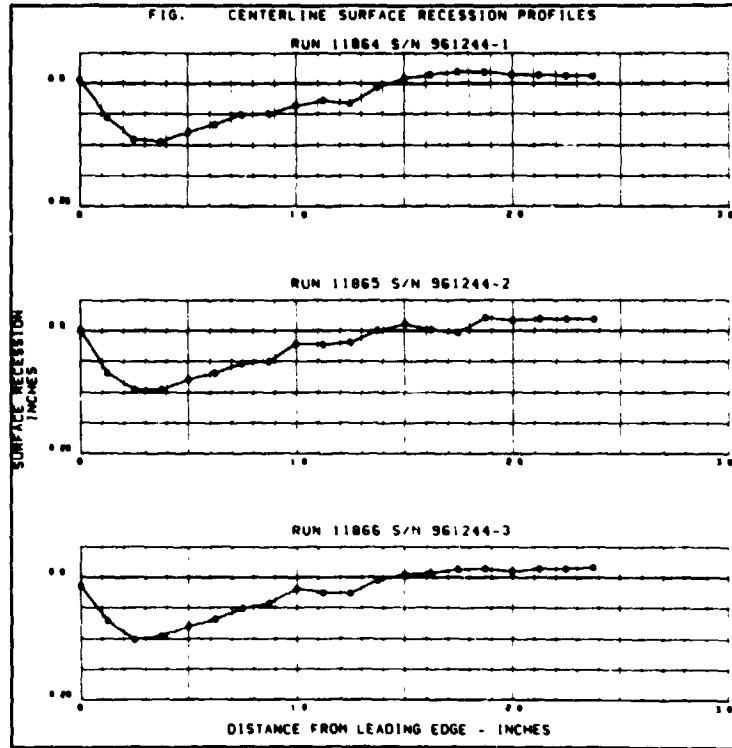Fig. 2. Temperature Distribution, 14 Seconds

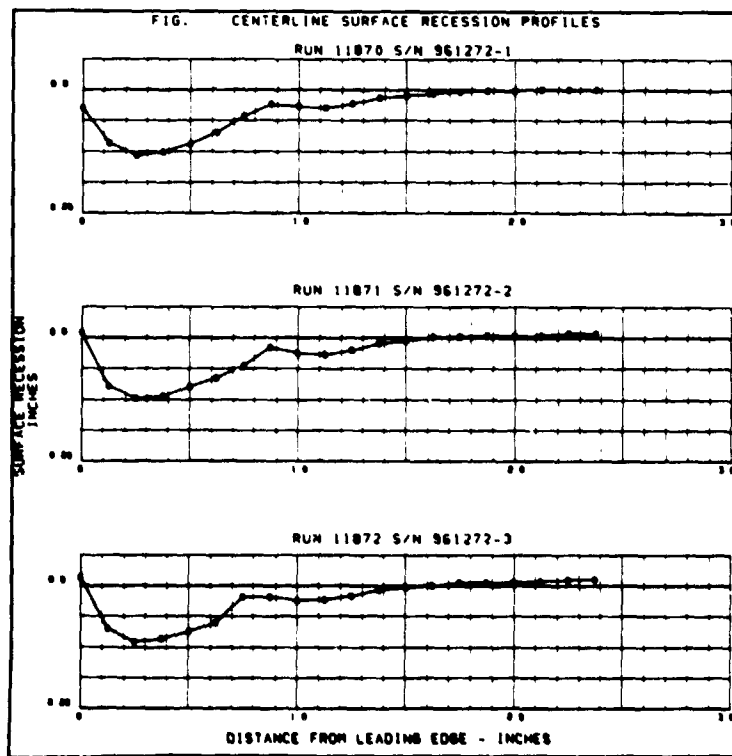Fig. 3. Centerline Surface Recession Profiles - Preheat Cycle, IRC FM5055A

Fig. 4. Centerline Surface Recession Profiles - Preheat Cycle, AVTEX (F) FM5055G